FERMILAB-Proposal-0875

NuMI-L-79

Addendum to P-875: A Long-baseline Neutrino Oscillation Experiment at Fermilab

April 21, 1995

The MINOS* Collaboration

E. Ables[10], W. W. M. Allison[13], G. J. Alner[14], D. S. Ayres[1], B. Barish[3], W. L. Barrett[19], R. H. Bernstein[5], R. Bionta[10], R. E. Blair[1], D. Bogert[5], P. M. Border[11], C. Bower[7], C. B. Brooks[13], W. L. Bryan[12], D. Burke[3], J. Byrne[16], R. Carney[10], V. A. Chechin[9], D. Ciampa[11], J. H. Cobb[13], S. Cooper[13], R. J. Cotton[14], H. Courant[11], D. A. Crane[1], P. Cushman[11], A. David[17], P. G. Dawber[16], J. W. Dawson[1], N. Diaczenko[17], T. H. Fields[1], H. Flick[6], W. S. Freeman[5], H. M. Gallagher[1,11], M. Gebhard[7], M. C. Goodman[1], K. Green[16], V. J. Guarino[1], J. Hanson[3], P. G. Harris[16], R. Hatcher[7], R. Heinz[7], K. Heller[11], N. Hill[1], Y. Ho[4], A. R. Holmes[13], G. Irwin[15], U. Jagadish[12], D. Johnson[5], T. Kafka[18], G. Koizumi[5], E. P. Kuznetsov[9], A. Lan[6], K. Lau[6], W. Lee[4], M. Libkind[10], P. J. Litchfield[14], J.Liu[6], N. P. Longley[3], W. A. Mann[18], M. L. Marshak[11], D. Maxam[11], E. N. May[1], B. Mayes[6], D. G. Michael[3], R. H. Milburn[18], L. Miller[7], W. H. Miller[11], G. Mitselmakher[5], G. Mo[6], J. Morfin[5], S. Mrenna[3], S. Mufson[7], J. Musser[7], A. Napier[18], D. Naples[5], F. Nezrick[5], S. O'Day[5], W. Oliver[18], H. Olsan[10], L. Ott[10], E. Parker[10], D. Parks[6], G. F. Pearce[14], C. W. Peck[3], D. H. Perkins[13‡], E. A. Peterson[11], D. A. Petyt[13], L. Pinsky[6], L. E. Price[1], J. Pyrlik[6], G. Rameika[5], A. L. Read[5], K. Ruddick[11], R. Rusack[11], J. Schneps[18], P. V. Schoessow[1], M. H. Schub[11], R. V. Seidlein[1], P. D. Shield[13], V. Singh[11], V. Smotriaev[8], J. Swan[10], J. Thomas[13], J. L. Thron[1], T. Toohig[2], H. J. Trost[17], I. Trostin[8], V. Tsarev[9], L. R. Turner[1], R. L. Wastie[13], R. C. Webb[17], R. Weinstein[6], S. J. Werkema[5], N. West[13], R. F. White[16], S. G. Wojcicki[15†], D. Wright[10], C. Wuest[10], and T. Yokota[10].

† Spokesman ‡ Retired

Argonne[1] - Boston College[2] - Caltech[3] - Columbia[4] - Fermilab[5] - Houston[6] - Indiana[7] - ITEP[8] - Lebedev[9] - Livermore[10] - Minnesota[11] Oak Ridge[12] - Oxford[13] - Rutherford[14] - Stanford[15] - Sussex[16] - Texas A&M[17] - Tufts[18] - Western Washington[19]

Main Injector Neutrino Oscillation Search

AA08514

Contents

1 Introduction **6**

2 Executive Summary **8**
- 2.1 Introduction 8
- 2.2 Physics motivation 8
- 2.3 Beams and experimental halls 9
- 2.4 Detectors 10
- 2.5 Physics analysis 11
- 2.6 Costs and schedules 16

3 Responses to PAC questions **17**
- 3.1 Question #1 17
- 3.2 Question #2 19
- 3.3 Question #3 20
- 3.4 Question #4 26
- 3.5 Question #5 28
  - 3.5.1 Wide-band beam 28
  - 3.5.2 Narrow-band beam 38
- 3.6 Question #6 43
- 3.7 Question #7 57
- 3.8 Question #8 61

4 Errata for the February 1995 MINOS Proposal **67**

5 References **68**

List of Tables

1 Wide-band beam results and significance for 5 scenarios described in the text. Integers represent number of events expected in two years. "TRUE" quantities indicate physics signatures. Column "0" shows expected event rates with no oscillations. Not shown are near detector event rates, which will be 60-1000 times higher than column "0", depending on the choice of radius cut. Observed quantities include all efficiencies, systematic errors and backgrounds described in the MINOS proposal. Errors quoted as σ are calculated assumed to be Gaussian. Errors quoted as σ' are calculated with Poisson statistics, and converted using a two-sided Gaussian for the same chance probability. "*" means no calculation has been done yet. "-" represents no signal. 55

2 Short description of rows and columns in Table 1. Numbers in parentheses are the page numbers of the MINOS proposal where the quantity is defined or described. 56

3 Nonaccelerator neutrino measurement capabilities for MINOS compared to other experiments in the year 2000. The first column lists those areas in which MINOS is likely to yield useful data. The next three columns show the capabilities of competing experiments. The last two columns indicate whether an active shield and/or internal timing are needed for MINOS. 64

4 Astro-particle physics measurement capabilities for MINOS compared to completed or running experiments in the year 2000. The first column lists those areas in which MINOS is likely to yield useful data. The next three columns show the capabilities of competing experiments. The last two columns indicate whether an active shield and/or internal timing are needed for MINOS. 66

List of Figures

1 Overview of the far detector for MINOS. 10

2 Upper plot: Energy spectrum of CC events in the wide-band beam *without* oscillations. Lower plot: Energy spectrum of CC events in the wide-band beam *with* oscillations for $\Delta m^2 = 0.1$ eV^2 and $\sin^2(2\theta) = 1$. The resolution of the detector has been included in both graphs. 12

3 MINOS two year 90% CL limit curves for $\nu_\mu \rightarrow \nu_\tau$ oscillations. Curve "A" is for the $\frac{cc}{total}$ test. Curve "B" is for the near/far rate comparison and is dominated by 4% systematic error. Curve "C" comes from the total energy measurement. The dashed curve shows measured limits from the CDHS experiment, and the dot-dashed curve shows FNAL E-531 limits. The diamond is the Kamiokande best-fit point. 14

4 MINOS two year 90% CL limit curves for $\nu_\mu \rightarrow \nu_e$ oscillations. Curve "A" uses longitudinal cuts. Curve "B" is for the $\frac{cc}{total}$ test. Curve "C" comes from the total energy measurement test. Curve "D" is for the near/far rate comparison and is dominated by 4% systematic error. Curve "A" is the statistical limit, and the other three curves combine statistics and estimated systematic error. The dashed curve shows measured limits from BNL E-776, and the dot-dashed curve shows the Bugey 4 reactor experiment limits. The diamond is the Kamiokande best-fit point. 15

5 Energy spectra for NC- and CC-like events for $\nu_\mu \rightarrow \nu_\tau$ oscillations at the Kamiokande point, for the NBB with a 45 GeV meson beam. The top two plots show the far (circles) and near (crosses) spectra separately, and the lower plots show the far - near difference spectra. 23

6 Energy spectra for NC- and CC-like events for $\nu_\mu \rightarrow \nu_e$ oscillations at the Kamiokande point, for the NBB with a 45 GeV meson beam. The top two plots show the far (circles) and near (crosses) spectra separately, and the lower plots show the far - near difference spectra. 24

7 Contour plot for χ^2, corresponding to an $\nu_\mu \rightarrow \nu_\tau$ oscillation signal with 1σ significance at the Kamiokande point, showing the correlation between errors in Δm^2 and $\sin^2(2\theta)$. 25

8 Schematic diagram of the angles associated with near and far neutrino energy spectra. 29

9 The neutrino decay angle with respect to the parent hadron for the central near detector and the far detector. 30

10 a) The distribution of ν_μ CC events (N_ν^{CC}) at the near and far detectors for the horn beam normalized to unit area. b) The difference $N_{Near}^{CC} - N_{Far}^{CC}$ for the horn beam. 32

11 a) The distribution of ν_μ CC events (N_ν^{CC}) at the near and far detectors for perfect focus normalized to unit area. b) The difference $N_{Near}^{CC} - N_{Far}^{CC}$ for perfect focus. 33

12 The distribution of the flux of neutrinos at the near and far detectors normalized to unit area a) for perfect focus and b) for the two horn beam. The difference $\phi^{Near} - \phi^{Far}$ c) for perfect focus and d) for the horn beam. 34

13 Radial dependence of the nu_μ CC-event energy distribution in the near detector. The spectrum for the far detector is on an arbitrary scale for presentation. 36
14 Change in the average ν_μ CC event energies $< E^{Near} >$ and $< E^{Far} >$ at the near and far detectors as a function of radius. 37
15 Neutrino energy distributions at the near and far detectors. The solid line is near detector and the dashed line is for the far detector, for the cases (a) and (b) described in the text. 40
16 The far/near neutrino flux ratios as functions of neutrino energy for the case (a) and (b) described in the text. 41
17 Secondary particle momentum spectra for π^+ (solid), K^+ (dashed), and protons (dotted) for 120 GeV incident protons. 42
18 90% CL curves for $\nu_\mu \rightarrow \nu_\tau$ hypothesis. Curve "A" is for the CC/total test. Curve "B" is for the near/far rate comparison and is dominated by the estimated 2% systematic error. Curve "C" comes from the total energy measurement test. The dashed (dash-dot) curve is the present accelerator limit from CDHS (FNAL E-531). The diamond point shows the Kamiokande best fit parameters. 45
19 90% CL curves for $\nu_\mu \rightarrow \nu_e$ hypothesis. Curve "A" uses longitudinal cuts to identify electron showers. Curve "B" is for the CC/total test. Curve "C" is for the near/far rate comparison and is dominated by 2% systematic error. Curve "D" comes from the total energy measurement test. The dashed (dash-dot) curve is the present limit from accelerator (reactor) data. The diamond point shows the Kamiokande best fit parameters. 46
20 90% CL curve for $\nu_\mu \rightarrow \nu_\tau$ hypothesis with a 45 GeV pion NBB, using inclusive CC and NC analysis. The mean E_ν is 19 GeV. The solid (dashed) curve is for a 2 year (1 year) run. 47
21 90% CL curve for $\nu_\mu \rightarrow \nu_\tau$ hypothesis with a 30 GeV pion NBB, using inclusive CC and NC analysis. The mean E_ν is 12 GeV. The solid (dashed) curve is for a 2 year (1 year) run. 48
22 90% CL curve for $\nu_\mu \rightarrow \nu_e$ hypothesis with a 45 GeV pion NBB, using inclusive CC and NC analysis. The mean E_ν is 19 GeV. The solid (dashed) curve is for a 2 year (1 year) run. 49
23 90% CL curve for $\nu_\mu \rightarrow \nu_e$ hypothesis with a 30 GeV pion NBB, using inclusive CC and NC analysis. The mean E_ν is 12 GeV. The solid (dashed) curve is for a 2 year (1 year) run. 50
24 Four σ plots for $\nu_\mu \rightarrow \nu_\tau$ hypothesis in the WBB. For neutrino oscillation parameter space to the right of each curve, we would get a 4σ or greater significance with a two year run in MINOS. Curve "A" is for the CC/total test. Curve "B" is for the near/far rate comparison and is dominated by 2% systematic error. Curve "C" comes from the total energy measurement test. The diamond point shows the Kamiokande best fit parameters. 51

25 Four σ plots for $\nu_\mu \rightarrow \nu_e$ hypothesis in the WBB. For neutrino oscillation parameter space to the right of each curve, we would get a 4 σ or greater significance with a two year run in MINOS. Curve "A" uses longitudinal cuts to identify electron showers. Curve "B" is for the CC/total test. Curve "C" is for the near/far rate comparison and is dominated by 2% systematic error. Curve "D" comes from the total energy measurement test. The diamond point shows the Kamiokande best fit parameters. 52

26 For $\nu_\mu \rightarrow \nu_\tau$ oscillation parameters to the right of the solid curve, MINOS can determine that oscillations are due to $\nu_\mu \rightarrow \nu_\tau$ and not $\nu_\mu \rightarrow \nu_e$ with a significance that is 3 σ or greater. Likewise, for $\nu_\mu \rightarrow \nu_e$ oscillation parameters to the right of the dashed curve, MINOS can determine that oscillations are due to $\nu_\mu \rightarrow \nu_e$ and not $\nu_\mu \rightarrow \nu_\tau$ with a significance that is 3 σ or greater. The dotdash curve shows the region of parameter space in which Δm^2 can be measured. The resolution in Δm^2 is 6 $\times 10^{-4}$ eV^2 or better. 53

27 P_τ *versus* P_e assuming measurements as expected for threefold maximal mixing. The three tests used are the T test, electrons, and NC^{far}/NC^{near}. The area between the lines indicates the combination of $\nu_\mu \rightarrow \nu_e$ oscillations (P_e on the horizontal axis) and $\nu_\mu \rightarrow \nu_\tau$ oscillations (P_τ on the vertical axis) which is consistent with the measurement made by that test. 54

28 $\nu_\mu \rightarrow \nu_e$ sensitivity plots for MINOS and COSMOS. The dash-dot curve is the 90%CL limit that MINOS can set using its far detector. The solid curve is the limit that both COSMOS and the MINOS near detector could set using all electron events and is dominated for both experiments by the systematic error in the beam. An estimate of this error is described in the text. The dashed curve is for both experiments cutting on $E_\nu < 15$ GeV. 60

1 Introduction

This Addendum to the Fermilab P-875 MINOS Proposal[1] was prepared in response to comments and questions from the Fermilab Physics Advisory Committee (PAC) following the presentation of the MINOS Proposal at the February 1995 PAC meeting. Specifically, this document addresses the eight "areas of concern," or questions, which were transmitted to the collaboration in the February 21st letter from Director John Peoples.

This Addendum is intended to be considered together with the companion report submitted to the PAC by the Fermilab NuMI Beam Design Group[2]. The latter report contains the response to the PAC's Question #2, concerning the design, cost, operation, and maintenance of the neutrino beam. In accordance with the PAC's suggestion in Question #6, Section 2 is a self-contained Executive Summary of the MINOS proposal, including a description of the subregions of $\sin^2(2\theta)$ and Δm^2 in which oscillations can be discovered and characterized by our experiment. Additional sensitivity calculations relevant to Question #6 are described in Section 3.6.

We fully concur with the PAC's summary of the salient features of our proposal:

1. The possibility of the production and identification on a statistical basis of τ's, which would provide direct evidence that an oscillation into ν_τ has occurred.

2. The possibility of performing a measurement of the parameters Δm^2 and $\sin^2(2\theta)$ once oscillations have been observed.

3. The large coverage in the plane of the mixing parameters, Δm^2 and $\sin^2(2\theta)$.

4. The possibility of performing the measurement in several different ways, which will lead to a credible exploration of the mixing plane.

We would like to reiterate the collaboration's strong opinion about the sensitivity (mass and granularity) of the MINOS experiment. Our continuing analyses of Monte Carlo simulations employing a variety of different neutrino oscillation scenarios has strengthened our belief that the 10 kT mass and 4-cm steel plate granularity of the reference detector provide the minimum acceptable sensitivity. Our conclusion is based on the following arguments:

1. If oscillations do not occur in the region suggested by the atmospheric neutrino anomaly, this experiment may be the only opportunity to extend the search in this region to smaller mixing angles. The 10 kT mass of the MINOS detector will yield statistics which are well matched to the achievable level of systematic uncertainties, which determines the practical limits to sensitivity in $\sin^2(2\theta)$.

2. Experimental sensitivity is usually presented in terms of 90% confidence-level limit curves in $\Delta m^2 - \sin^2(2\theta)$ parameter space, under the assumption that no oscillation signal is seen. However, a convincing discovery will require deviations from the no-oscillation expectations at a much higher level of significance, even if signals are seen in several different tests. Thus, the region of the mixing plane which characterizes the discovery potential of any experiment will be substantially smaller than that indicated by the no-oscillation limit curves.

3. If oscillations do occur, large numbers of neutrino events will be needed to characterize the phenomenon. For example, actual oscillations may well be more complex than the simple $\nu_\mu \rightarrow \nu_\tau$ model used to explain the atmospheric neutrino anomaly. The Harrison-Perkins-Scott scenario[3], which fits the atmospheric neutrino data with oscillations into both ν_τ and ν_e, is a case in point. If MINOS is to be capable of fully characterizing an observed signal, even at the "Kamiokande point," the high event rates and good resolution which we have proposed will be essential.

The remainder of this report is organized as follows. Section 2 consists of the Executive Summary, including the answer to PAC Question #6. Section 3 contains our responses to the other PAC questions. Finally, Section 4 is a list of errata to the February 1995 MINOS Proposal.

2 Executive Summary

Summary of the MINOS Proposal, A Long-baseline Neutrino Oscillation Experiment at Fermilab

April 1995

Argonne - Boston College - Caltech - Columbia - Fermilab - Houston - Indiana - ITEP - Lebedev - Livermore - Minnesota - Oak Ridge - Oxford - Rutherford - Stanford - Sussex - Texas A&M - Tufts - Western Washington

2.1 Introduction

The MINOS Collaboration proposes to conduct a search for $\nu_\mu \rightarrow \nu_\tau$ and $\nu_\mu \rightarrow \nu_e$ oscillations using a new ν_μ beam from the Fermilab Main Injector[1] with energies well above τ production threshold. Oscillations will be detected by the comparison of signals in a 'near' detector at Fermilab and a 'far' detector situated 730 km away in the Soudan underground laboratory. The experiment will require self-consistency among several tests for oscillations to build a compelling case for any discovery. A new 10 kton detector will be built at Soudan to allow the exploration of oscillation parameters down to $\Delta m^2 \approx 0.002\ eV^2$ and $\sin^2(2\theta) \approx 0.01$. In addition the existing, much finer grained but smaller, Soudan 2 detector will provide an independent check of any potential signal with $\sin^2(2\theta)$ larger than ≈ 0.1.

The proposal describes a baseline design (the reference detector) which we are confident can perform the experiment. We plan to continue simulations and detector R&D to further optimize the detector design for both cost and physics potential until the Technical Design Report is completed in late 1996.

2.2 Physics motivation

The MINOS experiment is designed to detect $\nu_\mu \rightarrow \nu_\tau$ oscillations if they occur with $\sin^2(2\theta) > 0.01$ and $\Delta m^2 > 0.002\ eV^2$. This includes the entire region suggested by the atmospheric neutrino anomaly (as reported by the Kamiokande experiment[4]), and also extends to much lower mixing angles. In addition, the experiment will be sensitive to $\nu_\mu \rightarrow \nu_e$ oscillations at even lower values of $\sin^2(2\theta)$ and Δm^2. MINOS will also be able to identify and characterize simultaneous $\nu_\mu \rightarrow \nu_\tau$ and $\nu_\mu \rightarrow \nu_e$ oscillations, as predicted by maximal mixing models[3].

Atmospheric neutrino data suggest that oscillations occur with $L/E_\nu \approx 100$ km/GeV. A ν_τ appearance experiment requires a neutrino beam energy well above τ production thresh-

old. The Main Injector can produce high flux neutrino beams with $E_\nu \approx 10\ GeV$, suggesting a distance similar to the 730 km between Fermilab and Soudan. Independent of the atmospheric neutrino anomaly, the neutrino energy and baseline of the MINOS experiment represent a good compromise between sensitivity to both low Δm^2 (long L) and small $\sin^2(2\theta)$ (high statistics, short L).

In addition to the accelerator neutrino oscillation search, we plan to study several particle astrophysics topics. The experiment will be sensitive to the oscillations of atmospheric neutrinos with energies of a few GeV and higher. MINOS is unique among underground detectors with its magnetic field capability, which allows us to extend the study of atmospheric ν interactions, both in the detector and in the rock surrounding the detector, from the few GeV available in current detectors up to around 100 GeV.

2.3 Beams and experimental halls

The very high intensity of the Main Injector will provide the high neutrino flux required for the detection of neutrinos in a realistic detector at a distance of 730 km. The MINOS experiment will use both a wide-band beam with a double-horn and a narrow-band beam with a lithium lens. The wide-band beam will provide a broad spectrum of neutrino energies up to about 30 GeV, peaking at 10 GeV, and giving ~2100 ν_μ charged-current events per kiloton-year at the far detector. If maximal $\nu_\mu \rightarrow \nu_\tau$ mixing is assumed, i.e. that half the beam is ν_τ and half ν_μ at Soudan, then this would give 312 charged-current ν_τ events per kton-year. The ν_τ rate is less than half of the unoscillated ν_μ rate because of the lower ν_τ charged-current cross-section in this energy range. The narrow-band beam can be tuned between 10 GeV and 30 GeV neutrino energies with an energy spread of $\pm 15\%$. Peak narrow-band beam ν_μ event rates are expected to be lower than wide-band beam rates by about a factor of 2.4 for $E_\nu > 10\ GeV$ (a factor of 4 for all E_ν). The ν_e backgrounds in both beams are calculated to be less than 1%.

Since the experiment is based on a comparison of event rates and distributions in the far detector with those expected in the absence of oscillations, a complete understanding of the beam is of crucial importance. The main systematic errors in the experiment are produced by the uncertainty in predicting the energy spectrum at the far detector from that observed at the near detector. To minimize these errors we plan an extensive beam monitoring system using a dedicated, fine-grained beam monitor calorimeter at Fermilab, in addition to conventional neutrino beam monitors. High statistics measurements of energy and angular distributions over a wide range of angle and position in the beam monitor detector will enable us to check and calibrate our beam Monte Carlo program, which will then be used to extrapolate the beam to the detectors at Soudan.

At the Soudan mine, a new hall will be excavated for the new detector, adjacent to the existing hall containing the Soudan 2 detector. It will be oriented towards Fermilab so that the beam is incident perpendicular to the face of the detector. The near detector hall at Fermilab will house the beam monitor and small versions of the MINOS and Soudan 2 detectors, and the E-803 short-baseline experiment.

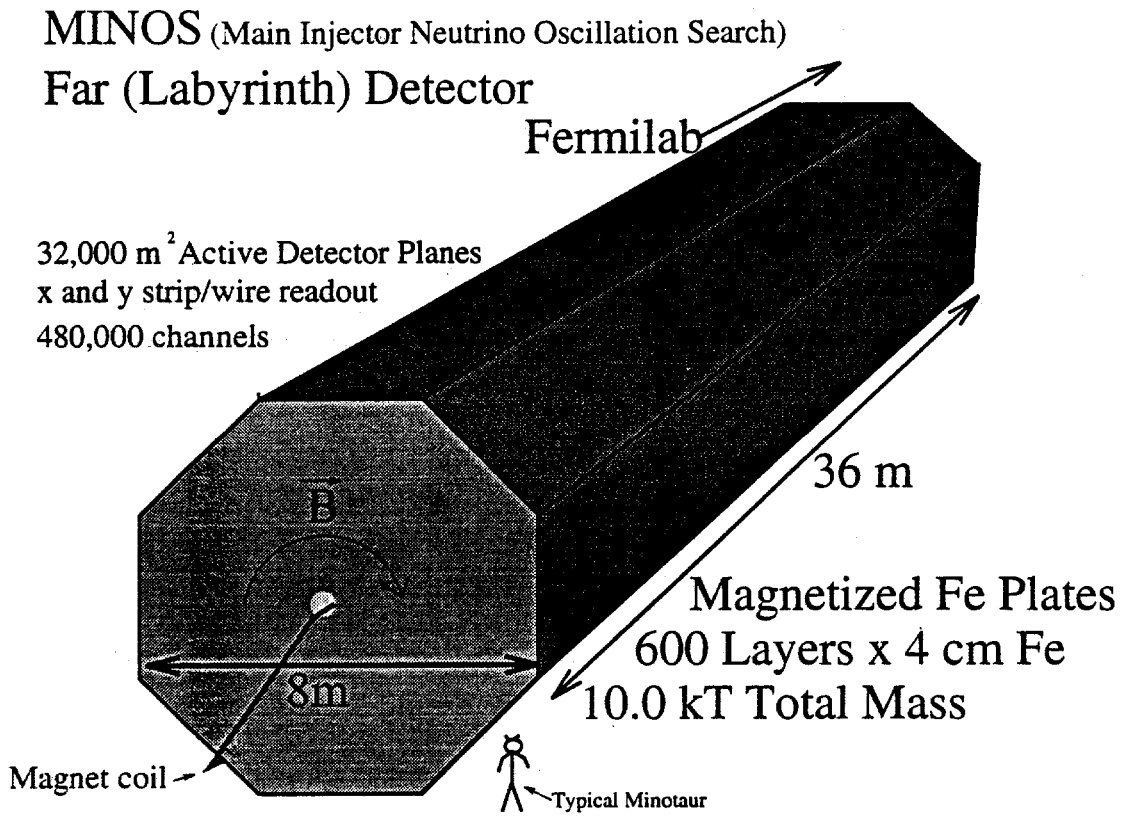

Figure 1: Overview of the far detector for MINOS.

2.4 Detectors

The MINOS proposal describes a 10 kton reference detector which can be built using well understood technology. The detector is designed to obtain measurements of muon momentum by range and/or curvature in magnetized steel, and to provide calorimetric measurements of hadronic and electromagnetic energy. Monte Carlo calculations performed to date give us confidence that this detector will reach the design goals of the experiment. We shall continue both detector R&D and simulation with the expectation of further improving the physics capabilities and reducing costs.

The reference detector is a 36-m long, 8-m diameter sandwich of 4-cm thick octagonal steel plates separated by 2-cm gaps containing the active detectors. A total of 600 such planes constitute the mass of 10 kton. A coil running through a central hole will produce a toroidal magnetic field of $\sim$ 1.5 Tesla. Figure 1 shows a schematic view of the detector.

The active detector elements will be 1-cm thick, 1-cm pitch limited streamer tubes. Both the wires and 2-cm pitch cathode strips perpendicular to the wires will be read out. The active detector area will be 32,000 m^2 with 480,000 readout channels. The electronics will utilize on-chamber chips to amplify, digitize and store information from the limited streamer

tubes, and to form triggers locally.

The near detector will be closely similar to the far detector, with the same granularity and detector technology. Unlike the far detector, which is small compared with the size of the beam ($\sim$ 1 km radius), the near detector will be comparable in size to the beam. Simulations show that the neutrino energy spectrum in the center of the beam ($\sim$ 25 cm radius) will be similar to that at the far detector.

2.5 Physics analysis

Extensive simulations of the reference detector have been made. The MINOS proposal discusses the expected angular and energy resolutions of the detector for muons, electrons and hadron showers. The explicit τ identification tests depend on cuts to isolate a τ sample from the large ν_μ interaction background and are particularly sensitive to tails of the resolution functions. We have made a careful study of these tails and are satisfied that they can be reduced to a level which is negligible for the analyses described in the proposal.

The experiment relies on multiple tests for neutrino oscillations, carried out with both wide-band and narrow-band beams. The results of these tests can be used to measure $\sin^2(2\theta)$ and Δm^2 and determine the oscillation mode ($\nu_\mu \rightarrow \nu_\tau$, $\nu_\mu \rightarrow \nu_e$ or a mixture of the two). Consistency between the results of the tests will be necessary before any discovery could be claimed. The experiment is therefore well protected against spurious effects and a positive result would be very convincing.

For a two year run in the wide-band beam we expect approximately 55,000 ν interactions in the far detector in the absence of oscillations. The MINOS proposal describes ten specific tests for oscillations; the most powerful of these are summarized here:

1. *Comparison of the fractional rate, cc/total, in the near and far detectors.* All ν_e and 82% of ν_τ charged current interactions will result in final states without muons. Such events will be classified as 'neutral current' events. Thus the measured fraction, cc/total, will decrease if oscillations have occurred. This is our most sensitive test and will reach limits of $\sin^2(2\theta)$ of ~ 0.02 for $\nu_\mu \rightarrow \nu_\tau$ and below 0.01 for $\nu_\mu \rightarrow \nu_e$.

2. *Comparison of the charged current total energy distribution in the two detectors.* The incoming ν energy is measured for charged current ν_μ interactions by summing the μ energy and the hadron shower energy. If oscillations occur, ν_μ will disappear from the beam at neutrino energies which depend on Δm^2. This creates distinctive dips in the far detector energy spectrum as shown in Figure 2. An analysis of the difference between the observed and expected energy spectra can *determine* Δm^2 and $\sin^2(2\theta)$ in a region approximately bounded by $0.005 < \Delta m^2 < 0.5$ eV^2 and $\sin^2(2\theta) > 0.05$.

3. *Observation of $\tau \rightarrow$ hadrons + ν in the neutral current energy distribution.* Most τ charged current events will be classified as neutral current events and will contain the energy of the τ decay in addition to that of the hadron vertex. Analysis of the shape of the energy distribution shows that at a Δm^2 of 0.015 eV^2 $\nu_\mu \rightarrow \nu_\tau$ oscillations can be detected if $\sin^2(2\theta) > 0.1$.

4. *Other, less sensitive, tests for τ appearance*, such as the planarity test, are described in the proposal.

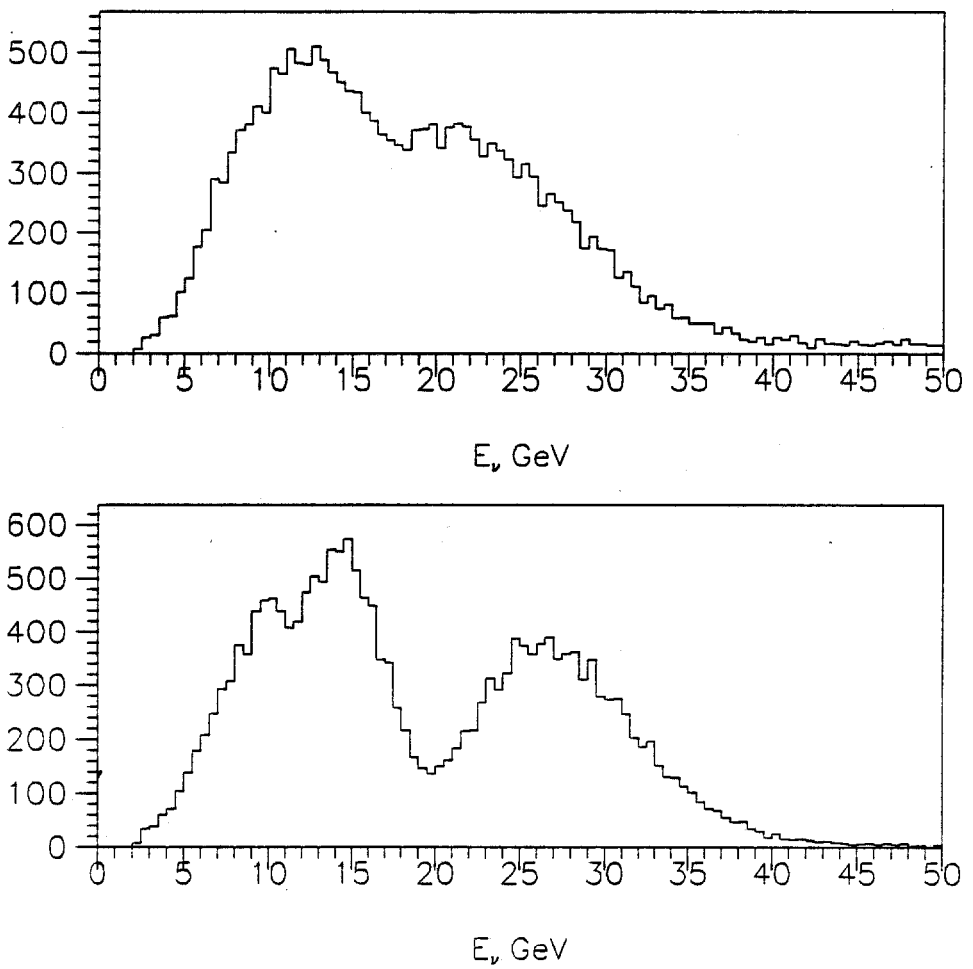

Figure 2: Upper plot: Energy spectrum of CC events in the wide-band beam *without* oscillations. Lower plot: Energy spectrum of CC events in the wide-band beam *with* oscillations for $\Delta m^2 = 0.1$ eV^2 and $\sin^2(2\theta) = 1$. The resolution of the detector has been included in both graphs.

5. *Appearance tests for $\nu_\mu \to \nu_e$.* As in the $\nu_\mu \to \nu_\tau$ case, $\nu_\mu \to \nu_e$ oscillations will reduce the cc/total fraction. Limits on $\sin^2(2\theta)$ of less than 0.01 for Δm^2 down to 0.001 eV^2 will be attainable.

Figures 3 and 4 show plots of the 90% confidence limits for the above tests for $\nu_\mu \to \nu_\tau$ and $\nu_\mu \to \nu_e$.

The narrow-band beam offers several important advantages over the wide-band beam in compensation for the lower ν intensity. First, the narrow energy distribution adds an extra kinematic constraint which significantly improves the separation of ν_μ, ν_e and ν_τ interactions. Second, the beam energy can be tuned to maximize any oscillation effect observed. Third, the narrow-band beam will allow us to minimize systematic errors arising from differences between the near and far detectors, including their absolute energy calibration. In a two year run in the narrow band beam tuned to 18.9 GeV we expect more than 10,000 ν interactions in the absence of oscillations. In addition to the wide-band beam tests listed above, the narrow-band beam provides the following new oscillation tests:

1. *Total energy measurements with final state μ events.* For ν_τ interactions followed by $\tau \to \mu\nu\nu$, the outgoing τ energy is shared among the three leptons. The signature for events with a $\tau \to \mu\nu\nu$ decay is the missing energy carried off by the neutrinos. For example, with a ν beam energy of 18.9 GeV, a cut on the measured total energy of less than 8 GeV accepts 63 ν_τ events with a background of four events for the Kamiokande oscillation parameters. The sensitivity to low-y $\tau \to \mu\nu\nu$ (quasi-elastic) events is particularly enhanced by the kinematic constraints of the narrow-band beam.

2. *Events with final state electrons.* For the Kamiokande parameters, we obtain a clear $\tau \to e\nu\nu$ signal by selecting quasi-elastic events with high (> 4 GeV) energy electrons. If $\nu_\mu \to \nu_e$, then a characteristic signal with a total energy equal to the beam energy is produced, yielding electron appearance sensitivity down to $\sin^2(2\theta) = 0.01$.

3. *Comparison of near and far energy distributions.* Because the neutrinos in the narrow-band beam are relatively monochromatic, the comparison of energy spectra for different classes of events between the near and far detectors can yield important information. For example, the ratio of neutral-current-like events observed in the two detectors plotted as a function of their measured energy can be a powerful discriminant between oscillations into ν_τ's or ν_e's.

If ν oscillations exist within our accessible parameter range we will, in general, obtain signals in many different tests simultaneously. *Consistency of all these signals would indeed present a compelling discovery.*

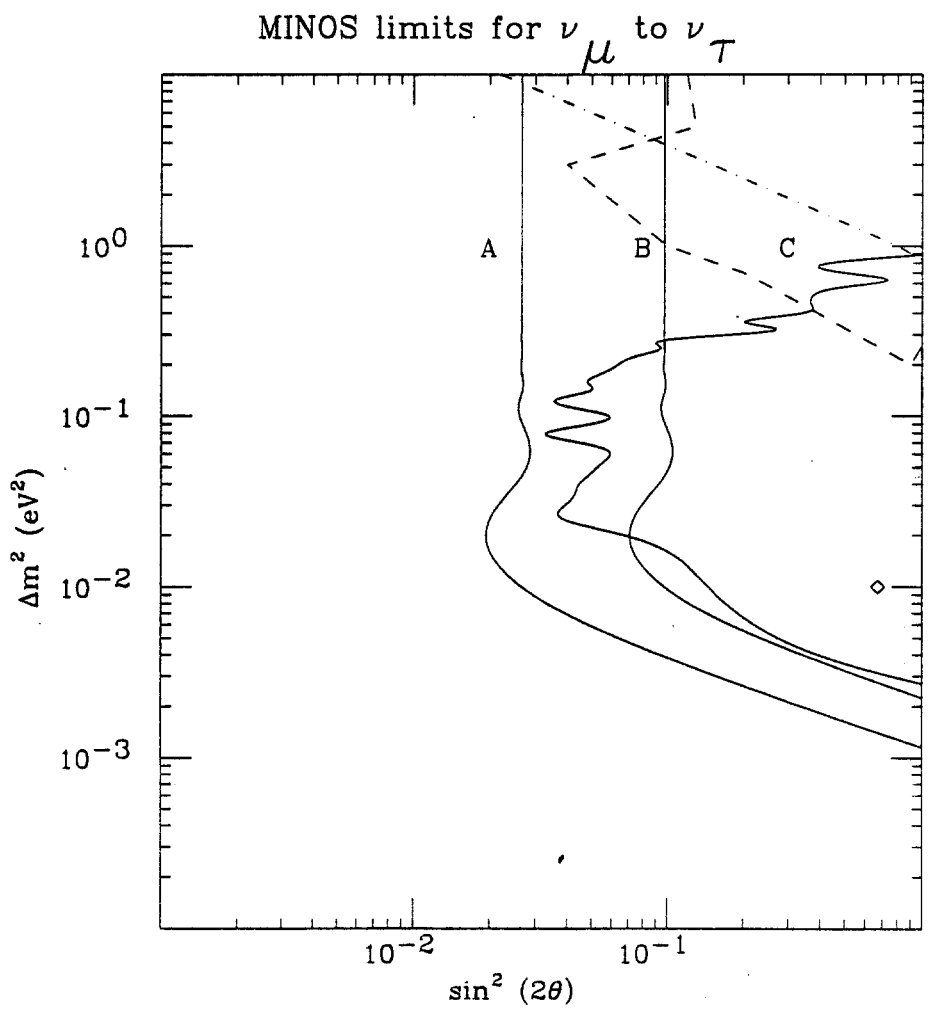

Figure 3: MINOS two year 90% CL limit curves for $\nu_\mu \rightarrow \nu_\tau$ oscillations. Curve "A" is for the $\frac{cc}{total}$ test. Curve "B" is for the near/far rate comparison and is dominated by 4% systematic error. Curve "C" comes from the total energy measurement. The dashed curve shows measured limits from the CDHS experiment, and the dot-dashed curve shows FNAL E-531 limits. The diamond is the Kamiokande best-fit point.

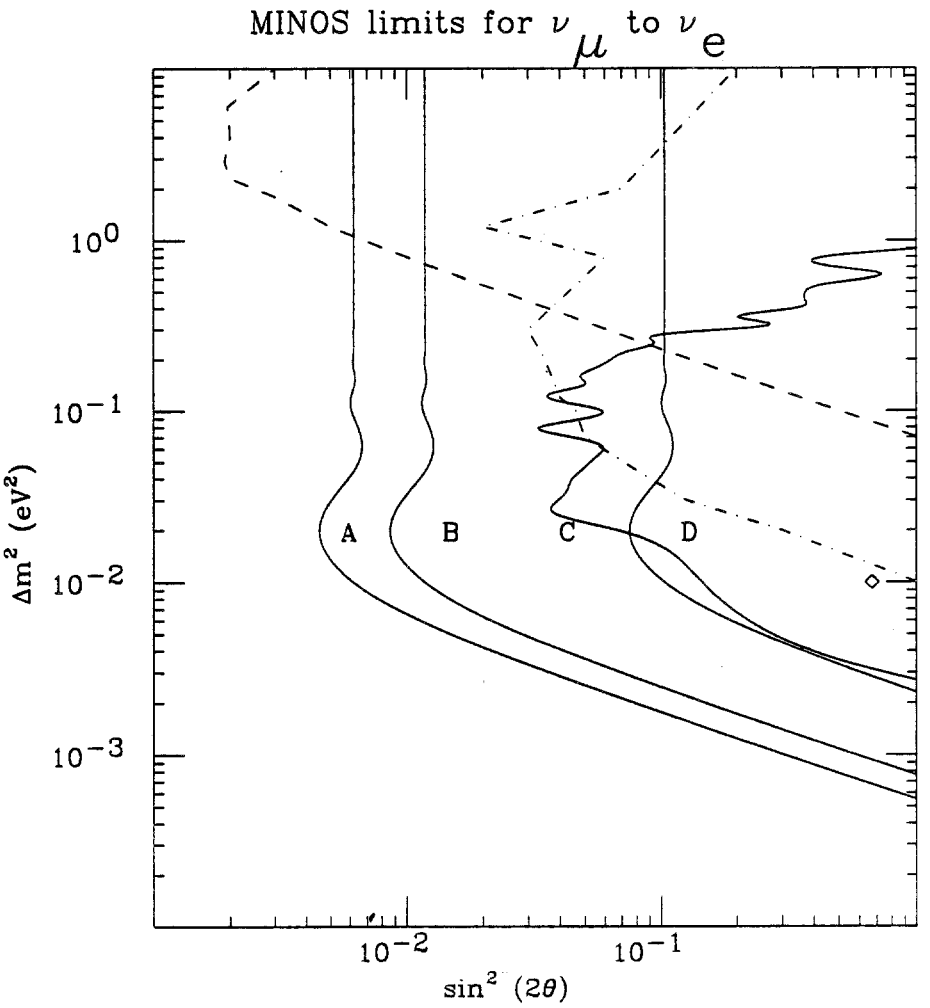

Figure 4: MINOS two year 90% CL limit curves for $\nu_\mu \rightarrow \nu_e$ oscillations. Curve "A" uses longitudinal cuts. Curve "B" is for the $\frac{cc}{total}$ test. Curve "C" comes from the total energy measurement test. Curve "D" is for the near/far rate comparison and is dominated by 4% systematic error. Curve "A" is the statistical limit, and the other three curves combine statistics and estimated systematic error. The dashed curve shows measured limits from BNL E-776, and the dot-dashed curve shows the Bugey 4 reactor experiment limits. The diamond is the Kamiokande best-fit point.

2.6 Costs and schedules

Since the technology of the experiment is conventional, our estimate of the cost of constructing the detector is quite reliable. The detailed cost breakdown in the MINOS proposal is summarized here. All costs are in FY 1995 dollars.

Passive detector elements (steel, magnets)	\$15.8M	
Active detector elements (limited streamer tubes)	\$13.1M	
Far detector installation and infrastructure	\$6.4M	
Near detector installation and infrastructure	\$1.1M	
Electronics	\$5.5M	
Subtotal		\$41.9M
Detector R&D	\$0.6M	
Contingency	\$12.0M	
Soudan laboratory outfitting	\$2.0M	
Total		\$56.5M

Our present schedule is to have one third of the MINOS far detector operational when the NuMI beam turns on in 2000, and the rest of the detector completed by the end of 2001. In order to achieve this, the new cavern excavation will start at Soudan in the autumn of 1996, and far-detector construction will begin in mid-1998. The funding profile needed to meet this schedule is as follows:

FY 1995	\$0.1M
FY 1996	\$0.8M
FY 1997	\$7.2M
FY 1998	\$15.3M
FY 1999	\$19.7M
FY 2000	\$12.7M
FY 2001	\$0.7M

The cost estimate of the MINOS experiment scales with far detector mass M as:

$$\mathbf{Cost(M\$) = 15.5 + 4.1 \times} M\mathbf{(kton)}.$$

3 Responses to PAC questions

3.1 Question #1

"The Committee notes that the cost of the experiment as now proposed exceeds the expected Fermilab budget for this experiment as presented at the June PAC meeting. In view of the speculative nature of a neutrino oscillation search, the Committee feels that the level of funding proposed by the Laboratory is appropriate. The experiment should plan to live within the financial guidelines provided by the Laboratory. Cost optimization of the total system of beam and detectors should be vigorously pursued."

We understand that approximately $55M of Fermilab capital equipment funds may be available for NuMI project construction, divided roughly as $30M for the beam and $25M for the long baseline detector. We are exploring possibilities to supplement these detector funds from other sources, which could add up to the $56.5M MINOS detector cost estimated in the P-875 proposal. We offer the following example breakdown of possible sources of funding for MINOS (in FY1995 dollars):

Fermilab capital equipment funds	$25.0M
DOE capital equipment funds, through University programs	$ 5.0M
U.K. contribution (requested), value equivalent	$ 3.0M
Other foreign contributions (possible), value equivalent	$ 5.0M
DOE line item funds for technical components	$18.5M
Total	$56.5M

Despite the uncertainties in these numbers, the MINOS collaboration is hopeful that some such funding package can be realized. The collaboration feels strongly that we must make every effort to achieve a sensitivity, i.e. mass and granularity, which is at least as good as that assumed in the proposal. Physics arguments supporting this view are outlined in Sections 1 and 2 above.

Our collaboration is continuing to pursue a vigorous development program with the goals of (1) reducing the cost of the 10 kT MINOS reference detector, and (2) enhancing the performance of the detector without increasing its cost.

For example, since the February PAC meeting we have been studying the engineering and cost consequences of a modified design of the steel structure. The axial bolts which were previously used to flatten the octagonal steel plates would be confined to the edges of the plates and now serve only to adjust their positions. This eliminates the dead regions around axial bolts in the active area, and also reduces the cost of the structure. The decrease in steel flatness would require an increase in the gap between plates to perhaps as much as 4 cm. In addition, we now believe that an inexpensive modification of the Soudan mine underground shaft station will allow us to assemble the steel octagons from eight 2-m wide strips (instead

of twelve 1.33-m wide pieces). Finally, we have received a reliable quotation for the price of far-detector steel which is 25% lower than that used for the MINOS proposal cost estimate. The contingency allowance for far detector steel has been reduced from 32% to 22% to reflect our greater confidence in this estimate. Taken together, these changes reduce the estimated total cost of the detector by about $6M.

Our goal is to reduce to the total detector cost to $45M, although we are still a long way from achieving this. Taken together with the incremental cost of the MINOS-plus-E803 beam over the $25M estimated for the E-803 stand-alone beam, this would give an incremental cost for MINOS of about $63M. This is comparable to the estimated cost of the long baseline program proposed by Brookhaven (after correcting for differences in their treatment of overheads and escalation).

The MINOS active detector R&D program is now focussed on two promising technologies, in addition to the limited streamer chamber reference detector. One alternative technology involves planes of scintillator-filled tubes which might be used in place of limited streamer chambers to improve calorimeter response. Encouraging light yields have recently been observed in our prototype tests of liquid-scintillator-filled tubes. Readout, trigger electronics, and cost issues are also under study for this technology. The second alternative technology is resistive plate chambers (RPC's). Recent progress includes the successful use of SF_6 as a substitute for Freon 13B1, a critical component of RPC gas which will not be available in the future. RPC's might be cheaper to construct than limited streamer chambers, and might also provide fast timing information.

In addition to this work on alternative detector technologies, we are developing cost effective mass production techniques for the limited streamer chambers used in the reference detector. We plan to study the calorimetric response of these detectors in a test beam in early 1996, and to take all steps necessary to ensure that chamber fabrication can begin on the schedule described in the MINOS proposal.

3.2 Question #2

"The collaboration and the Laboratory need to provide a more detailed conceptual design and cost estimate for the neutrino beam, both for the wide-band and narrow-band options. The method of switching between wide-band and narrow-band beams should be described. The plans for the maintenance of the beamline in the high radiation environment should also be included."

The response to this question is included in the report submitted to the PAC by the Fermilab NuMI Beam Design Group[2].

3.3 Question #3

"The strategy for the use of the narrow-band beam needs to be described further. The Committee appreciates that the efficacy of the narrow-band beam depends on the values of Δm^2 *and* $\sin^2(2\theta)$ *which obtain in nature. Nevertheless, in order to assess the importance of the narrow-band beam option, the Committee believes that the collaboration should choose possible values of the parameters and explore their consequences in detail for the narrow-band beam operated with several different momentum bites. The Committee would like to know how the narrow-band beam would be employed after a signal had been observed in the wide-band beam,*

1. *with* Δm^2 *and* $\sin^2(2\theta)$ *as suggested by the Kamiokande best solution, and*
2. *with* $\sin^2(2\theta) < 0.1$ *and unknown* Δm^2*."*

The narrow band beam (NBB) offers independent and complementary information regarding the existence and/or nature of neutrino mixing. In brief, the principal complementary advantages *vis-a-vis* the wide band beam (WBB) running are:

1. The knowledge of the energy provides an important constraint in identifying several τ production signatures, both in exclusive channels and in statistical analyses.
2. The ability to tune the energy allows one to maximize the signal, vary it in a controlled way, and measure oscillation parameters.
3. The NBB offers better understanding of the near-far detector flux comparison. This is due both to the ability to monitor the beam better (due to absence of primary proton beam) and to more control over beam parameters (energy, energy spread, etc.).
4. In a number of instances, the backgrounds are lower because of the absence of "off-momentum" neutrinos which do not contribute to the oscillation signal.
5. The NBB provides the ability to calibrate the energy response of the far and near detectors.

We can now turn to the discussion of running strategy. We anticipate that early in the run we will want to run in the NBB configuration (at least for a limited time) to perform energy calibration of the detectors. The subsequent running will depend very much on the overall state of our knowledge at that time regarding neutrino oscillations. We focus here on the two possibilities listed by the PAC:

a) Validity of the Kamiokande data. Currently there are two favored explanations of these data: $\nu_\mu \rightarrow \nu_\tau$ oscillations with $\sin^2(2\theta) = 1$ and $\Delta m^2 = 0.15\ eV^2$ and Harrison, Perkins, Scott (HPS)[3] hypothesis suggesting equal oscillations into ν_e and ν_τ with equivalent $\sin^2(2\theta) = 4/9$ and $\Delta m^2 = 0.0075\ eV^2$ for each.

If these parameters still look very plausible in the year 2000 or beyond (i.e., not contradicted by more atmospheric neutrino data, Super-Kamiokande accelerator neutrino data, or WBB running from MINOS) we would envisage running in the NBB configuration at two different energies. The oscillation parameters can be measured almost independently in two different ways namely:

i) Internal comparison of the far/near detector energy spectra for NC-like and CC like events for each energy. One can look at the ratio of the two or at algebraic differences. Simulated plots of NC-like and CC-like energy differences for 45 GeV primary meson beam and $\sin^2(2\theta) = 1$ and $\Delta m^2 = 0.15\ eV^2$ are shown in Figures 5 and 6. As can be seen from the figures, the data clearly distinguish the between the $\nu_\mu \rightarrow \nu_\tau$ and $\nu_\mu \rightarrow \nu_e$ hypotheses. Because the NBB covers a finite energy band one can observe differences as a function of energy. This effect will be maximized if the energy is chosen so that oscillation probability goes as $(\Delta m^2)^2$. The magnitude of this difference will depend on the values of the oscillation parameters and thus one can obtain a χ^2 for any given hypothesis. χ^2 contour plots in the Δm^2 - $\sin^2(2\theta)$ space will determine these two parameters. Figure 7 shows such a 1σ contour plot for the Kamiokande hypothesis of $\nu_\mu \rightarrow \nu_\tau$ oscillations. In principle, χ^2 can be calculated also as a function of the four parameters for the double oscillation hypotheses.

This method in principle is similar to the analyses that could be performed for the case of the WBB situation. The NBB situation should be however cleaner for reasons outlined at the beginning of this section and the effect is still quite strong even for a $\pm 20\%$ momentum bite (roughly a factor of two difference at the extrema). The two (or four) parameters are correlated in this analysis as can be seen from the contour plot displayed in Figure 7.

ii) Far/near comparison of NC- and CC-like events for two different energies. In principle, all of the data from each energy setting could be used, or limited energy cuts could be made to enhance sensitivity. This method minimizes (or eliminates) sensitivity to detector energy response. The probability for neutrino oscillations between two flavor eigenstates a and b is given by

$$P(\nu_a \rightarrow \nu_b) = \sin^2(2\theta)\sin^2(1.27\frac{\Delta m^2 L}{E}) \tag{1}$$

where $\Delta m^2 = \mid m_1^2 - m_2^2 \mid$ is measured in eV^2, L in km, and E in GeV.

Thus the ratio of the two far/near ratios will eliminate dependence on $\sin^2(2\theta)$ and Δm^2 can be obtained without correlation to $\sin^2(2\theta)$. Alternatively, one can look at the difference of the two far-near differences divided by the sum of the two near-far differences. Individual ratios (or near-far differences) will, of course, give then the value of $\sin^2(2\theta)$. We measure four different numbers i.e., number of NC- and CC-like events at two different energies and thus measurement of four parameters is possible in principle.

What are the optimum energies to run? They are different depending on whether the goal is ascertaining the existence of the effect (in which case ideally the arguments of the second factor for one energy should be $\pi/2$ and of the other π or a value close to zero) or whether one wants to have maximum sensitivity to Δm^2 determination (in which case they should be $\pi/4$ and $3\pi/4$). These theoretical values have to be weighed against such practical considerations as flux, signal to noise and τ production cross section dependance on energy. For the Soudan distance and $\Delta m^2 = 0.015\ eV^2$, $\pi/4$ occurs at 18 GeV. Thus for maximizing

the discovery potential, the two values might be about 12 and 25 GeV (central neutrino energy); for optimizing the measurement, the values might be around 8 and 18 GeV. The sensitivity is maximum if the energy spectrum is narrow but $\pm 20\%$ $\Delta p/p$ is quite adequate. We estimate that this method could measure Δm^2 to about 5% in one year, assuming the Kamiokande single oscillation hypothesis.

The discussion above focused entirely on the global analysis of the NC- and CC-like events. An important and frequently unique complementary part of the investigations with the NBB is the study of the exclusive channels. As was shown in the proposal, for example, $\tau \rightarrow \mu\nu\nu$ events can be identified quite clearly in the narrow band beam running, especially for low-y configuration. In addition, the identification of energetic electrons constitutes an observation of $\nu_\mu \rightarrow \nu_\tau$ and/or $\nu_\mu \rightarrow \nu_e$, as discussed in the MINOS proposal. Relative rates of exclusive channel signatures at two energies will provide important independent information on $\sin^2(2\theta)$ and Δm^2 values. Much more extensive simulation calculations are necessary before optimum final energies for all the possible channels taken together could be determined.

b) $\sin^2(2\theta) < 0.1$ and unknown Δm^2. For a significant fraction of the Δm^2 region (i.e., 0.02 to 0.2 eV^2) the CC test in the WBB will give some information on the Δm^2 value for somewhat lower values of $\sin^2(2\theta) < 0.1$. Thus more specific information may be available and would allow a more informed choice of running conditions. In the absence of such information, however, a following strategy might be appropriate:

i) The initial running at $E_\nu = 12$ GeV with $\Delta p/p = \pm 20\%$ (or larger if possible), corresponding to a phase of about $\pi/4$ for $\Delta m^2 = 0.01$ eV^2. Thus values of $0.005 < \Delta m^2 < 0.02$ eV^2 could be explored. Simultaneously, however, higher values of Δm^2 would also be investigated. For example, as seen in the proposal (p.51) $E_\nu = 12$ GeV corresponds to a minimum oscillation probability for Δm^2 equal to both 4 and 8×10^{-2}. The oscillation effect would be quite pronounced in the two wings of the distribution. Thus the results of such a run would preferentially pick certain values of the parameters, but might not be able to identify them unambiguously.

ii) Subsequent running at a different energy, probably as high as is compatible with reasonable flux. This might be about $E_\nu = 25$ GeV. The precise conditions could be chosen after looking at the results of the original run, so as to resolve in an optimum way all the ambiguities. In addition, if the value of $\sin^2(2\theta)$ is close to 0.1, there should be a sufficient number of neutrino events from K decays to provide additional constraints so that the region of exploration can be extended to values of Δm^2 beyond 0.1 eV^2.

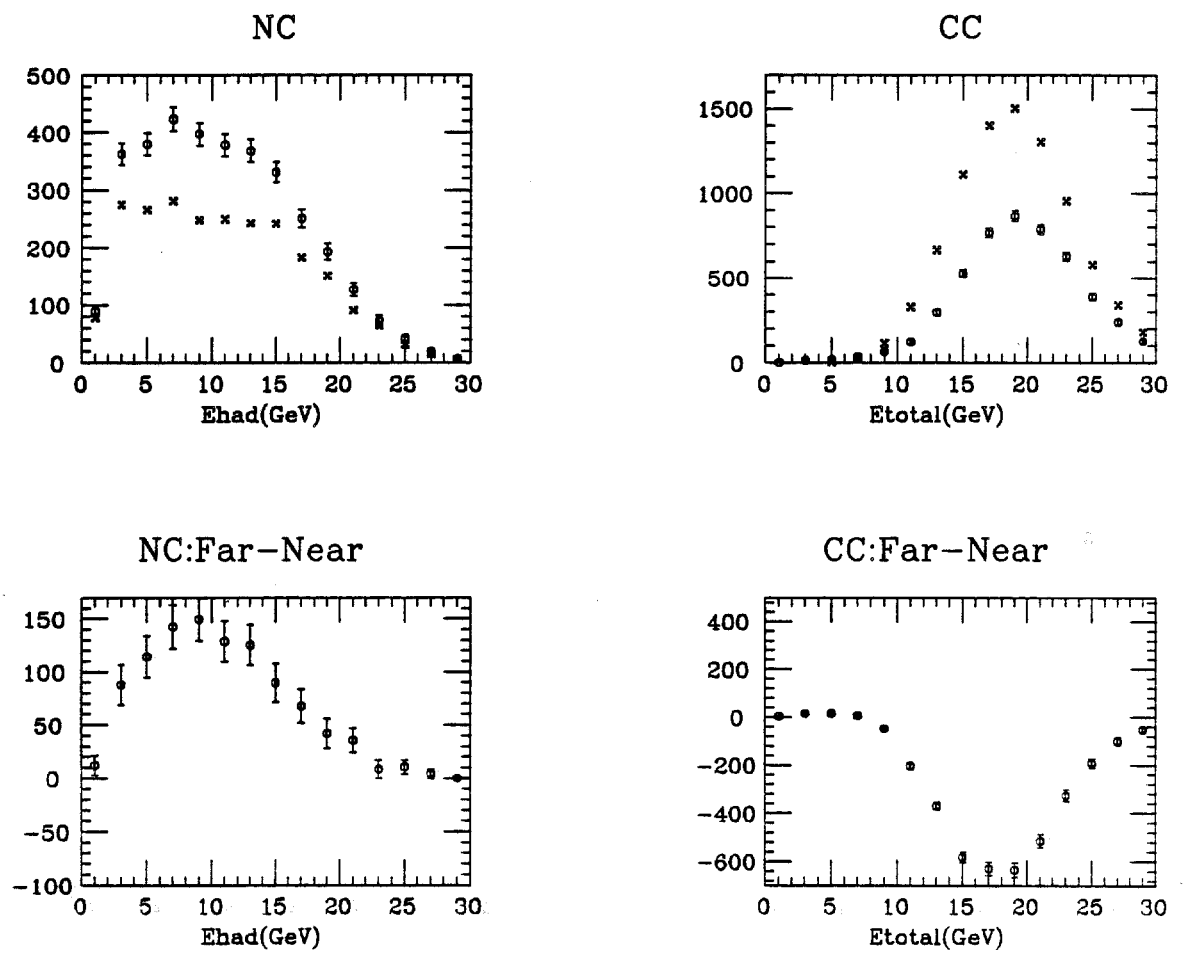

Figure 5: Energy spectra for NC- and CC-like events for $\nu_\mu \rightarrow \nu_\tau$ oscillations at the Kamiokande point, for the NBB with a 45 GeV meson beam. The top two plots show the far (circles) and near (crosses) spectra separately, and the lower plots show the far - near difference spectra.

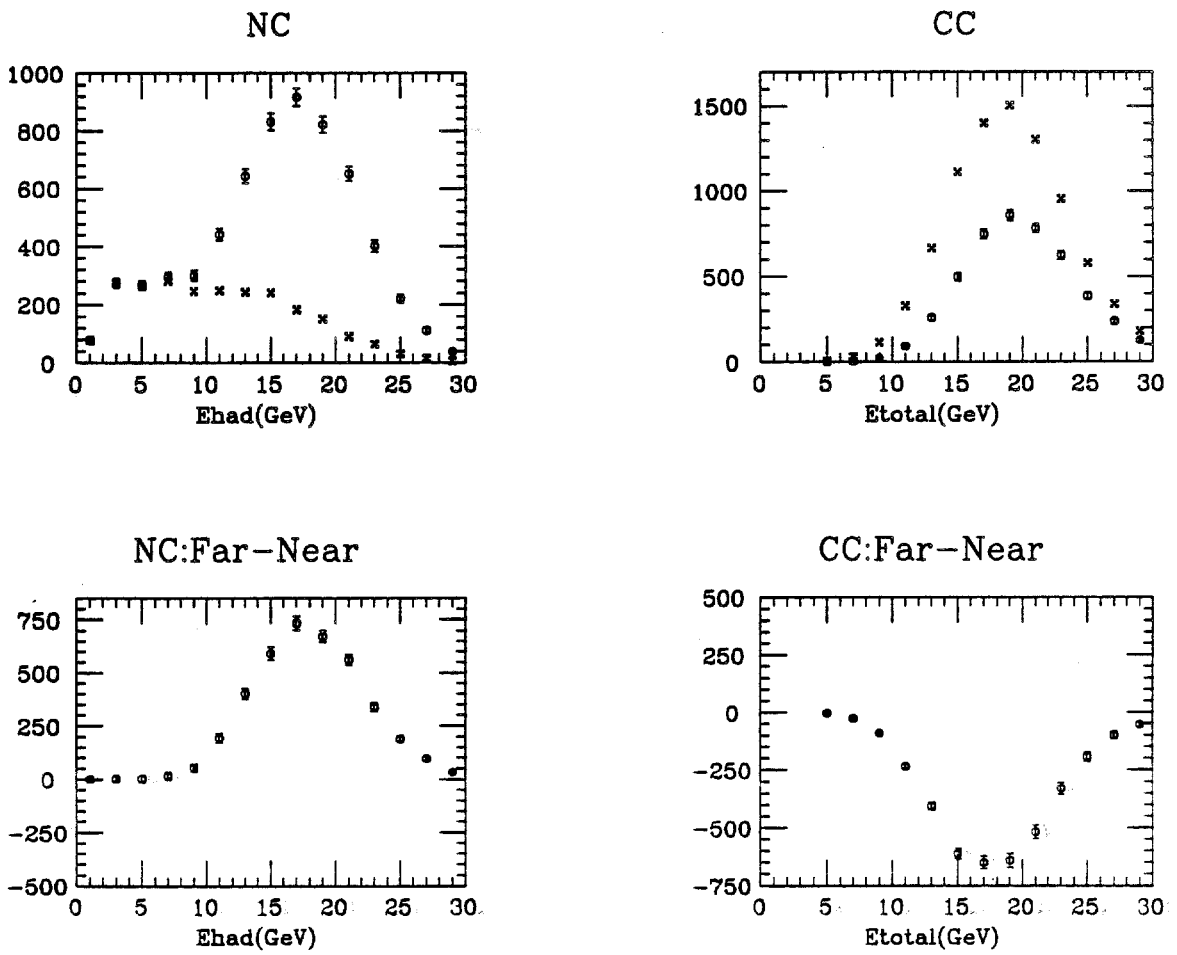

Figure 6: Energy spectra for NC- and CC-like events for $\nu_\mu \rightarrow \nu_e$ oscillations at the Kamiokande point, for the NBB with a 45 GeV meson beam. The top two plots show the far (circles) and near (crosses) spectra separately, and the lower plots show the far - near difference spectra.

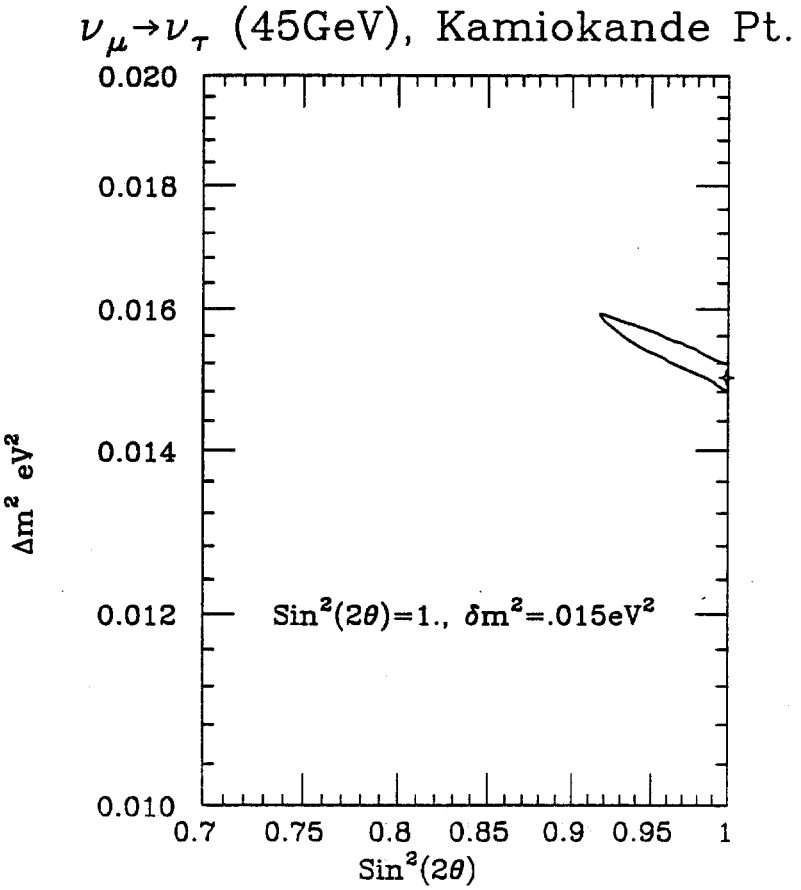

Figure 7: Contour plot for χ^2, corresponding to an $\nu_\mu \to \nu_\tau$ oscillation signal with 1σ significance at the Kamiokande point, showing the correlation between errors in Δm^2 and $\sin^2(2\theta)$.

3.4 Question #4

"The Committee would like to see as complete a simulation of the detector as possible. This should lead to a more coherent and consistent study of the detector and its sensitivity to oscillations. This will be an extremely useful guide in the required cost optimization."

The collaboration has utilized the Monte Carlo programs already available to the individual collaborating groups in order to make a quick start in simulating the detector and physics signatures. The programs differ in the completeness of the simulation but at least two of the programs, one based on GEANT and the other on the Soudan 2 Monte Carlo, make a very comprehensive simulation of the detector. Features included in the simulations include:

- The magnetic field in the iron.
- The shape of the iron plates, including the central hole for the magnet coils.
- The axial bolts included in the proposal version of the detector. However, further study of the mechanical construction of the detector has enabled us to dispense with the bolts in the detector active area, producing a more efficient and uniform detector.
- The full geometry of the limited streamer tubes.
- A realistic response for the limited streamer tube readout including the effects of close streamers and the production of multiple streamers on tracks crossing the chambers at large angles.

Although all the above features are not yet in all programs, we have been able to study the effects associated with all of them.

The simulations enable realistic separations between charged current, neutral current and electron-like events to be carried out using the simulated detector output. The energies of hadronic and electronic showers are calculated from the simulated detector hits, and realistic topology cuts are made for the identification of τ and electron final states. However, the trajectories of μ's in the magnetic field are complicated and a realistic energy measurement requires a full pattern recognition and reconstruction program which does not yet exist. Simulation of μ energies is thus currently made by Gaussian smearing of the generated energy. We have however comprehensively investigated non-Gaussian tails to the μ energy distribution and have shown in Section 7.4.2 of the MINOS proposal that non-Gaussian tails can be removed.

We consider that the availability of several independent Monte Carlo programs has been a distinct advantage for our work so far. The neutrino cross-sections in the 5-30 GeV range are not very well measured and the important quasi-elastic and resonance cross sections are particularly uncertain. We have compared the cross sections generated by the different programs and have been reassured that the physics output from the programs is not significantly different. However, in the future we clearly need a standard, complete MINOS Monte Carlo

program. We have instituted a committee to recommend the MINOS computing structure: platforms, languages, data structures, program packages, etc. When this committee reports we will be in a position to start on the first link in the MINOS software system which will clearly be the Monte Carlo program. However, we do not expect results from this program for at least one year.

3.5 Question #5

"The Committee looks forward to seeing a numerical corroboration of the arguments presented by the spokesman to justify the systematic uncertainties associated with the comparison of the energy spectra in the near and far detectors. This should be accompanied by a discussion of how well measurements performed in the near detector will constrain the difference between the energy spectra in the near and far detectors."

3.5.1 Wide-band beam

Introduction. The wide-band neutrino beam energy spectra at the near and far detectors turn out to quite similar, despite the different kinematical origins of the neutrinos at the two locations. Energy differences can be reduced even further by considering only neutrinos close to the beam center at the near detector (we used a 25-cm radius cut for calculations in the MINOS proposal). We present here a conceptual explanation of why this is the case, and include the quantitative results of Monte Carlo simulations of the beam characteristics at the two locations. In addition, we discuss how measurements of the beam by the near detector and the beam monitor calorimeter will tell us about the hadron beam which produces our neutrinos, and how we will use a comparison with Monte Carlo simulations of the hadron and neutrino beams to predict the energy spectrum in the far detector.

Meson decay kinematics. According to all of our beam simulation calculations the energy spectrum of neutrinos within the inner 25 cm region of the near detector is similar to the spectrum at the far detector. We shall first discuss the physical origins of this close similarity.

The near detector is situated 170 m from the downstream end of the decay pipe and 1 km from the meson production target. The far detector is 730 km further downstream. The neutrinos which reach the far detector are parallel to the beam axis within about 10^{-5} radians (in both planes); the angle of the decaying parent meson with respect to the neutrino beam axis must then be equal (to within 10^{-5} radians) to the decay angle of the neutrino with respect to the parent meson direction. This is illustrated schematically in Figure 8.

The neutrino energy is related to the angle between the parent meson and the neutrino in accordance with the well-known angular dependence of the two-body $\pi \to \nu$ (or $K \to \nu$) decay kinematics:

$$E_\nu = \frac{E_\nu^{max}}{1+\gamma^2\theta^2}, \quad \gamma = \frac{E_\pi}{m_\pi}. \tag{2}$$

The range over which this angle varies is related to the divergence and size of the meson beam in the decay pipe. Figure 8 shows the (larger) range of decay angles for neutrinos passing through the inner 25 cm of the near detector, relative to the range of decay angles for neutrinos which reach the far detector. Figure 9 shows the decay angle distributions for neutrinos passing through the inner 25 cm of the near detector and for those passing through the far detector. The mean decay angle in the two cases is quite similar.

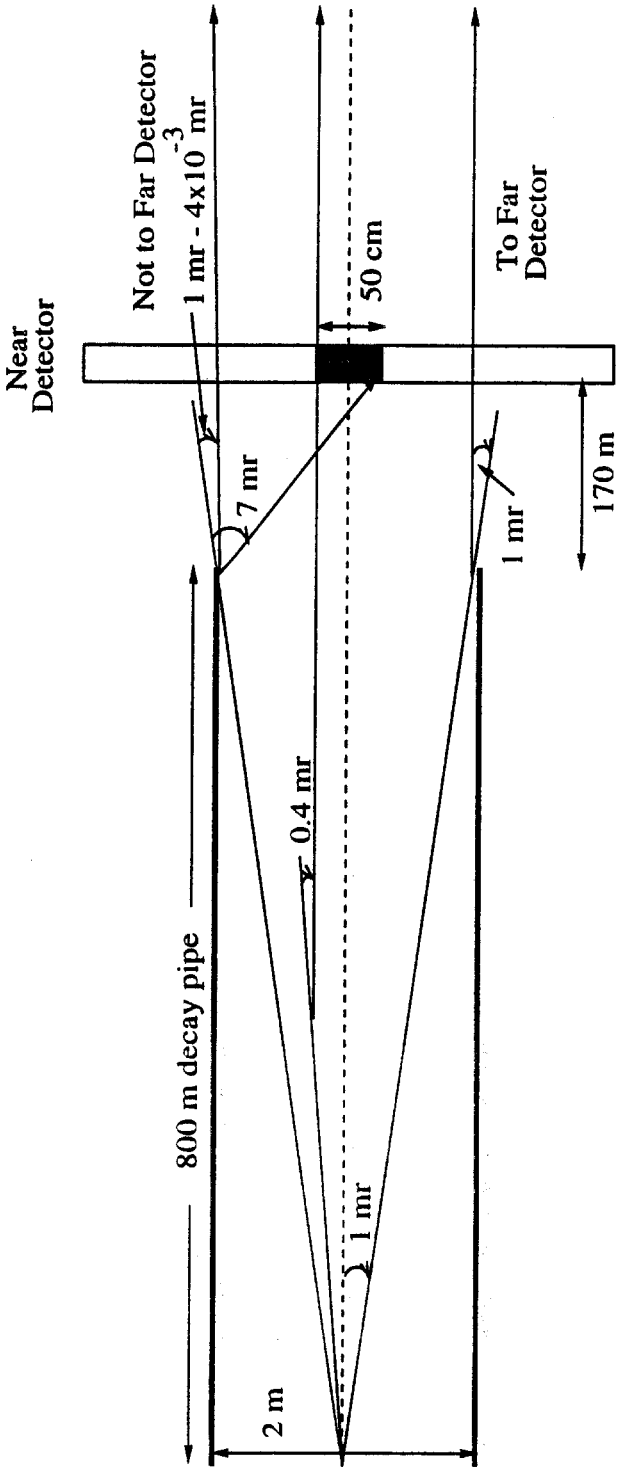

Figure 8: Schematic diagram of the angles associated with near and far neutrino energy spectra.

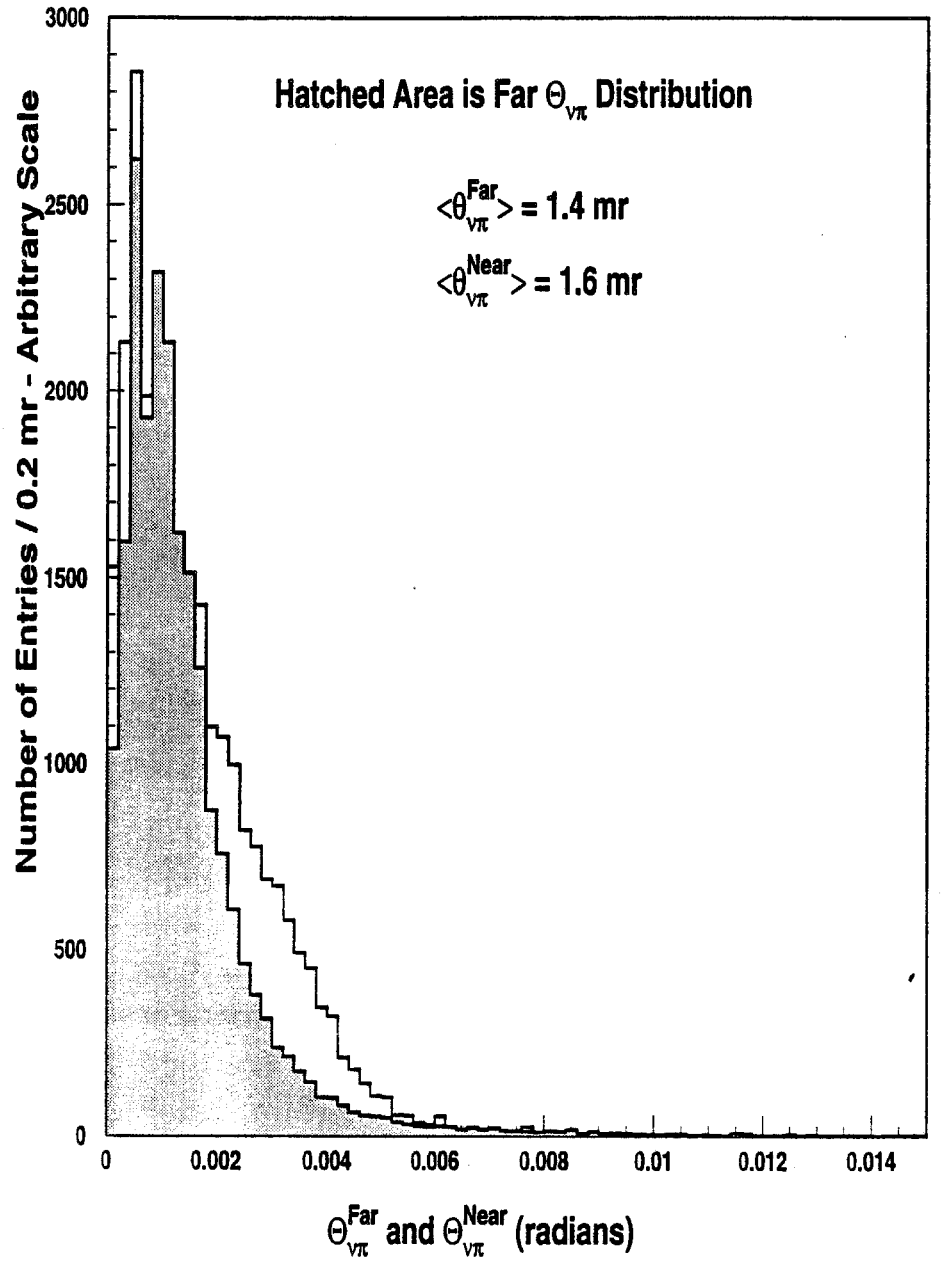

Figure 9: The neutrino decay angle with respect to the parent hadron for the central near detector and the far detector.

Relative to the energy spectrum at the far detector, the broader decay angular distribution for the neutrino beam at the near detector produces a softer beam energy spectrum, in accordance with Eq. 2. The detailed consequences of this softer spectrum at the near detector, across the entire energy range, have been studied in our Monte Carlo beam simulations, which are discussed next.

Simulations of near and far energy spectra. An important figure-of-merit for our discussion of the differences between the near and far energy spectra is the difference in the average neutrino event energies at the two detector locations. For the double-horn focusing system described in the MINOS proposal, our simulations predict a 4% difference in the average near and far detector neutrino event energies, after a 25 cm radial cut at the near detector. This comparison is shown in Figure 10, where the spectra have been normalized to equal areas. The large peaks in the distributions are due to the focusing actions of the two horns on parent mesons in specific energy regions. Figure 10 also shows the difference between the shapes of these two distributions as a function of energy. The near and far detector energy spectra shapes are quite similar, but the mean value is shifted to a lower energy for the near detector.

Our wide-band beam model, which includes the meson beam properties, the decay pipe geometry, the geometrical parameters of the two detectors, and meson decay kinematics, accounts for all the differences between the near and far energy spectra. The effects of decay kinematics alone, without the spectrum structure produced by the horn focusing, can be qualitatively understood in the case of "perfect focusing." In this idealized beam, all mesons travel exactly on the neutrino beam axis. Figure 11 shows the comparison between the near and far detectors for the perfect focusing case.

The effects of the horns on the neutrino beam spectra, and the consequent differences between the near and far spectra, are illustrated in Figures 12b and 12d, where the origins of the key features are labelled. The combined effects of the two spectrum peaks, and of the shifting to lower energy of these peaks in the near detector, are clearly seen. Figures 12a and 12c, which show the spectral shape differences for the case of perfect focusing, demonstrate the effect of the neutrino decay kinematics in softening the energy spectrum at the near detector relative to that at the far detector. In other words, Figure 12c illustrates those differences between the near and far spectra which are due entirely to the neutrino decay kinematics, while the additional structure in the energy region 10-25 GeV in Figure 12d is caused by the focusing action of the horns and by the decay kinematics of pions of those energies which are most strongly focused by the horns.

Another source of uncertainty in the near-far energy difference is our knowledge of secondary π and K production at the meson production target. All the simulations discussed above have used the particle production model of Atherton[5, 6, 7]. We have recently used two other models to obtain a measure of differences in the near and far beam spectra which may arise from uncertainty in particle production. The energy spectra in the inner 25 cm radius of the near detector and in the far detector have been compared for the Wang[7] and CKP[8] particle production models. The differences in the mean energies for the near and far spectra are found to be 5.2% for the Wang model and 4.9% for the CKP model, compared with 4% for the Atherton model.

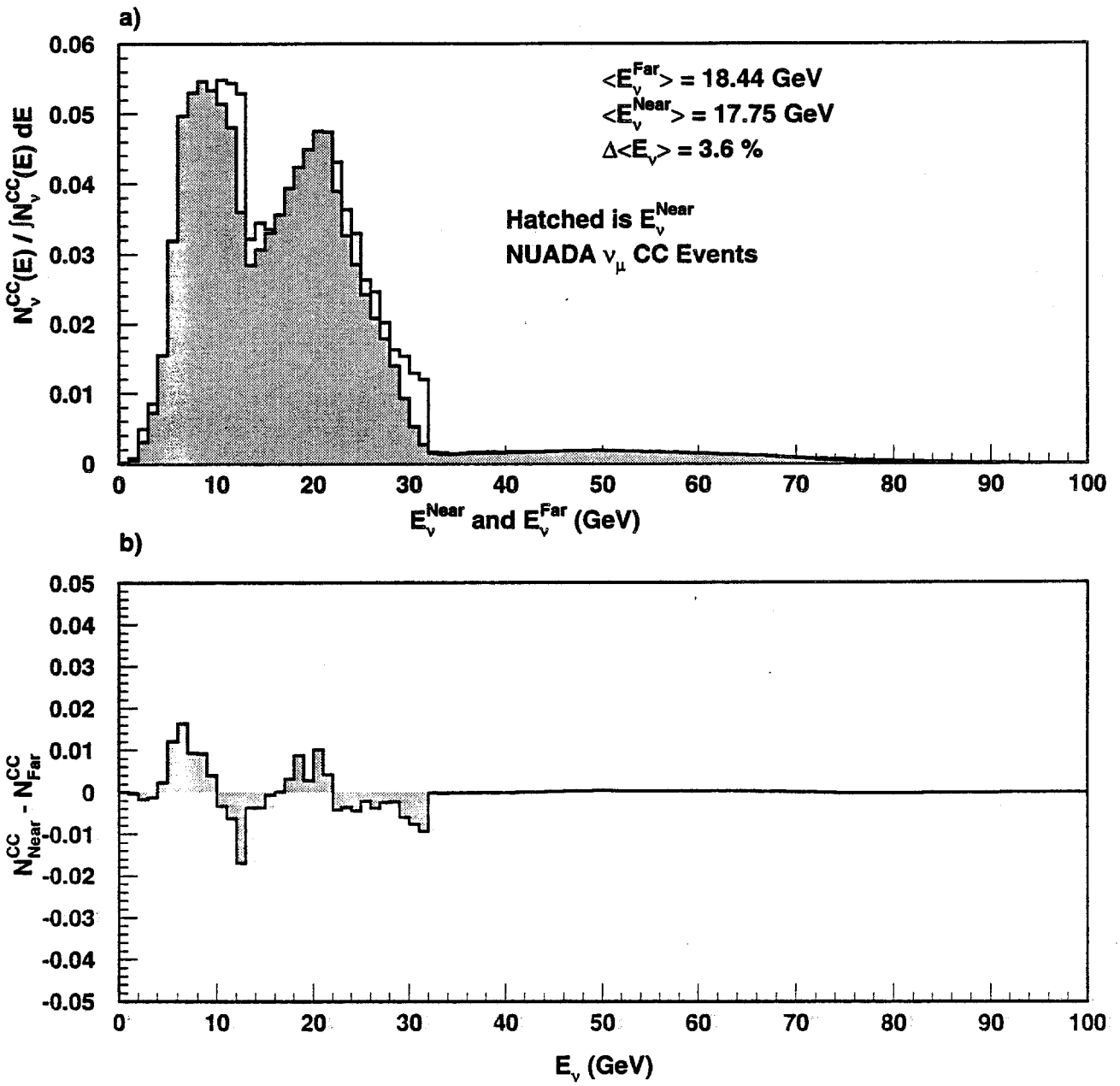

Figure 10: a) The distribution of ν_μ CC events (N_ν^{CC}) at the near and far detectors for the horn beam normalized to unit area. b) The difference $N_{Near}^{CC} - N_{Far}^{CC}$ for the horn beam.

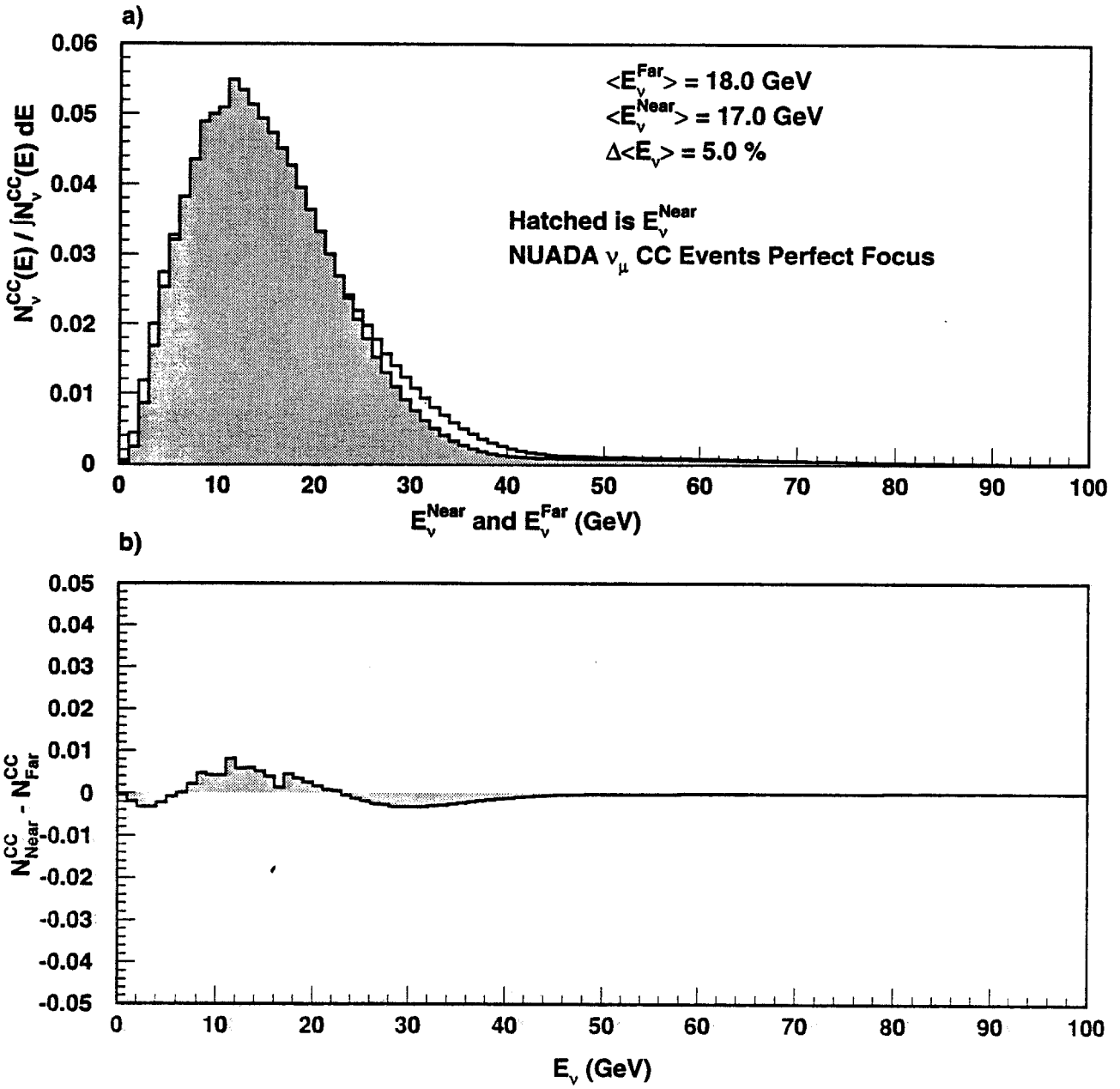

Figure 11: a) The distribution of ν_μ CC events (N_ν^{CC}) at the near and far detectors for perfect focus normalized to unit area. b) The difference $N_{Near}^{CC} - N_{Far}^{CC}$ for perfect focus.

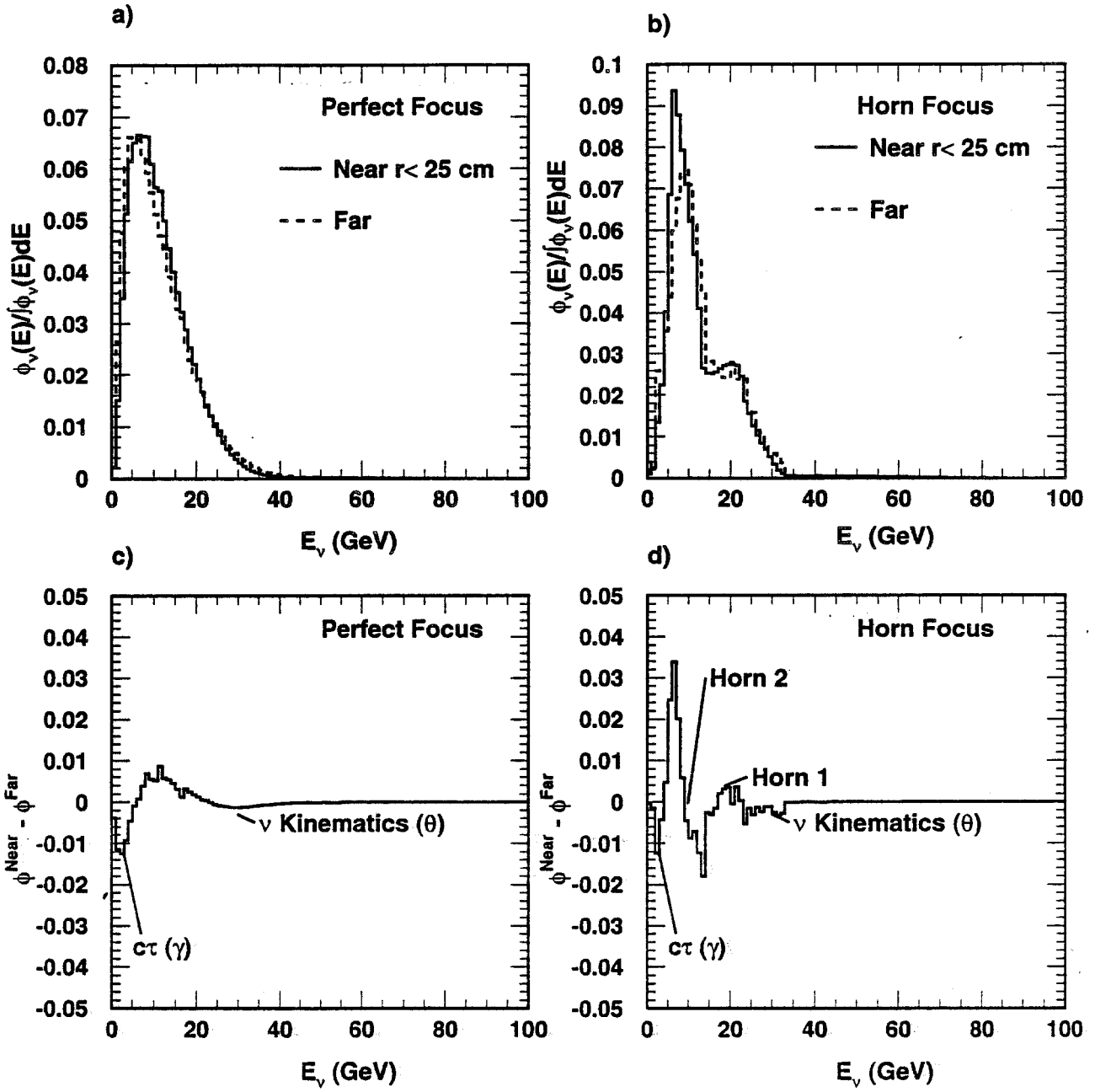

Figure 12: The distribution of the flux of neutrinos at the near and far detectors normalized to unit area a) for perfect focus and b) for the two horn beam. The difference $\phi^{Near} - \phi^{Far}$ c) for perfect focus and d) for the horn beam.

Beam measurements with the near detector. The near detector has a beam monitor calorimeter section which will have very good energy and position resolution. We propose to use quasi-elastic events in this section of the detector to measure the average incident angle of the neutrinos. Quasi-elastic events have little hadronic energy, which is difficult to measure with good angular accuracy in a calorimeter detector. Alternatively, for monitoring those distributions which have little or no angular dependence, we plan to use all charged current events in the beam monitor and make use of its superior energy resolution.

The beam monitor detector will measure the neutrino event energy (E), position (x,y) and average angle $< \theta_\nu >$ over the entire fiducial area. Distributions of these three observables will be used to monitor: (1) the day-to-day stability of the beam, (2) the left-right and up-down symmetry of the beam about the beam axis, and (3) the beam energy spectrum at the near detector. A careful comparison of the distributions of the three observables with the values predicted by Monte Carlo simulations will provide a measure of the systematic uncertainties in our beam calculations.

Figure 13 shows how the neutrino event energy spectrum in the near detector softens significantly as the radius increases. The motivation for using an inner radius cut for the near detector is illustrated in Figure 14, where the value of the mean event energy for the near and far detectors is shown as a function of the detector radius cut. The average event energy is a slowly changing (but measurable) function of the inner radius cut. Comparison of the measured radial dependence of the mean neutrino event energy as a function of the inner radius cut will provide an important consistency check on our understanding of the neutrino beam energy spectrum at the near detector.

Another possible check of the consistency of our data with the Monte Carlo simulation might be to compare $< \theta_\nu >$, as a function of position (x,y) in the near detector, with the simulated distribution of the neutrino events. We are currently performing numerical simulation studies to evaluate this check.

We believe that neutrino events in the beam monitor calorimeter will provide adequate constraints on our Monte Carlo simulation. However, we are also investigating the possibility of direct measurements on the meson beam itself. Such measurements, using ionization chambers and Cerenkov detectors, are difficult for the wide-band beam because the primary proton beam accompanies the meson beam in the decay pipe. This direct measurement of the meson beam properties would provide additional independent constraints on the parameters of the simulation, and would increase confidence in its accuracy.

The collaboration appreciates the critical need to model the quantitative relationship between measurements at the near detector and beam properties at the far detector. We have argued here that the near-far beam differences arise from well-understood and easily-modelled physical effects, which are already incorporated in our beam Monte Carlo simulations. Disagreements between measured beam characteristics and the simulation will then provide a measure of the systematic error in our prediction of beam properties at the far detector. The parameters which affect near-far beam differences in the simulation are already tightly constrained. Therefore, any adjustment of the Monte Carlo parameters (e.g., the energy and angular distributions of meson production) which is needed to obtain agreement with near detector measurements is unlikely to have a large effect on the beam properties at the far detector.

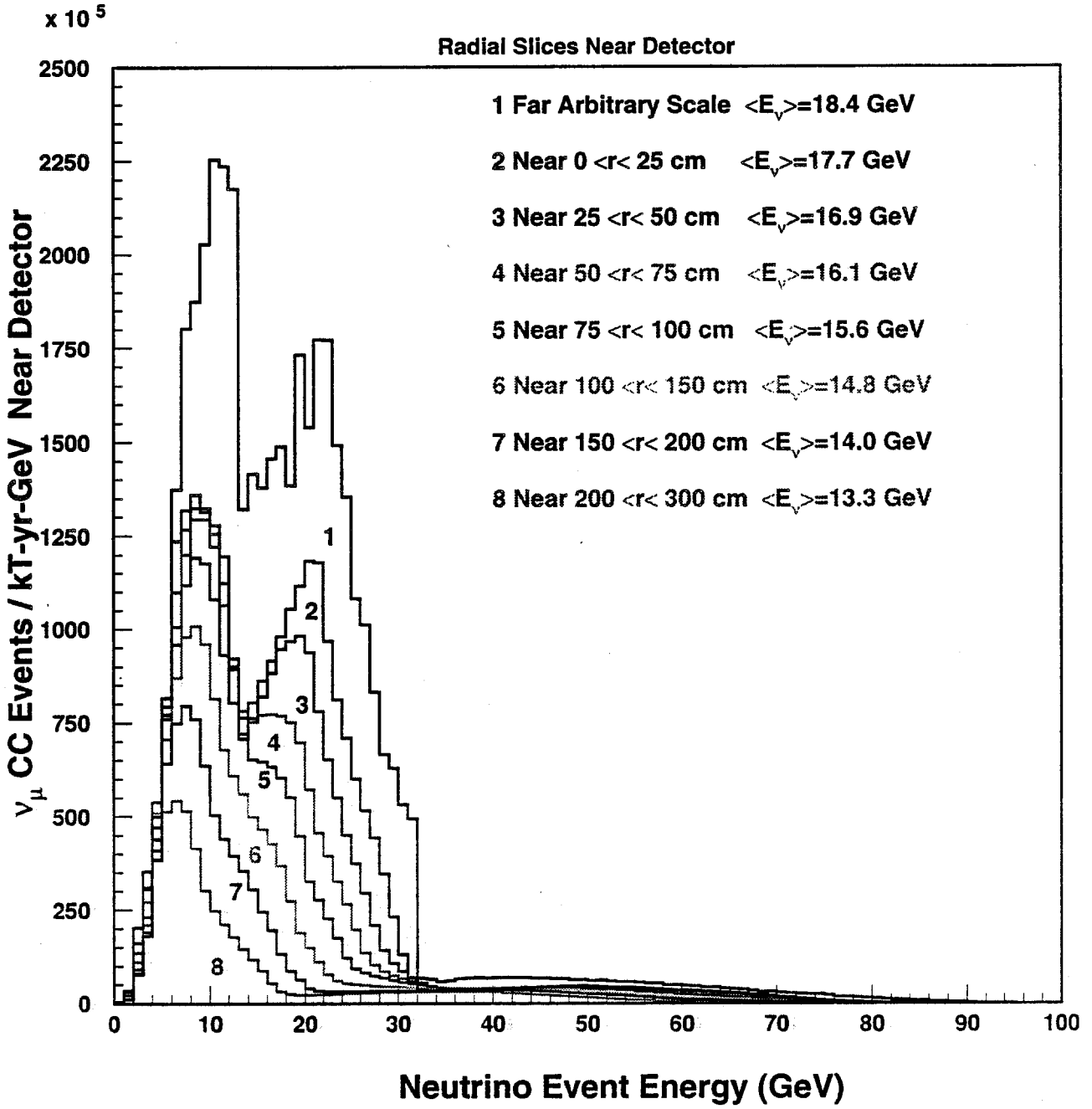

Figure 13: Radial dependence of the nu_μ CC-event energy distribution in the near detector. The spectrum for the far detector is on an arbitrary scale for presentation.

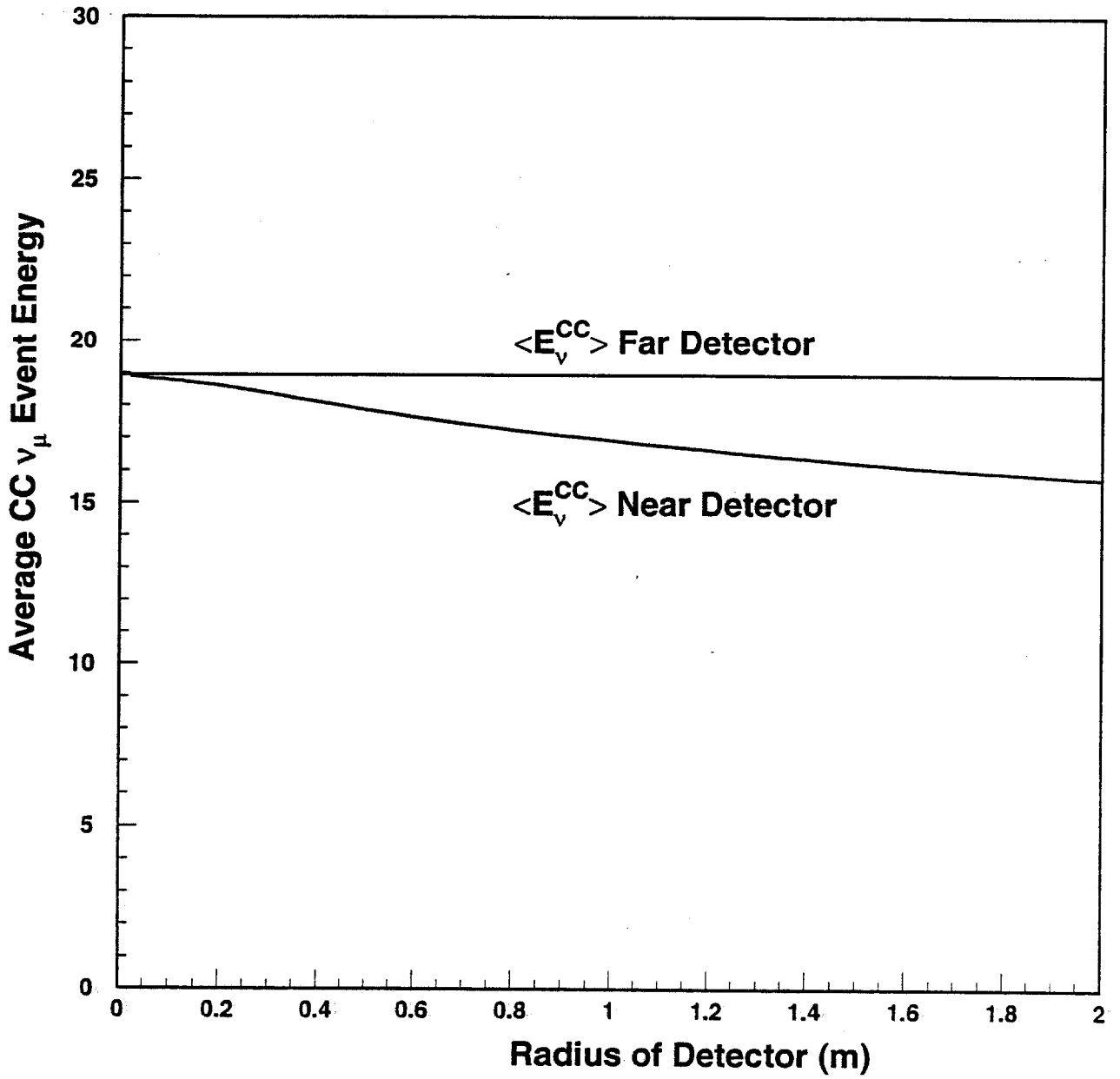

Figure 14: Change in the average ν_μ CC event energies $< E^{Near} >$ and $< E^{Far} >$ at the near and far detectors as a function of radius.

Conclusions. Back-of-the-envelope calculations and detailed simulations are in agreement that the neutrino energy spectra in the inner region of the near detector will be similar to that in the far detector. A measure of the uncertainty in our knowledge of the difference between the near and far beam spectra will be provided by measurements of neutrino energy distributions especially, and also of the mean neutrino angle as a function of radius in the near detector.

In the MINOS proposal we assumed that the uncertainty in the predicted far-detector beam spectrum was equal to the calculated difference between the spectra at the near and far locations. A normalization uncertainty of 4% was calculated under the pessimistic assumption that all near-far differences contributed with the same sign. The sources of these differences have now been identified as features of two-body decay kinematics and the well-understood properties of the double-horn focusing system. These turn out to be relatively insensitive to changes in the meson production spectra. As a result, a normalization uncertainty of 2% now seems appropriate.

Finally, our understanding of the origins of near-far beam differences suggests that the most accurate estimate of the systematic uncertainty in our prediction of the far-detector spectrum is given by the differences in this spectrum which result from changes in the beam simulation model, e.g., using different Monte Carlo programs and meson production spectra. This uncertainty is about a factor of four smaller than the 4% value used in the MINOS proposal.

3.5.2 Narrow-band beam

The narrow band beam (NBB) offers several advantages over the wide band beam (WBB) in neutrino oscillation experiments. One of these advantages is the possibility of making direct measurements of the meson beam within the decay pipe, which leads to a detailed understanding of the neutrino beam characteristics. This is possible because the primary proton beam is dumped upstream of the decay pipe in the NBB configuration. For the MINOS NBB design, the lower neutrino flux relative to the WBB is partially alleviated by the use of a Li lens, which provides both a large angular acceptance for pions and a very good momentum bite. This is described in detail in the MINOS proposal.

Here we address only the question of the near-far neutrino flux comparison. This calculation is difficult because the near detector is so close to the end of decay pipe, 170 m compared to 730 km for the far detector. Nevertheless, we believe that an adequate understanding of the near-far flux comparison is achievable for the following reasons:

1) The near/far neutrino flux ratio depends on the transverse size, angular distributions, and momentum distributions of parent pions. Using well known kinematics of pion decay, one can show that if transverse beam size is small (pencil beam), angular divergence is zero (typical angle much smaller than $1/\gamma_\pi$), and momentum bite is very small, then the energy distributions of neutrinos in the far and near detectors are the same.

In order to demonstrate this point, we consider the following examples. We assume the pion beam has a transverse size of 10 cm and Gaussian angular spreads of (a) 0.3 mrad and (b) 2 mrad. We chose the transverse size of the near detector to be the same as that of the pion beam at the exit of the last quadrupole. For purposes of this illustration, the far

detector size was taken to be one σ of the pion angular distribution times the 730 km. (Use of the actual far-detector size would accentuate the near-far differences calculated below.) We used a 45 GeV pion beam with a 20% momentum bite. In Figures 15a and 15b, we show the momentum distribution of near/far neutrino ratio for the two cases. The solid line is for the near detector and dashed line is for far detector normalized to the same flux. The difference between the near and far flux for case (a) is very small, but there is a clear near/far difference in case (b). In Figures 16a and 16b, we show the near/far ratio for cases (a) and (b). It is clear that we have a satisfactory result for case (a) but not for case (b).

2) We can achieve the conditions of case (a) in the MINOS beam. To prove that we have achieved this, it is very important to measure the charged particle flux in the decay pipe. This is not difficult, and has been successfully accomplished at both Brookhaven and Fermilab in narrow-band beams. This measurement is straightforward because the primary proton beam is dumped upstream immediately after the production target, and the meson beam has a well defined momentum.

For MINOS, we propose to place detectors at two locations, one right after the last quadrupole and the other just before the end of the decay pipe. We will use segmented ionization chambers to measure the position distribution of charged particles at the two locations. Figure 17 shows the production energy distributions of pions, kaons, and protons for 120 GeV incident protons. At 45 GeV, we see that there are approximately five times more protons than pions in the secondary beam. We propose to use differential Cerenkov counters at both locations to separate muons and pions from protons.

In the MINOS proposal, we discussed two preliminary designs of the NBB using the Li lens. In both cases, we demonstrated that the pion beam had a Gaussian angular spread of a little less than 1 mr and a transverse size of 10 cm. We believe that we can reduce the angular spread to significantly smaller than 1 mr by increasing the transverse dimension of the beam to about 30 cm. This approaches the case (a) conditions described above, and will ensure a good understanding of the near/far flux comparison.

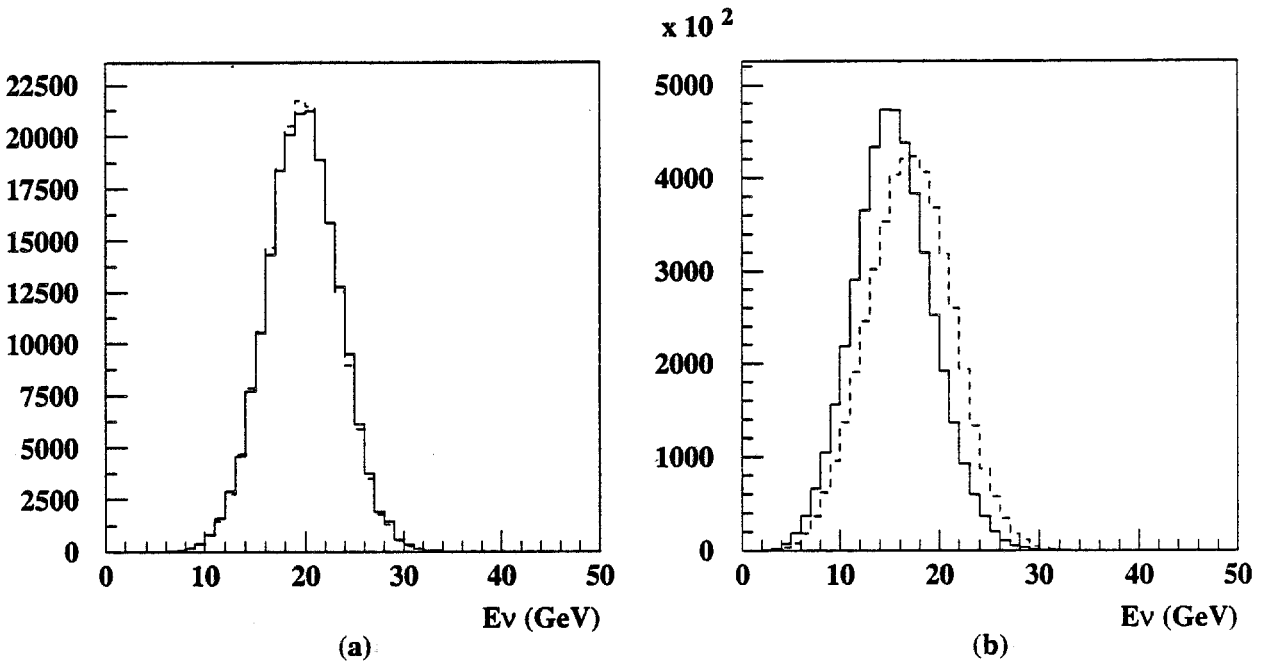

Figure 15: Neutrino energy distributions at the near and far detectors. The solid line is near detector and the dashed line is for the far detector, for the cases (a) and (b) described in the text.

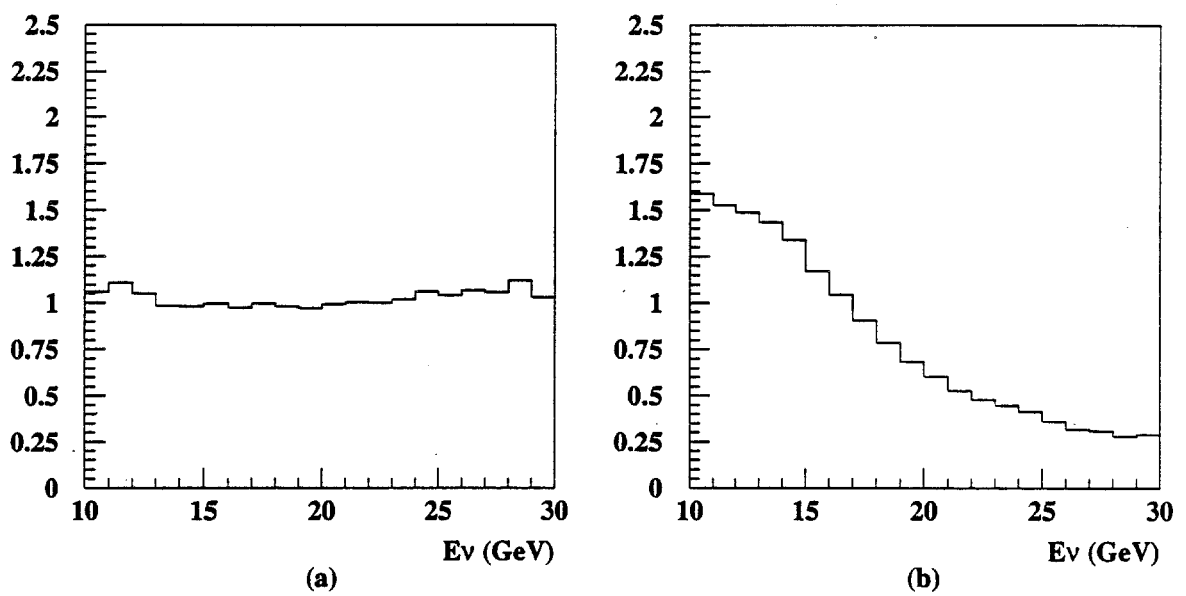

Figure 16: The far/near neutrino flux ratios as functions of neutrino energy for the case (a) and (b) described in the text.

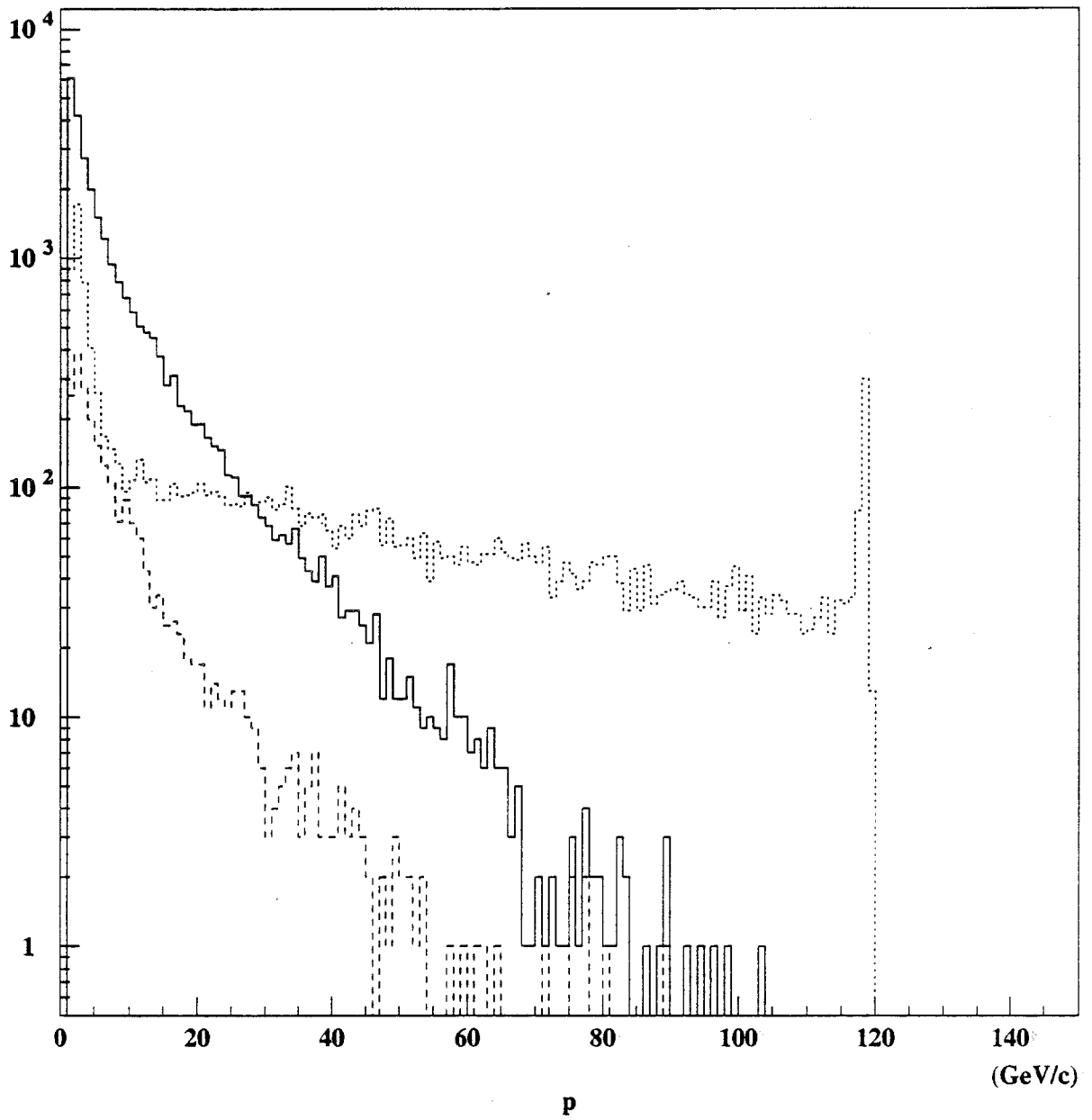

Figure 17: Secondary particle momentum spectra for π^+ (solid), K^+ (dashed), and protons (dotted) for 120 GeV incident protons.

3.6 Question #6

"The Committee feels that the clarity of the proposal could be improved by the addition of an executive summary, which displays in a clear fashion the region of $\sin^2(2\theta)$ *and* Δm^2 *in which oscillations can be discovered; the sub-region in which oscillations into* ν_τ *can be positively identified; the sub-region in which oscillations into* ν_e *can be positively identified; and lastly the sub-regions in which a measurement of the mixing parameters can be performed."*

It is the goal of the MINOS experiment to establish conclusive evidence for neutrino oscillations if they exist in our region of sensitivity, and to establish stringent limits on neutrino oscillation parameters if they do not. Unless otherwise stated, event rates and fluxes in this Section use the standard running assumptions of the MINOS proposal: two years of Main Injector running with 3.7×10^{20} protons/year on target and the full 10 kT MINOS detector.

In the absence of oscillations, it is customary to calculate 90% confidence-level (CL) exclusion plots in the $\sin^2(2\theta)$-Δm^2 plane. We have calculated 90% CL exclusion plots using several independent tests for $\nu_\mu \rightarrow \nu_\tau$ and $\nu_\mu \rightarrow \nu_e$ oscillations and they are shown in Figures 18 and 19. Limit curves from several other tests, such as the neutral current energy distribution, and quasi-elastic channels have not been shown, but they would not cover any additional parameter space besides what has been shown. Another analysis strategy would be to combine all information into one test, such as a χ^2 test for all distributions. The result would be slightly more sensitive than the best limit in each figure.

As described in Section 3.3, the NBB analysis is based on calculating the χ^2,

$$\chi^2 = \sum_i \{\frac{N_i^{far}(E_i) - N_i^{near}(E_i)}{\Delta N_i^{far}(E_i)}\}^2_{CC-like} + \sum_i \{\frac{N_i^{far}(E_i) - N_i^{near}(E_i)}{\Delta N_i^{far}(E_i)}\}^2_{NC-like} \qquad (3)$$

In Figures 5 and 6 in Section 3.3, simulated Monte Carlo data for this analysis are shown. The 90% CL NBB limits, calculated from this equation for NBB running with 45 and 30 GeV pion beams, are shown for $\nu_\mu \rightarrow \nu_\tau$ and $\nu_\mu \rightarrow \nu_e$ in Figures 20, 21, 22, and 23. In each figure, we show the limits based on 2 year and 1 year runs.

There are several ways to summarize how MINOS could discover oscillation signals if they exist. Figure 8.8 in the MINOS proposal, for example, shows the statistical effect in σ for maximal mixing as a function of Δm^2 for the ΔZ test. Here we show in Figures 24 and 25 the regions of parameter space in which we would observe a 4σ or higher effect in each test shown. We point out that for much of the parameter space shown, we would observe greater than 4σ effects in several tests using both the MINOS and Soudan 2 detectors simultaneously and independently.

A different way to express our capability of conclusively establishing neutrino oscillations is to consider specific scenarios. We consider five such scenarios and tabulate the results in Table 1. The scenarios we consider are:

1. Large $\nu_\mu \rightarrow \nu_\tau$ mixing to describe the atmospheric neutrino anomaly ($\sin^2(2\theta) = 1.0$; $\Delta m^2 = 0.01\ eV^2$).

2. Large $\nu_\mu \rightarrow \nu_e$ mixing to describe the atmospheric neutrino anomaly ($\sin^2(2\theta) = 1.0$; $\Delta m^2 = 0.015\ eV^2$).

3. Threefold maximal mixing[3] (e.g., $\Delta m^2 = 0.0072\ eV^2$; $\sin^2(2\theta_{\mu\tau}) = 4/9$; $\sin^2(2\theta_{\mu e}) = 4/9$).

4. Smaller $\nu_\mu \rightarrow \nu_\tau$ mixing ($\sin^2(2\theta) = 0.1$; $\Delta m^2 = 0.1\ eV^2$).

5. Smaller $\nu_\mu \rightarrow \nu_e$ mixing ($\sin^2(2\theta) = 0.1$; $\Delta m^2 = 0.1\ eV^2$).

In column "0" of Table 1 we show the expected results for the no oscillation case in the far detector. Rows in the Table for "TRUE" quantities show the physics implications of the scenario. Event rates listed, such as the number of charged current, neutral current, electron deep inelastic, muon quasi-elastic and electron quasi-elastic event rates include all resolutions, backgrounds and systematic errors described in the MINOS proposal. For each test, an estimate of the statistical and systematic significance for several tests is shown.

Hand-in-hand with the convincing establishment of a neutrino oscillation signature is the measurement of the oscillation mode and parameters. For large mixing, MINOS can separate $\nu_\mu \rightarrow \nu_e$ and $\nu_\mu \rightarrow \nu_\tau$ oscillation signatures from each other, and can measure the parameters Δm^2 and $\sin^2(2\theta)$. In Figure 26 we show the region of parameter space in which we can separate $\nu_\mu \rightarrow \nu_e$ and $\nu_\mu \rightarrow \nu_\tau$ oscillation hypotheses at the 3σ level. The separation is done using a simultaneous fit to the CC/total test and the electrons from longitudinal cuts. Also shown is the region of parameter space in which Δm^2 can be measured by the ΔZ test with a resolution of $8 \times 10^{-3}\ eV^2$ or better. The Z test resolution is always quite good $[\sigma(\Delta m^2) \sim 0.012\ eV^2/\sqrt{N \times \sin^2(2\theta)}]$, so the region shown is the same as that for which we get a 4σ effect or greater.

In the threefold maximal mixing scenario, we would observe both $\nu_\mu \rightarrow \nu_\tau$ and $\nu_\mu \rightarrow \nu_e$ oscillations simultaneously. In one reference for this scenario, the atmospheric, reactor, accelerator and solar data have been fit with $\Delta m^2 = 0.0072\ eV^2$[3]. One way to think about the scenario is with effective parameters $\sin^2(2\theta)(\nu_\mu \rightarrow \nu_e) = \sin^2(2\theta)(\nu_\mu \rightarrow \nu_\tau) = 4/9$; $\Delta m^2 = 0.0072\ eV^2$, which lead to $P(\nu_\mu \rightarrow \nu_e) = P(\nu_\mu \rightarrow \nu_\tau) = 0.13$ for our beam spectrum. In Figure 27, we show our ability to separate that possibility from pure $\nu_\mu \rightarrow \nu_\tau$ or pure $\nu_\mu \rightarrow \nu_e$ oscillations. Shown on the curve are allowed bands for three tests in the space of P_e *versus* P_τ, assuming that we measure the values predicted for the threefold maximal mixing scenario. Each test alone could be consistent with a different linear combination of $\nu_\mu \rightarrow \nu_e$ and $\nu_\mu \rightarrow \nu_\tau$ oscillations. The intersection of the three curves is at the value expected for threefold maximal mixing, and is inconsistent with a value on either the P_e or P_τ axis.

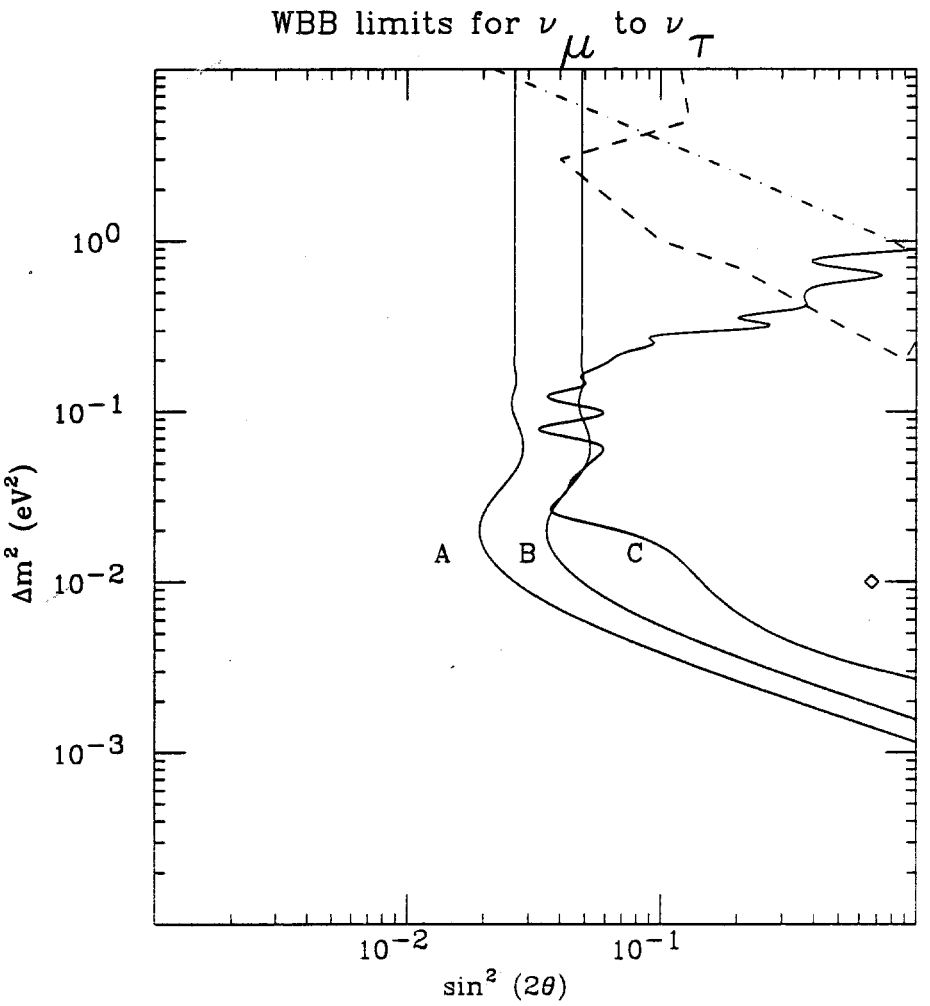

Figure 18: 90% CL curves for $\nu_\mu \rightarrow \nu_\tau$ hypothesis. Curve "A" is for the CC/total test. Curve "B" is for the near/far rate comparison and is dominated by the estimated 2% systematic error. Curve "C" comes from the total energy measurement test. The dashed (dash-dot) curve is the present accelerator limit from CDHS (FNAL E-531). The diamond point shows the Kamiokande best fit parameters.

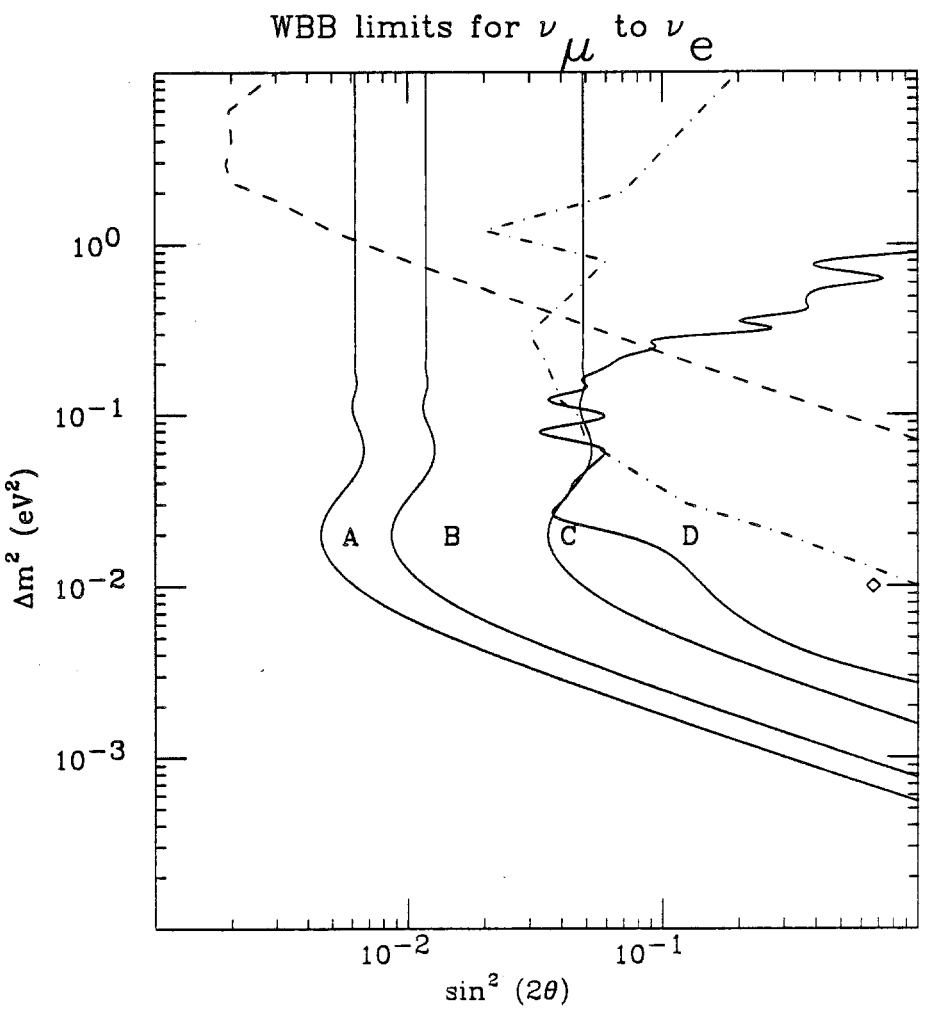

Figure 19: 90% CL curves for $\nu_\mu \rightarrow \nu_e$ hypothesis. Curve "A" uses longitudinal cuts to identify electron showers. Curve "B" is for the CC/total test. Curve "C" is for the near/far rate comparison and is dominated by 2% systematic error. Curve "D" comes from the total energy measurement test. The dashed (dash-dot) curve is the present limit from accelerator (reactor) data. The diamond point shows the Kamiokande best fit parameters.

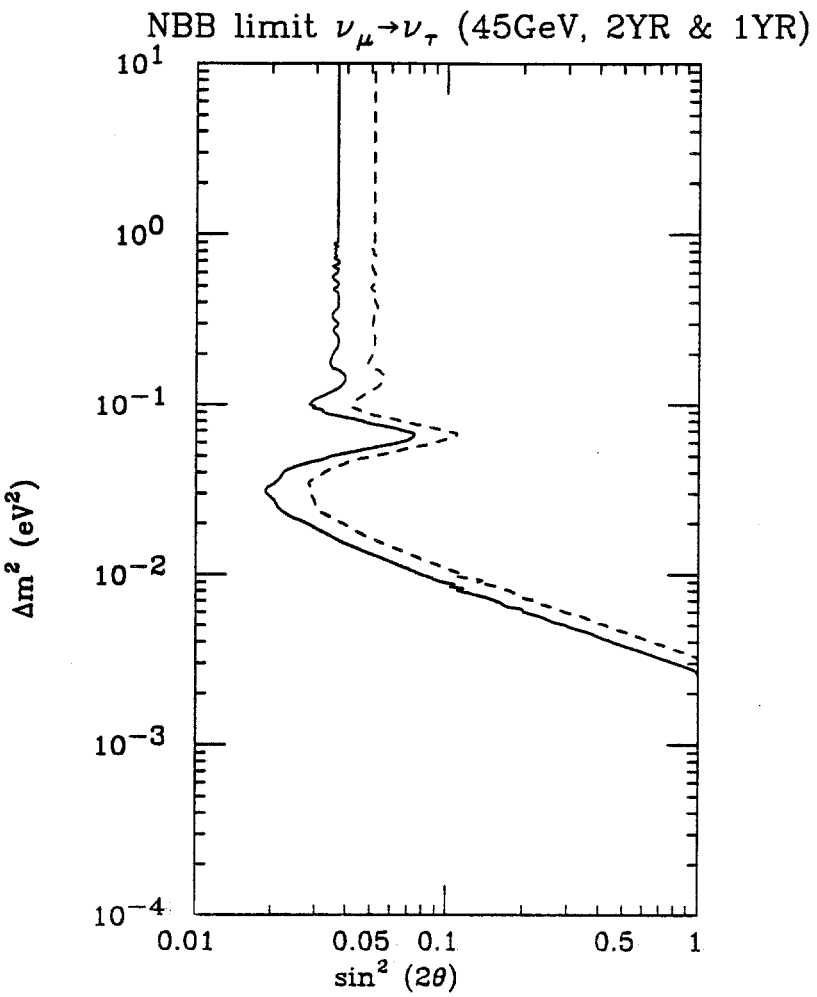

Figure 20: 90% CL curve for $\nu_\mu \to \nu_\tau$ hypothesis with a 45 GeV pion NBB, using inclusive CC and NC analysis. The mean E_ν is 19 GeV. The solid (dashed) curve is for a 2 year (1 year) run.

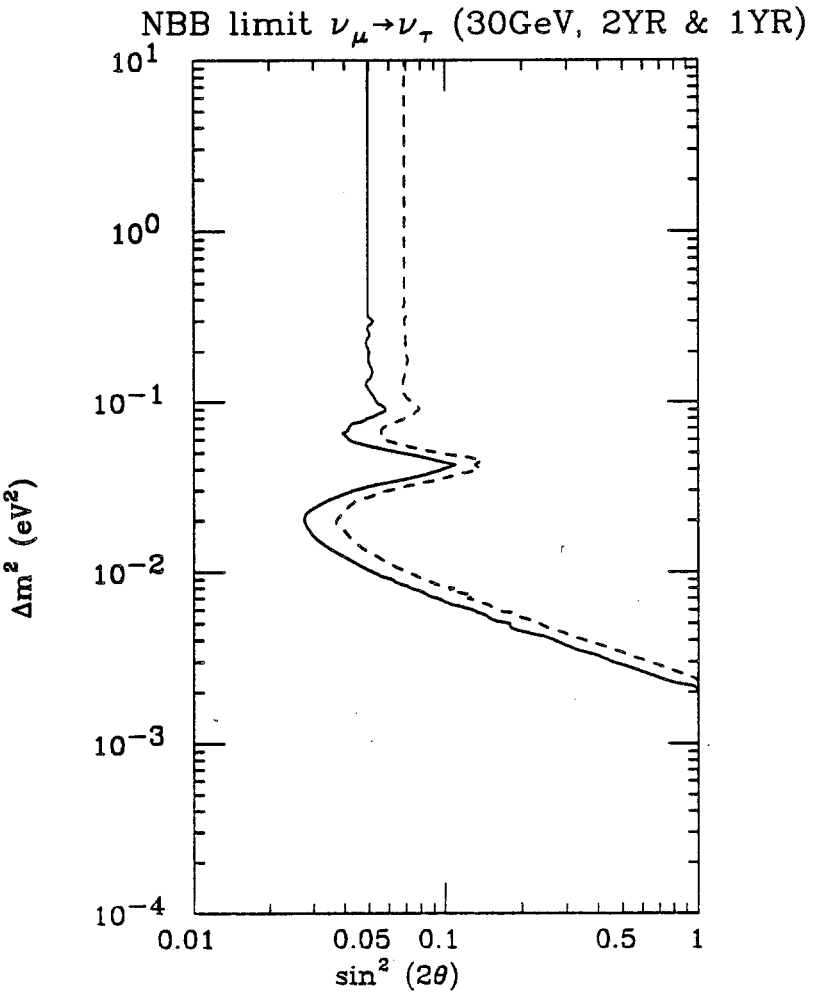

Figure 21: 90% CL curve for $\nu_\mu \to \nu_\tau$ hypothesis with a 30 GeV pion NBB, using inclusive CC and NC analysis. The mean E_ν is 12 GeV. The solid (dashed) curve is for a 2 year (1 year) run.

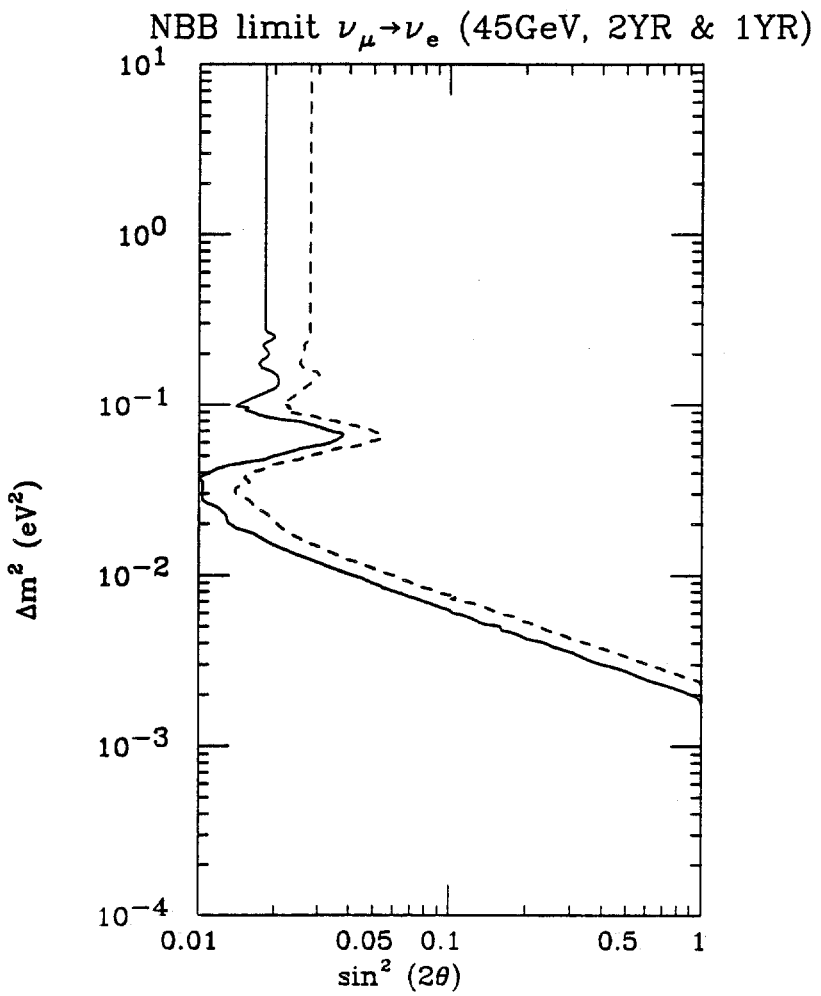

Figure 22: 90% CL curve for $\nu_\mu \to \nu_e$ hypothesis with a 45 GeV pion NBB, using inclusive CC and NC analysis. The mean E_ν is 19 GeV. The solid (dashed) curve is for a 2 year (1 year) run.

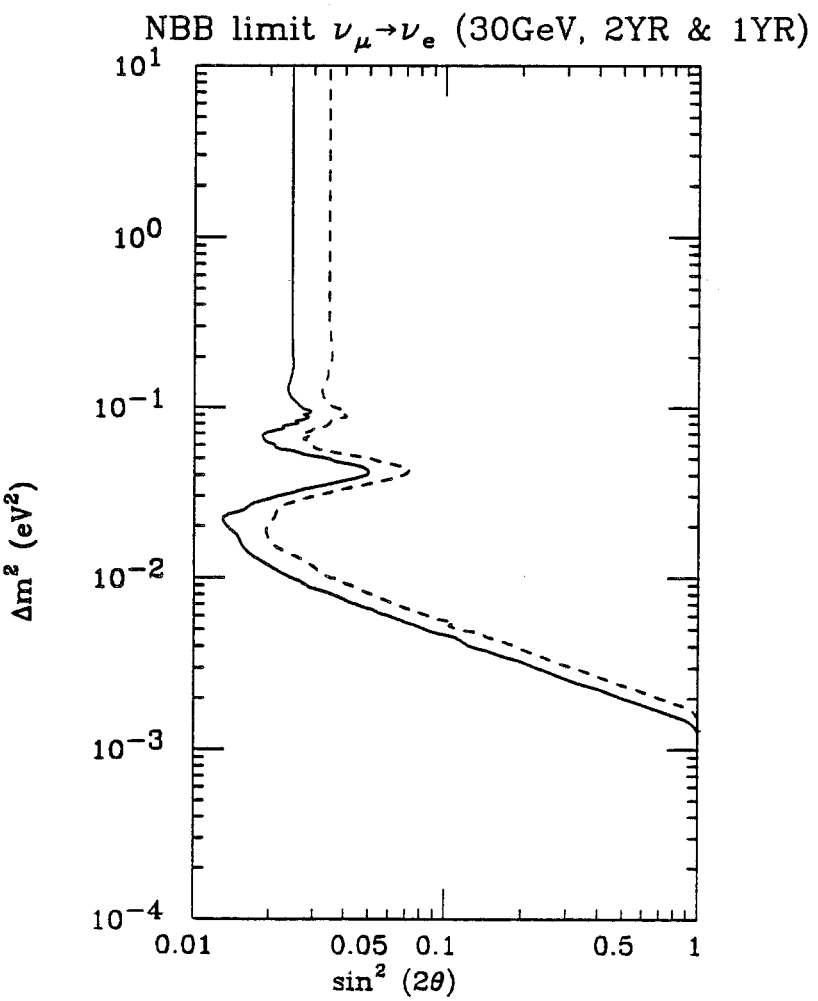

Figure 23: 90% CL curve for $\nu_\mu \to \nu_e$ hypothesis with a 30 GeV pion NBB, using inclusive CC and NC analysis. The mean E_ν is 12 GeV. The solid (dashed) curve is for a 2 year (1 year) run.

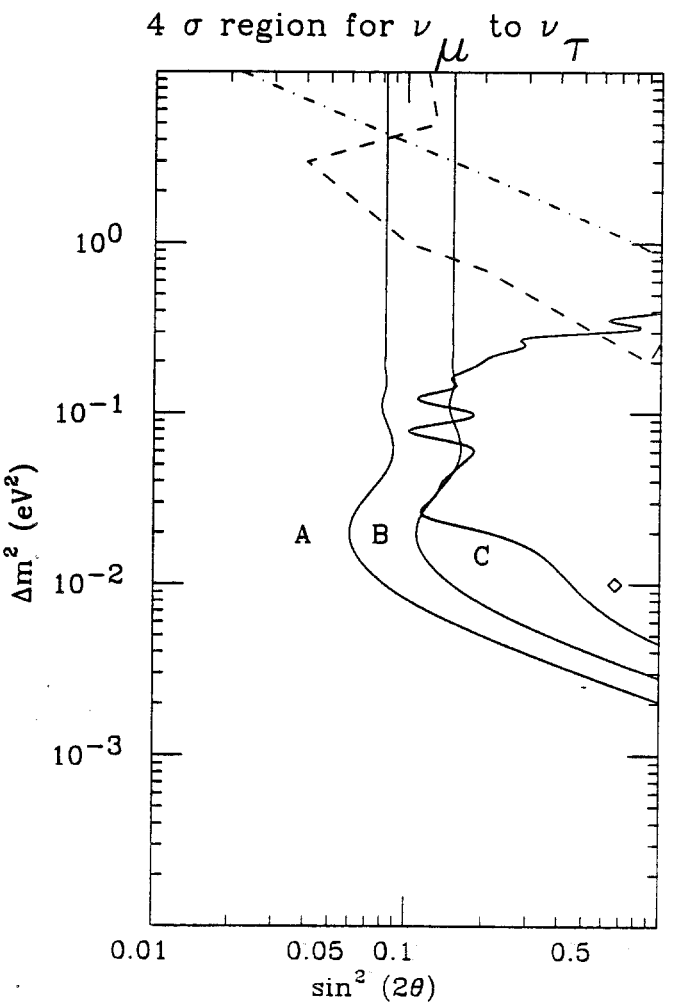

Figure 24: Four σ plots for $\nu_\mu \rightarrow \nu_\tau$ hypothesis in the WBB. For neutrino oscillation parameter space to the right of each curve, we would get a 4σ or greater significance with a two year run in MINOS. Curve "A" is for the CC/total test. Curve "B" is for the near/far rate comparison and is dominated by 2% systematic error. Curve "C" comes from the total energy measurement test. The diamond point shows the Kamiokande best fit parameters.

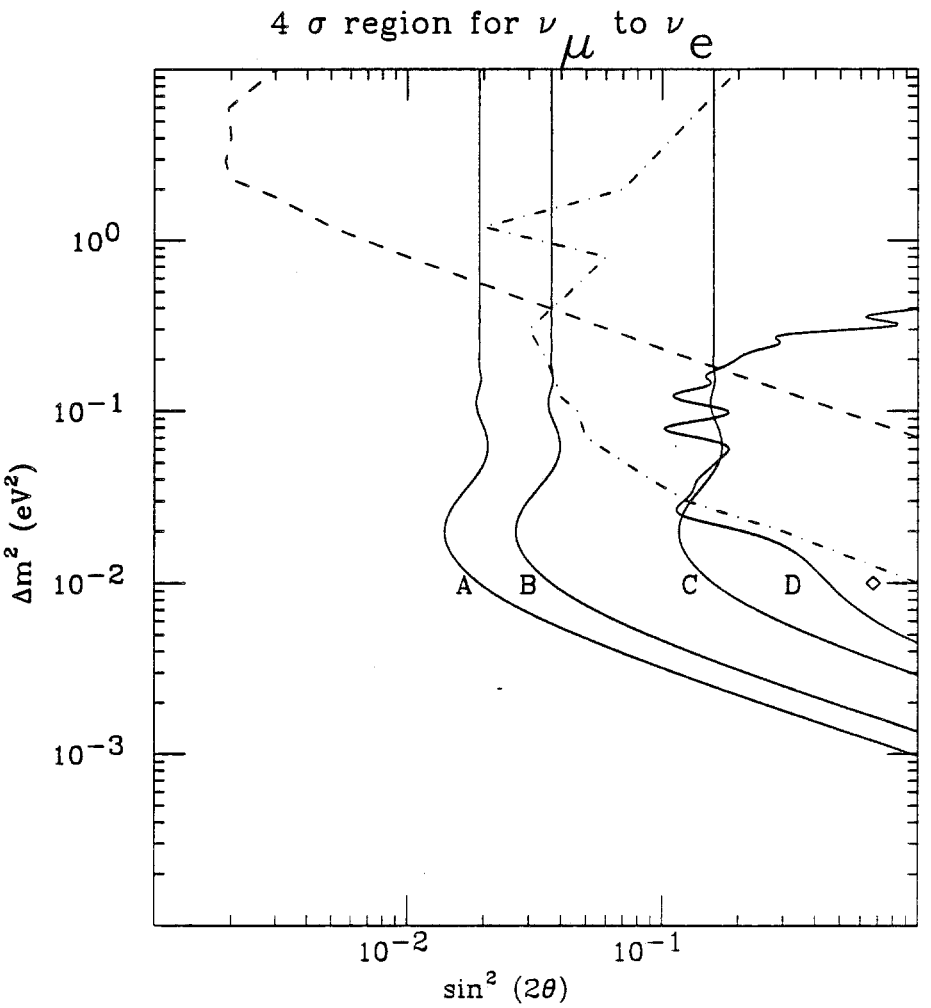

Figure 25: Four σ plots for $\nu_\mu \rightarrow \nu_e$ hypothesis in the WBB. For neutrino oscillation parameter space to the right of each curve, we would get a 4 σ or greater significance with a two year run in MINOS. Curve "A" uses longitudinal cuts to identify electron showers. Curve "B" is for the CC/total test. Curve "C" is for the near/far rate comparison and is dominated by 2% systematic error. Curve "D" comes from the total energy measurement test. The diamond point shows the Kamiokande best fit parameters.

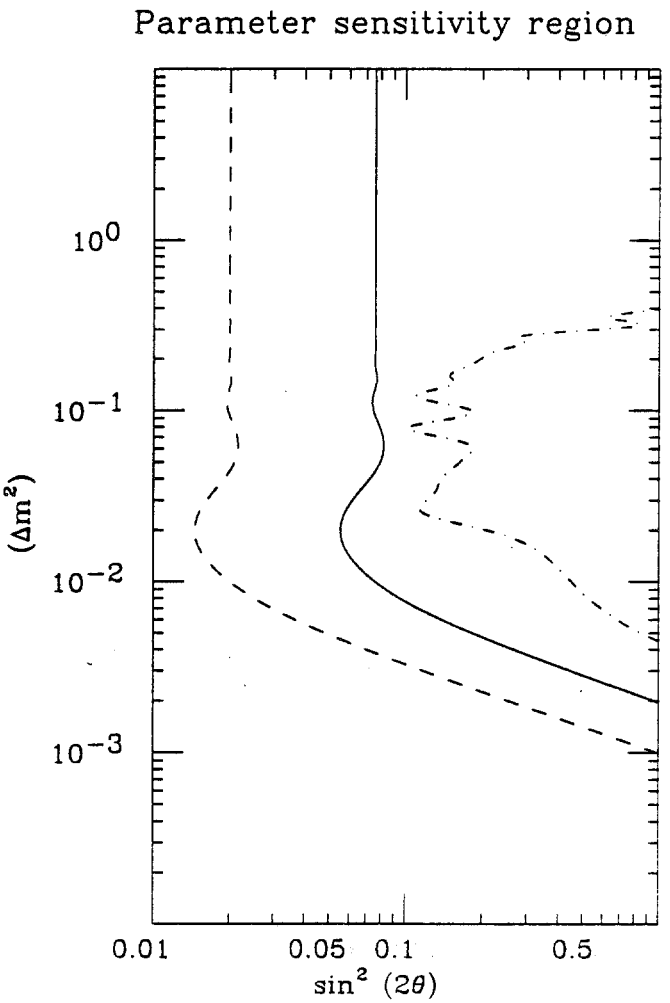

Figure 26: For $\nu_\mu \rightarrow \nu_\tau$ oscillation parameters to the right of the solid curve, MINOS can determine that oscillations are due to $\nu_\mu \rightarrow \nu_\tau$ and not $\nu_\mu \rightarrow \nu_e$ with a significance that is 3 σ or greater. Likewise, for $\nu_\mu \rightarrow \nu_e$ oscillation parameters to the right of the dashed curve, MINOS can determine that oscillations are due to $\nu_\mu \rightarrow \nu_e$ and not $\nu_\mu \rightarrow \nu_\tau$ with a significance that is 3 σ or greater. The dotdash curve shows the region of parameter space in which Δm^2 can be measured. The resolution in Δm^2 is 6 $\times 10^{-4}$ eV^2 or better.

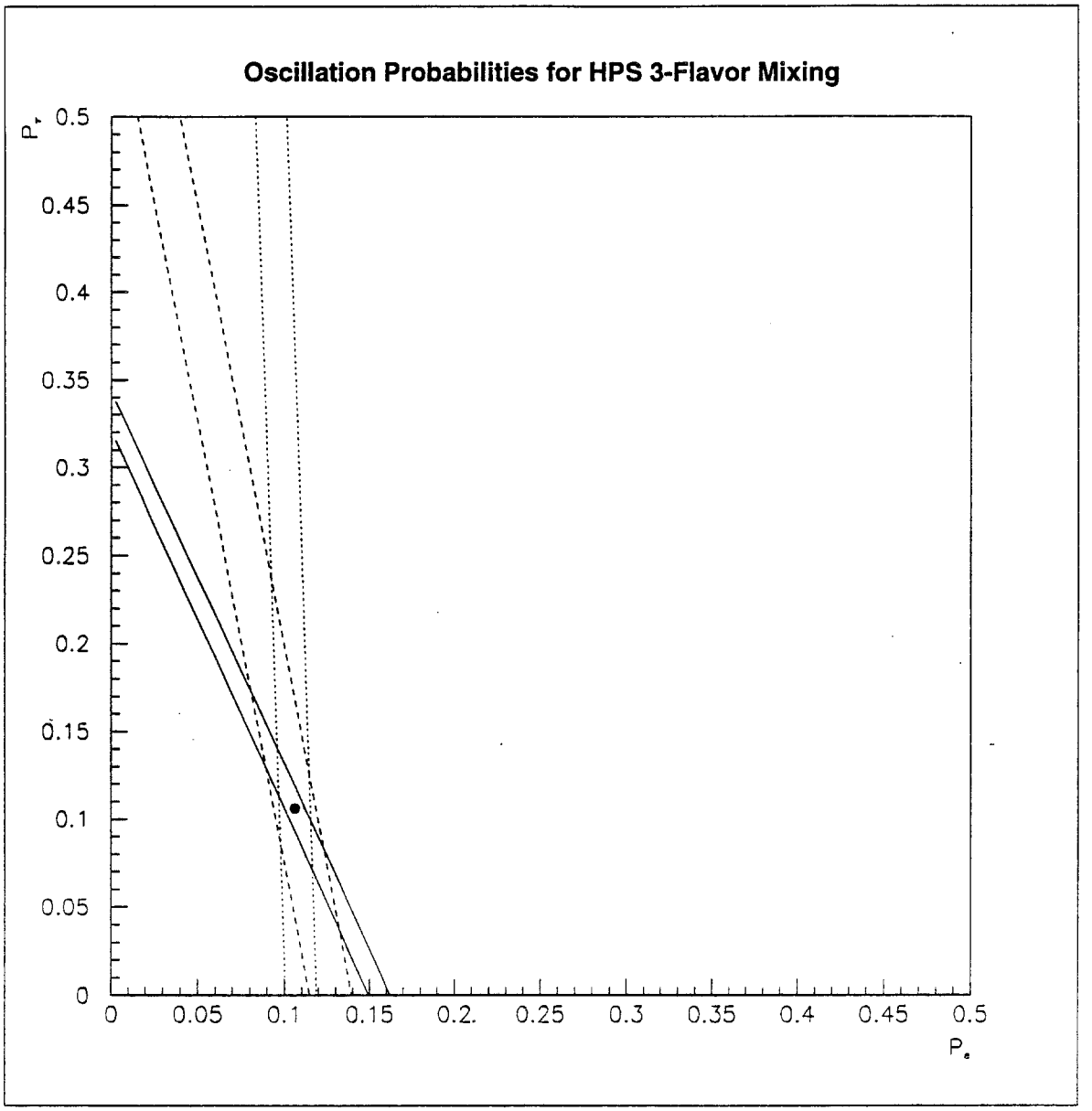

Figure 27: P_τ *versus* P_e assuming measurements as expected for threefold maximal mixing. The three tests used are the T test, electrons, and NC^{far}/NC^{near}. The area between the lines indicates the combination of $\nu_\mu \rightarrow \nu_e$ oscillations (P_e on the horizontal axis) and $\nu_\mu \rightarrow \nu_\tau$ oscillations (P_τ on the vertical axis) which is consistent with the measurement made by that test.

Scenario $\longrightarrow$	0	1	2	3	4	5
Quantity $\downarrow$	no	$\nu_\mu \rightarrow \nu_\tau$	$\nu_\mu \rightarrow \nu_e$	HPS[3]	$\nu_\mu \rightarrow \nu_\tau$	$\nu_\mu \rightarrow \nu_e$
$< P >$	0	0.369	0.551	0.212	0.051	0.051
MINOS events	40200	32360	40200	37948	39116	40200
"TRUE" μ	30793	20029	13826	24437	29305	29222
"TRUE" no μ	9407	12331	26374	13511	9811	10978
called "CC"	29015	19185	14382	23324	27652	27629
called "NC"	11185	13175	25818	14624	11464	12571
T	0.7218	0.5929	0.3578	0.6146	0.7069	0.6873
dT	0.0022	0.0025	0.0024	0.0024	0.0023	0.0023
"TRUE" electrons before cuts	282	881	17094	3658	365	1838
electron candidates	475	552	4846	1367	486	879
non-planar events	1	4	1	*	1	1
Δ Z(Δm^2)	NA	0.20	0.35	0.12	0.018	0.018
Rock μ's	17000	10727	6733	13396	16133	16133
Soudan 2 events	2462	2043	2462	2334	2393	2462
S2 called "CC"	1950	1322	1110	1610	1863	1872
S2 called "NC"	512	644	1418	724	530	596
S2 R	0.262	0.487	1.277	0.450	0.284	0.318
S2 dR	0.013	0.023	0.051	0.020	0.014	0.015
S2 quasi-elastic electrons	9	24	264	63	10	35
S2 quasi-elastic μp	1	6	1	2	2	1
Significance						
MINOS T test	NA	34σ	97σ	28σ	4σ	9σ
MINOS electrons	NA	4σ	200σ	41σ	1σ	19σ
MINOS near/far	NA	17σ	25σ	10σ	2σ	2σ
CC energy	NA	12σ	19σ	10σ	2σ	2σ
NC energy	NA	13σ	$>13\sigma$	*	1σ	*
Non-planarity	NA	$2\sigma'$	-	*	-	-
Soudan 2 R test	NA	10σ	20σ	9σ	2σ	4σ
S2 quasi-elastic μ's	NA	$3\sigma'$	-	$1\sigma'$	$1\sigma'$	-
S2 quasi-elastic e's	NA	$4\sigma'$	85σ	18σ	$1\sigma'$	9σ
Soudan 2 near/far	NA	9σ	12σ	5σ	1σ	1σ
R_μ from rock muons	NA	25σ	116σ	20σ	3σ	6σ

Table 1: Wide-band beam results and significance for 5 scenarios described in the text. Integers represent number of events expected in two years. "TRUE" quantities indicate physics signatures. Column "0" shows expected event rates with no oscillations. Not shown are near detector event rates, which will be 60-1000 times higher than column "0", depending on the choice of radius cut. Observed quantities include all efficiencies, systematic errors and backgrounds described in the MINOS proposal. Errors quoted as σ are calculated assumed to be Gaussian. Errors quoted as σ' are calculated with Poisson statistics, and converted using a two-sided Gaussian for the same chance probability. "*" means no calculation has been done yet. "-" represents no signal.

Scenario 0	No oscillations
Scenario 1	$\nu_\mu \rightarrow \nu_\tau$ for atmospheric; $\Delta m^2 = 0.01\ eV^2$, $\sin^2(2\theta) = 1.0$
Scenario 2	$\nu_\mu \rightarrow \nu_e$ for atmospheric; $\Delta m^2 = 0.015\ eV^2$, $\sin^2(2\theta) = 1.0$
Scenario 3	Threefold Maximal mixing; $\Delta m^2 = 0.0072\ eV^2$
Scenario 4	lower $\nu_\mu \rightarrow \nu_\tau$; $\Delta m^2 = 0.1\ eV^2$, $\sin^2(2\theta) = 0.1$
Scenario 5	lower $\nu_\mu \rightarrow \nu_e$; $\Delta m^2 = 0.1\ eV^2$, $\sin^2(2\theta) = 0.1$
$< P >$	$\int P(e_\nu)\phi_\nu(E_\nu)\sigma_{CC}^{tot}(E_\nu)dE_\nu / \int \phi_\nu(E_\nu)\sigma_{CC}^{tot}(E_\nu)dE_\nu$
MINOS events	Triggered events within the fiducial volume
"TRUE" μ	$\nu_\mu^{CC} + \nu_\tau^{CC}; \tau \rightarrow \mu$
"TRUE" no μ	NC + $\nu_e + \nu_\tau^{CC}; \tau \rightarrow e$ or hadrons
called "CC"	Reconstructed track longer than 20 plates (p124)
called "NC"	No reconstructed track longer than 20 plates
T	CC/total (p127)
dT	statistical error on T ; $dT_{syst} = 0.0029$ (p134)
"TRUE" electrons before cuts	e's from beam ν_e, oscillation ν_e, and $\nu_\tau; \tau \rightarrow e$
electron candidates	Events satisfying longitudinal e cuts (p163)
non-planar events	Event non-coplanarity in $\tau \rightarrow \mu$ decays (p147)
Δ Z(Δm^2)	CC Energy spectrum test (p136)
Rock μ's	μ from ν upstream of detector; μ in Soudan 2 / MINOS ν (p166)
Soudan 2 events	Event rate in Soudan 2 fiducial volume (p168)
S2 called "CC"	Events with 2 m reconstructed tracks
S2 called "NC"	Events without 2 m tracks
S2 R	NC/CC ratio (p168)
S2 dR	Systematic and statistical error on R
S2 quasi-elastic electrons	Identified ν_τ quasis, $\tau \rightarrow e$ (p171)
S2 quasi-elastic μp	Quasis $\tau \rightarrow \mu$ with recoil proton and angle cut (p169)

Table 2: Short description of rows and columns in Table 1. Numbers in parentheses are the page numbers of the MINOS proposal where the quantity is defined or described.

3.7 Question #7

"The collaboration should describe the exploitation of the complementary features of the MINOS and E-803 experiments, both with regard to the physics program and the beam measurements."

E-803 (COSMOS) and MINOS will share the same Main Injector beam and will be operating simultaneously most of the time. Although both experiments are seeking neutrino oscillations, there is little overlap in the primary physics regions covered. E-803 is mainly seeking $\nu_\mu \rightarrow \nu_\tau$ or $\nu_e \rightarrow \nu_\tau$ in a high Δm^2, small $\sin^2(2\theta)$ region not accessible to MINOS, whereas MINOS is mainly exploring a low Δm^2, larger mixing angle region not accessible to E-803. It is conceivable that both experiments could see oscillations. For example, if the correct explanation for the atmospheric neutrino anomaly is $\nu_\mu \rightarrow \nu_e$ oscillations, MINOS might see this and E-803 might see $\nu_\mu \rightarrow \nu_\tau$, where ν_τ is "cosmological". If one of the LSND interpretations of its data is correct — $\nu_\mu \rightarrow \nu_e$ with $\delta m^2 \approx 6\ eV^2$ and $sin^2 2\theta \approx 0.01$ — the situation at Fermilab would be very interesting. Both long and short baseline experiments might see the effect in $\nu_\mu \rightarrow \nu_e$, which could be a powerful confirmation. An estimate of the $\nu_\mu \rightarrow \nu_e$ sensitivity indicates both experiments cover this region, as shown in Fig. 28. The assumptions used for this estimate are discussed below. Understanding the ν_e content of the beam as well as the efficiency of each experiment to find ν_e events is crucial. Thus Fig. 28 should only be considered suggestive at this time.

To summarize, the physics programs complement each other in the following ways:

1. In the search for oscillations to ν_τ they cover quite different regions in $\sin^2(2\theta)$ - Δm^2 space.

2. It is conceivable that the two experiments will simultaneously observe oscillations, but into different flavors.

3. If LSND is observing $\nu_\mu \rightarrow \nu_e$ oscillations, either E-803 or MINOS or both should be able to confirm this in a convincing way.

Since E-803 sits a short distance upstream of the MINOS near detector the question has been raised as to what extent E-803 could supplement the calibration functions of the beam monitor: to determine the ν_e content of the beam, and the energy and radial distributions of neutrino events at the near detector location.

It should be pointed out here that any information that E-803 could provide in this respect does not depend in any way on locating or measuring neutrino events in the emulsion. All measurements would come from the downstream spectrometer system which will record essentially all events produced in the nuclear emulsion target. These data will be recorded on tape and presumably would be available on a time scale comparable to that for MINOS beam monitor data.

The energy and radial distributions, as well as energy as a function of radius, would be determined from identified ν_μ CC events in the E-803 data. The question is how well

E-803 can do this from the MINOS point of view. We emphasize that the energy *vs* radius measurement is extremely important to MINOS in predicting the beam at the far detector from its properties at the near detector. For this reason the beam monitor dimensions are set at 3 m $\times$ 3 m. On the other hand, the emulsion target in E-803 is 1.4 m $\times$ 1.8 m. Therefore, E-803 could be a very important check for the MINOS beam monitor, but could not be a substitute.

In addition, there could be serious acceptance corrections involved, particularly for low energy neutrinos, e.g., slow or large angle muons which do not reach the muon identifier. We point out that whereas the neutrino energy region of 5-10 GeV (where muon acceptance corrections could be large) is relatively unimportant for the primary E-803 goal (because of the low ν_τ cross section) this region could be very important for MINOS with regard to tests such as the CC/total or CC and NC energy distributions. If, for example, $\Delta m^2 \approx 0.01\ eV^2$ (the Kamiokande region) the oscillation effect at the far detector is greatest in just this energy range.

Other effects in E-803 which could degrade the energy resolution are the conversion of γ's in the emulsion rather than in the electromagnetic calorimeter, and the lack of a hadron calorimeter to catch neutrons and K_L^0. The former effect could be minimized by choosing neutrino events from the downstream third of the emulsion. Some information on neutral hadrons might be obtainable from interactions in the electromagnetic calorimeter or muon identifier, and corrections for missing neutrals might also be made kinematically. We understand that the E-531 emulsion-spectrometer did quite well at low energies, and E-803 should be much better. But a quantitative measure of how well E-803 can determine the energy distribution, particularly at the lower energies, requires a detailed Monte Carlo study which E-803 has not yet carried out.

E-803 could also provide information on the ν_e and $\bar{\nu}_e$ content of the beam. By using the downstream third of the emulsion, one can minimize the effect of electron conversion within the emulsion. The electron momentum and sign would be well measured from curvature in the E-803 magnetic field region, and the identification would be made by showering in the electromagnetic calorimeter. Again, there could be serious acceptance corrections for low energy events, and this would need to be studied by E-803.

Figure 28 shows estimated $\nu_\mu \rightarrow \nu_e$ limit curves from MINOS and COSMOS. The dot-dash curve is the limit using longitudinal cuts in the far detector. In the near detector, there is an estimated 0.670 $\pm$ 0.042% $\nu_e + \bar{\nu}_e$ background in the beam. Below 15 GeV, the estimated fraction is 0.170 $\pm$ 0.010 %. Both COSMOS and the MINOS near detector have very high statistics. For this measurement both experiments will be limited by the systematic error in the beam, which is discussed in the next paragraph. Since the beam systematic error is the same for each detector, the sensitivity for both experiments will be the same. The solid curve uses the full energy spectrum and the estimated 6% systematic error. Both MINOS and COSMOS will be able to reconstruct ν_e^{CC} energies, and sensitivity improves at low energy, where backgrounds and systematic errors are both lower. The effect for LSND parameters ($\Delta m^2 \sim 6\ eV^2$; $\sin^2(2\theta) \sim 10^{-2}$) is at quite low energy in this beam. The dashed curve in the figure is the limit that could be set by both experiments with an energy cut, $E_\nu < 15\ GeV$, and the more conservative 10% systematic error (see below).

The 6% estimated systematic error in this value comes mainly from the uncertainty in K_{long} production by 120 GeV protons. The fraction of events from charged K_{e3} decays is not

FERMILAB-Proposal-0875

P-875: A Long-baseline Neutrino Oscillation Experiment at Fermilab

February 1995

The MINOS* Collaboration

E. Ables[10], W. W .M. Allison[13], G. J. Alner[14], D. S. Ayres[1], B. Barish[3], W. L. Barrett[19], R. H. Bernstein[5], R. Bionta[10], R. E. Blair[1], D. Bogert[5], P. M. Border[11], C. Bower[7], C. B. Brooks[13], W. L. Bryan[12], D. Burke[3], J. Byrne[16], R. Carney[10], V. A. Chechin[9], D. Ciampa[11], J. H. Cobb[13], R. J. Cotton[14], H. Courant[11], D. A. Crane[1], P. Cushman[11], A. David[17], P. G. Dawber[16], J. W. Dawson[1], N. Diaczenko[17], T. H. Fields[1], H. Flick[6], H. M. Gallagher[1,11], M. Gebhard[7], M. C. Goodman[1], K. Green[16], V. J. Guarino[1], J. Hanson[3], P. G. Harris[16], R. Heinz[7], K. Heller[11], N. Hill[1], Y. Ho[4], A. R. Holmes[13], G. Irwin[15], U. Jagadish[12], D. Johnson[5], T. Kafka[18], G. Koizumi[5], E. P. Kuznetsov[9], A. Lan[6], K. Lau[6], W. Lee[4], M. Libkind[10], P. J. Litchfield[14], J.Liu[6], N. P. Longley[3], W. A. Mann[18], M. L. Marshak[11], D. Maxam[11], E. N. May[1], B. Mayes[6], D. G. Michael[3], R. H. Milburn[18], L. Miller[7], W. H. Miller[11], G. Mitselmakher[5], G. Mo[6], J. Morfin[5], S. Mrenna[3], S. Mufson[7], J. Musser[7], A. Napier[18], D. Naples[5], F. Nezrick[5], S. O'Day[5], W. Oliver[18], H. Olsan[10], L. Ott[10], E. Parker[10], D. Parks[6], G. F. Pearce[14], C. W. Peck[3], D. H. Perkins[13‡], E. A. Peterson[11], D. A. Petyt[13], L. Pinsky[6], L. E. Price[1], J. Pyrlik[6], G. Rameika[5], K. Ruddick[11], R. Rusack[11], J. Schneps[18], P. V. Schoessow[1], M. H. Schub[11], R. V. Seidlein[1], P. D. Shield[13], V. Singh[11], V. Smotriaev[8], J. Swan[10], J. Thomas[13], J. L. Thron[1], T. Toohig[2], H. J. Trost[17], I. Trostin[8], V. Tsarev[9], L. R. Turner[1], R. L. Wastie[13], R. C. Webb[17], R. Weinstein[6], S. J. Werkema[5], N. West[13], S. G. Wojcicki[15†], D. Wright[10], C. Wuest[10], and T. Yokota[10].

† **Spokesman** ‡ Retired

Argonne[1] - Boston College[2] - Caltech[3] - Columbia[4] - Fermilab[5] - Houston[6] - Indiana[7] - ITEP[8] - Lebedev[9] - Livermore[10] - Minnesota[11] - Oak Ridge[12] - Oxford[13] - Rutherford[14] - Stanford[15] - Sussex[16] - Texas A&M[17] - Tufts[18] - Western Washington[19]

* **Main Injector Neutrino Oscillation Search**

AA07127

Contents

1 Introduction **14**

2 Physics Motivations and Goals **16**

2.1 Physics motivations 16

2.1.1 Neutrino mass 16

2.1.2 Neutrino oscillations 17

2.1.3 The solar neutrino deficit 17

2.1.4 The missing matter problem 17

2.1.5 The atmospheric neutrino deficit 18

2.2 Discussion of atmospheric neutrino results 18

2.2.1 The flavor ratio 18

2.2.2 The Kamiokande angular distribution 21

2.2.3 Upward muons 22

2.3 Theoretical scenarios 23

2.4 Implications for a long baseline experiment 24

2.5 Sensitivity 26

2.5.1 Wide-band beam tests sensitive to both $\nu_\mu \to \nu_\tau$ and $\nu_\mu \to \nu_e$ 27

2.5.2 τ signatures in a wide band beam 27

2.5.3 τ signatures in a narrow band beam 28

2.5.4 Searches for $\nu_\mu \to \nu_e$ 28

2.5.5 MINOS sensitivity in Δm^2 and $\sin^2(2\theta)$ 28

3 Neutrino Beam **30**

3.1 Introduction 30

3.2 Running strategies 31

3.3 Focusing devices 31

3.4 Neutrino flux calculations 32

3.5 Decay pipe optimization 33

3.5.1 Optimizing the ν_τ rate at the far detector 34

3.5.2 Variation of the ν_τ rate at the near detector 38

3.6 Precision of beam pointing to the far detector 41

3.7 Wide band beam 43

3.7.1 WBB optics 45

3.7.2 WBB performance 46

3.7.3 WBB characteristics at near and far detectors 46

3.7.4 WBB backgrounds . . . 49
3.8 Narrow band beam . . . 50
3.8.1 NBB optics . . . 51
3.8.2 NBB performance . . . 54
3.8.3 NBB backgrounds . . . 58
3.9 Beam monitoring . . . 59

4 Far Detector Site **61**
4.1 Location, access, local facilities . . . 61
4.2 The Soudan Mine and the laboratory lease . . . 62
4.3 Soudan 2 Laboratory . . . 63
4.4 Excavation plan . . . 64
4.5 Lab outfitting and utilities . . . 66
4.6 Funding, costs and schedules . . . 67

5 Far Detector **70**
5.1 Introduction . . . 70
5.2 Overview of the detector . . . 70
5.3 Size and shape of the far detector . . . 72
5.4 Steel absorbers and construction . . . 73
5.5 Magnet coil and magnetic properties . . . 77
5.6 Active detectors . . . 78
5.7 Readout electronics . . . 82
5.8 High voltage system . . . 86
5.9 Gas system . . . 87
5.10 Online computing . . . 89
5.11 Construction and Installation . . . 91
5.12 Options for Detector Construction . . . 93
5.13 Soudan 2 detector . . . 94

6 Near Detector **96**
6.1 Near detector overview . . . 96
6.2 Description of the MINOS near detector . . . 97
6.2.1 The beam monitor calorimeter . . . 97
6.2.2 The steel calorimeter . . . 99
6.2.3 The Soudan 2 near detector . . . 100
6.3 Beam monitoring . . . 100
6.4 Detector elements . . . 102
6.5 Construction and installation . . . 102
6.6 Online data taking . . . 103
6.7 Experimental hall requirements . . . 103

7 Simulation of Detector Response **105**
7.1 Introduction . . . 105
7.2 Software . . . 105
7.2.1 General comments . . . 105
7.2.2 Simulation procedures . . . 106
7.3 Detector response . . . 107
7.4 Resolutions . . . 110
7.4.1 Muon angular resolution . . . 110
7.4.2 Muon momentum measurement and resolution . . . 111
7.4.3 Hadron energy . . . 116
7.4.4 Hadron angle . . . 118
7.4.5 Electron energy . . . 120
7.4.6 Shower axis reconstruction and angular resolution . . . 123
7.5 NC/CC separation . . . 124

8 Physics Signatures **126**
8.1 Introduction . . . 126
8.2 Measurement of CC/total . . . 127
8.2.1 Formalism . . . 127
8.2.2 Statistical errors . . . 129
8.2.3 Systematic errors . . . 130
8.2.4 Summary of $\frac{cc}{total}$ errors . . . 134
8.3 Tests using energy measurements of CC events . . . 136
8.4 Near/far detector comparison ("disappearance" experiment) . . . 141
8.5 Wide band beam, τ identification . . . 144
8.5.1 $\tau \rightarrow$ hadrons and $\tau \rightarrow$ e . . . 144
8.5.2 $\tau \rightarrow \mu\nu\nu$ planarity analysis . . . 147
8.5.3 τ detection in quasi-elastic channels . . . 150
8.6 Narrow band beam, τ signatures . . . 151
8.6.1 Introduction . . . 151
8.6.2 $\tau \rightarrow \mu$ for low-y events . . . 152
8.6.3 Total energy measurements with muons . . . 154
8.6.4 Near/far comparison of total energy measurements . . . 156
8.6.5 QE-like events: τ decaying into electrons . . . 160
8.7 $\nu_\mu \rightarrow \nu_e$ . . . 163
8.7.1 $\frac{cc}{total}$ analysis . . . 163
8.7.2 $\nu_\mu \rightarrow \nu_e$ oscillations using longitudinal cuts in the WBB . . . 163
8.7.3 Other wide band beam tests for $\nu_\mu \rightarrow \nu_e$ . . . 165
8.7.4 $\nu_\mu \rightarrow \nu_e$ oscillations, narrow band beam . . . 166
8.8 Rock muons . . . 166
8.9 Use of Soudan 2 . . . 168
8.9.1 $\frac{cc}{total}$ test . . . 168
8.9.2 ν_τ quasi-elastic events . . . 169
8.10 Summary and discussion . . . 173

9 Nonaccelerator Physics Opportunities **177**
9.1 Introduction 177
9.2 Atmospheric neutrinos in the MINOS detector 177
9.2.1 Interaction rates and trigger efficiency 178
9.2.2 Sensitivity to atmospheric neutrino oscillations 179
9.3 Cosmic ray muons 179
9.3.1 Cosmic ray composition 182
9.3.2 Point source searches 183
9.3.3 Large scale anisotropies 185

10 Evolution of the Detector Design **186**
10.1 Introduction 186
10.2 Absorber media and granularity 186
10.3 Other active detectors 187
10.4 Soudan 2 modifications 188
10.5 Active shield around the detector 188
10.6 Changes in minor parameters 189

11 Detector Development Program **190**
11.1 Introduction 190
11.2 Reference detector technology 190
11.3 Mechanical structure engineering 191
11.4 Alternative technologies 191
11.4.1 Scintillator 191
11.4.2 Resistive plate chambers 192
11.4.3 Other technologies 192

12 Cost Estimates and Schedules **193**
12.1 Cost Estimates 193
12.1.1 Introduction 193
12.1.2 Electronics 193
12.1.3 Active detectors 194
12.1.4 Calorimeter and magnet steel 194
12.1.5 Installation Costs 196
12.1.6 Level 3 WBS cost summary 198
12.1.7 Itemized WBS Costing 199
12.1.8 MINOS cost scaling with far-detector mass 204
12.2 Schedules 205
12.2.1 Construction and installation 205
12.2.2 Funding profile 205

13 Summary **211**

Appendices **213**

A The MINOS Collaboration **213**
A.1 Collaboration resources 213
A.2 Collaboration structure 214

B The Soudan 2 Detector **217**
B.1 Detector description 217
B.1.1 Electronics readout 218
B.2 Detector status and operation 219
B.3 Performance and calibration 220
B.3.1 Module performance 220
B.3.2 Module calibration 221
B.4 Detector summary 222
B.5 Soudan 2 upgrades proposed for P–822 223

C Bibliography **236**

List of Tables

2.1 The atmospheric neutrino flavor ratio. Quoted errors are statistical and systematic added in quadrature. 20
2.2 The data on the atmospheric neutrino deficit. TR refers to single tracks, SH to single showers 20
2.3 Neutrino induced upward event rates in IMB. 22
2.4 Upward muon fluxes. The units for Kamiokande are $10^{-13}\text{cm}^{-2}\text{s}^{-1}\text{sr}^{-1}$; for IMB, events per day; for Baksan and MACRO, the total number of observed events. 23
2.5 Several theoretical neutrino mass scenarios 24

3.1 Comparison of the NBB ν_μ and ν_τ charged current and quasi-elastic + single pion event rates per kT-year. The ν_μ rates assume no oscillations, and the ν_τ rates assume mixing parameters $\sin^2(2\theta) = 1$, and $\Delta m^2 = 0.015$ eV^2. 54

4.1 Preliminary cost estimates for the new laboratory construction 69

7.1 Values of the constants a and c in Equations 7.11 and 7.13 for three detector granularities. 122

8.1 Expected event ratios with and without $\nu_\mu \rightarrow \nu_\tau$ oscillations. Effects due to charm, ν_e background and misidentification are included. Errors in the second column are statistical. The number of sigma combining statistical and systematic errors in quadrature is in the last column. 130
8.2 Predicted charm cross sections as a fraction of the total charged current cross section. 133
8.3 Summary of statistical and systematic errors 134
8.4 NBB event rates without (left) and with (right) oscillations ($\Delta m^2 = 0.015\ eV^2$ and $\sin^2(2\theta) = 1.0$.) in a two year running period. 154
8.5 Table showing how the π^0 background reduces as we make cuts to select the QE-like electron signal. E'_{had} is the total energy minus the most energetic π^0 energy. 162
8.6 Expected event ratios with and without $\nu_\mu \rightarrow \nu_e$ oscillations. Effects due to charm, ν_e background and misidentification are included. Errors in the second column are statistical. The number of sigma combining statistical and systematic errors in quadrature are in the last column. 163

8.7 Percentage of events passing analysis cuts for a $\nu_\mu \rightarrow \nu_e$ oscillation appearance signature. The cuts are applied successively. 166
8.8 Rates for $R'' = nc/cc$; $R_{\frac{\mu}{\nu}}$ = Rock muons/contained vertex ν events; and $R_{near/far}$ = near/far event ratios. Rates are for the existing detector and include misidentification, charm and ν_e's. The column with P=0.345 corresponds to near maximal mixing as suggested by the Kamiokande data. . . . 169

9.1 Trigger efficiency for various event types and trigger requirements for ν's with energy greater than 3.5 GeV and averaged over all incidence angles out to 60 degrees (2π steradian acceptance). 180
9.2 Number of events in a 30 kT-year exposure for atmospheric ν's for various oscillation hypotheses. The errors shown are one σ statistical errors only. It is expected that there will be systematic errors of about 8% for the 'hadron-like' sample of events and 2% for the energetic muon and 'electron-like' event samples. 182

12.1 Manpower for the assembly of the main part of the detector. 197
12.2 Overhead cost during assembly period. 198

A.1 Full time equivalents for MINOS from 1995 through 2002 215

List of Figures

2.1 Atmospheric ν_μ energy spectra for different types of experiments. 19

2.2 The survival probability $P(l \rightarrow l)$ measured in solar, atmospheric, reactor and accelerator experiments, corrected according to the threefold maximal mixing scenario. 25

2.3 MINOS two year 90% CL limit curves for $\nu_\mu \rightarrow \nu_\tau$ oscillations. Curve "A" is for the $\frac{cc}{total}$ test. Curve "B" is for the near/far rate comparison and is dominated by 4% systematic error. Curve "C" comes from the total energy measurement test. The diamond point shows the Kamiokande best fit parameters. 29

3.1 Comparison of the ν_τ event rates at Soudan for decay lengths from 300 to 1000 m and decay pipe radii from 0.25 to 4.0 m using the WBB. 35

3.2 Comparison of the ν_τ event rates at Soudan for decay lengths from 300 to 1000 m and decay pipe radii from 0.25 to 3.0 m using a generic 45 GeV/c NBB. 36

3.3 Comparison of the ν_μ and ν_τ charged current and ν_τ quasi-elastic event rates for maximal mixing and the ν_τ event rates at the Kamiokande best fit $\nu_\mu \rightarrow \nu_\tau$ oscillation point versus decay pipe length. The event rates are at Soudan for the WBB with an optimized decay pipe radius for each decay pipe length. . 37

3.4 Comparison of the ν_τ event rates at Fermilab for decay lengths from 300 to 1000 m and decay pipe radii from 0.25 to 3.0 m for the WBB. Note the suppressed zero on the vertical scale. 39

3.5 Comparison of the ν_τ event rates at Fermilab for decay lengths from 300 to 1000 m and decay pipe radii from 0.25 to 3.0 m using a generic 45 GeV/c NBB. Note the suppressed zero on the vertical scale. 40

3.6 a) A comparison of NUADA and PBEAM calculations of the ν_μ beam profile at the far detector (note the suppressed zero on the vertical scale), b) The ν_μ flux normalized by the area of the 10 m bin size annulus, and c) the normalized ν_e flux *vs* distance from beam center at the far detector for a finer distance scale, using the PBEAM program. Only the relative values on the vertical scales are important. 42

3.7 Comparison of the ν flux (ν per meter^2) from the three beam programs at the near detector. NUADA results are shown by the solid histogram, NUANL by the points with error bars, and PBEAM by the dashed histogram. 43

3.8 Comparison of the ν flux from the three beam programs at the far detector. NUADA results are shown by the solid histogram, NUANL by the points with error bars, and PBEAM by the dashed histogram. 44

3.9 The shape and optics of the WBB horns. Rays 1, 2, and 3 illustrate the bending of particle trajectories in the B field between the inner and outer conductors. 45
3.10 Comparison of the ν flux (ν's per meter^2) *vs* energy using the $r < 25$ cm cut at the near detector (histogram) and all ν at the far detector (diamonds). . . 47
3.11 Ratio of the ν flux *vs* energy using the 25 cm cut at the near detector and all ν at the far detector. 48
3.12 The ν_μ, ν_e, $\overline{\nu}_\mu$, and $\overline{\nu}_e$ flux for the 800 m nominal decay pipe. The absolute value of the vertical scale is arbitrary. Only the relative values for each ν type are important. 49
3.13 Oscillation probability versus neutrino energy for $\sin^2(2\theta) = 1$ for neutrinos at Soudan for various Δm^2. 51
3.14 The layout in the beam direction of the two NBB options compared with that of the WBB. The vertical scale is in feet with each division equal to five feet. The arrows illustrate the lengths of the WBB and the NBB with a 1 cm radius lithium lens. 52
3.15 The optics of the two NBB options. 53
3.16 Energy spectrum of NBB ν_μ events for several radial slices at the near detector. 56
3.17 Energy spectrum of ν_μ events at the far detector from the NBB with a reduced low-energy tail. 57

4.1 Plan view of the proposed arrangement of the new and existing laboratories at Soudan. 65
4.2 Elevation view of the proposed arrangement of the new and existing laboratories at Soudan. 66

5.1 Overview of the far detector for MINOS. 71
5.2 Fiducial fraction of the total mass versus the detector half-width assuming containment parameters for optimum muon momentum measurement. 73
5.3 Fiducial fraction of the total mass versus the detector half-width assuming containment parameters for optimum hadron containment. 74
5.4 Details of steel absorber plate assembly and support. 75
5.5 Magnetic field contour map for the octagonal plates with 10^4 amp-turns. The innermost field contour is 1.8 T, and the outermost is 0.8 T. 78
5.6 Magnet coil installation on the steel will be in three separate segments along the detector. 79
5.7 Construction of individual streamer tube packages. Both an end view and an isometric view of the end of a chamber are shown. The tube pitch is 1 cm. . 80
5.8 Overview of the setup for the readout electronics. 83
5.9 Block diagram for components of the front-end electronics strip boards. . . . 84
5.10 Block diagram for logic in the front-end custom chips. 85
5.11 Block diagram for the gas mixing, circulation and distribution system. 88
5.12 Time-line for the far detector installation. 92
5.13 Layout of the detector halls showing space available for construction. 93
5.14 A possible arrangement of modules in a concrete/steel option. 94

6.1 Layout of the Near Detector 98
6.2 Magnet geometry for MINOS Near Detector. 100
6.3 Magnetic field in the near detector magnet 101
6.4 Layout of Soudan 2 modules for the near Soudan 2 detector. 101
6.5 Layout of the near detector hall 104

7.1 Simulated NC event in the MINOS reference detector. The horizontal scale is *detector planes* (6 cm per unit) and the vertical scale is *strip widths* (2 cm per unit). The event is approximately 90 cm long. 108
7.2 Simulated CC event in the MINOS reference detector. Same scales as in Figure 7.1. The event is approximately 12 m long. 109
7.3 Average angular resolution for muons. 111
7.4 Muon range in iron. 112
7.5 Resolution for range and magnetic momentum measurements. 113
7.6 Muon range measurement for 5 GeV muons. Events in which the number of hits divided by the number of planes is greater than 4 are shown in the unshaded region. 114
7.7 Distribution of momentum measurement using a simple tracking algorithm to study the non-Gaussian tails. Events which have more than 40 hits in addition to those associated with the muon track are shown in the non-shaded region. 115
7.8 Histograms of the number of crossings for the four hadron energy ranges shown. 117
7.9 Number of crossings as a function of hadron energy. The curve is a quadratic fit to the points. 117
7.10 Hadronic energy resolution as a function of hadronic energy. 118
7.11 Hadron shower angular resolution. 119
7.12 Number of crossings as a function of energy. 121
7.13 Difference of fitted - calculated energy. 121
7.14 $\frac{\delta(E)}{E}$ as a function of energy. 122
7.15 Angle between the generated and fitted electron direction. 123
7.16 Energy dependence of angular resolutions for electrons. 124
7.17 Event length (number of iron plates crossed) distributions for ν_μ CC events (top), ν_μ NC events (middle) and ν_τ cc events with the decay $\tau \rightarrow hadrons + \nu$ (bottom). 125

8.1 Simulation of neutral current trigger efficiency *versus* E_ν for a trigger of 3 hits in 5 planes 132
8.2 Simulation of neutral current trigger efficiency versus E_{had} for a trigger of 3 hits in 5 planes 132
8.3 Two year $\nu_\mu \rightarrow \nu_\tau$ oscillation limit curve for MINOS using the $\frac{cc}{total}$ test. Curve "A" is for statistics only, and represents the sensitivity if we can reduce systematic errors to a small fraction of the statistical uncertainty. Curve "B" includes systematic and statistical errors. The diamond point shows the Kamiokande best fit parameters. 135

8.4 Upper graph: Energy spectrum of CC events in the NuMI wide-band beam *without* oscillations. Lower graph: Energy spectrum of CC events in the NuMI wide-band beam *with* oscillations for $\Delta m_0^2 = 0.1$ eV^2 and $\sin^2(2\theta) = 1$. The resolution of the detector has been included in both graphs. 137
8.5 Expected oscillation signals using the CC energy test described in the text. Upper graph: $Z_f(\Delta m^2)$ (solid line) and $Z_n(\Delta m^2)$ (dashed line) for $\sin^2(2\theta) = 1.0$ and $\Delta m^2 = 0.1$ eV^2. Lower graph: The difference, $Z_f(\Delta m^2) - Z_n(\Delta m^2)$. These figures were obtained from simulations using 40,000 events; the statistical errors are invisible on this scale. 139
8.6 As for the previous figure but with $\Delta m^2 = 0.01$ eV^2. 140
8.7 Limits on $\sin^2(2\theta)$ and Δm^2 expected for the standard running assumptions. The dotted line shows the statistical limit for a perfect detector; the dashed line includes the effect of detector energy resolution. The solid line includes the systematic uncertainties associated with imperfect knowledge of the neutrino energy spectrum at the far detector and a 2% uncertainty in the energy calibration. 142
8.8 The effect, in standard deviations, as a function of Δm_0^2 that would be measured using the CC energy test given the standard running assumptions and $\sin^2(2\theta) = 1.0$. 143
8.9 Number of hits for selected "nc" events for neutral current, τ and μ charged current events with and without oscillations 145
8.10 Number of hits for selected "nc" events for $\sin^2(2\theta) = 1.0$ and $\Delta m^2 = 0.015\ eV^2$ (solid line) and no oscillations (dashed line) 146
8.11 Number of hits for selected "nc" events for $\sin^2(2\theta) = 1.0$ and $\Delta m^2 = 0.008\ eV^2$ (solid line) and no oscillations (dashed line) 147
8.12 $\vec{p_\mu} \bullet \vec{p_{had}} \times \hat{z}$ for ν_τA$\rightarrow \mu^- \nu_\tau \bar{\nu_\mu} + hadrons$ and ν_μA$\rightarrow \mu^- + hadrons$ events. The broader distribution for ν_τ events represents their non-planarity compared to the more planar ν_μ events. The width of the ν_μ distribution is indicative of the angular resolution of the hadron showers. 149
8.13 Number of $\tau \rightarrow \mu\nu\nu$ signal events remaining (with a background of less than one event) after planarity analysis cuts, as a function of Δm^2 (in eV^2). . . . 150
8.14 Distribution of experimentally measured fraction of neutrino energy carried by the muon vs the fraction of energy in the hadrons (actually hits divided by energy). All plotted events require that $p_\mu > 1.5$ GeV. 155
8.15 Two dimensional plot of the total energy (sum of muon energy and hadron energy) for $\tau \rightarrow \mu\nu\nu$ events (left) and for ν_μ CC events (right). 157
8.16 Plot of the total energy spectrum. The solid line is for ν_μ events and the dotted line is for $\tau \rightarrow \mu\nu\nu$ events. 158
8.17 The hadron energy distribution of CC-like, NC-like, NC-like (background), and NC-like (signal). 159
8.18 The ratio $[NC-like\ (with\ oscillation)]/[NC-like\ (without\ oscillation)]$ as a function of hadron energy. 161
8.19 (a) Energy *vs* transverse energy of electrons from $\nu_\mu \rightarrow \nu_\tau \rightarrow \tau \rightarrow e\nu\nu$. (b) Energy *vs* transverse energy of π^0's from ν_μ interactions. 162

8.20 Measured electron energy distributions from (a) $\nu_\mu \rightarrow \nu_\tau \rightarrow \tau \rightarrow e\nu\nu$, (b) $\nu_\mu \rightarrow \nu_e \rightarrow e$. 164
8.21 Reconstructed electron neutrino energy 167
8.22 Limit curves for two years using the Soudan 2 detector, including systematic and statistical errors. Curve "A" is the limit for $\nu_\mu \rightarrow \nu_e$ oscillations and curve "B" is the limit for $\nu_\mu \rightarrow \nu_\tau$ oscillations. 170
8.23 Distributions of azimuthal angle between the μ and p in (a) ν_μ quasi-elastic events (background) and (b) ν_τ quasi-elastic events followed by $\tau \rightarrow \mu\nu\nu$, in the Soudan 2 detector. 172
8.24 MINOS two year 90% CL limit curves for $\nu_\mu \rightarrow \nu_\tau$ oscillations. Curve "A" is for the $\frac{cc}{total}$ test. Curve "B" is for the near/far rate comparison and is dominated by 4% systematic error. Curve "C" comes from the total energy measurement test. The diamond point shows the Kamiokande best fit parameters. 175
8.25 MINOS two year 90% CL limit curves for $\nu_\mu \rightarrow \nu_e$ oscillations. Curve "A" is for the $\frac{cc}{total}$ test. Curve "B" uses longitudinal cuts. Curve "C" is for the near/far rate comparison and is dominated by 4% systematic error. Curve "D" comes from the total energy measurement test. Curve "B" is the statistical limit, and the other three curves combine statistics and estimated systematic error. The diamond point shows the Kamiokande best fit parameters. . . . 176

9.1 Areas of oscillation parameter space ruled out at the 90% confidence level for a 30 kT-year MINOS exposure to atmospheric neutrinos, compared to results from other experiments. Note that the allowed region is to the right of the Kamiokande curves, but is below and to the left of the other curves. 181

10.1 A possible arrangement of modules in a concrete/steel option. 187

12.1 Production schedule for the MINOS electronics. 206
12.2 Schedule for the active detector R&D, engineering and production. 207
12.3 Schedule for the steel production. 208
12.4 Schedule for the installation of the far detector. 209
12.5 Funding profile for MINOS construction and installation. 210

B.1 Soudan 2 main detector and active shield layout. 225
B.2 *Bandolier*, insulation sheets (inserts) and corrugated steel assembly (stack). 226
B.3 A single drift tube. The drift field is generated by the application of graded voltages on a series of 21 copper electrodes 227
B.4 Segment of a muon track and fit 228
B.5 A cosmic ray muon in the Soudan 2 detector. The anode-time (x), cathode-time (y), and matched (z) views are shown 229
B.6 Typical mean tube efficiency variation with cathode numbers. 230
B.7 Typical pulse height variation along the drift direction. 230
B.8 Electron shower energy versus number of hits from ISIS data and Monte Carlo simulations. 231
B.9 Energy resolution for electron showers. 231

B.10 Mean number of hits (a) and mean total pulse height (b) for different beam momenta versus the vertical angle, and mean number of hits (c) and mean total pulse height (d) versus the horizontal angle. 232
B.11 Invariant mass distribution for two shower events in the $\pi^{\pm}$ beam. 233
B.12 Number of shower hits at the end of μ^{+} and μ^{-} tracks. 234
B.13 Mean pulse height versus anode number (measured from the last anode in the μ trajectory). 235

Chapter 1

Introduction

Neutrino physics presents one of the most promising avenues to probe for extensions of the Standard Model. *A priori*, no fundamental reason exists why neutrinos should have zero mass or why there should be no mixing between different neutrino species. Thus, the existence of neutrino oscillations is quite plausible, maybe even likely, on theoretical grounds. The possible existence of this phenomenon has recently received some experimental support, both from the observations of a deficit of solar neutrinos and from the apparent ν_μ/ν_e anomaly in the interactions of atmospheric neutrinos observed by large underground experiments.

This document presents a proposal for a comprehensive investigation of neutrino oscillations, down to a level of about 10^{-2} or lower in both Δm^2 (eV^2) and $\sin^2(2\theta)$, using neutrinos produced by the Fermilab Main Injector beam and a large new detector located at the Soudan Mine in Minnesota, some 730 km away. (The existing Soudan 2 detector at the same site will also contribute to these studies.) A "near detector" located at Fermilab will monitor the beam and enable a comparison to be made between neutrino interactions in detectors at two quite different distances from the neutrino source. The approach of our experimental program is to perform a variety of different measurements, all of which would be sensitive to neutrino oscillations. A self consistent interpretation of all these measurements would be required for a claim of observation of neutrino oscillations.

This proposal is based on investigation of neutrino interactions with energies sufficiently above the τ production threshold that the presence of $\nu_\mu \rightarrow \nu_\tau$ oscillations, if they occur, can be convincingly demonstrated. The signal for $\nu_\mu \rightarrow \nu_\tau$ oscillations in our experiment relies on a measurement of ν_τ charged current events and the subsequent τ decay. In addition to this ν_τ sensitivity, our experiment will perform several additional measurements which will be sensitive to both $\nu_\mu \rightarrow \nu_\tau$ and $\nu_\mu \rightarrow \nu_e$ oscillations. Most of our tests will rely on near-detector/far-detector comparisons in order to minimize uncertainties due to imperfect knowledge of the neutrino beam energy spectrum and of the detector responses.

One of the design goals of our experiment is to provide the maximum possible flexibility to respond to future improvements in our knowledge of neutrino oscillations. For example, in collaboration with Fermilab, we are designing a neutrino beamline that is capable of operating in several modes. The two extremes would be a wide band beam which maximizes neutrino flux at the far detector and a narrow band beam, which has lower flux, but is free of low energy tails. Such flexibility would allow us to respond in an appropriate way to whatever may be the physics situation in the year 2000, the approximate starting time

of the experiment. Assuming that our knowledge of neutrino oscillations has not changed substantially by the year 2000, our plan would be to begin with a two year run using a wide band beam. However, as will be made clear in Chapter 8, we consider the narrow band beam option an integral and essential part of our experimental program. Several other options for follow-up running, based upon our initial results, are discussed in Section 8.10.

This proposal is focused around a "reference detector" defined as one which can be built with currently proven technology, can be costed with some degree of confidence, and can be used to address the physics goals described in the proposal. In that sense, it can be viewed as a "proof of the principle" detector. The parameters we have chosen are: 10 kT total mass, 4-cm thick magnetized steel plates with an 8 m transverse dimension, and limited streamer tubes as the active detector element. The reference detector is described in detail in Chapter 5.

Detector optimization requires a careful balance between granularity and mass. Some processes which we will use to study ν_μ oscillations are relatively insensitive to granularity, and their accuracy is limited by statistics. Others put a premium on fine granularity, and some demand it, even if it is obtained at the expense of statistics. To achieve optimization of the whole program we require a good understanding of the trade-offs in all of these measurements. We believe that we have made a good start in that direction, but our understanding is still far from complete. Thus, it is almost certain that the final detector will differ in a number of ways from the one described in this document. We expect that the final detector will provide a better performance at the same or lower cost and will be better optimized to achieve our physics goals.

Between now and the production of the Technical Design Report, we plan to devote a considerable additional effort to the design of the optimal detectors at both the near and far locations. This effort will probably result in an evolution of the reference detector design, as discussed in Chapter 10. Our development work will include additional simulation studies, as described in Chapter 8, as well as detector hardware R&D and detailed engineering designs, as outlined in Chapter 11. These studies will clearly have close interplay with the ongoing and future studies of the beam design. Chapter 3 reviews our work on beam design and monitoring, and Chapter 6 describes our requirements for the near detector hall at Fermilab. Both activities will continue to be closely coordinated with the plans of E–803.

The fine-grained Soudan 2 detector, which was the basis of the P–822 proposal, will be integrated into the experiment proposed here. The existing detector and its capabilities are described in detail in Appendix B. Chapters 8 and 10 discuss the sensitivity of Soudan 2 and some alternative configurations of its detector modules.

The MINOS collaboration is still in the formative stage. The majority of its present members are the authors of the Expressions of Interest submitted to Fermilab in the spring of 1994. The current proposal is an evolution of the ideas presented in those EoI's. Assuming a favorable response to this proposal, we anticipate that the collaboration will grow in the future, to perhaps twice its current size. Furthermore, as time progresses, more and more of its current members will focus their efforts exclusively on the MINOS program. Appendix A describes the current organizational structure of the collaboration. It is optimized for the near future, during which we will focus on design of the experiment, preparation of the Technical Design Report, and more detailed simulation studies. We expect that the administrative structure will evolve as the collaboration grows and the experiment progresses.

Chapter 2

Physics Motivations and Goals

2.1 Physics motivations

2.1.1 Neutrino mass

The origin of fermion mass is one of the most fundamental issues in particle physics. Neutrinos are either massless, or much less massive than other fermions. The present kinematic limits on neutrino mass are[1]:

$$m_{\nu_e} < 5.1\ eV \tag{2.1}$$

$$m_{\nu_\mu} < 0.27\ MeV \tag{2.2}$$

$$m_{\nu_\tau} < 31\ MeV \tag{2.3}$$

The ever-lower experimental upper limits on the neutrino mass indicated to many physicists that ν masses might well be zero. Neutrinos, as the only neutral fundamental fermions, could indeed be massless. More recently, the notion of quark-lepton universality and the experimental hints described below have moved theoretical attention toward considering nonzero neutrino masses.

If neutrinos do have finite masses, a framework to understand the low value of the mass is given by the seesaw mechanism [2]. In a general way, this framework suggests that if the neutrino has both Majorana and Dirac mass terms, then neutrino masses are related to other fermion masses by the following:

$$m_\nu \propto m_f(m_f/m_X)^n \tag{2.4}$$

where m_X is a high energy scale at which some new physics, such as unification, is expected. The exponent n is usually assumed to be 0 or 1. The parameter m_X could range from a few TeV up to the Plank mass, and m_f could range from the electron mass up to the top quark mass. Thus the "prediction" of the neutrino mass is not well constrained. However, in this picture the family relationship produces a normal mass hierarchy, *i.e.*

$$m_{\nu_e} < m_{\nu_\mu} < m_{\nu_\tau} \tag{2.5}$$

as a casual look at the lepton and quark generations would also suggest.

2.1.2 Neutrino oscillations

Neutrino mass and lepton number violation are the necessary ingredients for the existence of neutrino oscillations. By analogy with the quark sector, there is no fundamental symmetry requiring lepton number conservation, so it is generally expected that if neutrinos have nonzero masses, neutrino oscillations will also occur. Lepton number conservation has been stringently tested in the decays $\mu \rightarrow e\gamma$ and $K_L \rightarrow \mu e$, for which the branching ratios are measured to be less than 4.9×10^{-11} [3] and 3.3×10^{-11} [4] respectively. However, in the Standard Model such decays are strongly suppressed by the small neutrino mass. If the neutrino mass is below 1 eV, a $\mu \rightarrow e\gamma$ branching ratio no larger than 10^{-48} is implied[5].

The search for neutrino oscillations between two flavor eigenstates a and b is based on the well known formula:

$$P(\nu_a \rightarrow \nu_b) = \sin^2(2\theta)\sin^2(1.27\frac{\Delta m^2 L}{E}) \tag{2.6}$$

where $\Delta m^2 =\mid m_1^2 - m_2^2 \mid$ is measured in eV^2, L in km, and E in GeV.

Experimental hints which suggest the existence of neutrino oscillations include (1) the solar neutrino deficit, (2) the cosmological missing matter problem, and (3) the atmospheric neutrino deficit. These hints are described in the next sections.

2.1.3 The solar neutrino deficit

The results of four independent solar neutrino experiments indicate that the flux of electron neutrinos from the sun is lower than expected, based on detailed solar models which are constrained by the very well measured solar luminosity [6]. The reliability of the solar neutrino fluxes calculated by solar models has been a matter of recent controversy [7]. However, it has been shown that no solar model can, by itself, account for even three of the four solar neutrino experimental results [8]. In other words, either there is some new particle physics, such as neutrino mass, or at least two of the four solar neutrino experiments must be wrong (outside of their quoted statistical and systematic errors). This conclusion relies on the calculated flux of neutrinos from Be^7, which is much less sensitive to the solar temperature than the B^8 neutrino flux. A recent calibration of the GALLEX solar neutrino experiment with a Chromium-51 source adds confidence to the solar neutrino flux measurements [9].

One explanation of the solar neutrino deficit, namely neutrino oscillations enhanced by the MSW mechanism[10], is compatible with all of the solar neutrino flux measurements. This model implies ν_e disappearance with parameters $\Delta m^2 \sim 10^{-5} eV^2$ and $\sin^2(2\theta) \sim 0.01$ or alternatively, $\sin^2(2\theta) \sim 0.8$.

2.1.4 The missing matter problem

The neutrino is the only known particle that is a candidate for the missing matter sufficient to close the universe [11]. This solution is known as hot dark matter, because the neutrino would have been relativistic when radiation and matter decoupled. The mass hierarchy suggested in Section 2.1.1 makes the ν_τ the most popular candidate. Analyses of the recent COBE data are consistent with hot matter being 30% of the matter needed to close the

universe [12]. There are expected to be 100 cosmological $\nu's/cm^3/flavor$ in the universe from the big bang, analogous to the 2.7° black body photons. Depending on the Hubble constant and the fraction of the critical density in neutrinos, a mass of 1-10 eV is expected. Neutrino oscillations in this mass range can be well tested at accelerators. The best limit for $\nu_\mu \rightarrow \nu_\tau$ is from the E–531 experiment [13]. The major goal of the present short baseline experiments at CERN, CHORUS and NOMAD, as well as the short baseline experiment E–803[14], is to push sensitivity to lower values of possible mixing angles for $\nu_\mu \rightarrow \nu_\tau$ as well as $\nu_e \rightarrow \nu_\tau$. The LSND and KARMEN experiments are sensitive to $\nu_e \rightarrow \nu_\mu$ oscillations in this mass range, although stringent limits from Brookhaven already exist [15].

2.1.5 The atmospheric neutrino deficit

Both the Kamiokande and IMB groups have presented experimental results [16, 17] on the interactions of atmospheric ν_μ and ν_e in their underground water Cerenkov detectors, which have been claimed [16] as strong evidence for neutrino oscillations. Significant data on ν_μ and ν_e interactions have also been obtained by the Frejus and Soudan 2 underground iron-plate calorimeters. Measurements of underground upward-going muons also can give information on atmospheric neutrino oscillations. Because of the central relevance of the atmospheric neutrino results to our long baseline experiment, we shall discuss in more detail several aspects of the atmospheric neutrino experiments in the following section.

2.2 Discussion of atmospheric neutrino results

2.2.1 The flavor ratio

Atmospheric neutrinos are produced by decays of the π and K mesons which result from the collisions of primary cosmic rays in the spherical shell of the earth's atmosphere. In order to use atmospheric neutrinos for an oscillation search, we must know the distribution in energy and flight distance for each neutrino type produced. Different types of measurements, described here and in following sections, probe different parts of the neutrino spectrum, as shown in Fig. 2.1. Most neutrinos have energies below the threshold for τ-production, making a ν_τ appearance experiment impossible to perform with atmospheric neutrinos.

The sensitivity of neutrino oscillation searches with atmospheric neutrinos is limited in $\sin^2(2\theta)$ mainly by statistics, and in Δm^2 by E_ν and R_{Earth}. Uncertainties in the absolute flux of cosmic ray primaries, together with uncertainties in the production of pions and kaons in collisions between light nuclei, translate into significant uncertainties in the normalization and shapes of the atmospheric neutrino spectra at production. For this reason, conclusions based on measured ratios of neutrino types are the most reliable.

Atmospheric neutrino interactions observed in massive underground detectors are usually classified as fully or partially contained events, depending on whether all interaction products are contained within the fiducial volume or a high energy muon leaves the detector. The neutrino flavor ratio from experiments which measure fully contained events is shown in Table 2.1 while the input data and calculations are shown in Table 2.2. The flavor ratio is

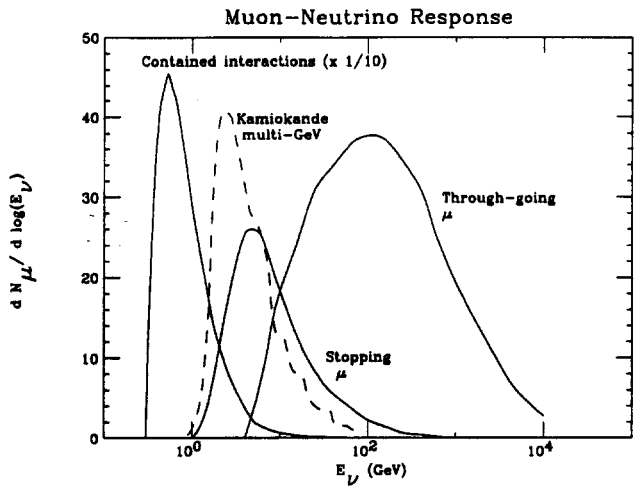

Figure 2.1: Atmospheric ν_μ energy spectra for different types of experiments.

defined as

$$R \equiv \frac{\nu_\mu/\nu_e)^{data}}{\nu_\mu/\nu_e)^{MC}} \tag{2.7}$$

while the experiments actually measure

$$R' \equiv \frac{track/shower)^{data}}{track/shower)^{MC}}. \tag{2.8}$$

The high statistics water Cerenkov experiments in Table 2.1 distinguish between quasi-elastic ν_μ and ν_e events in two ways. In one method, the shape of the Cerenkov ring on the wall of phototubes is used. In the other method, an excess in the number of phototube hits in a time window several microseconds after the event is used to identify μ decay. The two methods have different systematic errors, but are statistically correlated. Experimental measurements of e and μ identification properties of these detectors are now under way in a KEK test beam. Test beam results from the Kamiokande group presented at Eilat [18] give no indication of misidentification problems. Results from the IMB test beam calibration at KEK are expected to be available in the next few months.

All experimental results on contained atmospheric neutrino events are consistent with a 30-40% deficit of ν_μ events. Such a deficit could be the result of either $\nu_\mu \rightarrow \nu_\tau$ or $\nu_\mu \rightarrow \nu_e$ oscillations or both, or of some effect(s) other than neutrino oscillations. The assignment of the atmospheric neutrino anomaly to a specific neutrino oscillation channel requires knowledge of the absolute ν_μ and ν_e fluxes. In a conventional two-detector neutrino oscillation experiment at an accelerator, the flux normalization is obtained by measuring the interaction rate in the neutrino beam close to the source. The nearest analog of a close-in detector for atmospheric neutrino experiments is a measurement of the intensity of muons at the atmospheric altitudes where both the neutrinos and muons are produced (10 to 20 km). New, higher precision measurements of this flux are being made [19, 20], and preliminary results [19] are consistent with a relatively high normalization of the muon neutrino flux [21]. This favors a $\nu_\mu \rightarrow \nu_\tau$ interpretation of the atmospheric neutrino puzzle. On the other hand, a preliminary re-analysis of the Frejus data which was presented at Snowmass [22] seems to be even less consistent with the results of Refs. [16, 17] than the original published

Experiment	Exposure kT-year	R'
Contained Events only:		
IMB1	3.8	0.68 ± 0.08
Kamiokande ring	7.70	0.60 ± 0.06
Kamiokande decay		0.69 ± 0.06
IMB-3 ring	7.70	0.54± 0.05
IMB-3 decay		0.64 ± 0.07
Frejus contained	2.0	0.87 ± 0.13
Soudan 2	1.01	0.64 ± 0.19
NUSEX	0.5	0.99 ± 0.29
Uncontained events included:		
Kamiokande Multi-GeV	7.70	0.59 ± 0.08
Frejus total	2.00	0.96 ± 0.18

Table 2.1: The atmospheric neutrino flavor ratio. Quoted errors are statistical and systematic added in quadrature.

Experiment	TR^{data} (ν_μ^{data})	TR^{MC} (ν_μ^{MC})	SH^{data} (ν_e^{data})	SH^{MC} (ν_e^{MC})
IMB1	104	136	297	265
Kam. ring	234	356.8	248	227.6
Kam. decay	182	277.5	300	313.9
IMB-3 ring	182	268	325	257.3
IMB-3 decay	208	261.5	402	348.5
Frejus contained	94	100	89	82
Soudan	33.5	42.1	35.3	28.7
NUSEX	32	36.8	18	20.5

Table 2.2: The data on the atmospheric neutrino deficit. TR refers to single tracks, SH to single showers

Frejus result [23]. A simultaneous analysis of Frejus contained, partially contained, and through-going muons leads to a neutrino oscillation exclusion plot which is inconsistent with a neutrino oscillation interpretation of the data in Tables 2.1 and 2.2. Taken alone, the Frejus fully contained data are not in strong disagreement with the data from other experiments. However, their partially-contained event rates and the flux of neutrino-induced through-going muons seem to be inconsistent with the new Kamiokande result (described in the next section). An analysis of all Frejus neutrino data leads to the result $R' = 0.96 \pm 0.18$.

2.2.2 The Kamiokande angular distribution

The most striking new result on atmospheric neutrinos was presented during the 1994 Snowmass meeting [24]. This Kamiokande analysis of "multi-GeV" events includes fully-contained events with $E_{\rm vis} > 1.33$ GeV as well as partially-contained events. The mean neutrino energy responsible for this class of events is ~ 6 GeV, as shown in Fig. 2.1. This energy is nearly an order of magnitude higher than for the independent sample [16] of contained events with $E_{\rm vis} < 1.33$ GeV. In this new data sample, there is again evidence for a ν_μ deficit, characterized by the flavor ratio $R' = 0.59 \pm 0.08$.

The most remarkable feature of the data is the dependence of the flavor ratio on the calculated zenith angle of the incident neutrinos. This angular dependence agrees with a model in which downward ν_μ's have path lengths too short to oscillate, and the upward ν_μ's, which have travelled from the far side of the earth, have been depleted by oscillations. Given the range of E_ν and R involved for the multi-GeV sample, Equation 2.6 implies an upper limit on Δm^2. In contrast to the muon events, the angular dependence of the electron events suggests that ν_e are not affected by oscillations. The angular dependence alone therefore supports an interpretation in terms of ν_μ disappearance.

We also note a statistical point regarding Kamiokande's angular dependence. They plot R $= (\nu_\mu/\nu_e)^{data}/(\nu_\mu/\nu_e)^{MC}$ versus zenith angle. Part of that ratio, ν_e^{data}/ν_e^{MC}, is for flux normalization only, and should be flat within statistics in both the no-oscillation case and the $\nu_\mu \to \nu_\tau$ hypothesis. Normalizing to the binned ν_e data adds bin-to-bin statistical fluctuations to the angular dependence plot. We expect that a better representation may be $(\nu_\mu/ < \nu_e >)^{data}/(\nu_\mu/\nu_e)^{MC}$ where the ν_e average is over all angular bins. When this is done, the angular distribution still supports the oscillation hypothesis, but with a best-fit mixing angle which is no longer maximum.

One interesting feature of the new Kamiokande result is the relative excess of electron neutrinos and the relatively small deficit of muon neutrinos, compared to what is expected from the $\nu_\mu \to \nu_\tau$ hypothesis. Using the neutrino flux of Ref. [25], they find

$$e - \text{like} \left(\frac{\text{measured}}{\text{calculated}}\right) = 1.47 \pm 0.15$$

and

$$\mu - \text{like} \left(\frac{\text{measured}}{\text{calculated}}\right) = 0.83 \pm 0.07.$$

The corresponding numbers for the low-energy, fully contained event sample are 1.09 (electrons) and 0.66 (muons). Thus, while the low energy sample suggests $\nu_\mu \leftrightarrow \nu_\tau$, the high energy sample may suggest $\nu_\mu \leftrightarrow \nu_e$.

It is noteworthy that the experiments with the greatest statistical significance [16, 17] show a significant effect in the best understood feature of the atmospheric neutrino beam—the ν_e/ν_μ ratio. The measured ratio is apparently greater than the ratio at production. The possibility that the discrepancy might result from an incorrect use of the Fermi Gas Model (FGM) in calculating neutrino interaction rates is not borne out in a recent careful investigation [26]. This study concludes that the atmospheric neutrino energies are high enough that any deviation from the FGM would affect both flavors of neutrinos similarly. Other types of systematic errors in the measurement of the ν_μ/ν_e are now under study by several groups. These possibilities include contamination of the contained events by neutrons from cosmic-ray muon inelastic scattering in the surrounding rock, and possible proton decay to $e\nu\nu$ [27].

2.2.3 Upward muons

The measured ratio of stopping to through-going upward neutrino-induced muons is consistent with the no-oscillation expectation [28]. The IMB data are shown in Table 2.3. If the data are background free, this means *either* that there are no oscillations of ν_μ with mixing angle and Δm^2 large enough to be seen with upward neutrinos *or* that there is large mixing of ν_μ, but with Δm^2 large enough so that the lower energy stopping muons as well as the higher energy through-going muons are affected. The measured stopping/through-going ratio is used to rule out a range of $10^{-3} < \Delta m^2 < 10^{-2}$ eV^2 at large mixing angle for ν_μ disappearance [28].

The ratio of upward stopping muons to through-going muons is sensitive to the absence of background from events which are not initiated by neutrinos. In particular, down-going muons which initiate hadronic cascades in the rock could mimic upward going stopping muons in some cases. There is evidence for such events from Soudan, Kamiokande, and MACRO[29, 30, 31], but it is not straightforward to calculate the possible contamination of the IMB data sample. We do note, however, that a background of 12 events out of the 85 would lead to the absence of any neutrino oscillation limit from the IMB analysis, and also that the comparison of upward showers to expectation in IMB may be evidence that such a background could exist.

	Observed	Calculated
Stopping tracks	85	84
Exiting tracks	532	516
Showers	49	17

Table 2.3: Neutrino induced upward event rates in IMB.

The IMB group [28] calculated the rate of upward, through-going muons starting from a particular neutrino flux [32] and a particular representation of the neutrino cross section [33]. Their calculated rate agrees with their measured rate, apparently ruling out most of the available parameter space needed for a $\nu_\mu \leftrightarrow \nu_\tau$ interpretation of the low energy, contained event anomaly. Frati *et al.* [34] showed that the Kamiokande data on upward, through-going

muons [35] is similarly consistent with a calculation using the same input assumptions. On the other hand they found that, starting from different, more recent calculations of the neutrino flux [36, 37] and a different representation of the cross section [38] (the "high" case), the predicted rate is some 15% higher than the observed rate. They further showed that a discrepancy of this size is consistent with a range of parameters needed to explain the contained event anomaly as $\nu_\mu \leftrightarrow \nu_\tau$. Recently reported results from MACRO [39] similarly show a significant deficit of the measured upward rate as compared to a no-oscillation calculation with the "high" input assumptions. This matrix of measurements and calculations is indirect evidence that these experiments and calculations are all consistent with each other. The same cannot be said for Baksan [40] where there is agreement between measurement and expectation for "high" input assumptions, but an *excess* of measurements over calculation when the low input is used. In all cases the differences are only of marginal statistical significance, as indicated by the summary of measurements/calculations in Table 2.4.

Experiment	Observed	Calculated	
		"high"	"low"
IMB [28]	0.47 ± 0.02	—	0.455
KAM [35]	2.04 ± 0.13	2.36	2.18
Baksan [40]	161	162	142
MACRO [39]	$74 \pm 9 \pm 8$	101 ± 15	—

Table 2.4: Upward muon fluxes. The units for Kamiokande are $10^{-13}\mathrm{cm}^{-2}\mathrm{s}^{-1}\mathrm{sr}^{-1}$; for IMB, events per day; for Baksan and MACRO, the total number of observed events.

2.3 Theoretical scenarios

The richness of possibilities in the neutrino sector is indicated in Table 2.5, which lists several theoretical scenarios. Table 2.5 also shows the expectations of each model for the solar ν, atmospheric ν and missing matter problems. The NuMI program, consisting of the short baseline E–803 experiment, and the long baseline MINOS experiment, would be in a unique position to see signals for many of these scenarios.

The theoretical models for neutrino oscillations are too numerous to review here, but we shall describe one recent proposal with particularly interesting consequences [41]. At the GUT scale, a reasonable mixing matrix is one which is (threefold) maximal. The mixing matrix can be written explicitly:

$$U = \frac{1}{\sqrt{3}} \begin{pmatrix} \omega_1 & \omega_1 & \omega_1 \\ \omega_1 & \omega_2 & \omega_3 \\ \omega_1 & \omega_3 & \omega_2 \end{pmatrix} \tag{2.9}$$

where $UU^\dagger = 1$ and the ω_i $(i = 1 - 3)$ are the complex cube roots of unity. In contrast to the case of quarks, evolution with energy due to quantum corrections, is expected to have

Reference	m_{ν_μ} (eV)	m_{ν_τ} (eV)	Does it explain? Solar deficit	Atmospheric deficit	Dark Matter	E–803 signal	MINOS signal
Standard Model	0	0	$\mathcal{NO}$	$\mathcal{NO}$	$\mathcal{NO}$	$\mathcal{NO}$	$\mathcal{NO}$
Pakvasa[43]	10^{-3}	10^{-1}	$\mathcal{YES}$	$\mathcal{YES}$	$\mathcal{NO}$	$\mathcal{YES}$	$\mathcal{YES}$
Hall[44]	10^{-3}	10	$\mathcal{YES}$	$\mathcal{NO}$	$\mathcal{YES}$	$\mathcal{YES}$	$\mathcal{NO}$
Akhmedov[45]	10^{-1}	10	$\mathcal{NO}$	$\mathcal{YES}$	$\mathcal{YES}$	$\mathcal{YES}$	$\mathcal{YES}$
GINO[46]	0	0	$\mathcal{YES}$	$\mathcal{YES}$	$\mathcal{NO}$	$\mathcal{NO}$	$\mathcal{YES}$
Caldwell[47]	3	3	$\mathcal{YES}$	$\mathcal{YES}$	$\mathcal{YES}$	$\mathcal{YES}$	$\mathcal{YES}$
Wolfenstein B[48]	$3\ 10^{-4}$	$3\ 10^{-3}$	$\mathcal{YES}$	$\mathcal{NO}$	$\mathcal{NO}$	$\mathcal{NO}$	$\mathcal{NO}$
"Just So"	10^{-5}	10^{-5}	$\mathcal{YES}$	$\mathcal{NO}$	$\mathcal{NO}$	$\mathcal{NO}$	$\mathcal{NO}$
Albright[49]	10^{-3}	10^{-1}	$\mathcal{YES}$	$\mathcal{YES}$	$\mathcal{NO}$	$\mathcal{YES}$	$\mathcal{YES}$
Maximal mixing [41]	0.085	$< 3\ 10^{-6}$	$\mathcal{YES}$	$\mathcal{YES}$	$\mathcal{NO}$	$\mathcal{NO}$	$\mathcal{YES}$
Heavy ν_τ[50]	10^6	-	$\mathcal{YES}$	$\mathcal{NO}$	$\mathcal{NO}$	$\mathcal{NO}$	$\mathcal{NO}$

Table 2.5: Several theoretical neutrino mass scenarios

a negligible effect on the mixing matrix [42]. The neutrino survival probability approaches 5/9 at low Δm^2, which is compatible with both the atmospheric deficit and all solar data except that of Davis, which is lower (Figure 2.2). In this particular scenario, a long baseline experiment should measure an equal mixture of $\nu_\mu \rightarrow \nu_e$ and $\nu_\mu \rightarrow \nu_\tau$ oscillations.

2.4 Implications for a long baseline experiment

A ν_μ disappearance interpretation (*e.g.* $\nu_\mu \leftrightarrow \nu_\tau$) of the ratio ν_μ/ν_e in low-energy contained atmospheric neutrino events with $\Delta m^2 > 10^{-2}$ eV^2 and large mixing angle would imply disappearance of $\sim$ 100 GeV ν_μ with path-lengths $L > R_{Earth}$. This in turn predicts a deficit of ν_μ-induced, upward, through-going muons in underground detectors. As discussed in Section 2.2.3, measurements of this rate are inconclusive because of uncertainty in the normalization of the calculated neutrino flux. There is also some uncertainty in the neutrino cross section.

Combining all their data (sub-GeV and multi-GeV), the Kamiokande group find a rather limited allowed region, either for $\nu_\mu \leftrightarrow \nu_\tau$ or for $\nu_\mu \leftrightarrow \nu_e$ with nearly full mixing and with $\Delta m^2 \sim 1$ to 2×10^{-2} eV^2. A simultaneous analysis of all atmospheric and solar neutrino data sets (as of 1993) in the space of 3-flavor neutrino oscillations [51] favors oscillation predominantly in the $\nu_\mu \leftrightarrow \nu_\tau$ sector to explain the atmospheric anomaly and in the $\nu_\mu \leftrightarrow \nu_e$ sector for the solar neutrinos. This in turn implies a "natural" order for the neutrino masses, but with $m(\nu_\tau) \sim 0.1$ eV, rather than the value of $\sim$ 10 eV expected from a quadratic see-saw starting from $m(\nu_\mu) \sim 0.003$ eV to solve the solar neutrino puzzle.

A consistent picture of the solar and atmospheric neutrino experiments can be drawn in which neutrino oscillations exist with $\nu_e \rightarrow \nu_\mu$ responsible for the solar neutrino deficit and $\nu_\mu \rightarrow \nu_\tau$ responsible for the atmospheric deficit. Evidence for this scenario comes from the solar neutrino data, the data on contained-neutrino flavor ratio from IMB, Kamiokande

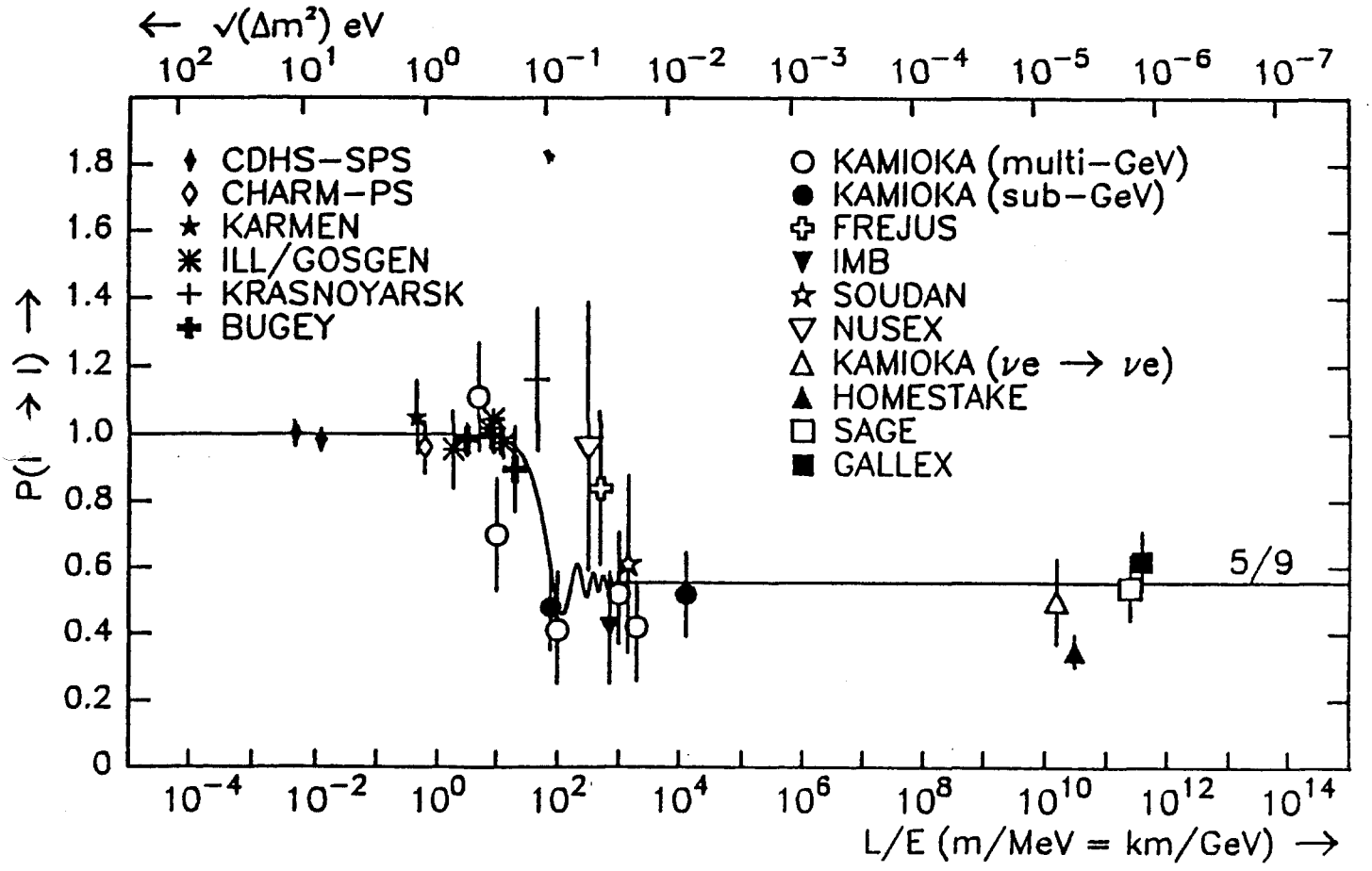

Figure 2.2: The survival probability $P(l \to l)$ measured in solar, atmospheric, reactor and accelerator experiments, corrected according to the threefold maximal mixing scenario.

and Soudan 2, and the angular distribution of multi-GeV data from Kamiokande. Recent calibration studies (GALLEX, and the test beam studies of the IMB, Kamiokande, and Soudan 2) have given support to the analysis methods used for data from these detectors.

However the experimental picture is not a compelling one, due in part to the upward muon data, the upward stopping muon data, and the Frejus data. This situation provides strong motivation for a study with the well controlled systematics of an accelerator experiment. The long baseline neutrino oscillation experiment described in this proposal will achieve this goal.

If the atmospheric neutrino anomaly is a signal of neutrino oscillations, the lack of observed angular dependence for low energy ($\lesssim 1$ GeV) events [16, 17] implies $\Delta m^2 > 10^{-3}$ eV^2. The large size of the anomaly requires $\sin^2(2\theta) \gtrsim 0.5$. The $\nu_e \leftrightarrow \nu_\mu$ explanation is ruled out by reactor limits for much (but not all) of the parameter space allowed by the atmospheric neutrino experiments [52].

The bottom line is that **a new accelerator based long baseline oscillation experiment is clearly desirable to clarify the situation.** There are several plausible physics scenarios in which our experiment could observe an oscillation signal:

1. If the atmospheric anomaly is due to $\nu_\mu \rightarrow \nu_\tau$, the MINOS long baseline experiment is sensitive to the suggested region of Δm^2 and will measure $\nu_\mu \rightarrow \nu_\tau$ oscillations with large mixing angle.

2. If the solar neutrino anomaly is due to $\nu_e \rightarrow \nu_\mu$, then whether or not the atmospheric results are caused by oscillations, the MINOS experiment is sensitive to $\nu_\mu \rightarrow \nu_\tau$ in the right region of Δm^2. In this case, the MINOS design goal of mixing angle sensitivity down to about 0.01 may prove to be important.

3. If the ν_τ mass is partly responsible for the missing matter problem then our sister experiment, E–803, may see a $\nu_\mu \rightarrow \nu_\tau$ oscillation signal. The possibility would remain that the MINOS experiment could measure $\nu_\mu \rightarrow \nu_e$ oscillations.

4. In the maximal lepton mixing scenario, the MINOS experiment would measure *both* $\nu_\mu \rightarrow \nu_\tau$ and $\nu_\mu \rightarrow \nu_e$ oscillations.

5. In the gravitationally-enhanced neutrino oscillation scenario [46], the combination of high neutrino energy and large distance is an ideal one for a neutrino oscillation signal.

2.5 Sensitivity

The MINOS long baseline neutrino oscillation experiment will provide an opportunity to measure neutrino oscillations in several possible modes over a wide range of parameter space. More importantly, using the beam from the Fermilab Main Injector with an average energy above ν_τ charged current threshold, and the distance from Fermilab to Soudan, we will be able to measure neutrino oscillations in a number of redundant and statistically independent ways. The signals for neutrino oscillations are outlined here, and will be described in detail in Chapter 8. Essentially all of our results will be based on a comparison of some particular

class(es) of events induced by the unoscillated beam in our near detector with those in our far detector, where the beam may have been changed by neutrino oscillations.

2.5.1 Wide-band beam tests sensitive to both $\nu_\mu \rightarrow \nu_\tau$ and $\nu_\mu \rightarrow \nu_e$

The MINOS experiment can perform several key measurements in a wide band beam which are sensitive to both $\nu_\mu \rightarrow \nu_\tau$ and $\nu_\mu \rightarrow \nu_e$:

1. Comparison of the absolute rate of ν_μ charged current events in the near and far detectors. A signal for oscillations would be a smaller number of events in the far detector.

2. Comparison of the fractions of charged current (defined for ν_μ) and neutral current events in the near and far detectors. A signal for oscillations would be a smaller fraction of charged current events in the far detector than the near detector.

3. Measurement in the far detector of the ratio of muons emerging from the rock to neutrino interactions in the detector. A signal for oscillations would be an unexpectedly low ratio of rock muons to detector interactions.

4. Measurement of the charged current energy distribution. A signal for oscillations would be a change in the shape of the energy distribution between the near and far detectors, which could be fit with a specific value of Δm^2.

2.5.2 τ signatures in a wide band beam

A search for $\nu_\mu \rightarrow \nu_\tau$ oscillations using neutrinos with an energy above ν_τ charged current threshold provides an opportunity to measure not only changes in the beam composition, but also to look for signatures due to the τ leptons themselves. Our sister experiment E–803 plans to use the τ lifetime in emulsion to see τ's on an "event-by-event" basis (*i.e.* with zero background). The MINOS detector is being designed to record several τ decay signatures with enough event information that an oscillation signal will be statistically distinguishable from ν_μ and ν_e backgrounds. The change in these signatures between near and far detectors will be an important feature in establishing such signals. Wide-band beam signatures include:

1. $\tau \rightarrow$ hadrons

2. $\tau \rightarrow \mu\nu\nu$ deep inelastic events

3. $\tau \rightarrow \mu\nu\nu$ quasi-elastic events

4. $\tau \rightarrow e\nu\nu$ quasi-elastic events

2.5.3 τ signatures in a narrow band beam

A narrow band beam provides knowledge of the neutrino energy with a relatively small spread. This gives an important kinematic constraint which is not available in a wide band beam. Not only will signals studied with the wide band beam have reduced backgrounds in the narrow band beam, but new signals will become available. Narrow band beam τ signatures include:

1. $\tau \rightarrow \mu\nu\nu$ quasi-elastic events
2. $\tau \rightarrow e\nu\nu$ quasi-elastic events
3. $\tau \rightarrow \mu\nu\nu$ deep inelastic events
4. Other tests described in Chapter 8.

2.5.4 Searches for $\nu_\mu \rightarrow \nu_e$

For the physics reasons discussed above, this proposal has focused on the neutrino oscillation mode $\nu_\mu \rightarrow \nu_\tau$. In fact, this detector will be even more sensitive to the neutrino oscillation channel $\nu_\mu \rightarrow \nu_e$. Measurements which are sensitive to this channel include all four tests in Section 2.5.1 above, as well as the $\tau \rightarrow e\nu\nu$ tests. Tests which are most directly sensitive to ν_e appearance are:

1. Comparison of the rate of ν_e quasi-elastic events in the near and far detectors. A signal for $\nu_\mu \rightarrow \nu_e$ oscillations would be an excess rate of such events at the far detector, compared to events in the near detector.
2. Measurements of the kinematics and electromagnetic energy spectra in neutral current events. A signal for $\nu_\mu \rightarrow \nu_e$ oscillations would be an increase in the rate of events with large shower energies and large electromagnetic components in the far detector.

2.5.5 MINOS sensitivity in Δm^2 and $\sin^2(2\theta)$

Fig. 2.3 shows the sensitivity of the MINOS experiment to $\nu_\mu \rightarrow \nu_\tau$ oscillations using three separate tests. The calculation of these and other limits is described in detail in Chapter 8.

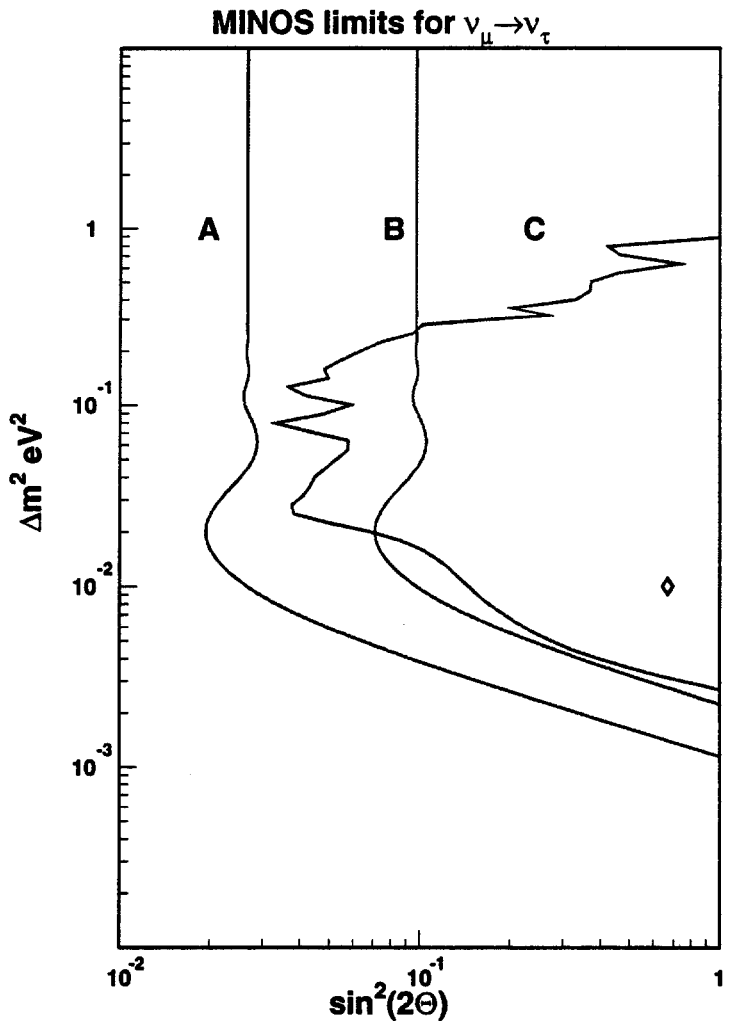

Figure 2.3: MINOS two year 90% CL limit curves for $\nu_\mu \rightarrow \nu_\tau$ oscillations. Curve "A" is for the $\frac{cc}{total}$ test. Curve "B" is for the near/far rate comparison and is dominated by 4% systematic error. Curve "C" comes from the total energy measurement test. The diamond point shows the Kamiokande best fit parameters.

Chapter 3

Neutrino Beam

3.1 Introduction

This Chapter describes the neutrino beams that are needed to pursue the physics described elsewhere in this proposal. The neutrino beams and the detectors must work together as a system to maximize data rates while facilitating the interplay of the near and far detectors to minimize systematic uncertainties. Two types of beams are being designed: (a) a wide-band beam (WBB) in which a pair of focusing horns are used to decrease the angular dispersion of a charged particle beam before a decay pipe in which a broad spectrum of neutrinos are produced; and (b) a narrow-band beam (NBB) in which the charged particles undergo focusing by a lithium lens and momentum selection so that the resulting neutrinos are quasi-dichromatic (different momenta coming from π and K decay). The WBB has the advantage of maximizing neutrino flux because of its broad momentum acceptance. The NBB, with lower flux, provides a known beam energy and facilitates kinematic checks that reduce backgrounds and permits some experimental measurements that would not be possible with the WBB.

The goal for the design of the WBB is to simultaneously maximize the exposure of the short baseline experiment E–803 and the long baseline MINOS experiment to neutrinos with energies above the ν_τ charged current threshold. The short baseline experiment requires a low and well understood background from $\overline{\nu}_\mu$[53], whereas the long baseline experiment requires a low and well understood background from $\nu_e + \overline{\nu}_e$. The WBB as presently conceived is a double horn beam with horn currents of 160 kAmp that has been designed for E–803. It has been studied and optimized over an extended time period.

The design goals for the NBB are to maximize the event rate from the beam with a well understood ν_μ energy distribution and a minimized low-energy tail. Work on the NBB has begun more recently than the WBB, so it has not been as extensively optimized. Already, however, a flux which is 40% of the WBB flux has been achieved for neutrinos with energies above 10 GeV. We are actively working on the low energy tail minimization and have made progress. Finally, we note that the near-to-far-detector flux ratio will be better understood for the NBB than for the WBB, thus reducing systematic uncertainties.

3.2 Running strategies

The collaboration is exploring the physics reach that could be achieved from running with either a WBB or a NBB, or splitting the running time between the two modes. The target and beam line enclosure has been designed to accommodate both beams. Since different physics channels are optimized with the different beams, the MINOS collaboration strategy is to design the beamline enclosure to accommodate both types of neutrino beams. The existing designs[54] have enough room in the beam enclosure for both beams so there is no additional cost associated with having both beams except for the beamline components themselves.

Assuming that our knowledge of neutrino oscillations has not changed substantially by the time running begins in the year 2000, our plan would be to start with a two-year run using the wide band beam. However, as will be made clear in Chapter 8, we consider the narrow band beam option to be an integral and essential part of our experimental program. Several other options for follow-up running, based upon our initial results, are discussed in Section 8.10.

3.3 Focusing devices

In this Section, we give a brief discussion of the focusing devices that permit neutrino beams to have adequate flux. Two types of focusing device are under consideration for our neutrino beams, namely horns and lithium lenses.

Double horn systems have been used for years at BNL, CERN, and Fermilab to produce WBB[54]. The horns focus particles with a toroidal magnetic field which varies as 1/R. The horns are designed to focus the particles produced in a target into a parallel beam that subsequently decays to neutrinos. A very high flux neutrino beam can be produced because the focusing increases acceptance.

The lithium lens is also a device for decreasing the angular divergence of particles emerging from a target. This is accomplished by applying a current pulse through the ends of a solid lithium cylinder (along the beam direction). The resulting Lorentz force on charged particles passing through the lens is a radially restoring one. Lithium is the lightest metal so that interactions are minimized. A lithium lens is the focusing device used in the Fermilab AP-2 beam line which collects antiprotons.

Horns and lithium lenses fill broadly the same functions, namely focusing a divergent beam into a parallel one. The horn is a more mature technology and was adopted when the WBB was designed a few years ago. In the intervening time, the reliability of the existing lithium lenses has improved significantly and it has become the technology of choice for the NBB, being designed now. It would also be possible to use the lithium lens for the WBB and that may be considered later.

The acceptance of the horn and the lithium lens are similar. The primary advantage of the lithium lens is its short focal length and this is of particular advantage for the NBB, where the needed bends make the beam longer than the WBB. Disadvantages of the lithium lens are its higher cost and possible failure modes.

The focal length of a lithium lens is given by

$$f = \frac{1}{k\tan(kl)} \tag{3.1}$$

where f is a focal length in meters, $k = \sqrt{0.3G/p}$, G is the field gradient in Tesla/meter (T/m), p is the momentum in GeV/c and l is the length of the device in meters. The AP-2 lithium lens, as an example, has a radius of 0.01 m, a length of 0.15 m and a constant field gradient of 10 T/m. The focal length of that lens is (0.67 m, 0.95 m, 1.28 m) for (30 GeV/c, 45 GeV/c, 60 GeV/c). Transverse momentum acceptance of the device, if the target is placed at the focal point, is 500 MeV/c for all three momenta, providing very good angular acceptance of pions. If the lens were 0.1 m in radius, 0.2 m long, and had a gradient of 120 T/m, the focal length at 45 GeV/c would be 6.2 meters. The transverse momentum acceptance would be 720 MeV/c.

The two lithium lenses under consideration are 1 cm and 10 cm in radius. The 1 cm version would be based on the present AP-2 device. The lengths of these lenses are 15 and 20 cm respectively. The neutrino production rates are comparable for both. The constraints involved in choosing the lens radius are three fold: (a) the surface field of the lens; (b) Joule heating; and (c) the ratio of the skin depth to the lens radius, which must be at least 0.45 for good field quality. Scaling the existing 1 cm radius lens to a 10 cm lens should produce a reliable design.

A reasonable design has an acceptable surface field in the range of 10 - 12 T. A 10 cm lens will have a temperature rise from Joule heating due to one pulse that varies with the square of the lens radius. The available surface cooling area rises linearly with radius so the cooling rate must rise by a factor of 10. Skin depth varies as the reciprocal of the square root of frequency ω. The frequency ω of the half-sine wave pulse is 9500 rad/sec for the 1 cm lens used in the Fermilab Antiproton Source. In order to maintain the ratio of skin depth to radius when scaling to a lens radius of 10 cm the half–wave sine pulse must have a duration of 30 msec. These requirements are achievable though the detailed design will be challenging.

The small radius lens has the advantage that a working model exists in the form of the AP-2 lens. The larger radius lens will be more expensive and more technically challenging, but there are three advantages to using a larger diameter lens. First, a larger lens results in a longer focal length. Since the line source target is further away, it appears to be more point like. This is good for focusing. Second, with the high intensity of this experiment, a larger spot size (probably a transverse size of 0.5 mm to 1 mm at one σ) is required. The larger the lens, the less sensitivity to spot size. Third, a larger lens also allows the beam to expand more. Since phase space is conserved, this results in a less divergent beam.

3.4 Neutrino flux calculations

We have used three programs to calculate neutrino flux because different calculational needs are met by each program. The three programs also allow us to perform cross checks of our calculations. In this Section, we give a brief description of the calculational strategy of each program and summarize their strengths and weaknesses for our purposes. In this Chapter

we will first present the event-rate results from these programs and then describe the layouts of the different beams and the neutrino spectra they produce.

The Fermilab neutrino beam program NUADA[55] is an analytic calculation using a parametrization of secondary hadron production[56] and decay kinematics. Only the two-body decays of π^+ and $K^+ \rightarrow \mu^+\nu_\mu$ are used to calculate the neutrino flux at the near and far detectors. The charged current ν_μ cross section for $\nu_\mu p$ or $\nu_\mu n$ is used to determine the ν_μ event rate at the detectors. NUADA is used for both WBB and NBB flux calculations.

The E–803 Monte Carlo[57] (PBEAM) follows each particle produced in the target and traces it through the horn focusing elements. The secondary particle production is a parameterization of data from S.P. Denisov, *et al.*[58]. The particles $\pi^\pm$, $K^\pm$ and K_L^0 are produced in the target and if they successfully exit the target are then allowed to decay with distances consistent with each particle's lifetime and momentum. The μ from the π and K two-body decays are also allowed to decay. Absorption by the horn and multiple scattering in the horns is modelled. This Monte Carlo allows realistic determination of the backgrounds to the ν_μ flux but requires huge amounts of computer time for studies in the far detector.

A third beam program NUANL has been developed for the MINOS collaboration[59]. NUANL uses as input the secondary particle production of the E–803 Monte Carlo. It is then an analytical calculation of the ν flux at both the near and far detectors. The NUANL program includes all leptonic decays of the $\pi^\pm$, $K^\pm$ and K_L^0 and the subsequent decays of the muons in those decays. It also includes decays of the secondary $\pi^\pm$ in the K_{e3} and $K_{\mu 3}$ decays and of the $\pi^\pm$ in the $K^+ \rightarrow \pi^+\pi^0$ and $\pi^+\pi^-\pi^+$ decays. This program offers the best determination of the ν_e, $\overline{\nu}_e$ and $\overline{\nu}_\mu$ backgrounds to the ν_μ events in each detector.

We have used these programs in the following way. Fermilab main injector 120 GeV protons on a carbon target produce secondaries that are focused either by the WBB or by the NBB with central momenta of 30, 45, or 60 GeV/c[60]. The target is a half–density two interaction length carbon pencil 1.8 m long with a radius of 3 mm. Multiple scattering and absorption are modelled in the target. The secondary π and K exiting the target are allowed to decay with the appropriate lifetimes. The surviving π and K pass through the focusing elements. The focused π^+ and K^+ decay within an evacuated decay pipe. The ν_μ are projected to a far detector of 4 m radius at a distance of L_F where

$$L_F = \text{decay pipe length} + 150\ m \text{ shielding} + 732\ km \tag{3.2}$$

or to a near detector of 1 m radius at a distance of L_N where

$$L_N = \text{decay pipe length} + 150\ m \text{ shielding} + 40\ m \text{ air.} \tag{3.3}$$

We calculate for a standard year defined as having 4×10^{13} protons on target every 1.9 seconds for 1.75×10^7 seconds/year. In a standard year there are then 3.7×10^{20} protons on target. The ν_μ flux into a one kiloton (kT) detector at L_N or L_F in a standard year defines a kT-year.

3.5 Decay pipe optimization

The decay pipe radius and length affect the ν_μ and ν_τ event rates for both the near detector at Fermilab and the far detector at Soudan. The ν_τ event rate at the near and far detectors

is calculated by assuming that the ν_μ oscillate to ν_τ with maximal mixing, $\sin^2(2\theta) = 1$ and $\Delta m^2 \rightarrow \infty$. The result of this assumption is that half of the ν_μ are transformed to ν_τ. However, for the NBB it is possible to tune the beam energy to the appropriate Δm^2 so the ν_τ rate will be twice the maximal mixing assumption rate. The ν_τ have the same energy spectrum as the ν_μ. The ν_τ event rate at the long baseline detectors is then calculated using the ν_τ charged current (CC) cross section for $\nu_\tau Fe$, including the energy dependence of $\sigma^{CC}_{\nu_\tau}$. This calculation shows that the ratio of ($\nu_\mu \rightarrow$ CC ν_τ) to (CC ν_μ) is $\approx 15\%$ for the WBB.

In the Section 3.5.1 we show results for beam parameters from both WBB and NBB (not tuned in energy for Δm^2) as a function of the length of the decay pipe.

3.5.1 Optimizing the ν_τ rate at the far detector

We studied the question of decay pipe radius by determining the ν_τ event rate at the far detector for various decay pipe radii from 0.25 m to 4 m. At the same time we studied the effect of decay pipe length by varying that parameter between 300 and 1000 m. Figure 3.1 illustrates the variation in the charged current ν_τ event rates at Soudan for different decay pipe radii and lengths for the WBB. The rates show a rapid increase with increasing decay pipe radius until a plateau is reached. The data suggest that the decay pipe radius should be optimized on or near the plateau for each decay pipe length in order to maximize ν_τ events at the far detector.

The variation of ν_τ rates for a NBB is presented in Figure 3.2. (This calculation was done for a different NBB focusing system than those presently under design. But the general dependence on decay pipe parameters should be quite similar.) The rapid event rate increase for increased decay pipe radius up to about 1 m, evident in the WBB case, is also present for the NBB. The onset of the plateau at larger radius for longer decay pipes in both beam options shows that the decay pipe radius must be optimized for the desired decay pipe length. The number of ν_τ events for any running period and detector mass can be increased by such an optimization.

Figure 3.3 shows the comparison of the charged current ν_τ and the quasi-elastic ν_τ event rates at Soudan for the maximal mixing assumption and the Kamiokande parameters using the WBB. The Kamiokande parameters for $\nu_\mu \rightarrow \nu_\tau$ are taken to be $\sin^2(2\theta) = 1$ and $\Delta m^2 = 10^{-2} eV^2$. The decay pipe radius has been optimized at the first plateau point for each decay pipe length. The first plateau point is approximately 90% of the maximum event rate achievable with a 4 m decay pipe radius. The plot is a graphical representation of the data assuming an optimized decay pipe radius.

The information presented in this Section indicates that for the long baseline neutrino oscillation search a decay pipe length of 1000 m with a decay pipe radius of 1.5 to 2 m provides more ν_τ events at the 732 km distant detector than for a decay pipe with a smaller radius or a shorter length. A radius of 1 m for the 1000 m long decay pipe results in approximately 10% fewer ν_τ events at Soudan. The optimization of the decay pipe length and radius must ultimately be traded off against the detector mass and cost and event rates for the final NuMI neutrino beam design.

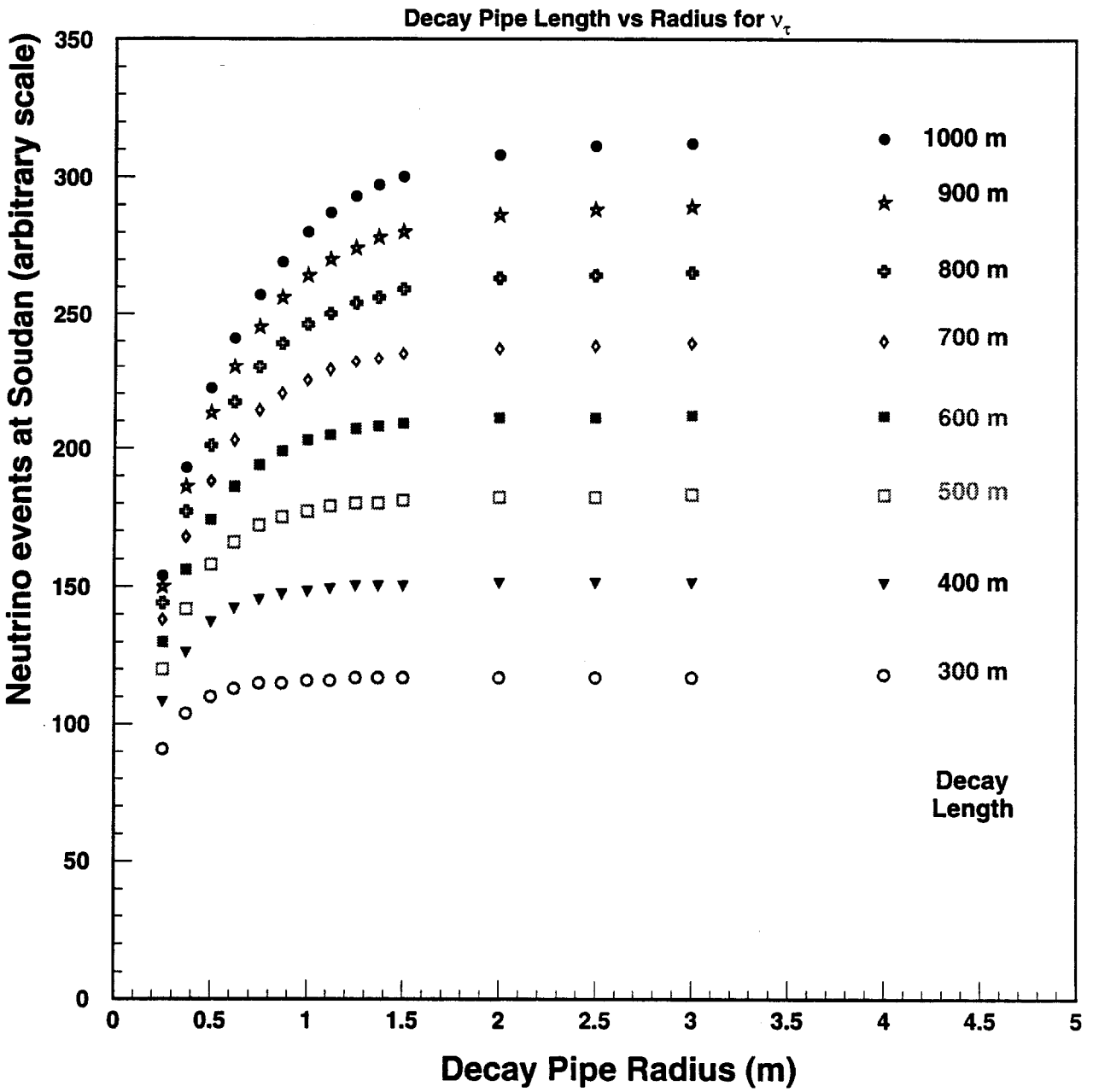

Figure 3.1: Comparison of the ν_τ event rates at Soudan for decay lengths from 300 to 1000 m and decay pipe radii from 0.25 to 4.0 m using the WBB.

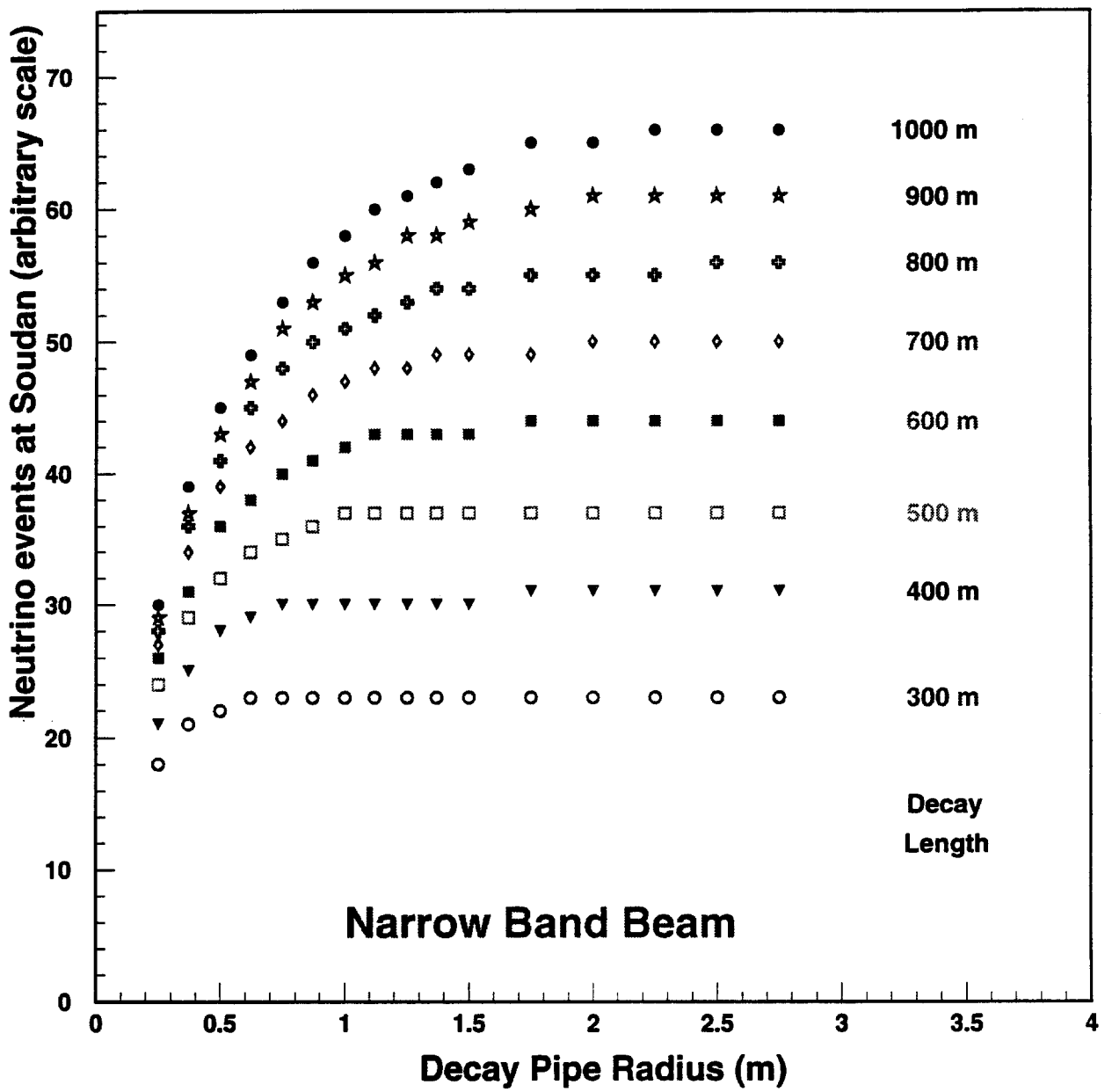

Figure 3.2: Comparison of the ν_τ event rates at Soudan for decay lengths from 300 to 1000 m and decay pipe radii from 0.25 to 3.0 m using a generic 45 GeV/c NBB.

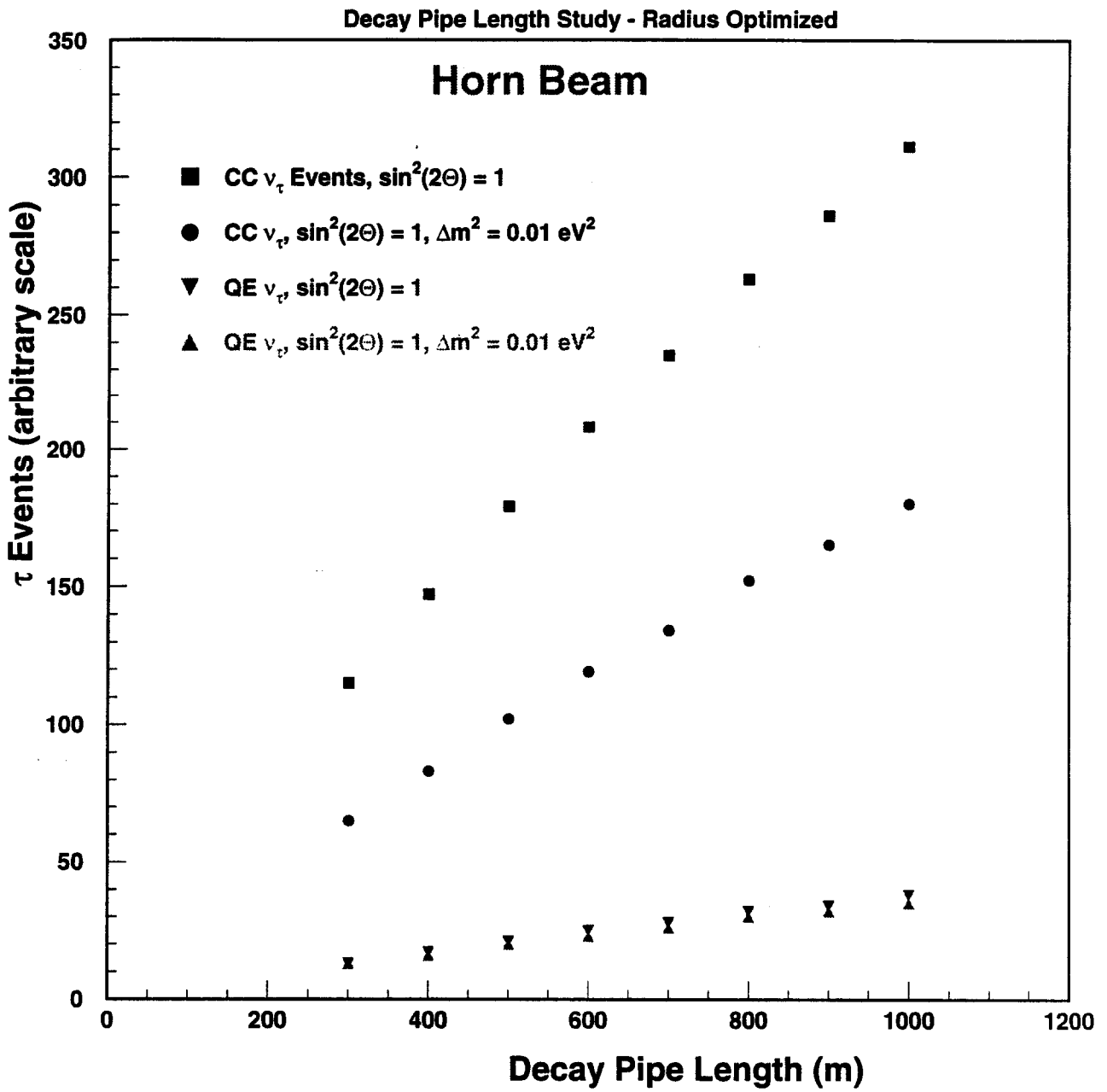

Figure 3.3: Comparison of the ν_μ and ν_τ charged current and ν_τ quasi-elastic event rates for maximal mixing and the ν_τ event rates at the Kamiokande best fit $\nu_\mu \rightarrow \nu_\tau$ oscillation point versus decay pipe length. The event rates are at Soudan for the WBB with an optimized decay pipe radius for each decay pipe length.

3.5.2 Variation of the ν_τ rate at the near detector

Event rates for the near detector are large enough that the rates do not need to be optimized for MINOS. But the decay pipe parameters also affect E–803 rates, as we describe briefly in this Section.

We have repeated the rate calculations as a function of the decay pipe parameters using a one kT iron detector with a radius of 1 m located 190 m beyond the end of the decay pipe. The results are shown in Figure 3.4 for the WBB, and in Figure 3.5 for the NBB design discussed in Section 3.5.1. We continue to assume neutrino mixing with $\sin^2(2\theta) = 1.0$ and $\Delta m^2 = \infty$.

The variation in event rates for the near detector behave oppositely to that for the far detector as a function of the decay pipe length. The maximum ν_τ event rates occur for a decay pipe length of 400 m and then decrease by approximately 25% for a length of 1000 m. However, the ν_τ event rates do show the same type of dependence on the decay pipe *radius* as do the rates at the far detector but over a smaller range of radius. The optimized pipe radius for the far detector varies from 0.62 to 2.5 m as the length is changed, whereas for the near detector it varies from 1.0 to 1.5 m. The event rates at both the near and far detector suggest that a decay pipe radius of 1.0 to 1.5 m is adequate for a long decay pipe.

Discussions with E–803 have resulted in a compromise that is suitable to both E–803 and MINOS. We have agreed to use a decay pipe with a length of 800 m and a radius of 1 m as the working hypothesis. According to E–803, for the region of Δm^2 they are studying, an 800 m decay pipe is the longest pipe that they can tolerate without sacrificing their sensitivity to $\nu_\mu \rightarrow \nu_\tau$ oscillations[61].

All of the beam calculations for this proposal that are not explicitly studying the effect of decay pipe length have used a decay pipe length of 800 m, unless stated otherwise.

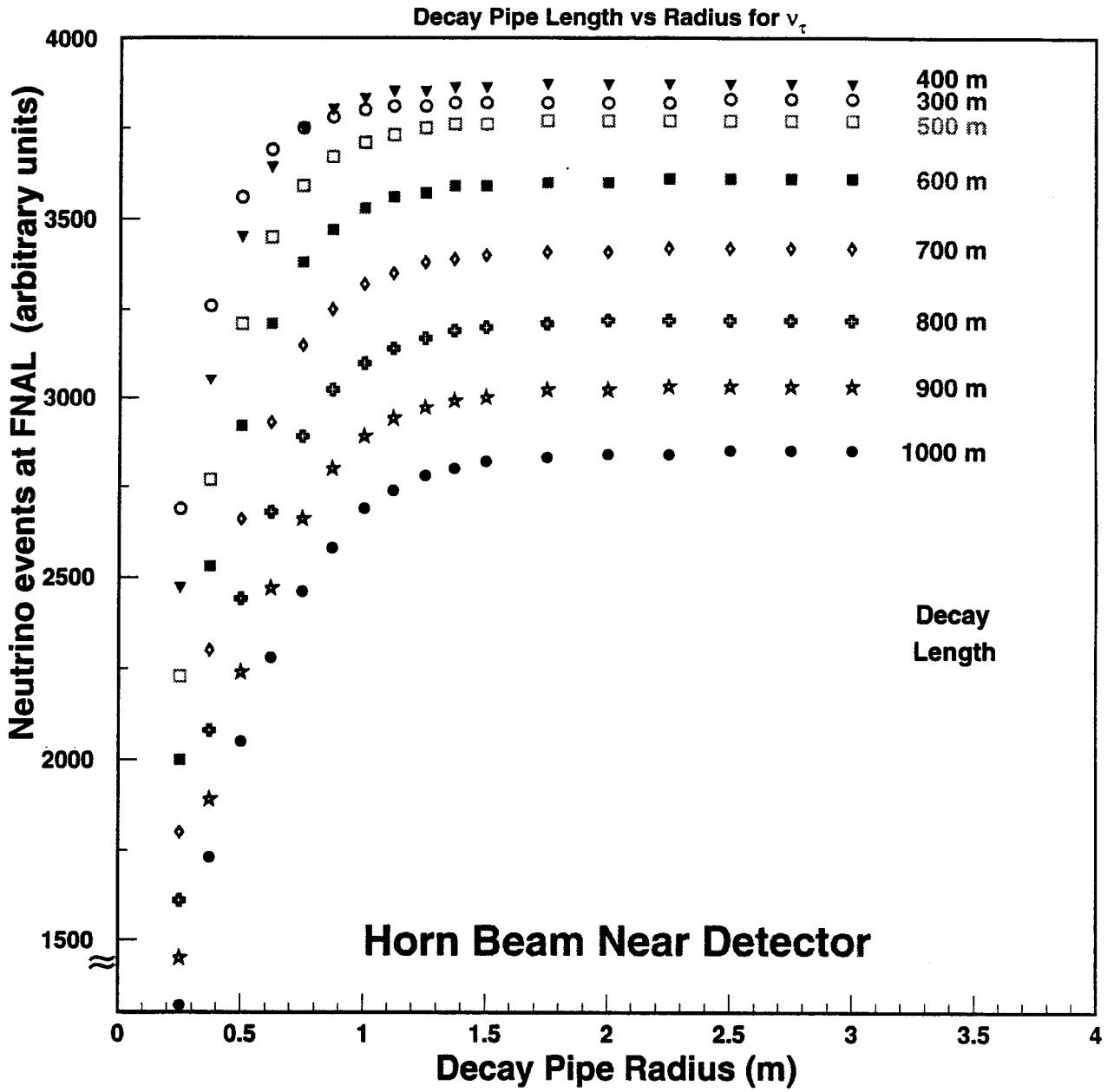

Figure 3.4: Comparison of the ν_τ event rates at Fermilab for decay lengths from 300 to 1000 m and decay pipe radii from 0.25 to 3.0 m for the WBB. Note the suppressed zero on the vertical scale.

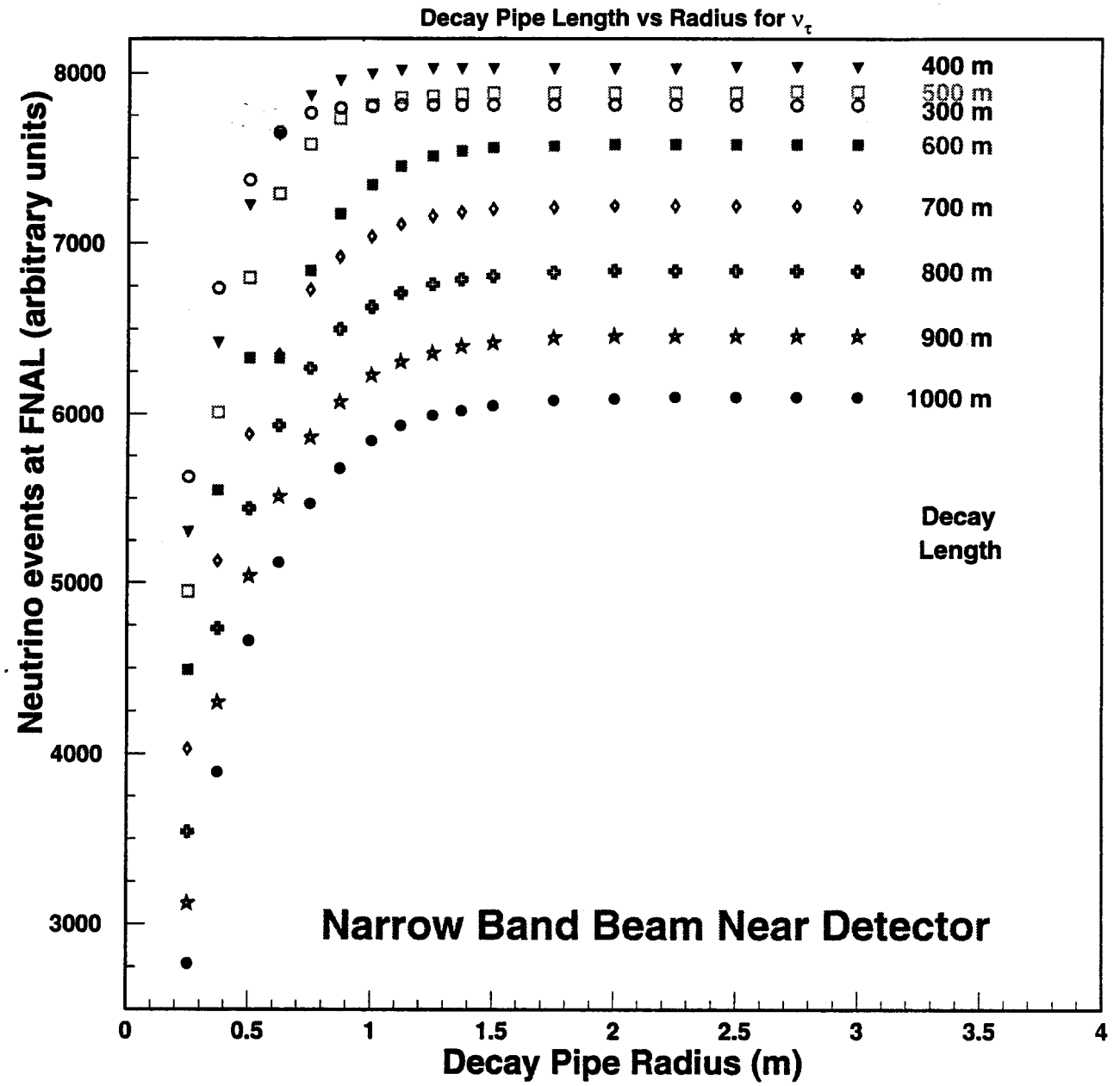

Figure 3.5: Comparison of the ν_τ event rates at Fermilab for decay lengths from 300 to 1000 m and decay pipe radii from 0.25 to 3.0 m using a generic 45 GeV/c NBB. Note the suppressed zero on the vertical scale.

3.6 Precision of beam pointing to the far detector

The decay pipe must be pointed towards Soudan with high precision in order to:

- Ensure maximum intensity at the far detector,
- Minimize sensitivity to very small changes in steering which might be amplified near the edges of the beam,
- Avoid possible differences in non-ν_μ beam backgrounds from those calculated under the assumption of perfect centering.

PBEAM and NUADA were used to obtain the profile of neutrino interactions as a function of the distance from the beam center at Soudan, which is illustrated in Figure 3.6 (a). The beam intensity is relatively flat out to about 400 m from beam center, followed by a rapid drop in intensity caused by the finite radius of the decay pipe. Our goal is to point the beam towards Soudan with a transverse precision of 100 m out of 732 km, or 0.14 mr, which should be easily attainable. The flux in the area near beam center is shown in Figure 3.6 (b). The beam profile is flat out to 100 m from beam center for ν_μ events.

We have also used PBEAM to study the ν_e component of the beam as a function of distance from the beam center at Soudan. Figure 3.6 (c) shows that this important background component will not be particularly sensitive to beam steering.

There should be no fundamental difficulty in pointing the Main Injector neutrino beam (*i.e.*, the beamline components and decay pipe) with a precision of 0.14 mr towards Soudan [62]. The fact that road tunnels bored from opposite sides of a mountain (or the Channel) meet routinely with a precision of 10 cm or better is an experimental proof of the capabilities of modern surveying technology. Nevertheless, a skeptical scientific community would like to have some experimental verification of the fact that the NuMI neutrino beam is indeed pointing precisely at the MINOS detector. To address this issue we are actively exploring the possibility of placing several sets of muon counters in the Soudan mine, probably about 400 m to both sides and above the detector. These counters would be sensitive to muons produced by beam ν's in the rock. Comparison of these muon rates would give experimental verification of the precision of beam centering on the MINOS detector. Precise verification would require several weeks of data, although gross missteering would be detected faster.

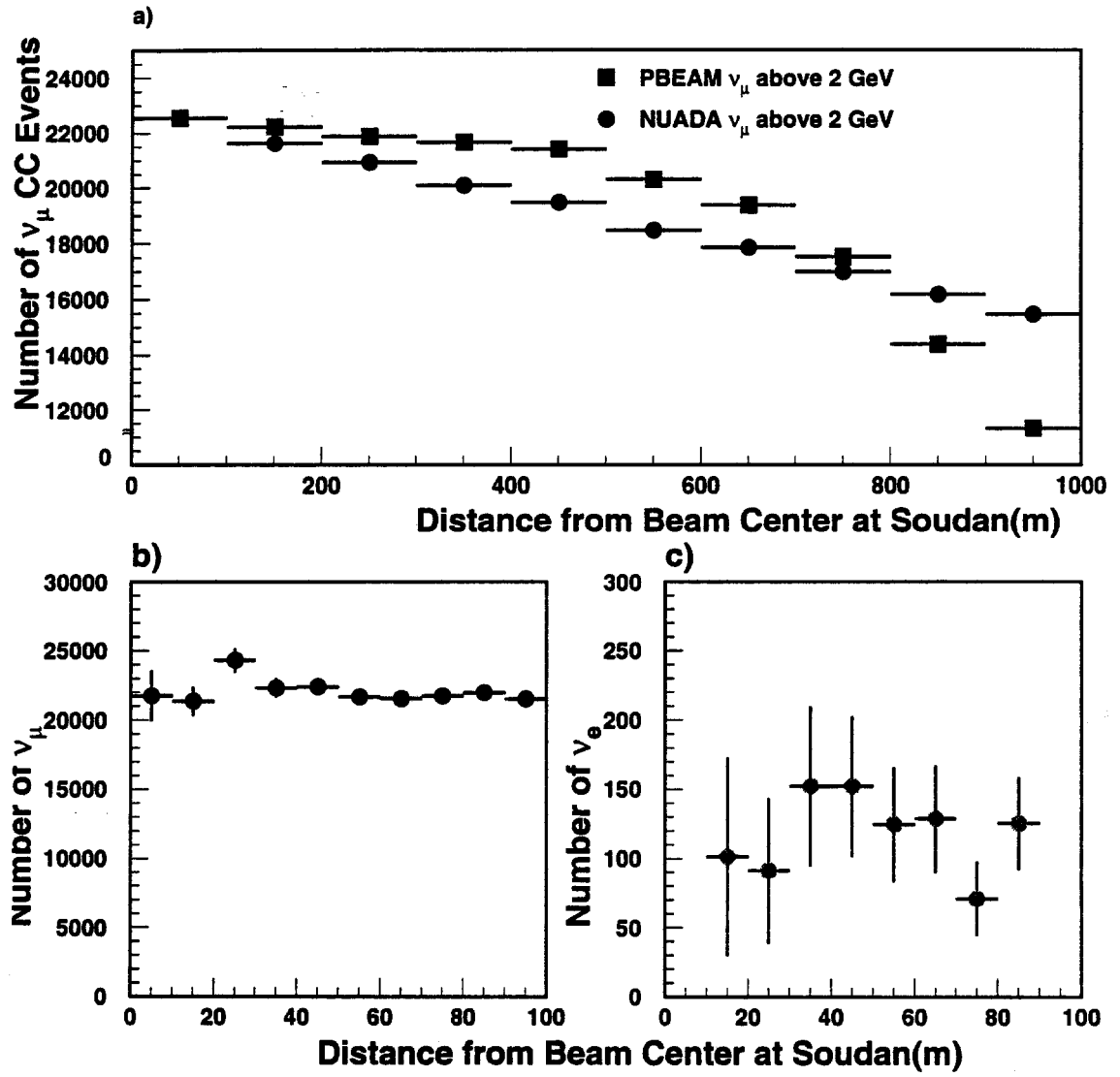

Figure 3.6: a) A comparison of NUADA and PBEAM calculations of the ν_μ beam profile at the far detector (note the suppressed zero on the vertical scale), b) The ν_μ flux normalized by the area of the 10 m bin size annulus, and c) the normalized ν_e flux *vs* distance from beam center at the far detector for a finer distance scale, using the PBEAM program. Only the relative values on the vertical scales are important.

3.7 Wide band beam

We now turn to a discussion of the beam fluxes and spectra at the near and far detectors produced by the WBB and NBB under consideration. As discussed in Section 3.5, calculations have been carried out with three different programs. For now, we consider differences between the programs to give an estimate of calculational uncertainties in the flux results.

Figure 3.7 illustrates the ν flux at the near detector as determined by the three beam programs. The shape of the flux distribution as a function of energy agrees sufficiently well among the programs that it will not be the dominant systematic uncertainty in the WBB physics analyses described in Chapter 8. Figure 3.8 presents the ν_μ flux at the far detector as a function of energy. Note that at both the near and far detectors, 92% of the interactions will be from π decay neutrinos and 8% will be from K decay neutrinos. We also note that the sharp drop in flux at 32 GeV is a result of the calculation method used by NUADA. The PBEAM far detector is placed at 10 km rather than at 732 km for the purpose of having adequate statistics to compare to the other two programs. The 10 km distance is well within the $1/R^2$ region, where the beam appears to originate from a point source.

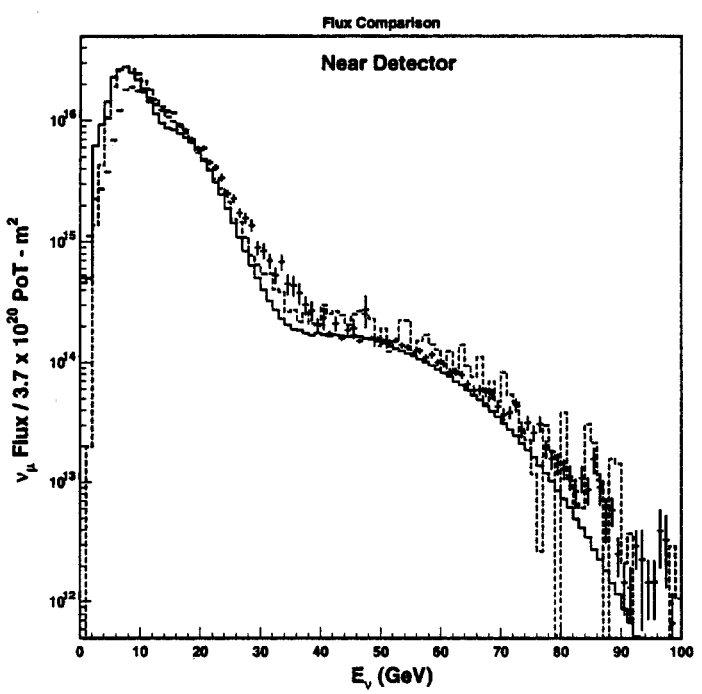

Figure 3.7: Comparison of the ν flux (ν per meter^2) from the three beam programs at the near detector. NUADA results are shown by the solid histogram, NUANL by the points with error bars, and PBEAM by the dashed histogram.

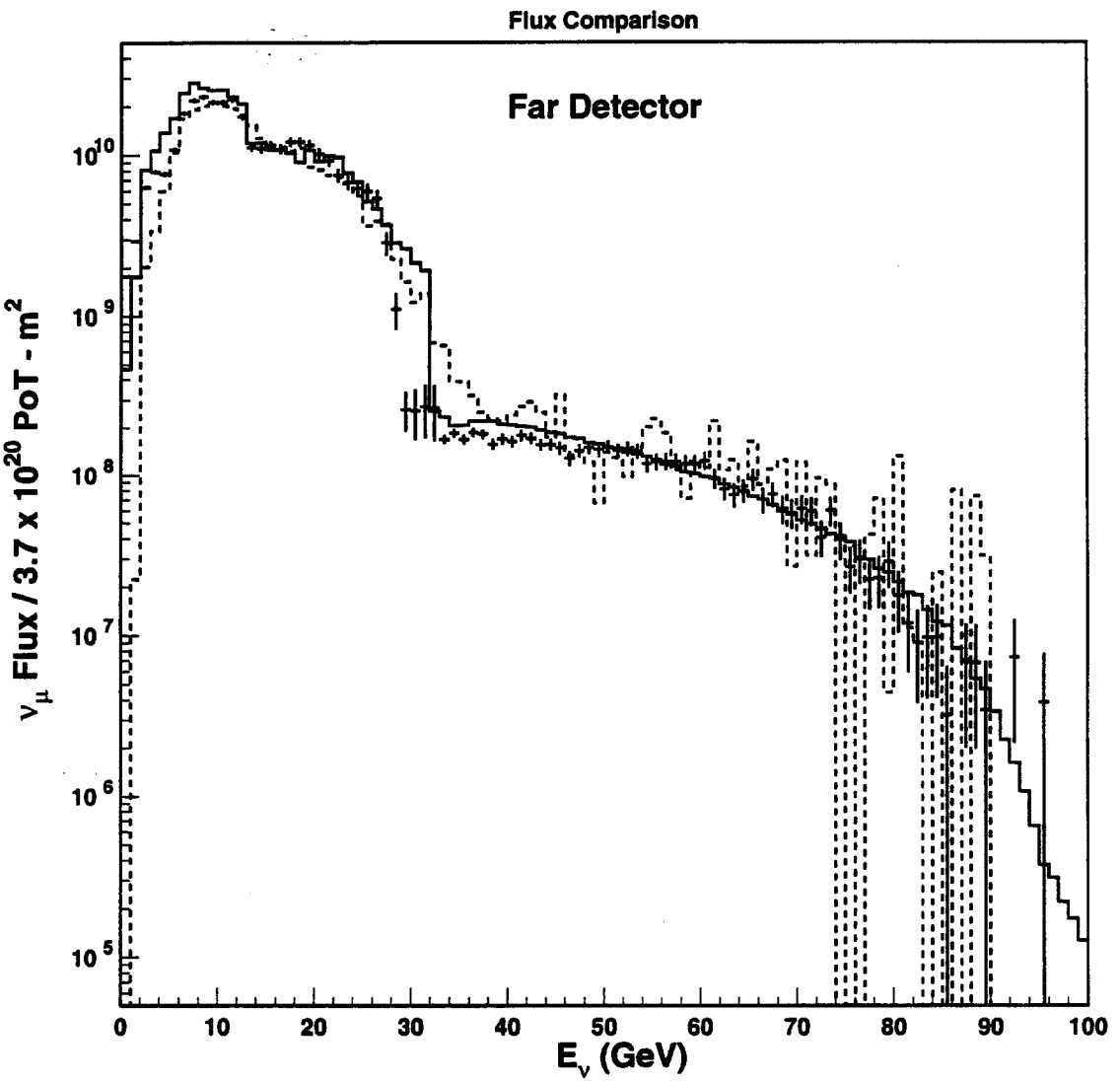

Figure 3.8: Comparison of the ν flux from the three beam programs at the far detector. NUADA results are shown by the solid histogram, NUANL by the points with error bars, and PBEAM by the dashed histogram.

3.7.1 WBB optics

A horn is a cylindrically symmetric current sheet constructed of two conductors. The outer conductor is a cylinder, while the inner conductor is shaped as two cones connected together with a narrow cylinder at their pointed ends. The shape of the horn is shown in Figure 3.9 along with rays displaying the optics of the two horn system. The magnetic field between the two conductors is

$$B = \frac{\mu_0}{2\pi}\frac{I}{r} \tag{3.4}$$

where $\mu_0/4\pi = 10^{-7}$ N/A. An ideal horn with no deformations has $B = I/5r$, with I measured in A, r measured in m to the axis of azimuthal symmetry, and B is in T. There is no magnetic field inside the inner conductor or outside the outer conductor. Particles which remain within the inner conductor do not have their trajectories modified but particles of the appropriate charge which enter the region between the two conductors are focused back toward the horn center line.

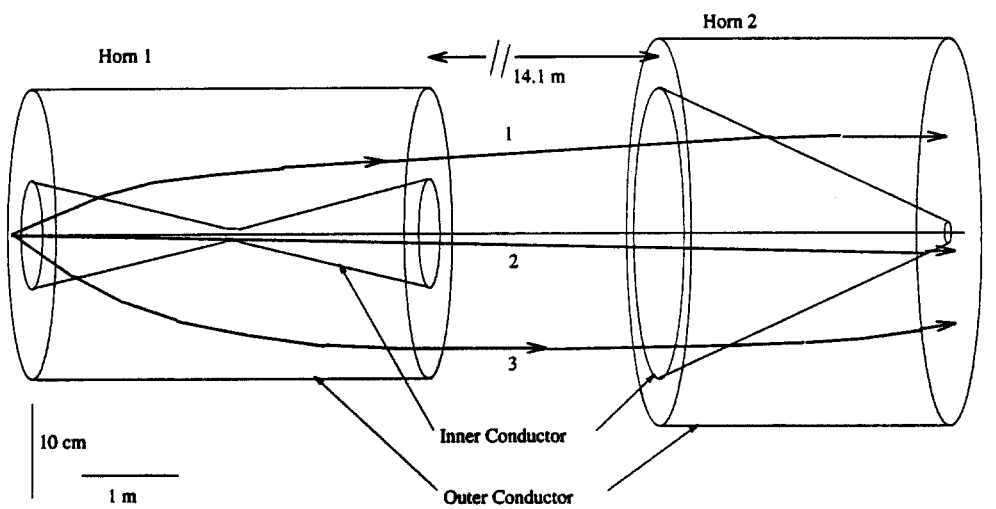

Figure 3.9: The shape and optics of the WBB horns. Rays 1, 2, and 3 illustrate the bending of particle trajectories in the B field between the inner and outer conductors.

The conical shape of the horn means that the horn focuses particles with the same transverse momentum p_T. The first horn is constructed of two cones with $l = 2$ m and $r_1 = 6$ cm so it focuses $p_T = 670$ MeV/c for $I = 160$ kA. The second horn is a single cone with $l = 3$ m and $r_2 = 15$ cm, so it focuses $p_T = 200$ MeV/c. The two horn system has a high efficiency for capturing particles produced by 120 GeV protons interacting with a two interaction length carbon target out to $p_\perp^{production} = 900$ MeV/c[54].

The target has been described briefly in Section 3.4 and much more extensively in an earlier Conceptual Design Report[54].

3.7.2 WBB performance

The WBB with a 1-m radius 800-m long decay pipe will produce 2085 CC ν_μ events per kT-year at the far detector. Using the maximal mixing assumption described in Section 3.5 this will result in 312 CC ν_τ events and 35 quasi-elastic (QE) ν_τ events per kT-year. For $\nu_\mu \rightarrow \nu_\tau$ mixing parameters $\sin^2(2\theta) = 1$ and $\Delta m^2 = 0.01$ eV^2 there will be 176 CC and 35 QE ν_τ events per kT-year at Soudan.

3.7.3 WBB characteristics at near and far detectors

Many of the physics measurements require knowledge that the beams at the near and far detectors are well known and alike in their characteristics. As described in Chapter 2 the MINOS collaboration proposes to study ν interactions in the near detector at 990 m from the target, and at the far detector 732 km away, and to use the near detector measurements as a calibration of the unoscillated interactions. A large difference in the energy distributions at the two detectors could compromise that comparison. In the near detector, there is a strong dependence of the beam energy distribution as a function of the beam radius. Although it is not an obvious result, we find that the ν beam close to the center of the near detector is a good representation of the ν beam at the far detector. An analytical demonstration of this close similarity is given in MINOS collaboration notes [63, 64]. There we show that the energy spectrum of the central 25 cm of the near detector beam is very similar to that at the far detector.

In addition to the analytical demonstration in References [63, 64], we have simulated the beam at the near and far detectors with PBEAM and NUADA. The simulations both show that the energy spectrum within a central 25 cm radius at the near detector is quite similar to that at the far detector. This comparison is illustrated for the NUADA calculation in Figure 3.10. The ratio of the two fluxes as a function of energy is one indication of the differences in the beam, and is shown in Figure 3.11.

The neutrino flux at the far detector can be predicted from measurements of the flux at the near detector. Differences between the near and far beam energy spectra are one measure of the possible systematic error in this extrapolation. To obtain an estimate of this uncertainty, we have calculated the difference in neutrino interaction event rates which would result from the predicted near and far energy spectra:

$$\frac{1}{2}\frac{\int \sigma^{CC} \mid \Phi_n - \Phi_f \mid dE}{\int \sigma^{CC}(\Phi_n + \Phi_f)dE} = 4.2 \times 10^{-2}, \tag{3.5}$$

where Φ_n is the ν_μ flux in the inner 25 cm of the near detector normalized to the same neutrino flux as Φ_f, the ν_μ flux at the far detector. All three beam programs agree on the absolute event rate to better than 2%. We expect to further reduce our systematic error on the event rate at the far detector by using measurements of the radial and energy dependence at the near detector to improve our beam simulations. At present, a conservative assumption is that the near-to-far event ratio can be calculated with an accuracy of 4%.

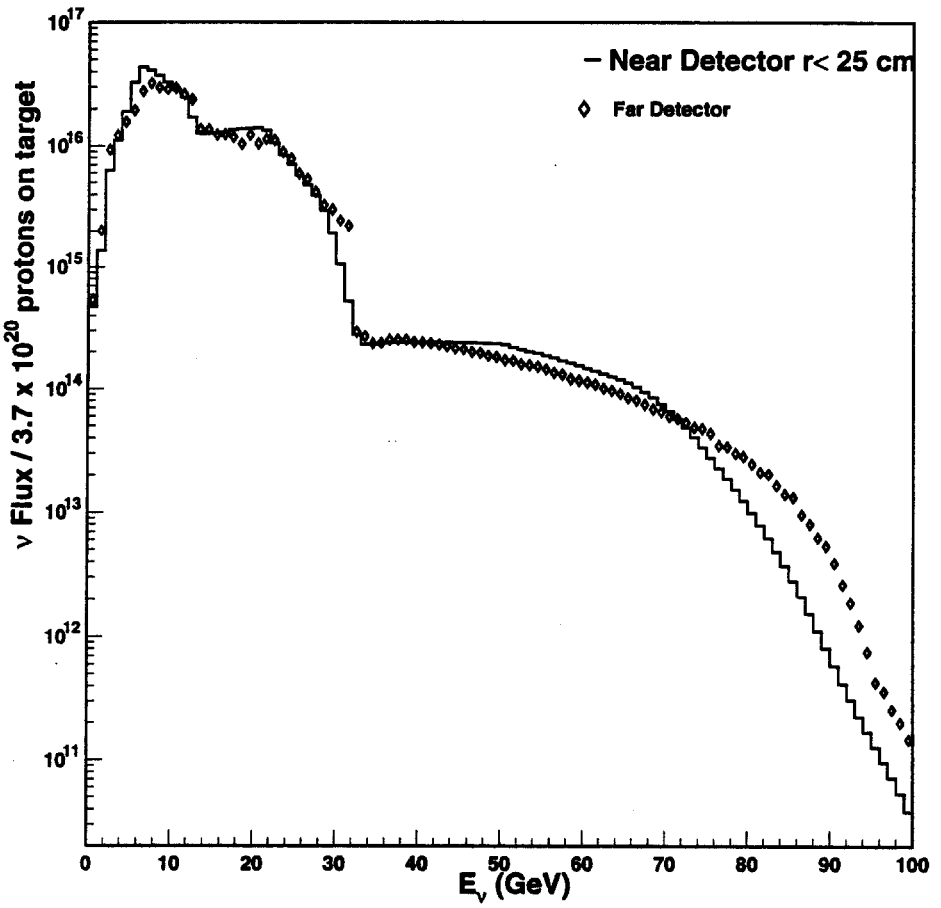

Figure 3.10: Comparison of the ν flux (ν's per meter^2) *vs* energy using the $r < 25$ cm cut at the near detector (histogram) and all ν at the far detector (diamonds).

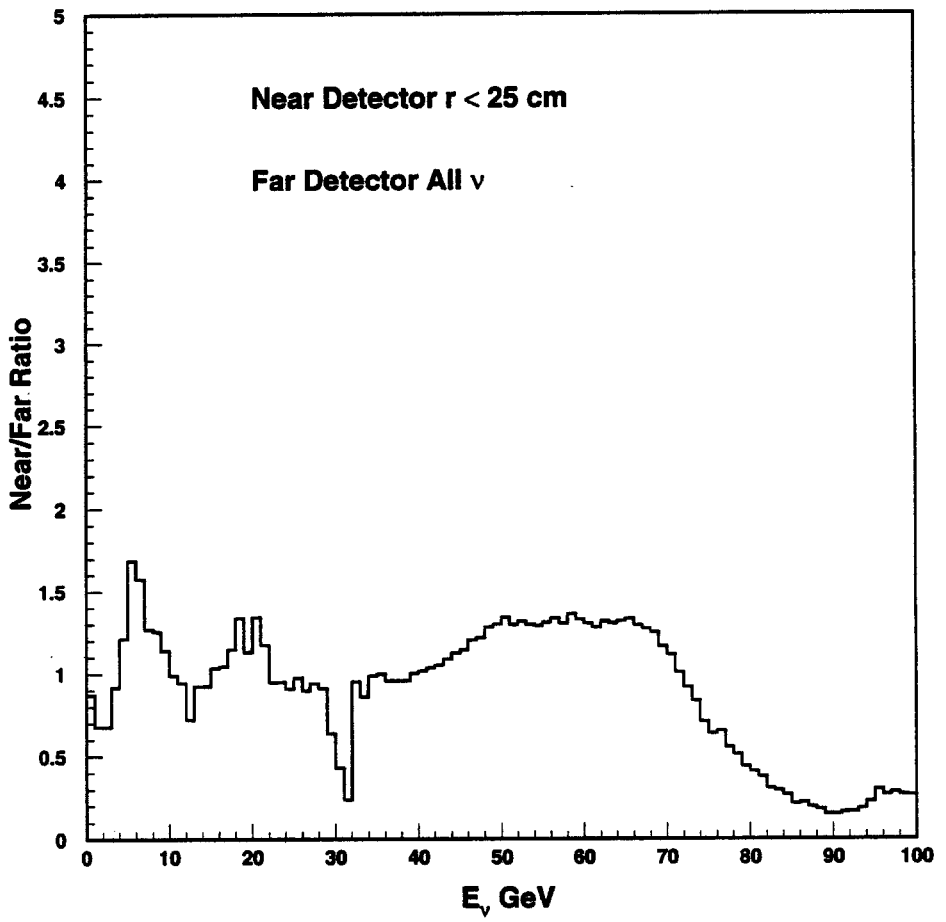

Figure 3.11: Ratio of the ν flux *vs* energy using the 25 cm cut at the near detector and all ν at the far detector.

3.7.4 WBB backgrounds

Figure 3.12 shows the expected WBB ν backgrounds for the full near detector from PBEAM. The most important background for the MINOS experiment is from the $\nu_e + \overline{\nu}_e$ component, which we calculate to be $0.682 \pm 0.0124\%$ of the ν_μ event rate at the far detector. The ν_e and $\overline{\nu}_e$ have a 37% contribution from μ decay, a 33% contribution from $K_L^0 \rightarrow \pi^\pm e^\mp \nu_e$ decays, a 30% contribution from $K^\pm \rightarrow \pi^0 e^\pm \nu_e$ decays and a 0.8% contribution from $\pi^+ \rightarrow e^+ \nu_e$.

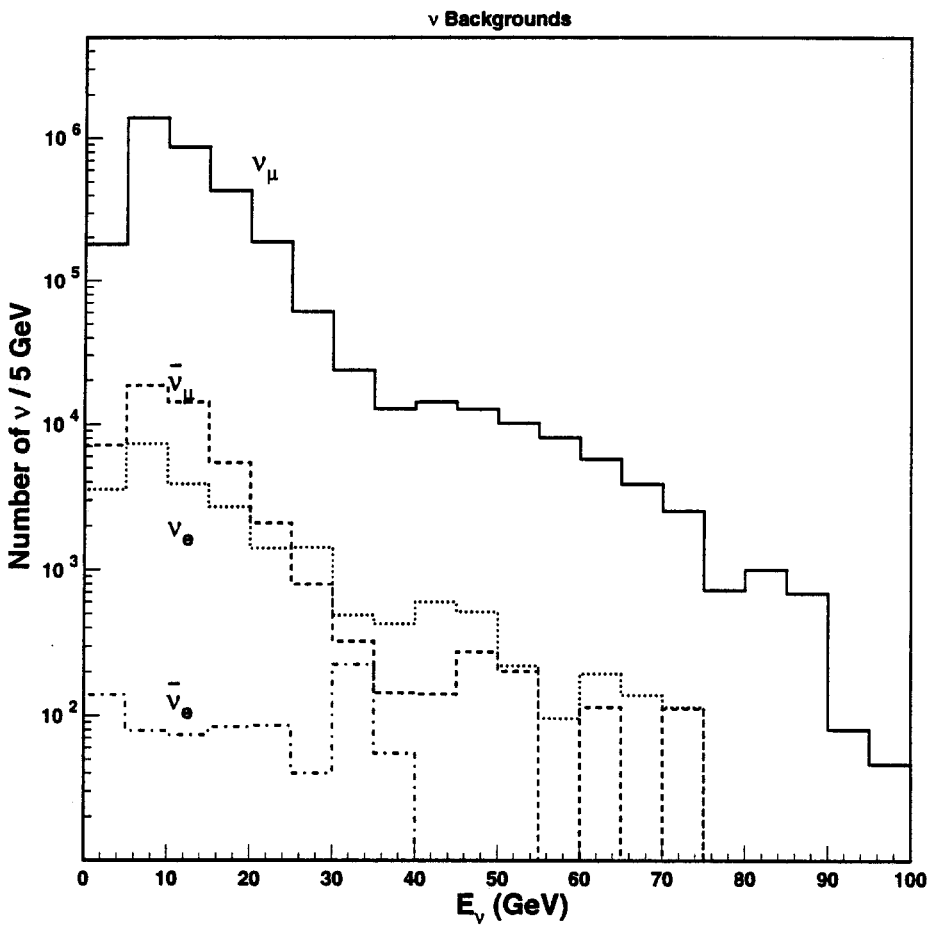

Figure 3.12: The ν_μ, ν_e, $\overline{\nu}_\mu$, and $\overline{\nu}_e$ flux for the 800 m nominal decay pipe. The absolute value of the vertical scale is arbitrary. Only the relative values for each ν type are important.

3.8 Narrow band beam

A narrow-band beam (NBB) will provide several important advantages to a search for neutrino oscillations for the MINOS experiment. These advantages are of particular interest for τ appearance signatures. The additional constraint allowed by the knowledge of the neutrino energy is important for a number of reasons:

- The ratio of ν_τ's in the beam to ν_μ's can be increased by selecting the beam energy to correspond to a maximum in the oscillation probability. Figure 3.13 shows the oscillation probability for neutrinos at Soudan for various Δm^2. It is clear that by tuning the beam energy appropriately the ratio of ν_τ to ν_μ in the beam can be significantly improved with a beam with $\Delta p/p$ around 0.2.

- Because neutrinos carry a substantial part of the energy in τ decays, typical ν_τ events will have reduced total energy of the observable final-state products. This means that ν_μ's of low energy present particular background problems for τ appearance and use of a NBB allows almost complete removal of such low energy neutrinos [65].

- Kinematic cuts which depend on knowledge of the neutrino momentum can be employed. The energy spread in the WBB is simply too broad for any of these cuts to be very useful. This allows more powerful and cleaner cuts.

- For a near detector, a narrow-band beam removes one possible source of background neutrinos which are neutrinos coming from heavy secondaries produced in the target.

- About 10% of the interactions will be from K-decay neutrinos. These high energy neutrinos can provide a consistency check for any oscillation signal observed. For example, values of Δm^2 which give a low oscillation probability for π-decay neutrinos may give a high probability for K-decay neutrinos.

For τ appearance, a NBB with very sharp cutoff on the low energy side is desired. When combined with other analysis cuts for τ appearance, the NBB can provide a powerful tool in reliably characterizing the nature of an oscillation signature.

We can reduce the low-energy tail of the neutrino energy spectrum by using a pion beam with a sharp low-energy cutoff and a very small angular divergence. This will also give very similar energy distributions at the near and far detectors, which will facilitate comparisons of analyses in those detectors. In particular, the background to a τ signal in the far detector will be calculated by performing the same τ analysis on near-detector data, which is assumed to contain no real τ events. The rate of spurious τ-like events will be significantly lower in the NBB than in the WBB experiment. Finally, the similarity of the energy distributions in the near and far detectors gives a smaller systematic uncertainty in a pure disappearance experiment. This could in fact offer the best reach in $\sin^2(2\theta)$ since the statistical uncertainty even for the NBB can be less than 1% for a two-year run.

To accomplish these goals, we have chosen a lithium lens as the pion collector in the beam optics.

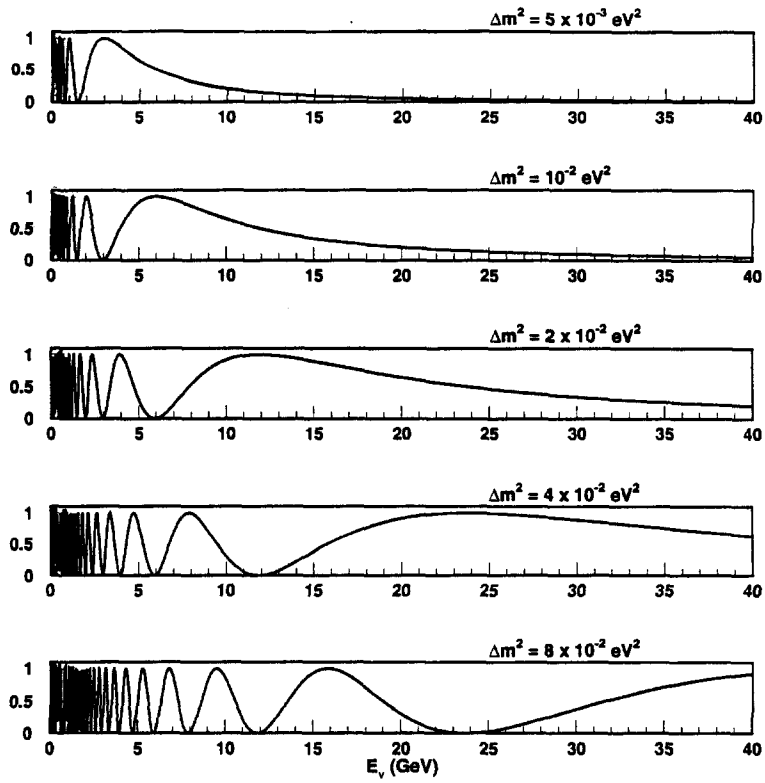

Figure 3.13: Oscillation probability versus neutrino energy for $sin^2(2\theta) = 1$ for neutrinos at Soudan for various Δm^2.

3.8.1 NBB optics

Two beams using lithium lenses are under consideration. The first beam uses a 1 cm (radius) lithium lens and subsequently a total bend for momentum selection of 14 mr is introduced. The lens is 15 cm long and the field at r = 1 cm is 10 T. The second uses a 10 cm (radius) lithium lens and a total bend of 31 mr. This lens is 20 cm long and the field at r = 10 cm is 12 T. The schematic of these beamlines as well as the wide band beam layout is shown in Figure 3.14. The dumping of the primary protons is essentially the same for both NBB's.

The optics of the two beams are slightly different and are compared in Figure 3.15. The optics of the 14 mr beam consists of:

- point to parallel: target through lithium lens,
- parallel to point: first doublet to momentum slit,
- point to parallel: momentum slit through second doublet.

The first bending magnet separates the secondary beam from the primary protons and also gives a dp/dx correlation at the momentum slit. The second bending magnet, along with the quadrupole near the slit recombine the momenta.

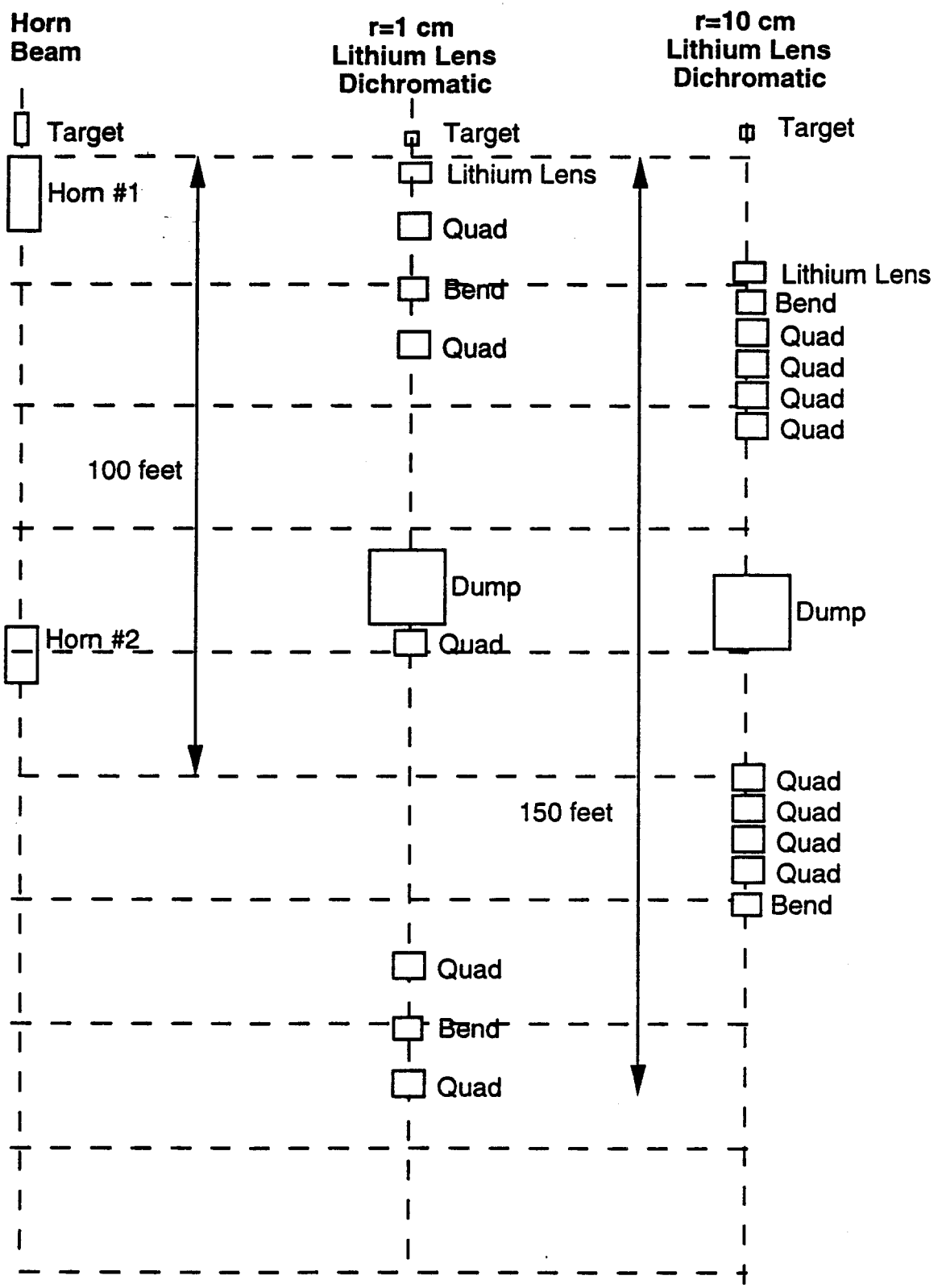

Figure 3.14: The layout in the beam direction of the two NBB options compared with that of the WBB. The vertical scale is in feet with each division equal to five feet. The arrows illustrate the lengths of the WBB and the NBB with a 1 cm radius lithium lens.

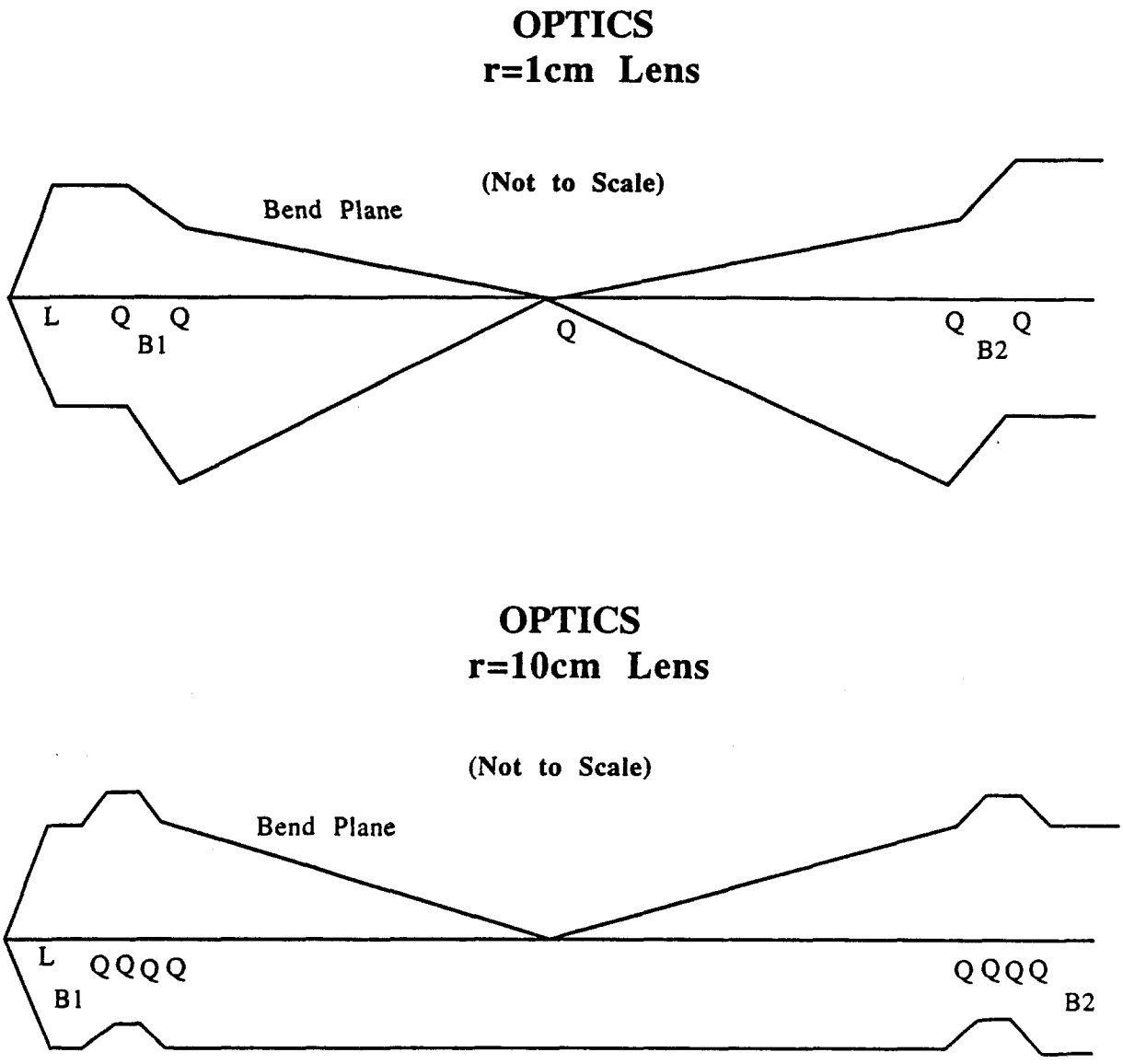

Figure 3.15: The optics of the two NBB options.

The optics of the 31 mr beam consists of:

- point to parallel: target through lithium lens,
- parallel to point(bend plane): Q1 thru Q4 to momentum slit,
- parallel to parallel(non bend plane): Q1 thru Q4 to momentum slit,
- point to parallel(bend plane): momentum slit through Q8.
- parallel to parallel(non bend plane): momentum slit through Q8.

The first bending magnet separates the secondary beam from the primary protons and also gives a dp/dx correlation at the momentum slit. The second bending magnet, along with the 8 quadrupoles, recombines the momenta.

The beamlines can be tuned to various momenta, by changing the focal length of the lithium lens, keeping its gradient constant, and then scaling the bends and quadrupoles. This retains the highest acceptance while moving a minimum number of elements. Only the distance from the target to the lithium lens needs to be varied. For tunes from 30 to 60 GeV/c, the corresponding target-to-beginning-of-lens distance varies from about 0.6 to 1.3 m in the first beam, and from 4 to 8 m in the second beam.

3.8.2 NBB performance

We have calculated the NBB event rates for the 45 GeV/c beam, which has $E_{\nu_\mu} = 18.9 \pm 2.8$ GeV/c. The ν_μ energy spread is 15%. For 3.7×10^{20} protons on target (one year), the ν_μ intensity is $1.7 \times 10^{16}/m^2$ at the near detector and $8.9 \times 10^{10}/m^2$ at the far detector. The far detector event rates per kT-year are given in Table 3.1. Assuming a 7 kT fiducial mass for the 10 kT MINOS detector, we expect to obtain approximately 9,000 ν_μ CC and 2,400 NC events in a two-year run with the NBB (assuming no oscillations).

CC ν_μ	QE+SP ν_μ	CC ν_τ	QE+SP ν_τ	CC $\tau \rightarrow \mu$ or e	$QE + SP$ $\tau \rightarrow \mu$ or e
640	41	121	17	41	5

Table 3.1: Comparison of the NBB ν_μ and ν_τ charged current and quasi-elastic + single pion event rates per kT-year. The ν_μ rates assume no oscillations, and the ν_τ rates assume mixing parameters $\sin^2(2\theta) = 1$, and $\Delta m^2 = 0.015$ eV^2.

The energy distributions of ν_μ events at the near detector for various radius cuts are shown in Figure 3.16. Although the event rate calculation shown in Figure 3.16 has relatively large uncertainties for $E_\nu < 10$ GeV, there is a significant low-energy tail. We can remove that tail by making the pion beam more parallel to the neutrino beam line direction and reconfiguring the momentum slit. Figure 3.17 shows the energy distribution of the ν_μ events at the far detector for this optimized beam, which exhibits a significantly reduced low energy tail compared to Figure 3.16. However, this improvement has been obtained at the expense

of ν_μ flux, which is lower than that used to calculate the NBB event rates in Table 3.1. Optimization of the NBB design is still in progress at this time.

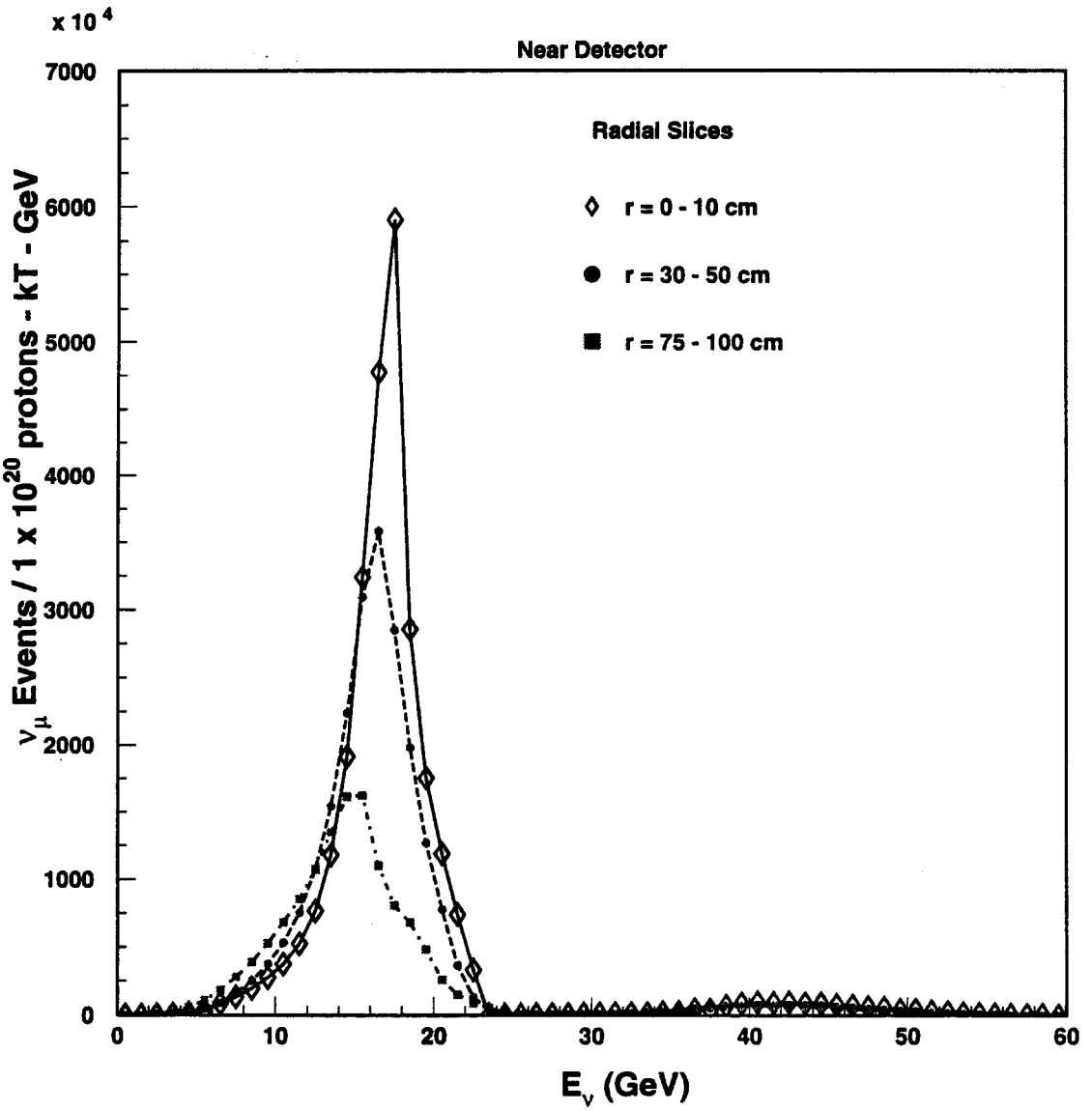

Figure 3.16: Energy spectrum of NBB ν_μ events for several radial slices at the near detector.

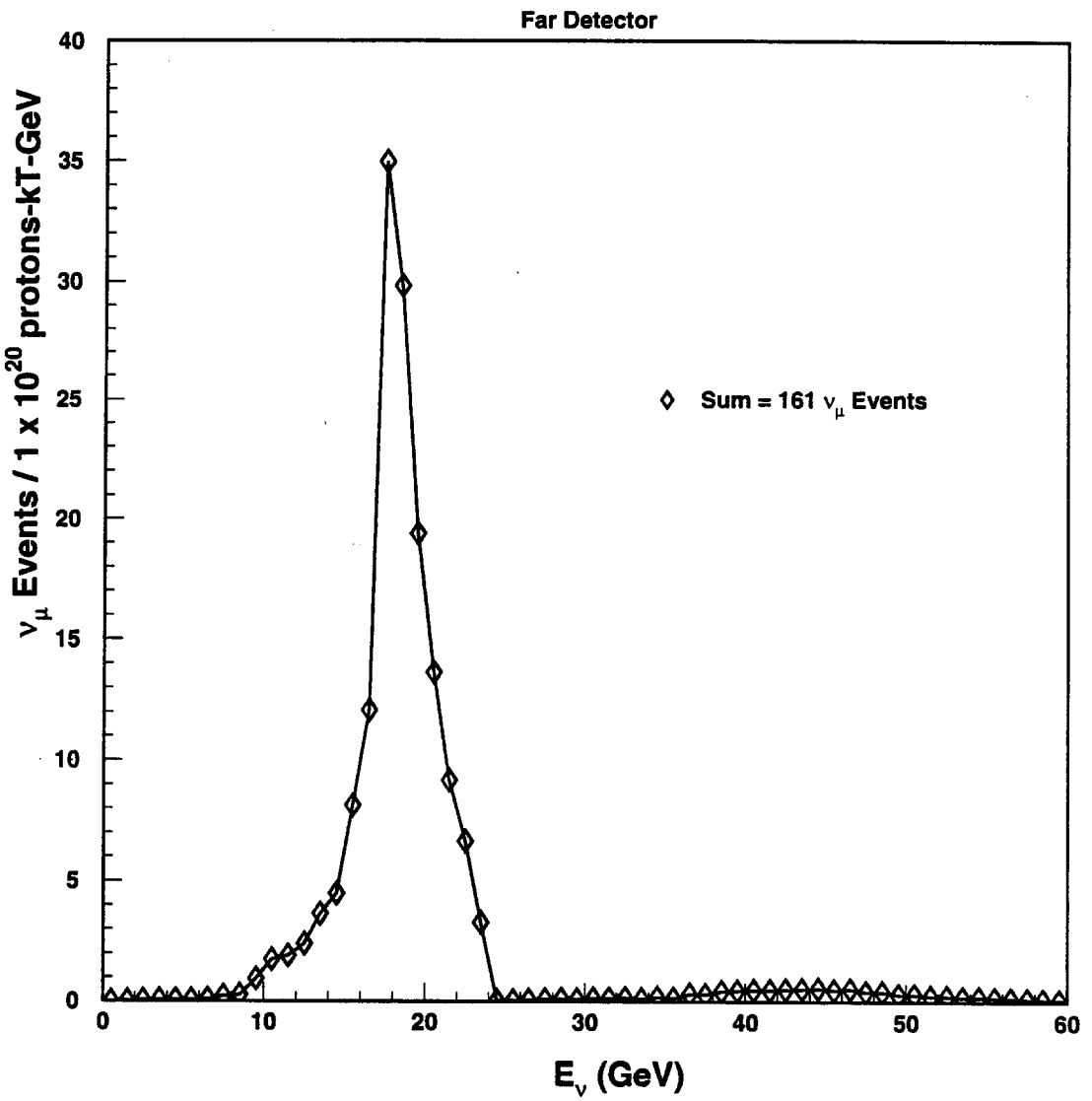

Figure 3.17: Energy spectrum of ν_μ events at the far detector from the NBB with a reduced low-energy tail.

3.8.3 NBB backgrounds

For the goals of our experiment the ideal NBB is one that is composed only of ν_μ's with energies close to the nominal value. Low energy ν_μ's or ν's of other species constitute background. Since the final beam has not been designed yet, no rigorous quantitative statements can be made at this time about the level of different backgrounds. However, we can make some semi-quantitative statements based on the more mature studies of WBB backgrounds, experience with other NBB designs, and the work to date on the NuMI NBB.

Low energy ν_μ's

One of the MINOS design goals for the NBB is to minimize the low energy tails of the beam energy spectrum. The current design is still not completely satisfactory in that regard (see Figure 3.17), and work is continuing on further optimization. There are several possible sources of low-energy ν_μ in the NuMI neutrino beam:

1. Nonparallel pions, *i.e.* those traveling at a finite angle to the beam axis, constitute the most important source of low-energy ν_μ's. In the NBB, neutrinos that reach the far detector must be produced at a finite angle, and therefore at less than the maximum energy.

2. Low momentum pions in the beam channel itself produce low-energy ν_μ. Because the NBB design requires the final hadron beam to point at a finite angle to the proton beam direction, very few ν's from decay of off-momentum mesons should be seen by our detectors.

3. Third generation ν_μ's, coming from processes like $K^+ \to \pi^+\pi^0$ (or $\to \pi^+\pi^+\pi^-$) followed by $\pi^+ \to \mu^+\nu$ also produce low-energy ν_μ.

4. Semileptonic decays of K^+ constitute an irreducible low-energy beam component. This is estimated to be roughly 0.2% of the total ν flux, but only a small fraction of these neutrinos have less than the nominal ν beam energy.

An optimized NBB design will reduce the first three contributions as much as possible, perhaps requiring some trade-offs with the total flux. There appears to be some advantage in keeping the transverse dimensions of the upstream end of the decay pipe as small as possible, so as to be able to provide effective collimation for decay particles (*e.g.* π's from $K \to \pi\pi$). The production target needs to be optimized to provide minimum phase space consistent with large flux of secondaries. Finally, the bending magnets and/or quadrupoles might be mistuned slightly between the two stages of magnetic analysis to make the lower momentum component of the pion beam as parallel as possible.

Neutrinos of other species

Because the NBB direction is at a finite angle with respect to the incident proton beam, ν_τ's coming from the short-lived secondaries made in the target constitute a negligible contamination. Similarly no significant sources of $\overline{\nu}_e$'s exist in the NBB at the 10^{-3} level. Thus we focus here on $\overline{\nu}_\mu$ and ν_e contamination. Probably the principal source of the $\overline{\nu}_\mu$ and ν_e

component is muon decay. The former are not a problem because they will be recognized most of the time by the presence of wrong sign muons, and their cross section is down by a factor of about 2.5. The $\overline{\nu}_\mu$'s will also prove to be a useful monitor of the size of the ν_e component. Another source of $\overline{\nu}_\mu$'s is the decays of π^-'s from $K^+ \rightarrow \pi^+\pi^+\pi^-$. This contribution is also expected to be below the 10^{-3} level.

The ν_e component receives roughly equal contributions, about 0.25% each, from both μ decays and K^+ semileptonic decays. The muon source might be reduced slightly by installing defocusing toroids around the beam at several places in the decay pipe. This method, which is currently under study, would be effective only if the radial π and μ distributions are significantly different.

3.9 Beam monitoring

The purpose of beam monitors in our experiment is twofold: to measure all the relevant characteristics of the neutrino beam, and to ensure that the beam properties are constant as a function of time. To achieve the first goal a special "monitor detector" will be constructed in the near hall in front of our near detector, as described in Chapter 6. It will also be able to measure the ν beam direction, but on a relatively long time scale. In this Section we focus on other monitors whose primary functions are to ensure the stability of the beam with time and to provide feedback which is fast enough to be useful for beam adjustments.

Monitoring neutrino beams is both an art and a science, which has over 30 years of history behind it. Over this period, a large body of knowledge has been accumulated about successful techniques and problems, as described for example in Reference [66, 67]. We plan to draw on this experience in designing our monitoring system. Our main new requirement for the NuMI beam, which was not a concern in historical ν beam experiments, is to ensure that the beam direction is held steady at a level of about 0.1 mrad. Our current ideas about an optimal monitoring system are still quite rudimentary. This Section will therefore focus mainly on the challenges that we see ahead, and on possible ways to overcome them

The problems encountered in the WBB and NBB are somewhat different. The WBB situation is the more difficult one because the unspent proton beam accompanies the focussed π/K beam all the way down the decay pipe. The proton flux is significantly higher than the meson flux, and thus any direct beam measuring device must identify pions and kaons in the presence of an intense background. The proton beam generally will not be affected by the horn and thus any horn malfunction will not be detected unless the meson beam is directly monitored. On the other hand, the WBB has only two active elements, the two components of the horn, which reduces the number of possible malfunctions.

We are exploring two possible approaches to WBB monitoring. The first involves ionization chambers on the periphery of the beam, probably placed near the end of the beamline. They should be located well outside of the proton beam. Measurement of the relative intensity at different azimuths would allow us to monitor the centering of the meson beam. An alternative approach is the traditional method of placing a number of muon counters around the decay pipe to detect muons from π and K decays.

The WBB monitors described above would also be useful for the NBB. In addition, we are exploring the possible use of integrating ionization chambers and Cerenkov counters in

the main part of the beam to monitor pions. Additional beam position monitors are needed for the upstream part of the NBB; those would be used to tune the beam and ensure its stability.

Finally, it is important to ensure for both WBB and NBB that the proton beam remains centered on the target. Conventional devices used for this purpose, including scintillation screens, secondary emission monitors, and telescopes viewing the target at 90 °, should be adequate for the NuMI beams.

Chapter 4

Far Detector Site

4.1 Location, access, local facilities

The proposed far detector site is the Soudan Underground Laboratory located in Soudan, Minnesota (48° North latitude, 92° West longitude), approximately 730 km 26° west of north from Fermilab, 150 km north of Duluth, Minnesota and 300 km north by northeast of Minneapolis-St. Paul. The Soudan Laboratory is at a depth of 713 m (2090 meters of water equivalent). It is located within the Soudan Underground Mine State Park, an approximately 4 km^2 property of the State of Minnesota.

Soudan, an unincorporated community with about 300 residents, is centered within 250 m of the shaft leading to the underground laboratory. Soudan is located on State Trunk Highway 169 in Breitung Township, St. Louis County. A U.S. post office, fire department and ambulance service and highway equipment maintenance garage are located within 250 m of the laboratory entrance. Tower, Minnesota, located about 3 km from the laboratory, has about 750 residents, a business district, a high school and swimming pool, an 8-room motel, a civic center, and a telephone exchange with microwave communications. About 20 restaurants and a gambling casino are located within a half hour drive of the Soudan Laboratory. Visiting scientists generally live in rented houses or apartments in Soudan or Tower.

Automobile transportation to Soudan from either Chicago or Minneapolis-St. Paul is primarily by freeway or 4-lane divided highway. For example, the driving time from Minneapolis is about 4 hours, with only about 35 km of two-lane highway. There are sufficient plows and sanding trucks to maintain all-weather access to the laboratory. Snow conditions cause access problems typically less than five days a year. Commercial air transportation is available by Northwest Airlink flights to Hibbing, Minnesota, about a 50 minute drive from the laboratory. There are five Airlink flights each day to Hibbing from Minneapolis-St. Paul (MSP) airport, as well as jet service to Duluth airport, which is a 90 minute drive from the laboratory. Daily non-stop or through service operates to MSP from most major airports in North America. MSP also has non-stop service to and from London/Gatwick and Amsterdam. Both Federal Express and United Parcel provide regular pick-up and delivery service to the Soudan Laboratory.

The Soudan Laboratory is located about 50 km south of the Minnesota-Ontario border.

The land north and northwest of the laboratory (the region in which a neutrino beam from Fermilab would exit the earth) is primarily federally-owned as part of Superior National Forest. This region is mostly a primitive area with dense, second-growth boreal forests and shallow lakes. It is used for outdoor recreation and logging. The permanent population within 25 km of the laboratory towards the north is only a few hundred people.

4.2 The Soudan Mine and the laboratory lease

The Soudan Mine is a registered national historic site and was the first iron mine in Minnesota. Surface mining began in the 1880's and was soon replaced by underground workings. The mining techniques at Soudan were copied from those in the Cornish tin mines and Cornish workers were recruited as mine captains in order to supervise the use of these methods. Immigrants were recruited from Eastern Europe (including Finland) as mine laborers. Employment at the Soudan mine peaked at about 5,000 men in the 1890's.

The ore at Soudan is almost pure hematite (Fe_2O_3), which was economically mined underground through the 1950's. Soudan hematite was used in the final steelmaking process to control the carbon content of the steel because of its precise oxygen content. When American steel plants converted to direct oxygen injection, U.S. Steel decided to close the Soudan Mine in 1962. They donated the mine and the surrounding land to the State of Minnesota, which decided to dedicate it as a state park.

The Soudan Mine is currently operated by the Department of Natural Resources (DNR), Division of State Parks. The mine staff, headed by Paul Wannarka, the park superintendent, includes about 8 full-time and an additional 20 seasonal employees. The park is most active during the late Spring, Summer and early Fall. Typically, 30,000-40,000 people per year travel underground to visit the last workings of the Soudan Mine. Public visits occur seven days a week from Memorial Day weekend to Labor Day. Other visitors are mostly school groups.

Because of the large number of public visitors and the unique deep underground environment, the DNR places a major emphasis on safety. Although the basic mine machinery was installed in 1924, the working parts are continually overhauled and replaced. For example, almost the entire electrical system, both surface and underground has been renovated during the past few years. Because it is located in ancient, pre-Cambrian rock, the Soudan mine has no methane or other organics and is low in radon and other radionuclides. The mine is ventilated almost entirely by natural air circulation through the myriad of underground workings excavated during almost a century of work.

Access to the underground for both tourists and physicists is *via* the No. 8 mine shaft, the only currently useable shaft. Both the tourist activities and the physics laboratory are located on the 27th level, the lowest developed area of the mine. The shaft is comprised of three compartments—two are used for hoisting and one houses utilities and a ladder. The internal hoisting compartment dimensions are approximately 1.2 m by 1.8 m. Lengths up to 8 m can be moved underground without difficulty. The nominal hoist capacity is 6 tons. The usual hoist trip takes about three minutes and can transport twenty people on two cage decks. The mine hoist is run by an operator who communicates with the passengers by both buzzer and telephone systems.

Physics activities at Soudan began in 1980 with construction of the Soudan 1 detector on the 23rd level of the mine, about 100 m above the current laboratory. In 1984, construction began on the current Soudan 2 Laboratory. Both the Soudan 1 and the Soudan 2 laboratories are leased from the State of Minnesota by the University of Minnesota. Legally, the University is a constitutional corporation chartered by the Territorial Legislature prior to the formation of the State. The current lease term began in 1984 for a 10-year term. It was renewed in 1994 for another 10-year term with minor amendments. The current leasehold includes the Soudan 2 Laboratory and a sufficient volume of unexcavated rock to construct a new laboratory. New construction is specifically permitted under the amended lease.

The lease does not require rent payments but the University is required to reimburse the DNR for expenses. These expenses include direct charges for consumables such as electricity and for labor such as outside-normal-hour hoisting operators. The University also pays the DNR $20 per hoist round trip used by the physicists as a reimbursement for general maintenance. This general maintenance charge includes all of the cost normally associated with a remote site such as road maintenance and snow plowing, water and power lines, *etc.*

4.3 Soudan 2 Laboratory

The Soudan 2 Laboratory is 14 m wide by 70 m long by 11.3 m high, oriented with its long axis almost exactly north-south. The laboratory has two entrances at its northern end: one connects *via* a 25 m tunnel to the area adjacent to the No. 8 shaft, the other has a shorter tunnel leading to the main 27th level east-west drift about 50 m west of the No. 8 shaft. The Soudan 2 detector, surrounded by a proportional-tube active shield, occupies the southern half of the laboratory. The shielded volume includes both the detector and a "clean room" that is used to prepare and repair Soudan 2 calorimeter modules. The northern end of the laboratory is occupied by a two-story "counting house" built over an electrical sub-station and a gas mixing area. The counting house has a floor area of 85 m^2 and houses computer facilities, a lunchroom and offices. The remaining laboratory floor houses a machine shop, a $\beta\beta$ decay experiment and a large (480 m^2) area that is used for assembly and storage.

The Soudan Laboratory has a considerable existing utility base. Current electrical capacity at the 27th level is 800 kVA at 2.4 kV. The Soudan 2 Laboratory has sufficient transformers to provide 230 kVA at 440, 220 and 110 V. The laboratory has 19 installed telephone twisted pair lines, of which 16 are currently in use. A single coaxial cable connection to the surface is used for the radio station WWVB clock antenna, which provides the absolute time to an accuracy of a few milliseconds. All these surface communication cables are installed in the utility/manway section of the No. 8 shaft. The laboratory has a fire suppression system including smoke and heat detection, automatic electrical power cut-off upon fire detection and a high-pressure water sprinkler system charged with approximately 100,000 l of water in a reservoir 60 m above the laboratory. The air in the cavity is exchanged approximately every hour by two large blower fans. After ten years of occupancy the laboratory temperature has stabilized at 22° C, at a relative humidity of 54%. These conditions are maintained by the heat input resulting from the consumption of electrical power in the laboratory. Atmospheric pressure in the underground laboratory is 8% higher than on the surface.

The Soudan 2 experiment has acquired useful equipment for moving heavy material, both on the surface and underground. Surface equipment includes a 12.5 ton mobile crane and a 5-ton forklift. Underground equipment includes a 7.5-ton bridge crane in the Soudan 2 detector area and a 5-ton battery-powered forklift. The Soudan Laboratory also has permanent use of two large truck bays in a maintenance building shared with the DNR located about 100 m from the mine shaft.

4.4 Excavation plan

The excavation of a new laboratory at the Soudan site will be facilitated by the experience of building the existing Soudan 2 Laboratory. Many of the key personnel in that project, including Dr. Charles Nelson, the engineer who planned and supervised the construction, are available and interested in working on a new laboratory. The costs and schedules described here are mostly derived from actual experience with the Soudan 2 Laboratory excavation. In addition, expensive equipment procured for that excavation, including a custom hoist cage and rock skip and a mobile crane, can be re-used at little or no cost.

The most likely location for the new laboratory is about 50 m east southeast (center-to-center) of the existing laboratory, as shown in Fig. 4.1.

The planned dimensions of the new laboratory are 14 m by 75 m horizontally by 12 m clearance height. The roof will be domed, so that the actual height in the center will be somewhat higher. The long axis of the laboratory will be oriented towards Fermilab. The new laboratory will have two access tunnels — one will connect directly to the shaft station, while the other will connect the new laboratory to the existing Soudan 2 Laboratory. This latter tunnel will have sufficient cross-section to permit moving entire detector assemblies from the Soudan 2 Laboratory, where much detector assembly and testing will be done, to the new lab. Figure 4.2 shows an elevation view of the new and existing laboratories and the tunnel which connects them.

The plan for constructing the new laboratory is as follows:

- An initial engineering investigation of feasibility, scheduling and cost estimates for the new lab construction has already been completed. The work was done by CNA Associates, the engineering firm which designed and supervised construction for the Soudan 2 Laboratory. This investigation involved a review of Soudan Mine geological records to identify likely areas of good rock and a review of records on the Soudan 2 lab construction to develop a schedule and cost model based on that experience. This schedule and cost model was updated to the present time by considering both new technology and construction cost inflation. The deliverables from this investigation include a laboratory site determination, a detailed preliminary cost estimate and a schedule for the new construction.

- The next step is core drilling and detailed geological characterization of the proposed lab site. The core drilling is currently planned for May 1995. It will likely involve drilling two bores, each approximately 125 m in length east southeast from the Soudan 2 access tunnel behind the shaft station through the center of the proposed laboratory site. One core will be horizontal. The other core will angle upward to probe the area

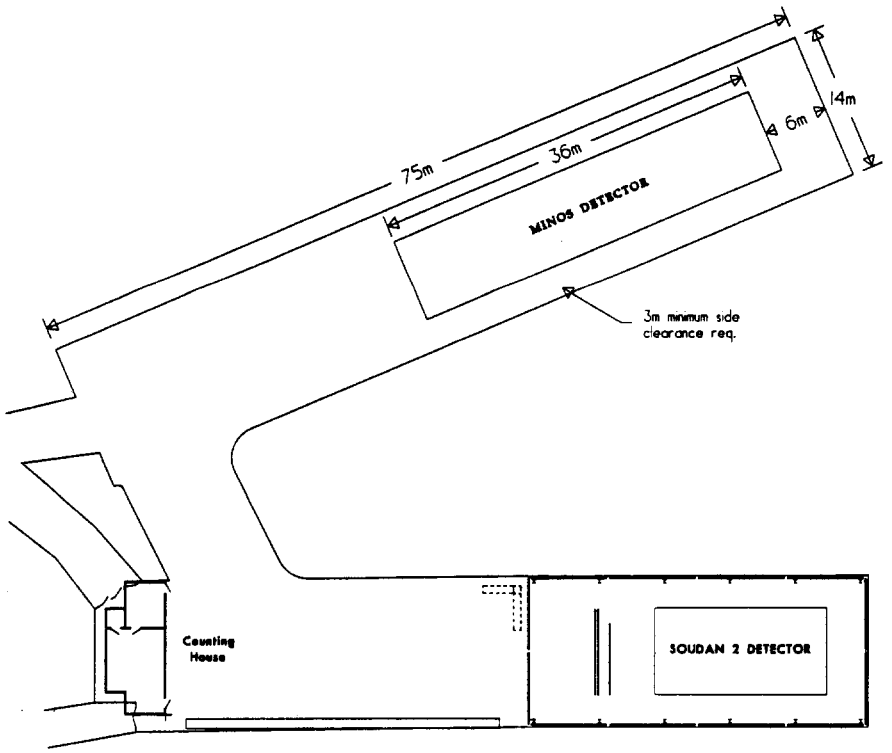

Figure 4.1: Plan view of the proposed arrangement of the new and existing laboratories at Soudan.

of the laboratory roof near the southeast end of the new lab. Core drilling will require about two months.

- The cores and other geological studies will provide a basis for developing a construction design and bid package between Fall 1995 and Spring 1996. In order to obtain low bid prices, it is important to develop a design package which is detailed enough to reassure prospective contractors that the laboratory can be built for a fixed price. The design must include specific examples of drill rigs, loaders and conveyors that can be moved down the shaft and used for the excavation, a specific order of excavation plan, drill hole patterns and explosive loading specifications, and a specific design for rock bolting and other supports. Design plans must also include provisions for utilities including electricity, HVAC (heating, ventilation, air conditioning), detector gas, communications, fire suppression and other life safety systems. We expect to

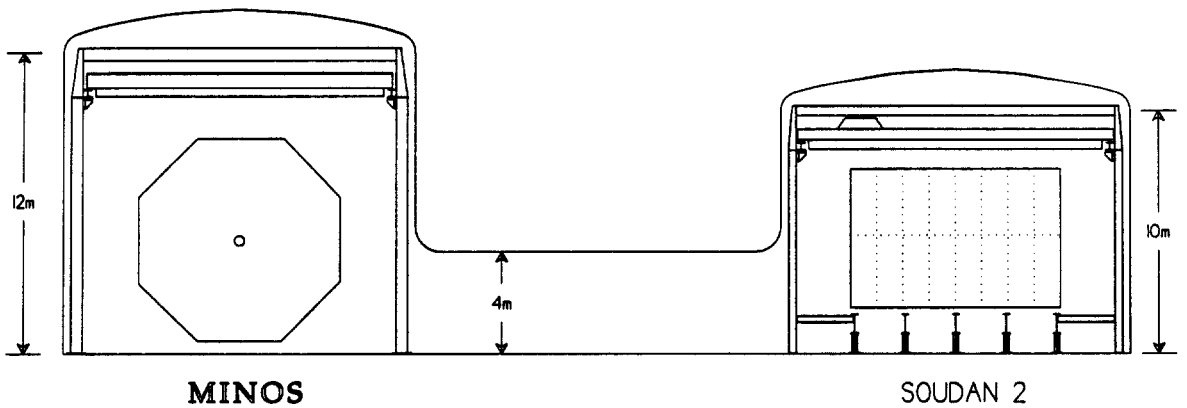

Figure 4.2: Elevation view of the proposed arrangement of the new and existing laboratories at Soudan.

advertise for bids in Summer 1996.

- We propose to begin construction of the laboratory in September 1996, with completion of construction, including utilities and detector support and crane structures, in Winter 1997-98.

4.5 Lab outfitting and utilities

The fixed equipment and utilities for the new laboratory will be similar to those already installed in the existing Soudan 2 Laboratory. Also, some existing facilities in the Soudan 2 Laboratory, such as the electrical substation, machine shop, lunch room, office space and toilet facilities, will be available and thus do not need to be rebuilt in the existing laboratory. Some of these facilities including the electrical substation and the toilet facilities, will however

require upgrading to meet the increased needs associated with the MINOS detector.

The first utilities installed in the new laboratory will be electrical lighting, electrical power, HVAC and fire suppression. The lighting system will include large mercury vapor flood lamps for area lighting and spot lighting for special work areas. Battery-powered emergency lighting will also be provided. Electrical power will include 220/440 V for compressors for the gas system and local air conditioning needs. Separate 110 V feeds out of the substation will be used to partially isolate "clean power" used for electronics from 110 V power for general use. The HVAC system will take fresh air through a duct from the west access tunnel to the Soudan 2 Laboratory and exhaust air through the new lab access tunnel to the mine shaft. Fresh air will be dehumidified. Initially, electric heaters will be used to raise the lab temperature to about 20° C. When the lab reaches thermal equilibrium, waste heat from the electronics will provide sufficient heat to keep the laboratory warm. The lab temperature will be controlled by varying the volume of fresh air moved through the HVAC system. The fire suppression system will include both smoke and heat detectors. Baffles and special smoke detectors will be used on the electronics racks to insure quick detection at the most likely location for a fire. Fire detection will initiate an alarm, followed by an electrical power interruption with a 5 minute delay when the lab is occupied and no delay when the lab is not occupied. The current Soudan 2 sprinkler system will also be extended into the new laboratory.

Because of the likely use of flammable components in the detector gas, the gas mixing system will be located on the surface. The gas will be piped down the shaft at positive pressure and vented up the shaft at atmospheric pressure through dedicated supply and vent lines. The mixing system will be set and alarmed, so that any gas mixtures underground are well below the explosive limit. The detector gas system is described in Chapter 5. The laboratory will also have a gas safety system with flammable gas detectors and emergency purge fans with explosion-proof motors. This system will be connected with the fire-suppression system, so the two systems will work in a coordinated way in case of emergency.

We expect to install an overhead bridge crane to facilitate installation of the MINOS detector. The crane will be similar to the one in the Soudan 2 lab, except it will have a 20 ton capacity. The crane rails will be supported on columns spaced along the long axis of the detector hall. The crane structure could also be used to support an active shield, if one is installed around the detector. The detector support structure is described in Chapter 5.

4.6 Funding, costs and schedules

We expect to seek University of Minnesota and State of Minnesota funding for the cost of constructing a new laboratory and part of the cost of installing utilities and fixed equipment. We estimate the possibly obtainable state contribution as $3,350,000 divided as follows:

- $100,000 is required in early 1995 for core drilling and geological investigations. These funds have already been allocated for the MINOS experiment by the University of Minnesota. They are conditional only on Fermilab Phase 1 approval of the experiment.

- $250,000 is required for engineering design leading to a bid package. We expect to request these funds in Spring 1995 from the Iron Range Resources and Rehabilitation

Board (IRRRB). (The IRRRB is a state agency which distributes economic development funds generated by a dedicated tax on iron ore.) Preliminary conversations with responsible officials indicate that our chances for obtaining these funds are good, provided that we can show strong evidence that the long baseline experiment will really happen. (The IRRRB has in the past received bad publicity for investing in projects such as Northwest Airlines maintenance bases that were never actually built.)

- $3,000,000 is the expected state contribution for laboratory construction. These funds will be requested as part of the University bonding request during the 1996 Legislative Session. The University again believes there is a good possibility for obtaining these funds, provided the long baseline project is progressing and that there is a good indication from both the Department of Energy and, perhaps, the appropriate Congressional leaders that the project will likely proceed.

Table 4.1 lists the preliminary cost estimates for the new laboratory developed by CNA Associates based on the actual costs for the Soudan 2 Laboratory. These costs include EDIA and 20% contingency. A summary of the estimated costs are as follows: Construction: $3.311 million, Fixed Equipment: $0.786 million, Engineering and Construction Supervision: $0.679 million, Hoisting Operations to Support Construction: $0.552 million. The Total Project Cost is $5.328 million with $3.350 million expected from the State and University of Minnesota and $1.978 million from MINOS project costs.

MINOS Laboratory Cost Estimate

Description	Quantity	Unit	Unit Price	Cost
A. Construction				
Mobilization and Bond	1		$150,000	$150,000
Surface Preparation and Rehabilitation	1		$25,000	$25,000
Shaft, Hoisting System and Shaft Station Rehabilitation	1		$150,000	$ 150,000
Entrance Tunnel Including Excavation and Support	125	LF	$1,300	$162,500
Laboratory Excavation	19125	CY	$60	$1,147,500
Muck Hoisting and Disposal	19125	CY	$25	$478,125
Shotcrete	185	CY	$500	$92,500
Shotcrete Rebar	20500	LB	$2	$41,000
Rockbolts	825	EA	$150	$123,750
Tunnel to Soudan 2 Lab	75	LF	$1,800	$135,000
Concrete Floor	425	CY	$300	$127,500
Finishing (Cleanup, Doors, Paint)	1		$50,000	$50,000
Trucking Premium for Low Background Concrete	1300	TON	$59	$76,700
Sub-total				$2,759,575
20% Contingency				$551,915
Sub-total for Construction				$3,311,490
B. Fixed Equipment				
Permanent Ventilation	1		$125,000	$125,000
Permanent Electrical System and Lighting	1		$100,000	$100,000
Fire Suppression	1		$30,000	$30,000
Crane and Crane Support	1		$400,000	$400,000
Sub-total				$655,000
20% Contingency				$131,000
Sub-total for Fixed Equipment				$786,000
Sub-total for Construction and Fixed Equipment				$4,097,490
C. Engineering, Testing and Construction Supervision				
Boring Mobilization	1		$5,000	$5,000
Boring and Testing	450	LF	$40	$18,000
Engineering (8% of $4,013,490)				$327,799
Construction Supervision (8% of $4,013,490)				$327,799
Sub-total for Engineering and Supervision				$678,598
D. Hoisting Operations to Support Construction				
Hoisting and Maintenance Personnel for Non-Day Access	8	FTE	$45,000	$360,000
Electricity and Equipment Replacement	1		$100,000	$100,000
Contingency (20 %)				$92,000
Sub-total for Hoisting Operations				$552,000
Grand Total				$5,328,088
Anticipated State and University Funds				$3,350,000
MINOS Project Funds				$1,978,088

Table 4.1: Preliminary cost estimates for the new laboratory construction

Chapter 5

Far Detector

5.1 Introduction

The plan for the MINOS experiment is to have both a near and far detector which are as identical in physics measurement capabilities as possible. This will allow cancellation of possible systematic errors which can arise due to uncertainties in acceptance (particularly at low neutrino energies) for the two different detectors. This requirement does not demand that the near and far detectors are identical but rather that the two detectors have fiducial volumes which will act the same and be exposed to a neutrino flux with similar energy distributions in both detectors. In order to achieve this, the basic technology employed in each of the detectors will be the same. However, the arrangement and the total masses will be different. The basic description of the detector philosophy and technology apply to both the near and far detector.

The underlying philosophy of MINOS is to provide the ability to identify and make precise measurements for any oscillation mechanism which may be present in the region of parameter space of interest. This demands ability to be able to identify and measure several different physics signatures. The relatively high energy provided by the Fermilab Main Injector beam will typically yield events with considerable complexity which will require a detector with good longitudinal and transverse granularity. We believe that the most economical way to achieve this is the use of a sampling/tracking calorimeter. Neutrino events with muons will benefit from a very massive detector with capability for measurement of the muon momentum. A number of possible options exist in the detector construction. Here, we present a particular construction option which we believe is clearly achievable using proven technologies. A detector development effort is planned to determine what the final construction techniques might be (see Chapter 11).

5.2 Overview of the detector

The detector will have 600 octagonal cross-section steel absorbers which are 8 m across and 4 cm thick. Figure 5.1 shows an overview of the full detector. The total length of the detector is 36 m with a total mass of 10 kT. The iron will be magnetized toroidally by running a coil through a hole in the center of the absorber plates to produce a reasonably uniform field

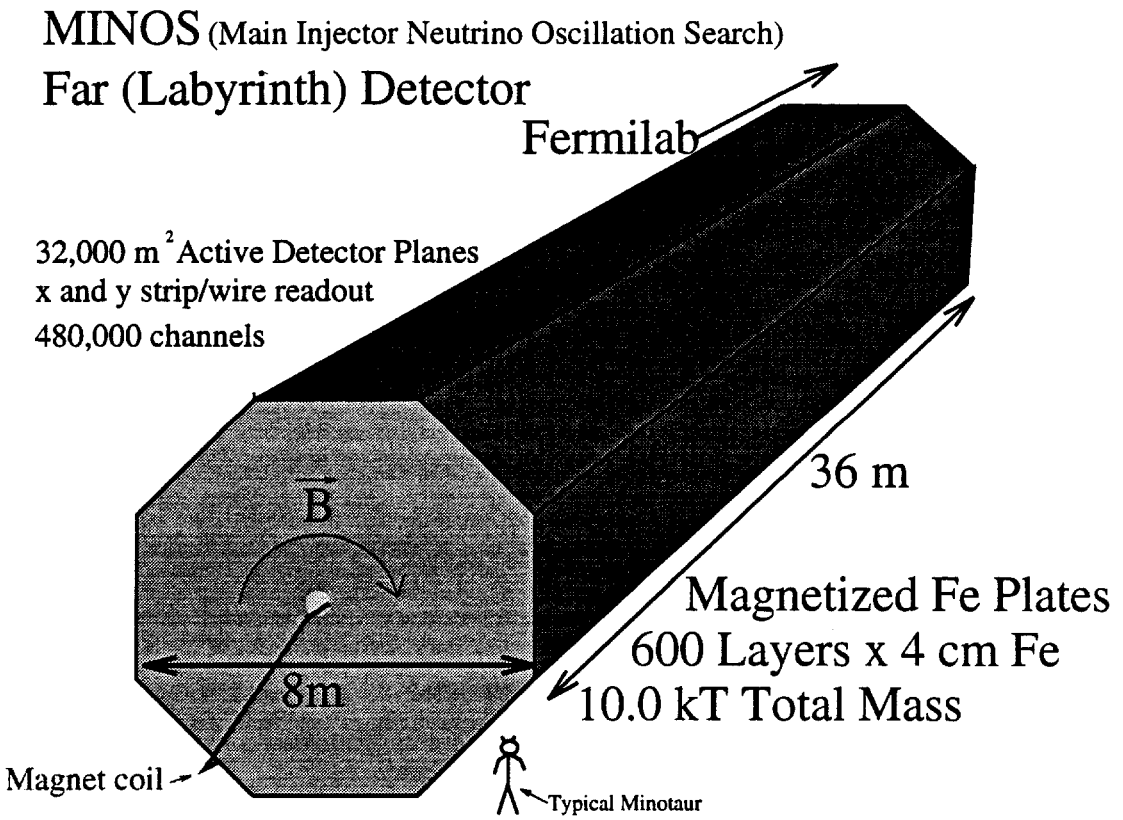

Figure 5.1: Overview of the far detector for MINOS.

with typical strength of about 1.5 T. The magnetization allows measurement of high-energy muon momenta.

The active detector elements which we consider here consist of planes of plastic limited-streamer tubes which are 1 cm thick and with 1 cm pitch along the wire cells. The tubes will be installed at a 45° angle with respect to the horizontal so that they run parallel with the diagonal sides of the octagon. The cathode strips will be installed perpendicularly to this. This arrangement allows for support of all of the bottom edges of the detector. Both the wires themselves and transverse cathode strips can be read out to provide an x and y readout dimension for each plane. Both the wires and strips will run the full width/height of the detector and be read out on the sides and top. The length of the tubes will vary according to the width of the steel plates for the octagon. The pitch of the cathode strips will be 2 cm and adjacent pairs of wires will be summed together in order to provide 2 cm pitch for the wire readout as well. The tubes in successive planes will be offset slightly in order to provide effective position resolution over several planes which is considerably better than the nominal 2 cm pitch and the direction of wires and strips will be reversed in every other plane. The total area of active detector planes to be instrumented in this scheme is

32,000 m^2. The total number of strip/wire channels which are to be read out is 480,000.

5.3 Size and shape of the far detector

The size, shape and granularity of the far detector are driven by the need to get as large a fiducial mass as possible for neutrino interactions while simultaneously providing good measurement for the interaction products. Sensitivity to oscillations in the CC/total ratio will require at least 50,000 events to provide a positive signature of oscillations for mixing strength of 1%. Since the number of neutrino events per year of operation with the Main Injector beam with a detector located at Soudan is about 3000 per kT, a detector in the mass range of 10 kT is required in order to meet this goal in a reasonable running period. This demand for very large mass necessarily constrains all decisions about the detector construction and technology.

Counteracting the demand for large mass is the need for fine-grained readout in order to make sense of complex neutrino events and thereby clearly demonstrate oscillation signatures and provide precise determination of oscillation parameters. As discussed in Chapter 8, signatures based on total energy, hadronic energy, event shapes of NC and ν_μ CC events or muon measurements can be done with relatively coarse longitudinal sampling. For these measurements 4 cm iron absorbers will provide adequate sampling for the measurements that we envision. However, precision measurements on events with electrons, and the ability to separate such events from those with π^0's, makes even more stringent demands on the longitudinal sampling. In this case, since there are few ν_e's in the beam, the background for events with electrons is relatively small, and useful signatures for events with electrons could probably be obtained with a smaller mass detector. This suggests that a natural course of action could be to split a large detector into finer-grained but smaller mass sections and coarser but larger mass sections. The finer-grained section could also be used to check the reconstruction of events in the coarser section. More study needs to be done to decide whether this kind of approach can add useful physics measurements and thus compensate for the reduction in total mass for the full detector assuming a fixed cost.

In order to reliably reconstruct events, it will be necessary to define a fiducial volume in the far detector where interaction vertices occur and/or limits on how near the edge of the detector interaction products can come. For fixed total mass, the fiducial mass of the detector will vary depending on the requirements of these cuts. A detector which is either very wide (and therefore very short) or very long (and therefore very narrow) will give unacceptably small fiducial masses. Other considerations to take into account are containment for atmospheric neutrinos, number of electronics channels for readout, mechanical integrity of the structure, ease of construction and logistics in building a staged detector. Figures 5.2 and 5.3 show the fiducial fraction of the total mass as a function of detector width for a square cross section detector assuming 50 cm and 100 cm fiducial cuts around the edges of the detector for the position of the primary vertex. Figure 5.2 shows the fiducial fraction for optimal muon measurement (assumes 10 m downstream of vertex is needed) and 5.3 shows the fiducial fraction for good hadron containment (assumes 2 m downstream of vertex is needed). Although the total length of the detector is affected, the results of fiducial fraction versus detector width do not change significantly for a circular cross-section detector (or

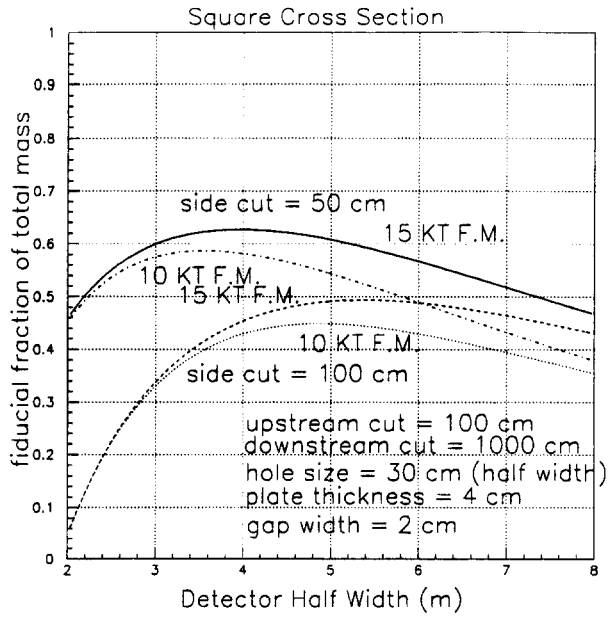

Figure 5.2: Fiducial fraction of the total mass versus the detector half-width assuming containment parameters for optimum muon momentum measurement.

anything in between such as an octagon). Studies of this type have driven the decisions on the aspect ratio of the far detector with the resulting 8 m wide detector giving optimal acceptance.

5.4 Steel absorbers and construction

The steel absorbers for the far detector consist of octagonal planes which are 4 cm thick and 8 m across from flat to flat on the sides of the octagon. The gap between planes is nominally 2 cm. Each plane of steel has a total mass of 16.8 metric tons. Each plane will be assembled from six vertical plates and six horizontal plates, all 2 cm thick with each plate being 1.33 m wide and as long as necessary to complete the octagon shape. See Figure 5.4 for details of the construction of the steel absorber planes. The maximum size for the plates (and hence the number of plates required to form each octagon) are governed by the width of the access shaft to the mine.

The steel plates will be fabricated from AISI 1010 or equivalent steel. This steel is both relatively inexpensive and provides good magnetic permeability. The standard thickness tolerance for 2 cm thick plates of this sort is 3 mm. This should be an acceptable variation in the plate thickness based on precision of energy measurements for hadronic or electromagnetic showers. For muon range measurements, if we imagine that the location of thickness variation is correlated from plane to plane then this could lead to a maximum of 15% systematic error in muon energy reconstruction due to this variation. Although this variation is not very bad, half this number would be more comfortable. We believe that this precision should be easily reached since it is unlikely that all thickness variations are perfectly correlated. Furthermore, one U.S. steel mill has already indicated that they normally do better than this standard by a factor of two and that they would guarantee better on the large

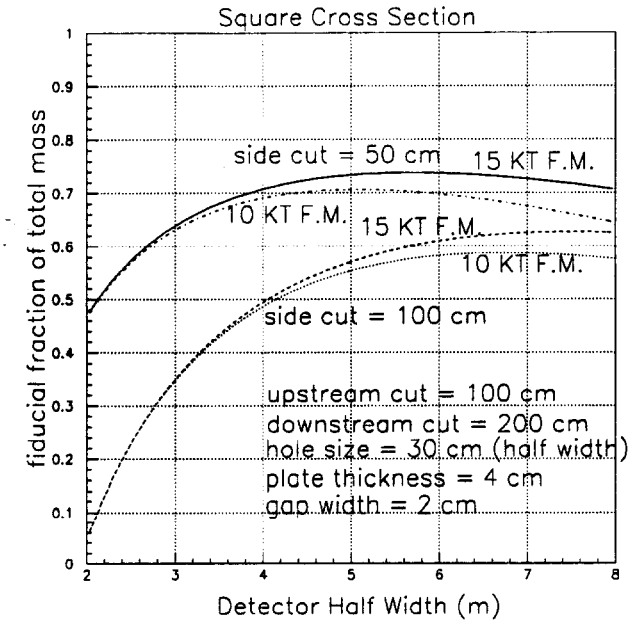

Figure 5.3: Fiducial fraction of the total mass versus the detector half-width assuming containment parameters for optimum hadron containment.

number of plates required for the far detector.

The individual plates must be tied together to form the octagon. The crossed layers of plates provide a strong basic structure for the octagon. The plan is to weld the plates together with plug welds. This approach is attractive both from a mechanical aspect and from a physics aspect since it completely eliminates gaps in the absorber planes. Potential concerns with this are impact on the assembly schedule, warping of the plates and air quality in the hall with significant amounts of welding. Alternatives for the assembly technique will be studied carefully.

Although thickness variation is unlikely to pose a problem, flatness of the plates is an issue which will likely require an active engineering solution. Although the American Society for Testing and Materials provides a standard for flatness for such plates, this standard applies only to plates lying horizontally on a flat surface. The vertical plates may present different challenges for flatness. The parameter which drives the flatness requirement is the width of the gap between absorber planes. This has been nominally set to 2 cm which is thick enough for installation of the detector planes with a bit of room left over as long as the variation in the flatness of the plates is no more than a few millimeters. The 2 cm number is an attempt at minimizing the gap-width in order to give optimal containment properties transverse to the detector planes and prevent excessive transverse spread of showers. However, there is no magic in the 2 cm gap-width and if necessary to reduce the cost for steel plate construction the width can be increased without substantially impacting the physics measurements. Increasing the gap-width from 2 cm to 3 cm for instance would change the average interaction length or radiation length of the detector by only 17%. We plan to carefully study the costs versus flatness requirement in order to optimize the final gap width.

The active engineering solution that we envision for forcing the plates to be sufficiently flat is to add axial support rods or bolts on a 1.33 m grid. The rods will be adjustable

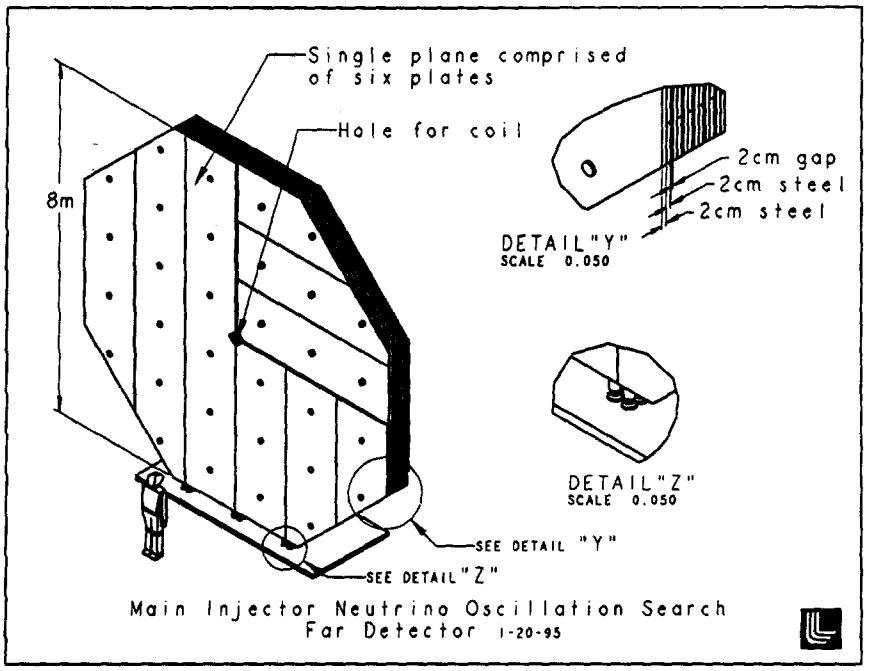

Figure 5.4: Details of steel absorber plate assembly and support.

allowing plates to be forced further apart or drawn closer together depending on the local flatness and plate thickness. In addition to forcing flatness of the plates, these bolts also serve several other important functions including securing the plates in place, prevention of seismic failure and prevention of bow due to magnetic loads. It is expected that use of 1.5 cm diameter support rods will be adequate to handle all of the envisioned loads with the 1.33 m grid spacing.

The matrix of bolts which secure the planes together will introduce dead space between chamber planes. The bolts will be precisely placed in order to avoid excessive dead space due to misalignment. It is expected that the gap between successive detectors along a line of bolts will be about 1.5 cm every 1.33 m. This represents a dead area for each detector plane of about 1.3% on the wire view. The strip view will be affected in a somewhat different way since gaps under strips will not completely hide the streamers in the tubes located under that gap (the gaps are perpendicular to each other) but the response will be diminished. The dead space which is intrinsic to limited streamer tubes due to the walls and gaps between tubes results in roughly a 13% dead space averaged over the full area of the detector. In addition to these dead regions, the 0.3-m diameter coil hole in the center of each steel plate accounts for a 0.13% dead area. We anticipate that except for electromagnetic showers located immediately over gap locations, the effect on physics measurements coming from these gaps will be minimal. Even for electromagnetic showers, a modest fiducial cut requiring that shower cores be a couple of centimeters away from such gaps will remove any significant systematic effect at a cost of about 10% in fiducial mass. More precise Monte-Carlo calculations will be performed to understand the effect that this construction technique will have on physics measurements. With more advanced engineering we may reduce the number and/or diameter of the axial rods.

The octagonal plates will be supported on shims or adjustable feet which sit on steel plates on the floor. This is a particularly inexpensive technique for supporting the structure but does not permit any access to the bottom side of the detector. No particular difficulties are expected from this other than if a bottom active shield might be desired.

The Soudan mine is located in an area rated as 'seismic zone 0'. This means that the seismic load for typical structures can be assumed to be zero. However, large, thin plates are not typical structures and therefore the effect of even small seismic loads must be considered. The support rods previously mentioned will provide adequate restraint for any expected seismic loads. Although the magnetic forces are nominally in the plane of the plates, tolerances in the assembled planes and installation tolerances will result in axial loads that will be restrained by the axial rods. Detailed engineering studies will be performed to ensure that all loads can be safely handled but such studies are beyond the scope of the current work.

Individual pieces of the raw steel are of a size and weight that can be manufactured by a large number of steel mills in the US. The manufacturing cycle for the raw steel will depend on mill capacity and their need to continue to meet other customer needs. A one year manufacturing cycle appears to be realistic and should fall within the constraints of other schedule requirements.

The fabrication of the finished plates that make up each octagon requires a vertical or horizontal mill capable of handling 8 meter long steel plates in order to make smooth edges which match closely together in the plane. Mills are available which can simultaneously machine 5 plates which helps to reduce the total machining costs since there is only one setup cost for each 5 plates. One source for this large quantity of machining would be McDonnell Douglas, St. Louis, MO. They currently have fifty-four 90-120 foot vertical milling machines capable of fabricating 5 plates at a time. They could, subject to other obligations (primarily aircraft wing structures), fabricate the plates over a one year period.

Transportation of the steel between the manufacturer, fabricator and the site can be a major cost. The location of the manufacturer and fabricator relative to each other and to the site will be an important consideration in deciding where the steel should be fabricated. The size and weight of individual plates permit use of both truck and rail without extra costs associated with wide loads. It is expected that some combination of the two will be employed.

The aspect ratio of the plates will require that the plates be handled using special lifting fixtures to prevent permanent deformation during handling. Each plate will include an array of tapped holes for attachment of the lifting fixture. These holes will be filled with threaded plugs after installation. The octagons will be assembled according to the following procedure, which requires a crane:

- Weld plates together to form plane (octagon)
- Install active detector plane
- Lift plane to vertical position
- Adjust shims or support feet
- Install axial support rods (flatten and set axial position of plane)

The first planes which are installed will require a separate 'bookend' structure to support them until sufficient planes are in place so that the whole structure becomes free standing.

5.5 Magnet coil and magnetic properties

The steel part of the detector will have a central hole through which a current-carrying coil can run in order to magnetize the steel plates toroidally. Figure 5.5 shows the strength of the magnetic field as a function of position within an octagonal plane of the steel. With 10^4 amp-turns running through the coil, the average field in the steel is 1.5 T with the field near the center being about 2.0 T and 50 cm from the edge of the detector about 1.1 T. The field changes relatively smoothly and slowly across the face of the detector. Figure 5.5 has been calculated assuming AISI 1010 steel and no gaps in the assembly of the octagon. Although the individual steel plates in the octagon will have some effect on the field, the planned overlapping layers should keep irregularities due to the joints to a minimum.

The magnet coil will be a normal-conducting copper coil. It will be installed in three separate sections along the length of the detector, each section servicing 200 planes of steel. Figure 5.6 shows how the coil will run around the ends of the detector segments. Sufficient gaps will be allowed between the steel plates at these locations to allow access for servicing the coil if necessary. Installation of the coil in sections will allow the first sections of the detector to begin normal data acquisition while the remainder of the detector is under completion. Each of the coils will consist of 72 turns of square, hollow, copper conductor which is 12 mm across on the outside and with a 7 mm hole in the center. It will be installed slightly away from 45° from horizontal in order to allow for access to half-length chambers where the central hole is located. The total length of copper conductor in each third of the detector will be 2300 m. Cooling will be provided by flowing low-conductivity water through the coils with a pressure drop of 60 psig across the coil. With a total water flow rate of 2.5 gallons/minute, this will maintain an average conductor temperature of 55°C assuming an inlet water temperature of 20°C. A heat exchanger will be provided to exhaust the heat to the mine up-shaft. The coil will be operated with 139 amps at a voltage of 128 volts resulting in total power consumption of 8.5 kW per third of the detector or a total of 25 kW for the full detector. This presents only modest power-supply and heat-exchange demands.

The coil conductor will be transported underground wound in 40 foot elements onto reels. Underground, the conductors will be unwound, straightened, taped with insulation and assembled into rows on a backing sheet of epoxy-fiberglass composite. The assembled sections of coil will then be pulled through the central hole of the assembled detector. The hole will be lined with a U-shaped nonmagnetic metal to provide a smooth surface. Sections of the coil will be brazed together into 8 individual water circuits and connected to the power supply. All of these techniques represent standard technology for construction of magnets. In particular, very large scale toroidal magnets of similar construction (but somewhat smaller) have been successfully operated in previous high energy physics experiments (*e.g.*, BCDMS [68] and CDHSW [69]).

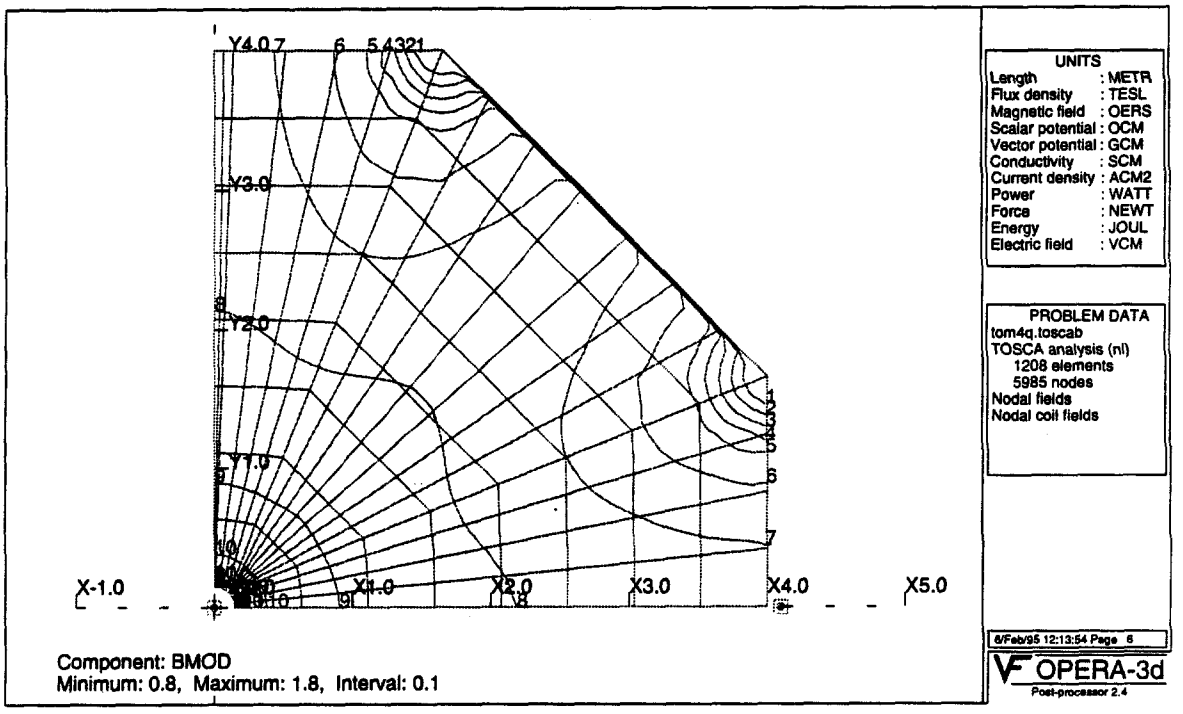

Figure 5.5: Magnetic field contour map for the octagonal plates with 10^4 amp-turns. The innermost field contour is 1.8 T, and the outermost is 0.8 T.

5.6 Active detectors

Although a number of possible alternatives will be investigated, we propose here that the active detector planes will be constructed from plastic streamer tubes similar to those used in the hadron calorimeters of LEP detectors and the MACRO detector [70, 71, 72, 73]. The total area of active detectors required for the far detector is 32,000 m^2. This compares to approximately 20,000 m^2 used in the MACRO detector and therefore represents only a modest extrapolation of this technology. Other possible technologies include scintillator tubes, resistive plate counters (RPC's) or drift tubes any of which (see Chapter 11) may allow reduction in cost or improved physics signatures compared to streamer tubes. Here we have chosen to propose a well-proven technology as a baseline design.

The streamer tubes will be based on plastic extrusions with a modular construction similar to the construction used in previous experiments. Each module (see Figure 5.7)

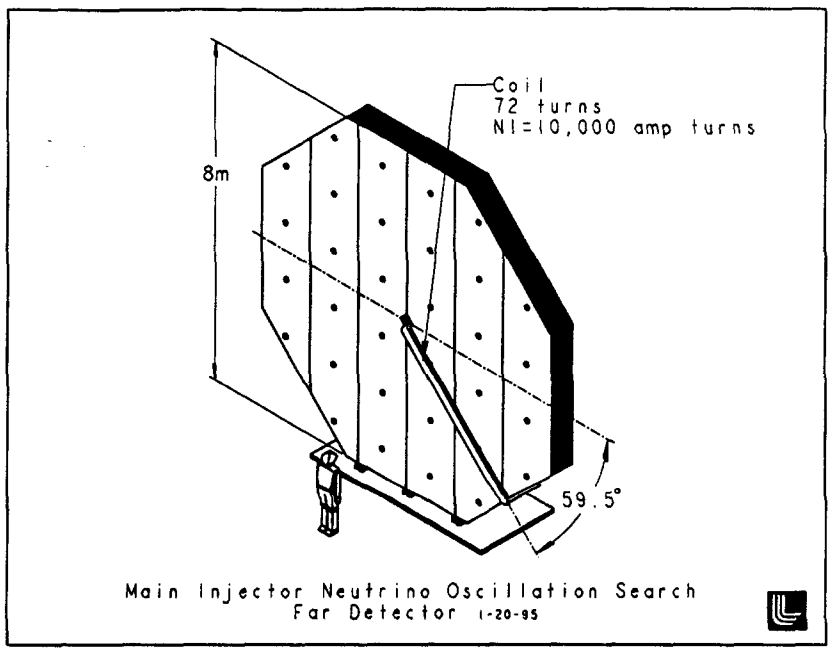

Figure 5.6: Magnet coil installation on the steel will be in three separate segments along the detector.

will be 8 cm wide, 1 cm thick and as long as necessary to reach across the full width of the detector (with the module installed with the long direction running at 45° to the horizontal). Each module will have an inner and outer plastic extrusion. The outer extrusion will form the gas envelope and will have a rectangular cross section approximately 8 cm wide and 1 cm thick. The inner extrusion will be a 'comb' which is 8 cm wide and with 1.2 mm thick walls which are 1 cm wide placed every 1 cm across the extrusion. This forms 8 cells, each with a 1 cm square cross section. The top of the comb is left open. The walls of the comb will be painted with resistive graphite paint which is connected either to high voltage or ground, so that the wires can be read out as planned for the reference detector. (Placing the wires at ground eliminates the need for a blocking capacitor if they are to be read out.) The traditional material for construction of these tubes is PVC. Recent discussions on safety have suggested that PVC should not be used in particle physics detectors so other plastics may have to be employed. This situation is not unique to this experiment and will be studied further.

Wires are strung down the center of each of the square-cross section cells. For operation in limited-streamer mode, 100 micron diameter, silvered, copper-beryllium wire is used. The wires are supported every 1 m along the length of the tube with 0.5 cm wide plastic bridges. The wires are soldered onto printed circuit boards at each end of the tube. This whole structure is then inserted into the outer gas-envelope and end-plugs are heat-sealed and glued into place in order to provide a gas-tight enclosure. Connectors for gas flow can be placed on the same end of the detector if a gas 'U-turn' is provided at the far end of the outer gas envelopes. Connections for HV and signal lines are passed through one of the end connectors. The construction technique used for the MACRO streamer tubes has proven to

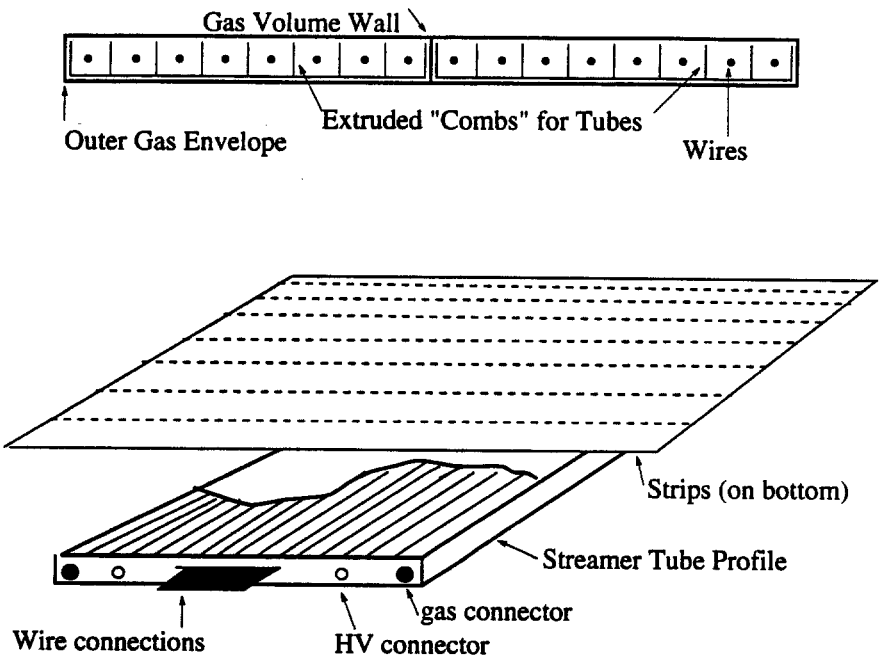

Figure 5.7: Construction of individual streamer tube packages. Both an end view and an isometric view of the end of a chamber are shown. The tube pitch is 1 cm.

be very reliable for gas seals.

The gas volume per plane of the detector is about 0.53 m^3 for a total gas volume in the detector of about 320 m^3. Several different gas mixtures have been used successfully in operation of limited streamer tubes. Typically, limited-streamer tube gasses involve argon and one or more hydrocarbon gasses as a quencher. For instance, in MACRO three different mixtures have been used including 70% argon, 5% CO_2 and 25% n-pentane or 25% argon with 75% isobutane [73] and more recently a mixture with helium, isobutane and n-pentane. Concerns about the safety of such gas mixtures have driven several searches for reliable replacement gasses. To date, all successful gas mixtures rely on some component of a flammable gas. However, studies [74] have shown that operation in limited-streamer mode is possible with a mixture containing as little as 9.5% isobutane with varying mixtures of argon and CO_2 with the CO_2 fraction being greater than 80% of the total mix. Such mixtures are nonflammable when mixed with air but are just below the limit of flammability.

Operation of detectors of this type with nonflammable gasses is a common problem in particle physics and is not unique to this experiment. We intend to study gas properties and research requirements for use of low concentrations of flammable gas in the far detector. The very large volume of air in the underground hall suggests that there should be no difficulty as long as pre-mixed gas is piped from the surface. A fall-back solution will be to run the tubes in proportional mode for which gas mixtures with no hydrocarbons have already been proven. The cost for running in such a mode is that the resulting smaller signals require

more amplification from electronics which places the experiment at greater risk to possible noise problems. The gas gain in proportional mode can be boosted somewhat by reducing the diameter of wires in the tubes but cannot equal that of limited-streamer mode. The benefit of high-gas gain and running in a partially saturated mode are very attractive and we intend to pursue this possibility but if necessary we believe that a reasonable fall-back strategy exists.

The primary plan for signal readout is to read wire signals along one edge of the detector and read strip signals along the other edge of the detector. The streamer tubes will be installed at alternating 45° angles to the horizontal in every other plane and with the strips running perpendicularly in both cases. The plastic walls of streamer tubes can support a surprising amount of weight so that they are essentially self-supporting. The only requirement is that they be held snugly in place to keep from buckling within the gap and pushed firmly against the readout strips. The strips will run the full length of the detector perpendicular to the tubes providing a transverse readout view.

The strip pitch will be 2 cm. The strips are facing the open side of the inner plastic extrusion so that they have optimal coupling to the discharges near the wires. (This helps to reduce the need for careful balancing of the resistive properties of the graphite coating.) Tubes in successive planes of the detector may be installed with the walls slightly offset to allow for better precision in position measurements for muon tracks which cross many planes in the detector. It is anticipated that this approach will allow an effective transverse position measurement of about 2 mm for tracks which cross through several planes of detector. Rough amplitude measurements can allow measurements in the strip-view of the detector to have a precision of about 1/10 of the pitch (2 mm in this case).

There are several options for the readout-strip configuration. One possibility is to put a second set of strips at a non-90° angle with respect to the wires in order to help eliminate x-y ambiguities which are inherent in perpendicular readout coordinates. This would require more channels of readout for each plane of the detector. Another possibility is to run strips at stereo angles on both sides of the tubes instead of reading out the wires. This has the benefit of improving the per-plane resolution compared to having one coordinate read by the wires. Technically, this simplifies the end connections for the streamer tubes but places more stringent demands on the properties of the graphite coating of the inner streamer tube profile in order to make sure that the coating is transparent to the signals. Finally, only one strip view might be read for each plane of the detector. This would cut the number of channels to be read in half but at the cost of poorer overall resolution and more positional ambiguities. Detailed Monte-Carlo calculations combined with cost estimates for implementation are needed to determine which, if any, of these options might be desirable.

The typical operating voltage for limited streamer tubes is around 4500 V. Under these conditions, wire pulses for a minimum ionizing particle are typically around 50-100 mV in amplitude terminated at 50 Ω. These signals require little or no amplification. The amplitude of the strip signals is determined by the capacitive coupling of each strip to the wires. For the strip geometry described here, it is expected that the amplitude of the strip signal for a strip which is centered directly over the discharge will be about 30% of the wire signal's amplitude. For a discharge which is located below the boundary between two strips, the amplitude of the two closest strip signals will each be about 20% of that from the wire. Hence, only modest amplification is necessary for operation in limited-streamer mode. If it is

necessary to run in proportional mode, the typical signal amplitude is expected to be about a factor of 100 times smaller, resulting in significant electronic amplification requirements.

5.7 Readout electronics

The total number of strips/wires to be read out in the far detector is 480,000. This places stringent demands on the design and cost of the readout electronics. Fortunately, modern tools make it easy to design and build custom chips which can deliver exactly the functions needed for a minimal cost per channel. The philosophy of the readout electronics is to distribute front-end and digitization circuits along the edges of the active detector planes. This minimizes the need to send analog signals over any significant distance, helping to keep costs down and reduce noise problems. Only digital signals or DC voltages will be transmitted over any significant distance. The distributed electronics will be tied to a ribbon cable bus which will be used for trigger information, setting discriminator thresholds and readout of the front-end electronics. Power distribution will run along a separate, parallel bus. The bus will link the front-end cards to electronics modules in VME crates where experiment triggers are formed and data are read and stored prior to being transferred to the online computers. An overview of the readout electronics is shown in Figure 5.8.

The front-end electronics will consist of two stages of custom monolithic chips mounted on PC strip-boards which will be directly connected to the edge of the active detector planes. Figure 5.9 shows a block diagram for these boards while Figure 5.10 shows a block diagram of the logic internal to the monolithic chips. Each strip-board will service 50 strips or 100 wires along the edge of one detector plane. (Wires will be summed together for readout and obviously will carry opposite polarity signals.) The custom chips will be built to accommodate as many channels as possible but it is likely that each board will contain a few sets of chips. Each of the 50 inputs will first go to a preamplifier and shaping/stretching circuit. These amplified analog signals are then sent to the second stage of custom chips which contain discriminators and various logic functions. The analog signals are split to two discriminators with separate thresholds. The thresholds are supplied externally from the bus or if necessary could be locally produced *via* a DAC.

When the first discriminator level is crossed, a time-stamp register is latched to record the time at which the event occurred. Each of the custom logic chips will have an input 40 MHz clock signal from the common bus which causes all of the chip times to be synchronous. While a pulse is above this threshold, a counter is gated on and the time over threshold is accumulated using the common clock. This gives ≈ 6 bits of information for a 1 μs analog pulse shaping time. The time of the event and time-over-threshold are recorded in a local FIFO buffer which can hold at least tens of μs of information.

The second discriminator is used to give a signal for triggering. The trigger from a given logic chip will consist of an OR of an appropriate number of contiguous strips. This number is determined by the need to keep random trigger rates from radioactivity sufficiently low. The current plan is that roughly every 16 strips will form a trigger unit. All trigger signals will be driven onto the trigger bus to be combined in the trigger modules with signals from other parts of the detector to determine an experiment-wide trigger. It could also be possible to provide various levels of trigger which depend on amplitude or multiplicity within a single

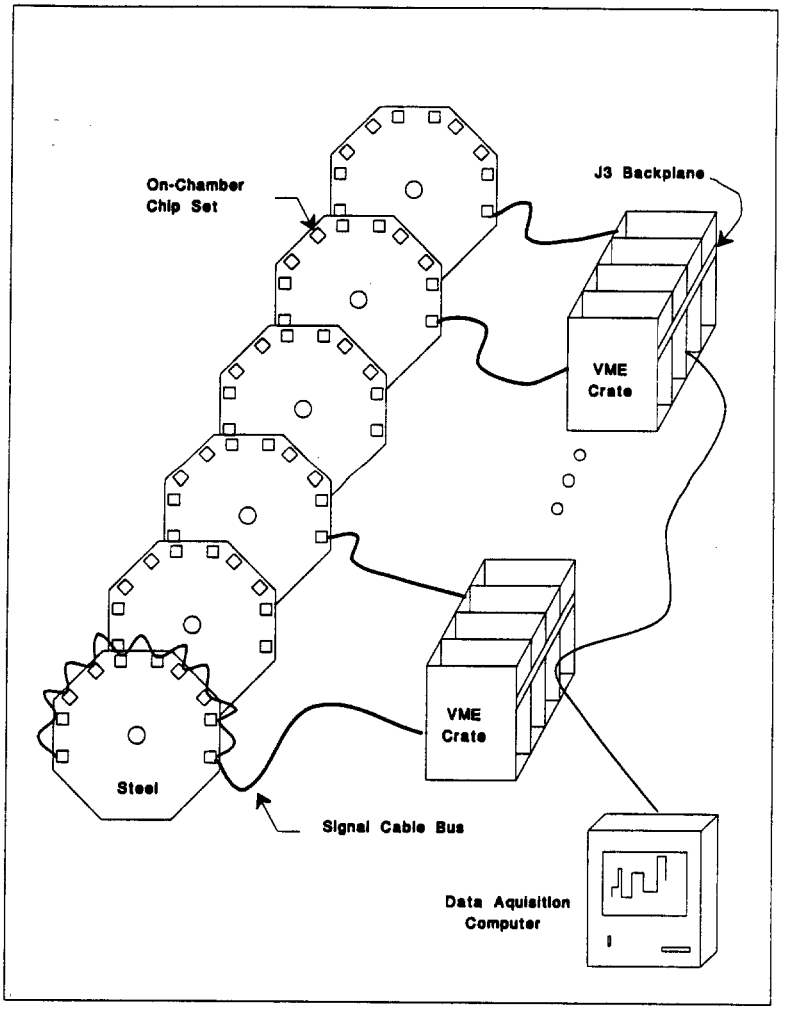

Figure 5.8: Overview of the setup for the readout electronics.

set of electronics. It is possible that a single channel could become noisy and dominate the trigger rate. However, this channel could still be useful for readout information. To cover this possibility, a register with a bit for every channel will be included which can disable the participation of any given channel in the trigger.

Trigger signals from each plane are combined in a single VME trigger module. This module combines signals from the various distributed cards for each plane with those from neighboring planes. The particular triggering condition will depend on noise levels in the active detector planes. However, we anticipate that a trigger which is based on $x - y$ coincident hits, in 3 out of any 5 contiguous planes firing within a 1 μs window over a 1 m^2 area of the detector, will provide very high efficiency with an acceptably small false trigger rate. We expect that the rate of pulses from radioactivity (the primary noise source in limited streamer tubes) is less than about 200 Hz per m^2. In that case the false trigger rate based on this trigger condition will be no more than a few Hz for the full detector depending on the local radioactivity conditions. This is a comfortable rate of false triggers which will

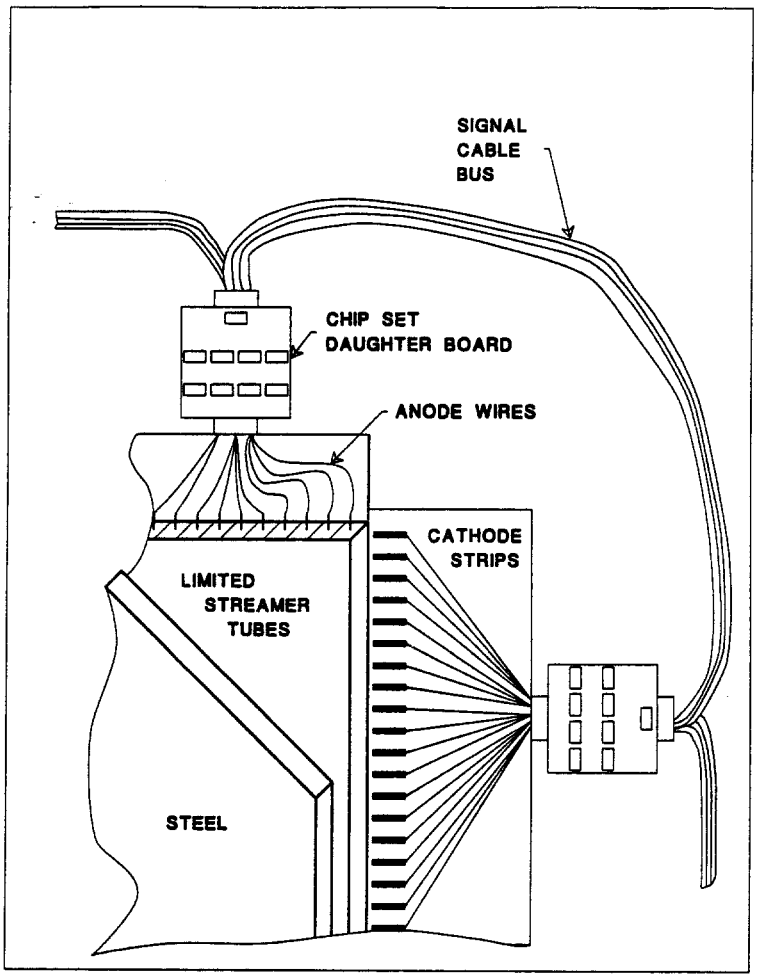

Figure 5.9: Block diagram for components of the front-end electronics strip boards.

not place any extra constraints on the data acquisition system. The rate of triggers from real cosmic ray events will be around 1 Hz. Other possible trigger conditions and rates will be studied.

When a global trigger condition is determined, a signal will be sent to all front-end electronics cards to switch into a readout mode. The readout of the information stored in the front-end cards will proceed serially for each system tied to a single VME module. The readout may proceed *via* an addressing scheme for the front-end cards or may be treated using a simple serial system where each card enables the following card for data transfer. Only data which satisfy minimal trigger conditions within a set time-period (in time with the trigger condition) will be transferred. Hence, other than the actual hits associated with the event, it is expected that no more than about 60 additional random (radioactivity) hits will be recorded over the entire detector within a 10 μs window of the triggering condition. A typical neutrino event will result in as much as a few hundred hits (events with muons will tend to provide the most hits) where each hit contains on the order of 32 bits of information. Hence, the typical event size will be less than 1 kB for random triggers and around 2 kB for cosmic ray muons or neutrino interactions. Once readout of the front-end electronics is

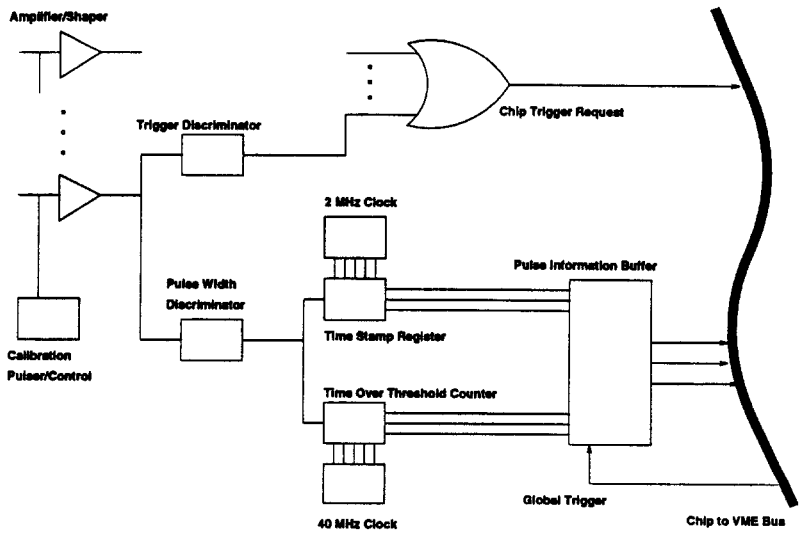

Figure 5.10: Block diagram for logic in the front-end custom chips.

complete, a reset pulse will be distributed which will zero the distributed registers and the detector will once again be live for further data acquisition.

A pulse injection system will be provided for calibration and monitoring of the front-end electronics. A pattern will be downloaded to each chip set indicating which channels are to be pulsed and then a synchronous signal will be sent to initiate a pulse. The pulses can either be generated by on-board test pulsers or a distributed pulse could be used depending on which provides the best stability and reproducibility. The resulting event will be treated in the same manner as a normal data event (but will be flagged in the readout). This system can be used for trigger diagnostics, calibration of the time-over-threshold pulse-height measurement, diagnosis of electronics problems and even for producing simulated events in the data stream.

The front-end chip set will be fabricated using CMOS technology in order to keep power requirements as low as possible. Each of the front-end boards will be provided with local fuses and the power buses will have additional fuses in order to ensure against any failures which could result in a fire. In order to keep the number of readout/trigger bus lines to a minimum (keeping the cost of connectors and cables down) functions on the bus and chip pins will be multiplexed. During data acquisition, most of the lines will be dedicated to carrying trigger signals. During the readout phase, most lines can be devoted alternately to addressing and data. Finally, during calibration setup the lines can be devoted to setting individual channels on or off. It is anticipated that a 32 pair bus will be sufficient for all functions.

The VME-based trigger/readout cards will each handle at least one plane of the detector (both readout views). (Perhaps as much as two planes could be handled per card with corresponding reduction in the total number of cards and crates needed.) The cards will form triggers based on coincidence with neighboring planes in local areas (on the order of 1 m^2 with overlapping adjacent sections). Trigger signals will be transmitted from one card to neighboring cards *via* a custom backplane. This allows each card to declare a trigger

according to its own local trigger information and that of the neighboring cards. Trigger information will be carried across adjacent crates *via* ribbon cable connectors on the backplane. The trigger conditions will be programmable with the nominally planned condition being hits in the local module and any additional two of the neighboring 4 modules. Once a module determines that an experiment trigger condition exists, a signal will be sent to all of the VME crates in order to close data acquisition and read out the full detector. Each of the readout modules will have local buffering for event information so that once the information is read into the VME modules the experiment can be re-enabled for further data acquisition. Computer readout can then occur at a leisurely pace following the event acquisition. A master trigger module will order the resetting of the front-end electronics once all trigger/readout modules report completion of readout.

In addition to the trigger and readout capabilities, the VME modules will also provide the various control functions needed by the front-end circuits. This includes controlling the state of the readout/trigger bus, loading and reading registers in the front-end electronics, distribution of DC levels and distribution of essential signals such as the global reset and trigger conditions, global clock and test-pulse initiation or distribution signals. These control functions will be governed by downloading information into registers on each of the VME cards. Computer readout and control will be *via* a master module in each VME crate which communicates with the other modules *via* the backplane. The master module may contain local processing capability and will communicate with the data acquisition computers *via* Ethernet or other communications protocol.

5.8 High voltage system

The required voltage for limited-streamer operation is about 4500 V and can be positive or negative depending on whether it is desired to read out the wires in one view or to use only cathode strips for readout. Positive HV is used if no wires are to be read and the wires are hooked to the HV through current-limiting resistors. If the wires are to be read out then negative HV is used with the HV connected to the graphite coating on the inside of the plastic streamer tubes. This technique has been used successfully in previous experiments.

The current draw is roughly proportional to the area of streamer tubes to be operated. Typical current draws in the type of tube that we propose to employ are less than 1 μA per square meter (frequently only tens of nA per square meter). Hence, the total current demand for the entire detector is about 100 mA at 4500 V. This demand is easily met by a number of commercially available systems. The CAEN SY403 HV system is an example of a system which will provide all of the necessary features. It allows computer control and readback of voltages and current limits and many channels can be driven through a single unit. It is desirable to have the detector segmented into parts not only from the point of view of current demand but also to keep most of the detector functional if some problem occurs or maintenance is being done. We anticipate that 10 of the CAEN mainframes will be sufficient to cover all HV needs for the far detector.

The HV distribution will be *via* coaxial cable using SHV connectors to local distribution panels located on the detector. Each HV channel will drive one plane of the detector. HV connections on the plane are made by a simple daisy-chain network which runs along the end

of the detector plane. Hence, about 600 cables, each of about 20 m length are needed to run the HV from the mainframes to the detector. The distribution on the chambers is typically made with "plug-in" connectors for each profile of streamer tubes which are single conductor cables and covered with a grounded aluminum housing along the edge of the detector for safety.

5.9 Gas system

The total gas volume for the far detector is 320 m^3. This is only about half that in the MACRO detector. Hence, the gas system for that detector provides a good model for how this system might operate. The main difference which we expect here is that the safety requirements for flammable gasses are more strict in the United States than in Italy where the MACRO detector is installed. However, we believe that the safety issues can be addressed through several measures, including placing the mixing operations on the surface instead of inside the mine. In that case, the gas which is actually piped into the mine will be below the limit of flammability when mixed with air. However, there are additional requirements to ensure a large margin of safety.

Figure 5.11 shows a block diagram for the planned gas system. The starting point is on the surface where mixing of gasses will be done in order to avoid transporting and housing pure isobutane underground. The gas will be a mixture of argon, CO_2 and about 10% isobutane. The argon will be delivered as dewars of liquid while the CO_2 and isobutane will be high-pressure cylinders (liquid phase). The gas will be mixed to its final concentration in a temperature-controlled building. The mixing will be under computer control using commercially available mass-flow meters. The gas will be tested for mixture control and purity by a gas-gain monitor and a commercial gas chromatograph. The mixture needs to be controlled to keep the isobutane fraction constant to within about 0.2% (i.e. 2% of 10%). This is easily achieved by use of mass-flow controllers with a modest downstream buffer volume. The rate at which new gas will be mixed is 1/10 of the total gas volume in the detector per day, or 1.3 m^3/hour. This rate is readily achieved using commercially available flow controllers.

The mixed gas will be piped to the underground laboratory *via* a 1500 m long one-inch diameter stainless steel pipe. Since the flow rate is relatively low, a pressure of 10-20 psig will be sufficient to drive the flow to the underground detector and give sufficient overpressure to drive across any flow-checking devices. The pipe will be insulated outside of the mixing building until it is sufficiently deep underground that the cold winter conditions of northern Minnesota will not cause any difficulties with condensation of any gas components (including traces of various hydrocarbons which if condensed out at one time can re-evaporate when it is warmer). The installation of the pipe in the mine-shaft is not an unusual operation and requires only a small fraction of the total labor involved in the gas system installation.

Underground in the experimental hall, the pipe from the surface will enter into a master gas control/circulation system. This system will be under computer control and will provide for recirculation of gas through the detector (one volume recirculated per day), filtering of the gas and removal of oxygen by 'burning' it with hydrogen (a standard technique), control of the absolute pressure of the full system, addition of 10% new gas per day, regulation of

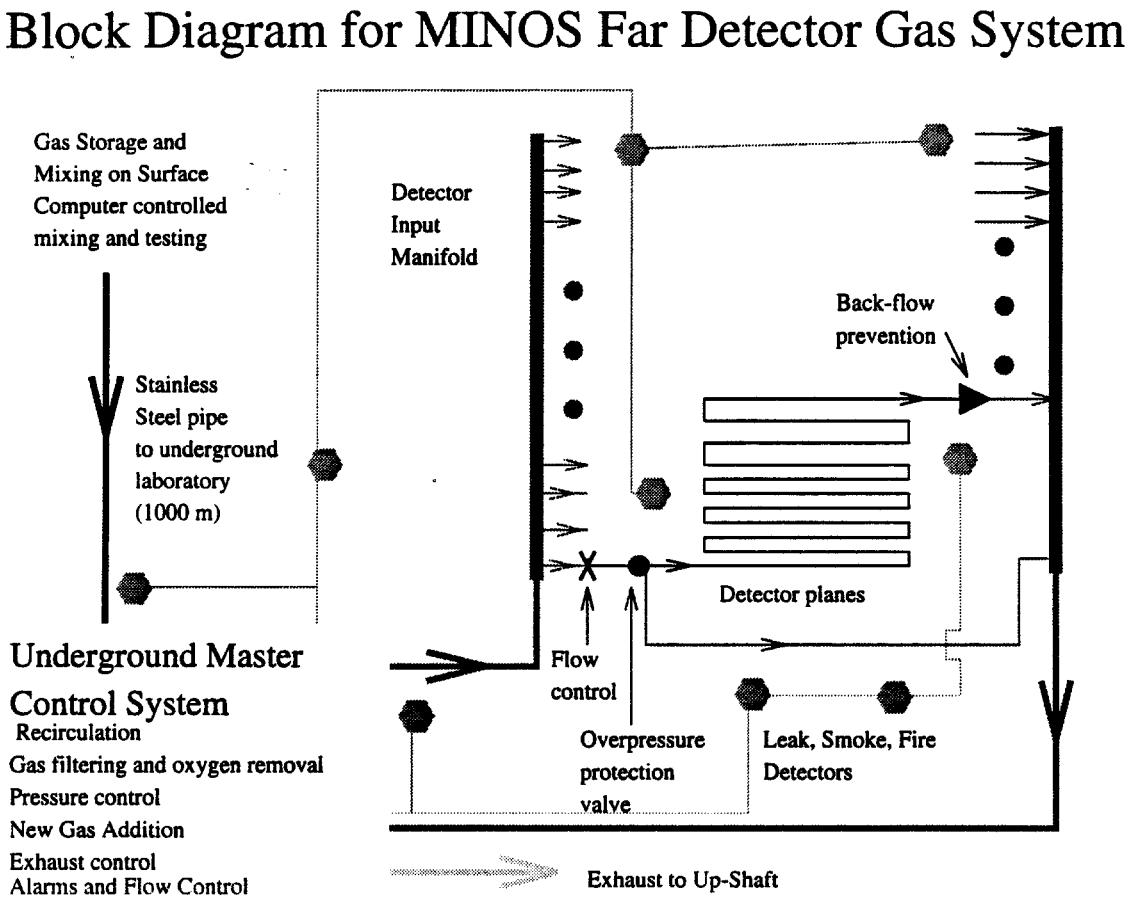

Figure 5.11: Block diagram for the gas mixing, circulation and distribution system.

the exhaust flow, monitoring of the gas quality, control of gas flow to different parts of the detector and monitoring of any alarms which indicate dangerous conditions or gas leaks in which the gas flow should be cut off.

An output pipe will carry gas from the central system to a distribution manifold which runs along the detector. Each plane in the detector will have a local valve coming off the distribution manifold and the manifold itself will be divided into several sections. Since the impedance of detector planes vary, it is necessary to provide local flow controllers to each plane in order to ensure that equal gas flow is achieved throughout. Typically, simple visual readout flow-controllers are used for this kind of task as the precision of the gas flow is not very important and the cost is lower than electronic readout and control. All of the streamer-tubes in a single plane will be daisy-chained together in a serial flow pattern. The exchange of one volume of gas per day will not produce any significant pressure differential across the plane of tubes. The exhaust from each plane is driven into a common manifold through a device which is designed to prevent backflow of gas. At the upstream input to each plane, an over-pressure relief valve will be installed in order to ensure that the chambers are not damaged if a gas-line is crimped somewhere in the system. These over-pressure valves

are usually simply visual bubblers with a few inches of oil to provide the pressure setting.

The exhaust from the planes will be returned to the central control system where it is cleaned, some is replaced, and then is recirculated. The quality of the mixture is continuously checked. Experience with the MACRO detector suggests that even complete cutoff of gas for periods of a few days does not strongly affect the behavior of the tubes so the system does not need to respond very quickly to slight anomalies. The exhaust from the central control system will be vented into a special duct in the utility shaft of the mine, as described in Chapter 4. Small quantities of chamber gas which leak from the system will be mixed with the ambient air and moved by the laboratory exhaust fans to the hoist shaft where it is mixed with the continuous shaft air flow of 500 cubic feet per second. Even quite large leaks will therefore present no danger for gas accumulation.

Safety regarding the operation of the gas system will be a primary concern. The system will have an extensive network of leak detectors which will isolate the location of any leak and if sufficiently large, automatically halt gas flow to that section of the distribution manifold. In addition, the system will monitor other alarms such as fire or smoke alarms and automatically cut off gas flow in the presence of such alarms. Finally, gas flow will require that power is present so that if a power outage occurs, gas flow will automatically be cut off.

5.10 Online computing

The online computing needs for the far detector are relatively pedestrian compared to most large high-energy physics experiments. This is due to the low trigger rate that is expected. We expect that the data which are read out will be dominated by events resulting from passage of cosmic-ray muons through the detector and from random radioactive coincidence. The rate of cosmic ray events will be about 1 Hz with an average event size of about 2 kB while the random trigger rate will be about 5 Hz but with only 0.2 kB of data per event. This average data throughput is so low that it essentially places no constraint on the capabilities of the data acquisition computers. In particular, since we envision that some modest data buffering capabilities will exist in the VME electronics, there is little need for the readout speed to be very fast. Virtually any modern computer which is capable of driving a data acquisition interface and writing data onto some external device will suffice. This allows us to design the acquisition system based on ease of use, good data monitoring capabilities and implementation of standard equipment and tools.

A simple system for event concatenation can be devised using local processors in each of the VME crates which communicate with a central computer *via* Ethernet. After data acquisition, each of the local nodes queues a data packet to be sent to the central computer. A program running on the central computer receives all of the packets from the distributed nodes and assembles them into a single event according to a common hardware event number which is automatically distributed between the VME crates for every trigger. Once the central computer has concatenated all of the data packets, the complete event is written to disk where it can be accessed by reconstruction and monitoring programs which run in parallel with the event concatenation program. We anticipate that it is the event reconstruction and monitoring programs which will provide the biggest CPU demands on the central computer. Even this is easily solved if necessary by assigning different tasks to several CPU's within

a cluster of machines which all have access to the data on disk. The expected event rate will result in about 300 MB of data being written to disk per day which corresponds to one Exabyte tape (or storage device with equivalent capacity) about every two weeks.

At this time, we refrain from specifying the particular elements of the computing system since anything we list here will certainly be obsolete by the time the experiment will be built. However, the generic needs are:

1. A central computer for communication with the distributed processors in the VME crates and concatenation of events.

2. Five multi-gigabyte disk drives for storage of data prior to writing to tape and local processing of data for reconstruction and monitoring purposes.

3. Five workstation processors for local reconstruction of events and running monitoring tasks.

4. Five high-quality color screens for event display and output from monitoring programs. (These may be the screens for the workstations in the previous item.)

5. Four workstations for local program development and data analysis work.

6. Five 'hard-copy' data storage/reading systems. The standard in the last few years for this has typically been Exabyte tapes but by the time this experiment will be taking data we anticipate that optical disks are more likely to be the favored technology.

7. Two 'carousel' or stacking systems for the data storage technology for production of distribution copies.

8. Local network hardware to tie everything together.

9. A fiber-optic data-link between the surface and underground.

All of the technologies listed above are readily available today at relatively small cost. We anticipate that the cost of these capabilities will remain stable at worst. Our cost estimates are based on purchasing the relevant equipment which exists now.

In order to take advantage of the small duty-cycle of the neutrino beam from the main injector (a 2 ms spill every 2 s) and to correlate the data acquired at the far detector with the near detector and accelerator operating conditions, some type of timing information is required. The technique now used by a number of underground experiments is simply to use clocks which are synchronized to broadcast signals from satellites. This permits absolute time measurements to within about 1 μs and hence will allow synchronization of the far detector with events at Fermilab. Any drifts in the spill time at Fermilab must be communicated to the far detector site by recording the time relative to a clock receiver at Fermilab and transmitting this information to the far detector site where the gates for electronics can be appropriately timed to the Fermilab time. Sending such information *via* software over normal computer links should be sufficient to maintain good timing for these purposes. Since the far detector will have an open trigger, it will be possible to use actual neutrino events over a period of a few days to verify the actual arrival time of the neutrinos at the far detector. The

ability to set a gate for triggering will allow even lower threshold trigger conditions to be set during that period of time. This may help reduce systematic errors involved in uncertainties in acceptance of very low-y neutral-current events.

5.11 Construction and Installation

It is our intention to have at least half of the full detector installed by January 1, 2000 and the full detector by the following January. We anticipate occupancy of the far detector hall in mid-1998. The schedule is driven by the desire to make the best use of the neutrino beam from the Main Injector. With 600 planes of detector to build and install underground, the installation work will require careful planning and coordination in order to maintain the desired schedule. Although it presents a challenge, we do not see any fundamental technical or cost barriers to meeting this schedule. Figure 5.12 shows the time-line for the major installation tasks.

Installation of half of the detector by January 1, 2000 will require that 300 planes of the detector be installed and brought into operation in about 450 calendar-days. Hence, the average rate of installation will have to be about one plane of passive and active detector elements per day. In order to accomplish this, the fabrication of steel and active detector elements must be scheduled to begin delivery of materials to the Soudan site by spring of 1998. Although transportation of materials from the surface to the underground laboratory is a non-negligible task, it should not represent a bottle-neck to the construction schedule. It is anticipated that the transfer of steel to the underground hall will take approximately 100 days of lift operation with a 6-person crew. Although less massive, transport of the active detector elements will require a similar amount of time since the lift load is constrained more by the area of the shaft than the mass which can be lifted. (Remember that this used to be an iron mine producing hundreds of kilo-tons of iron ore per year. Although rich in irony, putting iron back in is not substantially more difficult than taking it out.)

In order to maintain the installation schedule underground, detector planes will be assembled in parallel. The detector planes will be fashioned by first assembling the absorber steel horizontally on a special strong-back lifting structure. The active detector planes will then be installed on top of the steel, taking care to place the detectors with precision of a few millimeters. The detector elements will all be tested following delivery to the underground laboratory and prior to installation on a layer of steel. However, in order to ensure minimal failures, the active detectors will be tested a final time after being assembled into a plane. The planes of steel and detectors will be lifted up and the assembly structure on the back of the steel removed. The entire assembly will then be put into place on the face of the existing planes of the detector with the active detectors facing out. (The first plane needs a special 'book-end' fixture to hold it in place.) The positions of the detectors in the plane will then be surveyed to a precision of 1 mm. Any settling which occurs when additional planes are added will result in overall shifts of the entire plane which can be measured externally. Active detectors will be permanently entombed once the next plane of steel is added. This may suggest that a final test of the active detectors be performed once they are in place vertically.

It is anticipated that having four assembly structures for building planes will be adequate

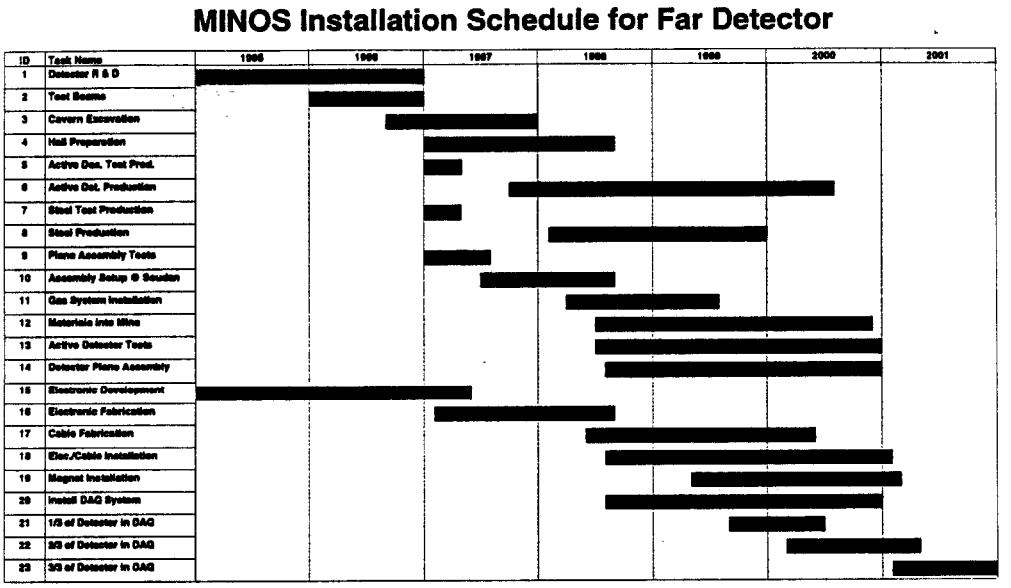

Figure 5.12: Time-line for the far detector installation.

to meet the schedule described above. Figure 5.13 shows the layout of the detector hall. The space in the new hall combined with the space in the existing hall and the planned interconnection will be sufficient for locating these assembly structures. In order to allow work to proceed simultaneously at the four assembly stations, we plan to employ two separate crews of 16 workers each. This will keep assembly in the mine under way two thirds of all assembly days. These workers are in addition to the expected participation of physicists, engineers and technicians from the participating institutions who will have responsibility for large amounts of testing, debugging and data checking on newly installed detectors. If sufficient money is available at a fast enough pace, we could add one more shift in order to complete assembly sooner.

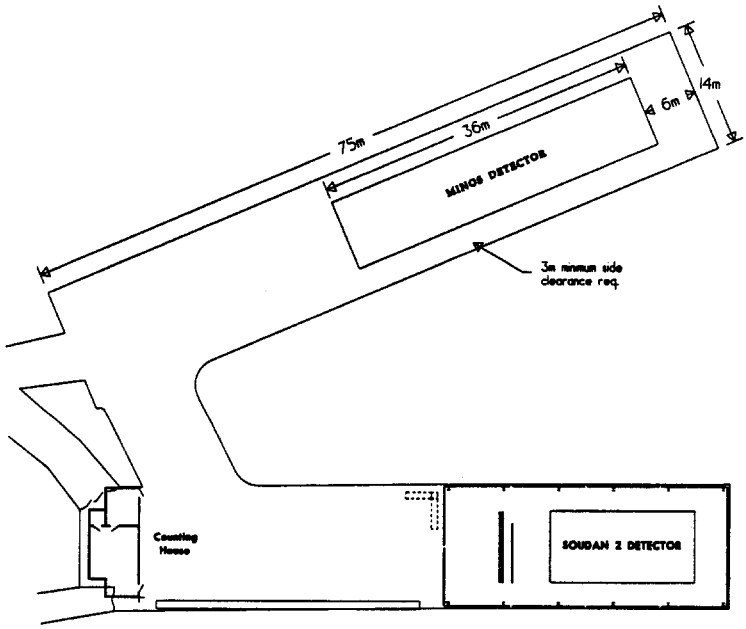

Figure 5.13: Layout of the detector halls showing space available for construction.

5.12 Options for Detector Construction

There are a number of possible options for detector construction which we will study prior to a technical design report. One particularly fundamental option is to make part of the detector from a low Z material with thinner sampling than in the iron section. One possibility could be to build absorber layers from specially designed concrete blocks roughly 5 cm thick (0.5 radiation-length sampling). This would be useful for measurement of kinematics for events which contain electrons (allowing $\tau \rightarrow e\nu\nu$ signatures) and for measuring kinematics of the hadronic part of events due to improved angular resolution on hadronic showers. In this case, it is anticipated that a modular construction would be attractive since it would allow optimal acceptance for muons which originate in the concrete to be measured in the steel part of the detector. In addition, a modular construction will most easily allow a staged construction allowing completed sections of the detector to be in data acquisition while construction continues on the remainder of the sections. Figure 5.14 shows a sketch of a possible combined steel/concrete detector.

Although probably not necessary for the accelerator neutrino experiment, an active shield around the top and sides of the detector will be essential for measurements on atmospheric neutrinos. The shield could be built using the same technology as the active detector or perhaps with a fast-timing technology such as RPC's instead of streamer tubes. Using streamer tubes, the active shield would consist of a double layer of tubes with wire readout only with the wires offset in the two planes in order to provide maximal efficiency.

A number of different options exist for the active readout technology. These include scin-

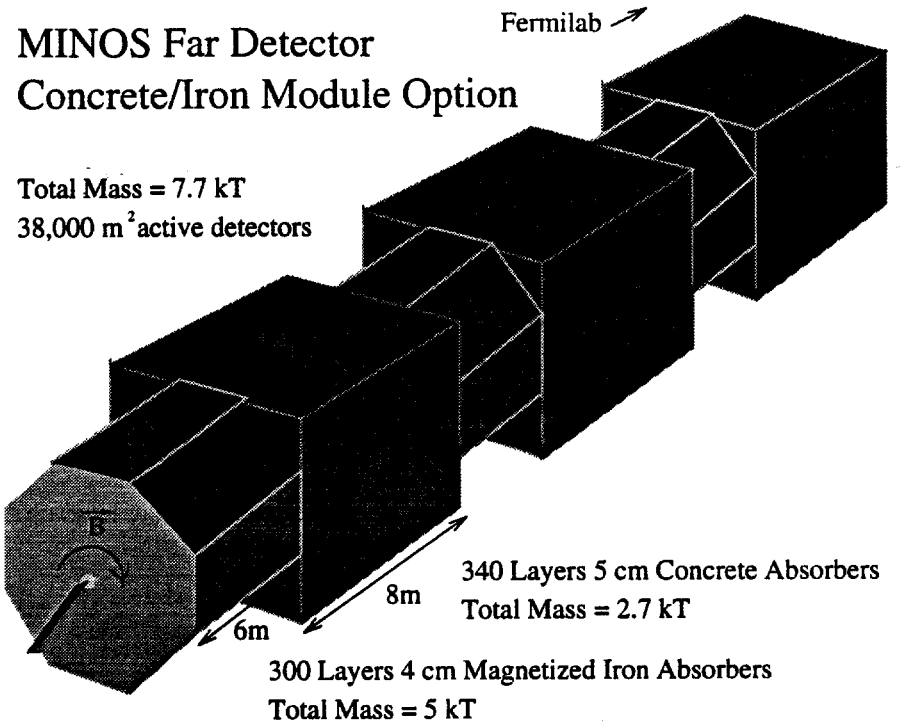

Figure 5.14: A possible arrangement of modules in a concrete/steel option.

tillator tubes, resistive plate counters (RPC's), proportional mode cathode strip chambers (CSC's) and drift tubes. Each of these has various advantages and disadvantages compared to limited streamer tubes. This will be discussed in detail in Chapter 11. It is conceivable that a final detector design could include more than one of these technologies in order to achieve some particular goal. For instance, a hybrid solution might include some layers of RPC's in addition to the limited streamer tubes in order to provide fast-timing for at least part of the detector. In any case, the far detector provides the most serious challenges for the active detector construction and will drive the decisions related to the appropriate readout technology. The near detector will always mimic whatever is needed for the far detector in order to keep the detector response as similar as possible.

5.13 Soudan 2 detector

In addition to the new detectors to be built for the long baseline neutrino oscillation experiment, we anticipate that the Soudan 2 detector will continue to be available as part of the overall experiment. This may be by keeping it in its current configuration (with removal of some modules to be used as part of a suite of near detectors, as described in Chapter 6 and Appendix B) or reconfigured to take maximal advantage of its very fine-grained readout combined with the new, much larger detector. One possibility is that the existing modules would be moved to be the most upstream part of the far detector so that muons and hadrons exiting the relatively thin Soudan 2 modules would be captured and measured in the down-

stream detector. Such a reconfiguration would be undertaken only once it is clear that the new detector construction is sufficiently well advanced that the overall measurements will benefit from the work.

In order to make optimal use of the existing detector, some upgrades to the electronics may be beneficial. In particular, the current detector has an 8-to-1 multiplexing of drift tubes to electronic channels. Reduction of this multiplexing could improve measurements for a long-baseline experiment. If new electronics are to be built for this purpose, it is likely that all of the electronics would be replaced using the most modern technology. This option requires further study to evaluate the cost and benefits which it offers.

See Appendix B for a more detailed description of the Soudan 2 detector and its role in the long baseline experiment.

Chapter 6

Near Detector

6.1 Near detector overview

The P–875 near detector will be installed in the Main Injector neutrino beam in the near detector hall at Fermilab, downstream of the E–803 experiment. It will consist of three different sections:

- The beam monitor calorimeter – a fine sampling calorimeter for beam measurements,
- The steel calorimeter – a smaller version of the far detector,
- The Soudan 2 near detector – twenty Soudan 2 detector modules.

The beam monitor calorimeter provides accurate measurements of neutrino beam characteristics which serve as input for the calculation of beam properties at the far detector. In order to determine the beam momentum spectrum as a function of radius, the monitor calorimeter measures neutrino interaction event vertices with 1 cm accuracy. It also identifies ν_e beam background events with known efficiency.

The steel calorimeter has two separate functions. First, a ν_τ appearance signal observed in the far detector must be compared with background predictions based on events measured only within the steel calorimeter. Any ν_τ appearance signal is likely to consist of a small number of τ lepton events in the far detector, so an accurate assessment of events which can mimic ν_τ charged current interactions in the far detector is crucial.

Second, the steel calorimeter will be used in a direct comparison of event characteristics in near and far detectors, as described in Chapter 8. The statistical comparisons of four independent ratios are used to characterize changes in the flavor composition of the beam as it travels the 730 km from Fermilab to the Soudan Laboratory:

1. $\frac{\nu_\mu(cc)_{near}}{\nu_\mu(cc)_{far}}$

2. $\frac{E_{total}(cc)_{near}}{E_{total}(cc)_{far}}$

3. $T \equiv \frac{CC/total(near)}{CC/total(far)}$

4. $\frac{E_{had}(NC)_{near}}{E_{had}(NC)_{far}}$

These tests require that the measurements be as similar as possible at the near and far detectors. Ideally, events will be measured by identical methods and selected by identical criteria. This would ensure the same momentum and angular resolutions for muons and hadrons in the near and far detectors.

Both of these near-detector functions are made difficult by the fact that the beam is quite different at the near and far detector locations. The transverse dimensions of the beam at the far site are much larger than the detector, while the beam at the near location is smaller than the detector. Furthermore, the near detector observes neutrinos from both small and wide angle pion and kaon decays, while the far detector sees only small angle neutrinos, as discussed in Chapter 3. We have attempted to address these problems by employing somewhat different geometries in the near and far detector designs.

6.2 Description of the MINOS near detector

Figure 6.1 shows the layout of the MINOS near reference detector. The beam monitor section is made of a low-Z material (probably aluminum) and is backed up by the (larger) steel calorimeter. Both parts have an active instrumented area of 3 m by 3 m to contain the 1 m radius neutrino beam (the same area as the decay pipe) plus a 0.5 m allowance on all sides for shower containment. The steel calorimeter duplicates the far detector as closely as possible. This rear section is magnetized, and is used as both a muon spectrometer for the beam monitor calorimeter, and for measurement of neutrino interaction events occurring within its fiducial volume.

6.2.1 The beam monitor calorimeter

The design of the beam monitor calorimeter is patterned after that of the MINOS far detector, except that absorber plates will be thinner and unmagnetized. The active elements are limited streamer chambers of the same design (1 cm square tubes, 2 cm wide strip and wire readouts, as described in Chapter 5). Low-Z aluminum plates allow the identification and measurement of electrons. This capability is particularly important because the ν_e and $\bar{\nu}_e$ component of the beam is a potentially serious background for some of the neutrino oscillation tests described in Chapter 8. This design also provides the good hadronic angular resolution needed to determine the average neutrino beam direction. Our current design uses

Reference Near Detector for MINOS

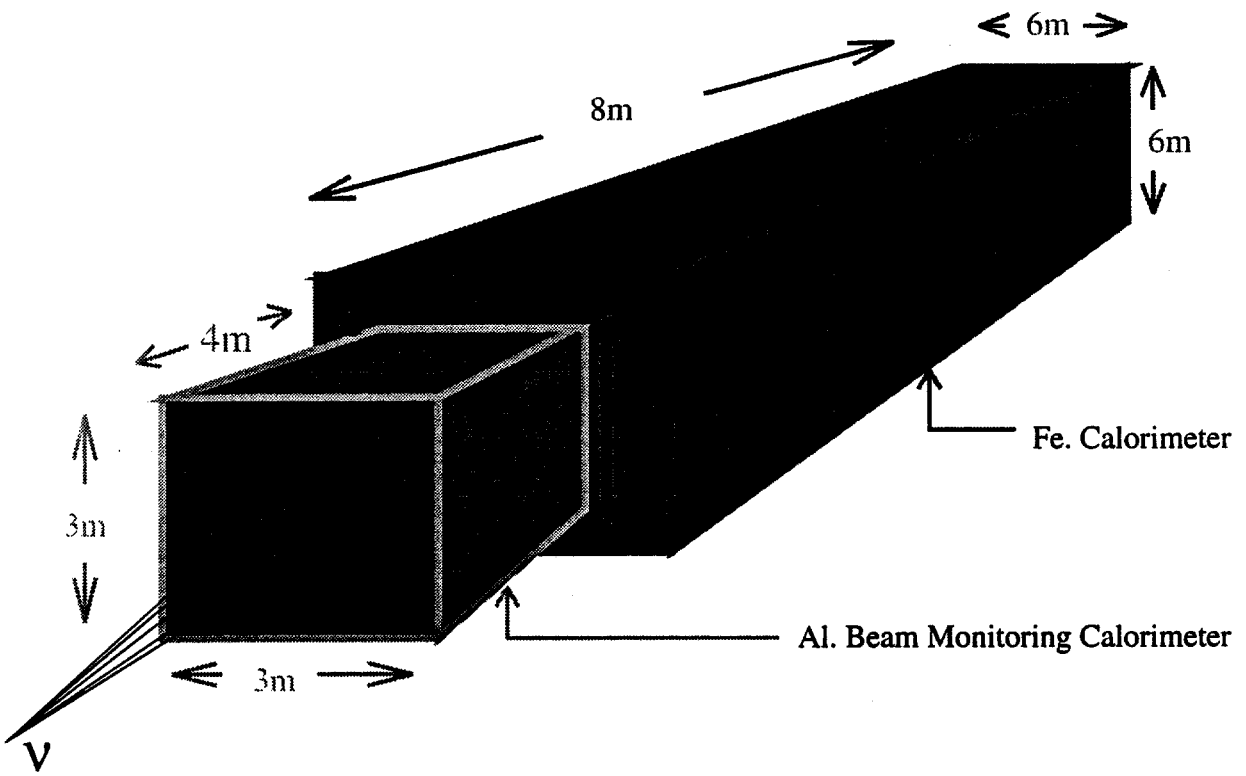

Figure 6.1: Layout of the Near Detector

2 cm thick aluminum plates, or about 5% of an interaction length and 22% of an interaction length per plate.

The first two to three interaction lengths serve to absorb beam-related neutrons from upstream neutrino interactions, and also to measure the longitudinal dependence of interactions. Beam-related hadron-induced reactions will be attenuated with longitudinal depth into the calorimeter. An additional two interaction lengths provide the target mass for the high neutrino interaction rate needed for accurate beam measurements. Measurement of the longitudinal dependence of interactions will allow us to determine the neutron contamination (if any) of the interactions in the target mass section. This geometry leads to a total length of 4 m for the beam monitor calorimeter.

With the present wide band beam design, neutrino event rates in the last two interaction lengths of the beam calorimeter will total 11 million per year, of which 0.9 million are in the central 25 cm region.

6.2.2 The steel calorimeter

In addition to its role in providing normalization and background information for far detector measurements, the magnetized steel also serves as a muon spectrometer for the beam monitor calorimeter. The depth of the MINOS near detector steel has been chosen to provide muon momentum measurements accurate to 10% or better in $\frac{\Delta p}{p}$. Muons with momenta higher than 5 GeV/c will be measured magnetically, requiring a path length of at least 5 m in the steel calorimeter to achieve the desired accuracy. Muons with momenta lower than 5 GeV/c may be stopped and measured also by range, which requires a path length of 7.5 m or more.

Near detector data may be analyzed by dividing the calorimeter into separate functional regions. The first 0.5 m serves as a target mass. The current wide band beam design gives 13 million neutrino interactions per year within the 1 m diameter beam area. The last 7.5 m of calorimeter depth is needed to measure the momenta of muons from these events, giving a total calorimeter depth of 8 m. The 1.5 m depth immediately downstream of the target region is also used to contain and measure hadron showers originating in the upstream region.

Magnet

The magnetized steel plates of the MINOS near detector are necessarily rather different from the 8 m diameter octagons of the far detector. Such large area plates are unnecessary (and would be excessively expensive) for the small beam area at the near detector. We have designed a near detector magnet with an "H" geometry and 6 m by 6 m rectangular plates. This magnet produces the same average field in the central 3 m by 3 m area as in the far detector octagons. The magnet is shown schematically in Figure 6.2. The "H" geometry minimizes the amount of iron in the flux return path. The magnetic field uniformity achieved with this design is shown in Figure 6.3. Conventional copper coils carrying a current of 7,500 A produce the average 1.5 T field in the central 3 m by 3 m instrumented area. The lack of a central hole in the near detector plates maximizes the useful area and simplifies event reconstruction in this detector.

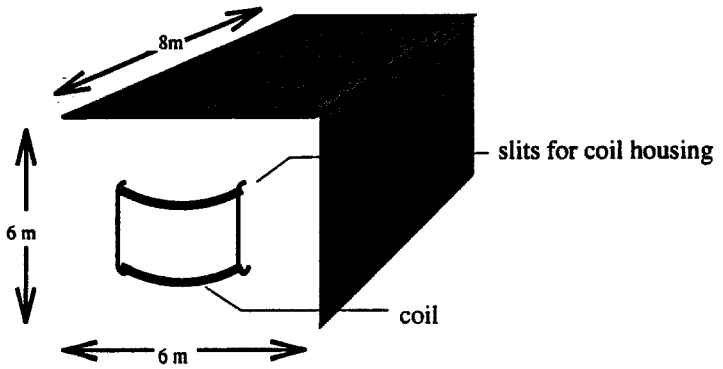

Figure 6.2: Magnet geometry for MINOS Near Detector.

6.2.3 The Soudan 2 near detector

A near detector constructed of Soudan 2 modules will be installed in the near detector hall in order to calibrate measurements made in the far Soudan 2 detector. Figure 6.4 shows the configuration of these modules as well as the beam direction. The modules are oriented at the same angle to the neutrino beam as the Soudan 2 far detector. The 4.3-ton calorimeter modules are arranged in a single-layer, 2.5-m high array. The mechanical support structure, gas system, electronic readout and data acquisition systems will be very similar to those currently in use at the Soudan Laboratory. These are described in detail in Appendix B, and will not be discussed further in this Chapter.

6.3 Beam monitoring

The beam monitor calorimeter is designed to perform measurements which will yield a precise characterization of the neutrino beam properties. However, the results of these measurements will not be available on the short time scale needed for beam tuning feedback during operation. Beam diagnostic instruments which can provide such instantaneous measurements of muon and hadron flux around the target area are discussed in Chapter 3. Because our knowledge of the momentum spectrum of the beam is so crucial to many aspects of this experiment, it is essential that we monitor it as thoroughly as possible. To this end we have designed the dedicated beam monitor calorimeter described here.

As described in Section 3.7.3, the neutrino energy spectrum of the inner 25 cm radius of the beam is expected to be very similar to that in the far detector (at the 4% level). This is true despite the fact that most of the neutrino flux at the near detector comes from wider angle decays (an off-axis pion decays to a neutrino with a wide angle, sending the neutrino back towards the center of the detector); such wide angle neutrinos cannot reach the far

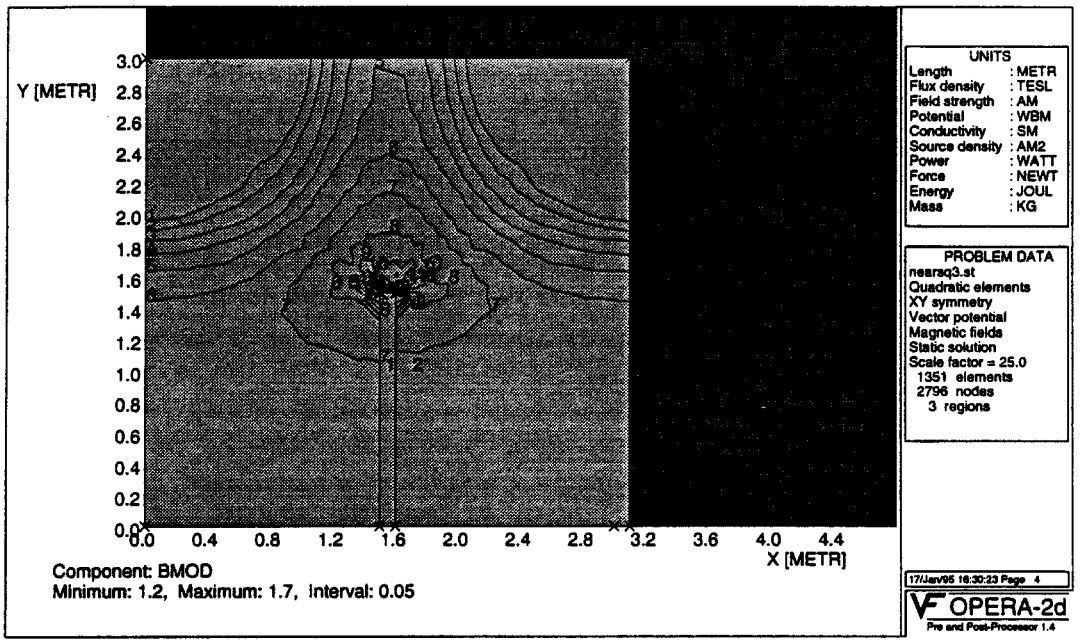

Figure 6.3: Magnetic field in the near detector magnet

Configuration of SOUDAN modules in Near Hall.

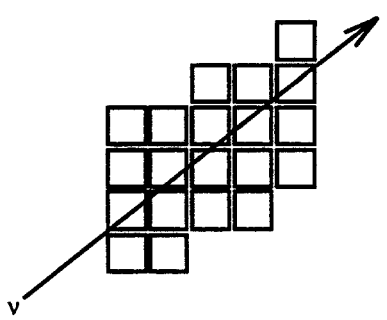

Figure 6.4: Layout of Soudan 2 modules for the near Soudan 2 detector.

detector. An important function of the beam monitor calorimeter will be to compare the predictions of the beam Monte Carlo simulation programs with the measured beam energy spectra as a function of radial position, from the central region out to where the beam is cut off by the decay pipe walls. In addition, the monitor calorimeter will measure the average neutrino direction as a function of radius, giving yet another check of the beam Monte Carlo programs.

As discussed above, an important function of the monitor calorimeter is to measure the ν_e and $\bar{\nu}_e$ contamination of the beam. This background has been calculated to be about 0.7% of the total neutrino flux in Chapter 3. The monitor calorimeter will measure both the absolute rate and the spectrum of these neutrinos.

The near detector must also determine the characteristics of the neutrino beam in the presence of beam-related backgrounds which are different from those at the far detector. The most serious of these backgrounds is the flux of muons produced in the dolomite shield and in the E–803 detector upstream of the MINOS near detector. The 150 m dolomite shield between the beam dump and the near detector hall will stop all muons produced in the beam dump itself. We expect beam neutrino interactions in the dolomite shield to produce about 8.8 μ/m^2 in each 1 msec long pulse [75]. The low rate and distinctive topology of these events should make them relatively easy to deal with. For example, we will probably employ a trigger veto at the upstream end of the beam monitor detector to avoid the data-acquisition dead time caused by triggers from these muons. This veto would give a trigger dead time of about 5%.

6.4 Detector elements

The limited streamer chamber active elements of the near detectors will be identical to those in the far detector except that the cathode strips and anode wires will be somewhat shorter than the 8 m lengths used in the far detector.

The passive material in the beam monitor detector is aluminum. The 3 m by 3 m plates are 2 cm thick and separated by 2 cm wide gaps for chambers. The 4 m depth of the monitor detector will require 100 planes of limited streamer chambers.

The MINOS near detector magnetized steel plates are 6 m by 6 m. The 4 cm thick plates are separated by 2 cm wide gaps for chambers. The 8 m depth of this calorimeter will require 133 planes of limited streamer chambers.

We have not yet begun detailed engineering designs of the near detectors. We do not expect these designs to present any unusual challenges or opportunities for significant cost savings. The mechanical structures and the magnet are rather conventional, while the active elements, electronics, data acquisition and gas systems will all be similar to those in the far reference detector, as described in Chapter 5.

6.5 Construction and installation

The only significant installation challenge will be the assembly of the MINOS near detector magnet in the underground hall. This device includes both the 6 m by 6 m steel planes

and a steel support structure. As in the far detector, the steel planes will be supported on adjustable feet, resting on a 7.5 cm thick steel base plate. Access to the chamber gaps between planes is from the top and sides only. The coils will block access to limited regions of the top and sides of each chamber gap, but are spaced far enough apart to allow the entire 3 m by 3 m area to be instrumented. The MINOS near detector chambers and strip planes will be 4.5-m long so that the wire and strip electronics can be mounted along the outside edges of the 6 m steel plates.

The 7.6 m by 3 m elliptical cross section elevator shaft is large enough to accept the full 6 m by 6 m square detector planes. The plates can therefore be installed as completed units, and will require very little assembly work in the underground hall.

Each 6 m by 6 m steel plane is preassembled from a central 3 m x 6 m plate and two 1.5 m by 6 m flanking plates which are joined with minimal air gaps to obtain the desired magnetic field quality. To minimize the fabrication costs, the plates would not be bolted together. The central plate would cover the entire active detector area while the two flanking plates would be notched to accommodate the magnet coil. A plane which is preassembled on the surface would be attached to a fixture and lowered into the hall. Axial support rods, similar to those used in the far detector, but outside of the instrumented area, will be used to flatten the planes. The planes will be stabilized by attaching the support rods to one wall of the near detector hall.

The aspect ratio of the 6 m by 6 m steel planes requires handling with special lifting fixtures to prevent permanent deformation. Each plane has an array of tapped holes for attachment of the lifting fixture. These holes will be filled with threaded plugs after installation.

6.6 Online data taking

The expected neutrino event rate in the near detectors will require data storage capacity for about 5 x 10^7 events per year. This is very similar to the event rate expected in the far detector, although the latter sample is composed primarily of the cosmic ray events which will not be recorded by the near detector. This rate is quite low compared to modern collider experiments, and will not create much of a challenge to a conventional online data acquisition system. Due to the rapid development of computer technology, it is not sensible to design the MINOS computing system in detail at this time. General requirements for disk storage, online monitoring, event reconstruction and networking are well within the reach of current technologies.

6.7 Experimental hall requirements

The near detector hall layout is shown in Figure 6.5. The hall dimensions are 18 m by 32 m by 13 m (height). The figure shows the beam monitor calorimeter, the MINOS near detector, and the Soudan 2 near detector. The detailed design of the near detector hall facilities is being closely coordinated with the E–803 experimenters. Careful coordination with E–803 will also be required for use of elevators and floor space during the installation period.

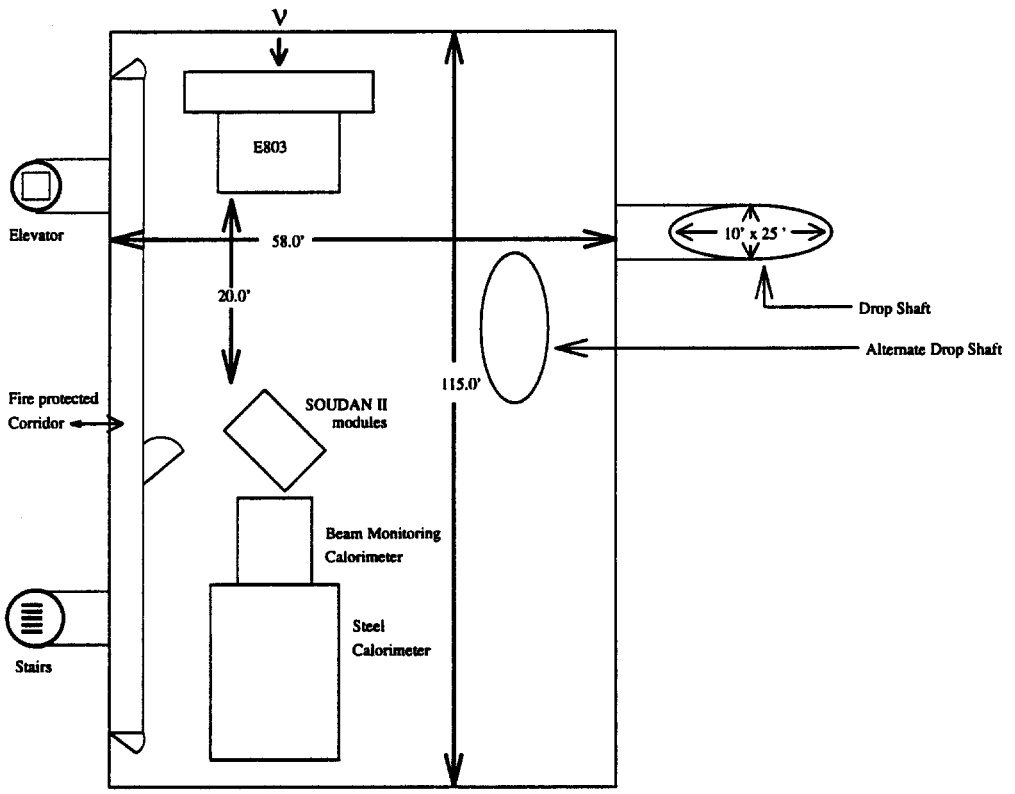

Figure 6.5: Layout of the near detector hall

Chapter 7

Simulation of Detector Response

7.1 Introduction

In this Chapter we describe the results of simulations of the response of the MINOS detectors to neutrino interactions in the energy range defined by our beams. We focus here on the quantitative measurement of kinematic quantities such as the angles and energies of hadronic showers, electrons, and muons. We attempt to understand the detector behavior as a function of shower and particle energies and of the granularity and composition of the passive absorber. The main thrust of the work reported here is on the properties of the reference detector defined in Chapter 5, *i.e.*, a tracking calorimeter with 4 cm thick magnetized steel plates. In parallel with this work we have also initiated, and will intensively pursue in the near future, simulations of other detector configurations. Such studies are essential to our ongoing process of optimizing the detector.

Following this Chapter's descriptions of simulation methods and of the predicted response of the reference detector, Chapter 8 will apply these results to the study of neutrino interactions in the MINOS detector. A thorough understanding of the requirements posed by the neutrino oscillation physics channels, and of how well the different detectors can meet these requirements, is essential to the optimization of our detector design.

This Chapter is organized in the following way. Section 7.2 is a general overview of the Monte Carlo programs used in the simulations. Section 7.3 describes the assumptions we have made about the detector response to the passage of charged particles: measurement accuracy for single space points as well as multi-track resolution. Section 7.4 describes the angular and energy resolutions. Finally, Section 7.5 discusses our ability to separate neutral and charged current ν_μ interactions.

7.2 Software

7.2.1 General comments

The collaboration has at its disposal several Monte Carlo programs. While we expect that a single experiment Monte Carlo will be developed in the relatively near future, for the time being each group in the experiment has used the program with which it is familiar. Programs

based on GEANT, the Soudan 2 Monte Carlo, the E–815 Monte Carlo and the Columbia group Monte Carlo have been used in the analyses reported here.

Similarly, different analysis strategies have been adopted. The ultimate Monte Carlo analysis will involve full tracking through the detector and the passing of a simulation of the detector output data through the experiment's pattern recognition and reconstruction program. However at this early stage of the experiment no fully functional off-line analysis program exists. Two methods have been used to generate the results detailed below:

- Tracking of outgoing particles through the detector has been carried out and hits obtained in simulated detectors. Event cuts based on relatively unsophisticated measurements such as event length can be made and quantities such as hadron energies based on numbers of hits determined. This method works well for tests such as the search for $\tau \rightarrow hadrons + \nu$ and the $\frac{cc}{total}$ test.
- More complicated tests that require, for example, the reconstruction of the μ momentum cannot be done without a full reconstruction program. For these tests we have calculated particle resolutions as detailed below in Section 7.4. Generated events are then smeared by these resolutions and kinematical quantities examined to define selection cuts which can isolate the required events.

7.2.2 Simulation procedures

The formalisms differ in detail between the different Monte Carlo programs used. Here, as an example, we describe the one that is incorporated in the Soudan 2 Monte Carlo [76]. While there are detailed differences in the other programs, no significant differences have been found between analyses using different programs. In the following sections a note of the programs which were used will be made.

The beam is simulated according to the prescriptions given in Chapter 3. At both the near and far detectors a neutrino energy spectrum is input for both the dominant ν_μ and for the background $\bar{\nu}_\mu$, ν_e and $\bar{\nu}_e$. The background events are generated in the predicted ratio of the four species. Tests of the effects of uncertainties in the beam at the far detector were carried out by determining the differences in observable quantities using the input spectra from two beam simulation programs, NUADA [55] and the E–803 PBEAM Monte Carlo [57]. At the near detector, beam spectra for various cuts on beam radius were generated. For the comparison with the far detector a beam radius cut of 25 cm was used as described in Chapter 3.

Neutrino cross sections were calculated using a sum of deep inelastic, elastic, quasi-elastic (QE) and resonance production. Deep inelastic cross sections were calculated using the CTEQ1M structure functions for ν_μ and ν_e interactions [77]. For ν_τ charged current cross sections, where the τ mass is important, the calculations of Albright and Jarlskog [78] were compared with an independent calculation of Phillips [79]. The two calculations were found to be in good agreement. In the measurement of changes in the ratio $\frac{cc}{total}$, uncertainties in the charm cross section near threshold are important. Again two calculations due to Phillips [80] and E–803 [14] were compared and the differences used as an indication of systematic errors. The hadronization process in deep inelastic scattering was parametrized in different fashions in the different programs. The JETSET formulation was used in the GEANT based

simulations and a parametrization based on KNO scaling in the Soudan 2 Monte Carlo. Quasi-elastic cross sections for τ production must include terms proportional to the lepton mass that are normally neglected. We have followed the calculation of Llewellyn-Smith [81]. These terms are also important in resonance production where the resonance cross sections were parametrized according to the model of Rein and Sehgal[82].

Quasi-elastic and resonance production are important at these beam energies, comprising up to about 20% of the total τ cross section. Such events can be easily selected since they typically have little or no hadronic activity (detector hits) at the event vertex. Because the hadron mass is constrained to be small, the event kinematics are well defined with the outgoing lepton taking most of the neutrino energy. This will be shown to be an important constraint that allows selection of τ events, particularly when used in conjunction with the narrow band beam which further constrains the event kinematics.

Our Monte Carlo programs simulate the near and far detectors described in Chapters 5 and 6. A simulated neutral current event with an 18 GeV hadron shower is shown in Figure 7.1. A simulated charged current event with a 10 GeV muon and a 10 GeV hadron shower is shown in Figure 7.2.

7.3 Detector response

We recall the parameters of the detector designs described in Chapters 5 and 6 which are most relevant to the simulation work. First, the thickness of the steel absorbers is 4 cm, corresponding to 2.3 radiation length or 0.24 interaction length for particles perpendicularly incident on the steel plates. (The neutrinos are actually 3° away from horizontal.) Since the edges of the plates will be machined to tolerances of a few millimeters and the plates will be assembled in an overlapping design in each plane, we do not expect any significant gaps or cracks in the absorbers, and none have been simulated at this time. Although not explicitly included in calculations at this time, the occasional gaps (1.5 cm every 1.3 m) between the chambers, resulting from the axial bolts in the detector, as well as the axial bolts themselves, are assumed to be addressed *via* application of fiducial cuts which require that the vertex of an event is more than 3 cm (approximately 0.6 Moliere radius) away from the center of a gap. This results in a 12% reduction in fiducial mass of the detector. Analyses which are particularly sensitive to resolution on EM showers may benefit from a more severe fiducial cut. Cuts requiring vertex positions to be 50 cm away from an edge of the detector and 20 cm from the central hole, result in a fiducial mass which is about 70% of the total mass.

The readout of the streamer tubes has a 2 cm pitch in both the wires and strips, with the direction of the wires alternating plane by plane. A rough pulse amplitude measurement (an approximate resolution of 10% from time-over-threshold) will improve energy resolution for electromagnetic showers where the hits are relatively close together, and will also allow approximately 2 mm transverse position resolution on the strip planes for single particles traversing the detector perpendicular to the plates. The position resolution obtained from the wire readouts will be somewhat worse than that achieved with the strips because wire hits cannot be located within the 2 cm wide 2-tube units. Pulse sharing between neighboring strips will allow strip hit positions to be located somewhat more accurately. The walls between individual streamer tubes result in dead spaces which have not been explic-

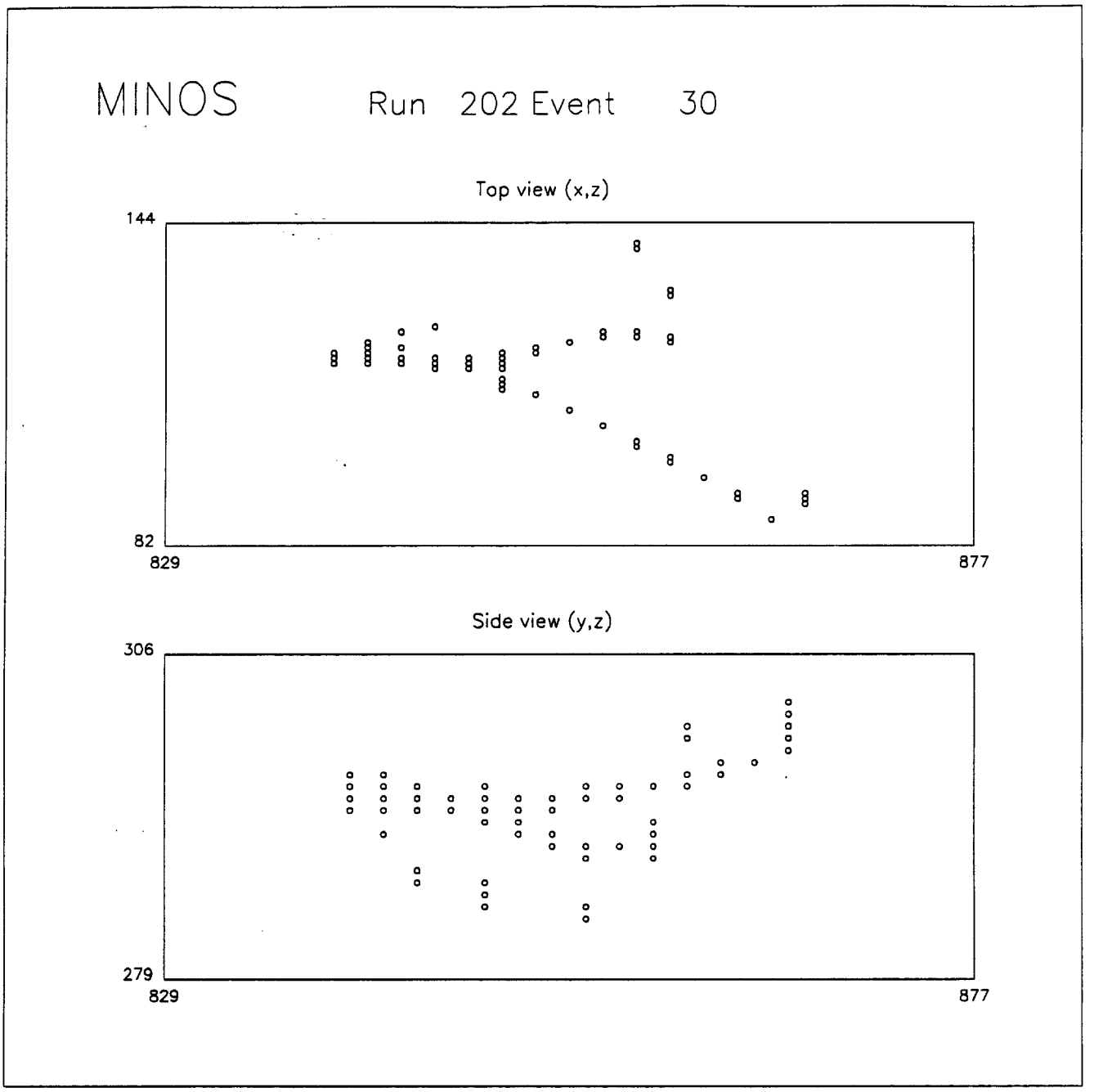

Figure 7.1: Simulated NC event in the MINOS reference detector. The horizontal scale is *detector planes* (6 cm per unit) and the vertical scale is *strip widths* (2 cm per unit). The event is approximately 90 cm long.

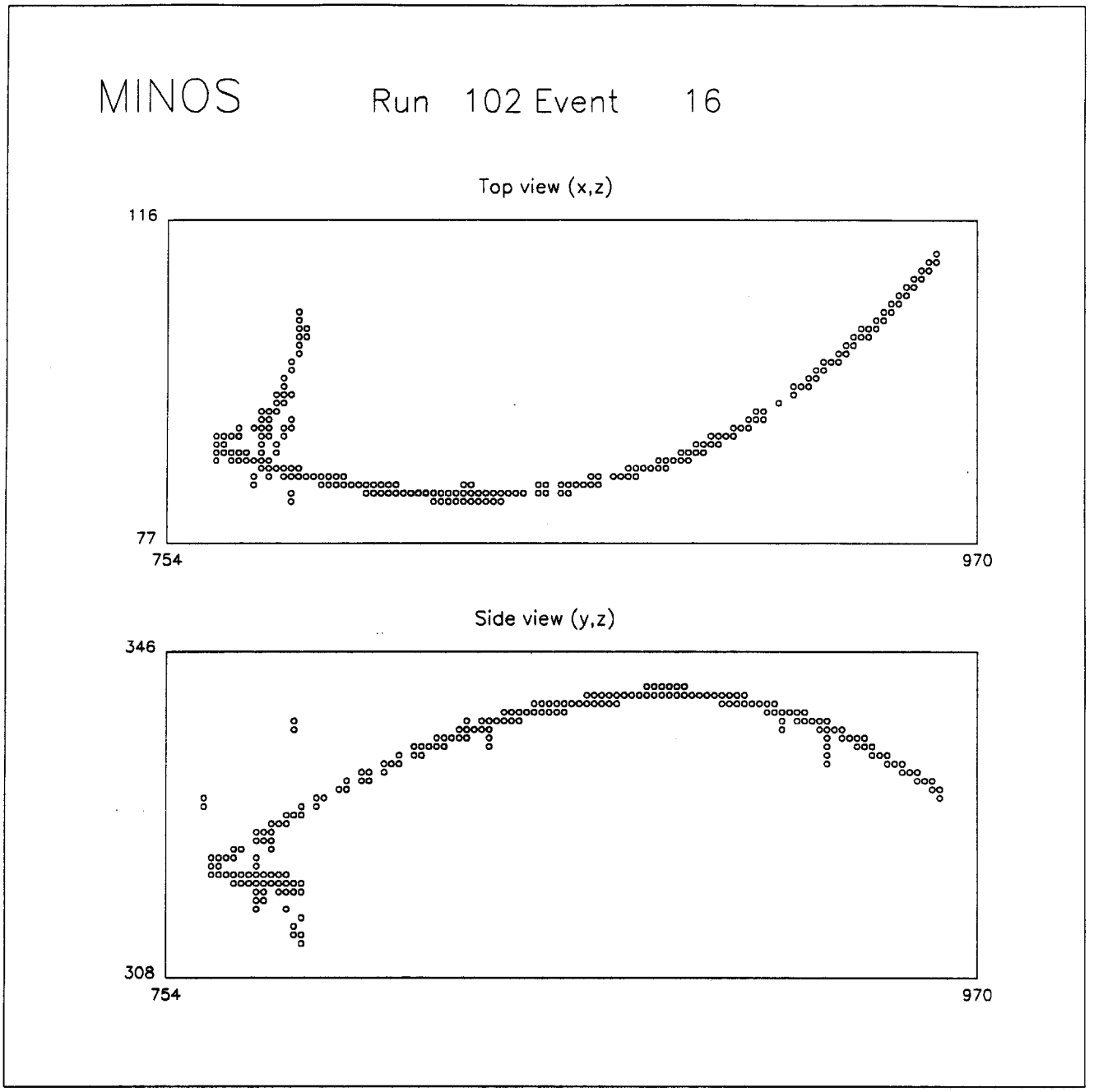

Figure 7.2: Simulated CC event in the MINOS reference detector. Same scales as in Figure 7.1. The event is approximately 12 m long.

itly simulated but for some analyses an average 13% inefficiency has been applied for this effect. Since the walls of the tubes are very thin compared to any relevant transverse shower properties this will not have any serious effect on the resolution. It is expected that the approximations made here will have little impact on the energy or angular resolutions. The resolutions derived from the somewhat idealized simulations presented here for EM showers have been compared to those from the CHARM II calorimeter [83].

Finally, the reference detector has a typical magnetic field of 1.5 T which is assumed in magnetic tracking measurements. We have verified that the magnetic field has no significant effect on shower resolutions.

7.4 Resolutions

7.4.1 Muon angular resolution

The angular resolution for muons is limited by the finite transverse spatial resolution for measuring hits, and by multiple scattering in the iron. The angular resolution from finite transverse resolution, $\delta\theta_{res}$, for a single measurement is given by $\delta\theta_{res} = \frac{\epsilon}{\lambda N}$, where $\delta\theta$ is in radians, ϵ is the transverse resolution, λ is the distance between planes, and N is the number of planes downstream from the interaction vertex used for the measurement. However, the resolution is improved by making multiple measurements at each plane up to the final plane. The final angular resolution (in radians) is:

$$\delta\theta_{res} = \frac{\epsilon}{\lambda \bar{N}}, \bar{N}^2 = N^2 + (N-1)^2 + \ldots + 1. \tag{7.1}$$

The angular resolution from multiple scattering, $\delta\theta_{ms}$, is given by the equation:

$$\delta\theta_{ms} = \frac{13.6 \times 10^{-3}}{\beta c p}\sqrt{\frac{\lambda_{Fe} N}{X_0}}[1 + 0.038 \ln\left(\frac{\lambda_{Fe} N}{X_0}\right)], \tag{7.2}$$

where the momentum p is measured in GeV/c, the radiation length of iron $X_0 = 1.76$ cm, and λ_{Fe} is the thickness of iron in each plane. Since $\delta\theta_{res}$ decreases (independent of momentum) and $\delta\theta_{ms}$ increases (for fixed momentum) with the number of planes, we must optimize the number of planes used for the measurement as a function of momentum. This optimization occurs when the two resolutions contribute equally to the full resolution $\delta\theta = \sqrt{(\delta\theta_{res})^2 + (\delta\theta_{ms})^2}$.

The full resolution using this optimal length is shown in Figure 7.3 as the solid line. We have used a plane thickness $\lambda = 6$ cm, an iron thickness $\lambda_{Fe} = 4$ cm, and a transverse resolution $\epsilon = 2$ mm. The inner plot shows the optimal length, which must be a multiple of the plane thickness, as a function of momentum. If an event has a large number of additional hits from hadrons (other than the muon) it may be necessary to use a track length longer than optimal. We estimate that the worst case would require measurement at the plane 96 cm from the interaction vertex. Because the multiple scattering is already dominant at this point, we expect that a single measurement at the first plane where the muon track is clear will provide the best measurement. The angular resolution using only a single measurement at a fixed length of 96 cm is also shown in Figure 7.3 as a dot-dashed line. For this case,

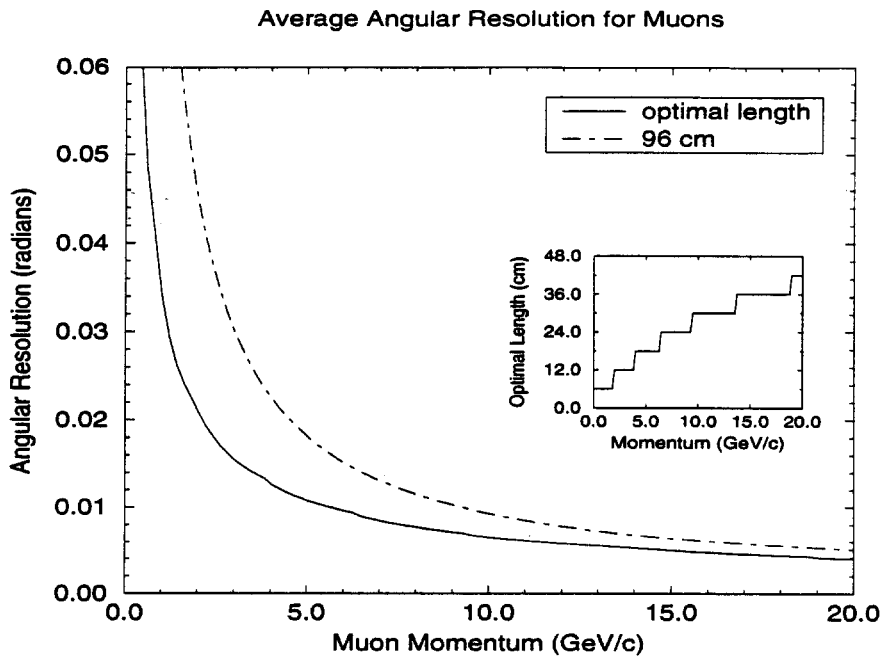

Figure 7.3: Average angular resolution for muons.

$\delta\theta_{ms} \gg \delta\theta_{res}$, confirming that the shortest possible length gives the best measurement. This has little effect for large momenta, but might double the angular resolution for momenta near a few GeV. Since non-Gaussian tails are understood and small for the momentum resolution, as demonstrated in Section 7.4.2, we expect that such effects will be equally small for the angular resolution.

7.4.2 Muon momentum measurement and resolution

Several of the neutrino oscillation signatures in MINOS rely on the measurement of a muon in the final state. In this section, we will discuss the average momentum resolution as well as non-Gaussian tails. A ν_τ appearance signature, such as $\nu_\tau n \rightarrow \tau^- p \rightarrow \mu^- \overline{\nu}_\mu \nu_\tau p$, requires good momentum resolution to distinguish the decay product μ^- from a prompt μ^-. Since decay muons have lower momentum and the oscillation probability decreases rapidly with energy beyond the maximum probability, there is a danger that high energy muons from $\nu_\mu n \rightarrow \mu^- p$ will feed down into the signal region. We expect of the order of 10^4 ν_μ interactions per year with a narrow band neutrino beam. As a result, we need the probability of a momentum measurement beyond a Gaussian distribution to be below about 10^{-4} in order to provide minimal background for oscillation signatures, particularly if $\sin^2(2\theta)$ is small. While previous neutrino beam experiments have used iron planes with toroidal magnetic fields to measure muon momentum, none of them have needed to study non-Gaussian tails in such detail. Therefore, understanding these tails is important to proving the viability of a ν_τ appearance signal with the MINOS detector. In the following sections, we present the muon momentum measurement using range and magnetic bending information separately. We expect that an optimal analysis would take advantage of both measurements simultaneously

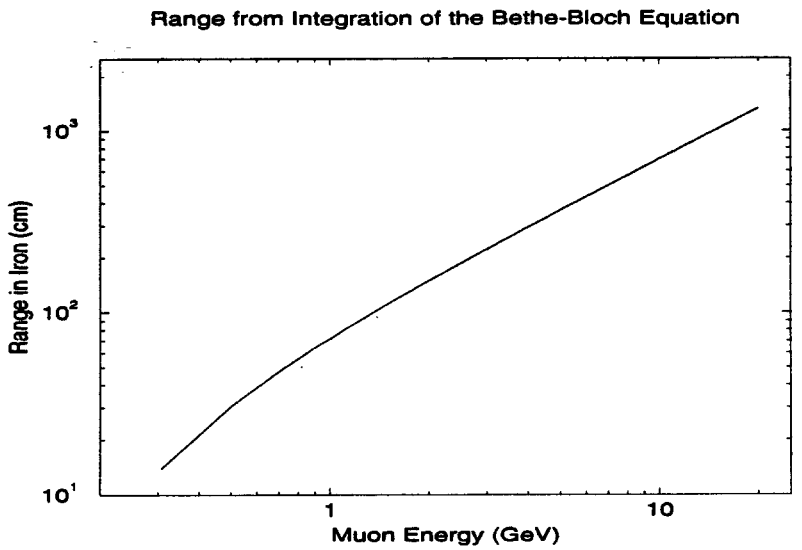

Figure 7.4: Muon range in iron.

in order to give the best possible resolution. An algorithm with sufficient sophistication to do this is beyond the scope of our current simulations.

Average resolution for the range measurement

For muons with an energy of less than a few hundred GeV, the primary mechanism for energy loss is ionization. The energy loss as a function of distance is given by the Bethe-Bloch equation,

$$-\frac{dE}{dx} = K\frac{Z}{A}\frac{1}{\beta^2}\left[\frac{1}{2}\ln\frac{2m_e c^2\beta^2\gamma^2 T_{max}}{I^2} - \beta^2 - \frac{\delta}{2}\right], \tag{7.3}$$

where βc is the muon velocity, $\gamma = \frac{1}{\sqrt{1-\beta^2}}$, $m_e c^2$ is the rest energy of an electron, T_{max} is the maximum kinetic energy transferable to an electron in a single collision, Z, A, I and δ are properties of the stopping material, and K is a conversion constant so that the units of energy loss are GeV g^{-1} cm^{-2}. This equation can be integrated to give the particle range as a function of energy. The range as a function of muon energy for iron is shown in Figure 7.4.

From this figure, we see that muons with energy less than 10 GeV will travel a distance of 10 meters or less. For thick layers of material, $\frac{dE}{dx}\delta x \gg T_{max}$, the fluctuations in the range measurement are Gaussian. This condition is satisfied for all muons in iron with energy greater than 1 GeV. The average energy resolution for a range measurement is determined from a full GEANT level simulation of a simplified detector geometry. A Gaussian fit to the distribution of ranges for muons of fixed energy leads to the resolution curve shown as a

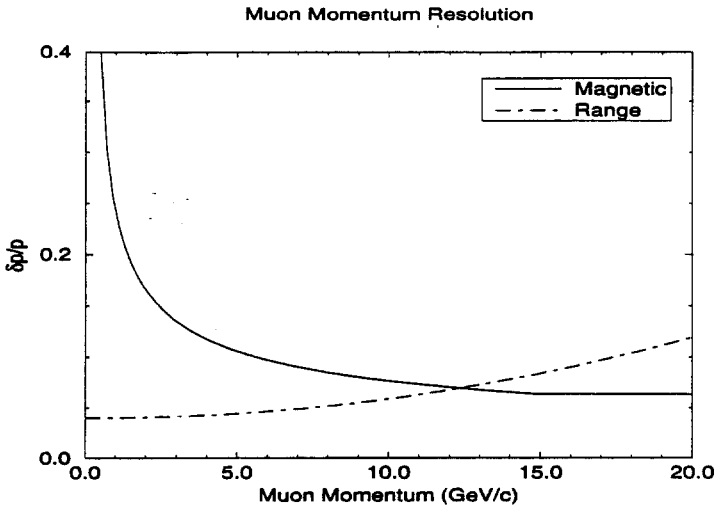

Figure 7.5: Resolution for range and magnetic momentum measurements.

dot-dashed line in Figure 7.5. The curve is extrapolated beyond 10 GeV; muons above this energy are likely to exit the detector.

Non-Gaussian resolution for the range measurement

There are at least three sources of non-Gaussian fluctuations in the energy measurement by range. First, there are fluctuations from ionization in a finite thickness of material. These are unavoidable once the detector geometry is chosen. Second, tails in the range distribution result from muons exiting the detector. These events are rejected by a fiducial volume cut. Third, hard interactions, such as bremsstrahlung or pair production, can cause large energy losses that can significantly shorten the range. To estimate the size of these fluctuations, we again used a full GEANT simulation. A typical resolution distribution exhibits a non-Gaussian tail skewed towards lower range values. In Figure 7.6, we show simulated range measurements for events with a muon energy of 5 GeV. All of the events in the tail have a substantial number of extra hits beyond those associated with a minimum-ionizing particle. Events in which the number of extra hits divided by the number of planes hit is greater than 4 are shown in the unshaded region of Figure 7.6. All events to the left of the arrow are eliminated if a cut on this ratio is applied, leaving only those indicated by the dark histogram. Visual inspection of these events shows that the extra hits are clustered in groups of 3 planes and could be easily removed with a standard pattern recognition algorithm. We have performed the simulation with and without hard interaction processes to verify that they are indeed the source of the tail.

Based on our simulations, the probability of a range mismeasurement outside of a Gaussian distribution is less than 3×10^{-5}.

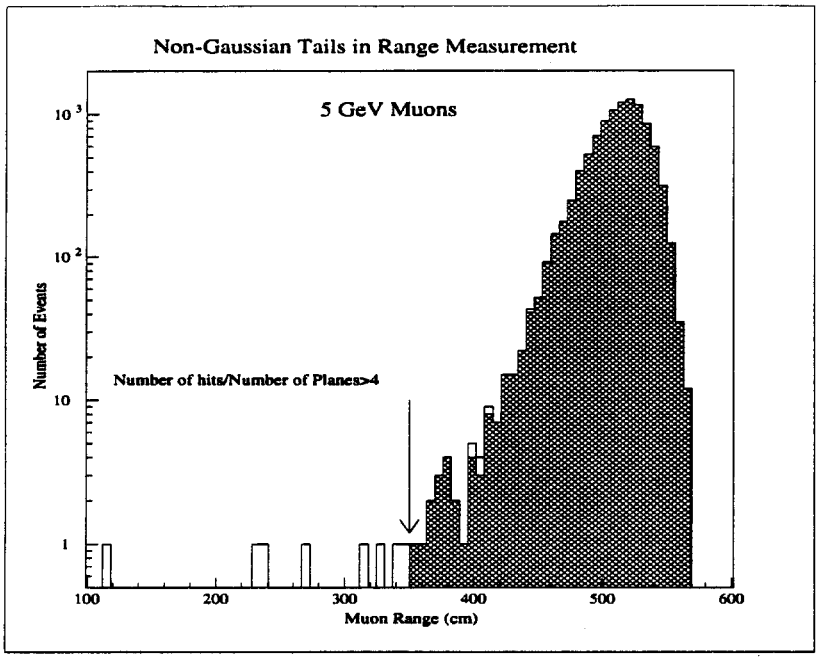

Figure 7.6: Muon range measurement for 5 GeV muons. Events in which the number of hits divided by the number of planes is greater than 4 are shown in the unshaded region.

Magnetic measurement

Muons which exit the detector must be measured by the curvature of their trajectories in the toroidal field. The relation between the magnetic field B, the momentum component perpendicular to the field p, and the curvature k is given by

$$k \equiv \frac{1}{R} = \frac{0.3B}{p}, \tag{7.4}$$

where the radius of curvature R is expressed in meters, B in Tesla, and p in GeV/c. The curvature k is approximately Gaussian for a large number of position measurements. The Gaussian error in the curvature δk has two components, a resolution error δk_{res} for determining the transverse position of a hit, and an error from multiple scattering δk_{ms} in any material the muon transverses. Simple formulae for these errors are

$$\delta k_{res} = \frac{\epsilon}{L^2}\sqrt{\frac{720}{N+4}}, \qquad \delta k_{ms} = \frac{0.016}{Lp\beta}\sqrt{\frac{L}{X_0}}, \tag{7.5}$$

where ϵ is the transverse resolution, L is the track length, N is the number of hits used in the measurement, and X_0 is the radiation length of the scattering material. For iron, $X_0 =$ 1.76 cm. (Note that this is for a fixed muon energy so that a correction factor will need to be applied in further work.) We can use these formulae to calculate an average resolution function for the magnetic measurement of momentum. We take conservative values for the two free parameters, $\epsilon = 2$ mm and L equal to the smaller of the expected range, based on the Bethe-Bloch equation, and 10 m. The resulting function is shown as the solid curve in Figure 7.5. The behavior of this curve is dominated by δk_{ms} for low momenta and δk_{res} for

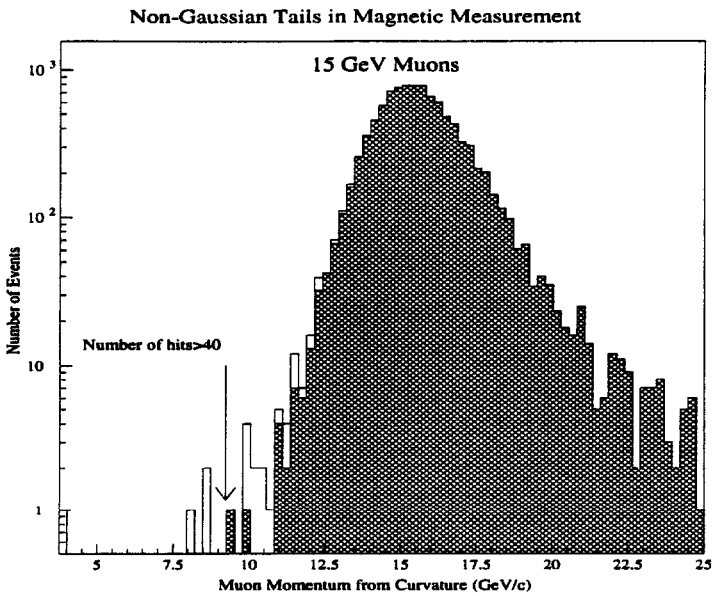

Figure 7.7: Distribution of momentum measurement using a simple tracking algorithm to study the non-Gaussian tails. Events which have more than 40 hits in addition to those associated with the muon track are shown in the non-shaded region.

large momenta. Above 15 GeV/c, where the expected range of the muon is greater than 10 m, the magnetic resolution becomes constant.

Non-Gaussian resolution for the magnetic measurement

We expect similar sources of non-Gaussian resolution for the magnetic measurement of momentum as for the range measurement. Hard interactions, however, can skew the curvature measurement to larger or smaller values than average. We have studied these tails in a similar fashion to those in the range measurement. The momentum distribution for measurements of 15 GeV/c muons is shown in Figure 7.7. This momentum is an average over curvature fits to 10 segments of the total track length, which is approximately 10 m. The algorithm for determining the muon momentum does not incorporate the finite transverse resolution. However, it is still a useful model for studying the tails. The worst low momentum measurements are removed by requiring that the total number of extra hits be less than 40. After this cut, all measurements to the left of the arrow are eliminated, leaving only those in the dark histogram. The remaining low measurements result from large multiple scattering. We are confident that a more detailed track fitting routine will identify kinks and remove those segments of the muon track from the final measurement. We have performed a similar simulation for 5 GeV/c muons, where the range measurement is clearly superior. For this energy, the low momentum tail is the same size as for 15 GeV/c muons, but it cannot be removed with a cut on the number of hits. We estimate the non-Gaussian contribution to the low energy momentum distribution for magnetic measurements to be of the order $4 - 5 \times 10^{-5}$, which is similar to that for range measurements, even for 5 GeV/c muons.

Conclusions on muon momentum

The average resolution is clearly best for a range measurement at low energies. Above about 10 GeV, where we must rely on magnetic measurements, the resolution is roughly constant and equal to the range measurement at 10 GeV. Neither measurement suffers from dangerously large non-Gaussian tails and both will probably improve after more thorough study. The two separate momentum measurements are beneficial not only to improve the total resolution, but also as a consistency check on non-Gaussian tails. In particular, for muons with energy below 10 GeV, it is extremely improbable to have a non-Gaussian fluctuation for both the range and magnetic measurements. Finally, we expect that by making a combined range/magnetic analysis, the overall resolution function will improve beyond that presented here.

7.4.3 Hadron energy

In a gas sampling calorimeter the energy of a hadron shower can be determined by counting the number of particles crossing the gas planes of the calorimeter. In our detector with a 2 cm readout granularity several particles may traverse the gas volume read out by a single strip. The limited streamer tubes and their associated electronics proposed for this experiment will give a pulse proportional in size to the number of particles seen by the strip. Thus by summing the pulse height observed in a plane of tubes a count will be obtained of the number of particles crossing the gap between steel absorber planes. It is assumed in the following simulation, carried out using the Soudan 2 Monte Carlo, that this measurement saturates at 20 particles. To distinguish between counting just hit strips and strips weighted by pulse height, the former will be called hits and the latter crossings. The inefficiency of a plane of tubes, mainly due to tube walls but also including structural effects, was taken to be 13%.

Hadron energy resolutions have been determined by generating neutral current events and counting the numbers of crossings as a function of hadronic energy. It is important to use the actual hadron shower at the hadronic vertex to define the resolution rather than a single incoming hadron since fluctuations in the composition of the shower and its angular divergence will broaden the distributions. Figure 7.8 shows typical crossing distributions for various hadron energies.

For each crossing distribution the mean number of crossings, $< N >$, and the rms, σ, of the distribution are calculated. Figure 7.9 shows the mean number of crossings as a function of energy and a second order fit to the distribution. The quadratic term is different from zero indicating some saturation at the highest energies.

Figure 7.10 shows $\frac{\sigma}{<N>}$ plotted against $\sqrt{E}$ (with E in GeV). A straight line is fitted, giving a resolution function:

$$\frac{\sigma}{< N >} = 0.03 + \frac{0.76}{\sqrt{E}} \tag{7.6}$$

Simulations of other thicknesses of steel and with concrete instead of steel for the absorber indicate that the resolution is not a strong function of steel thickness or absorber material. This is because the major contribution to the spread in the number of crossings is the intrinsic fluctuations in the hadron shower rather than the sampling frequency. At finer

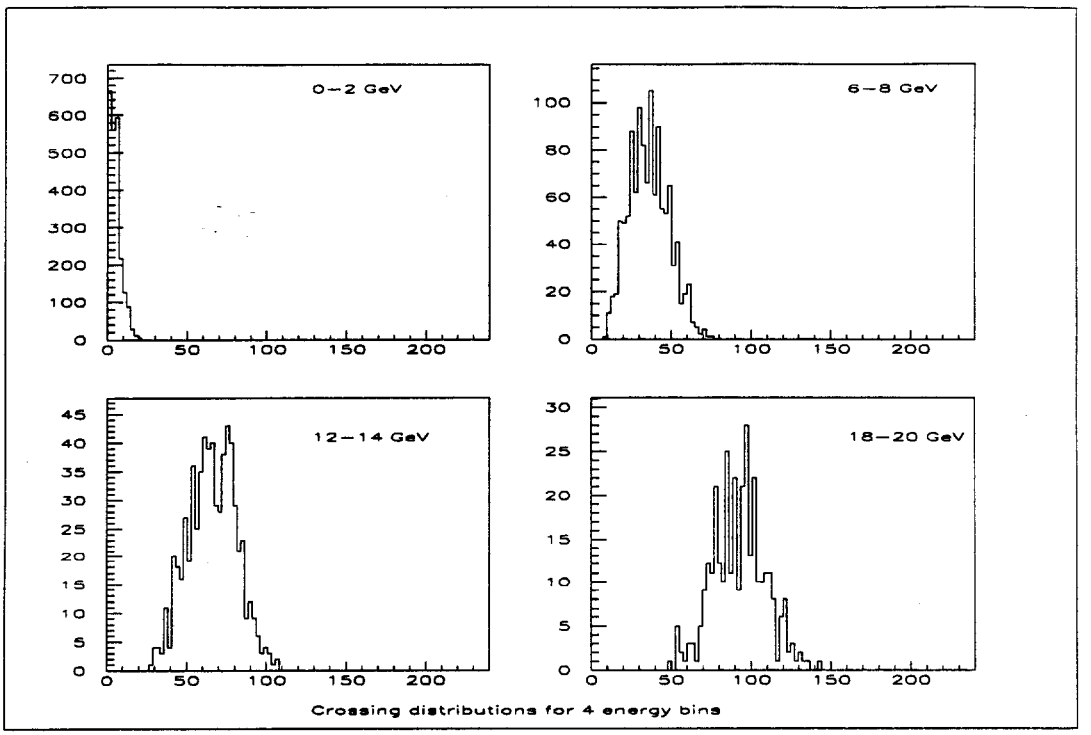

Figure 7.8: Histograms of the number of crossings for the four hadron energy ranges shown.

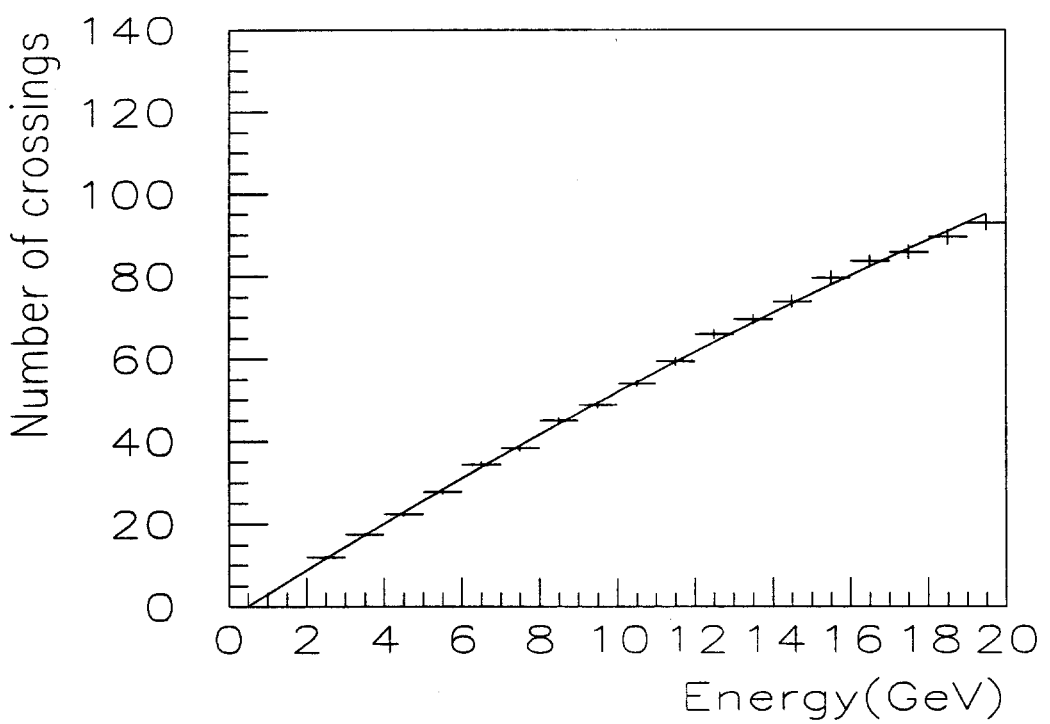

Figure 7.9: Number of crossings as a function of hadron energy. The curve is a quadratic fit to the points.

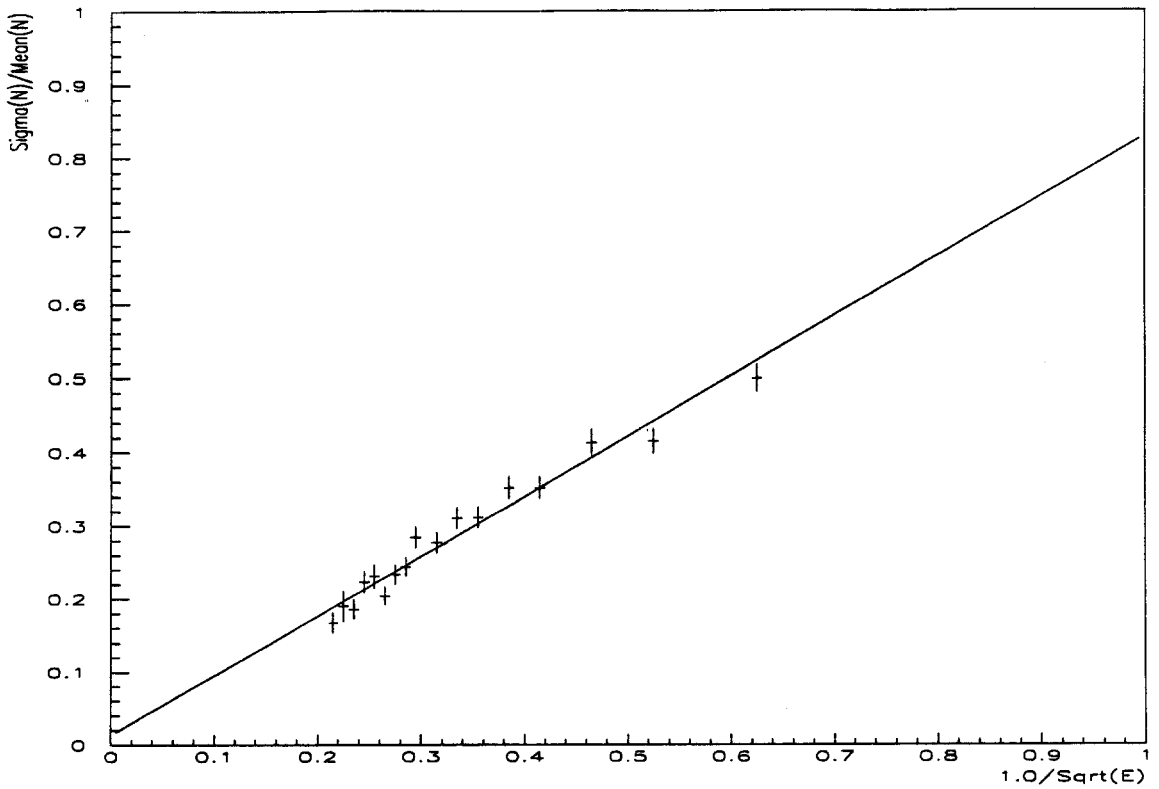

Figure 7.10: Hadronic energy resolution as a function of hadronic energy.

sampling, for example 2 cm steel, the peaks in the number of gas crossings become narrower but the tails at large numbers of crossings become longer. The distributions are no longer well represented by Gaussian peaks. This is probably due to the different response of the detector to showers which are predominantly hadronic or predominantly electromagnetic. Counting only hit strips rather than summing the pulse height in each strip reduces the tails. However since some of the tests described below are sensitive to tails of distributions, more work is required to quantify any benefits from finer sampling in this measurement.

7.4.4 Hadron angle

We have estimated the ability of a large detector to determine the direction of hadronic showers. Using the Soudan 2 Monte Carlo, we generated ν neutral current interactions in the reference detector with hadronic systems of energies 2, 5, 10, and 20 GeV. The wide band beam spectrum was used so that the hadron showers in question have the correct angular and invariant mass distributions. Each event was required to have at least one hit in each readout view. For 2 GeV showers, 6.5% of the events failed to meet this constraint. All showers at higher energies had at least one hit in each readout view. No hardware trigger requirement was imposed for this study. The centroid of the shower is formed by summing over the positions of the hits in the event. A vector is then drawn from the event vertex, which we assume is known perfectly, to the shower center. This vector is taken to be the reconstructed shower direction. The angle between the reconstructed shower direction and

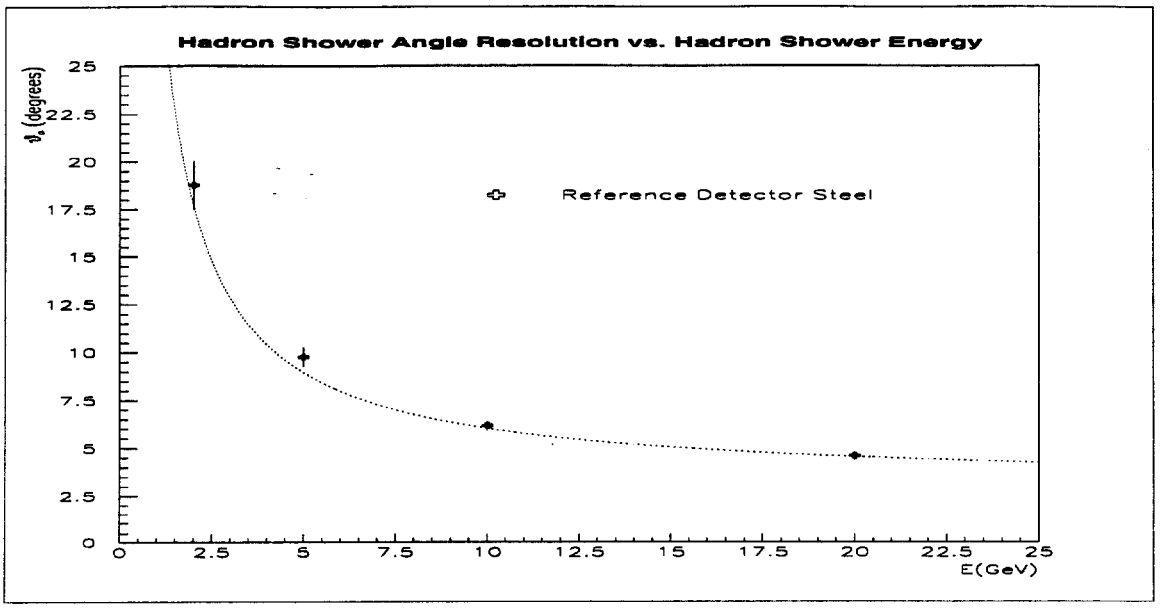

Figure 7.11: Hadron shower angular resolution.

the true shower direction is then calculated. At each energy, the resulting distribution in θ_{space}, the space angle between the true and reconstructed directions, is plotted and fit to a two parameter function of the form:

$$N(\theta) = \frac{N}{2\pi\theta_0^2} exp\left(\frac{\theta_{space}^2}{-2\theta_0^2}\right) d\Omega. \tag{7.7}$$

The hadron shower angular resolutions calculated in this way are shown in Figure 7.11. The resolutions can be well parametrized over this energy range by

$$\theta_0 = \frac{16.67}{\sqrt{E}} + \frac{12.15}{E} \tag{7.8}$$

with θ in degrees and E in GeV.

The detector simulation was also done with different assumptions about the detector readout. Equation 7.8 assumes x and y readout for each detector plane. A simulation was also done where we assume only 1-D readout, alternating between x and y in each plane. The degradation in angular resolution coming from only having one electronics view per detector plane is approximately 10% at all energies. The main disadvantage of having only 1-D readout is a loss of events at low hadronic energy; with 1-D readout 31.5% of the 2 GeV events were rejected because they failed to have at least one hit in each readout view.

Simulation of a finer grained detector (with 5 cm concrete absorber plates) has also been carried out. The expression for θ_0 obtained is

$$\theta_0 = \frac{8.87}{\sqrt{E}} + \frac{25.60}{E} \tag{7.9}$$

with θ in degrees and E in GeV.

Although the coefficients of the expression are different, the calculated values of θ_0 in the range of interest are not very much improved. 1-D readout is less of a problem in that only 15% of the events were rejected as having no hits in at least one readout view.

7.4.5 Electron energy

We have calculated the energy resolution and the angular resolution for electrons in a GEANT-based detector simulation. We studied three calorimeter configurations: an 8 kT iron calorimeter with 2 cm iron plates; an 8 kT iron calorimeter with 4 cm iron plates; and a composite concrete/iron calorimeter with 3.5 kT of concrete in 5 cm plates and 8 kT of iron in 4 cm plates.

For these studies we generated events from quasi-elastic ν_τ interactions ($3.5\ GeV < E_\nu < 40\ GeV$), selecting the electron τ decay channel. We used the Caltech neutrino generator with $\Delta m^2 = 0.008\ eV^2$ and $\sin^2(2\theta) = 0.87$. The electrons were started randomly in the iron in the first two detector configurations and randomly in the concrete in the composite detector.

For each shower, we counted the total number of crossings, N, recorded in the detector. In this study we assumed that pulse height information was available so that we could count every crossing. We used the known energy of the electrons to derive the linear energy reconstruction relation

$$E = E(N) = aN \tag{7.10}$$

Showers in which the number of crossings deviated by more than 3 σ from the line were excluded and the energy reconstruction relation was refit. In Figure 7.12 we show this relation for the 4 cm iron calorimeter.

The energy resolution was determined from the distribution of the difference between the known electron energy and the computed electron energy, $E_0 - E(N)$, for narrow ranges of N. A Gaussian function was fitted to these distributions and σ was taken as a measure of the energy resolution, $\delta(E)$. In Figure 7.13 we show a fit to 10,000 5 GeV electron showers in 4 cm iron. The simplicity of our current detector simulations for electromagnetic showers leads to an optimistic energy resolution. In order to quantify this, we have compared a calculation using our GEANT-based Monte-Carlo of a low Z concrete detector to the results from the similar CHARM II detector [83]. This comparison suggests that a scale factor of 1.4 should be applied to the resolution for EM showers from the Monte Carlo. The results including this factor are shown in Figure 7.14, where we plot $\frac{\delta(E)}{E}$ as a function of energy for the three detector configurations. The three data sets were fitted to the functional form

$$\frac{\delta(E)}{E} = \frac{a}{\sqrt{E}} + b \tag{7.11}$$

where E is measured in GeV. The parameter b was consistently found to be small. The results of these fits for parameter a are given in Table 7.1.

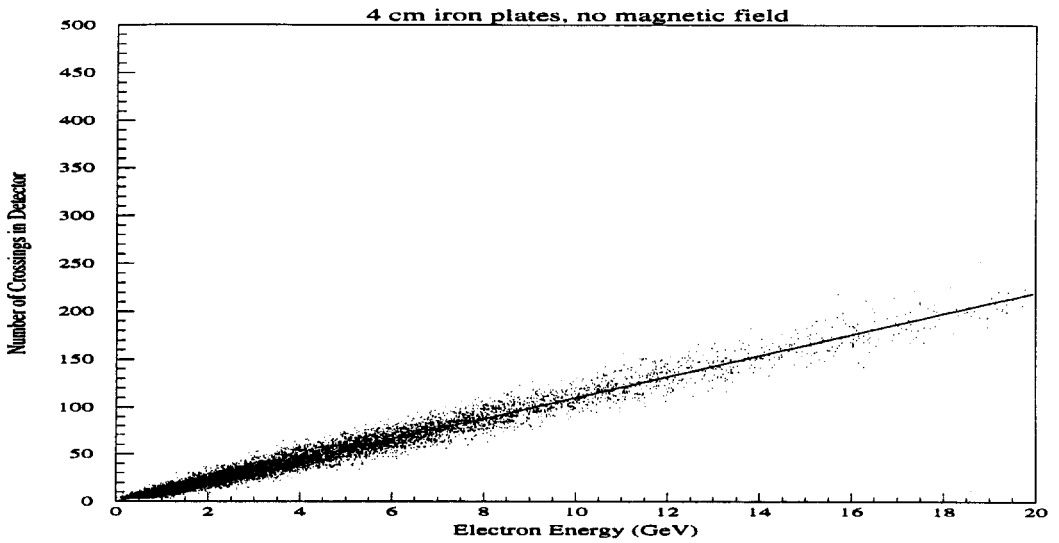

Figure 7.12: Number of crossings as a function of energy.

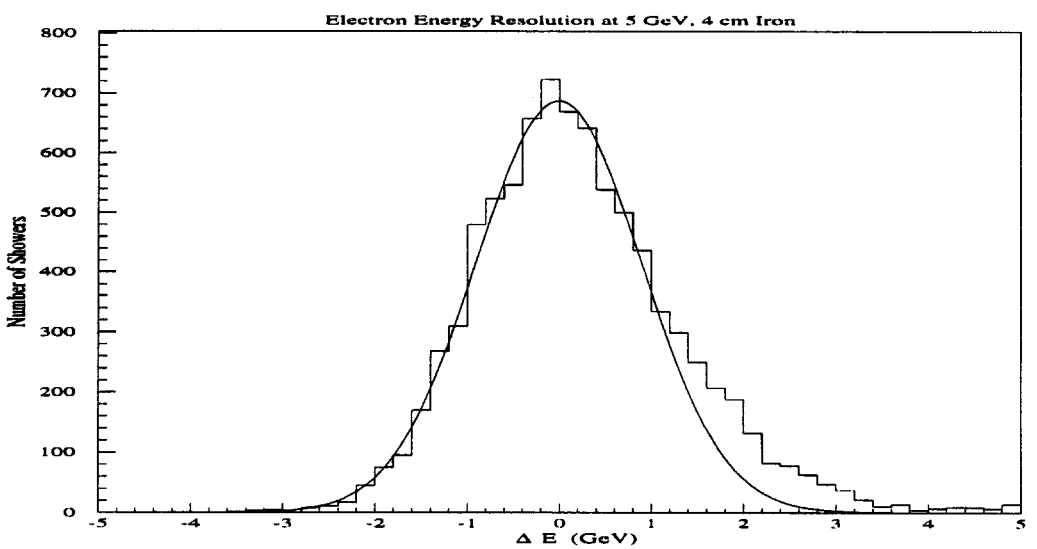

Figure 7.13: Difference of fitted - calculated energy.

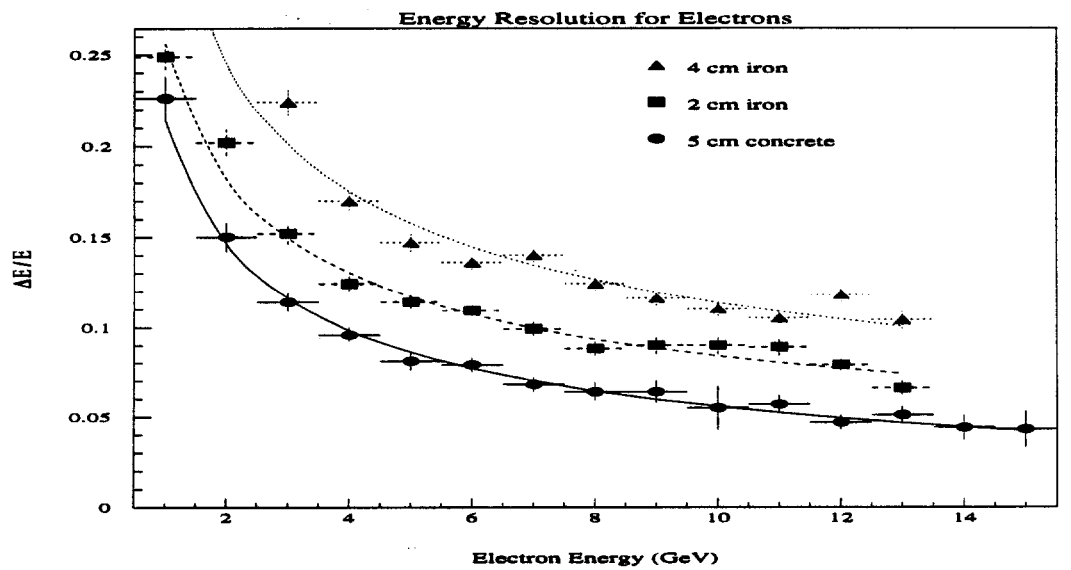

Figure 7.14: $\frac{\delta(E)}{E}$ as a function of energy.

Material	a (%)	c (mrad)
4 cm iron	33.7	30.2
2 cm iron	25.2	27.9
5 cm concrete	23.2	19.1

Table 7.1: Values of the constants a and c in Equations 7.11 and 7.13 for three detector granularities.

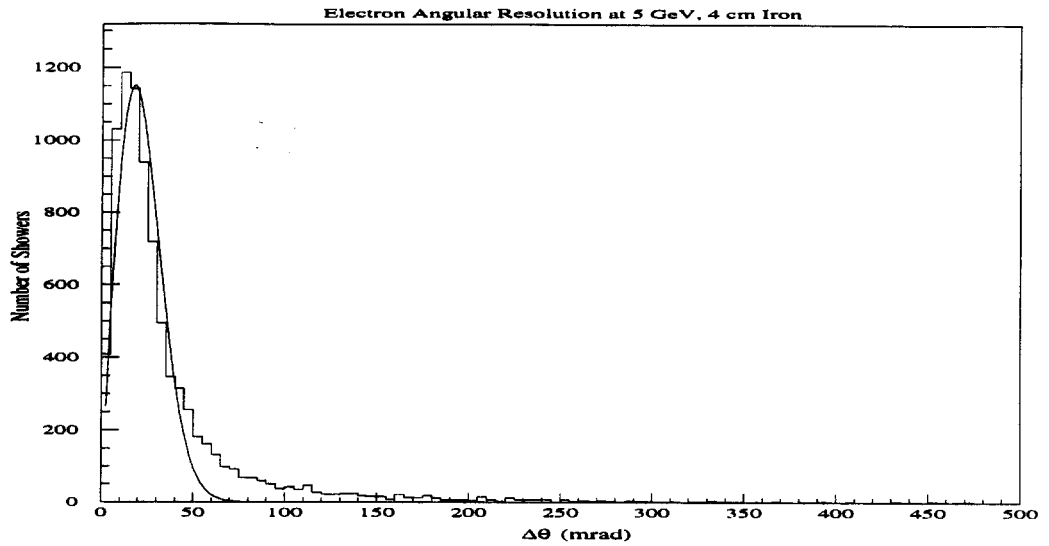

Figure 7.15: Angle between the generated and fitted electron direction.

7.4.6 Shower axis reconstruction and angular resolution

For each shower we fitted the crossing positions to a three dimensional straight line. The space angle θ of this line with respect to the known electron momentum vector was computed for narrow ranges of known electron energy. These distributions were fitted to a function of the form

$$\frac{\sin(\theta)}{\delta(\theta)^2} \exp\left(-\frac{\theta^2}{2\delta(\theta)^2}\right) \tag{7.12}$$

where $\delta(\theta)$ is a measure of the angular resolution. This is simply a Gaussian resolution folded with a solid angle effect for small scattering angles. In Figure 7.15 we show this distribution for 10,000 5 GeV electron showers in 4 cm iron. Significant non-Gaussian tails are visible compared to the best Gaussian fit function.

In Figure 7.16 we show these angular resolutions as a function of energy. Again these resolutions were normalized to the results of the CHARM II detector. The three data sets were fitted to the functional form

$$\delta(\theta) = \frac{c}{\sqrt{E}} + d \tag{7.13}$$

where E is measured in GeV. The results of these fits are given in Table 7.1. Again the value of the constant term, d, was found to be small.

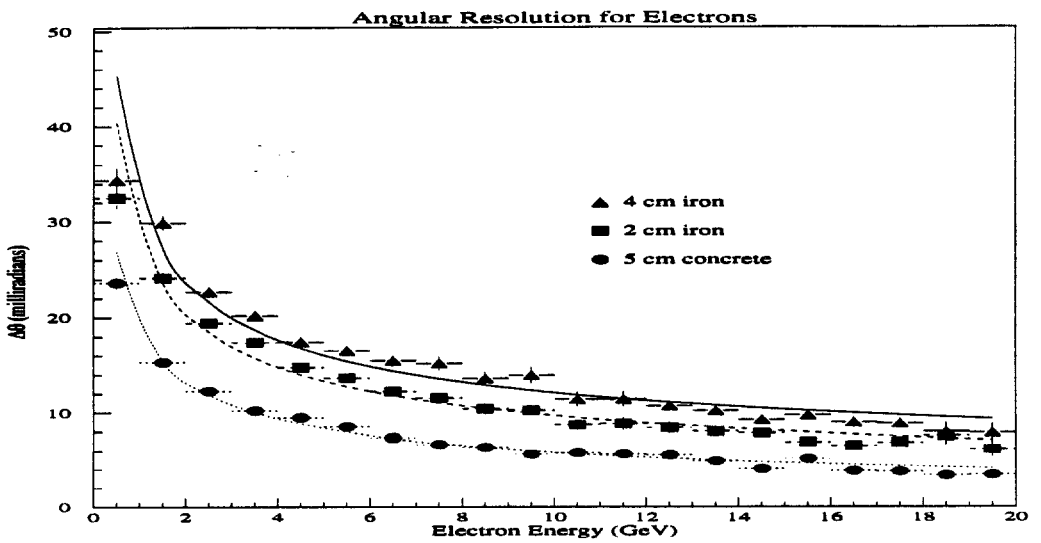

Figure 7.16: Energy dependence of angular resolutions for electrons.

7.5 NC/CC separation

The separation of charged and neutral current ν_μ events is based on the penetration of the muon and the fact that the flow of the event energy is perpendicular to the absorber plates. We define an event length (L) which is the number of absorber plates between the first and last hits associated with an event. We will show in this Section that an event length cut of 20 plates gives a good separation between neutral current (NC) and charged current (CC) events. To obtain a clean separation it is necessary to define a fiducial volume such that all CC events have a potential length to the edge of the detector of greater than 20 planes. An event vertex is defined as the mean coordinates of the hits in the first detector plane crossed by the event. The fiducial volume is defined as having this vertex more than 50 cm from the outside of the detector, more than 10 plates from the front of the detector, and 30 plates from the rear. A trigger of 3 hit planes out of any 5 consecutive planes was also required. An overall acceptance of 69% was obtained. The muon energy distribution of CC events within the fiducial volume and with $L < 20$ only contains low energy muons with insufficient range to pass the cut. The loss of high energy muons is negligible.

Figure 7.17 shows the event length distributions of neutral current and charged current events within the fiducial volume. We find that 6.2% of charged current events have muons with range less than 20 plates and 7.4% of neutral current events have lengths longer than the cut.

This separation is, of course, relatively crude. It may be possible to pattern recognize a fraction of the muons which produce long noninteracting tracks within the cut, thus reducing both the loss and the contamination.

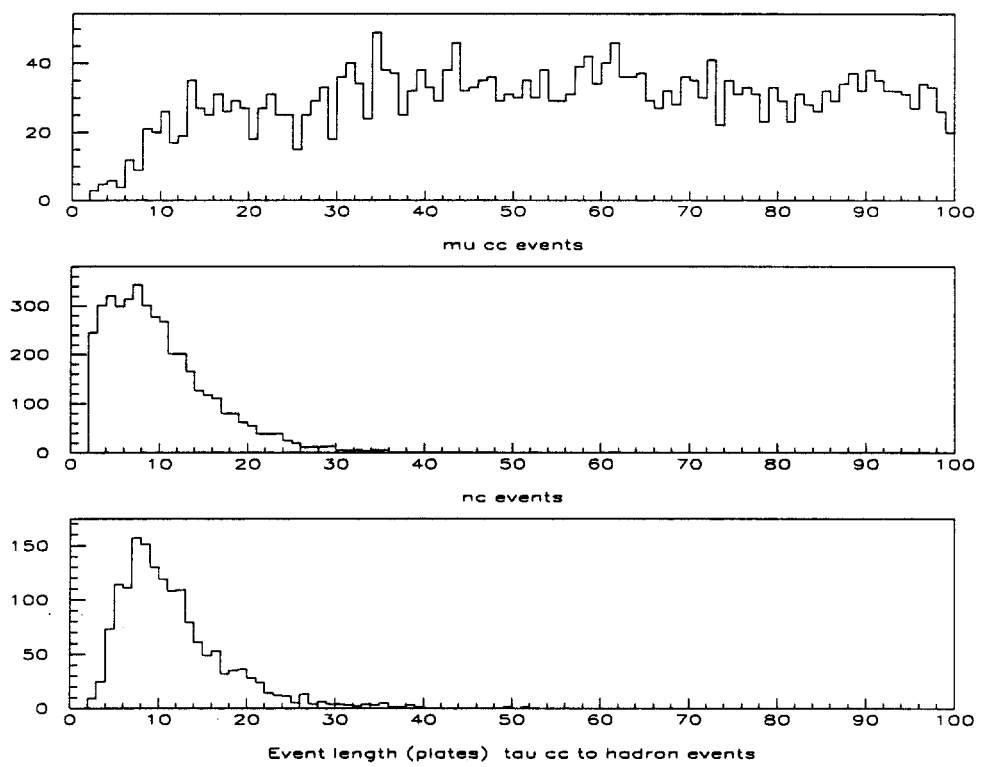

Figure 7.17: Event length (number of iron plates crossed) distributions for ν_μ CC events (top), ν_μ NC events (middle) and ν_τ cc events with the decay $\tau \rightarrow hadrons + \nu$ (bottom).

Chapter 8

Physics Signatures

8.1 Introduction

This Chapter describes the physics simulations of the MINOS detector's response to potential ν_μ oscillations. The results of this Chapter are the engine that drives the design of the detector. The input to the calculations are the detector response characteristics described in Chapter 7, the expected properties of both the WBB and the NBB described in Chapter 3, and the physics of neutrino interactions.

The Monte Carlo simulations described in this chapter demonstrate our ability to detect neutrino oscillations into both ν_τ and ν_e. We show that we can observe τ appearance signals in a variety of channels, by analyzing distributions of kinematical variables as well as by statistical tests.

We shall take the reference detector described in Chapter 5 as the basis of the simulations described here. Other possible options for the final detector will be discussed in Chapter 10. Simulation is in progress on these alternative detector configurations, particularly those with finer granularity. This work may in the future lead to improved sensitivity of our experiment to channels such as $\nu_\mu \rightarrow \nu_\tau$ with the decay $\tau \rightarrow e\nu\nu$.

Several of our tests for τ appearance involve the ability to distinguish between the range of kinematic variables for leptons arising from τ decays and those produced in the background ν_μ or ν_e charged current interactions. For example, if a ν_τ produces a μ through the decay $\tau \rightarrow \mu\nu\nu$, the energy of the τ is shared among the three decay leptons. The μ has, in general, a lower energy than a μ produced by an incident ν_μ of similar energy to the ν_τ. However in the wide-band beam such a low energy μ could also be produced by a lower energy ν_μ, giving a substantial background to the signal. In our narrow-band beam experiment this background is removed, thus much improving the power of these tests. Simulation of data in both the narrow- and wide-band beams will be described. Numbers of events are calculated for two years running in each beam.

This Chapter has the following layout. The first three sections discuss the general statistical tests that can provide the best $\sin^2(2\theta)$ limits on oscillations, and which have only a mild dependence on whether the oscillations occur into ν_e or ν_τ. Section 8.2 describes the comparison of the ratio CC/total between the near and far detector, probably the test with the best $\sin^2(2\theta)$ limit. In Section 8.3 we demonstrate how the oscillations can be directly

observed in the charged current total energy distribution. Section 8.4 discusses the "disappearance" experiment, the ratio of the rates of the CC events at the far and near detectors. Potentially, this is the test with the lowest statistical errors but which may be dominated by systematic errors at the level of a few percent.

We subsequently turn to the identification of specific τ production and decay channels. Section 8.5 describes tests performed in the WBB, and Section 8.6 those done in the NBB. Then in Section 8.7 we focus on our sensitivity to $\nu_\mu \rightarrow \nu_e$ oscillations. In Section 8.8 we comment on the information that can be provided by the neutrino-produced μ's emerging from the rock upstream of the detector. Section 8.9 summarizes the capabilities of the fine grained Soudan 2 detector to observe neutrino oscillations. The general assessment of our capabilities and summary of the results of this Chapter is provided in the concluding Section 8.10.

8.2 Measurement of CC/total

8.2.1 Formalism

The P–822 collaboration previously developed a formalism for the analysis of an experiment measuring the change in the fraction of apparent neutral current and charged current events between a near detector and a far detector using Soudan 2 as the target [76]. The analysis of the MINOS experiment has the following differences:

1. The planar detector makes the differentiation of charged and neutral currents (as described in Section 7.5) simpler than in Soudan 2, with consequently less systematic error.

2. The extra available mass enables us to choose a restricted fiducial volume in the far detector. This dramatically reduces the number of events which were defined in Soudan 2 as "out of acceptance" since the muon did not have sufficient potential length for the event to be distinguished from a neutral current event.

3. The neutral current trigger loss, which was negligible in Soudan 2, becomes an important potential source of systematic error in our much coarser detector.

The analysis is carried out in terms of the ratio of charged current events to the total number of events, $\frac{cc}{total}$, integrated over the neutrino energy spectrum. The *physical* value of this ratio is defined as T in the far detector and t in the near detector (far detector quantities are in upper case characters and near detector in lower case). Any difference between the two is either due to oscillations or to differences in the beam at the two detectors.

In Reference [76] we calculated a formula for P_e, the oscillation probability of $\nu_\mu \rightarrow \nu_e$ in terms of the *measured* $\frac{cc}{total}$ ratio in the far detector (T'') and near detector (t''), assuming full trigger acceptance and that in the absence of oscillations T = t, *i.e* that the beam is identical at the two locations. The measured quantities obviously differ from the physical quantities because of event misidentification and losses.

We repeat this formula here.

$$(1 - P_e) = \frac{(T'' - F_{nc})(f_{cc} - f_{nc})}{(t'' - f_{nc})(F_{cc} - F_{nc})} \tag{8.1}$$

where, in the far detector
F_{cc} is the fraction of Monte Carlo events having a muon and selected as a muon event as defined in Section 7.5
F_{nc} is the fraction of Monte Carlo non-muon events selected as muon events
F_{cn} is the fraction of Monte Carlo muon events selected as non-muon events
F_{nn} is the fraction of Monte Carlo non-muon events selected as non-muon events
and the variables in lower case (f_{cc}, *etc.*) are the same quantities for the near detector.

It can be seen that P_e turns out to be simply the ratio of the measured values of T'', t'', divided by the ratio of the acceptances for CC muons near and far, all quantities being corrected for the misidentification of NC events.

If instead of $\nu_\mu \rightarrow \nu_e$ oscillations we consider $\nu_\mu \rightarrow \nu_\tau$ then we can carry out the same analysis except that we have to correct for the fact that the integrated ν_τ cc cross section is lower than the ν_μ CC cross section at these low energies by a factor η (0.31) and that a fraction B (0.18) of τ's decay into μ's. Both of these effects reduce the size of changes in T'' produced by $\nu_\mu \rightarrow \nu_\tau$ oscillations compared with $\nu_\mu \rightarrow \nu_e$ oscillations. We then obtain

$$P_\tau = \frac{(t'' - f_{nc})(F_{cc} - F_{nc}) - (T'' - F_{nc})(f_{cc} - f_{nc})}{(t'' - f_{nc})((1 - B\eta)(F_{cc} - F_{nc}) - (T'' - F_{nc})(1 - \eta))} \tag{8.2}$$

It can be seen that the effect is to replace the factor $(F_{cc} - F_{nc})$ in Equation 8.1 by

$$(1 - B\eta)(F_{cc} - F_{nc}) - (T'' - F_{nc})(1 - \eta)$$

Using the values obtained below the ratio of these factors is 1:2.25 and this quantifies the difference in sensitivity between $\nu_\mu \rightarrow \nu_e$ and $\nu_\mu \rightarrow \nu_\tau$.

Using the above formulae we can calculate the statistical and systematic errors that we anticipate in our experiment. We emphasize that by performing a two station experiment we are, in general, only sensitive to changes between the two detectors. We do not have to determine the ***physical*** value of $\frac{cc}{total}$ though it will clearly be a useful check of our analysis that we find consistency in the near detector with both previously measured quantities and the value found by E-803.

In order to calculate the systematic errors on P_e and P_τ we relax our assumption that in the absence of oscillations $T = t$. That is, we investigate how much spurious oscillation probability can be introduced by differences in the beam between the near and far detectors. Defining the change in the ***physical*** ratio in the absence of oscillations as $dT = T - t$, Reference [76] showed that

$$dP_e = -\frac{(f_{cc} - f_{nc})}{(t'' - f_{nc})} dT \tag{8.3}$$

Again substituting the numbers listed below we find

$$dP_e = -1.25dT \tag{8.4}$$

The equation for dP_τ has the same correction factor as Equation 8.2 and therefore

$$dP_\tau = 2.25dP_e \tag{8.5}$$
$$= -3.8dT \tag{8.6}$$

The following sources of differences between T and t are considered below in Section 8.2.3:

- Changes in the neutrino energy spectrum between the near and far detectors.
- Uncertainty in the charm cross section folded with the beam differences between the two detectors.
- Changes in the ν_e contamination between the near and far detector.

Other sources of error whose contribution to the systematic error on P_e and P_τ can be calculated from the above formulae and which are also further considered in Section 8.2.3 are:

- Differences in backgrounds at the near and far detector.
- Errors in the calculation of the acceptance factors F_{cc} etc.

8.2.2 Statistical errors

We assume that the statistical errors in the near detector are negligible compared with all other errors and do not consider them further. Based on the standard running assumptions (10 kT, 2 years of $3.7 \times 10^{20} protons/year$,) we expect 40,000 neutrino triggers (NC+CC) from an unoscillated beam in the far detector. We use a fiducial volume 50 cm in from the outside edges of the detector, and more than 20 planes from the back of the detector, and 20 cm from the hole in the magnet. This corresponds to a fiducial mass which is 75% of the total mass, or 7.5 kT. The combined acceptance and trigger efficiency in the 10 kT is 69%.

From the simulation for the far detector, we find that $F_{cc} = 0.938$, $F_{nc} = 0.074$, $F_{nn} = 0.926$, and $F_{cn} = 0.062$. This leads to an expectation $T'' = 0.766$, before corrections due to ν_e and charm are included. The effect on the ratio of various $\nu_\mu \rightarrow \nu_\tau$ oscillation assumptions is shown in Table 8.1 where the ratio includes corrections due to charm, ν_e background and misidentification.

The statistical error (dT'') on T'' is given by the binomial form

$$dT'' = \sqrt{T''(1-T'')/N''} \tag{8.7}$$

which gives dT''=0.00203 for the 2 year run. The comparison of systematic and statistical errors is summarized later in Table 8.3.

$< P_\tau >$	$T'' \pm dT_{stat}$	$n_\sigma^{stat+syst}$
$< P_\tau > = 0$	$29015/40200 = 0.7218 \pm 0.0022$	0
$< P_\tau > = 0.1$	$26352/37956 = 0.6943 \pm 0.0023$	7.5
$< P_\tau > = 0.2$	$23688/35713 = 0.6633 \pm 0.0023$	15.8
$< P_\tau > = 0.345$	$19826/32460 = 0.6108 \pm 0.0024$	29.6

Table 8.1: Expected event ratios with and without $\nu_\mu \rightarrow \nu_\tau$ oscillations. Effects due to charm, ν_e background and misidentification are included. Errors in the second column are statistical. The number of sigma combining statistical and systematic errors in quadrature is in the last column.

8.2.3 Systematic errors

The systematic errors involved in comparison of the ratio $\frac{cc}{total}$ in the near and far detector and the contributions of these systematic errors to a limit on $\sin^2(2\theta)$ were discussed in detail in the Update to the P–822 Proposal [76]. There were two broad categories of systematic error:

1. Errors due to event losses and misidentification
2. Errors due to uncertainties in the beam and neutrino cross sections.

We consider both kinds of errors in the following:

Reconstruction errors

The neutral current/charged current separation algorithm defined in Section 7.5 is very simple, much simpler than the reconstruction algorithm which is necessary in the Soudan 2 detector. Also, the near and far reference detectors are functionally identical within their fiducial volumes for the algorithm we are using. Thus differences due to reconstruction failures, which was a major systematic error in P–822, will not be a significant source of systematic error in the MINOS detector.

Beam differences, near/far

The errors associated with the beam uncertainties will be very similar to those discussed in Reference [76]. Comparison of measurements in the near and far detector would be compromised if the energy spectrum of the beam were significantly different in the near and far detectors. While the radial variation of the average beam energy is substantial at the near detector, the beam simulations described in Chapter 3 show that the central 25 cm of the near detector has a very similar beam spectrum to that in the far detector [63, 64]. For a parallel beam, this can be understood from the kinematics of pion decay. The size of the central spot which has a flat energy distribution can be derived from pion decay kinematics, the beam energy, and geometry. The divergence of the beam within the decay pipe causes some differences which are accounted for by the beam simulations. We take the

difference between the near and far energy spectrum (shown schematically in Figure 3.11) as a conservative estimate for our uncertainty in the beam energy spectrum. This leads to several uncertainties in T based on our uncertain knowledge of the beam, as discussed below.

CC misidentification

The identification of charged current events is based on the length of the longest track in the event. The fraction of true CC events which fail this cut is 6.2%. The average neutrino energy for charged current events in the far detector is 18.94 GeV, as opposed to 18.22 GeV in the near detector. We take this difference as the uncertainty in the average beam energy, which leads to a systematic error $dN_{CC}/N_{CC} = 0.0025$ or dT = 0.0018.

Electron neutrinos

For an 800 m decay pipe, ν_e and $\bar{\nu}_e$ in the beam come from K_L (33%), K_{e3} decays (30%), μ decay(37%) and a small amount from π decay (0.8%). Our simulations show that $(\nu_e+\bar{\nu}_e)/\nu_\mu$ = 0.701% $\pm$ 0.009% at the far detector, and 0.715% $\pm$ 0.023% for the inner 25 cm radius at the near detector. The errors are due to the statistics of the beam simulation. We take twice the difference as a conservative estimate of the uncertainty in the ν_e fraction. This leads to a systematic error on dT = 0.00022. This does not take into account the uncertainty in the ν_μ flux. In Section 3.7.3 we estimate the systematic error on the flux at the far detector to be 4%, given a measurement at the central part of the beam at the near detector. (We hope to be able to reduce this by over a factor of 4 with further beam simulation and appropriate beam monitoring.) Then the uncertainty in the relative ν_μ portion of the beam leads to a systematic error dN_{cc}/N_{cc} of 0.04×0.007 or dT=0.00021.

Trigger efficiency

The neutral current trigger efficiency in the reference detector is based on a trigger requirement of 3 hit planes out of 5. The trigger efficiency for neutral current events is shown in in Figure 8.1 as a function of neutrino energy, which is more related to analysis issues, and Figure 8.2 as a function of hadron energy, which is related to detector properties. Integrated over the event energy spectrum, we find an efficiency of 81% in the center of the near detector and 82% in the far detector. The systematic error due to the uncertainty in the beam is $dN_{nc}/N_{nc} = 0.0113 =$ dT/[T(1-T)]. Further differences in the trigger efficiency could arise if the streamer tube efficiencies were different in the near and far detector in a way which could not be corrected. The neutral current trigger efficiency was calculated under the assumption that the streamer tubes will be 87% efficient. The trigger efficiency assuming 100% efficient tubes was calculated to be 86% in the center of the near detector and 87% in the far detector. The streamer tube inefficiency will be dominated by the geometric construction of the tubes. But it is possible that gas impurities or other effects could cause an average difference in efficiency in the near and far detector. A 1% difference in that efficiency that is not corrected would cause a systematic error of $dN_{nc}/N_{nc} = 0.0049$ which implies dT = 0.00087.

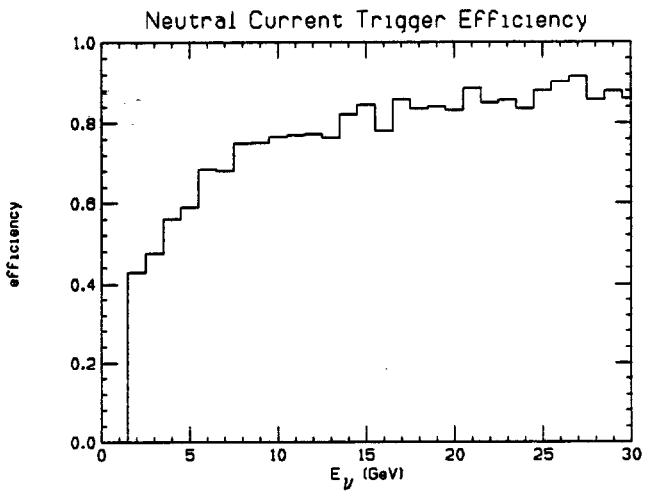

Figure 8.1: Simulation of neutral current trigger efficiency *versus* E_ν for a trigger of 3 hits in 5 planes

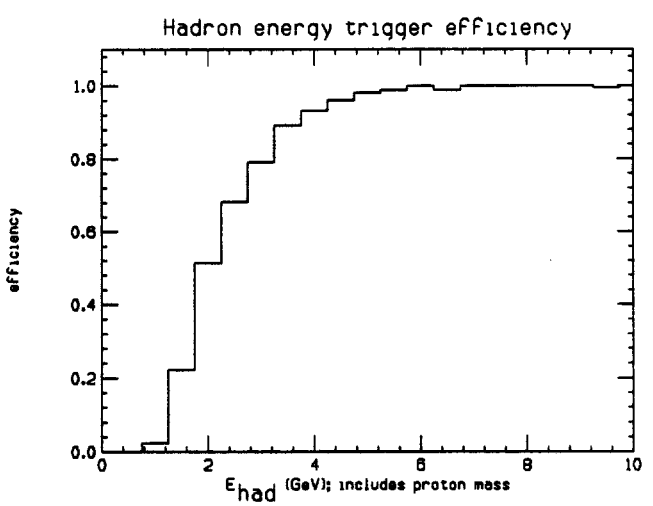

Figure 8.2: Simulation of neutral current trigger efficiency versus E_{had} for a trigger of 3 hits in 5 planes

Physics uncertainties

The systematic errors on physics cross sections and beam uncertainties were derived in the P–822 Proposal [76]. Here we ignore those systematic errors which were found to be negligible (due to uncertainties in the axial vector mass and uncertainties due to the choice of Q^2 cutoffs at low energy). The largest physics systematic error was the uncertainty in the charm cross section. We show the results of two beam Monte Carlos and two estimates of the range of the charm cross section in Table 8.2.

		high	mid	low
PBEAM Monte Carlo: E-803 $\sigma's$	near	2.41%	1.67%	1.06%
	far	2.67	1.87	1.22
	(near-far)	0.26	0.20	0.16
		high	mid	low
NUADA Monte Carlo: E-803 $\sigma's$	near	1.90%	1.30%	0.90%
	far	2.18	1.50	0.95
	(near-far)	0.28	0.20	0.15
		high	mid	low
PBEAM Monte Carlo: Phillips' $\sigma's$	near	2.02%	1.34%	0.87%
	far	2.34	1.59	1.06
	(near-far)	0.32	0.25	0.19
		high	mid	low
NUADA Monte Carlo: Phillips' $\sigma's$	near	1.51%	0.98%	0.62%
	far	1.81	1.21	0.79
	(near-far)	0.30	0.23	0.17

Table 8.2: Predicted charm cross sections as a fraction of the total charged current cross section.

Using the most conservative result in the table (0.32%) for the difference (near-far) in the contribution from charm, we assign a systematic error dT = 0.00057. We point out that we expect these cross sections to be measured in E-803, but we have not used that fact in this analysis.

Backgrounds

In both the near and far detectors, there could in principle be backgrounds from (1) cosmic rays and (2) beam associated tracks caused by ν interactions outside the detector. The expected rate of NC events from cosmic rays in the far detector is less than 7 in 2 years, within the beam spill-time gate. Less than one event is expected in the near detector. The only potential beam associated background which we have been able to identify is from NC events in the rock, in which a neutron or K_L^o is the most penetrating particle, no other particle from the shower enters the detector, and the neutral hadron goes more than one interaction length into the detector. A rough calculation of this background for the near detector shows that there should be about 100 such events in a two year run (*versus* several million NC events in the detector). If the result of a more detailed calculation suggests this

is an underestimate, we could probably reduce it further by accepting only those NC events which occur several interaction lengths into the near detector.

8.2.4 Summary of $\frac{cc}{total}$ errors

Table 8.3 summarizes the contributions of the above effects to the errors and limits. The systematic errors have been added in quadrature. It can be seen that at the present level of statistics, our experiment must control its systematic errors very carefully in order to take full advantage of the expected statistical precision. In particular, present estimates for two systematic errors in Table 8.3 are limiting the sensitivity of the experiment (see Figure 8.3)—these result from a combination of beam uncertainties with CC misidentification for short muon tracks, and the neutral current trigger efficiency. In the evolution of the design of the reference detector, the collaboration intends to reduce the effects of these potential systematic errors. This can be done through the following steps:

1. Better understanding of the differences between the near and far energy spectra, and quantitative beam monitoring to show that the beam is understood;
2. More sophisticated CC recognition algorithms, particularly to identify muons within hadron showers, and also for quasi-elastic and other low-y events;
3. A lower energy neutral current trigger threshold, by optimizing the trigger ;
4. A better understanding of the sources of inefficiency in streamer tubes, leading to a plan to monitor efficiencies with an accuracy of 0.2% or better.

Contribution	dT	dP_e	dP_τ	$\sin^2(2\theta)$ $\nu_\mu \rightarrow \nu_e$	$\sin^2(2\theta)$ $\nu_\mu \rightarrow \nu_\tau$
Statistics	0.0020	0.0025	0.0056	0.0065	0.0145
MisID-energy cut	0.0018	0.0023	0.0051		
ν_e fraction,$\Delta\nu_e$	0.00022	0.00028	0.00062		
ν_e fraction,$\Delta\nu_\mu$	0.00021	0.00026	0.00059		
NC trigger	0.0020	0.0025	0.0056		
Tube efficiency	0.00087	0.00109	0.00245		
Charm	0.00057	0.00071	0.00160		
Total Systematics	0.00290	0.00363	0.0082	0.0094	0.0210
Statistics and Systematics		0.0044	0.0099	0.0114	0.0255

Table 8.3: Summary of statistical and systematic errors

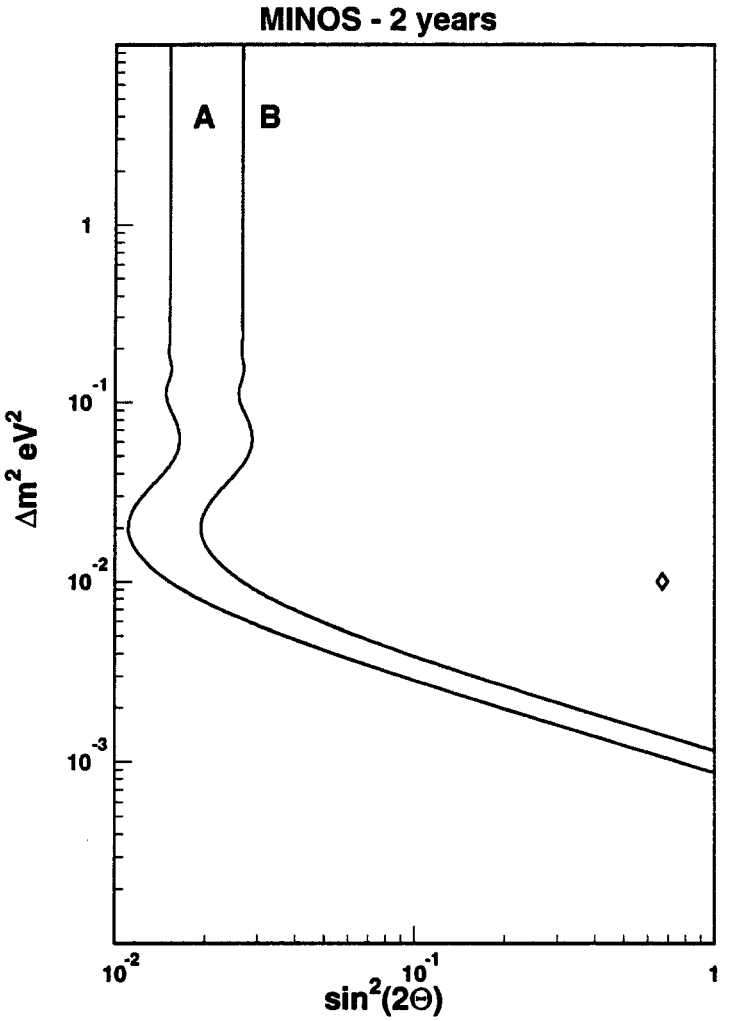

Figure 8.3: Two year $\nu_\mu \rightarrow \nu_\tau$ oscillation limit curve for MINOS using the $\frac{cc}{total}$ test. "A" is for statistics only, and represents the sensitivity if we can reduce systematic e a small fraction of the statistical uncertainty. Curve "B" includes systematic and statistical errors. The diamond point shows the Kamiokande best fit parameters.

8.3 Tests using energy measurements of CC events

For a nonzero value of $\sin^2(2\theta)$ the probability of a ν_μ surviving as a ν_μ after travelling a distance L is a function of E_ν:

$$P(\nu_\mu \to \nu_\mu) = 1 - \frac{1}{2}\sin^2(2\theta) + \frac{1}{2}\sin^2(2\theta)\cos\left(2.54\Delta m^2 L E_\nu^{-1}\right). \tag{8.8}$$

Observation of this dependence of P on E_ν would be a powerful demonstration of neutrino oscillations and provide a direct measurement of Δm^2 and $\sin^2(2\theta)$.

The energies of the neutrinos making charged current interactions in the far detector can be estimated as the sum of the muon energy and the hadronic energy, *i.e.*, $E_\nu = E_\mu + E_{\rm had}$. E_μ will be measured either from range, or by curvature in the magnetic field. $E_{\rm had}$ will be measured calorimetrically. A comparison of the measured energy spectrum of CC events with the spectrum expected in the absence of oscillations can be used as a test for oscillations. Use of the NuMI *wide-band* beam is essential to extend this measurement to the lowest accessible Δm^2 since the range of E_ν must encompass a phase change of $\sim \frac{\pi}{2}$ in the energy dependent term in the formula for the survival probability, Equation 8.8. Specifically, the *highest* energy minimum of $P(\nu_\mu \to \nu_\mu)$ occurs at $E_\nu \sim 6$ GeV if $\Delta m^2 = 0.01$ eV^2.

Figure 8.4 shows the expected distribution of the energies of CC events in the absence of oscillations (upper graph) and the distribution expected at the far detector if $\sin^2(2\theta) = 1.0$ and $\Delta m^2 = 0.1$ eV^2 (lower graph). The detector resolutions of $\Delta E_{\rm had} = 0.08E_{\rm had} + 0.7\sqrt{E_{\rm had}}$ and $\Delta p_\mu = 0.1p_\mu$ have been included. The finite resolution of the detector means that the minimum at $E_\nu \sim 19$ GeV does not go down to zero. Even with a modest energy resolution the modulation of the energy spectrum by $P(\nu_\mu \to \nu_\mu)$ is clearly visible. The resolution of the detector will clearly prevent this measurement reaching to the highest values of Δm^2 ($> \sim 1$ eV^2) but is unimportant for the lower Δm^2 region which is limited by the lowest useful neutrino energies in the beam.

The advantage of a test based on the measurement of neutrino *energies* is that, in contrast to the normal disappearance test based on simply counting events, it is unnecessary to know the absolute normalization, in terms of exposure, of the number of events. We have developed a test which is based solely on the *shape* of the energy spectrum, and is thus relatively immune to systematic effects. Despite the arbitrary normalization it achieves an ultimate statistical error equivalent to that of half the total number of CC events observed and is therefore an efficient use of neutrinos.

The test is based on the simple normalized statistic, Z, computed from the energies, E_i, of the measured CC events as:

$$Z_f(\Delta m^2) = \frac{1}{N_f}\sum_{i=1,N_f}\cos(2.54\Delta m^2 L E_i^{-1}) \tag{8.9}$$

where N_f is the number of events measured in the far detector. Z is an approximation, for a finite number of events, to the Fourier cosine transform of the distribution $dN/d(E^{-1})$. $Z_f(\Delta m^2)$ can be computed for the entire range of interest of Δm^2 and compared with the the value expected in the absence of oscillations, $Z_n(\Delta m^2)$. A statistically significant difference between $Z_f(\Delta m^2)$ and $Z_n(\Delta m^2)$ can be taken as evidence of oscillations. The difference will

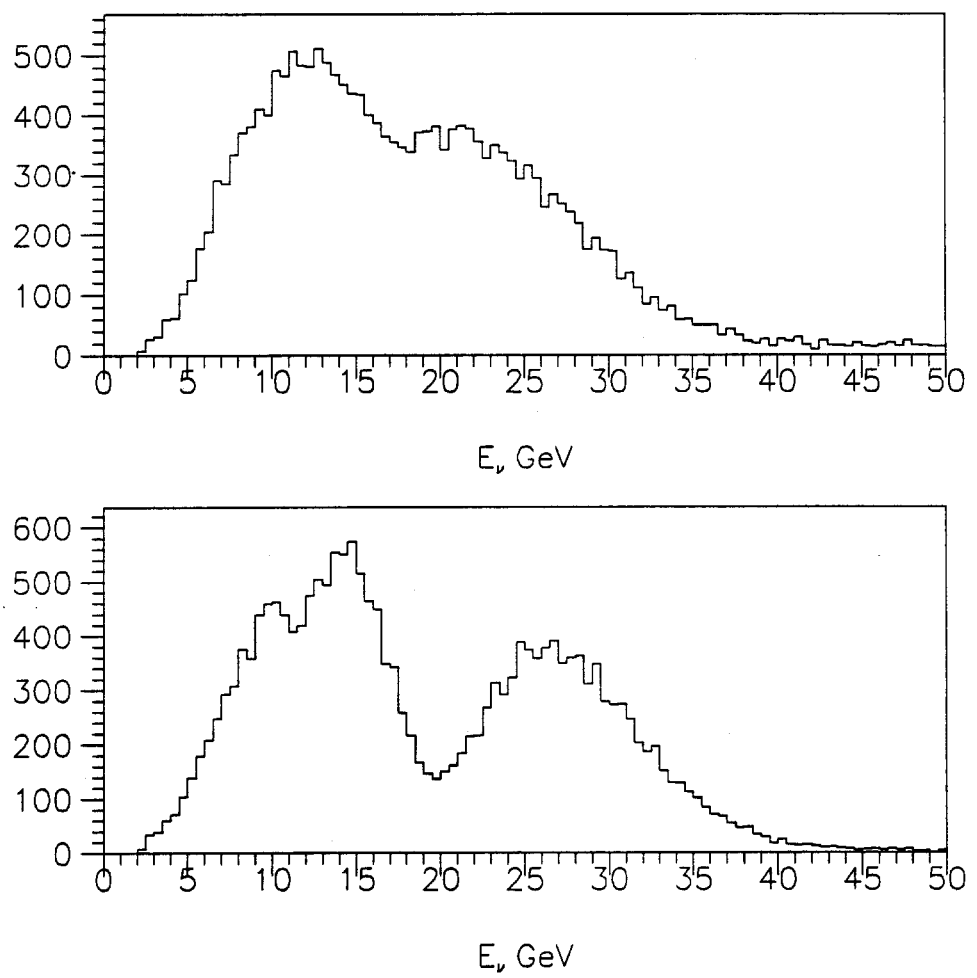

Figure 8.4: Upper graph: Energy spectrum of CC events in the NuMI wide-band beam *without* oscillations. Lower graph: Energy spectrum of CC events in the NuMI wide-band beam *with* oscillations for $\Delta m_0^2 = 0.1$ eV^2 and $\sin^2(2\theta) = 1$. The resolution of the detector has been included in both graphs.

be maximum at $\Delta m^2 = \Delta m_0^2$ where Δm_0^2 is the true value of Δm^2. This test produces the most direct measurement of Δm^2 of all those described in this proposal.

$Z_n(\Delta m^2)$ must be predicted by using the energy spectrum of CC events in the near detector and extrapolating the flux to the far detector.

Figures 8.5 and 8.6 show examples of the oscillation signatures that could be obtained with this analysis for $\Delta m_0^2 = 0.1$ eV^2 and 0.01 eV^2 with $\sin^2(2\theta) = 1.0$ in both cases.

The upper graph of each figure shows $Z_f(\Delta m^2)$ and $Z_n(\Delta m^2)$, the lower figure shows their difference. These figures were obtained from a simulation using the wide-band NuMI beam and include the resolution of the detector. In each case the difference, $Z_f(\Delta m^2) - Z_n(\Delta m^2)$, is maximum at Δm_0^2. It can be shown that for a detector with perfect energy resolution the height of the maximum at $\Delta m^2 = \Delta m_0^2$ is related to $\sin^2(2\theta)$ by:

$$\begin{aligned} Z_f(\Delta m^2) - Z_n(\Delta m^2) &= \frac{\sin^2(2\theta)}{2}\left(\frac{1 - 2Z_n^2(\Delta m^2) + Z_n(2\Delta m^2)}{2 - \sin^2(2\theta)(1 - Z_n(\Delta m^2))}\right) \\ &\rightarrow \frac{\sin^2(2\theta)}{4 - 2\sin^2(2\theta)}. \end{aligned} \tag{8.10}$$

The asymptotic limit given in Equation (8.10) is reached in the high Δm^2 region where $Z_n(\Delta m^2)$ is negligible. $Z_n(\Delta m^2)$ starts to become appreciably different from zero for $\Delta m^2 < E_{\rm min}/2.54L \sim 0.003$ eV^2 where $E_{\rm min}$ is the lowest neutrino energy with a useful interaction rate, $\sim$ 6 GeV for the wide-band beam. Below this value of Δm_0^2 the sensitivity of the measurement to $\sin^2(2\theta)$ is reduced.

The variance of Z as defined by Equation (8.9) is $\mathrm{var}(Z) \leq 1/2N_f$ and the test for oscillations is therefore simply a χ^2 test with $\chi^2 = (Z_f(\Delta m^2) - Z_n(\Delta m^2))^2/\mathrm{var}(Z)$. Only a positive difference would be taken as evidence for oscillations.

The finite resolution of the detector also reduces the sensitivity of the measurement to $\sin^2(2\theta)$ by an amount dependent on Δm_0^2, $f(\Delta m_0^2)$. Since the resolution is a function of both $E_{\rm had}$ and E_μ, $f(\Delta m_0^2)$ has been determined for the range 10^{-3} eV$^2 < \Delta m_0^2 < 1.0$ eV^2 by a Monte Carlo simulation. The value of $\sin^2(2\theta)$ is extracted by the use of Equation (8.10) when the detector resolution is included for an imposed signal of $\sin^2(2\theta) = 1$. $f(\Delta m_0^2)$ is close to unity for $\Delta m_0^2 < 0.02$ eV^2, ~ 0.5 at $\Delta m_0^2 = 0.1$ eV^2 and approaches zero for $\Delta m_0^2 > 1$ eV^2.

The reduction in sensitivity of the test to $\sin^2(2\theta)$, due to the effects of the finite value of Z_n at low Δm^2 and the resolution of the detector at high Δm^2, is apparent in Figures 8.5 and 8.6, where the maxima do not reach the value of 0.5 given by the asymptotic limit of Equation (8.10).

The most important systematic errors that have been identified for this type of analysis are (1) the uncertainties in the extrapolation of the energy dependence of the neutrino flux to the far detector, and (2) any energy scale uncertainty of the far detector. Since a subtraction is required to extract a signal at the lowest values of Δm_0^2, both of these systematic uncertainties affect the confidence with which limits to $\sin^2(2\theta)$ can be set at the lowest values of Δm^2. The dominant systematic effect is any uncertainty in the energy calibration of the detector. For the sensitivities discussed below it is assumed that the systematic uncertainty in the neutrino energy spectrum at the far detector is equivalent to

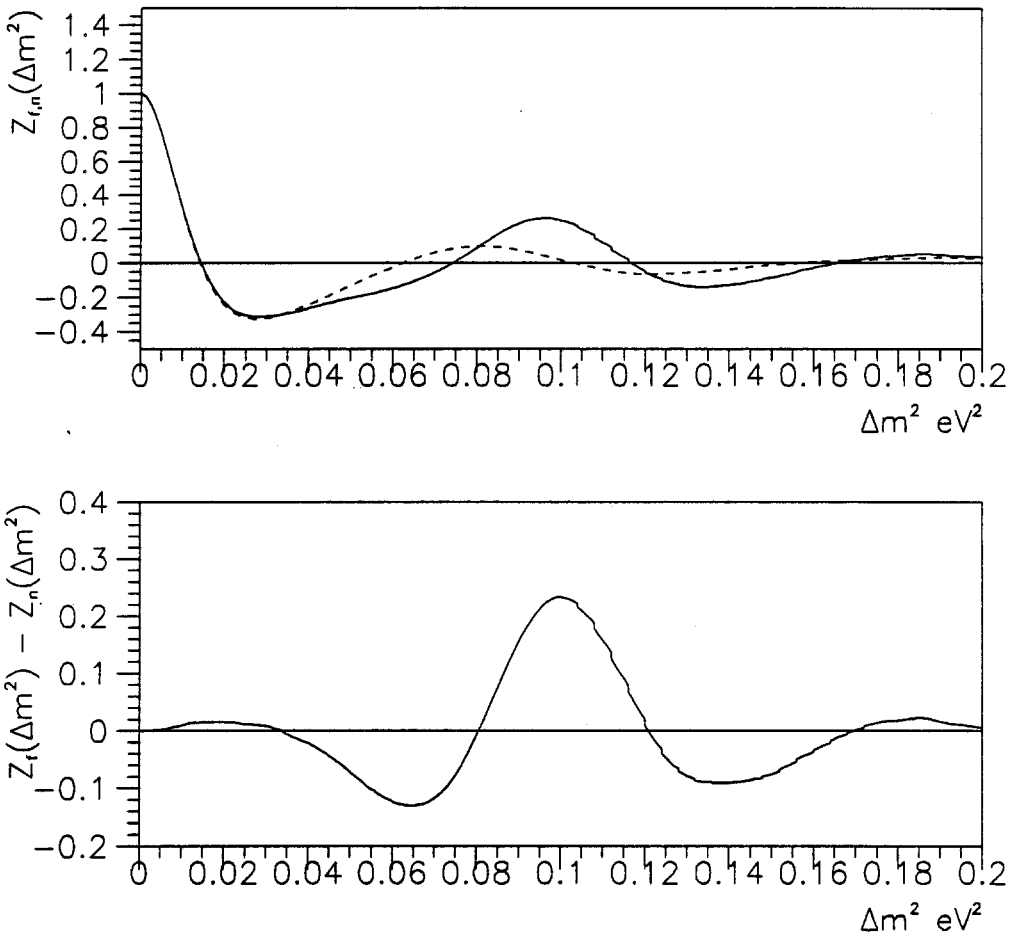

Figure 8.5: Expected oscillation signals using the CC energy test described in the text. Upper graph: $Z_f(\Delta m^2)$ (solid line) and $Z_n(\Delta m^2)$ (dashed line) for $\sin^2(2\theta) = 1.0$ and $\Delta m^2 = 0.1$ eV^2. Lower graph: The difference, $Z_f(\Delta m^2) - Z_n(\Delta m^2)$. These figures were obtained from simulations using 40,000 events; the statistical errors are invisible on this scale.

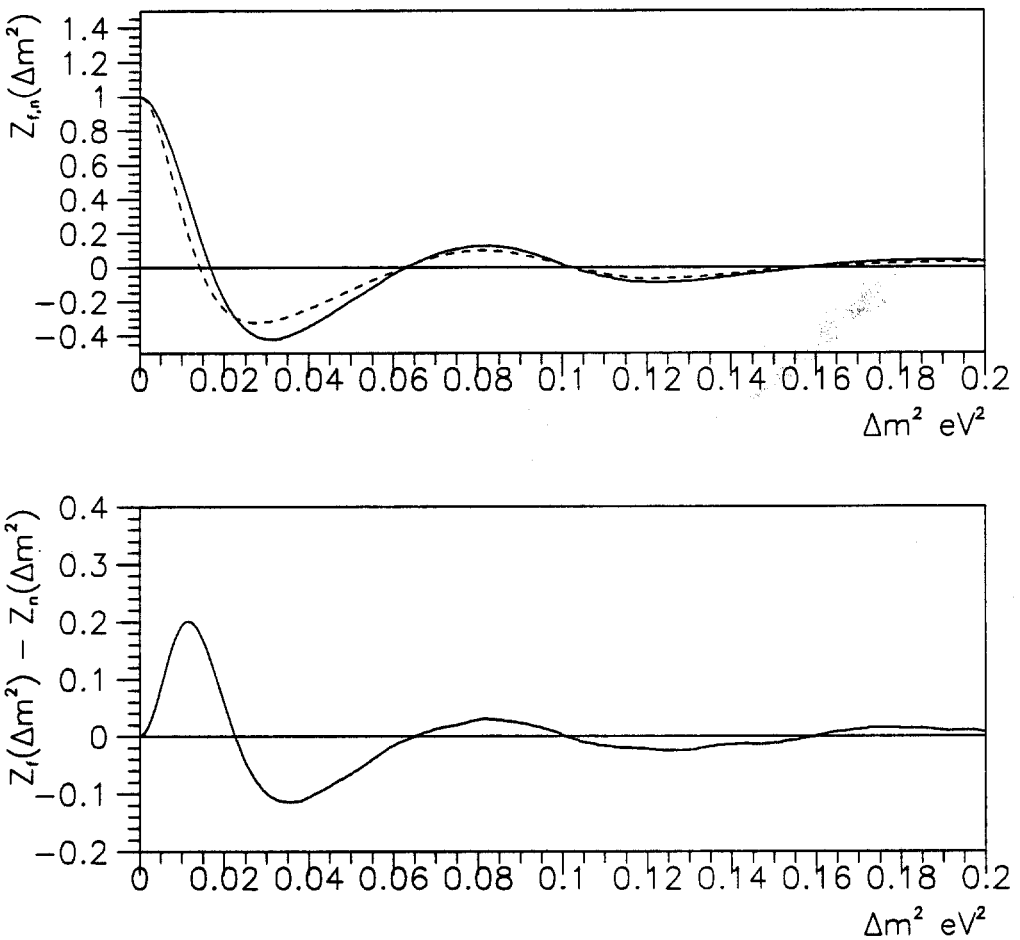

Figure 8.6: As for the previous figure but with $\Delta m^2 = 0.01$ eV^2.

$\pm 5\%$ admixture of the energy spectrum at the near detector, and that the energy calibration of the detector is known to $\pm 2\%$.

Figure 8.7 shows the 90% CL limits to $\sin^2(2\theta)$ that could be achieved with this analysis for the standard running assumptions. The outer, dotted, line is the statistical limit (*i.e.*, perfect detector resolution), the dashed line includes the detector resolution and the inner, solid, line includes the systematic uncertainties discussed above. Figure 8.8 shows the effect, in standard deviations, as a function of Δm_0^2 that would be obtained with the standard running assumptions. A quite unambiguous signal of $> 50\sigma$ would be found if the true values of Δm_0^2 and $\sin^2(2\theta)$ were 0.01 eV^2 and 1.0. An effect of $> 10\sigma$ would be observed after only 1 – 2 months running.

8.4 Near/far detector comparison ("disappearance" experiment)

If ν_μ oscillations exist (independent of the mode of oscillation), the rate of interactions characteristic of ν_μ at the far detector will be depleted with respect to that expected from the near detector rate. Two-detector comparisons generally are subject to rather low statistical errors but are potentially subject to significant systematic errors. In a two year run the statistical error for the number of CC events (characteristic of ν_μ interactions) will be about 0.5% for a WBB exposure and about 1% for the NBB exposure. The systematic error depends on our ability to extrapolate the beam from the near to the far detector. As described in Section 3.7.3, we are confident that less than 4% of the WBB flux in the central part of the near detector is not directly related to the flux that we measure at the far detector, based on the predicted energy distribution differences from Monte Carlo beam studies. As an absolute worst case we can assume that we do not understand this part of the beam and thus a 4% systematic error is possible. Because one can define and measure the characteristics of the NBB much better than for the WBB, it is probable that the NBB exposure will have smaller systematic errors and may give the optimum overall sensitivity for this test.

The general problem in the near/far detector comparison stems from the fact that the near detector sees more "wide angle" neutrinos, i.e. ν's emitted by π's (or K's) traveling at a relatively large angle to the beam axis. These neutrinos have to be emitted at a large angle with respect to the hadron's line of flight to be able to strike the detector. Accordingly their energy tends to be relatively low. As one limits the acceptance in the near detector to the central region of the detector, there is an increase in the fraction of events with the spectrum characteristic of the far detector flux.

Our strategy for reducing the systematic errors in the near/far comparison is threefold:

1. We plan to define a relatively small area of the near detector which will see a beam very comparable in its characteristics to the one seen by the far detector. Only the interactions in this part of the detector, estimated to comprise the central circle of radius 25 cm, will be used for the comparison. Because of the very large interaction rate at the near detector this will not compromise our overall statistical accuracy.

2. We plan to study the beam at the near detector over a much larger area than this central circle using the beam monitor detector, with dimensions 3 m by 3 m. As

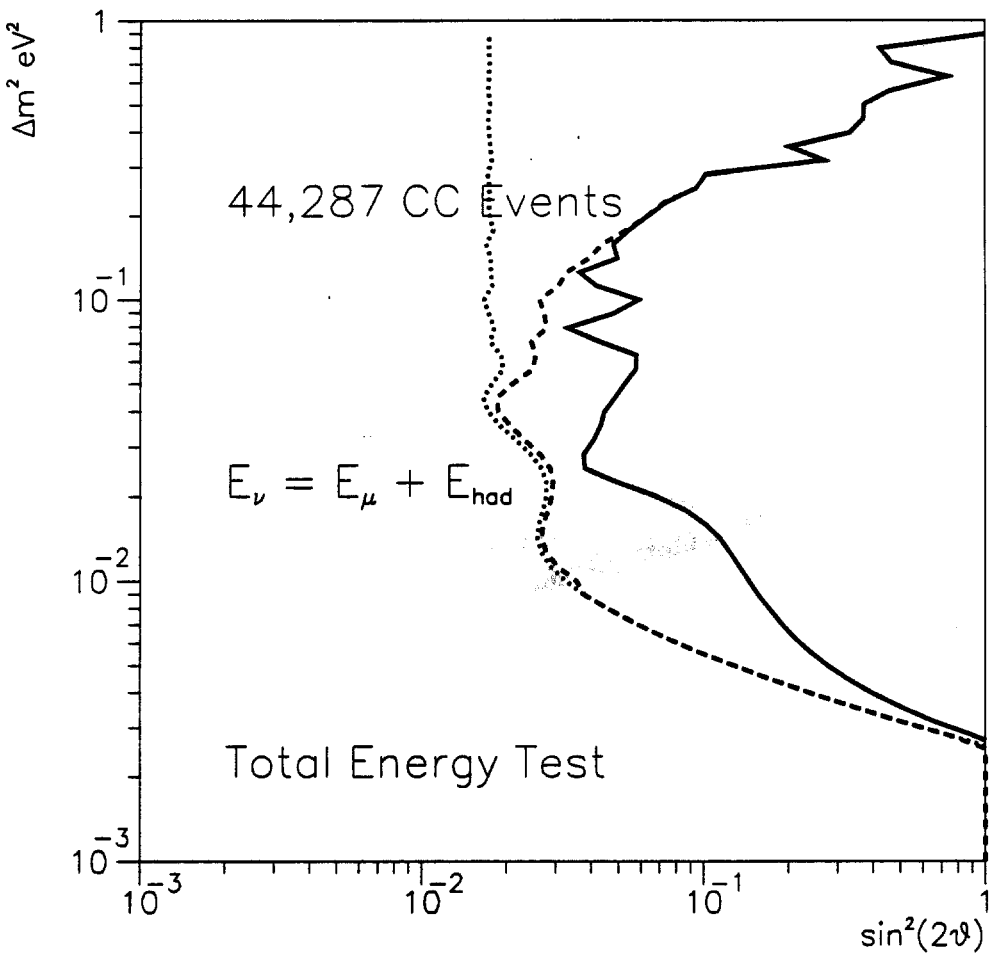

Figure 8.7: Limits on $\sin^2(2\theta)$ and Δm^2 expected for the standard running assumptions. The dotted line shows the statistical limit for a perfect detector; the dashed line includes the effect of detector energy resolution. The solid line includes the systematic uncertainties associated with imperfect knowledge of the neutrino energy spectrum at the far detector and a 2% uncertainty in the energy calibration.

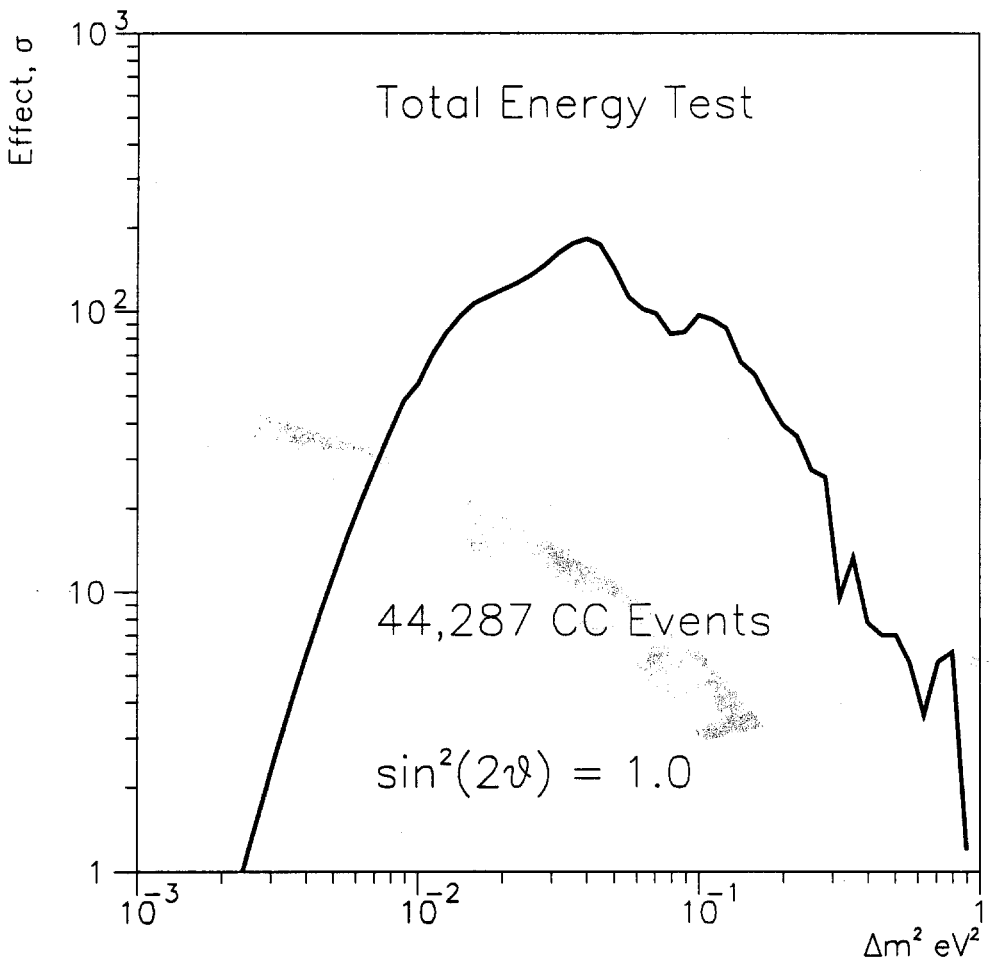

Figure 8.8: The effect, in standard deviations, as a function of Δm_0^2 that would be measured using the CC energy test given the standard running assumptions and $\sin^2(2\theta) = 1.0$.

discussed in Chapter 6, this will allow us to verify that the actual neutrino beam does have the characteristics expected from the beam Monte Carlo.

3. Extensive beam measurements will be made. There is now a great deal of experience in monitoring and measuring the characteristics of ν beams. We plan to take full advantage of this storehouse of knowledge.

8.5 Wide band beam, τ identification

8.5.1 $\tau \rightarrow$ hadrons and $\tau \rightarrow$ e

Tau neutrino charged current events, where the τ decays into hadrons or an electron, will look like neutral current events in the detector. However, in addition to the normal hadron production at the target vertex, a substantial amount of hadronic energy will be added to the event from the τ decay. The signatures of τ production in this channel are thus (1) an increase in the number of apparent neutral current events, and (2) a change in the event energy (number of hits) distribution, compared with the unoscillated distribution at the near detector.

This channel has a number of advantages which make it an attractive choice for a first search for τ production:

- 82% of the τ branching fraction is available, so the statistics are much more favorable than in the leptonic channels which have only 18% branching ratios.
- The background to τ in this channel is neutral current interactions, which are less than 1/3 of charged current interactions (the background in μ channels).
- The signature relies predominantly on the hadronic energy resolution of the detector which was shown in Chapter 7 not to be a strong function of the detector granularity. The detector granularity is thus not a major constraint in detecting these events.
- The selection procedure is simple and has a high efficiency. The results are thus relatively insensitive to small tails of distribution functions.
- Since neutral current events are spatially compact, the acceptance of the events within the far detector fiducial volume is very similar to that of the events in the center of the beam in the near detector. Thus the shape of the unoscillated hadronic energy distribution in the near detector will require only minor acceptance corrections to provide a comparison for the shape in the far detector.

We have generated events in the far detector for oscillation parameters $\sin^2(2\theta) = 1.0$, $\Delta m^2 = 0.015\ eV^2$, the best fit parameters to the Kamiokande atmospheric neutrino data, using the Soudan 2 Monte Carlo.

The event length (L) distribution for the charged current τ events is shown in Figure 7.17 in Section 7.5. This should be compared with the same distribution for neutral and charged current ν_μ events in the same figure. The $L < 20$ cut (defined in Section 7.5) selects 92% of the $\tau \rightarrow$ hadron events.

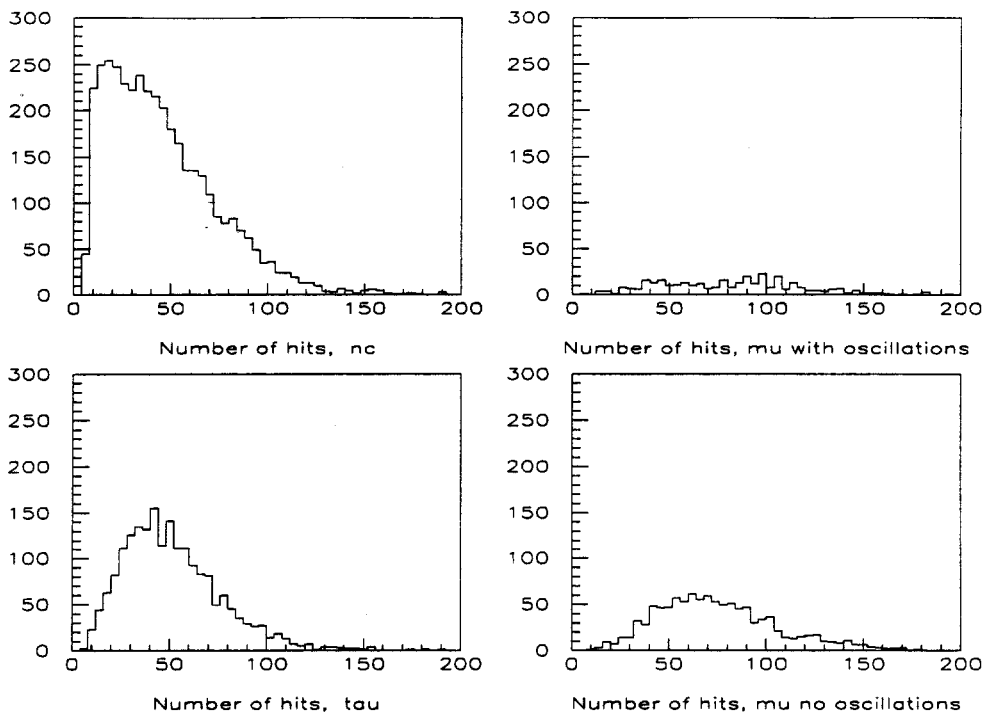

Figure 8.9: Number of hits for selected "nc" events for neutral current, τ and μ charged current events with and without oscillations

The short events remaining after the length selection consist of three types (ignoring the ν_e background):

- ν_τ charged current events, including $\tau \rightarrow \mu\nu\nu$ events with a short, low energy muon,
- neutral current events,
- ν_μ charged current events where the muon is too short to pass the event length cut.

The event energy was measured in Section 7.4.3 by counting the number of hit strips weighted by their pulse height to allow for multiple particles hitting one strip. In the present analysis we found that the unweighted number of strips hit was a better discriminant between τ and non-τ events. This is probably because the weighted distribution favours π^0 production and produces a broader distribution when the hadronic showers have a broad spread in the number of π^0. The distributions of numbers of hits for the three classes are plotted in Figure 8.9 and their sum in Figure 8.10.

The unoscillated distributions have to be calculated from the events in the near detector. The distributions measured there have to be extrapolated to the far detector using the measured beam parameters and the Monte Carlo extrapolation of the beam spectrum to the far detector. This is the largest source of systematic error in the measurement. The accuracy with which this extrapolation may be made is discussed in Section 8.2.3. We expect to obtain an accuracy of 2% in absolute normalization and 5% in the energy spectrum between the near and far detectors. For the present comparison we have generated events with no oscillations using the far detector beam spectrum. The above uncertainties have to be folded in, but will have only a small effect on the sensitivity to oscillations.

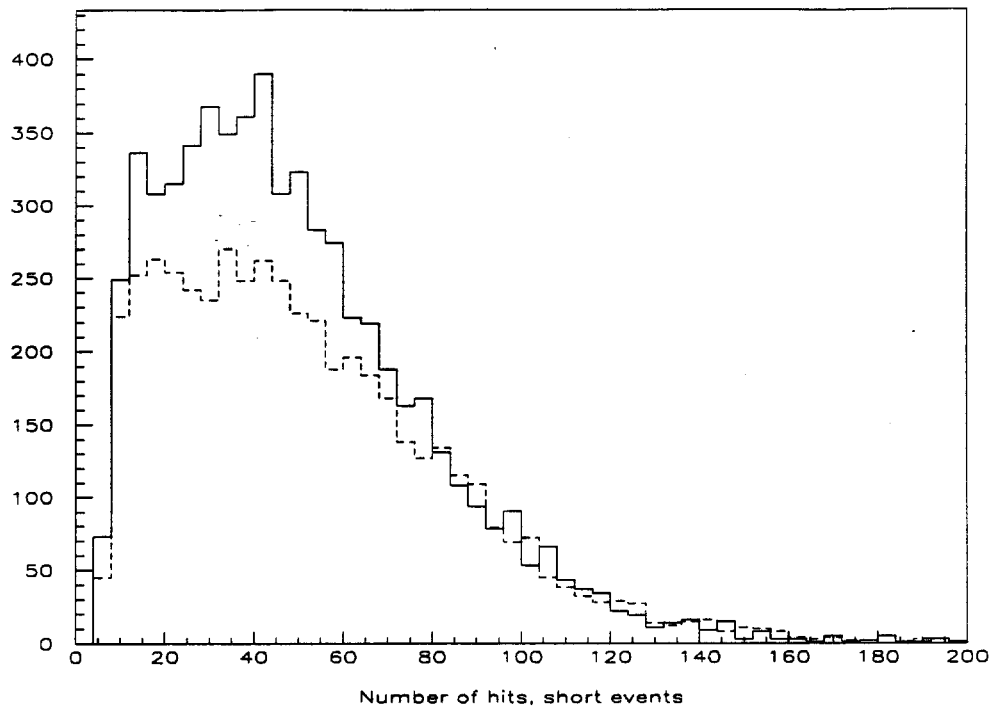

Figure 8.10: Number of hits for selected "nc" events for $\sin^2(2\theta) = 1.0$ and $\Delta m^2 = 0.015\ eV^2$ (solid line) and no oscillations (dashed line)

The neutral current distributions will, of course, be the same in the oscillated and unoscillated cases. However the short muon distributions will be different because the ν_μ energy distributions are different. The short muon hit distribution for $\sin^2(2\theta) = 0$ is plotted in Figure 8.9 and the total unoscillated distribution in Figure 8.10. The signal for oscillations is the difference between the oscillated and unoscillated distributions in Figure 8.10. The numbers of events in the plots are those expected for a one year run.

We may now test for the presence of oscillations by making a χ^2 comparison between the two distributions. We discuss two cases:

1. The relative normalization of the near and far detector distributions are known, *i.e.*, we can compare the two distributions directly.

2. The relative normalization is unknown and we have to compare only the shapes of the distributions with an arbitrary normalization. As discussed above this is far from the expected understanding of the normalization but it gives a worst case for the possible signal.

For case 1 the χ^2 difference is 508 for 37 bins. For case 2 the χ^2 difference is 149. In both cases the signal is very clear. The renormalization factor is 1.28, much larger than the expected systematic error.

An approximation to the distributions at other values of $\sin^2(2\theta)$ can be obtained by summing the neutral current distribution with a scaled version of the τ distribution and a short muon distribution interpolated between the $\sin^2(2\theta) = 1.0$ and $\sin^2(2\theta) = 0$ distributions, and comparing this with the unoscillated distribution. Taking a 90% confidence level

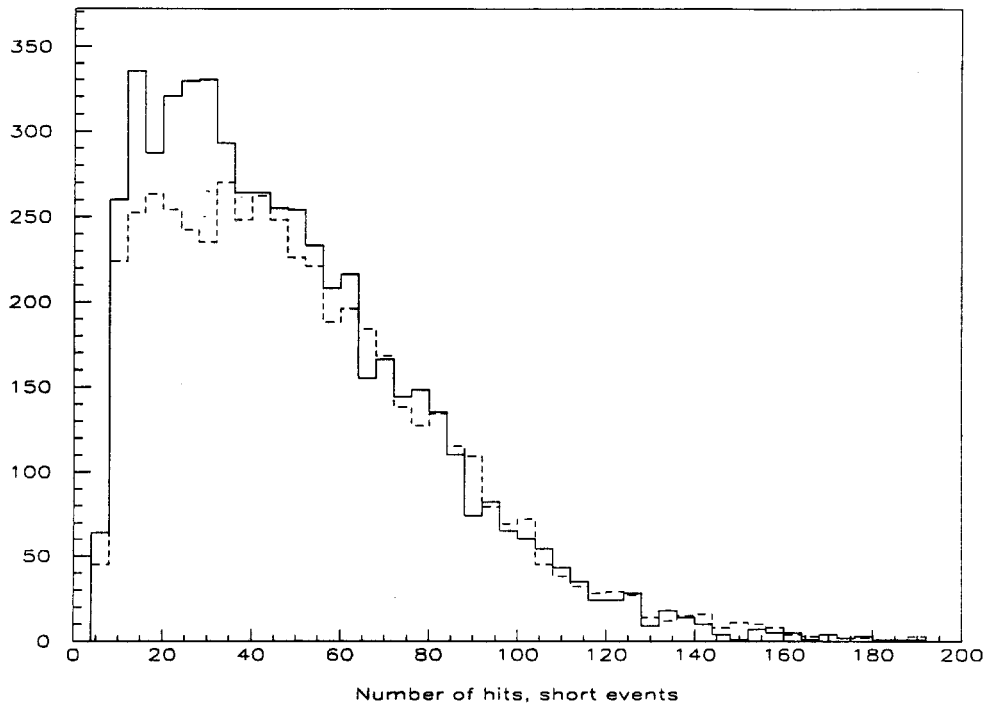

Figure 8.11: Number of hits for selected "nc" events for $\sin^2(2\theta) = 1.0$ and $\Delta m^2 = 0.008\ eV^2$ (solid line) and no oscillations (dashed line)

limit as the point where the probability that the two distributions are the same has fallen to 10%, we obtain a limit of 0.10 on $\sin^2(2\theta)$ in a two year run, if no allowance is made for systematic beam uncertainties. The limit including these uncertainties will depend on Δm^2 and the detailed energy variation of the uncertainties.

We have also compared the distributions for other values of the oscillation parameters. The hit distribution for $\Delta m^2 = 0.008\ eV^2$ and $\sin^2(2\theta) = 1.0$ is shown in Figure 8.11. At this low value of Δm^2, only low energy ν_μ have oscillated into ν_τ, thus producing the peak at low event energies. The shape of the hit distribution changes with Δm^2, providing a measurement of its value.

The χ^2 for the comparison of these two histograms is 176 for the normalized case and 116 for the unnormalized.

No attempt has been made in this analysis to refine the separation between ν_μ neutral current events and τ production events. These limits might be reduced by cuts that exploit the differences in topology between the τ events, which include extra high energy forward hadrons, and the ν_μ events. Work is in progress to investigate this possibility.

8.5.2 $\tau \rightarrow \mu\nu\nu$ planarity analysis

This analysis attempts to statistically identify $\tau \rightarrow \mu\nu\nu$ events. It was motivated by topological differences between the Deep Inelastic Scattering (DIS) events, $\nu_\mu \rightarrow \mu^- + hadrons$ and $\nu_\tau \rightarrow \mu^- \nu_\tau \bar{\nu}_\mu + hadrons$, stemming from the loss of visible energy in the ν_τ events from the two neutrinos. In the ν_μ events, the final state of the muon plus hadrons will lie in a

plane which includes the incoming neutrino direction. In the ν_τ events, this will usually not be the case.

Procedure

In the analysis outlined below, we assume full mixing ($\sin^2(2\theta) = 1.0$) with different values of Δm^2. The numbers of events quoted will be those in the far detector (732 km) for one year of running with an 800 m decay pipe and the 10.0 kT steel reference detector.

Of great importance to this analysis are the angular resolutions for muons and hadron showers which are described in detail in Sections 7.4.1 and 7.4.4. However, in view of the very small number of signal events and the very large background, a proper treatment of the tails from any resolution function is very important. In this case, the actual histograms from the full simulation were sampled to generate an accurate picture of the hadronic resolution, including the non-Gaussian tails.

Cuts

There are basically four parameters which enter into the cuts used. These are the muon momentum, its angle, the hadron energy and the hadron direction. These four parameters can be combined to form six variables on which the cuts are imposed. These are E_{had}, p_μ, E^T_{had}, p^T_μ, $E^T_{miss}=E^T_{had}$ - p^T_μ, and the event non-coplanarity. It is possible to adjust these cuts for a particular value of Δm^2 in order to minimize the background events from ν_μ, the magnitude of which depends on Δm^2 and can be as high as 100 times the number of signal events. Signal to background ratios of 1:1 are achieved after these cuts.

A very important characteristic of the background ν_μ events is that the muon, hadron shower and incoming neutrino lie in a plane. This is not true for the signal events. This is demonstrated in Figure 8.12 where the quantity $\vec{p_\mu} \bullet \vec{p_{had}} \times \hat{z}$ is plotted, where $\hat{z}$ is the z axis and represents the direction of the incoming neutrino.

With the relatively poor hadronic angular resolution which is available, the effects of the topological differences between the signal and background are rather washed out. Using this method with $\Delta m^2 = 0.015\ eV^2$ and $\sin^2(2\theta) = 1.0$ we have calculated a signal of 6 events over a background of less than 1 event. If a detector with 2 cm steel plates were used, the number of signal events would improve by a factor of two. Figure 8.13 shows the number of events expected for less than 1 event of background as a function of Δm^2. Also shown are the results for 2 cm steel plates. The number of events seen in a hybrid detector of 4 cm steel and 5 cm concrete plates (as described in Chapter 10) is very similar to the number found with the 4 cm steel plate detector. Although the improvement in hadron angular resolution is moderate, the mass of the 5-cm concrete plates is much smaller than the mass of the same number of 4-cm steel plates.

Narrow Band Beam

The main problem in this analysis is the huge number of background events compared to the signal, such that distribution tails become all important. Several of the cuts employed seek to reduce the background simply on the basis of total energy deposited in the detector. The majority of the background events passing such cuts are from the low energy tail of

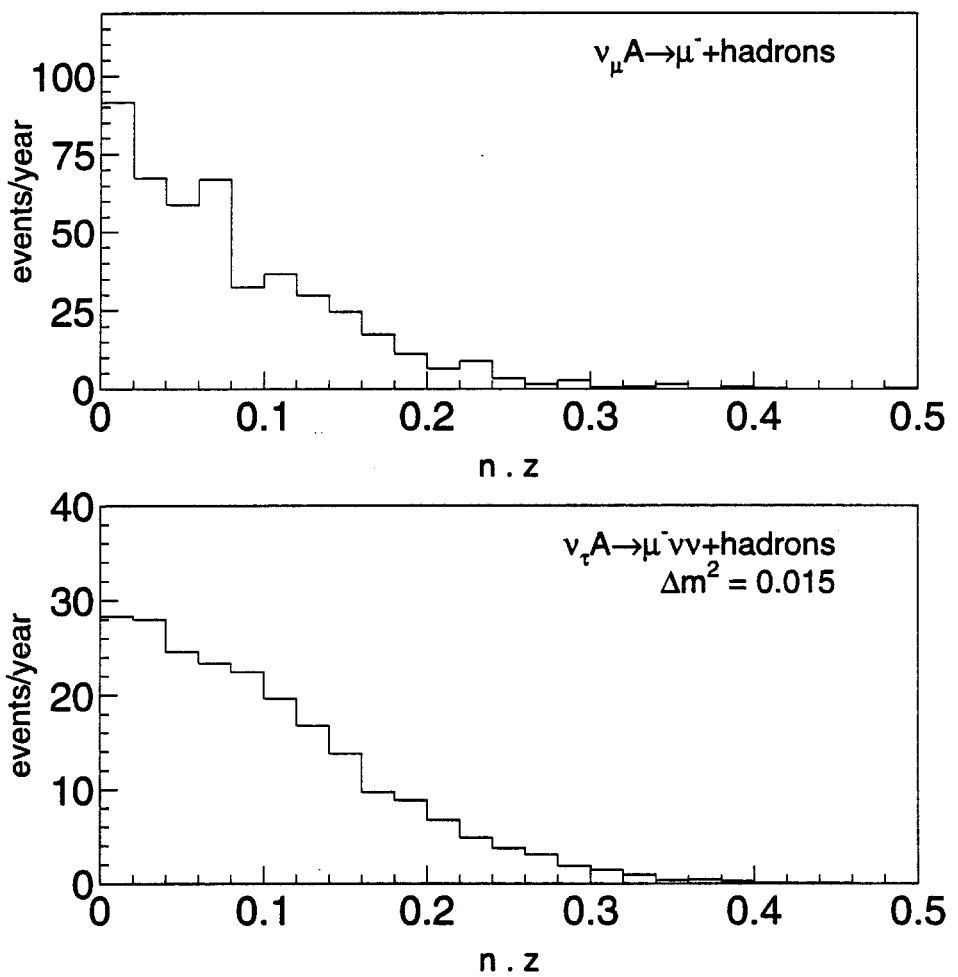

Figure 8.12: $\vec{p_\mu} \bullet \vec{p_{had}} \times \hat{z}$ for ν_τA$\rightarrow$ $\mu^- \nu_\tau \bar{\nu_\mu}$ + *hadrons* and ν_μA$\rightarrow$ μ^- + *hadrons* events. The broader distribution for ν_τ events represents their non-planarity compared to the more planar ν_μ events. The width of the ν_μ distribution is indicative of the angular resolution of the hadron showers.

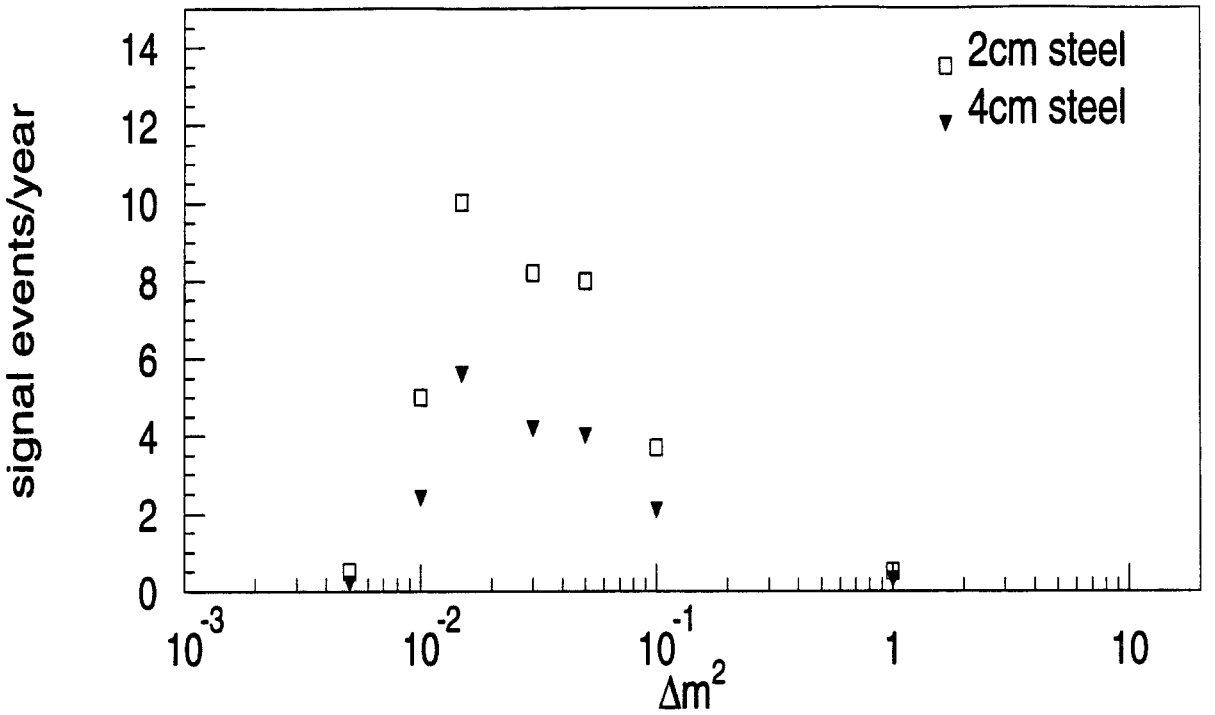

Figure 8.13: Number of $\tau \rightarrow \mu\nu\nu$ signal events remaining (with a background of less than one event) after planarity analysis cuts, as a function of Δm^2 (in eV^2).

the ν_μ beam energy spectrum. If a tail-less narrow band beam were employed much of this background would be absent, and a better separation using these cuts would be achieved. Such an analysis is in progress.

8.5.3 τ detection in quasi-elastic channels

For $\Delta m^2 \approx 0.01\ eV^2$, the maximum of the oscillation probability occurs at an energy of 5.9 GeV. At this energy, around 23% of the ν_τ interactions would be quasi-elastic. Because the q^2 spectrum for quasi-elastic scattering is strongly peaked at low q^2, these events deposit very little energy to the hadronic system and will have simple topologies. For these reasons, we believe that quasi-elastic tau production provides an excellent opportunity to see τ's for the values of Δm^2 and $\sin^2(2\theta)$ suggested by the Kamiokande results.

In events where the recoil proton is visible, one can make strong kinematic cuts on $\phi(\mu - proton)$, the angle in the transverse plane between the outgoing muon and recoil proton. This approach has been investigated in the fine grained Soudan 2 detector and the results are described below in Section 8.9.2. We have attempted to employ this same approach in the much coarser grained MINOS reference detector. The difficulty is that such an approach strongly depends on the ability to see the recoil proton from the quasi-elastic scattering, as well as the ability to separate out such events from the much larger number of resonance production or DIS events which have only one visible hadronic track. Because of the plate thickness in the MINOS reference detector, and the low q^2 of typical quasi-elastic events, this approach will not be effective. However, we have carried out an analysis using

the finer grained concrete detector discussed in Chapter 10. This analysis is described next.

A reconstruction program was written which separated out 'quasi-elastic like' events on the basis of event length, maximum number of hits in one plane, average hits per plane, and a number of other event parameters. The events passing the above cuts were then scanned, and events were kept only if they possessed a clean recoil proton track, with no additional hits. The vertex, proton track, and muon track were then reconstructed by hand, and the angle $\phi(\mu - proton)$ was calculated. We analyzed an exposure of 8 kT years in a concrete detector with 5 cm thick plates. In this sample, no non-τ events passed the cuts $\theta(\mu - beam) > 7^o$ and $\phi < 140^o$, while 3 τ events passed all cuts. There are large errors on the background due to the limited size of the event sample that could be scanned. We conclude from this analysis that a fine-grained detector is required to identify quasi-elastic $\tau \rightarrow \mu$ production in a wide-band beam.

We also attempted to detect quasi-elastic τ production in the mode $\tau \rightarrow e$. Again a reconstruction routine was used to reduce the complete event sample to a smaller sample with topologies characteristic of the production of a single electron. One can roughly distinguish the longitudinal shower development of single electron events from the much larger sample of regular neutral current events by looking at the distribution of hits in the first few planes near the vertex. With a few cuts on hit distributions, we were able to isolate a sample consisting of equal numbers of $\tau \rightarrow e$ and neutral current single π^o events. Without better electron/π^o separation, however, these $\tau \rightarrow e$ events cannot be further separated to statistically significant level.

8.6 Narrow band beam, τ signatures

8.6.1 Introduction

The narrow band beam (NBB) offers an important extra constraint on the ν beam momentum which much improves the signal to background ratio in a number of oscillation tests. The negative feature is, of course, that the overall ν flux and thus event rate is lower than in the wide-band beam. As an example of the gains that can be made, we consider the case of μ production in τ decay. The distinguishing features of events with a τ decaying to a μ result from the fact that neutrinos carry off some fraction of the initial total and transverse momentum and that the τ has a non-negligible mass. As a result, the final state μ in charged current ν_τ events will typically carry less than half of the momentum of the τ, and it can have a momentum below the kinematic limit for the μ from a CC ν_μ interaction of similar beam energy and topology. In the wide band beam the τ signal from this effect is much diluted because of the presence of lower energy ν_μ in the beam.

Several promising signatures for ν_τ events are available in our proposed detector. We consider the following reactions in the narrow band beam:

1. $\tau \rightarrow \mu\nu\nu$ for low y events,

2. Total energy measurements of events with muons,

3. NC/CC ratio measurements,

4. QE-like events with τ decaying to an electron.

There are other interesting final states such as the decay of the τ into $\pi\nu$. We plan to study these final states in the future as we increase the sophistication of our current simulation study.

These analyses have been carried out using the Columbia and the Caltech (GEANT-based) Monte Carlo programs and use the Gaussian smearing of kinematic quantities according to the resolutions described in Section 7.4.

8.6.2 $\tau \rightarrow \mu$ for low-y events

Although the number of ν_μ interactions containing energetic muons will far outweigh any other type of event, the ease of measurement of muons in a very large, coarse detector makes the use of the $\tau \rightarrow \mu$ channel as an appearance signature possible. As discussed in Section 7.4.2, the momentum of muons (both magnitude and direction) is the best measured quantity of any final state particle in ν interactions in this calorimeter. In a very massive coarse-grained detector, precise measurement of the properties of the recoiling hadronic state from a ν interaction is difficult. Fluctuations in hadronic showers produce a relatively large probability that an apparently large missing total or transverse momentum will be found, particularly if the hadrons carry a large fraction of the initial ν momentum. Hence, events where muons *should* be carrying a large fraction of either the transverse or total momentum will provide the cleanest measurements. The detector measurement uncertainties will be minimized for events where essentially only a μ is visible. In this case, the distinguishing feature of $\tau \rightarrow \mu$ events is that the magnitude of the μ momentum will be much smaller than expected for ν_μ events of the same total E_ν. Although the muons also populate larger laboratory scattering angles, this difference is generally small compared to our detector resolution. However these distinguishing features will be washed out if the beam contains a wide range of ν energies since low momentum muons could also be produced by low momentum ν_μ in the beam. We thus require the narrow band beam, as described in Section 8.6.1, to perform this experiment.

This analysis is based on 10,000 CC ν_μ events and 2000 CC ν_τ events generated using a tunable narrow-band beam with central $E_\nu = 11$ GeV and a Gaussian distribution with $\sigma_E = 15\%$. The calculation for the ν_μ's assumes no oscillations and that for ν_τ's assumes maximal mixing; both $\Delta m^2 = 0.01\ eV^2$ and $\Delta m^2 = 0.015\ eV^2$ cases were considered. JETSET has been used for fragmentation of DIS events into final-state hadrons and all final state particles have been simulated in the detector using GEANT with GHEISHA as the hadronic interaction package. The muon momentum resolution is based on the studies presented in Section 7.4.2.

The analysis consists of only two or three simple cuts. First, events with energetic muons are selected. Since we do not have a sophisticated reconstruction algorithm at this point, we require that an event have a muon with true energy greater than 1.5 GeV as the first cut. This very conservative cut ensures that no charged pions will be mistaken for muons. We anticipate that this cut could be relaxed when improved analysis techniques are available with a resulting increase in the fraction of τ events passing the cuts of perhaps as much as 30%. For the events which pass this cut, we then define two experimental quantities. The

first quantity is the fraction of the neutrino energy carried by the muon: $f_\mu = p_\mu/E_\nu$ where p_μ is the experimentally measured muon momentum and E_ν is the nominal peak momentum for the narrow-band neutrino beam. The second quantity is the ratio of hits observed in the first 16 detector planes of the event to the ν energy: $f_h = \mathrm{N_{hits}}/E_\nu$. This is effectively the fraction of energy going into hadrons, but no explicit normalization to energy is made.

Figure 8.14 shows f_μ versus f_h for events which pass the $p_\mu > 1.5$ GeV cut. A dramatic difference in the average distributions for ν_μ and ν_τ events is immediately visible. However, since we are interested in the smallest possible oscillation probability, even very small tails in the distribution for ν_μ's are of concern. Closer inspection of Figure 8.14 reveals several interesting features which are relevant to optimizing cuts. First, in the region between $f_\mu = 0.9$ and $f_h = 2$ there is a cluster of events which result from quasi-elastic scattering and resonant single pion production. These events funnel almost all of their energy into the muon (this value of f_h corresponds to only 6 hits in addition to those from the muon in the first 16 planes), and hence there is very little uncertainty in the total energy coming from fluctuations in measurement of the hadronic energy. In this region, the dominant smearing effect comes from the width of the neutrino energy distribution. On the other hand, near the low energy limit of muon momenta, the dominant resolution effect becomes the hadronic energy resolution as can clearly be seen by the much wider spread in the distribution of f_μ *vs* f_h. In between, the resolution coming from the beam width and that from the hadronic energy smearing will contribute roughly equally to the overall spread in this distribution and tails on the low energy side in either case pose a particular threat to the τ appearance signature.

Based on this Monte Carlo simulation, a cut value requiring that $f_\mu < 0.8 - 0.23 f_h$ allows for a 20% efficiency for all ν_τ events with $\tau \rightarrow \mu$ while only 0.011% of CC ν_μ events pass. Applying this result to an expected 5500 CC ν_μ events in two years of running with a narrow-band beam at 12 GeV, would yield 43 signal events for $\sin^2(2\theta) = 1$ and $\Delta m^2 = 0.015\ eV^2$, or 25 events with $\Delta m^2 = 0.01\ eV^2$. Calculations based on the hypothesis of no oscillations for muon neutrinos predict a background of less than about 1 event in the same period. (Note: the rates for $E_\nu = 12\ GeV$ have been extrapolated from the rate in Chapter 3 for a 45 GeV secondary beam to a 30 GeV secondary beam [60]. Oscillation probabilities have then been scaled from $E_\nu = 11\ GeV$ used in this analysis to 12 GeV, which is appropriate for the 30 GeV secondaries. Explicit calculations for different beam energies with the narrow-band beam are in progress.) The background has been calculated assuming no loss of muon neutrinos from oscillations, so in fact the situation for large mixing would be better than that presented here. In the region of parameter space suggested by the atmospheric neutrino anomaly, there will certainly be no difficulty in observing oscillations. Assuming that the central momentum of the narrow-band beam can be optimized to give maximal oscillation probability for the far detector site, this means that a τ appearance signature will be available using this analysis technique down to about $\sin^2(2\theta) = 0.05$ over a large region of Δm^2.

Detailed understanding of the tails of the beam energy distribution and experimental measurement resolutions are crucial to this analysis. In particular, tails in the signal region at the level of 10^{-3} could limit the available sensitivity to $\sin^2(2\theta) > 0.1$. Hence, detailed understanding of all sources of tails must be pursued. For muon momentum measurement, we believe that this level is already reliably demonstrated, as discussed in Section 7.4.2.

Although the Monte Carlo simulation shows that tails in the hadronic energy fluctu-

ations are manageable at the necessary level, real calorimeters tend to always have worse measurement effects than predicted by Monte Carlo simulations. Fortunately, the worst tails in hadronic energy measurement for gas-sampling calorimeters tend to over-estimate rather than under-estimate the hadronic energy. Under-estimation of the hadronic energy comes from gaps and dead-spaces in the detector. By taking care to require that the primary event vertex is sufficiently distant from any dead space, edges or gaps, these problems should be minimal. In the present analysis, this is assumed to be accomplished by drawing fiducial cuts around all such expected dead spaces so that the resulting fiducial mass of the detector is 70% of the full mass. Checks between the acceptance in the near and far detectors will be important to verify understanding of these effects. Finally, it is possible to guarantee that fluctuation in hadronic energy measurements are minimized by placing a cut on the total number of hits other than those on the muon track. As can be seen in Figure 8.14, placing a cut which requires no more than 10 additional hits (other than the muon track) in the first 16 planes can help to reduce problems coming from hadronic showers by relying much more heavily on the relatively precise measurement of the muon momentum. This cut is only slightly more restrictive than the one already imposed and is attractive since it is possible to be more certain that no ill effects have been suffered due to hadronic shower fluctuations.

The last source of potential tails which could limit this analysis comes from the neutrino beam itself. The most outlying events in Figure 8.14 result from the Gaussian tails of the assumed 15% σ on the beam energy. It is possible that the true beam could in fact have better properties in these extreme tails but it could also be worse. More study will be necessary to verify that there is no large tail introduced from this.

8.6.3 Total energy measurements with muons

The analysis described here is similar to that described in Section 8.6.2 in that it is sensitive to the loss of energy *via* the ν's in the decay $\tau \rightarrow \mu\nu\nu$. In the present treatment we use a different analysis strategy based on the total event energy (μ plus hadronic).

In this and the following two sections, we simulated a narrow band beam of 18.9 GeV with a Gaussian distribution of 15% width. Table 8.4 gives the numbers of events which we expect in a two year run, with and without oscillations.

without oscillations		*with oscillations*	
ν_μ CC	9,000	ν_μ CC	4,500
ν_μ NC	2,400	ν_τ CC	1,700
		$\nu_\mu + \nu_\tau$ NC	2,400

Table 8.4: NBB event rates without (left) and with (right) oscillations ($\Delta m^2 = 0.015\ eV^2$ and $\sin^2(2\theta) = 1.0$.) in a two year running period.

We select events with a clear μ (energy greater than 1.5 GeV). We make no other cuts. In Figure 8.15 we show a plot of the total energy (sum of μ energy and hadron energy) *vs* μ

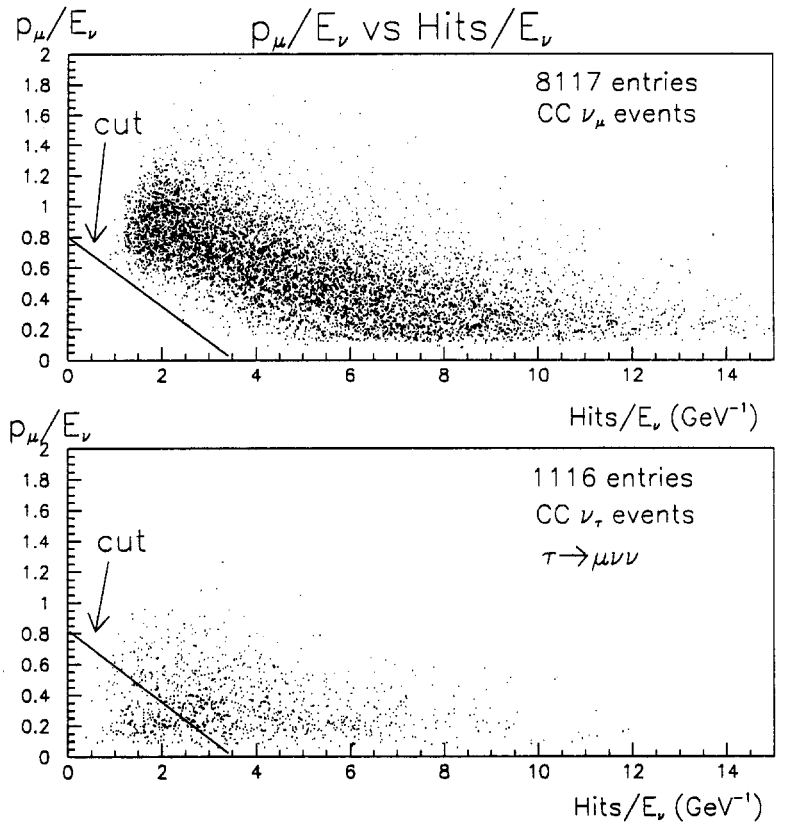

Figure 8.14: Distribution of experimentally measured fraction of neutrino energy carried by the muon vs the fraction of energy in the hadrons (actually hits divided by energy). All plotted events require that $p_\mu > 1.5$ GeV.

energy for ν_μ CC events and for $\tau \rightarrow \mu\nu\nu$. We clearly see a difference in the lower left hand corner which will allow detection of oscillations for sufficiently large mixing probability.

In Figure 8.16 we show the total energy distribution. The solid line is for ν_μ CC events and the dotted line is for the tau decaying into muon. By making the total energy cut of 8 GeV, we have an excess of 67 events with background of 4 events. Assuming we can calculate the background from the near detector with small statistical error, we have a 63 event signal which is clearly observable. The limit on $\sin^2(2\theta)$ at this Δm^2 is approximately 0.06, before the inclusion of systematic errors.

In this analysis, we assumed the NBB as described in Chapter 3. The analysis depends critically on the low energy tails of the NBB. We have not yet demonstrated that our low energy tails would be less than the form we have assumed. We intend to continue working on the design of the beam to obtain the low energy tails we require.

This analysis is also dependent on the hadron energy resolution. A realistic detector may introduce low-energy tails. Our GEANT studies indicate that these tails will not produce a large increase in our $\sin^2(2\theta)$ limit but a full simulation of the events is necessary to finally define these systematic limits.

It is in principle possible to reduce the background by using extra cuts based on the transverse properties of the events [78]. However the relatively poor angular resolution of the hadron shower described in Section 7.4.4 presently limits this analysis. However if further investigation can produce a better algorithm, thus reducing these errors, significant gains may be available.

8.6.4 Near/far comparison of total energy measurements

In this analysis, we study ratios of CC and NC events in a similar approach to that used for the wide-band beam in Section 8.2, but now taking advantage of the additional constraints afforded by the narrow-band beam. To account for the trigger inefficiency, we make a conservative requirement that the total energy of the hadrons must be greater than 1.5 GeV. This cut will be applied to both NC and CC events. Note that trigger inefficiency will be a smaller problem for the narrow-band beam than the wide-band beam since a much smaller fraction of NC events will be below trigger threshold. We also require a 1 GeV cut on the μ energy to ensure that we have a clear μ signal (this is very similar to the analysis approach described for the wide-band beam). For this study it is not critical if a small number of NC events are identified as CC events.

We select a sample of "CC-like" events, containing ν_μ charged current events plus ν_τ-produced τ's with subsequent decay to μ's. ν_μ and ν_τ NC events with a hadron energy greater than 1.5 GeV, and CC events with a μ energy smaller than 1 GeV, are called "NC-like (background)" events. Finally the production of τ and its subsequent decay into all channels other than μ are called "NC-like (signal)". Our exposure with oscillations resulted in 4000 CC-like events, 2200 NC-like (background) events, and an additional 1140 NC-like (signal) events. Assuming that the background can be measured with high statistical accuracy in the near detector, we have 1140 excess events with an error of 60. With 90% confidence, we will reach a $\sin^2(2\theta)$ limit of 0.05, before the addition of systematic errors.

It is instructive to examine the ratio as a function of hadron energy. In Figure 8.17 we show the hadron energy distribution of CC-like, NC-like, and NC-like (signal) and NC-like

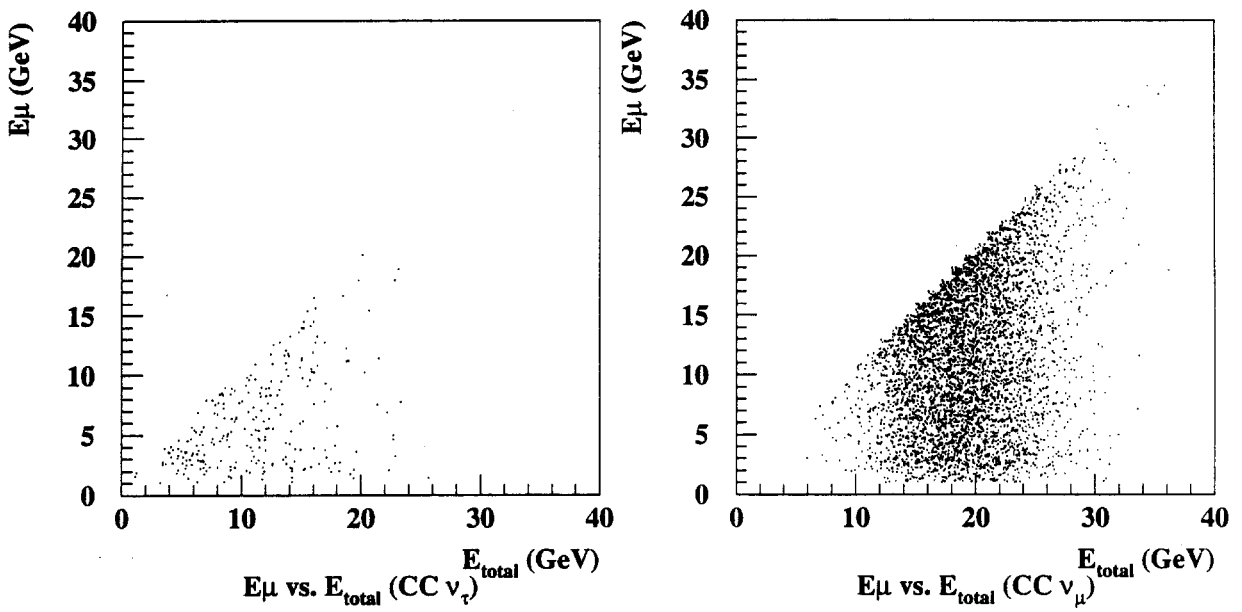

Figure 8.15: Two dimensional plot of the total energy (sum of muon energy and hadron energy) for $\tau \rightarrow \mu\nu\nu$ events (left) and for ν_μ CC events (right).

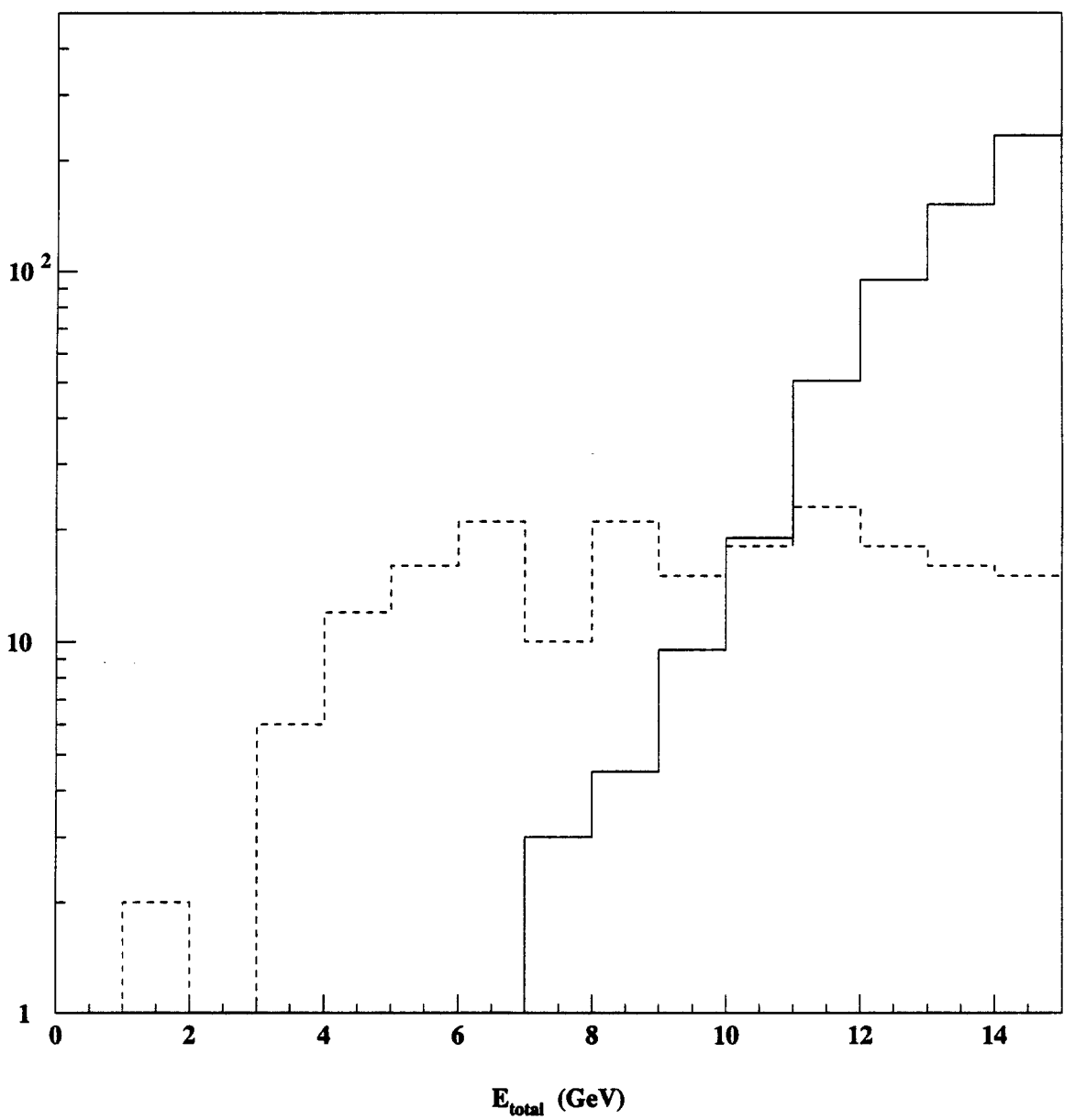

Figure 8.16: Plot of the total energy spectrum. The solid line is for ν_μ events and the dotted line is for $\tau \rightarrow \mu\nu\nu$ events.

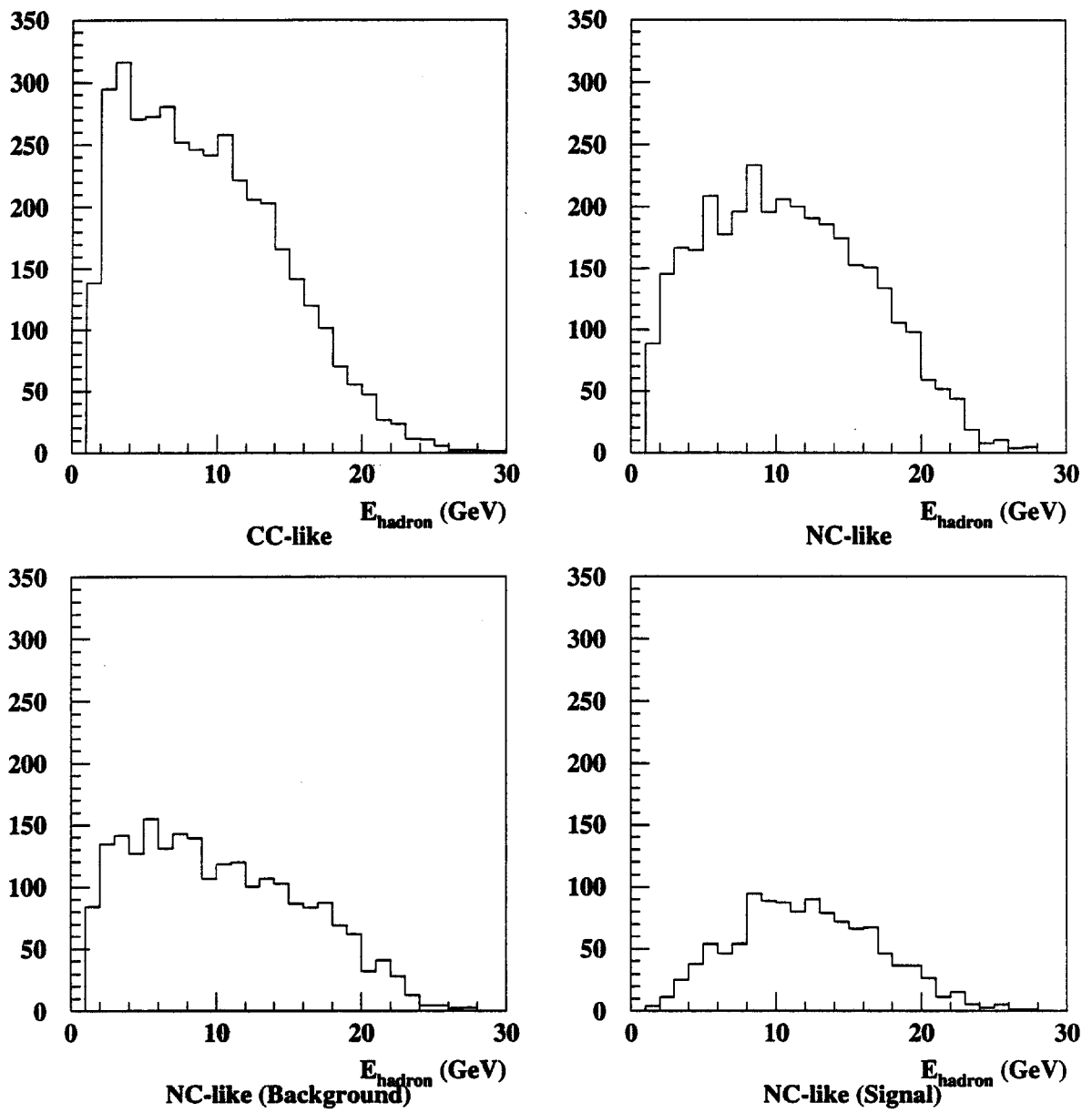

Figure 8.17: The hadron energy distribution of CC-like, NC-like, NC-like (background), and NC-like (signal).

(background) separately.

In Figure 8.18 we show the ratio of

$$[NC - like\ (with\ oscillation)]/[NC - like\ (without\ oscillation)] \tag{8.11}$$

as a function of hadron energy. A clear, statistically significant signal is visible.

An intrinsic systematic uncertainty in this analysis is our ability to subtract the background using the near detector data. We believe that this is a significant advantage of the NBB over the WBB since the pion beam is much better defined and extrapolation of the neutrino flux from the near to far detector is much easier. All of the systematic uncertainties associated with the beam in Section 8.2.3 for the wide band beam will be significantly reduced. A second important source of systematic errors is tails of detector resolutions not taken into account by the Gaussian smearing used in this analysis. Further work will be necessary to establish the lower limit on $\sin^2(2\theta)$ from this effect.

8.6.5 QE-like events: τ decaying into electrons

For this analysis we select events with a single isolated electromagnetic shower unaccompanied by any other visible particle. Our study of Monte Carlo events shows that identification of events with an electromagnetic shower energy greater than 4 GeV (from either an electron or a π^0) should be detected with good efficiency. In this analysis, we assume that π^0 showers cannot be distinguished from electron showers in the MINOS reference detector. We require a muon energy of < 1 GeV to remove charged current events and we apply a cut on the hadron energy < 1.5 GeV to select quasi-elastic (low-y) events. All cuts are made on Gaussian-smeared kinematic quantities. The method of implementing these cuts on actual data quantities is under study.

The signal in this type of event is the quasi-elastic-like production of τ and its subsequent decay into an electron. Backgrounds come from three sources:

1. The production of π^0 events in DIS NC events,
2. Quasi-elastic-like production of electrons from ν_e in the beam,
3. Coherent production of π^0.

Figure 8.19 compares the kinematics of (a) electrons from $\nu_\mu \rightarrow \nu_\tau \rightarrow \tau \rightarrow e$ with (b) the π^0 background. Both scatter plots show the transverse shower energy *vs* the total shower energy. The electron signal in Figure 8.19 (a) consists of 130 events from a sample of 1000 τ's decaying into electrons. The π^0 background in Figure 8.19 (b) consists of the 10 events which remain after cuts are applied to a sample of 10,000 CC + NC ν_μ events. Table 8.5 shows in detail how the π^0 background is reduced by the successive cuts. The ν_e beam background was taken to be 0.7% of the ν_μ flux.

Normalizing to event rates given in Section 8.6.3, we predict a signal of 40 τ's decaying to electrons in a two-year run. The background to this signal would consist of 11 π^0 events after the cuts, plus 1 event from the ν_e beam background. The coherent π^0 production is negligible. We thus expect a signal of 40 ± 7 events, assuming there is no additional uncertainty from the background calculation using data from the near detector.

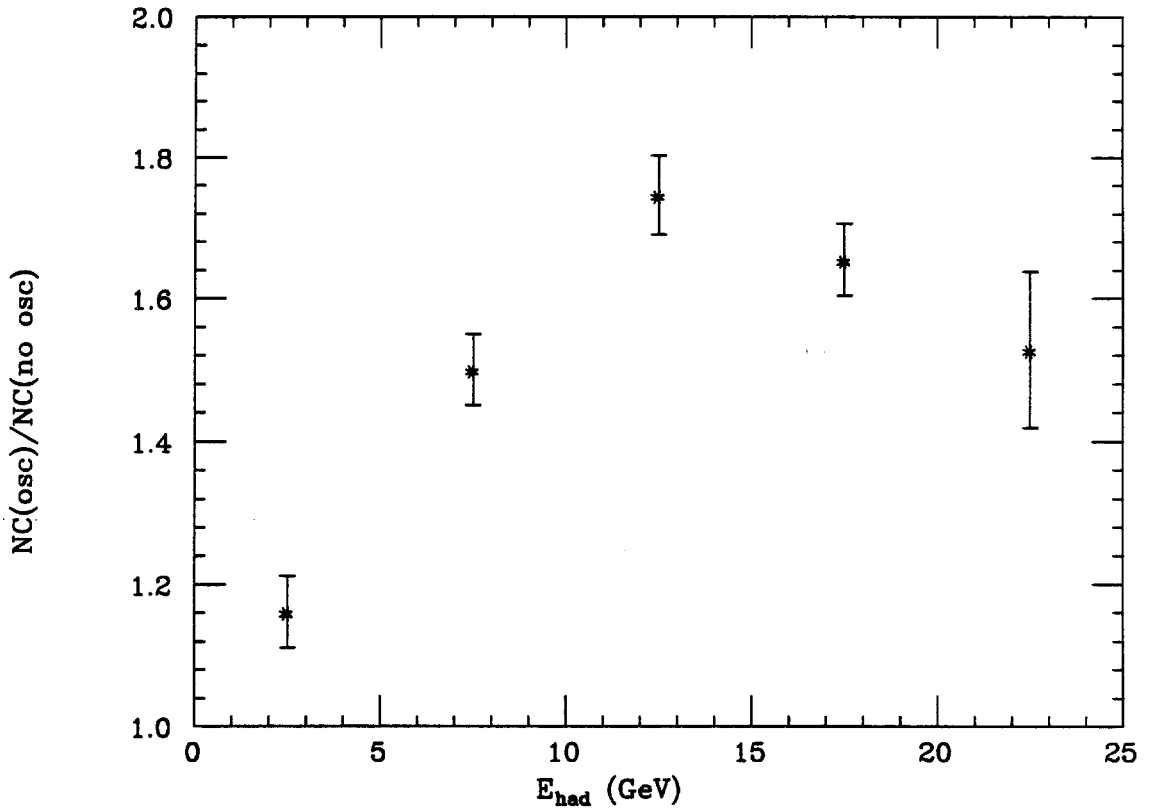

Figure 8.18: The ratio $[NC - like\ (with\ oscillation)]/[NC - like\ (without\ oscillation)]$ as a function of hadron energy.

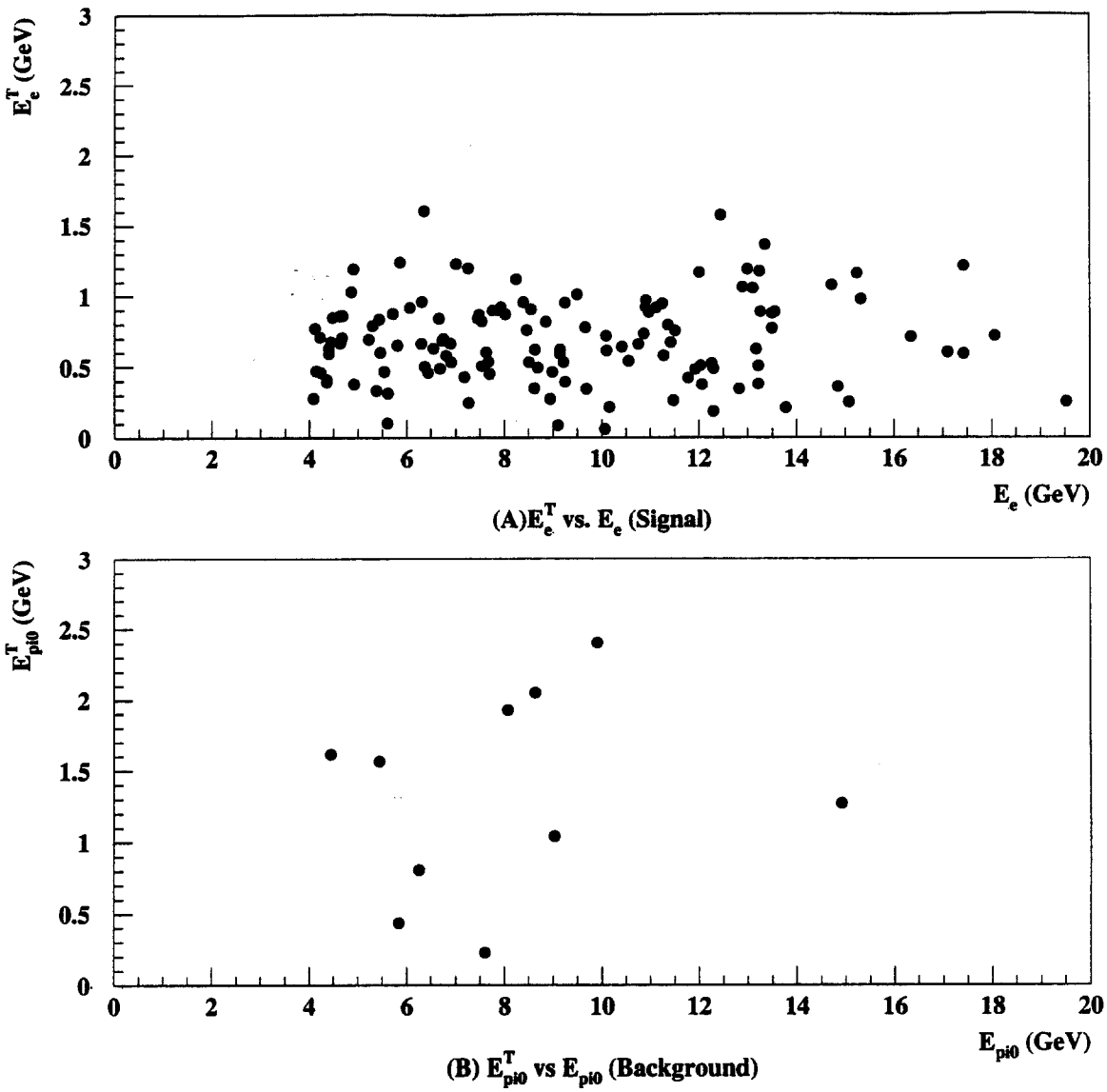

Figure 8.19: (a) Energy *vs* transverse energy of electrons from $\nu_\mu \rightarrow \nu_\tau \rightarrow \tau \rightarrow e\nu\nu$. (b) Energy *vs* transverse energy of π^0's from ν_μ interactions.

Total ν_μ int. (CC+NC)	10,000
$E_\mu < 1GeV$	2,421
$E_\mu < 1GeV$, $E'_{had} < 1.5GeV$	213
$E_\mu < 1GeV$, $E'_{had} < 1.5GeV$, $E_{\pi^0} > 4GeV$	10

Table 8.5: Table showing how the π^0 background reduces as we make cuts to select the QE-like electron signal. E'_{had} is the total energy minus the most energetic π^0 energy.

The transverse energy distributions of signal and background in Figure 8.19 suggest that we may be able to improve the signal/background ratio by applying cuts on the transverse energy. In addition, some fraction of π^0 events may be separable from electrons by topology cuts. Work is in progress to implement these improvements.

We can distinguish whether a possible electron signal arises from $\nu_\mu \rightarrow \nu_\tau$ or $\nu_\mu \rightarrow \nu_e$ oscillations by studying the electron energy distribution. Figure 8.20 shows the distributions for both cases. We find a peak close to the NBB beam energy for $\nu_\mu \rightarrow \nu_e$, while for $\nu_\mu \rightarrow \nu_\tau$ the distribution will be displaced to lower energies due to the energy carried off by the decay ν's. The numbers of events in Figure 8.20 are correctly normalized for $\Delta m^2 = 0.015\ eV^2$ and $\sin^2(2\theta) = 1.0$ for each case.

8.7 $\nu_\mu \rightarrow \nu_e$

8.7.1 $\frac{cc}{total}$ analysis

The previous sections have dealt with $\nu_\mu \rightarrow \nu_\tau$ oscillations. Many of the same tests in the wide band beam can also be used to search for or exclude $\nu_\mu \rightarrow \nu_e$ oscillations. For example, the formalism of the T test discussed in Section 8.2.3 was explicitly calculated for the case of $\nu_\mu \rightarrow \nu_e$ oscillations. If no signal is seen, the limit for $\nu_\mu \rightarrow \nu_e$ oscillations would be 2.25 times more restrictive than the limit for $\nu_\mu \rightarrow \nu_\tau$ oscillations. Limits for a two year run including systematic and statistical errors are shown in Figure 8.25 at the end of this Chapter. Statistical errors for this test are given in Table 8.6.

$< P_e >$	$T'' \pm dT_{stat}$	$n_\sigma^{stat+syst}$
$< P_e > = 0$	$29015/40200 = 0.7218 \pm 0.0022$	0
$< P_e > = 0.1$	$26034/40200 = 0.6543 \pm 0.0024$	18
$< P_e > = 0.2$	$23618/40200 = 0.5875 \pm 0.0025$	35
$< P_e > = 0.345$	$19767/40200 = 0.4917 \pm 0.0025$	60

Table 8.6: Expected event ratios with and without $\nu_\mu \rightarrow \nu_e$ oscillations. Effects due to charm, ν_e background and misidentification are included. Errors in the second column are statistical. The number of sigma combining statistical and systematic errors in quadrature are in the last column.

8.7.2 $\nu_\mu \rightarrow \nu_e$ oscillations using longitudinal cuts in the WBB

The distinguishing characteristic of most CC ν_e events is, of course, an energetic electron in the final state. In an iron calorimeter as proposed here, identification of events with electrons as distinct from events with π^0's is difficult. However, the electrons from ν_e CC events can frequently carry a large fraction of the neutrino momentum whereas the probability for π^0's to carry a large fraction of the neutrino momentum is relatively small. This means that a few simple cuts can give good sensitivity to an appearance signal for $\nu_\mu \rightarrow \nu_e$ oscillations, even though π^0/e separation is not possible.

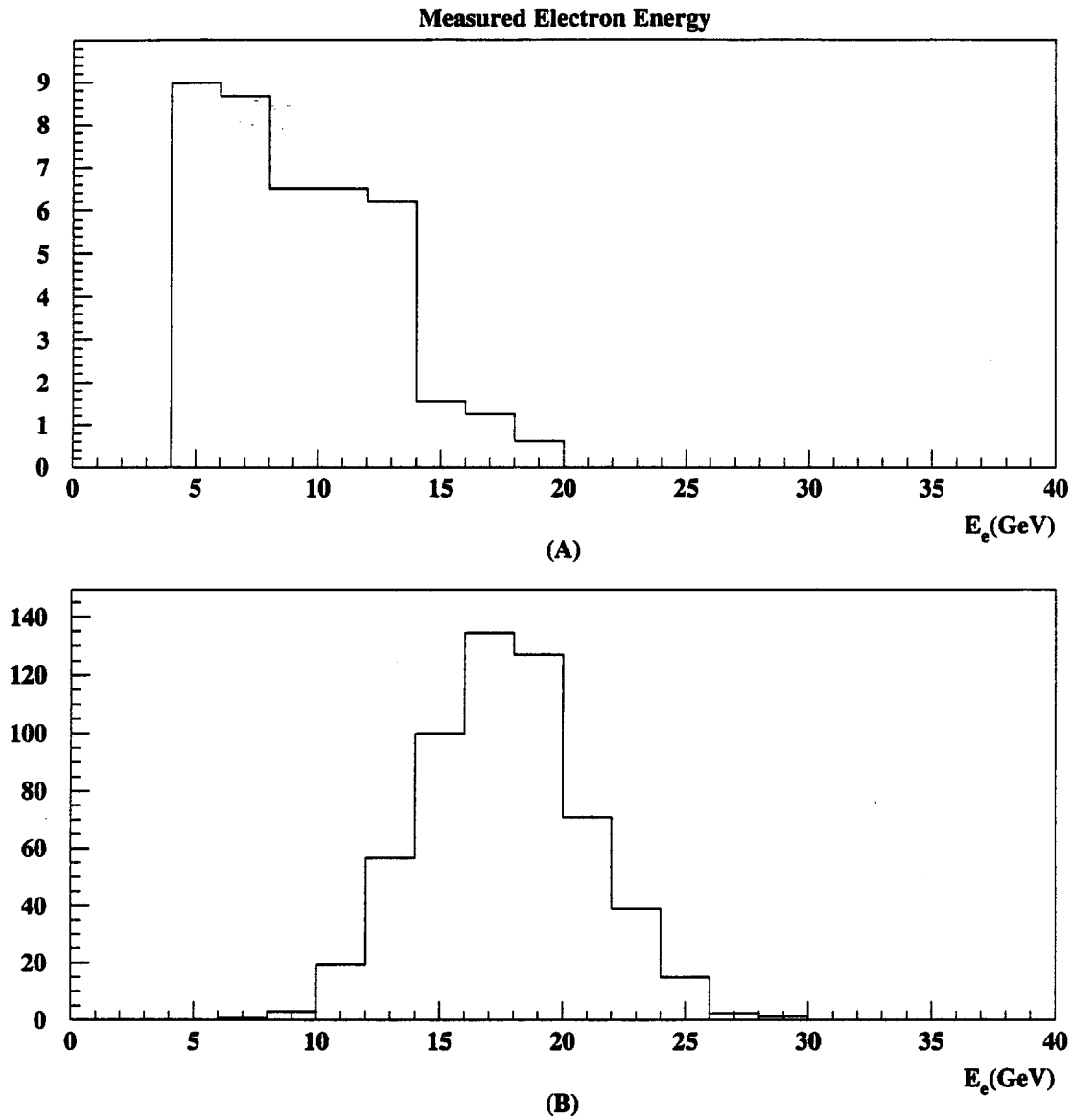

Figure 8.20: Measured electron energy distributions from (a) $\nu_\mu \to \nu_\tau \to \tau \to e\nu\nu$, (b) $\nu_\mu \to \nu_e \to e$.

For this analysis simulation, 2000 ν_e events and 2000 ν_μ events were generated and the final state products were tracked in the 4 cm iron calorimeter using GEANT. The ν_e events for the particular analysis presented here were calculated using $\Delta m^2 = 0.01\ eV^2$ and $\sin^2(2\theta) = 1$. The analysis steps for picking out ν_e CC events are summarized in Table 8.7, which briefly describes each cut and gives the percentage of ν_μ and CC ν_e interactions which pass each one (with cuts being made successively) , assuming the standard wide-band beam distribution. Similar cuts can be devised for different beam energies and/or Δm^2.

The first cut in the statistical identification of ν_e events is to reject all events with any hits beyond the 16th detector plane downstream of the first plane hit in the event. This removes most of the CC ν_μ events. Next, a requirement is imposed that the ratio of hits observed in the first 4 planes of the event over the total number of hits should be greater than 0.75. Since the typical shower maximum for EM showers is around 4-6 radiation lengths and each absorber is about 2.2 radiation lengths thick, this cut strongly favors events which have a significant fraction of the final state energy as EM showers. In addition, it will also remove most of the remaining CC ν_μ events in which the final muon energy was very low. The final cut is to require that the total number of hits in the first four planes is greater than 90 (assuming pulse-height measurement capability is used to correct for multiple hits/strip). This cut removes many low energy NC events and preferentially selects electron events over NC events with π^0's. The background and efficiencies for each cut are presented in Table 8.7. With these cuts, it is estimated that there is about a 10% systematic uncertainty in the efficiency for ν_e CC events to pass the cuts. The remaining ν_μ background comes completely from NC events with π^0's carrying a significant fraction of the momentum of the incoming neutrino. Hence, additional rejection of background will require a more sophisticated approach than the simple one presented here. Furthermore, the reliability of the probability estimate for ν_μ NC events to pass these cuts is limited by the idealized Monte Carlo employed here. Hence, further improvements in this analysis will require a more complete Monte Carlo simulation.

The limit curve in mixing parameter space for this analysis based on a 2 year run with the wide-band beam and a 7 kT fiducial mass for the far detector is shown as curve "B" in Figure 8.25. The 7 kT fiducial mass allows for avoidance of events which are too near an edge or the central coil hole in the calorimeter active detector area.

A final point of interest is that almost all of the remaining ν_μ events which remain as background for this analysis come from neutrinos with energy greater than 13 GeV, while the events from ν_e's have energy less than 13 GeV. Cuts which limit the total number of hits are not very efficient for the ν_e's, but a narrow-band beam can improve the signal/background (at a reduction in statistics) for this particular analysis by about a factor of 3.

8.7.3 Other wide band beam tests for $\nu_\mu \rightarrow \nu_e$

The hadron energy distributions discussed in Section 8.5.1 represent a very powerful test for $\nu_\mu \rightarrow \nu_e$ since the full energy of the outgoing electron would be added to the hadron energy in neutral current events. A much larger effect would be produced than in τ production because there are no missing neutrinos, and electrons are more efficient at producing hits than hadrons. We plan to perform detailed simulations of this analysis in the near future.

Cut	Percentage of all ν_μ events passing cuts	Percentage of CC ν_e events passing cuts
No hits beyond plane 16	26	90
Sum of hits in planes 1-4/ total hits > 0.75	10	49
Sum of hits in planes 1-4 > 90	1.0	27

Table 8.7: Percentage of events passing analysis cuts for a $\nu_\mu \rightarrow \nu_e$ oscillation appearance signature. The cuts are applied successively.

Statistically, the near/far test for $\nu_\mu \rightarrow \nu_e$ oscillations would be improved by 6% compared to $\nu_\mu \rightarrow \nu_\tau$ oscillations due to $B(\tau \rightarrow \mu) = 0.18$ and η (ν_τ/ν_μ cross section ratio) $= 0.31$.

An extremely powerful test for ν_e appearance is the signature $\nu_e N \rightarrow e^- N'$ quasi-elastic scattering. The analysis would be the same as that described in Section 8.5.3 for $\tau \rightarrow e$ decays following ν_τ quasi-elastic scattering, which was done in the alternative concrete detector. In that section the signal to background was found to be 1 : 1, but the signal for the same $\nu_\mu \rightarrow \nu_e$ mixing parameters would be about a factor of 20 higher. A factor of 6 comes from the τ decay branching ratio and a factor of 3 from the relative ν cross sections. For maximal mixing at $\Delta m^2 \sim 10^{-2}\ eV^2$, the signal to background would be about 20 to 1.

8.7.4 $\nu_\mu \rightarrow \nu_e$ oscillations, narrow band beam

The analysis for this reaction is the same as the one we described in Section 8.6.5. However, in addition, for quasi-elastic events the ν energy can be calculated from the momentum and angle of the final state electron.

We calculate that we will observe 570 events with background of 11 events. In Figure 8.21, we show the ν energy distribution of ν_e events. The signal for $\sin^2(2\theta) = 1.0$ is very clear. In the absence of oscillations we will reach a $\sin^2(2\theta)$ 90% confidence level limit of 0.01.

8.8 Rock muons

The rate of observation of muons produced by neutrinos in the rock upstream of the detector ("rock muons") and their relevance for ν_μ oscillations in the Soudan 2 detector has been described in the P–822 document[76]. The front area of the MINOS detector (64 m^2) is similar to the projected area of the Soudan 2 detector (70 m^2), but less than the area of the Soudan 2 shield. However, MINOS has a much larger mass than Soudan 2. Thus, in MINOS the relative importance of the rock muon test compared to the tests involving CC interactions will be less than in Soudan 2. Nevertheless, we are performing detailed simulations of muon production in the rock, their energy loss, transport, and angular distributions. The rock muon measurements can give independent evidence for neutrino oscillations, although they

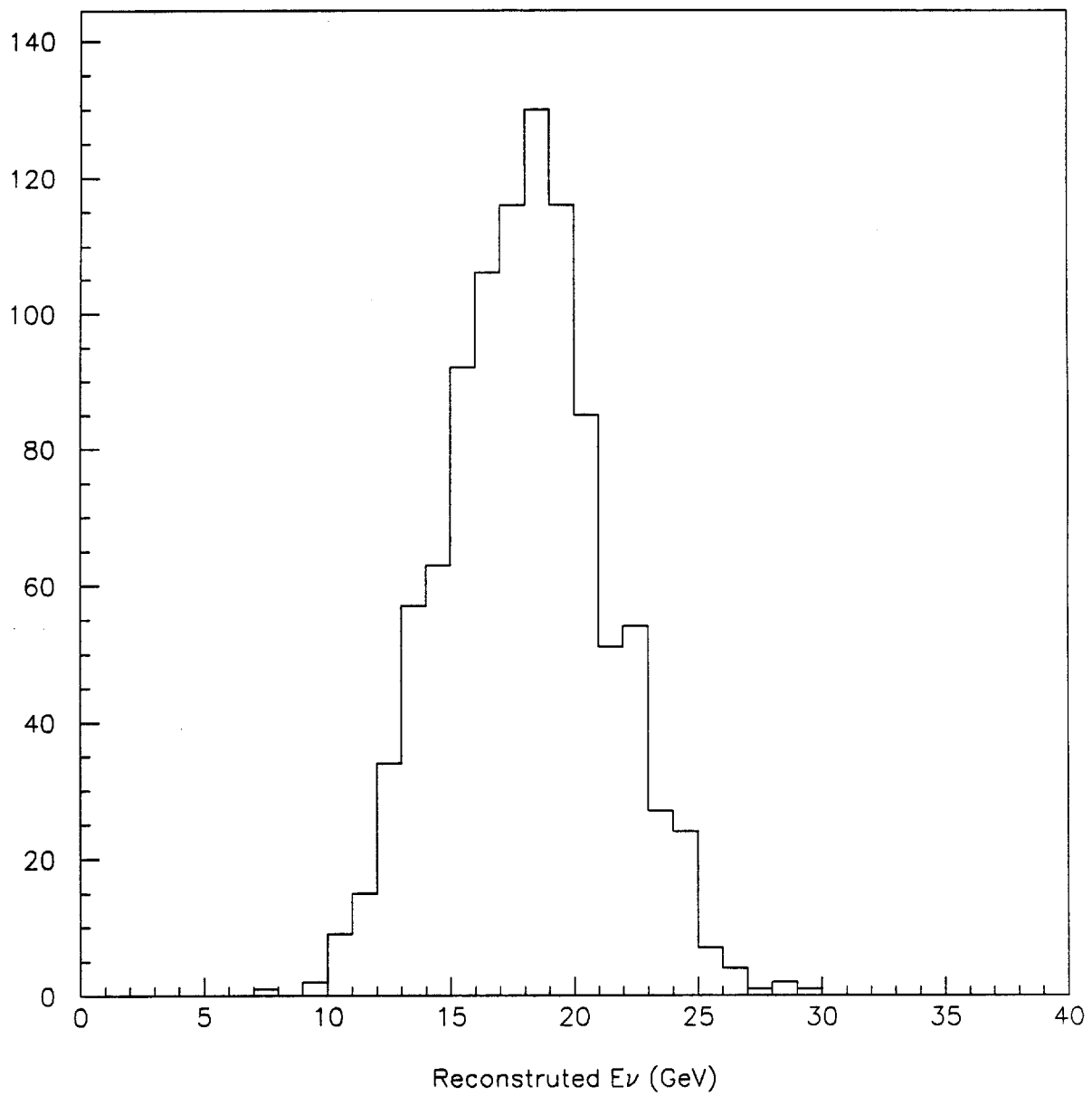

Figure 8.21: Reconstructed electron neutrino energy

may be limited by systematic errors due to uncertainties in the low energy portion of the beam. These errors are likely to be smaller in a NBB experiment and thus the test would be more sensitive than with the WBB.

8.9 Use of Soudan 2

Use of the existing Soudan 2 detector for a long baseline neutrino experiment has been described in considerable detail in previous documents submitted to Fermilab for proposal P–822 [76]. In this Section, we summarize those results which are applicable to Soudan 2 running during the MINOS experiment. In addition, we present here some new results on the search for quasi-elastic ν_τ interactions followed by τ lepton decays. In this Section, previous results have been scaled to the current neutrino running assumptions.

Some assumptions which have changed since the March 1994 update include:

- The length of the neutrino decay pipe is presently planned to be 800 m rather than 320 m. This gives 2.4 times more neutrino events for the same number of protons on target.
- The shield enhancement and toroid which were proposed in P–822 are not envisaged as part of the MINOS reference detector. The rate of rock muons will thus be reduced, and the increase in acceptance which the toroid had provided will not be realized.

As in the P–822 proposal, twenty Soudan 2 modules from the existing detector will be brought to Fermilab as a near detector. This will reduce the size of the far detector to 25 halfwalls (from 28), with a total mass of 840 tons.

The increased neutrino flux more than compensates the other losses. The lack of the toroid prevents the use of the test on total visible energy described in Section 3 of the March 1994 update. However, the MINOS detector will do an excellent job on that measurement, and there is no particular advantage in using a fine grained detector for that test. It is possible that there will be an opportunity to put a prototype magnetic detector behind Soudan 2 as the new detector design evolves, and regain some magnetic measurement capability. The incremental cost would be small, but we have not developed a specific plan so we do not consider this option further here.

8.9.1 $\frac{cc}{total}$ test

The event rates now expected in Soudan 2 are shown in Table 8.8. Note that the ratio $R_{n/f}$ for the near/far test has very small statistical error, but that we have assumed a 4% systematic error on knowledge of the beam at the far detector, calculated from the measurement at the near detector (Section 8.4). Without the far detector toroid, the misidentification matrices at the bottom of page 5 in the March 1994 update are relevant. As a reminder, these are based on a full event simulation in the detector, the creation of data files similar to actual data, and processing by a track reconstruction program. The larger acceptance in the smaller near detector is due to the use of a restricted fiducial volume cut, made possible by the high near-detector event rate.

For the Soudan 2 experiment, the event identification parameters defined in Section 8.2 are: $F_{cc} = 0.54$, $F_{cn} = 0.024$, $F_{nn} = 0.35$, $F_{nc} = 0.070$, $f_{cc} = 0.91$, $f_{cn} = 0.038$, $f_{nn} = 0.58$, $f_{nc} = 0.097$.

	$P_\tau = 0$	$P_\tau = 0.1$	$P_\tau = 0.2$	$P_\tau = 0.345$
R''	$\frac{512}{1950} = 0.262 \pm 0.013$	$\frac{550}{1780} = 0.308 \pm 0.015$	$\frac{583}{1610} = .362 \pm 0.018$	$\frac{635}{1363} = 0.466 \pm 0.022$
$R_{\frac{\mu}{\nu}}$	$\frac{17000}{4840} = 3.51 \pm 0.057$	$\frac{15300}{4570} = 3.35 \pm 0.056$	$\frac{13600}{4290} = 3.17 \pm 0.055$	$\frac{11100}{3900} = 2.86 \pm 0.053$
$R_{n/f}$	$\frac{1.0\times10^8}{17000} = 5880 \pm 240$	$\frac{1.0\times10^8}{15300} = 6540 \pm 267$	$\frac{1.0\times10^8}{13600} = 7350 \pm 301$	$\frac{1.0\times10^8}{11100} = 8980 \pm 369$

Table 8.8: Rates for $R'' = nc/cc$; $R_{\frac{\mu}{\nu}}$ = Rock muons/contained vertex ν events; and $R_{near/far}$ = near/far event ratios. Rates are for the existing detector and include misidentification, charm and ν_e's. The column with P=0.345 corresponds to near maximal mixing as suggested by the Kamiokande data.

Systematic errors on the neutral current to charged current ratio are described in Section 2.4 and Table 3 of the March 1994 update. Since these original calculations were performed, we have obtained higher statistics on the beam simulation and have been able to lower our estimate of the systematic error on the ν_e background correction. Other beam-related systematic errors are slightly worse for the 800 m decay pipe than for the original 320 m pipe. We conclude that for a two year run, results in the Soudan 2 detector are not limited by systematic errors. We find $dP_\tau^{stat} = 0.0285$, and $dP_\tau^{syst} = 0.0071$. Limit curves for the Soudan 2 experiment are shown in Figure 8.22.

8.9.2 ν_τ quasi-elastic events

Section 5.8 of the October 1991 Proposal [76] discussed ν_τ quasi-elastic scattering followed by τ lepton decay as a potential ν_τ appearance signature. Recent progress in detecting events of this type in the very fine-grained Soudan 2 detector is presented here.

$\tau \rightarrow \mu$

Quasi-elastic and other low multiplicity events are particularly useful in the Soudan 2 detector since all outgoing particles can often be individually identified. In quasi-elastic scattering the typical q^2 transfer to the struck nucleon is small. The outgoing lepton retains most of the energy of the incident neutrino and typically proceeds in a direction close to the beam direction. One can place an effective cut on $\phi_{\mu-proton}$, the angle between the outgoing muon and the recoil proton in the plane transverse to the beam. For muons produced from ν_μ charged current interactions, the transverse momentum from the muon should balance that

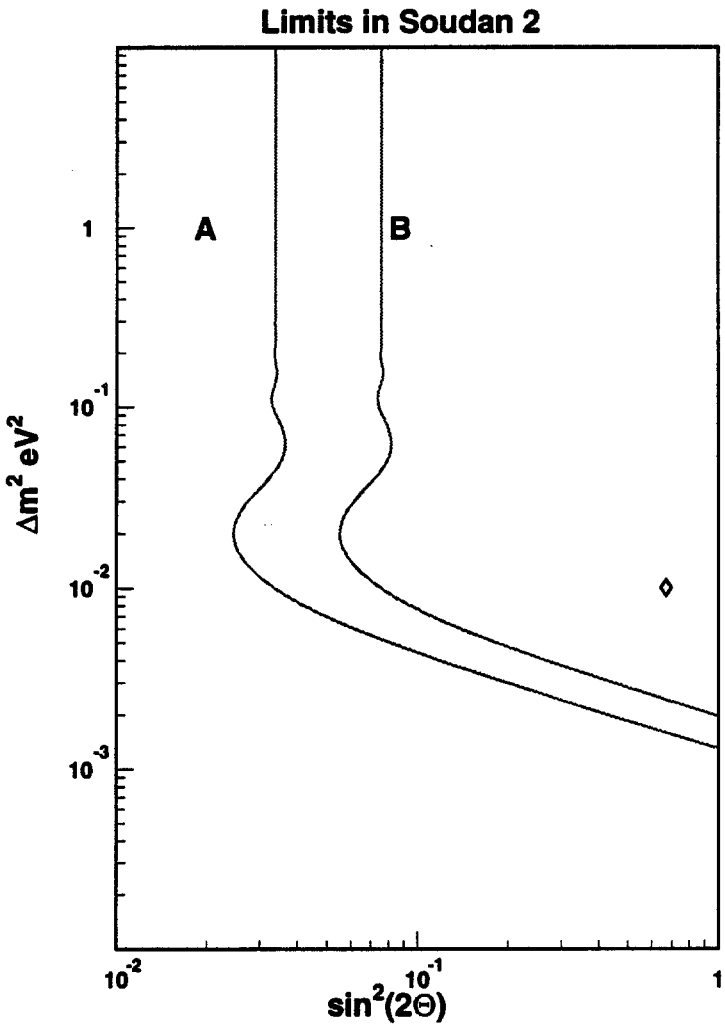

Figure 8.22: Limit curves for two years using the Soudan 2 detector, including systematic and statistical errors. Curve "A" is the limit for $\nu_\mu \rightarrow \nu_e$ oscillations and curve "B" is the limit for $\nu_\mu \rightarrow \nu_\tau$ oscillations.

of the proton, hence in the transverse plane the muon and proton should be back to back. Muons coming from tau decays, on the other hand, do not necessarily balance p_t with the recoil proton. For example, in the limit of $q^2 \rightarrow 0$, the outgoing tau proceeds along the beam direction, and the angle in the transverse plane between the recoil proton and the muon from the tau decay will be essentially random. Figure 8.23 shows the distribution of this angle, $\phi_{\mu-proton}$, for muons from ν_μ charged current interactions and muons from tau decays, where the angle between the outgoing muon and the beam direction is greater than 7°. The normalization in Figure 8.23 is arbitrary. The struck nucleon was given an initial Fermi momentum selected from the Bodek and Ritchie distribution [84]. Intranuclear rescattering can occur as the recoil nucleon emerges from the target nucleus, this was modelled using the INTRANUKE library of routines [85]. In addition, tau decays were generated with the TAUOLA package to produce the correct angular distributions for the outgoing muons [86]. By placing a cut at $\phi_{\mu-proton} < 125°$, and normalizing to the correct number of events we expect to obtain in a two year Soudan 2 run, we find that this test would allow us to identify ≈ 4.5 tau events with a background of ≈ 1.2 for oscillation parameters of $\Delta m^2 = 0.01\ eV^2$, $sin^2(2\theta) = 1.0$.

$\tau \rightarrow e$

Quasi-elastic and resonance tau production followed by the decay $\tau \rightarrow e$ will be identified by the presence of an energetic electromagnetic shower accompanied by very little hadronic activity. The two main sources of background to this channel come from the 0.7% ν_e in the beam, and from neutral current events in which most of the hadronic energy goes into a single π^o which is subsequently mistaken for an electron. In the Soudan 2 detector, most neutral current events have a clearly identifiable hadron track. We make the following cuts to reduce background:

1. We require $E < 10\ GeV$. The distribution of shower energies for ν_e-produced quasi-elastic and resonance production events is relatively flat with energy, while for $\Delta m^2 = 0.01\ eV^2$ electromagnetic showers from τ decays will typically have $E < 10\ GeV$.

2. We require 75% of the hits in the event to be within 3 and 10 radiation lengths from the vertex.

3. We require the angle between the reconstructed shower direction (using all the hits in the event) and the beam direction to be less than 15°. Only 18% of neutral current resonance production events have a reconstructed shower direction within 15° of the beam direction while 72% of $\tau \rightarrow e$ quasi-elastic and resonance production events have a reconstructed direction within 15° of the beam direction.

We believe that a rejection factor for neutral current events of 5×10^{-3} is attainable with moderate π^o/electron separation capabilities in Soudan 2, leaving a $\tau \rightarrow e$ efficiency of 50%. We find a signal of about 15 events with a background of about 9 (7 neutral current + 2 ν_e) in two year's running with oscillation parameters of $\Delta m^2 = 0.01\ eV^2$, $sin^2(2\theta) = 1.0$.

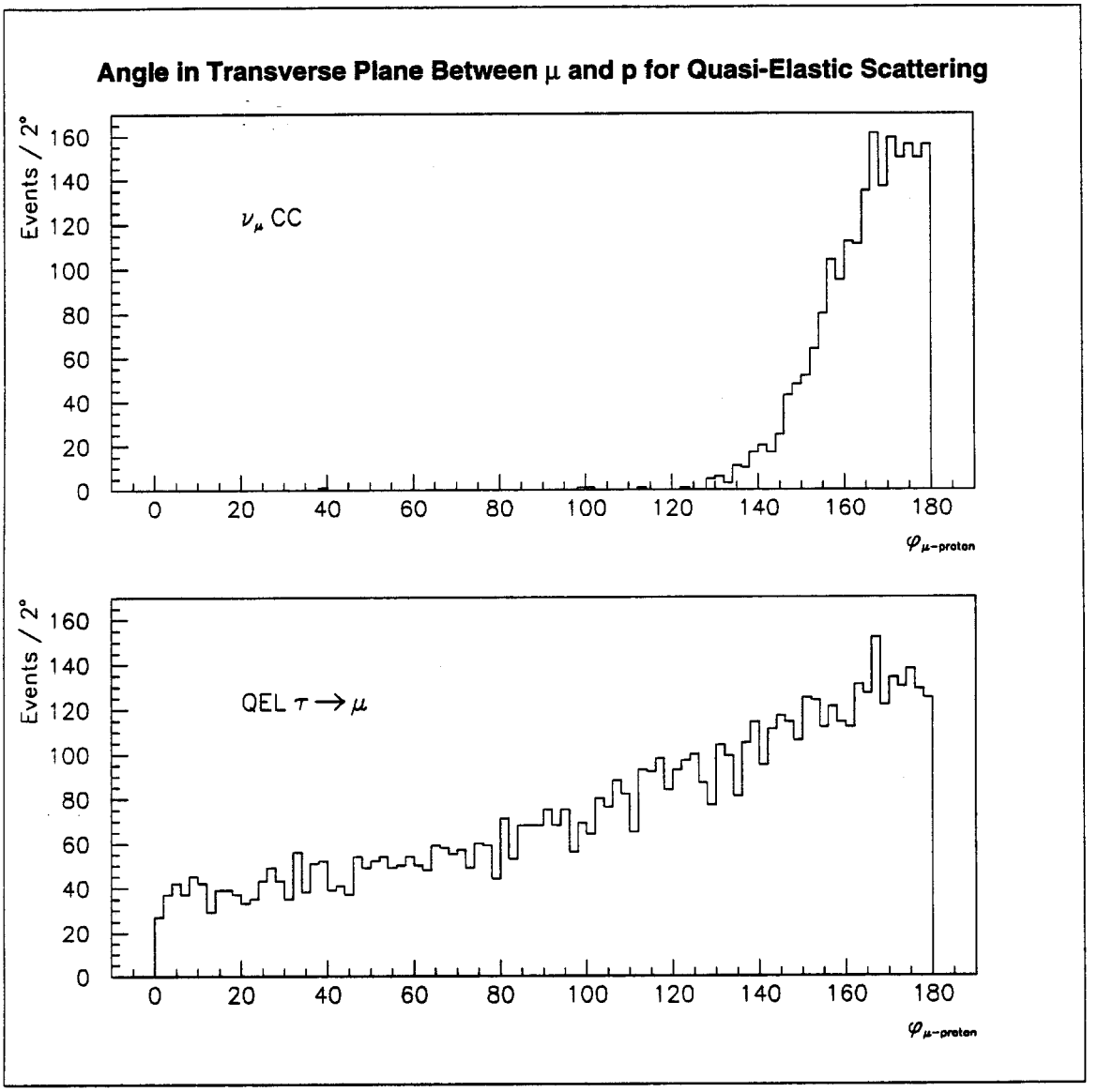

Figure 8.23: Distributions of azimuthal angle between the μ and p in (a) ν_μ quasi-elastic events (background) and (b) ν_τ quasi-elastic events followed by $\tau \rightarrow \mu\nu\nu$, in the Soudan 2 detector.

8.10 Summary and discussion

The MINOS experiment offers an opportunity to search for neutrino oscillations in the region of parameter space $\Delta m^2 > 10^{-3}\ eV^2$ and $\sin^2(2\theta) > 10^{-2}$. This program fully and unambiguously covers the region of parameter space for neutrino oscillations suggested by the atmospheric neutrino deficit.

We emphasize that our experimental program is able to clearly distinguish between oscillations into ν_τ or ν_e, or into an equal mixture of both. Furthermore it is able to do so by requiring internal consistency for a given hypothesis among several independent channels. How such an analysis might proceed is described below.

In the absence of any new information pointing to specific values of the parameters Δm^2 and $\sin^2(2\theta)$, we would initiate the program with the WBB running. We assume that this will still be the case when the MINOS experiment is ready to begin operation. The statistical analyses which would provide evidence for oscillations most quickly are the $\frac{cc}{total}$ test, ν_μ charged current total energy test, and the near/far test. The charged current total energy test would give a clean determination of Δm^2. The limits which are achievable through these tests in a two year run with the WBB, when oscillations are interpreted as $\nu_\mu \rightarrow \nu_\tau$, are shown in Figure 8.24.

When interpreted as $\nu_\mu \rightarrow \nu_e$ oscillations, the parameters derived from the positive signal in the last two tests would be identical to those obtained under the $\nu_\mu \rightarrow \nu_\tau$ assumption. The $\frac{cc}{total}$ test, however, for the same parameters, would predict an effect 2.2 times larger for oscillations into ν_e. This is illustrated in Figure 8.25, where we show that this test gives a better limit for oscillations into ν_e than into ν_τ. An independent test which could distinguish between these two hypotheses is the search for the $\nu_\mu \rightarrow \nu_e$ oscillations using the longitudinal cuts. There the effect is about a factor of 20 greater for the $\nu_\mu \rightarrow \nu_\tau$ hypothesis.

If the signals are relatively large ($\sin^2(2\theta) >\sim 0.1$), the $\tau \rightarrow hadrons + \nu$ test would provide a specific τ appearance signal. This signal would also be very different for the case $\nu_\mu \rightarrow \nu_e$. For very large values of $\sin^2(2\theta)$, consistent with the Kamiokande atmospheric neutrino result, a signal could be seen in the planarity analysis and the Soudan 2 detector would be sensitive to τ signals in the quasi-elastic channels.

A completely independent confirmation and/or improved measurement of the oscillation parameters could then be obtained from the NBB running. Using the Δm^2 value obtained from WBB running, we would tune the beam energy to maximize the effect of oscillations. Definitive signatures would be seen in $\tau \rightarrow \mu\nu\nu$ decays and in the NC(far)/NC(near) test as a function of hadronic energy if $\sin^2(2\theta) >\sim 0.05$. Clearly, the $\nu_\mu \rightarrow \nu_e$ oscillation scenario would give a null result in the $\tau \rightarrow \mu$ decay test and a larger effect in the NC(far)/NC(near) test. Other tests, applicable to both the WBB and NBB, would be much cleaner because of the lower background. The disappearance test (near/far comparison) might be possible even at lower values of $\sin^2(2\theta)$. As a consistency check, the beam could then be tuned to an energy where minimal effect is expected. If $\sin^2(2\theta)$ is large, *i.e.* > 0.1, only few months of running at each energy would be required for a definitive answer.

We are, of course, continuing simulation work both to refine our search methods and to investigate the possibilities of the different options for the detector discussed above. In particular we are studying finer granularity detectors to try to improve our experiment's performance in the $\tau \rightarrow e$ channels which are poorly separated from background in a 4 cm

steel plate MINOS reference detector.

In Figure 8.3 we show the limit curve for a two year run using the $\frac{cc}{total}$ test for $\nu_\mu \rightarrow \nu_\tau$. We have shown both the expected limit curve with our present estimate of systematic errors "B", and a curve with only statistical errors "A". As discussed earlier in this Chapter, we will continue to improve the detector design to minimize systematic errors in order to achieve the greater reach of curve "A". In Figure 8.22 we show the limits for $\nu_\mu \rightarrow \nu_\tau$ and $\nu_\mu \rightarrow \nu_e$ oscillations for the $\frac{cc}{total}$ test in just the Soudan 2 detector. The more sensitive tests in the MINOS detector are shown in Figure 8.24 for $\nu_\mu \rightarrow \nu_\tau$ oscillations and in Figure 8.25 for $\nu_\mu \rightarrow \nu_e$ oscillations. All of these curves represent 90% CL upper limits. Four σ effects would be seen for parameters a factor of 3 to the right of each limit curve.

The MINOS experiment has a number of options for follow-up running after the initial wide-band and/or narrow-band exposures described above. Our choice among these would of course depend on the knowledge of neutrino oscillations at the time, and in particular on the initial results from our own experiment. These additional scenarios include:

- Antineutrino running would allow the first tests of CP violation in the lepton sector [51], although the event rate will be much reduced due to the lower flux and lower cross section.

- Running with a different proton energy, or different focusing devices, would change the energy spectrum of the neutrino beam. This might allow sensitivity to be optimized for particular neutrino oscillation tests, as well as providing valuable studies of beam-associated systematic effects.

- If no evidence for oscillations is found in our initial running, we will need to determine if systematic errors on the most sensitive tests can be reduced to justify further running. Statistical sensitivity in $\sin^2(2\theta)$ will grow with the square root of the number of events in the absence of systematic errors. Of course, if clear appearance signatures are found, the sensitivity will grow linearly with running time.

The discovery potential for neutrino oscillations and the exclusion plots that we can establish in the absence of oscillations are closely linked. For the MINOS experiment, the appearance signatures do not by themselves provide sensitivity at as low values of $\sin^2(2\theta)$ as the $\frac{cc}{total}$ test. However, at higher mixing values, we have the capability of **simultaneously finding evidence for neutrino oscillations in more than ten different tests**. Such a consistent measurement of neutrino oscillations would be a compelling discovery.

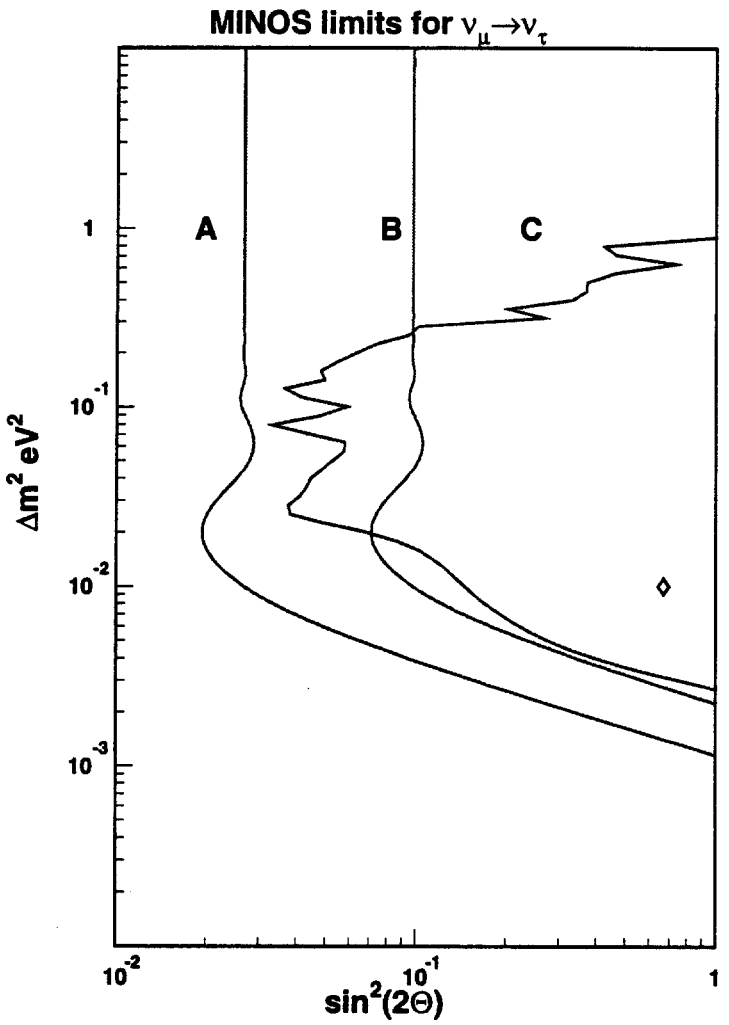

Figure 8.24: MINOS two year 90% CL limit curves for $\nu_\mu \rightarrow \nu_\tau$ oscillations. Curve "A" is for the $\frac{cc}{total}$ test. Curve "B" is for the near/far rate comparison and is dominated by 4% systematic error. Curve "C" comes from the total energy measurement test. The diamond point shows the Kamiokande best fit parameters.

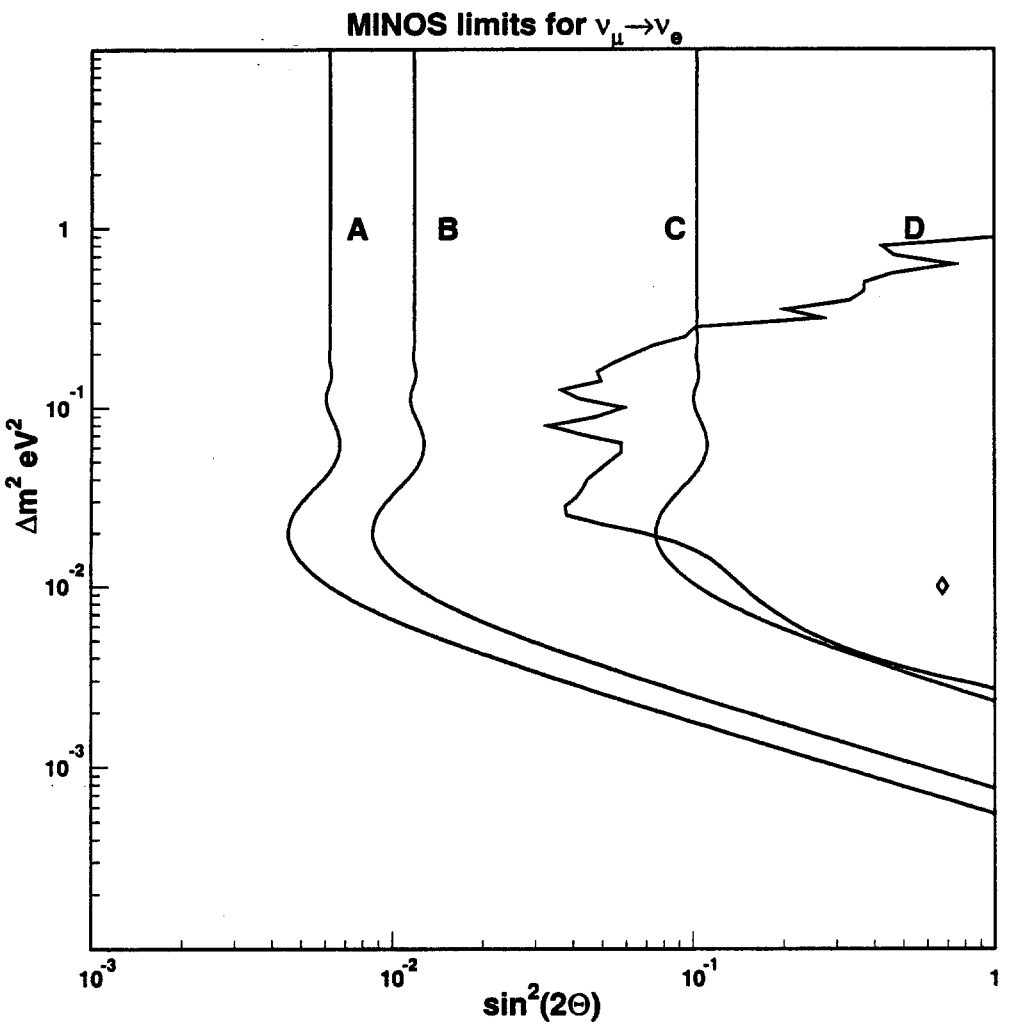

Figure 8.25: MINOS two year 90% CL limit curves for $\nu_\mu \rightarrow \nu_e$ oscillations. Curve "A" is for the $\frac{cc}{total}$ test. Curve "B" uses longitudinal cuts. Curve "C" is for the near/far rate comparison and is dominated by 4% systematic error. Curve "D" comes from the total energy measurement test. Curve "B" is the statistical limit, and the other three curves combine statistics and estimated systematic error. The diamond point shows the Kamiokande best fit parameters.

Chapter 9

Nonaccelerator Physics Opportunities

9.1 Introduction

The construction of the large, underground MINOS tracking calorimeter adjacent to the existing Soudan 2 detector will substantially enhance the opportunities for nonaccelerator physics studies at Soudan. Topics that can be investigated include atmospheric neutrino oscillations, cosmic ray muon studies, searches for neutrino point sources, and searches for magnetic monopoles and other exotic particles. These studies will exploit unique features of the MINOS far detector. In particular, its large area, magnetic field, thickness and granularity will allow rough energy determination for muons in the TeV range. Some attractive features of the Soudan Laboratory include moderate depth (which provides a high cosmic-ray muon counting rate), relatively flat overburden, and surface air-shower detectors which permit coincident surface-underground measures of a single air shower.

9.2 Atmospheric neutrinos in the MINOS detector

Atmospheric neutrino interactions in the MINOS detector can be used to extend our sensitivity down to $\Delta m^2 \sim 10^{-3}$ eV^2. Furthermore, unless the long-baseline experiment discovers neutrino oscillations with oscillation parameters consistent with the atmospheric flavor-ratio anomaly, this anomaly will still require detailed investigation. The MINOS detector will provide unique capabilities for studying atmospheric neutrinos, and will be able to perform a number of measurements which cannot be made by Super-Kamiokande, despite its greater tonnage.

First, MINOS will record a sufficient number of ν_μ CC and ν_e CC contained events to provide an absolute measurement of the flux of each of these neutrinos as a function of zenith angle and neutrino energy up to about $E_\nu = 10$ GeV. We will of course also measure the ν_μ/ν_e ratio from these events over the same energy range, which is predicted with a smaller systematic uncertainty than are the absolute fluxes. Integrating over a range of neutrino energies from several GeV up to about 10 GeV, we will also measure the apparent NC/CC ratio for atmospheric neutrinos.

The MINOS magnetic field can provide charge determination, enabling us to measure the flux of atmospheric muon neutrinos and antineutrinos separately, and providing a constraint on models of the atmospheric neutrino flux. If fast timing information is available either in the detector or in an active 'shield' of chambers surrounding the detector, the toroidal magnetic field in the iron will enable us to measure the momentum spectrum of neutrino-induced upward-going muons from the rock as a measure of ν_μ disappearance.

Even without fast timing, MINOS will be able to address in detail the problem of the ν_μ/ν_e ratio in the GeV region. Most of the muons in this energy range will stop in the detector, and the field will allow us to distinguish μ^+ from μ^-. Electron and, to a lesser extent, hadronic showers should give a pattern of hits which will also allow determination of their directions with reasonable accuracy. Thus we hope to be able to measure the ν_μ/ν_e ratio as a function of energy and zenith angle, although detailed simulations of atmospheric neutrino interactions in the MINOS detector still have to be carried out to verify this expectation.

Hence, MINOS could provide the first differential energy measurement for atmospheric (and astrophysical) muon neutrinos from the range of a few GeV up to a few hundred GeV, and could also separate the neutrino and antineutrino parts of the spectrum.

At even higher neutrino energies for nearly horizontal or upgoing muons we can use the very thick MINOS calorimeter to distinguish statistically between high-energy and low-energy muons by pair production and bremsstrahlung. This gives yet another differential energy measurement and may be of particular interest in searching for possible point sources of high energy neutrinos. (The spectral index for point source objects is expected to be less steep than that of the atmospheric neutrinos, resulting in an emergence of signal above atmospheric background in the range from 1-10 TeV.)

As discussed in Chapter 10, some additions to the detector which are not included in the reference design can increase our capability to do atmospheric neutrino physics. Experience with other underground detectors has shown that an active shield is a great help in cleanly separating real atmospheric neutrino interactions from the interactions of neutrals produced by atmospheric muons in the rock surrounding the detector. Having fast timing available in part of the MINOS detector (perhaps on one detector plane out of ten) would allow us to increase the fiducial volume of the detector by enabling us to distinguish incoming and outgoing muons, and would also separate upward- and downward-going muons, which is necessary for measuring the spectrum of the up-going muons. In the near future we plan to initiate a study of the detailed requirements for the active shield and for fast timing in the MINOS detector.

9.2.1 Interaction rates and trigger efficiency

We have calculated the interaction rate of atmospheric neutrinos in the MINOS detector as a function of energy using the atmospheric flux calculated by Agrawal, Gaisser, Lipari, and Stanev [37], the quasi-elastic cross sections of Llewellyn-Smith [81] with axial vector mass from Reference [87], and deep-inelastic cross sections from Albright and Jarlskog [78]. Our calculation includes only neutrinos with directions within 60 degrees of the normal to the detector plates, since the reaction products of neutrinos at larger angles are not as likely to be well measured.

Clean separation of interaction types in the MINOS detector is possible only for comparatively high-energy neutrinos, so trigger requirements for atmospheric neutrino studies can be similar to those used for beam neutrinos. A trigger might simply require that some number of planes contain at least one hit, or it might require some minimum number of total hits in the detector. Table 9.1 shows the trigger efficiency as a function of various requirements, for neutrino energies above 3.5 GeV. For purposes of the NC/CC study, a combination trigger was defined, as shown at the bottom of the table.

9.2.2 Sensitivity to atmospheric neutrino oscillations

Reference [88] is a detailed study of the NC/CC ratio in a detector very similar to the reference MINOS detector. Using the combination trigger described in Section 9.2.1, and classifying Monte Carlo events as 'muon-like' (containing a long muon track), 'electron-like' (a short, showering event primarily from electron neutrino interactions), 'hadron-like' (a long showering event with no clear muon track; primarily NC interactions), or 'other', we calculate the event rates shown in Table 9.2 for various oscillation probabilities. The oscillation limit curves expected from the atmospheric neutrino ratio for a 30 kT-year exposure are shown in Fig. 9.1.

9.3 Cosmic ray muons

The Soudan 2 detector currently records $\sim 5 \times 10^5$ reconstructable muon events each month by running with 85% livetime and 90% efficiency after run and event cuts. The combined muon counting rate for the MINOS and Soudan 2 detectors will be approximately four times higher, that is, 2.5×10^7 events per year, assuming similar livetime and efficiency. The minimum energy for an air shower muon to penetrate to the MINOS-Soudan 2 depth is ~ 800 GeV.

Most of these underground muons are produced by pion decay in proton or heavy-nucleus-induced cosmic ray air showers. The number of muons in a photon-induced air shower are at least a factor of 10 fewer than in a hadron-induced shower. At higher energies where pion decay is disfavored, a fraction of the underground muons result from prompt decays, for example, from vector mesons and heavy quark states. Most upward muons and a varying fraction of downward muons at large zenith angles are produced by neutrino interactions in the rock around the detector.

Possible cosmic ray underground muon studies include:

- A study of cosmic ray composition by measurement of underground muon rates as functions of multiplicity, muon separation and muon angular distribution. The power of these measurements to distinguish among competing models may be enhanced by correlating these parameters with the characteristics of associated air showers. In addition to composition, the analysis of these measurements is sensitive to very high energy interaction parametrizations. Although this will probably already be extensively studied by MACRO, it is possible that the use of MINOS as a muon calorimeter may add information for very high energy muons.

Minimum Number of Hits	trigger efficiency (percent) CC ν_e	CC ν_μ	CC ν_τ	NC events
0	100	100	100	100
1	100	100	99	92
2	100	100	98	85
3	100	100	98	79
4	100	100	96	74
5	100	100	95	68
6	99	100	94	62
7	99	100	93	58
8	99	100	91	53
9	98	100	90	49
10	97	100	88	46
15	90	99	77	31
20	76	97	69	22

Minimum Number of Planes	trigger efficiency (percent) CC ν_e	CC ν_μ	CC ν_τ	NC events
0	100	100	100	100
1	100	100	99	92
2	100	100	97	77
3	90	100	90	60
4	63	99	78	44
5	43	99	65	31

Combined Trigger (see text)	trigger efficiency (percent) CC ν_e	CC ν_μ	CC ν_τ	NC events
$\geq$ 3 planes OR $\geq$ 2 planes AND $\geq$ 8 hits	99	100	94	65

Table 9.1: Trigger efficiency for various event types and trigger requirements for ν's with energy greater than 3.5 GeV and averaged over all incidence angles out to 60 degrees (2π steradian acceptance).

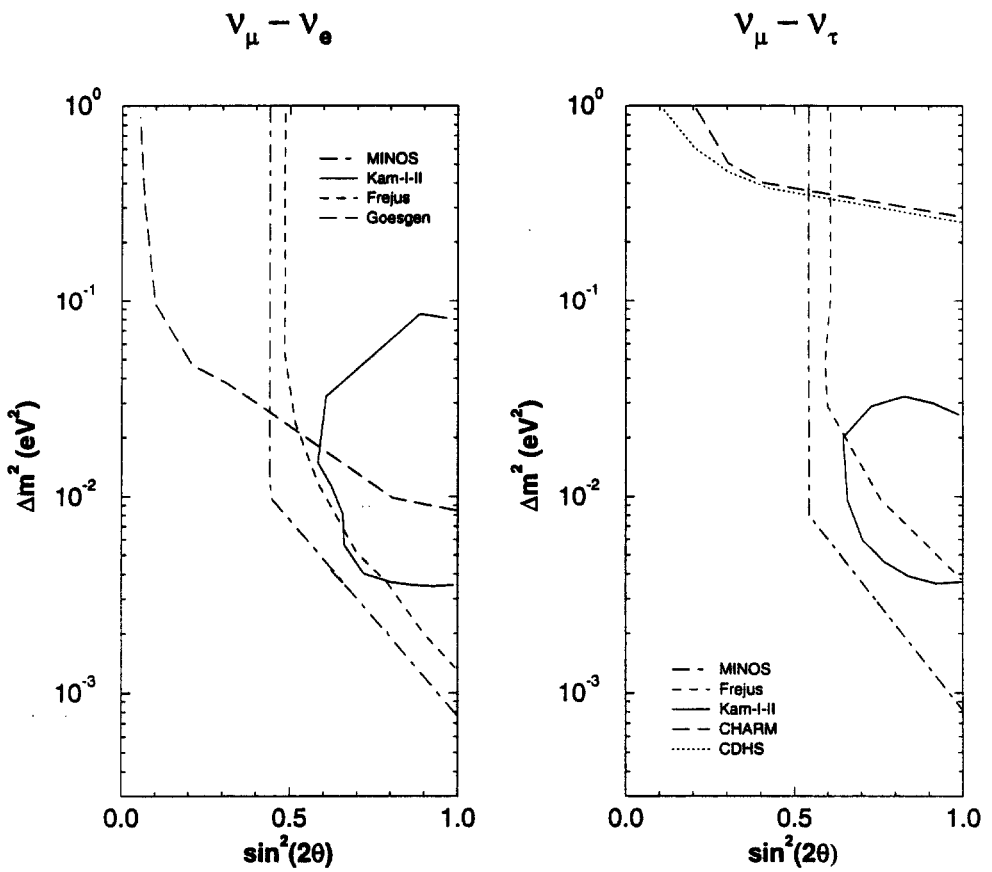

Figure 9.1: Areas of oscillation parameter space ruled out at the 90% confidence level for a 30 kT-year MINOS exposure to atmospheric neutrinos, compared to results from other experiments. Note that the allowed region is to the right of the Kamiokande curves, but is below and to the left of the other curves.

Osc. type →	No Osc.	$\nu_\mu \leftrightarrow \nu_e$	$\nu_\mu \leftrightarrow \nu_\tau$	$\nu_\mu \leftrightarrow \nu_\tau$
$\Delta m^2(\mathrm{eV}^2)$ →		.01	.001	.008
$\sin^2 2\theta$ →		.4	.87	.87
event type or ratio				
'muon like'	410 ± 20	350 ± 18	310 ± 18	310 ± 18
'electron-like'	230 ± 15	290 ± 17	230 ± 15	230 ± 15
'hadron-like'	150 ± 12	160 ± 13	160 ± 13	170 ± 13
h-like/μ-like	$.37 \pm .04$	$.46 \pm .04$	$.52 \pm .03$	$.55 \pm .04$

Table 9.2: Number of events in a 30 kT-year exposure for atmospheric ν's for various oscillation hypotheses. The errors shown are one σ statistical errors only. It is expected that there will be systematic errors of about 8% for the 'hadron-like' sample of events and 2% for the energetic muon and 'electron-like' event samples.

- A search for muon point sources over varying intervals of time. There is no known physical mechanism for such point sources, because most underground muons result from hadron-induced air showers. Stable hadrons are electrically charged and therefore made isotropic by galactic magnetic fields. Nonetheless, there is evidence suggesting both a sustained excess of muons from the direction of the x-ray binary Cygnus X-3 (from the Soudan 1 and NUSEX detectors) and a burst of muons coincident with a Cygnus X-3 radio flare (from the Soudan 2 detector).

- A search for large-scale cosmic ray muon anisotropies. In addition to point sources, previous underground detectors have searched for anisotropies due to the local galactic plane as well as anisotropies due to the motions of the solar system through the galaxy, toward the local supercluster or through the cosmic microwave background radiation. The relatively flat overburden at Soudan will be a benefit to this analysis.

9.3.1 Cosmic ray composition

The composition of the cosmic rays in the "knee" ($\sim$ 10,000 TeV/nucleus) region of the cosmic ray all-particle spectrum has consequences for astrophysical models of particle acceleration and propagation. For example, a model of accretion onto a black hole in the center of an Active Galactic Nucleus predicts an excess of protons around the knee region in the cosmic ray flux [89], while a model of shock acceleration during a supernova blast into a stellar wind environment predicts an excess of heavy nuclei in the cosmic ray flux in the knee region [90, 91]. Unfortunately, the composition at energies above $\sim$ 1000 TeV/nucleus is difficult to measure directly due to the steeply falling spectrum of cosmic ray primaries. The flux of particles with energies greater than 1000 TeV/nucleus is only $\sim 60/\mathrm{m}^2/\mathrm{sr}/\mathrm{year}$. Therefore measurements of cosmic rays in this energy regime require detectors of either very large acceptance or long exposure, neither of which is currently feasible for measurements near the top of the atmosphere or above. Instead, studies of the composition of cosmic ray primaries in this high energy regime can be carried out indirectly through measurements of aspects of the atmospheric cascade generated by the interaction of a cosmic ray primary

with the earth's atmosphere.

Deep underground experiments, such as the investigation carried out with the Soudan 2 detector, attempt to indirectly study the composition of cosmic rays by comparing observations of multiple muon event rates to expectations derived through Monte Carlo simulations using various trial composition models as input [92, 93]. A multiple muon event is one in which two or more nearly parallel, time-coincident muon tracks are observed in the detector. These muons are the decay products of parent mesons which are generated in the hadronic core of the atmospheric cascade. At high energies, massive primaries will generate more muons per event than proton primaries of the same total energy. This is because pion multiplicities are larger from the massive primary. In addition, the pions are more likely to be generated high in the atmosphere where the decay probability is greater than the interaction probability. At the Soudan site, the measurement of the high energy muon component underground is coupled with sampling of the electromagnetic component of the air shower at the surface with a small proportional tube array [94], and a Cerenkov light detector array. A correct interpretation of the cosmic ray composition should yield consistent results using all three experimental techniques in all possible combinations.

The addition of the MINOS detector will improve the current studies of composition at Soudan 2 in several ways. First, the large size of the new detector will decrease the dependence of the composition measurement on the simulation of the muon lateral spread. At the Soudan 2 depth, the mean perpendicular distance of a muon from the core is approximately 12 meters and is therefore comparable to the size of the Soudan 2 detector. The larger size of the MINOS detector will decrease the correction factor for containment efficiency and therefore make the measurement of composition more reliable. Second, the MINOS detector will have increased containment probability for high multiplicity events, which are most sensitive to primary composition at the high energies near the knee region. Third, the absolute rate of muon events will increase by a factor of ~ 5 due to the increased area of the combined detector. This will allow a check on results coming from the large data sample of existing, fine-grained tracking detectors. Finally, we may be able to make use of the calorimetric properties of MINOS to make additional cuts on the data which are unavailable to existing detectors. Since other detectors with good tracking capabilities will already have performed extensive measurements on this subject, this new information may prove to be of particular interest. We need to study this possibility further to evaluate its usefulness.

Monte Carlo simulations of the MINOS detector show that it should be sensitive to multiple muons generated by primary cosmic rays in the energy region 5 - 50,000 TeV/nucleus. This includes the energy region just below and around the knee in the all-particle spectrum. This energy region also significantly overlaps that of direct measurements (which currently extend out to ~ 1000 TeV/nucleus [95, 96]), which allows for calibration of the measurement in the low energy regime.

9.3.2 Point source searches

The search for muon point sources has always been controversial for a number of reasons. First, there is no known physical mechanism for correlating underground muons with a

specific astrophysical source. With the exception of neutrinos from Supernova 1987a, all known astrophysical observations are based on photons carrying energy from the source to earth. Many model calculations and simulations show that photon-induced air showers are very inefficient at producing muons. Less than a few percent of a very high energy photon fluence (energy per unit area per unit time) would appear in the muon channel. Since the efficient large air shower detectors such as CASA have never detected point sources, it would seem unlikely to find them in smaller, less efficient underground muon detectors.

A second reason for skepticism is that past evidence for muon point sources has unexpected properties. For example, both the Soudan 1 and NUSEX detectors reported a possible correlation between underground muons and Cygnus X-3, but in each case the apparent size of the source was clearly larger than the detector angular resolution. For the Soudan 2 data on the 1991 Cygnus X-3 radio flare, the time structure of the data with two high days separated by two low days was arbitrary. In all cases, these data are background limited. That is, there are no clear characteristics of events that can be used to separate signal from background.

A third problem is that reported effects are transient which makes confirmation difficult. For example, Soudan 1 and NUSEX reported excess muons from Cygnus X-3 during the interval 1981 to 1984. Both collaborations agreed independently by 1990 that post-1984 flux from Cygnus X-3 was much reduced. Partially overlapping data from other detectors showed no anomaly for muons from the direction of Cygnus X-3. The Soudan 2 Cygnus X-3 radio flare result was even more transient, lasting only two days. The number of these large flares is small, so a long time may elapse before there is another opportunity to observe one.

Despite all these uncertainties, the striking parallels between the independent Soudan 1 and NUSEX observations argues for an admittedly speculative point source analysis of underground muon data. Indeed, the Compton GRO EGRET detector has shown that there exist more than 30 high energy sources, mostly active galactic nuclei, and that these sources are indeed variable. Although we can and should analyze our data by a search across the sky for muon point sources, a complementary and potentially more sensitive way to proceed is to examine muons from the directions of the known EGRET sources. Indeed, the transient nature of these sources raises the possibility of a temporal cross-correlation analysis between MINOS and EGRET data.

The MINOS and Soudan 2 detectors combined should record about 2.5×10^7 muons per year, about 4 times the flux recorded by Soudan 2 alone and about 50 times the flux of either the Soudan 1 or NUSEX detectors. Since the angular resolution of all these detectors is comparable, the sensitivity is roughly proportional to the square root of the flux. Thus, the MINOS and Soudan 2 combination will be approximately twice as powerful as Soudan 2 alone with the additional advantage of showing that any real effect occurs in each of the two detectors independently but at the same time.

The MACRO detector can, of course, provide complementary information as well. Although MACRO has about twice the detection area as MINOS, the raw data rate is comparable to that of the smaller Soudan 2 due to its greater depth underground. It does, however, provide a greater mean muon energy (by a factor of ~ 2) and this might help to elucidate the underlying physics of any effects discovered in concert. Muon calorimetry information may provide similar capabilities to understand muons from a point source, if observed. The fact that point sources of muons seem to be episodic (if they exist) suggests that it is necessary

to have multiple detectors running over long periods of time to resolve the questions about these sources.

9.3.3 Large scale anisotropies

Although individual sources may have variable flux, large-scale angular flux variations (if they exist) should be relatively constant in time. For example, at GRO EGRET energies, the galactic plane is a strong source of photons. The galactic center is the brightest region of the plane, followed by the Cygnus direction, which is down the local spiral arm, and the anti-center direction, which includes the bright Crab nebula. While one might hypothesize the galactic plane as a source of cosmic rays because of the large number of accreting binaries in the plane, there have also been reports of the galactic plane as an anti-source. The most straight-forward explanation for such an effect, if it were true, would be that some fraction of the cosmic rays are extragalactic in origin and that the higher column mass density in the galactic plane acts as a differential absorber of extragalactic flux.

Another possible source of a large scale anisotropy is the Compton-Getting effect, which characterizes the result when an isotropic flux $\frac{d^2N}{d\Omega dE}$ is transformed into an observer frame moving at velocity β. The result is a dipole anisotropy with a dipole coefficient $D = (2+\gamma)\beta$, where γ is the exponent in the power-law equation $\frac{dN}{dE} = E^{-\gamma}$. For example, for the motion of the solar system through the cosmic microwave background, $\beta = 1.2 \times 10^{-3}$ and $\gamma \sim 3$, so the maximum value of D is $\sim 7 \times 10^{-3}$. The observed effect due to motion through the cosmic microwave background could be much smaller, if only a fraction of the underground muon flux has an extragalactic origin.

The sensitivity of a detector to a dipole anisotropy is $\sigma \sim \frac{2}{\sqrt{N}}$. For the combination of the MINOS and Soudan 2 detectors, the sensitivity is $\sigma \sim 4 \times 10^{-4}$ or 10% of the cosmic microwave Compton-Getting effect per year. Again, in this study, the possibility of comparing data between the two detectors provides a good check on possible systematic effects. Finally, the relatively level overburden at Soudan may allow the systematic error on this measurement to be smaller than for the MACRO detector which is located under the Gran Sasso mountain with its rapidly changing overburden for different azimuthal angles. In addition, due to several subtle effects which can mimic a possible anisotropy, independent checks between multiple detectors with very large statistics may prove useful.

Chapter 10

Evolution of the Detector Design

10.1 Introduction

The reference detector described in this proposal represents a conservative design based on proven technology. We do not believe, however, that it necessarily represents the optimum possible instrument for the physics goals of this experiment, for the total amount of money indicated. The focus of our work during the next 1-2 years will be to improve on this design through detector R&D, further engineering studies, better understanding of various tradeoffs, and more detailed and extensive simulations. Better understanding of the neutrino beams will also be an important input in the effort.

In this Chapter we consider some of the possible improvements in the reference detector. They range from rather radical modifications to more minor changes of the current detector parameters. We group these ideas under several different headings.

10.2 Absorber media and granularity

One of the key choices in the design of the detector is the compromise between total mass and granularity. The number of events will clearly increase with the total mass, but the quality of measurements will improve with granularity. Thus for example, π/e separation becomes possible at lower and lower energies as granularity of the detector becomes finer. But the finer granularity carries with it serious cost implications, not only because of additional active detector elements but also because of additional costs associated with the manufacture and installation of a larger number of steel plates.

Our reference detector choice of 4-cm thick steel represents a relatively simple design which we have been able to study in some detail using simulations. But the final optimum solution might be different in a number of ways. Some possibilities are:

1. The use of equal numbers of plates of thickness 2 cm and 6 cm, keeping the total mass constant. The cost would be very similar to the reference design and would result in half of the detector having significantly better resolution at the expense of the other half.

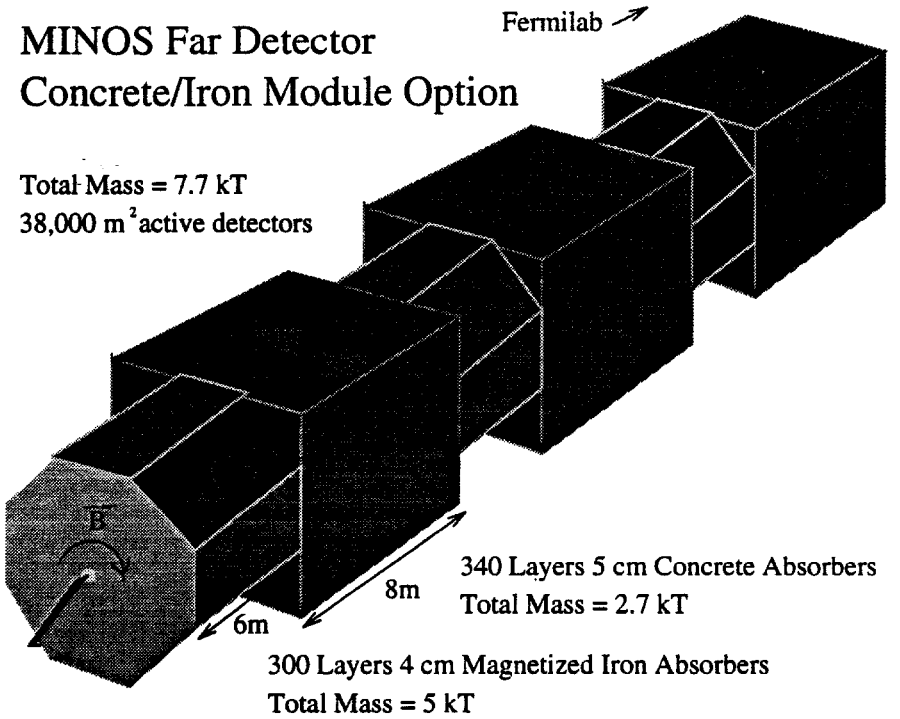

Figure 10.1: A possible arrangement of modules in a concrete/steel option.

2. The use of thinner plates, *e.g.*, 2 cm or 3 cm, and reducing the total detector mass to satisfy the constant cost constraint.

3. The use of a lower Z material, *e.g.*, concrete, for part of the detector. Such a detector probably would be modular, each module being constructed of concrete absorber in front and magnetized iron in the rear. The detector at the near site might consist of a single such module, making it very similar to the far detector. The logical choice would be to use concrete thickness of about 5 cm (*e.g.*, like the CHARM II detector at CERN). If the iron thickness were kept at 4 cm, some reduction in total mass would be necessary to keep the cost constant. A possible layout of such a detector is shown in Fig. 10.1.

We have already initiated preliminary simulations to study these alternatives. But our current results are not advanced enough at this time to allow a clear decision. Our intention is to await fuller simulations and calorimeter module tests in charged beams before a final decision is made.

10.3 Other active detectors

Iarocci tubes (limited streamer tubes, or LST's) represent a well tested and proven technology that has now been used successfully for several years in a number of collider and

nonaccelerator experiments on a scale comparable to what we are proposing. For this reason, we have adopted that technology for the reference detector. However, other active detector technologies may have significant advantages, as described in Chapter 11. The foremost among these are liquid scintillator and resistive plate chambers (RPC's). Either technology could replace the limited streamer tubes used for the reference detector without significant design changes in the passive part of the detector. Thus investment in the design of the latter can proceed in parallel with the studies of the detector technology.

One can visualize the use of an alternative technology in two different ways:

- Replacement of all LST's with the other-technology detector.
- Augmentation of the LST's with the other-technology detectors every n'th plane, to enhance the capability of the overall instrument. For instance, RPC's would provide better timing, which is important for some nonaccelerator physics goals of our experiment (as discussed in Chapters 9 and 11). Clearly, the time pressure to make a decision is much less in this situation than if we planned to replace all the LST's.

10.4 Soudan 2 modifications

The existing Soudan 2 detector represents almost 1 kT of fine granularity instrument (about 0.1 radiation length typical absorber thickness). Besides its relatively low mass, there are several potential drawbacks for neutrino oscillation experiments in its current configuration:

1. Its nonmagnetic nature does not allow the measurement of high muon momenta.
2. The 8-fold multiplexing in the electronics generates frequently confusing "ghosts" in the track reconstruction.
3. The electronics represents a rather old technology (it was designed twelve years ago).

We intend to determine whether it is cost effective to alleviate these potential shortcomings. Thus, for example, one might consider moving the Soudan 2 modules to the new hall and placing them in an optimum orientation in front of the magnetic detector. Whether or not the existing Soudan 2 detector is mechanically reconfigured, it may be useful to replace the current electronics with a nonmultiplexed system which makes use of current technology.

10.5 Active shield around the detector

An active shield is not necessary for the long baseline neutrino oscillation experiment because of the low cosmic ray background in the Soudan mine. On the other hand, a shield will be important for achieving some of the nonaccelerator physics goals of our experiment, as discussed in Chapter 9. Even though this proposal describes the detector without the shield, its addition would be relatively straightforward. An active shield might use the same chamber technology as the main detector. Alternatively, the shield might employ a detector technology such as RPC's with fast timing capability. If in addition a subset of the

main detector (*e.g.* every 10th chamber plane) were upgraded to also provide fast timing information, the direction of partially contained muon tracks could be determined by time of flight. This would extend the atmospheric neutrino event sample to higher energies. The physics implications of this enhancement are discussed in Chapter 9.

10.6 Changes in minor parameters

There are several parameters in the currently described detector that will probably undergo changes as work proceeds. To give an example, a currently unresolved question is whether a 2 cm gap between steel plates is adequate. Increasing it to 3 cm would relax some of the tolerances on the steel and make assembly easier. It would require (in the current design) a volume 17% larger. The physics repercussions would be minimal: muon momentum measurement and angle measurements for hadrons and electrons would improve slightly; muon containment would get slightly worse.

A number of other parameters will undoubtedly need fine tuning even if the major features of the reference detector remain intact. Some of these are the LST cell size, the length of the near detector, and a number of electronics response parameters. Such changes do not have major physics or cost consequences and do not impact the overall design in any major way. Thus their resolution can easily await the results of additional studies. As described in Chapter 11, some of the development work needed to optimize the reference detector design has already begun.

Chapter 11

Detector Development Program

11.1 Introduction

The long baseline neutrino oscillation experiment can be constructed using well-established particle detection technology with standard electronic readout as described in this proposal. Our development program is designed to hone this technology to its most cost effective form when incorporated into a large underground detector designed to detect a positive signature of tau neutrino interactions. For the purpose of this discussion, the detector can be considered as having three aspects, the active detector elements, the electronics, and the mechanical structure. The collaboration will continue to investigate, and hopefully improve, these aspects until the detector design is frozen in 1997.

The time scale for the investigation of the detector is set by our desire to have a working detector in place when the neutrino beamline is commissioned in 2000. To meet that schedule, detector installation must begin in 1998. Thus the underground laboratory must be completed and the tooling for detector construction must be ready by that time. This leads to freezing almost all aspects of the detector design in 1997. This time scale fits in well with the availability of test beams in the 1996 Fermilab fixed target run. At that time we plan to expose a prototype of our detector in a Fermilab test beam; alternatively, earlier beam tests could be performed at Brookhaven starting in January 1996. Final design changes, if any, as a result of the beam tests can then be incorporated in the construction process.

11.2 Reference detector technology

The thrust of most of the development work is to investigate procedures which will simplify the detector in order to reduce construction or operating costs. The Argonne, Oxford and Tufts groups are currently developing techniques for streamlining the mass production of limited streamer chambers, for example by using wider extrusions than are currently available, or by improving wire stringing techniques. They are also studying the capacitive coupling of the cathode strip readout to iron sheets so that pulse height information is more reliable, and are designing low cost electronics for two dimensional readout.

The collaboration is also devising procedures for safe handling of the isobutane-CO_2 gas mixture used by limited streamer chambers. Even small concentrations of isobutane can

pose special safety hazards in the underground environment. In the unlikely event that we are unable to develop satisfactory techniques for handling flammable gas, the Oxford group is studying the operation of limited streamer chambers in proportional mode, which would use a gas mixture of Ar-CO_2.

Throughout this proposal we have used the performance characteristics of limited streamer tubes which have been well established by previous experiments, for example MACRO. We expect to expose a prototype of our detector in a test beam in 1996 to verify that design changes we have implemented do not degrade the expected performance. The main goal of this test would be to determine the detector's response to hadron and electromagnetic showers. At the same time we would test different material thicknesses and densities to verify the simulations used to optimize the identification of tau events. It is possible that we would eventually wish to expose a large (50 ton) prototype in the Fermilab E–872 neutrino beam in order to calibrate directly the tau neutrino detection capabilities of the detector.

11.3 Mechanical structure engineering

The mechanical structure of the detector will continue to be the subject of engineering efforts from the collaboration. The Livermore engineering group is currently refining the design of the steel plate support structure. Engineering studies by the collaboration will continue to investigate the optimal procedure for installing and securing the detector structure in the mine. We expect to erect a test version of a wall of the detector at one of our collaborating laboratories to test the structure and assembly procedures in 1996 followed by a test in the existing Soudan 2 underground laboratory. Meanwhile, the Argonne and Livermore groups are determining the optimal design of the magnetic toroids including the geometry, power considerations, and controls.

11.4 Alternative technologies

Because the limited streamer tubes do not give a fast timing signal, which would be useful for some of the particle astrophysics measurements identified in this proposal, we are investigating two other technologies which might be integrated into the final design if they can be used at a reasonable cost. These technologies are scintillator and resistive plate chambers (RPC's). Both are rugged technologies which potentially can be constructed in large quantities at low cost. Neither technique requires wires, which simplifies their assembly and makes them less susceptible to failure. Each has to overcome technical and cost challenges to become an acceptable system in the detector.

11.4.1 Scintillator

The scintillator technology, investigated by Indiana and Minnesota, has the potential advantage of a simple construction needing no gas system or wires. Using standard photomultiplier tubes for readout would make this technology expensive. The challenge is to extract enough photons from a long tube of liquid scintillator or extruded plastic scintillator to allow the use of low cost/channel image intensifiers. Two designs are being investigated. One is similar to

MACRO in that it uses a liquid scintillator with a long attenuation length. Another design increases the light yield of the scintillator at the expense of transmission. The light is transmitted to the end of the tube through a wavelength shifting fiber. A single fast timing signal would be picked off a microchannel plate serving many tubes while the actual hit pattern would be read out slowly from the image intensifier by a CCD array. Pulse height would also give good information on the number of particles crossing each scintillator.

11.4.2 Resistive plate chambers

The Caltech, Livermore, and Rutherford groups are investigating the applicability of RPC's as fast timing elements. The challenge for this system is to find an operating gas which is both ozone and mine friendly. While searching for such a gas, another solution being investigated is to run these chambers in the proportional mode with Ar-CO_2. The RPC design that we are investigating is similar to that being proposed for the BABAR detector using ABS plastic for the resistive plate. Argonne is investigating the design of electronics to take advantage of the fast pulses from the RPC's.

11.4.3 Other technologies

If the cost of an all-scintillator or all-RPC detector were less than or equal to the cost of the reference detector, then the physics advantages of fast timing would make these technologies very attractive. Provided that the challenges outlined above can be overcome, the next important step is therefore to accurately determine their manufacturing costs. Both technologies could use the same steel granularity as the reference detector with LST's.

In case the structure itself provides an unforeseen problem, the Minnesota group is developing a plan to build the nonmagnetic part of the detector using a modified Soudan 2 technology with fine granularity 5-10 mm steel plates. The challenge is to keep that detector below the cost profile of a detector using limited streamer tubes.

Our intent is to eliminate any of these shadow technologies as soon as it is determined that it is not superior to our reference technology on the basis of cost and resolution. Small scale beam tests of one or more of these technologies might be required before the 1996 fixed target run. These tests could be carried out at a lower energy accelerator.

Chapter 12

Cost Estimates and Schedules

12.1 Cost Estimates

12.1.1 Introduction

This Chapter presents the results of our first attempt to estimate the bottom-up cost of the MINOS experiment, including both the far and near detectors. Throughout we have used the standard U.S. accounting system, even though it is quite likely that significant components of the detector would be built by our overseas collaborators (already signed on or potential new ones) in Europe, Asia, or Latin America.

We have tried to estimate as well as possible the EDIA (Engineering, Design, Inspection, Administration) costs for each subsystem. Because our detectors are relatively large but monolithic, we believe that engineering and design costs will be rather low when expressed as a fraction of the total costs. We have applied relatively conservative 20-30% contingency to all the subsystems.

The total costs of the detector are broken down in the accompanying WBS format. Below we give a short explanation of the basis for estimating the costs for some of the main cost components of the detector: electronics, active detector, magnet steel/absorber and installation.

The estimates presented in this Chapter give a total experiment cost of $54.5M, including EDIA and contingency. However, this total does not include the site preparation costs which are discussed in Chapter 4. As described in detail in Chapter 4, the difference between the total site preparation cost (including EDIA and contingency) and the funds expected from the State and University of Minnesota, is $2.0M. Thus, the total MINOS project cost estimate consists of the $54.5M from the WBS calculation outlined below plus $2.0M for site preparation costs.

12.1.2 Electronics

The costs for the electronics were estimated by several methods with varying uncertainties. The cable and connector costs are the best known. These are standard off the shelf items with the prices taken from current catalogs. This includes the power cables, their connectors, the signal busses and their connectors. The signal bus cable costs were reduced by 30% to

reflect the experience from Soudan 2 where significant price reductions were negotiated for these very large cable orders.

The VME system estimate is based on the recent experience of the Argonne HEP Electronics Group. The costs for the crates, processor cards and power supplies are well known. There is more uncertainty on the readout/trigger cards and the J3 backplane. These costs were estimated from ongoing and recently completed experience with work for the ZEUS detector. These include VME systems for the calorimeter readout and triggering and the small angle rear tracker trigger. For the MINOS detector, the major uncertainty arises from the fact that the actual circuits which will be on the boards are not yet known.

The monolithic chips have the largest cost uncertainty. These cost estimates came from discussions with chip design experts at the Oak Ridge National Laboratory Instrumentation and Controls group. They have worked on chips for a number of high energy physics experiments and have extensive experience with the readout for the various types of detectors used in these experiments. Their recent experience is with the PHENIX and PHOBOS experiments at Brookhaven. The uncertainties here are again due to the actual circuits needed for MINOS not being precisely defined yet, and the fact that small changes in circuit parameters (*e.g.*, amplifier slew rate) can have large effects on the chip area required.

12.1.3 Active detectors

Cost estimates for active detector production are based on the U.S. experience with streamer tube production at the University of Houston SCARF factory. For production at SCARF, many materials were purchased from Bindi (Italy), which supplied not only SCARF but all the other major streamer tube producers in the world. However, there is nothing unique about the production of these materials, which can also be obtained in the U.S. Our cost estimates assume a 70% yield of chambers from the input raw materials, which is realistic for the "high resistivity painting" and is pessimistic for "low resistivity painting" techniques.

Labor costs are based on the SCARF experience, as are the costs of running the factory. We also have at our disposal cost estimates from Russia (JINR, Dubna). They have a similar factory and comparable experience in mass production of the streamer tubes. Cost estimates from Russia are slightly lower but certainly consistent with the U.S. estimates.

A major uncertainty is the cost of extrusion material if we are required to change from the usual PVC to some less toxic plastic. The cost may be somewhat higher but the factor is not known at this time. Other cost estimates are based on the U.S. experience with the production of similar detectors. We believe that they are quite reliable, and that there is still room for optimization and cost reduction.

Five percent of the total cost is allocated for EDIA. Its main components would be the cost of designing detectors and tooling for factories as well as the cost for commissioning of factories and pilot production.

12.1.4 Calorimeter and magnet steel

The steel-plate, support-structure, and magnet-coil costs are based on conceptual engineering designs developed by the Applied Research Engineering Division at Livermore, drawing on their recent experience with the design of the one kiloton steel structure and conventional

magnet for the PHENIX detector at Brookhaven. We discuss the basis for cost estimation of various components in more detail below.

EDIA. Approximately one year of engineering manpower is required for each of the two engineering phases (design phase and fabrication phase) for the steel absorber plates. The effort estimates are based on actual expenditures for the design and construction of the PHENIX magnet, flux return and muon identifier (which is currently in fabrication). The total cost for EDIA includes overhead charges, technical support and travel during the fabrication phase.

Fabrication. The individual steel pieces that comprise the absorber planes for the far detector weigh up to 1.4 tons and can be produced by a number of industrial sites in the U.S. The maximum dimensions of each piece are limited by the size of the access shafts to the underground hall. Maximizing the size of the steel pieces helps to reduce cost by reducing the total length of machined edges and reducing the number of assembly tasks. The largest steel piece, 8 m by 1.33 m, is small enough to fit on a single milling machine so that all the edges can be machined with a single setup. The current design of crossed and welded 2 cm plates is constructed entirely with 90° cuts and no bolts. The simple 90° cut allows multiple plates to be machined simultaneously, while welding eliminates the need for counter-sunk bolts, both of which result in significant cost savings.

The steel plates will be produced at a mill by forging and rolling an iron ingot. Typical lengths for a 2 cm thick rolled plate are on the order of 30 m. The mill will torch cut the plates into a size that is ready for machining. After optimizing the cutting procedure to accommodate the 45° angle cut on 2/3 of the steel plates, approximately 10% of the volume of excess steel will be lost in the process of machining the plates. This loss is added into the cost of producing 10 kT of machined steel.

Bethlehem Steel of Burns Harbor, Indiana, estimated a cost at $ 0.353/lb for AISI 1010 steel, including an extra stress relief step that is required for welding plates. This is consistent with estimates from other mills and estimates for the PHENIX detector. Burns Harbor could produce 10 kT of steel in a year using less than 10% of their total capacity. Bethlehem Steel was chosen as a good source for an estimate because of the large size of this company and their multiple locations throughout the country. There are no mills or machine shops in Minnesota that can handle this job.

Most mills do not have large machine shops, so we have solicited estimates from a number of shops that could handle a job of this magnitude. For example, McDonnell Douglas in St. Louis, Missouri has 54 mills that machine plates up to 35 m in length. The machining costs include a setup cost that is nominally independent of the size of the plate and a cost that scales with the length of the edges being cut and the number of holes that must be drilled. The total fabrication cost includes a significant cost saving by machining about five plates (each 2 cm thick) simultaneously.

The basic design and construction concept for the near detector steel is similar to that for the far detector. The cross sectional area of the plates is significantly smaller than the far detector, and the Fermilab near hall access shaft is large enough to accommodate an entire preassembled absorber plane. The three steel plates that make up a plane do not need to be bolted or welded together and are shaped in a way to minimize the need for precise machining. The Bethlehem Steel estimate for non-stress relieved AISI 1010 steel is $ 0.32/lb. Since the absorber planes are rectangular and have fewer machined edges than do the far

detector planes, the amount of excess material prior to machining is only about 5% of the desired volume.

Transportation. Transportation costs are based on shipping by railroad from the mill in Burns Harbor, Indiana to the machine shop in St. Louis, Missouri and then to Aurora, Minnesota. From Aurora the steel will be hauled by truck to the Soudan Mine. The steel will be transported in roughly twelve shipments over the span of one year.

Prototype. Prior to the procurement of the full 10 kT of steel, we envisage the construction of a prototype consisting of three full size absorber planes.

Magnet. The 10,000 amp-turn magnet design is well within the scope of conventional construction techniques. The magnet is composed of 72 turns of hollow copper conductor that can be easily built by industry. The major material cost is for the special fixtures and jigs required to assemble and wind the conductor underground.

The magnet installation cost was determined from a detailed analysis of the tasks involved with unreeling, brazing, insulating and winding the conductor. The cost includes all the electrical and cooling water hookups, as well as testing and magnetic field mapping along the coil bore.

The magnet coil construction for the near detector is similar to the far detector coil described above and the costs were calculated by scaling based on conductor length.

Contingency. Standard Livermore procedures were used in estimating the contingency. They are based on the estimated risk factors in technical design, potential cost basis and the schedule.

12.1.5 Installation Costs

The installation costs for the far detector can be broken into three major categories: setup, cost per plane of detector installed and overhead costs during the installation process. The largest single expense in all of these steps is manpower for work done at the far detector site. Based on salaries for the technical crew already employed for the Soudan 2 detector, we estimate the average cost per year per FTE will be $40K. The mine is run by the State of Minnesota Department of Natural Resources (DNR). The DNR maintains the lift, shaft and tunnels of the mine. They provide one shift per day of operators for the lift. Any additional lift operators must be hired through the DNR at an average annual cost of $50K per FTE. In addition, certain jobs such as maintenance work in the shaft must be performed by DNR personnel.

Since the installation work will require many repetitions of the same tasks, we expect that substantial overall savings will be realized by investing in extensive setup prior to beginning the installation work. This setup will involve preparations for moving materials into the mine, preparation and construction of the various lifting strongbacks and assembly jigs, setup of test equipment and procedures. It is estimated that the setup period will require about one year with a 7-person crew at the mine (in addition to physicists, engineers and technicians from participating institutions). The initial crew members hired in this time period will form the basis for the assembly crews during the main installation period which will follow. In addition to manpower, there will be costs for fixture construction, electricity, and setup of office and laboratory space on the surface.

Work Item	*People* ⊗	*Days*	= *Person-Days*
Assembly of steel into plane	3	0.75	2.25
Assembly of active detector plane on top of steel layer	3	1.0	3.0
Testing of active detector plane prior to installation (note, elapsed time is longer than person-time)	2	1.0	2.0
Mount steel/detector plane onto detector	4	0.7	2.8
Testing of active detector plane following installation	1	0.7	0.7
Survey of active detector plane positions	2	0.5	1.0
Electronics installation and cabling (Note: this does not include debugging and operation tests which are assumed to be carried out by collaborating technicians/engineers/physicists.)	2	1.5	3.0
Moving materials and other work in hall	2	1.5	3.0
Loading materials at surface	2	0.75	1.5
Unloading materials underground	2	0.75	1.5
Manpower per detector plane			20.8
Manpower required for 600 planes			12,500
x 1.2 due to overlap in jobs			15,000

Table 12.1: Manpower for the assembly of the main part of the detector.

The manpower required for assembly of the main part of the detector is best calculated as a cost per plane of assembly. The breakdown of the expected manpower required per plane is shown in Table 12.1.

Making a conservative assumption of 230 person-days per year per FTE, this corresponds to 65 FTE-years. Hence, at $40K per FTE the marginal cost per plane comes to $4.3K or $2600K for 600 planes of detector.

It is estimated that the assembly could be completed in a total of 450-500 assembly days with two shifts working 40 hour weeks. This corresponds to 2.2 calendar years assuming 230 assembly days per year. In addition to the per-plane costs, there will be overhead costs during this assembly period. These costs are shown in Table 12.2.

Of course, if the assembly work is stretched over a longer period of time, the resulting overhead costs will be higher. The installation and assembly costs listed here do not include any costs related to preparation of the experimental hall, installation of the gas system, installation of the HV system, testing of electronics or installation of the online computing system. Installation costs for these areas are either listed explicitly for each item in the appropriate cost section of the WBS, or it is assumed that the installation work will be carried out by collaborating technicians, engineers and physicists.

Item	*Cost per year ⊗ 2.2 years*	*= Total*
Hoist operators: 2 FTE's (DNR)	$100K	$220K
Administrative: 2 FTE's	$ 80K	$176K
Electricity, other DNR	$150K	$330K
Gas	$ 50K	$110K
Surface Office Space	$ 25K	$ 55K
Infrastructure and Misc.	$200K	$440K
Total Overhead Costs	$605K	$1331K

Table 12.2: Overhead cost during assembly period.

12.1.6 Level 3 WBS cost summary

2.2.1	**Detector R&D**	**$605K**
2.2.2	**Far detector gas, HV, computing, installation**	**$6,387K**
2.2.3	**Near detector gas, HV, computing, installation**	**$1,125K**
2.2.4	**Active detector elements, near and far**	**$13,099K**
2.2.5	**Passive components (steel, magnet), near and far**	**$15,819K**
2.2.6	**Electronics, near and far**	**$5,464K**
2.2.7	**Contingency**	**$12,024K**
	Total MINOS experiment cost (with EDIA and contingency)	**$54,523K**

12.1.7 Itemized WBS Costing

2.2 MINOS Experiment (level 2 MINOS Project Manager) : $42,499,821 ($54,523,622 including contingency)

2.2.1 Detector R&D (level 3 system manager) : $605,200

2.2.1.1 FY 1995 : $105,200

2.2.1.2 FY 1996 : $500,000

2.2.2 Far Detector (level 3 system manager) : $6,387,000

2.2.2.1 Installation and Assembly : $6,387,000

2.2.2.1.1 EDIA : $2,005,000

2.2.2.1.1.1 Setup costs : $675,000

2.2.2.1.1.2 Overhead for 2.2 Years : $1,331,000*

2.2.2.1.2 Materials and Services : $4,381,000

2.2.2.1.2.1 HV System : $370,000*

2.2.2.1.2.1.1 10 CAEN SY403 @ $20,000/crt : $200,000

2.2.2.1.2.1.2 600 SHV cbl & con @ $50/unit : $30,000

2.2.2.1.2.1.3 Distribution system @ $200/plne : $120,000

2.2.2.1.2.1.4 Racks and Miscellaneous : $20,000

2.2.2.1.2.2 Gas System : $690,000

2.2.2.1.2.2.1 Surface Building : $100,000

2.2.2.1.2.2.2 Comp controlled mass flow mixer : $50,000

2.2.2.1.2.2.3 Gas Analysis System : $30,000

2.2.2.1.2.2.4 Surface to undergrnd pipes : $60,000

2.2.2.1.2.2.5 Gas Cleaning System : $200,000

2.2.2.1.2.2.6 Flow meters, piping, conncts : $150,000

2.2.2.1.2.2.7 Leak Detection, Auto cutoff : $100,000

2.2.2.1.2.3 Online Computing : $321,000

2.2.2.1.2.3.1 Central DAQ Computer : $40,000

2.2.2.1.2.3.2 8 Disk Drives @ $2000/pce : $16,000

2.2.2.1.2.3.3 5 Wrkstns @ $8,000/pce : $40,000

2.2.2.1.2.3.4 4 Wrkstns @ $5,000/pce : $20,000

2.2.2.1.2.4.5 5 Hrd Cpy Strge @ $3,000/pce : $15,000

2.2.2.1.2.4.6 2 Carousel @ $25,000/pce : $50,000

2.2.2.1.2.4.7 Local Network Hardware : $70,000

2.2.2.1.2.4.8 Surface-undergrnd link $50,000

2.2.2.1.2.4.9 Universal Time System $20,000

2.2.2.1.2.4 Services : $3,000,000

2.2.2.1.2.4.1 Assembly of planes : $2,800,000*

2.2.2.1.2.4.2 Coil Installation : $200,000

2.2.3 Near Detector (level 3 system manager) : $1,125,000

2.2.3.1 Installation and Assembly: $1,125,000

2.2.3.1.1 EDIA : $273,000

2.2.3.1.1.1 Setup Costs : $55,000

2.2.3.1.1.2 Overhead : $218,000

2.2.3.1.2 Materials and Services : $852,000

2.2.3.1.2.1 HV System : $146,000

2.2.3.1.2.1.1 4 CAEN SY403 @ $20,000/crt : $80,000

2.2.3.1.2.1.2 233 SHV cbl & conn @$50/cbl : $11,600

2.2.3.1.2.1.3 Distribution System @ $200/pln : $46,400

2.2.3.1.2.1.4 Racks and Miscellaneous : $8,000

2.2.3.1.2.2 Gas System : $140,000

2.2.3.1.2.2.1 Comp Controlled mass mixer : $50,000

2.2.3.1.2.2.2 Gas Analysis System : $30,000

2.2.3.1.2.2.3 Flow meters, pipes, conns : $60,000

2.2.3.1.2.3 Online Computing : $146,000

2.2.3.1.2.3.1 Central DAQ Computer : $40,000

2.2.3.1.2.3.2 8 DD @ $2,000/pce : $16,000

2.2.3.1.2.3.3 5 Wrkstns @ $8,000/pce : $40,000

2.2.3.1.2.3.4 Hard Copy Hardware : $30,000

2.2.3.1.2.3.5 Universal Time System : $20,000

2.2.3.1.2.4 Services : $420,000

2.2.3.1.2.4.1 Assembly of planes : $320,000

2.2.3.1.2.4.2 Coil Installation : $100,000

2.2.4 Active Detector (level 3 system manager) : $13,099,295

2.2.4.1 Design and Prototype : $1,750,000

2.2.4.1.1 EDIA (5% of detector cost) : $600,000*

2.2.4.1.2 Materials and Services : $1,150,000

2.2.4.1.2.1 Pre-production : $400,000

2.2.4.1.2.2 3 Production lines @ $250,000/setup : $750,000

2.2.4.2 Near Detector Production : $857,295

2.2.4.2.1 Materials and Services : $857,295

2.2.4.2.1.1 Beam Monitor Detectors : $361,500

2.2.4.2.1.1.1 100 planes @ $3615/plane : $361,500

2.2.4.2.1.2 Main Detectors : $480,795

2.2.4.2.1.2.1 133 planes: $480,795

2.2.4.2.1.3 Services : $15,000

2.2.4.2.1.3.1 Transportation of Detectors : $15,000

2.2.4.3 Far Detector Production : $10,492,000*

2.2.4.3.1 Materials and Services : $10,492,000

2.2.4.3.1.1 Detectors : $10,392,000

2.2.4.3.1.1.1 600 planes @ $17,320/plane: $10,392,000

2.2.4.3.1.2 Services : $100,000

2.2.4.3.1.2.1 Transportation of Detectors : $100,000

2.2.5 Passive Detector (level 3 system manager) : $15,819,340

2.2.5.1 Design and Prototype : $250,000

2.2.5.1.1 EDIA : $50,000

2.2.5.1.1.1 Site Preparation : $50,000

2.2.5.1.2 Materials and Services : $200,000

2.2.5.2 Near Detector Production : $2,239,340

2.2.5.2.1 EDIA : $296,000

2.2.5.2.2 Materials and Services : $1,943,340

2.2.5.2.2.1 Steel: $1,420,000

2.2.5.2.2.1.1 1,546.5 Tons Steel @ $0.32/lb:$1,089,000

2.2.5.2.2.1.2 Steel consumed by machining : $54,000

2.2.5.2.2.1.3 Floor Support : $50,000

2.2.5.2.2.1.4 Fixturing & Fasteners : $50,000

2.2.5.2.2.1.5 Steel Plate Machining : $177,000

2.2.5.2.2.2 Magnet : $108,000

2.2.5.2.2.2.1 Magnet Power Supplies : $6,000

2.2.5.2.2.2.2 Water Cooling System : $50,000

2.2.5.2.2.2.3 Coil Materials : $52,000

2.2.5.2.2.3 Aluminum : $257,840

2.2.5.2.2.3.1 48.6 Tons Aluminum @ $2/lb:$213,840

2.2.5.2.2.3.2 Aluminum Plate Machining : $44,000

2.2.5.2.2.4 Services : $157,500

2.2.5.2.2.4.1 Transportation of Steel: $143,000

2.2.5.2.2.4.2 Transportation of coil materials : $10,000

2.2.5.2.2.4.3 Transportation of Aluminum : $4,500

2.2.5.3 Far Detector Production : $13,330,000

2.2.5.3.1 EDIA : $408,000

2.2.5.3.2 Materials and Services : $12,922,000

2.2.5.3.2.1 Steel : $11,650,000*

2.2.5.3.2.1.1 10 kT Steel @ $0.353/lb:$7,766,000

2.2.5.3.2.1.2 Steel consumed by machining : $777,000

2.2.5.3.2.1.3 Fixturing & Fasteners : $250,000
2.2.5.3.2.1.4 Steel Plate Machining : $2,168,000
2.2.5.3.2.1.5 Axial Rod Fabrication : $342,000
2.2.5.3.2.1.6 Floor support : $347,000
2.2.5.3.2.2 Magnet : $302,000
2.2.5.3.2.2.1 Magnet Power Supplies : $18,000
2.2.5.3.2.2.2 Water Cooling System : $50,000
2.2.5.3.2.2.3 Coil Materials : $234,000
2.2.5.3.2.3 Services : $970,000
2.2.5.3.2.3.1 Transportation of Steel: $924,000*
2.2.5.3.2.3.2 Transportation of coil materials : $46,000

2.2.6 Electronics (level 3 system manager) : $5,463,986

2.2.6.1 Design and Prototype : $1,000,000
2.2.6.1.1 EDIA of Monolithic Chips : $900,000
2.2.6.1.2 Materials and Services : $100,000
2.2.6.2 Near Detector Production : $853,120
2.2.6.2.1 EDIA : $12,000
2.2.6.2.2 Materials and Services : $841,120
2.2.6.2.2.1 Cables and Connectors : $74,380
2.2.6.2.2.1.1 10765 ft cable @ $3/ft : $32,295
2.2.6.2.2.1.2 1631 x 2 connectors @ $7/piece : $22,834
2.2.6.2.2.1.3 1398 x 2 board cons @ $4.5/pce : $12,582
2.2.6.2.2.1.4 10765 ft pwr cable @ $0.1/ft : $1,077
2.2.6.2.2.1.5 1398 pwr cbl cons @ $1/pce : $1,398
2.2.6.2.2.1.6 1398 pwr brd cons @ $1/pce : $1,398
2.2.6.2.2.1.7 Cable Trays 5592 ft @ $0.5/ft : $2,796
2.2.6.2.2.2 VME Crates and Cards : $585,000
2.2.6.2.2.2.1 15 VME crts @ $2000/pce : $30,000
2.2.6.2.2.2.2 15 J3 bckplnes @ $3000/pce : $45,000
2.2.6.2.2.2.3 15 crte pwr supl @ $3000/pce : $45,000
2.2.6.2.2.2.4 15 processr crds @ $4000/pce : $60,000
2.2.6.2.2.2.5 240 readout crds @ $1500/pce : $360,000
2.2.6.2.2.2.6 30 misc crds @ $1500/pce : $45,000
2.2.6.2.2.3 Monolithic Chips : $181,740
2.2.6.2.2.3.1 4,194 analog chips @ $10/pce : $41,940
2.2.6.2.2.3.2 4,194 digtal chips @ $10/pce : $41,940
2.2.6.2.2.3.3 1,398 interface chips @ $10/pce : $13,980
2.2.6.2.2.3.4 1,398 daughter boards @ $50/pce : $69,900

2.2.6.2.2.3.5 1,398 daughtr brd cons @ $10/pce : $13,980

2.2.6.3 Far Detector Production : $3,221,724*

2.2.6.3.1 EDIA : $86,400

2.2.6.3.2 Materials and Services : $3,135,324

2.2.6.3.2.1 Cables and Connectors : $405,324

2.2.6.3.2.1.1 45540 ft cable @ $3/ft : $136,620

2.2.6.3.2.1.2 10200 x 2 connectors @ $7/pce : $142,800

2.2.6.3.2.1.3 9600 x 2 board cons @ $4.5/pce : $86,400

2.2.6.3.2.1.4 45540 ft pwr cable @ $0.1/ft : $4,554

2.2.6.3.2.1.5 9600 pwr cbl cons @ $1/pce : $9,600

2.2.6.3.2.1.6 9600 pwr brd cons @ $1/pce : $9,600

2.2.6.3.2.1.7 31500 ft cable trays @ $0.5/ft : $15,750

2.2.6.3.2.2 VME Crates and Cards : $1,482,000

2.2.6.3.2.2.1 38 VME crts @ $2000/pce : $76,000

2.2.6.3.2.2.2 38 J3 bckplnes @ $3000/pce : $114,000

2.2.6.3.2.2.3 38 crte pwr supl @ $3000/pce : $114,000

2.2.6.3.2.2.4 38 processr crds @ $4000/pce : $152,000

2.2.6.3.2.2.5 608 readout crds @ $1500/pce : $912,000

2.2.6.3.2.2.6 76 misc crds @ $1500/pce : $114,000

2.2.6.3.2.3 Monolithic Chips : $1,248,000

2.2.6.3.2.3.1 28,800 analog chips @ $10/pce : $288,000

2.2.6.3.2.3.2 28,800 digtal chips @ $10/pce : $288,000

2.2.6.3.2.3.3 9,600 interface chips @ $10/pce : $96,000

2.2.6.3.2.3.4 9,600 daughter boards @ $50/pce : $480,000

2.2.6.3.2.3.5 9,600 daughtr brd cons @ $10/pce : $96,000

2.2.6.4 Spares : $389,142*(**partially**)

2.2.7 Contingency (level 3 system manager) : $12,023,801

2.2.8.1 Far Detector @ 25% : $1,596,750 *(**partially**)

2.2.8.2 Near Detector @ 25% :$281,250

2.2.8.3 Active Detector @30% : $3,929,788 *(**partially**)

2.2.8.4 Passive Detector @ llnl rates : $5,038,549

2.2.8.4.1 Far detector Steel : $4,229,240 *(**partially**)

2.2.8.4.2 Far detector magnet : $97,440

2.2.8.4.3 Near detector Steel and Aluminum : $678,829

2.2.8.4.4 Near Detector Magnet : $33,040

2.2.8.5 Electronics : $1,177,464 *(**partially**)

2.2.8.5.1 Electronics Development: $300,000

2.2.8.5.2 Electronics Production : $877,464

The items marked * are items which will scale with tonnage of the far detector.

12.1.8 MINOS cost scaling with far-detector mass

The costs of the MINOS experiment can be broken down into those which scale with the mass of the far detector and those which are fixed, one time costs. In the WBS, the items marked with a star are those which scale (*e.g.*, steel in the far detector). The other items are independent of the far detector size (*e.g.*, detector R&D or a data acquisition computer). The costs are summarized at WBS level 3 as follows:

- One Time Costs
  - Detector R & D : $605K
  - Far Detector : $1,886K
  - Near Detector : $1,125K
  - Active Detector : $2,007K
  - Passive Detector : $3,245K
  - Electronics : $1,969K
  - Contingency : $2,648K
  - **Total Fixed Costs : $13,486K**
- Scalable Costs for 10 kT Far Detector
  - Detector R & D : $0
  - Far Detector : $4,500K
  - Near Detector : $0
  - Active Detector : $11,092K
  - Passive Detector : $12,574K
  - Electronics : $3,495K
  - Contingency : $9,376K
  - **Total Scalable Costs for 10 kT Far Detector : $41,036K**

The resulting cost of the MINOS experiment as a function of the far detector mass is:
Total Cost = $13,486K + $4,104K × Far Detector Mass(kT).

12.2 Schedules

12.2.1 Construction and installation

The schedules below represent our current estimates of the length of time required to design, prototype, manufacture, test and install the major components of the detector.
The project is broken up into four time-line schedules, as follows:

- Figure 12.1 shows the production schedule for the MINOS electronics.
- Figure 12.2 shows the schedule of the active detector R&D, engineering and production.
- Figure 12.3 shows the steel production schedule.
- Figure 12.4 shows the installation schedule for the far detector.

Although these four schedules are shown separately, the dependencies of the time lines on each other have been taken into account. Thus, for example, steel shipments to the mine do not begin until the cavern excavation is completed.

12.2.2 Funding profile

Figure 12.5 shows the schedule of funding required to construct and install the MINOS detector on a time scale compatible with current plans for NuMI beam operation. This funding profile is derived from the WBS cost estimate and the production and installation schedules presented in this Chapter. As for those estimates, the funding schedule should be regarded as preliminary and subject to change as the design, fabrication techniques, and schedules evolve.

Production Schedule for MINOS Readout Electronics

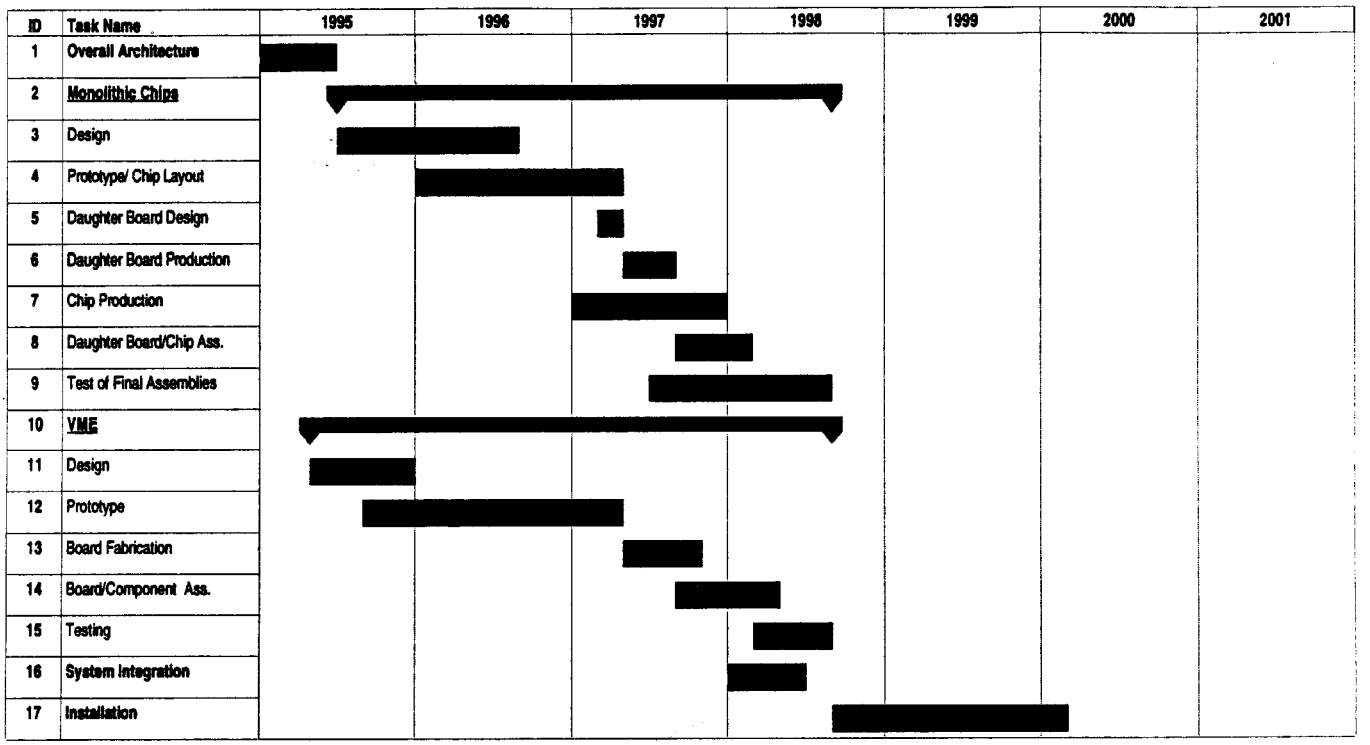

Figure 12.1: Production schedule for the MINOS electronics.

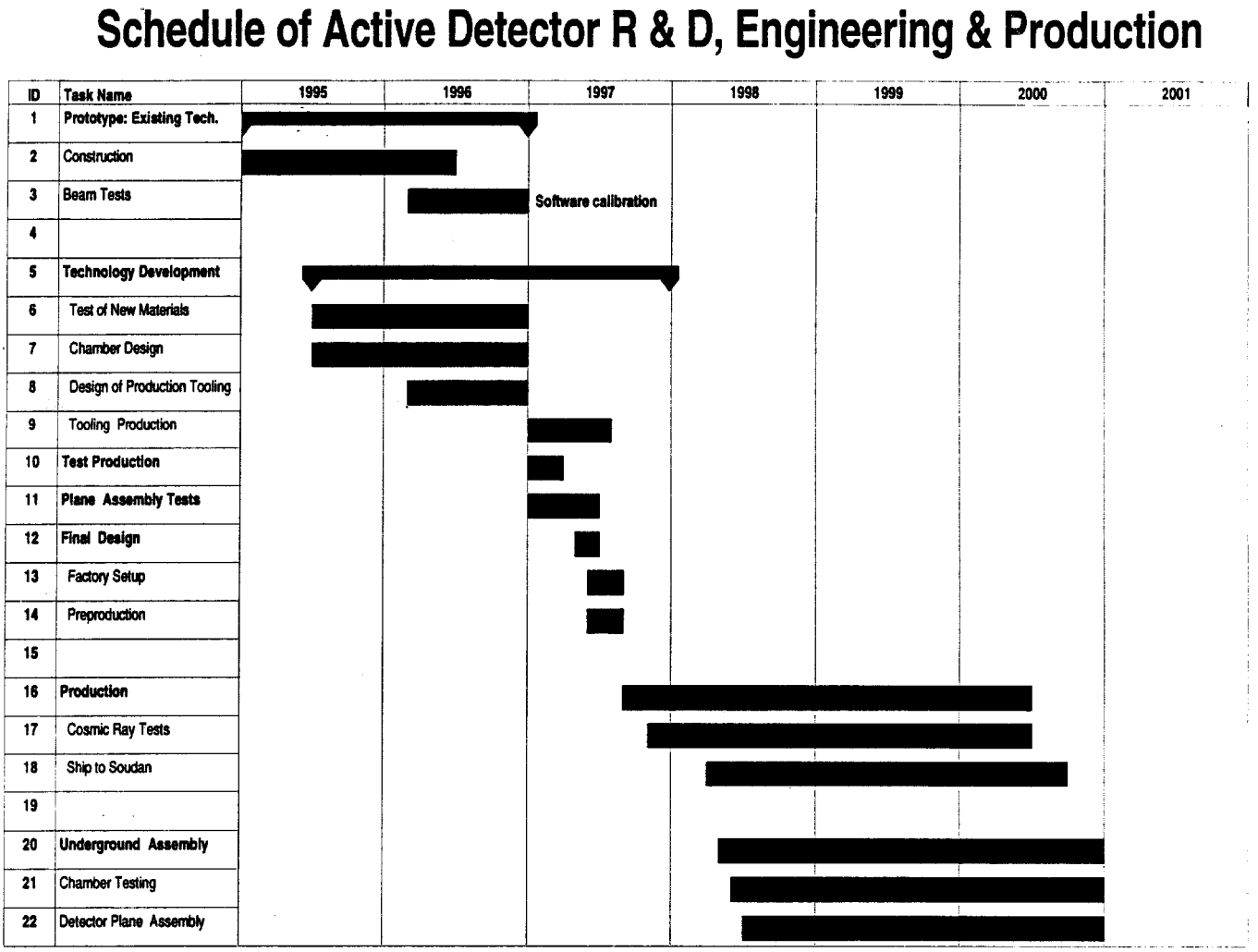

Figure 12.2: Schedule for the active detector R&D, engineering and production.

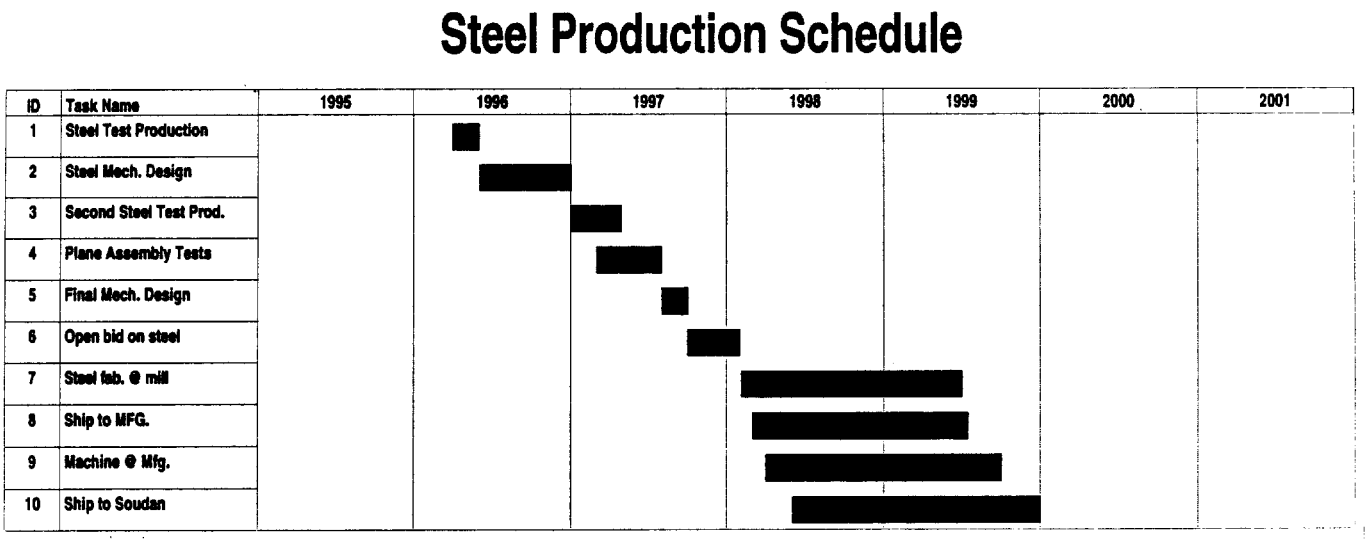

Figure 12.3: Schedule for the steel production.

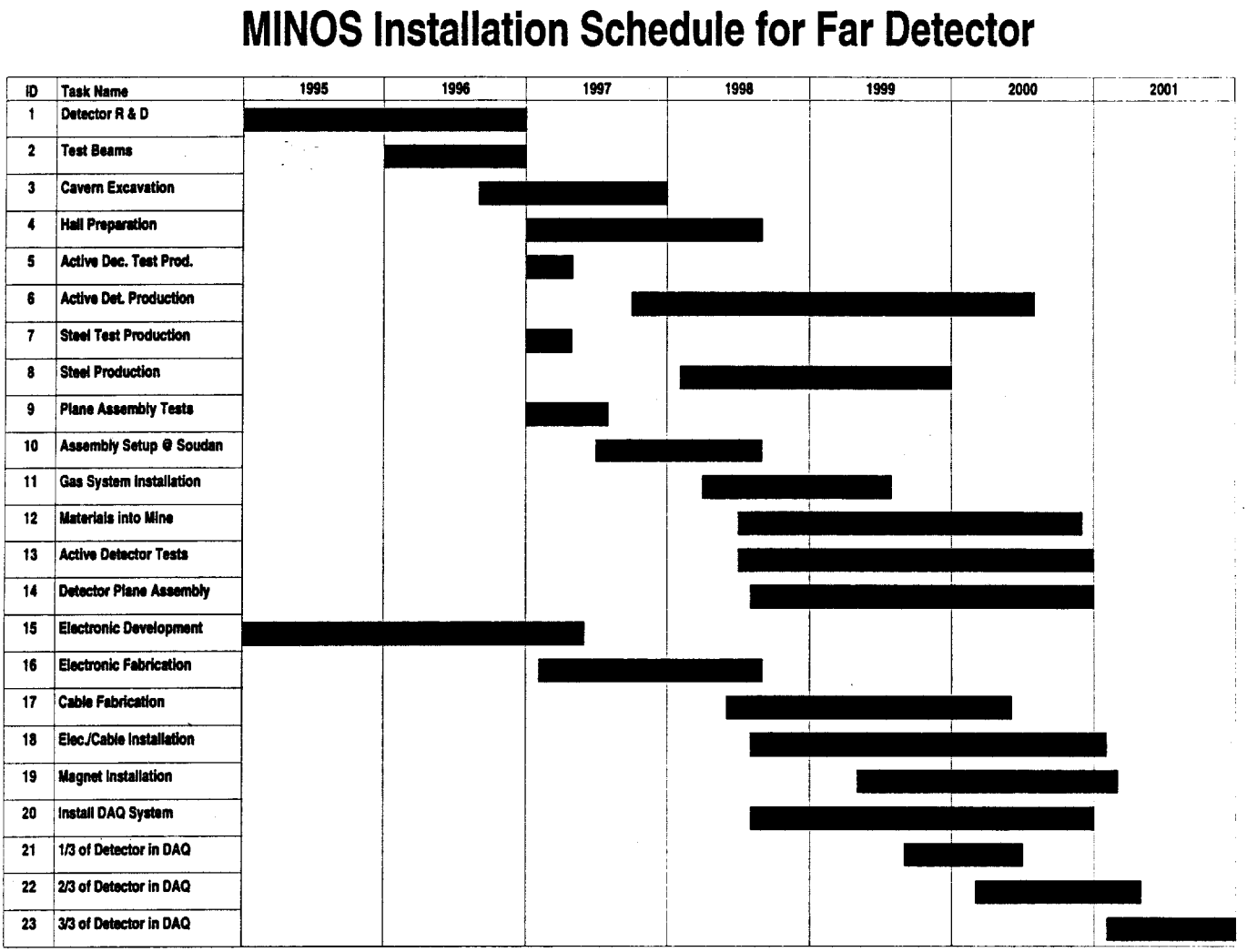

Figure 12.4: Schedule for the installation of the far detector.

MINOS Funding Profile

Tasks	FY1995	FY1996	FY1997	FY1998	FY1999	FY2000	FY2001	TOTALS
Detector R & D	$105,000	$500,000						$ 605,000
Excavation & Hall Prep.			$1,192,000	$786,000				$ 1,978,000
Far Detector			$506,250	$1,141,750	$2,148,500	$2,032,500	$558,000	$ 6,387,000
Near Detector				$634,345	$2,537,378	$1,903,033		$ 5,074,756
Active Detector			$1,750,000	$3,497,333	$3,497,333	$3,497,333		$ 12,241,999
Passive Detector			$250,000	$4,284,000	$6,665,000	$2,381,000		$ 13,580,000
Electronics		$200,000	$2,300,000	$1,722,000	$389,000			$ 4,611,000
Contingency		$ 43,100	$1,226,838	$3,249,622	$4,510,715	$2,853,992	$139,500	$ 12,023,766
Fiscal Total with Cont.	**$105,000**	**$743,100**	**$7,225,088**	**$15,315,050**	**$19,747,926**	**$12,667,858**	**$697,500**	**$ 56,501,521**

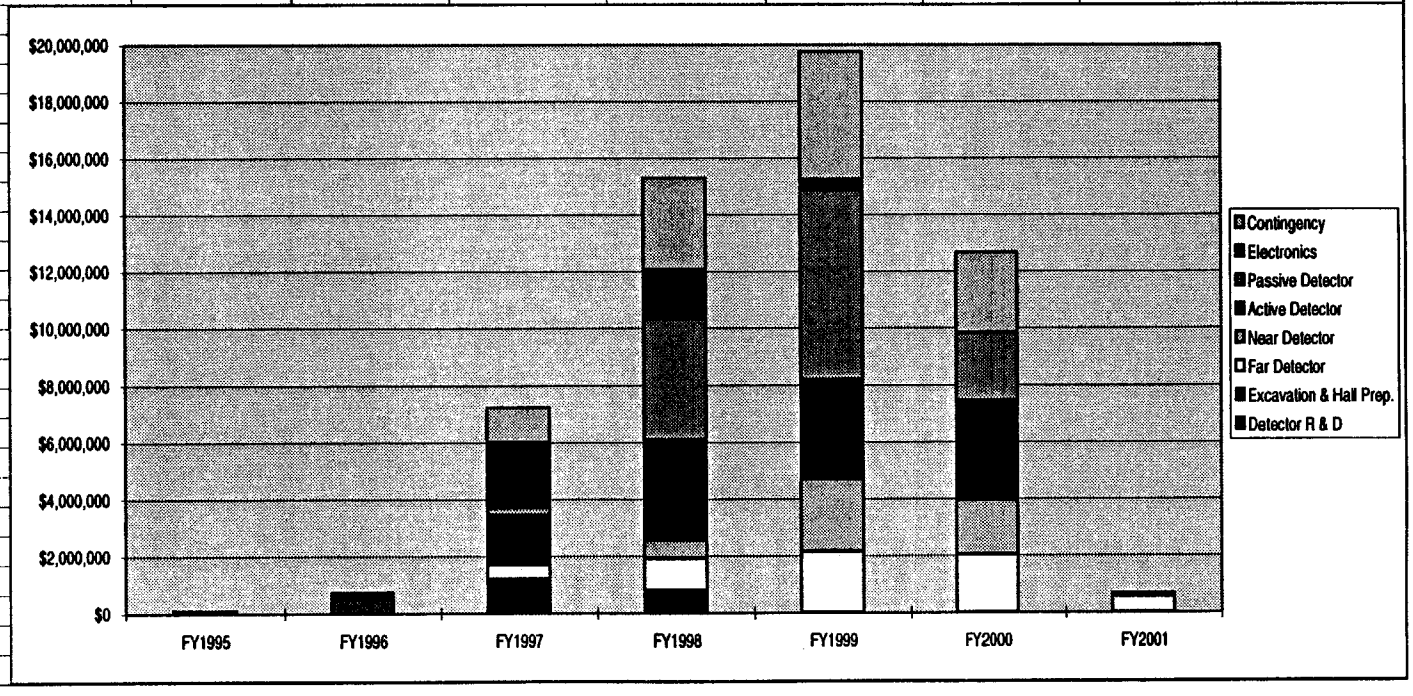

Figure 12.5: Funding profile for MINOS construction and installation.

Chapter 13

Summary

In this proposal the MINOS collaboration has presented the current status of our effort to design an optimum long baseline neutrino oscillation experiment based on a beam from the Fermilab Main Injector and a 10 kT magnetized iron detector located in the Soudan mine. Although our studies are far from complete, we believe that our work to date demonstrates that a sensitive oscillation search can be performed for a reasonable cost.

We are pleased with our progress to date. We have formed the nucleus of a strong collaboration with sufficient strength to complete the design of an optimum experiment. We expect that the strength and size of the collaboration will increase with time. We have obtained a good estimate of costs and our reference detector can now serve as a basis of comparison as we try out new ideas. We have acquired a preliminary understanding of various possible signatures and of the demands that they make on the detector. We have initiated studies on the production and installation of the detector calorimeter. Finally, in collaboration with the Fermilab staff, we have made much progress in understanding how to optimize the neutrino beam and at the same time maintain maximum flexibility.

The initial results of our simulation studies look very promising, although they are far from complete. We have shown that the presence of ν_μ oscillations can be demonstrated for mixing angles down to $\sin^2(2\theta) \gtrsim 0.01$. Production and decay of τ.leptons can be clearly seen for $\sin^2(2\theta)$ down to about 0.1. This sensitivity is more than adequate to fully and unambiguously explore the range of oscillation parameters suggested by the Kamiokande experiment. Finally, our experiment will be sensitive to oscillations into ν_e, and will be able to distinguish $\nu_\mu \rightarrow \nu_e$ from $\nu_\mu \rightarrow \nu_\tau$, down to $\sin^2(2\theta) \gtrsim 0.01$.

But much work remains to be done. We want to reduce the costs of the detector and at the same time improve its performance. We need to obtain a better understanding, through simulation, of the performance of the detector and the impact of that performance on the physics output.

Probably our most important challenge is to understand the physics trade-offs between good statistics and cleanliness of the signal. Good statistics require a large mass, hence coarse granularity, and maximum neutrino flux. The cleanliness of the signal can be improved by finer granularity (at the expense of the detector mass for total fixed cost) and a cleaner and better understood neutrino beam. We intend to focus our work this year on the optimization of such trade-offs. Our studies will encompass all oscillation channels, so that the detector solution ultimately adopted will be optimized not only for identifying (and distinguishing)

$\nu_\mu \rightarrow \nu_\tau$ and $\nu_\mu \rightarrow \nu_e$ oscillations, but also for measuring the mixing parameters, Δm^2 and $\sin^2(2\theta)$.

We are confident that the concept of a magnetic detector, conceivably with interleaved low-Z material, is the proper way to address the issue of neutrino oscillations given our current physics knowledge. It is also clear that the MINOS detector will be capable of providing important new information in the area of nonaccelerator physics.

Whether neutrinos oscillate or not is an unsolved problem today. The MINOS collaboration is looking forward to making a major contribution towards resolving this fundamental physics issue.

Appendix A

The MINOS Collaboration

A.1 Collaboration resources

Designing, constructing and running the MINOS detector will be a challenging process requiring the commitment of a sizeable group of physicists, engineers, students, and technicians. It is, however, still a smaller enterprise than the major collider detectors that have set the scale for HEP projects in recent years. Estimating just how much effort is required is necessarily imprecise. However, we believe that the experiment could be done comfortably with an author list of 200, including Ph.D. physicists, graduate students and those engineers and other technical specialists expected to make major contributions. These 200 would then be backed up by the efforts of other technical specialists for specific tasks. As is usually the case, the level of commitment of the average author would grow with time. In the early period starting now, we expect an average commitment, after teaching duties and commitments to current experiments, of about 25% or 50 FTE plus 10 FTE from non-authors. This would grow to roughly 50% or 100 FTE (plus about 30 FTE from non-authors) for the construction and commissioning phase when the work will be intense, and some current commitments will be tapering off. Then during the running and data analysis phase, some of the technical effort will no longer be required, while there will be an influx of students and postdocs to take part in running and data analysis. During that phase, the effort level needed will be perhaps 40 FTE (plus about 10 FTE from non-authors).

Where does the collaboration stand now with respect to these effort goals and other resources? The current MINOS Collaboration institutions are a healthy blend of large national laboratories, with their extensive infrastructure, and universities, which supply much of the intellectual horsepower of the field as well as graduate students. Present authors of the MINOS proposal, over 100, are Ph.D. physicists, engineers, technical specialists and graduate students whose theses will be based on this experiment.

In order to respond to the PAC's request for information on expected levels of commitment of the collaborators, we have asked each of the initial institutions for their estimate of effort levels during four different time periods. These periods correspond to:

1. 1995-1996: design, detector R&D
2. 1997-1998: engineering, prototyping
3. 1999-2000: construction and commissioning
4. 2000-2002: initial running and data analysis

Then we add together the FTE contributions of Ph.D.'s, engineers, and technical and software specialists from each institution. The results are shown in the Table A.1. We see an initial team of 51 FTE, growing to 94 FTE as other commitments fade and MINOS demands grow.

In addition to the FTE's listed in Table A.1, we estimate the number of graduate students working on MINOS to be 4, 15, 22, and 27 during the four periods indicated above.

We have also polled the institutions about other resources that they can provide. Not surprisingly, we find that we are well supplied with both technical infrastructure and specialized expertise. Collaborating institutions expect to provide over twelve R&D laboratories, eight production laboratories, and access to a large number of other laboratories on an as-needed basis. We have cutting-edge equipment such as extensive computer farms, specialized software (CADENCE for chip design, AUTOCAD, COSMOS, Finite Element Analysis), specialized laboratories for the design and production of chips and boards, and high bay areas with cranes for maneuvering large detector components.

We have experience with the design and production of all relevant types of particle detectors including tracking detectors, calorimeters, and scintillators. This experience includes electronics, gas systems, and software for these detectors. Our extensive software experience includes Monte Carlo simulations, online control and data acquisition, and offline data analysis. In the past, members of our collaboration have built a number of magnets for accelerators and large high energy physics experiments. Of particular relevance, we have experience with large arrays of Iarocci tubes in our previous work on DELPHI at CERN (160,000 4-m long tubes) and MACRO at the Gran Sasso (50,000 12-m long tubes).

Finally, the MINOS Collaboration has extensive experience in conducting experiments both at accelerators (including Fermilab) and at underground laboratories (Soudan and the Gran Sasso).

We believe that the present collaboration has appropriate size, experience and infrastructure to begin work on the MINOS experiment. From our estimates of required effort, it is clear that additional collaborators will be needed. We are in discussions with several other interested groups, including some from abroad. There is good reason to expect that a number of additional groups will join once the experiment has been approved by Fermilab.

A.2 Collaboration structure

The MINOS collaboration has adopted an initial organizational structure in which the ultimate authority rests with an Institutional Board (IB) consisting of one member per institu-

MINOS FTE's, Excluding Students

Institution	1995-96	1997-98	1999-00	2000-02
Argonne	4.6	10.6	10.8	9.1
Boston College	0.4	0.4	0.4	0.4
Caltech	2.5	2.8	4.6	5.5
Columbia	0.7	0.7	0.7	0.7
Fermilab	6.5	7.0	10.0	11.0
Houston	4.3	6.6	9.0	9.0
Indiana	3.0	3.0	3.0	3.0
ITEP	2.0	3.0	4.0	3.0
Lebedev	2.0	3.0	4.0	3.0
Livermore	5.2	9.7	9.7	9.7
Minnesota	5.0	6.0	8.5	9.0
Oak Ridge	2.0	2.0	2.0	2.0
Oxford	3.9	4.7	6.0	6.0
Rutherford	2.0	4.5	5.0	6.0
Stanford	1.5	3.5	4.5	5.0
Sussex	0.5	1.5	3.0	3.0
Texas A&M	1.4	3.0	3.0	3.0
Tufts	3.0	4.5	5.0	5.0
West. Wash.	0.3	0.3	0.3	0.3
Total	50.8	76.8	93.5	93.7

Table A.1: Full time equivalents for MINOS from 1995 through 2002

tion, with members selected by their institution. The IB elects its Chairperson, who serves for a one year term.

The MINOS Spokesperson is selected by the IB, which establishes a search committee and then must approve the recommendation of the search committee. The Spokesperson is responsible to the IB. The Spokesperson is the scientific representative of the Collaboration to Fermilab, to the funding agencies, and to other collaborations. The Spokesperson functions as the executive manager of the collaboration. In general, the Spokesperson's term of office will be up to three years, the specific term to be negotiated with the search committee.

The IB is responsible for admitting new institutions to the collaboration. (Collaborating institutions may add members from their institutions without an approval process.)

A Deputy Spokesperson is chosen by the Spokesperson and ratified by the IB. The primary function of the Deputy Spokesperson will be to represent the collaboration in the absence of the Spokesperson.

The Executive Committee (EC) consists of the Spokesperson, Deputy Spokesperson, and others elected by the IB to total eight members. Those elected by the IB initially have staggered terms, to lead into rotating three year terms. The EC sets scientific and technical policy for the experiment, and establishes procedures for making technical choices, such as the formation of technical panels.

A Project Manager (PM) is chosen by the Spokesperson and ratified by the IB. The PM is responsible for establishing the Work Breakdown Structure schedules and for the preparation of the Technical Design Report. The PM manages the funding, project plan, and schedule.

The MINOS Collaboration has begun the process of establishing the administrative infrastructure outlined here, and plans to fill all major positions within the next few weeks.

At present, the following positions are filled:

IB Chairperson:	Richard Heinz
Spokesperson:	Stanley Wojcicki
Deputy Spokesperson:	David Ayres
Executive Committee Secretary:	Maury Goodman
Executive Committee Member:	Ken Heller
Executive Committee Member:	Wonyong Lee
Executive Committee Member:	Peter Litchfield
Executive Committee Member:	Doug Michael
Executive Committee Member:	Jenny Thomas

Appendix B

The Soudan 2 Detector

B.1 Detector description

The Soudan 2 experiment uses a currently operating detector in an underground laboratory 713 m (2090 meters water-equivalent) beneath Soudan, Minnesota. The detector consists of a 963 metric ton fine-grained tracking calorimeter surrounded on all sides by a two-layer active shield of proportional tubes. Its primary goal is to search for nucleon decay in modes which may be dominated by neutrino-interaction background in other experiments. The fine-grained sampling of the Soudan 2 calorimeter makes it an ideal instrument for the study of high energy neutrino interactions in the Main Injector neutrino beam. Compared to neutrino detectors which have been used in past experiments at Fermilab and CERN, Soudan 2 has similar mass and better resolution.

The performance of the calorimeter modules has been studied using cosmic ray muon tracks, both on the surface and underground. A charged particle test beam, at the Rutherford Laboratory ISIS accelerator, has been used to study detector response to low energy particles. The test beam studies have provided the energy calibration for electromagnetic showers and tracks, and have measured the ability of Soudan 2 to identify muon charge and direction.

The Soudan 2 detector [97] consists of 224 identical 4.3-ton calorimeter modules, which were constructed at the Argonne National Laboratory and the Rutherford Appleton Laboratory. The modules are arranged in a rectangular parallelepiped which is two modules high, by eight modules in the east-west direction, by 14 modules along the north-south axis of the cavity. The full detector is 5 m by 8 m by 16 m. This layout is illustrated in Figure B.1.

Each module is composed of 240 layers of 1 m by 1 m by 1.6 mm corrugated steel sheets, interleaved with an insulated "bandolier" assembly of 1 m long by 0.5 mm thick by 15 mm diameter resistive Hytrel drift tubes (see Figure B.2). The insulation consists of two layers of 125 μm mylar, laminated together with long pockets to accommodate the drift tubes, and 0.5 mm thick polystyrene inserts which are vacuum formed to fit the steel corrugation. The steel sheets and the bandolier are stacked in 240 layers (2.5 m high) by fanfolding the bandolier back and forth with steel sheets interleaved. The stack is then compressed with about 15 tons of force. Each module is enclosed in a gas-tight sheet steel enclosure consisting of welded sideskins to maintain compression and removable covers to allow access to the readout proportional wireplanes and stack faces. The assembled detector has a density

1.6 g/cm^3, a radiation length of 9.7 cm and a nuclear interaction length of $\sim$ 81 cm.

The basic detector element of the experiment is shown in Figure B.3. It is a tube made of resistive ($\sim 2\text{x}10^{12}\Omega - cm$) plastic Hytrel (DuPont Corporation). Each module contains 7560 drift tubes. A linearly graded electric field is applied by 21 1.5 mm wide copper electrodes (see Figure B.2). These have a voltage of -9 kV at the middle of the tube and 0 V at the two ends. The resistive tube grades the voltage between electrodes, creating a uniform axial drift field of 180 $volt/cm$ inside the tube. The modules are filled with a drift gas mixture of 85% argon, 15% CO_2 and 0.5% of H_2O (from the plastic). When a charged particle passes through the tube it ionizes the gas; the liberated electrons then drift (with a velocity of 0.6 $cm/\mu sec$) up to 50 cm to the ends of the tube where they are collected and amplified on a 50 μm diameter anode wire (gold plated tungsten). The gas is circulated through the modules and filtered to remove oxygen and hydrocarbons which absorb the drifting electrons.

The tubes are arranged in a close-packed hexagonal array as shown in Figure B.2. The anode wires run vertically in a plane 10 mm from the tube ends and are spaced every 15 mm so that they are aligned with the centers of the tubes. Cathode pads are connected in horizontal strips orthogonal to the anode wires and 5 mm behind them, and are aligned with the tubes. Thus it is possible to identify which tube a signal came from, since the anode wires and cathode pads form a grid centered on the tube ends. The position along the tube length is obtained from drift-time information. Three correlated spatial coordinates and a dE/dx measurement are recorded for every charged particle crossing of a drift tube.

The main detector is surrounded on all sides by a 2-layer array of extruded aluminum proportional tubes [98]. This active shield is mounted against the cavity walls to signal the presence of cosmic ray events in the cavity and the surrounding rock. The tubes are up to 7 m long and 20 cm wide and have a time resolution of 1 μs. Cosmic ray muons can create contained event candidates by entering the detector through the spaces between main detector modules, or by creating neutrons, photons and K_L^o's in the nearby rock which penetrate to the interior without leaving tracks. Such neutral particle production is almost always associated with charged particles which are detected in the shield. Because the 1700 m^2 shield has nearly 3.5 times the area of the main detector in the direction of Fermilab, it can also be used to increase the effective area for the measurement of the flux of muons from ν interactions in the rock upstream of Soudan 2.

B.1.1 Electronics readout

The detector is read out by 28,224 anode wires and 107,520 cathode pads through 5,888 electronics channels. The reduction in the number of channels is accomplished in two stages. Groups of 8 modules are stacked 2 high by 4 across to form a halfwall. The detector consists of 28 halfwalls. The two large faces of each halfwall each contain 8 wireplanes. Anode signals from the upper modules are bussed to the lower modules and cathode signals are bussed across the halfwall to give an equivalent readout plane which is 5 m high by 4 m wide and is known as a *loom*. Each loom consists of 252 anode channels and 480 cathode channels. Preamplifier signals from 8 anodes are then summed together by connecting the anode channels from 8 separate looms to one digitization crate. The preamplifier signals from each cathode pad are also summed 8-fold, but in a different pattern, ensuring that the looms served by one anode crate are served by different cathode crates. Since any one loom

is served by a unique anode crate and cathode crate combination, a tube anywhere in the detector may be located by matching the anode and cathode pulses.

The resulting 5888 channels of ionization signal are digitized by flash ADC's every 200 ns and stored in RAM. The digitization and data acquisition process occurs in a system of 24 parallel MULTIBUS crates each containing an Intel 80C86 microprocessor, which supervises a pipe-lined data compactor (which removes digitizations below a programmable threshold), and manages transfer of the compacted data *via* CAMAC to the host computer. Within each data crate there is a calibration card which, under local processor control, can be used to calibrate all the analog channels and verify the trigger logic within the data crate. The calibration card controls an array of pulsers which can send pulses to various combinations of the preamp inputs.

Digitization proceeds asynchronously in each of the 24 data crates with the RAM's used as circular data buffers. When a trigger decision is positive, the digitization is continued for an additional time beyond trigger time. This allows all the ionization for that event to drift out of the tubes so a complete drift history is stored for each channel.

To prompt the Soudan 2 detector to read out and store an event, it is necessary for the event to satisfy the trigger requirements. The raw data pulse patterns at the ADC inputs are continuously compared with programmable trigger conditions to detect localized clusters of hits in the drift tubes. The primary trigger requirement in the Soudan 2 detector is the "edge" trigger. A detailed description of the edge trigger will not be given here, for a complete account, see Reference [99]. Compton electrons produced by photons interacting in module wireplanes are a primary source of the noise rate in the detector. The edge trigger was designed to reject these events, so an event must have some minimum extent in the drift direction to satisfy this trigger. Since every readout channel contributes equally, the trigger requirement is uniform throughout the detector volume. Efficiency is high for muons above 230 MeV/c and falls linearly to zero at 90 MeV/c (for muons which do not have a visible decay). The electron (shower) triggering threshold is about 50 MeV. The rate of random triggers from natural radioactivity is less than 0.5 Hz in the full detector under these conditions. The trigger efficiency for neutrino events produced by the Fermilab beam will be essentially 100%. The deadtime will be less than 6%.

B.2 Detector status and operation

The Soudan 2 experiment has been operational since July 1988 when the first 275 tons of detector was turned on. Data were taken while the detector was being constructed; operation of the complete 963 ton detector began in November 1993. A total exposure of 2.2 kiloton years has been obtained to date (February 1995). Reconstruction and filtering of contained neutrino events and cosmic ray muons is performed at the Soudan site immediately after data acquisition. Detailed analysis has been completed on all data taken before November 1992 (1.0 fiducial kton-years). The analysis of data from the second kiloton year exposure will be completed during the spring of 1995. The detector is now in routine data taking operation more than 80% of the time. Most of the down time is associated with the upgrade of older modules which will be completed in 1995. The performance of the detector has been reliable and stable over the past four years of operation. We do not anticipate any problems

with continuing operation through the time period when a neutrino beam might be available. We are in any case committed to running Soudan 2 at least through 1998 to obtain a proton decay exposure of 5 fiducial kton-years. The detector performance is entirely consistent with the original Soudan 2 proposal and more than adequate to perform this experiment.

Data at the Soudan site are stored on disk in runs of $\sim$ 1 hour length, and is processed immediately after the end of a run on a local VAX Cluster with an analysis package SOAP (Soudan Offline Analysis Program). SOAP performs noise rejection, pulse matching, track reconstruction, and sorting of events into various categories of physics interest, such as muons, multimuons, monopole candidates, (contained) neutrino candidates, and semi-contained events. Muons from neutrino interactions in the rock from the direction of Fermilab would all be found in the muon sample. Neutrino events would be in either the contained or semi-contained event classifications. An additional processor would be established to flag events that were in time with a Fermilab beam pulse. This event sample would be compared with the contained and semi-contained event samples to ensure that all Fermilab events were being found with high efficiency.

The detector is monitored in several ways to assure that it is operating properly. The pulser system is used to inject signals into the preamp inputs. These signals then work their way through the readout chain and check the operation of the electronics. Pulser calibration runs are performed daily to find amplifiers with incorrect gain, disconnected cables, *etc.* The response of the detector (as well as the electronics) is continuously monitored by analyzing the data from through-going cosmic ray muons. These muons trigger the experiment at a rate of about 0.3 Hz. One to two days of data are sufficient to detect larger effects such as air leaking into a module or bad electrical connections inside a module. A sample of tracks accumulated over about one month is used to measure the detailed pulse height response at the level of individual drift tubes and can be used to correct the pulse heights in the region of nucleon decay or neutrino interaction candidate events.

An example of part of a cosmic ray muon track is shown in Figure B.4. The fine detail of a few pulses can be seen. This shows both the pulse shape information and the 200 ns digitization time. The result of the fit to that part of the track in relationship to the pattern of the stack is also shown. A complete muon track traversing the detector is shown in Figure B.5. Comparing the two figures, the large amount of information that is available for each event is apparent.

To provide pulse height uniformity over time, the atmospheric pressure is monitored and the anode wire high voltage is adjusted to compensate the effect of pressure changes on gas gain in both the modules and the shield.

B.3 Performance and calibration

B.3.1 Module performance

In order to optimize the operating parameters (*e.g.*, gas and electronic gains), a few modules were initially operated on the surface where the cosmic ray flux is high enough to do high statistics studies rapidly. Some of the results on performance of the modules operated on the surface are presented in this Section.

For the study of tube efficiency the cosmic ray muon trajectories were fitted. By comparing the number of hit tubes crossed by the trajectory with the number predicted to be hit, the tube efficiency is determined. Such a definition not only considers if the tube is working, it also includes the anode-cathode matching efficiency and the track fitting efficiency. Moreover, the efficiency will be decreased due to deviations of the actual tube position from its nominal position, and random scattering of the muon from a smooth trajectory. In the case of perfect geometry, for Monte Carlo data, the tube efficiency is 85%. Under actual operating conditions the mean tube efficiency is of the order of 75%. The mean tube efficiency is very uniform throughout a module, as is shown in Figure B.6, where the efficiency is plotted along the cathode direction. The variations seen in Figure B.6 are correlated with the pulse height variations along the cathode direction. The maximum tube efficiency that is reached is 80% for very high pulse heights, but the modules were operated at the knee of the efficiency plateau to remain in the proportional gain region.

Typical drift attenuation lengths are of the order of 70 *cm*. For the pulse height distribution shown in Figure B.7 the attenuation lengths for the two 50 *cm* drift regions are 71 and 63 *cm*. Such attenuation is well understood in terms of electron diffusion during drifting and electron attachment due to O_2 contamination at the few ppm level. Some variations from module-to-module can be observed, even with the same gas composition, due to imperfections in the electric field which show up as a difference in the effective radii of the tubes. In the absence of oxygen attachment, attenuation lengths are expected to be about 70 *cm*. The spatial resolution is determined by the anode and cathode spacing, the drift time digitization unit and the drift velocity. Spatial resolutions are obtained from the residual distributions of fits to cosmic ray muon tracks. The resolution of the wireplanes is found to be 0.35 *cm* RMS (in the $x - y$ plane), compatible with expectations from anode and cathode spacing. The spatial resolution in the drift (z) direction is measured to be 1.12 *cm* RMS.

One of the main characteristics of the Soudan 2 detector is its ability to yield pulse height information for track direction determination and particle identification. To make maximum use of this information, the pulse height variation between modules must be smaller than Landau fluctuations (20%). Typical pulse height fluctuations along the wire plane are of the order of 30%, while in the drift direction, due to pulse height attenuation, a 50% reduction in pulse height can be observed (see Figure B.7). However, these variations are corrected by calibrating out the effects of measured pulse height attenuation, wire plane nonuniformities, module-to-module variations, and gas composition. After pulse height calibration, a 10% variation is obtained.

B.3.2 Module calibration

At the Rutherford Laboratory's ISIS pulsed neutron source, a Soudan 2 calorimeter module was exposed to beams of positive and negative pions, muons, and electrons at momenta between 140 and 400 MeV/c, and protons at 700 and 830 MeV/c, for several angles of incidence. Analysis of the data is in progress but preliminary results are available on the detector resolution, ionization response, and particle identification. These studies have confirmed that the detector modules are performing as expected, and also have provided detailed response parameters which can be used in the Monte Carlo detector simulation.

The electromagnetic shower energy is determined by counting tube crossings (hits). Fig-

ure B.8 shows the number of tube crossings as a function of the electron beam energy, for ISIS and Monte Carlo data. The non-linear dependence upon the energy reflects the high density of tube crossings at high energy. The measured energy resolution can be represented as in Figure B.9.

Although the Soudan 2 detector is designed to be relatively isotropic, its geometry is not completely uniform. This fact will affect, at some level, the number of hits counted for shower energy measurement. Figure B.10 (a) shows the number of hits observed for different vertical incidence angles of the beam, for tracks perpendicular to the tubes. The maximum variation (8%) is obtained for small vertical angles. This variation is easily calibrated. The total pulse height is independent of the vertical incidence angle as is shown in Figure B.10 (b). When the dependence upon horizontal angle (angle with the z direction) was measured, a variation of the number of hits was observed where the beam is almost parallel to the tubes (see Figure B.10 (c)). The total pulse height does not vary with horizontal angle (Figure B.10 (d)). Therefore, the Soudan 2 detector is isotropic after some small corrections. The small detector anisotropy observed is confirmed with the Monte Carlo and does not compromise the energy resolution.

A sample of $\pi^{0's}$ produced in charged pion interactions has been reconstructed. The events were selected by scanning for events with two well separated showers. The π^0 peak is centered at 136 ± 3 MeV/c^2 and has an RMS of 40 MeV/c^2 (see Figure B.11). When the production vertex is known it is possible to distinguish electrons from photons by measuring the distance between the vertex and the first hit (conversion length). If the distance is smaller than 4 cm the relative probability to be $e : \gamma$ is $8 : 1$, for a distance larger than 4 cm the shower is more likely a photon with $e : \gamma$ a probability of $1 : 14$.

Muon momentum is calculated from the range obtained by measurement of the muon track length (L) and using a mean detector density (1.6 g/cm^3). The average length for 245 MeV/c muons is 40.6 cm, with $\Delta L/L = 20\%$, giving a momentum resolution of 8%. This resolution is independent of momentum for the ISIS energies.

Soudan 2 can distinguish between stopping positive and negative muons because most negative muons are captured by iron nuclei and do not decay visibly. The decay positrons from positive muons are usually detected. Figure B.12 shows the number of extra hits at the ends of tracks for samples of negative and positive muons. Two or more shower hits are observed at the end of 85% of the positive muon tracks. No hits are observed for 75% of the negative muon tracks.

The expected ionization response of a slowing muon is observed. Figure B.13 shows the mean pulse height along the muon trajectory measured from the end of the track. Crude measurement of the track direction (choosing the end with the higher mean ionization on the last 5 hits as the stopping end) yields the correct direction 80% of the time.

B.4 Detector summary

Some advantages of the Soudan 2 detector for detecting and identifying neutrino events are:

- The fine granularity gives very good track and vertex resolution. The result is high quality pictorial event information, comparable to, or better than that from previous

electronic neutrino experiments. The spatial resolution is 1 cm or better in all three spatial coordinates.

- The ionization measurement yields particle identification information (*e.g.*, proton/pion-muon separation) not available in some other detectors.
- μ^- absorption in iron gives track charge information. (about 2/3 of stopped μ^+'s decay visibly in Soudan 2.)
- In a moderate density iron calorimeter, high energy muon/hadron separation is easy.
- The energy threshold of the trigger for muons is lower than in any other underground ν detector.
- The observation of shower development yields better low energy electron-muon separation than in water Čerenkov detectors.
- The modularity of the detector has allowed detailed test beam calibration studies. Detector modules will also be calibrated in a high energy charged particle test beam at Fermilab at energies appropriate for the P–822 proposal.
- The modularity of the detector will allow us to operate an almost identical type of near detector in the P–822 neutrino beam at Fermilab.

The particular features which make this detector powerful for the proposed neutrino experiment are the excellent pattern recognition and particle identification of hadrons, muons and electrons. This capability will enable reliable separation of charged and neutral current events and the identification of the flavor of the final state lepton.

B.5 Soudan 2 upgrades proposed for P–822

The P–822 proposal [76] envisioned the use of existing Soudan 2 modules for both the near and far detectors of a two-station neutrino oscillation experiment. The far detector would consist of the existing detector, minus about 10% of its modules, which would be taken to Fermilab for calibration in a high energy hadron beam. These 20 modules would also be used to construct the Fermilab near detector for the experiment. The Soudan detector itself would be upgraded by (1) enhancing the active shield to improve the detection of neutrino-induced muons emerging from the upstream rock walls, and (2) adding a downstream muon spectrometer, consisting of a large iron toroid and drift chambers.

For the present experiment the Soudan 2 detector would perform an independent, lower statistics search for neutrino oscillations, in parallel with that in the new MINOS detector. The experiment with Soudan 2 would still require a near detector built from Soudan 2 modules, but the shield enhancement and the addition of a downstream muon spectrometer would no longer be essential. These upgrades were expected to be fairly expensive ($1.2M for the shield and $2.4M for the muon spectrometer) and we do not plan to implement them in the context of the present experiment. Excellent measurements of rock muons and the muon momentum spectrum will both be made by the new detector. We plan to perform

the hadron beam calibration of Soudan 2 modules at Fermilab at the same time as the similar calibration of the new detector prototype. These same modules would then be used to construct the Soudan 2 near detector, as described in Chapter 6.

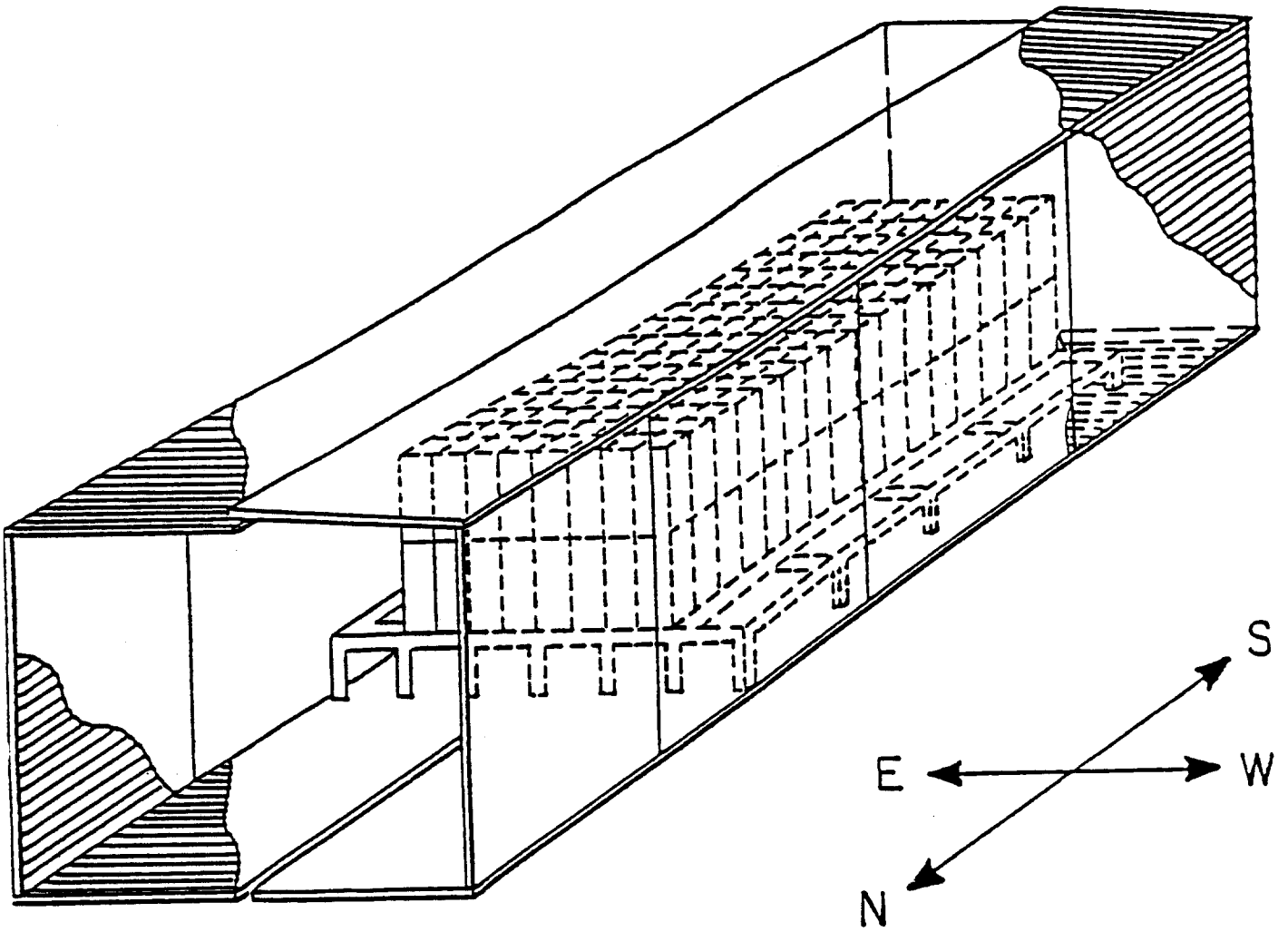

Figure B.1: Soudan 2 main detector and active shield layout.

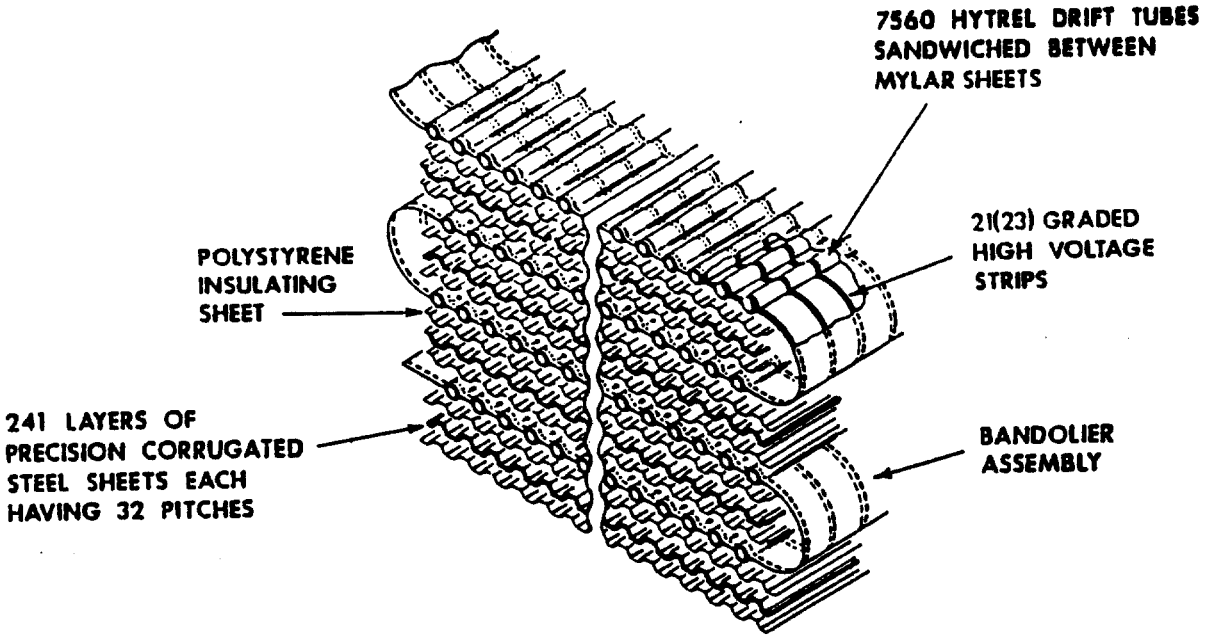

Figure B.2: *Bandolier*, insulation sheets (inserts) and corrugated steel assembly (stack).

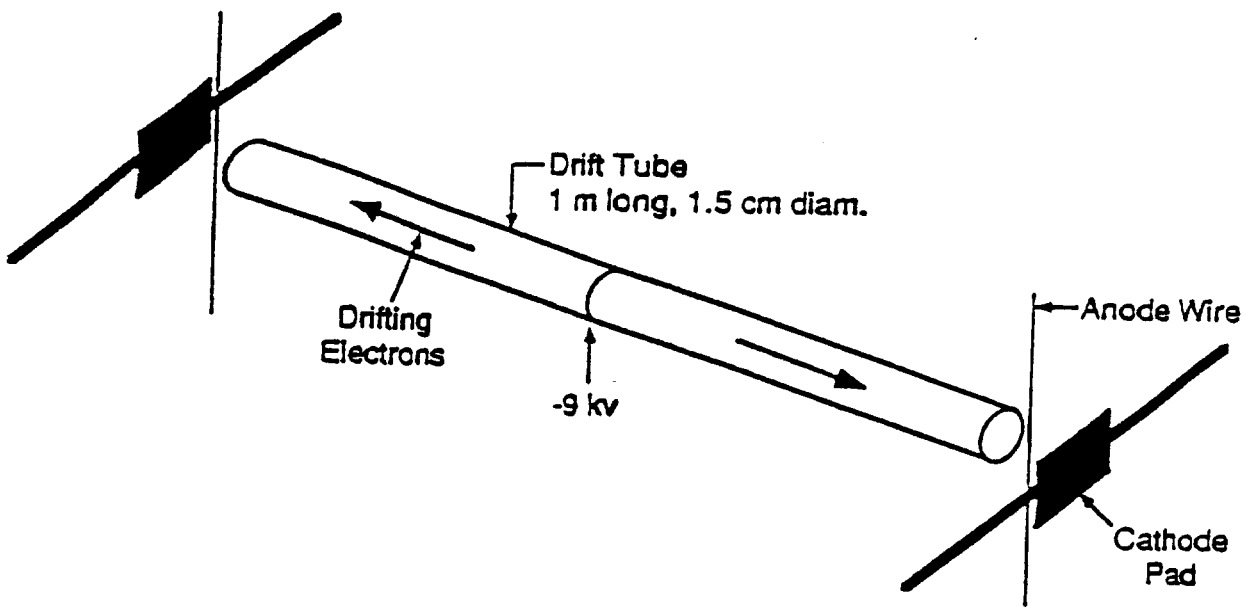

Figure B.3: A single drift tube. The drift field is generated by the application of graded voltages on a series of 21 copper electrodes

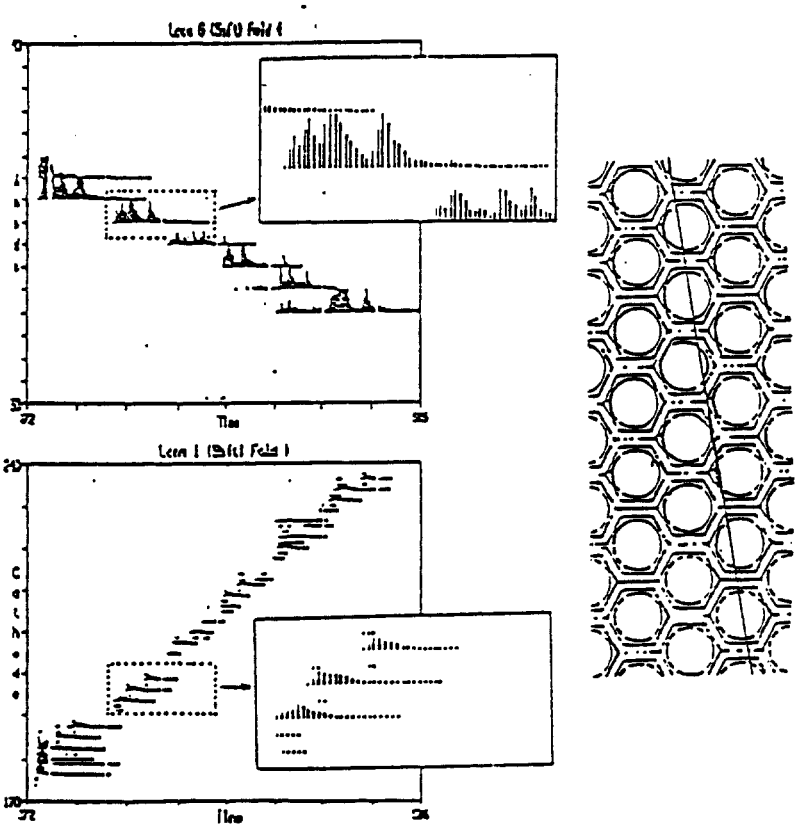

Figure B.4: Segment of a muon track and fit

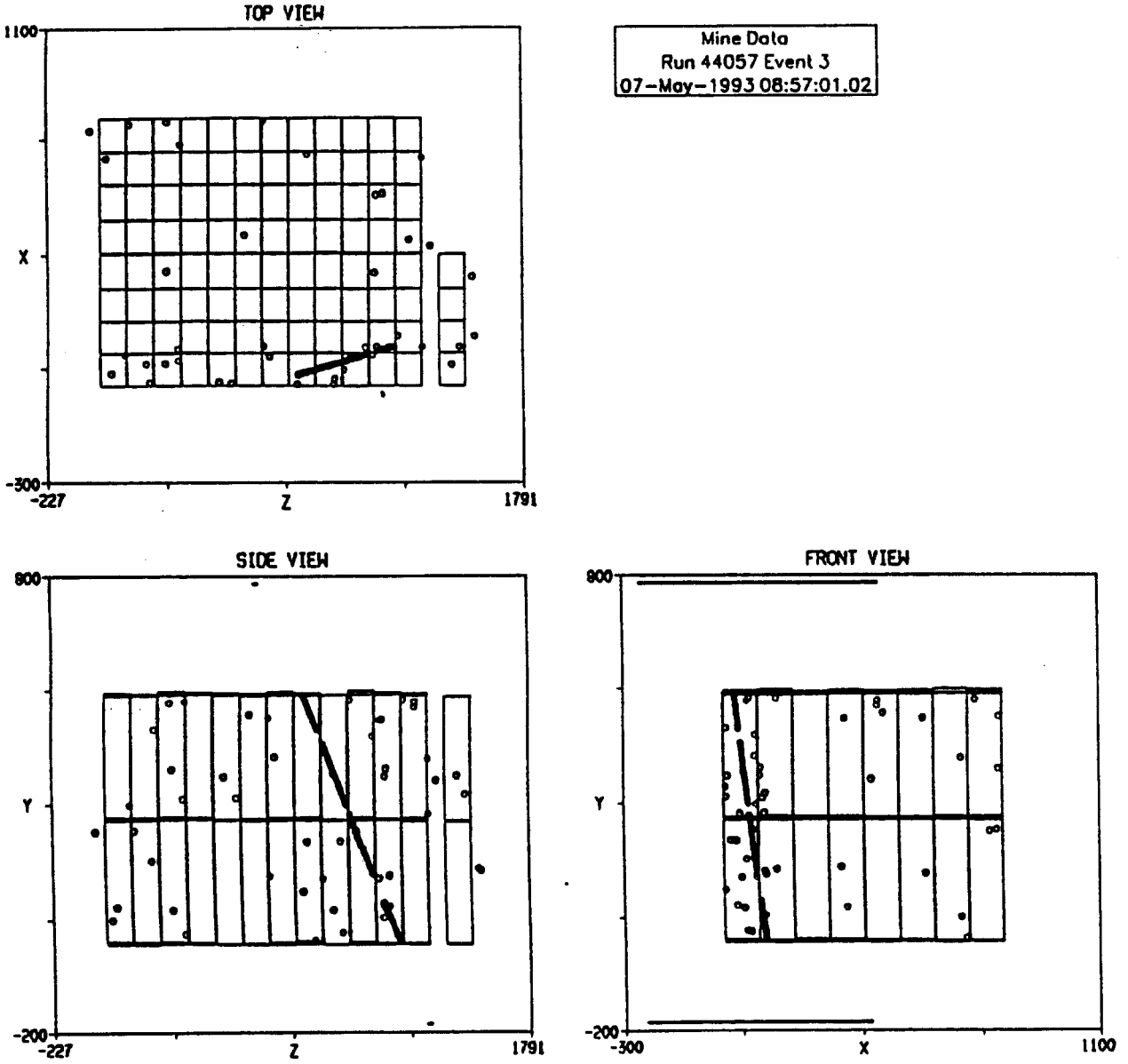

Figure B.5: A cosmic ray muon in the Soudan 2 detector. The anode-time (x), cathode-time (y), and matched (z) views are shown

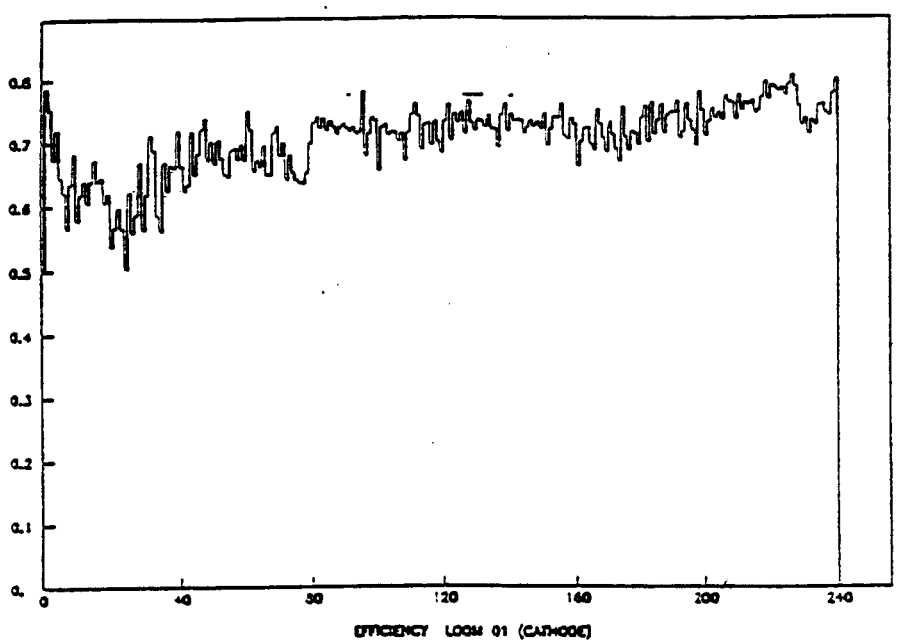

Figure B.6: Typical mean tube efficiency variation with cathode numbers.

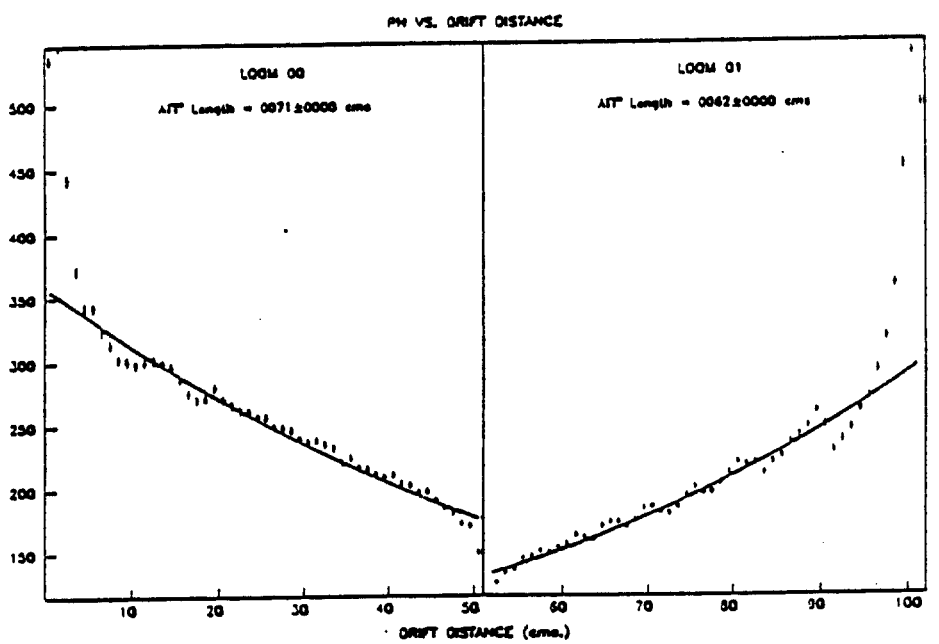

Figure B.7: Typical pulse height variation along the drift direction.

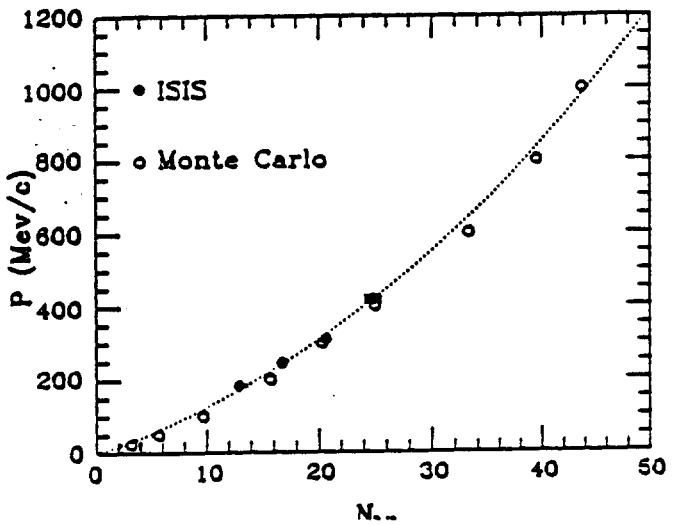

Figure B.8: Electron shower energy versus number of hits from ISIS data and Monte Carlo simulations.

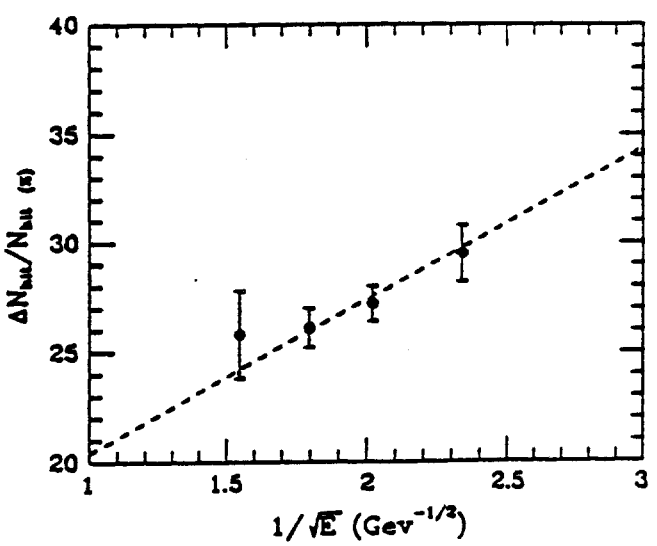

Figure B.9: Energy resolution for electron showers.

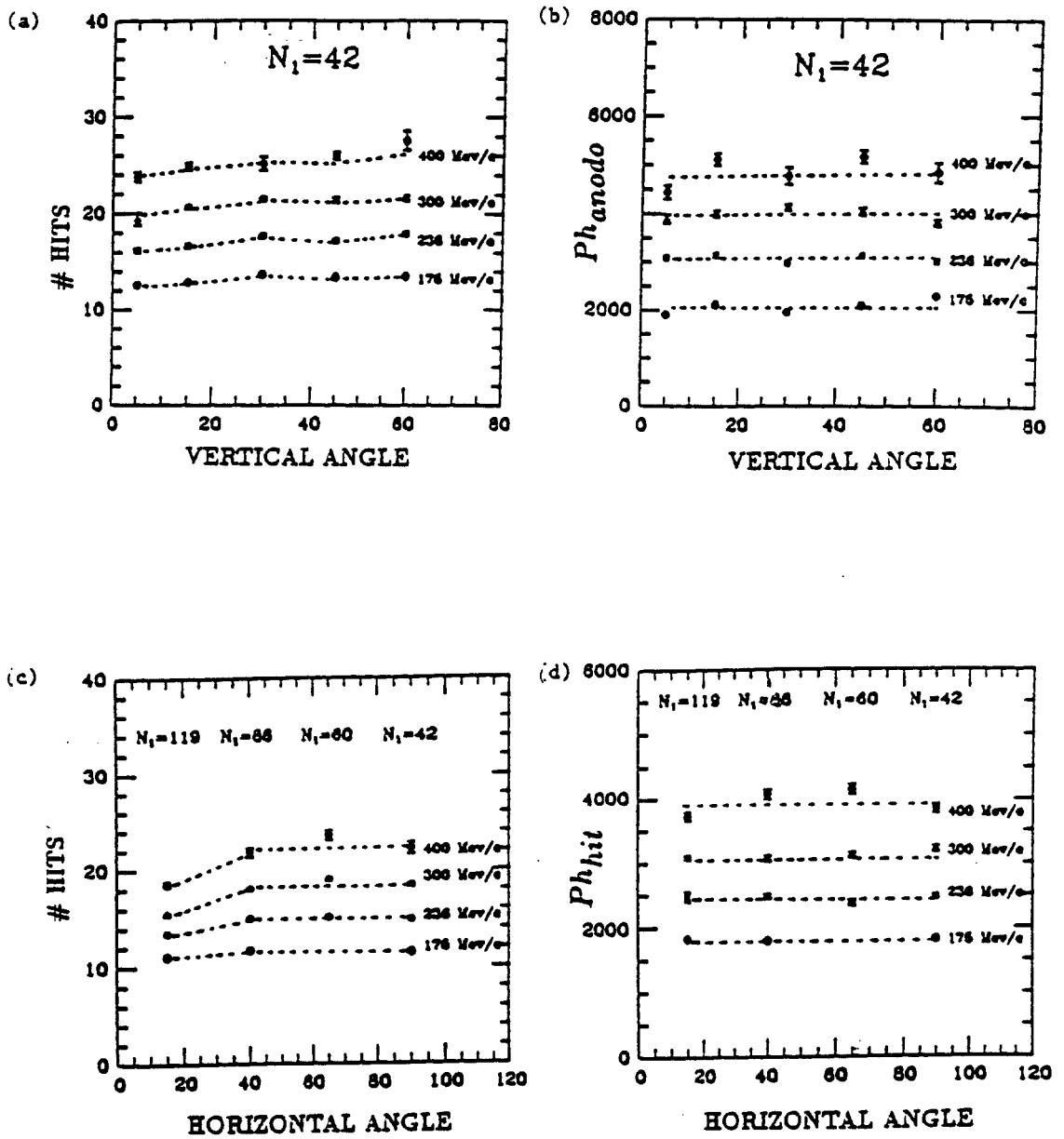

Figure B.10: Mean number of hits (a) and mean total pulse height (b) for different beam momenta versus the vertical angle, and mean number of hits (c) and mean total pulse height (d) versus the horizontal angle.

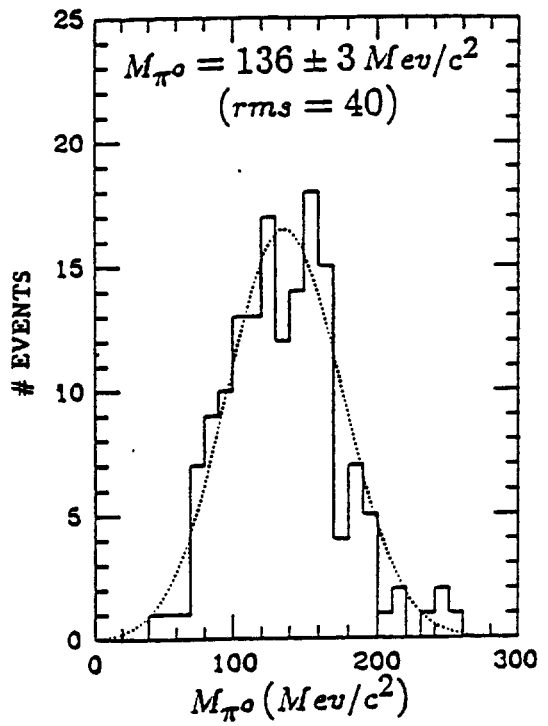

Figure B.11: Invariant mass distribution for two shower events in the $\pi^{\pm}$ beam.

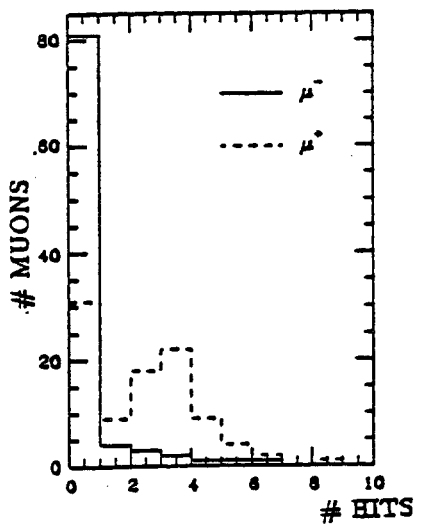

Figure B.12: Number of shower hits at the end of μ^+ and μ^- tracks.

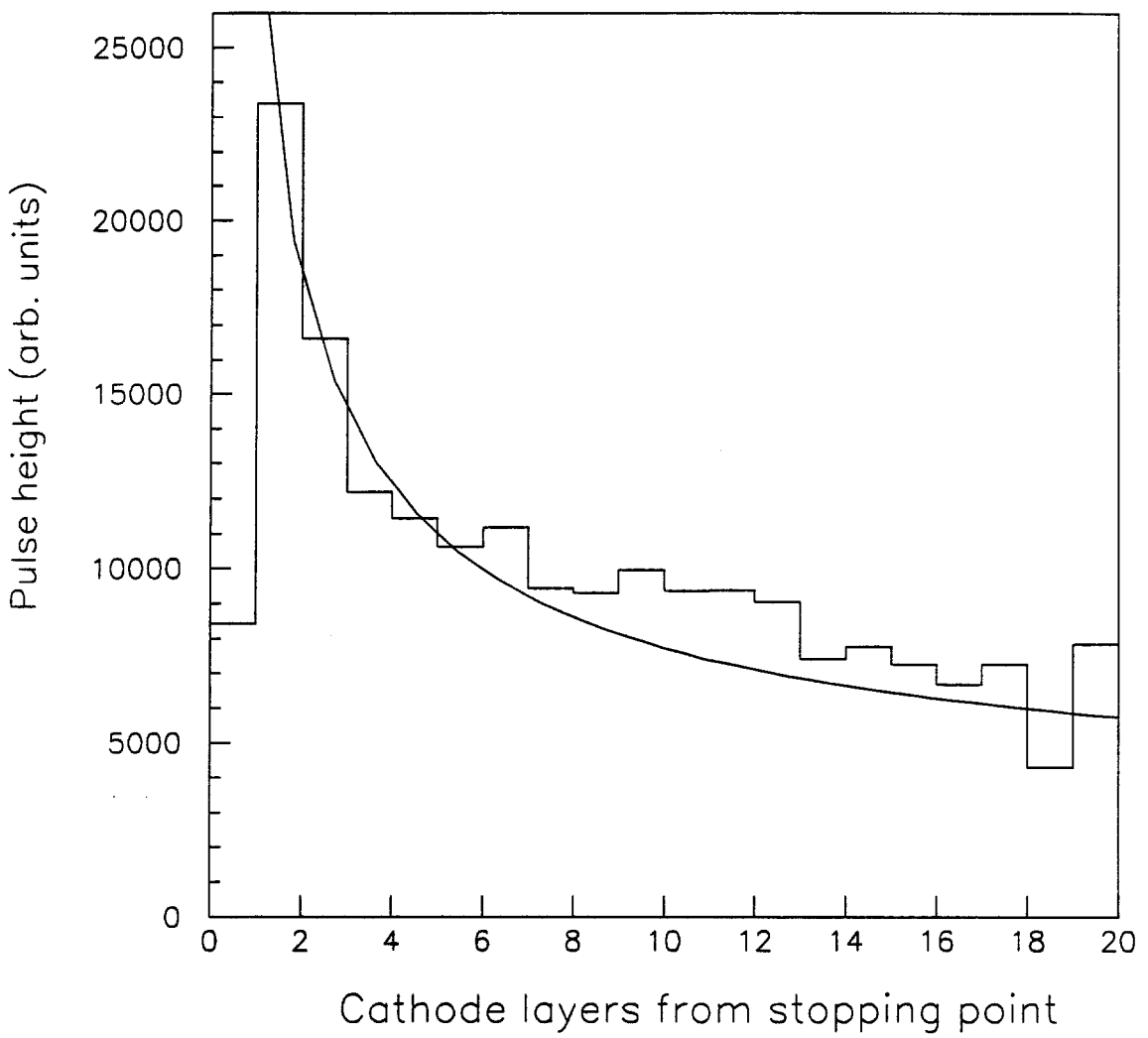

Figure B.13: Mean pulse height versus anode number (measured from the last anode in the μ trajectory).

Bibliography

[1] Review of Particle Properties, Phys. Rev. **D50**, 1173 (1994).

[2] See, *e.g.*, H. Harari, Summary talk of Neutrino '94, Eilat, Israel, 1994 (to be published in the Proceedings).

[3] R.D. Bolton *et al.*, Phys. Rev. **D38**, 2077 (1988).

[4] K. Arisaka *et al.*, Phys. Rev. Lett. **70**, 1049 (1993).

[5] F. Boehm and P. Vogel, *"Physics of Massive Neutrinos"* (Cambridge University Press, Cambridge, 1987), p. 82.

[6] R. Davis *et al.*, in *Proc. 21st Int. Cosmic Ray Conference, Adelaide, 1990*, Vol. 12, p. 143; P. Anselmann *et al.*, Phys. Lett. **B285**, 376 (1992), Phys. Lett. **B285**, 390 (1992), Phys. Lett. **B314**, 445 (1993); A.I. Abazov *et al.*, Phys. Rev. Lett. **67**, 3332 (1991); K.S. Hirate *et al.*, Phys. Rev. Lett. **65**, 1297 (1990), Phys. Rev. Lett. **66**, 9 (1991), Phys. Rev. **D44** 2241, (1991).

[7] Proceedings of Neutrino '94, Eilat, Israel, 1994 (to be published).

[8] J. Bahcall, *"How Many Solar Neutrino Experiments are Wrong?"*, preprint IASSNS-AST-94-37, Institute for Advanced Studies, Princeton, July 1994 (submitted to Physics Letters B).

[9] P. Anselmann *et al.*, Phys. Lett. **B342**, 440 (1995).

[10] See, *e.g.*, J. Bahcall, *"Neutrino Astrophysics"* (Cambridge University Press, Cambridge, 1989).

[11] See, *e.g.* H. Harari, Phys. Lett. **B216**, 413 (1989).

[12] G.F. Smoot *et al.*, Astrophys. J. **396** 3, 155-B5 (1992); G.F. Smoot *et al.*, Astrophys. J. **396** L1, 160-B1 (1992); G.F. Smoot *et al.*, COBE preprint, 1992; E.L. Wright *et al.*, COBE preprint, 1992.

[13] N. Ushida *et al.*, Phys. Rev. Lett. **57**, 2897 (1986).

[14] N. Reay (spokesman), *E-803 proposal for a short baseline experiment at Fermilab*, October 1990; revised October 1993.

[15] L. Borodovsky *et al.*, Phys. Rev. Lett. **68**, 274 (1992).

[16] K.S. Hirata *et al.* (Kamiokande Collaboration), Phys. Lett. **B280**, 146 (1992). This paper reported on a 4.92 kT-year exposure. The exposure for sub-GeV, fully contained events is now 7.7 kT-year [24].

[17] R. Becker-Szendy et al. (IMB Collaboration), Phys. Rev. **D46**, 3720 (1992).

[18] Kamiokande presentation at Neutrino '94, Eilat, Israel, 1994 (to be published in the Proceedings).

[19] M. Circella *et al.*, in *Proc. 23rd Int. Cosmic Ray Conf., Calgary, 1993*, Vol. 4, p. 503.

[20] D. Müller *et al.*. (HEAT Collaboration), in *Proc. 22nd Int. Cosmic Ray Conf., Dublin, 1991*, Vol. 2, p. 177.

[21] D.H. Perkins, Astroparticle Physics **2**, 249 (1994).

[22] H. Meyer, for the Frejus collaboration, talk presented at the 1994 Snowmass Summer Study, July 7, 1994.

[23] Ch. Berger *et al.*. (Frejus), Phys. Lett. **B245**, 305 (1990); **B227**, 489 (1989).

[24] Y. Fukuda *et al.*, Phys. Lett. **B335**, 205 (1994).

[25] M. Honda, K. Kasahara, K. Hidaka and S. Midorikawa, Phys. Lett. **B248**, 193 (1990).

[26] J. Engel, E. Kolbe, K. Langanke and P. Vogel, Phys. Rev. **D48**, 3048 (1993).

[27] W. A. Mann *et al.*, Phys. Lett. **B291**, 200 (1992).

[28] R. Becker-Szendy et al., Phys. Rev. Lett. **69**, 1010 (1992).

[29] M. Goodman, in *Proceedings of the Atmospheric Neutrino Workshop, 6-8 May 1993*, LSU-HEPA-93-6.

[30] T. Kajita, in *Proceedings of the Atmospheric Neutrino Workshop, 6-8 May 1993*, LSU-HEPA-93-6.

[31] D. Michael (private communication).

[32] L.V. Volkova, Sov. J. Nucl. Phys. **31**, 1510 (1980).

[33] E. Eichten, I. Hinchcliffe, K. Lane and C. Quigg, Rev. Mod. Phys. **56**, 579 (1984); **56**, 1065(E) (1986).

[34] W. Frati, T.K. Gaisser, A.K. Mann and Todor Stanev, Phys. Rev. **D48**, 1140 (1993).

[35] M. Mori *et al.*, Phys. Lett. **B270**, 89 (1991).

[36] A.V. Butkevich, L.G. Dedenko and I.M. Zheleznykh, Sov. J. Nucl. Phys. **50**, 90 (1989).

[37] V. Agrawal, T.K. Gaisser, Paolo Lipari and Todor Stanev (unpublished).

[38] J.F. Owens, Phys. Lett. **B266**, 126 (1991).

[39] D. Michael for the MACRO Collaboration, talk presented at the 1994 Snowmass Summer Study, July 7, 1994.

[40] M.M. Boliev et al. (Baksan Collaboration), in *Proc. 3rd Int. Workshop on Neutrino Telescopes, Venice, 1991*, edited by M. Baldo-Ceolin, p. 235.

[41] P.F. Harrison, D.H. Perkins and W.G. Scott, "Threefold Maximal Lepton Mixing and the Solar and Atmospheric Neutrino Deficits", submitted to Phys. Lett. B, December (1994); also C. Giunti, C.W. Kim and J.D. Kim, "Atmospheric Neutrino Problem in Maximally Mixed Three Generations of Neutrinos", DFTT-54-94, submitted to Physics Letters B, October (1994).

[42] P.F. Harrison and W.G. Scott, Phys. Lett. **B333**, 471 (1994).

[43] J. Learned, S. Pakvasa, and T.J. Weiler, Phys. Lett. **B207**, 79 (1988).

[44] S. Dimopoulos, L. Hall and S. Raby, Phys. Rev. **D47**, R3697 (1993).

[45] S. Pakvasa (private communication); E.K. Akhmedov *et al.*, Phys. Lett. **69**, 3013 (1992).

[46] J. Pantaleone, A. Halprin and C. Leung, Phys. Rev. **D47**, 4199 (1993); also M.N. Butler, S. Nozawa, R.A. Malaney and A.I. Boothroyd, Phys. Rev. **D47**, 2615 (1993).

[47] D. Caldwell and R. Mohapatra, Phys. Rev. **D50**, 3477 (1994).

[48] L. Wolfenstein, as reported at the Workshop on The Many Worlds of Neutrino Physics, Fermilab, October 1991.

[49] C. Albright *et al.*, *"Construction of Fermion Mass Matrices Yielding Two Popular Neutrino Scenarios"*, preprint FERMILAB-PUB-94/061-T, 1994.

[50] S. Dodelson, G. Gyuk and M. Turner, Phys. Rev. Lett. **72**, 3754 (1994).

[51] G.L. Fogli, E. Lisi and D. Montanino, preprint CERN-TH.7491/94.

[52] G.S. Vidyakin *et al.*, J. Exp. Theor. Phys. Lett. **59**, 390 (1994).

[53] N. Stanton, *"E-803 Sensitivity to Antineutrino Contamination in the Beam"*, NuMI-S-25 (1994).

[54] R. Bernstein *et al.*, *"Conceptual Design Report: Main Injector Neutrino Program"*, FNAL, 1991; *"Project Definition Report: NuMI Project"*, FNAL F.E.S.S., 1993; *"Project Definition Report: NuMI Project (LBL MI-60)"*, FNAL F.E.S.S., 1994.

[55] D.C. Carey and V.A. White, *"NUADA, the Fermilab Neutrino Flux Program"*, Note PM0011, Fermilab, June 1975.

[56] A.J. Malensek, *"Empirical Formula for Thick Target Particle Production"*, Note FN-341, Fermilab, 1981; *"Comparison of Particle Production Measurements and FN-341 with 100 GeV Protons"*, Note NuMI-B22, Fermilab, 1994.

[57] Noel Stanton, Kansas State University (private communication).

[58] S.P. Denisov *et al.*, Nucl. Phys. **B61**, 62 (1973).

[59] The NUANL Monte Carlo is by Robert E. Blair and Daniel A. Crane, Argonne National Laboratory.

[60] The horns and dichromatic beam line are designs by Anthony Malensek, see notes NUMI-B24, NUMI-B34, NUMI-B39, and NUMI-B56.

[61] N. Stanton, *"Beam Issues from a Short-Baseline Perspective"*, NuMI-S-40 (1994).

[62] T. Sager, *"P-875 Survey and Alignment, Status and Costs"*, NuMI-L-62 (1995).

[63] D. Crane and M. Goodman, *"Study of Neutrino Beam Properties"*, NuMI-L-64 (1995).

[64] R. Blair *et al.*, *"Long Baseline Neutrino Beam Calculations"*, NuMI-B-27 (1994).

[65] J. Bofill *et al.*, Phys. Rev. **D36**, 3309 (1987).

[66] T. Eldridge, *"Total Cross Section Measurements for $\nu_\mu + \bar{\nu}_\mu$ Charged Current Deep Inelastic Scattering"*, Ph.D. thesis, Massachusetts Institute of Technology, 1985, p. 49.

[67] A. Bodek *et al.*, Z. Phys. **18C**, 289 (1983).

[68] D. Bollini *et al.*, Nucl. Instr. Meth. **A204**, 333 (1983).

[69] M. Holder *et al.*, Nucl. Instr. Meth. **A148**, 235 (1978).

[70] M. Catanesi *et al.*, Nucl. Instr. Meth. **A247**, 438 (1986).

[71] K. Ahmet *et al.*, Nucl. Instr. Meth. **A305** 275, (1991).

[72] P. Aarnio *et al.*, Nucl. Instr. Meth. **A303**, 233 (1991).

[73] S.P. Ahlen *et al.*, Nucl. Instr. Meth. **A324**, 337 (1993).

[74] S. Cartwright *et al.*, Nucl. Instr. Meth. **A277**, 269 (1989).

[75] J.D. Bjorken, in *Proceedings of the Workshop on New Directions in Neutrino Physics, Fermilab, 1988*, p. 262.

[76] The P-822 proposal is described in the following documents submitted by the P-822 Collaboration:
"Proposal for a long baseline neutrino oscillation experiment using the Soudan 2 neutrino dectector", March 1991;

"Progress report and revised P–822 proposal for a long baseline neutrino oscillation experiment from Fermilab to Soudan", October 1993;
"Update to P–822: proposal for a long-baseline neutrino oscillation experiment from Fermilab to Soudan", March 1994;
"P–822 response to the PAC's questions of 11th April 1994", May 1994.

[77] J. Botts *et al.*, Phys. Lett. **B304**, 159 (1993).

[78] C. Albright and C. Jarlskog, Nucl. Phys. **B84**, 467 (1975).

[79] Roger Phillips (private communication).

[80] Roger Phillips (private communication).

[81] C. Llewellyn-Smith, Phys. Rep. **3C**, 261 (1972).

[82] D. Rein and L.M. Sehgal, Ann. Phys. **133**, 79 (1981).

[83] K. de Winter *et al.*, Nucl. Instr. Meth. **A277**, 83 (1989).

[84] A. Bodek and J. L. Ritchie, Phys. Rev. **D23**, 1070 (1981).

[85] R. Merenyi *et al.*, Phys. Rev. **D45**, 743 (1992).

[86] S. Jadach *et al.*, Comp. Phys. Comm. **64**, 275 (1990).

[87] S.V. Belikov *et al.*, Z. Phys. **A320**, 625 (1985).

[88] D. Michael, *"Searching for Oscillations of Atmospheric and Accelerator Neutrinos"*, August 1992 (unpublished).

[89] A.P. Szabo and R.J. Protheroe, Astroparticle Physics **2**, 375 (1994).

[90] P.L. Biermann and J.P. Cassinelli, Astron. Astrophys. **277**, 691 (1993).

[91] P.L. Biermann, Astron. Astrophys. **271**, 649 (1993).

[92] W.W.M. Allison *et al.*, in *Proc. of the 23rd Intl. Cosmic Ray Conf., Calgary, 1993,* Vol. 4, p. 398.

[93] S. Ahlen *et al.*, Phys. Rev. **D46**, 895 (1992).

[94] N.P. Longley *et al.* (submitted to Phys. Rev. D).

[95] I.P. Ivanenko *et al.*, in *Proc. of the 23rd Intl. Cosmic Ray Conf., Calgary, 1993,* Vol. 2, p. 17.

[96] K. Asakimori *et al.*, in *Proc. of the 23rd Intl. Cosmic Ray Conf., Calgary, 1993,* Vol. 2, p. 21.

[97] J.L. Thron, Nucl. Instr. Meth. **A283**, 642 (1989).

[98] W. P. Oliver *et al.*, Nucl. Instr. Meth. **A276**, 371 (1989).

[99] S. Werkema, *"Monte Carlo Evaluation of the Atmospheric Neutrino Background to Nucleon Decay in the Soudan 2 Detector"*, Ph.D. thesis, University of Minnesota, 1989.

P875

Response to PAC Question No. 2 relating to the NuMI Beam Line

Dan Crane, Bill Freeman, Gordon Koizumi, Anthony Malensek,
Jorge G. Morfín, Steve O'Day, Tim Toohig
Revised: 25 April 1995

2. The collaboration and the Laboratory need to provide a more detailed conceptual design and cost estimate for the neutrino beam, both for the wide-band and narrow-band options. The method of switching between wide-band and narrow-band beams should be described. The plans for the maintenance of the beamline in the high radiation environment should also be included.

In preparation for the HEPAP Sub-panel visit in mid-June the NuMi Beam Group has contracted Fluor-Daniel to produce engineering drawings for a civil construction Conceptual Design Report (CDR) which will include all below-ground enclosures and surface buildings. The enclosures themselves have been sized following several rounds of discussions with the COSMOS and MINOS collaborations to ensure that the size is minimal but adequate to do the physics. These engineering drawings will be available at the time of your meeting on 28/29 April. For this written report we have included the simple conceptual drawings, used for the costing, for your information.

The costing procedure for the civil construction is still underway. A costing model, developed by Tim Toohig and briefly described to you at the February PAC meeting, has been used to arrive at the totals. An independent confirmation of the model has been contracted to Sverdrup Civil, Inc. which performed similar services for the Main Injector Project. The full cost endorsement will be ready for the HEPAP sub-panel visit. An interim report is enclosed for your information. It compares the costs of Rev 0 (the "deep" Soudan design described in the report), Rev 1 (the "shallow" Soudan design) and the current costing model. The bottom line, before escalation, of the current costing model is $18.1M which is $8.3M less than Rev 0. After full escalation the comparison is $45.7M for Rev 0 compared to $31.7M for the Toohig Model.

A full technical design report (TDR) is also being prepared for the HEPAP sub-panel visit. A fairly complete WBS costing of the technical components is attached. Our confidence in the costing of most of the technical systems is quite high since we have designed, built and installed such systems before. The items which currently have the highest degree of uncertainty are the dichromatic element costs and the cost of the horn and its power supply. Due to these items the contingency is currently set at 25%. By the time of the HEPAP review this could be reduced to 15%. The total cost, before escalation, of just under $4.0M is consistent with earlier estimates since this total now includes $1.2M for a narrow band beam.

The time involved in switching from horn wide-band to narrow-band beam (NBB) is, as one might expect, dominated by radiation safety concerns. The actual removal of the horn beam and installation of the NBB components can be performed in 12-15 four-hour shifts if the NBB components are stored in the transfer hall of the target enclosure and pre-alignment of stands and fixtures has taken place. The important concern of how long one must wait before beginning the change-over has been briefly examined. We have determined that with a shield of marble (Calcium Carbonate) surrounding the steel we would probably have to wait on the order of 1 week after shut-off before commencing the switch. The total time from wide-band beam shut off to turn-on of the NBB is of the order of two weeks.

AAO 8513

COST ESTIMATE FOR NUMI CIVIL CONSTRUCTION

G. Koizumi and T. E. Toohig

The attached cost estimate is based on the Revision 0 (November 1993) and Revision 1 (June 1994) Project Definition Reports (PDR) for the NuMI Project provided by the Facilities Engineering Services Section of Fermilab. The details of the estimate for the tunneled portions of the Project in the PDRs, which were produced under subcontract by Sverdrup Civil, Inc., are contained in three subcontract reports dated November 5, 1993, May 26, 1994 and June 1, 1994. The design basis for the Rev 0 PDR was a facility that was entirely sited in the bedrock underlying the Fermilab site, except for the beam pipe carrying the incident proton beam from the Main Injector, the various access shafts, and the supporting surface facilities. The primary modification to the design between Rev 0 and Rev 1 was to raise the facility so that the pre-target area was partly in the bedrock and partly in the glacial till overlaying the bedrock. The design basis for the present estimate is a facility sited in the bedrock to avoid environmental and construction complications, so the Rev 0 cost estimate was used as a basis to derive unit costs to factor into the facility model as shown in Figures 1-5, below. Since the cost of the facility is driven by the underground construction, the present cost estimate simply repeats the costs for the surface facilities as given in Rev 0 and Rev 1. Additional savings could accrue from a more detailed review of those facilities.

The outstanding change in the design basis of the facility for the present estimate is the lengthening of the decay distance from 340 meters to 800 meters. This increased length results in a substantially deeper experimental hall, since the beam is pointed down by approximately three degrees relative to the surface in order to intercept the detector at the Soudan location in Minnesota. At the same time the size of the experimental hall was increased to accommodate the evolving detector designs.

To compensate for the increased costs associated with these incremental features, the costs were analyzed to determine where the cost drivers lay. At the same time, the civil design parameters were revised to match more closely the revised technical requirements, including environmental and operational constraints. These revisions are reflected in Figures 1-5.

A general revision evident in the figures is a reduction in the cross-section of the shafts, since the excavation volume is driven by the cross-section rather than the length, and the cost is driven by the excavation volume. The reduction in shaft cross-section also improves the containment of radiation below ground. A potential further benefit from reducing the diameter of shafts is to make feasible the augering of the shafts; a very substantial reduction in shaft costs and schedules was achieved at the SSC by this simple expedient. This potential reduction has not been factored into the present cost estimate.

The costs for the increased length of the decay pipe were offset by utilizing an improved environmental design based on the geotechnical and hydrogeological characteristics of the dolomite in which the facility will be sited. This allows the

tunnel cross-section, and therefore the excavated volume and unit cost, to be substantially reduced, resulting in essentially wash between the costs for the 340-meter design and the 800-meter design. The present design recognizes that the presence of an unlined tunnel creates a negative gradient to the pore pressure in the rock so that there is a net inward flow of water to the tunnel to be collected at the dump location. The downward slope of the tunnel facilitates this collection. The design involves pressure grouting any locations where the rock may be fractured to limit the inflow. An additional feature for monitoring the radiation environment is to incorporate loss monitors along the beam pipe to measure the actual radiation history, rather than rely entirely on the difficult model calculations.

The volume of excavation for the pre-target and target areas has been substantially reduced by shorter pre-target optics, utilization of local shielding containment in place of target trains, and elimination of expensive underground shielded storage for radioactive components. The last provision recognizes that damaged, highly-radioactive components are replaced, rather than repaired, and Fermilab already provides shielded storage for radioactive components. The proximity of the MI8 service building to the NuMI target area may impact the final design and cost of this complex, but will not substantially change the current cost estimate which is driven by the underground work.

The detector configurations have evolved considerably from the design bases of the earlier estimates; the E803 detector has grown substantially, the MINOS near detector has come into existence, and space is requested for exposure of some of the Soudan 2 modules in the hall. In spite of this, the estimated cost of the facility has been maintained substantially the same as in the older design bases by optimizing the shaft sizes and placements, by offsetting the detectors in the hall to maximize the useful space, by utilizing the space available above (beneath for Soudan 2) the detectors for electronics racks, and by a certain amount of tailoring of the excavation to the detailed requirements of the detectors, especially for E803.

NuMI Project Summary Cost Analysis

WBS #	Cost Element	Rev. 0 ($K)	Rev. 1 ($K)	Cost Model ($K)	Revised CM ($K)
1.2.1.1	WETLANDS MITIGATION	400	500	500	
1.2.1.2	SITE WORK AND UTILITIES	1,535	1,604	1,604	
1.2.1.3	LANDSCAPING	180	180	180	
1.2.2.1	EXTRACTION ENCLOSURE	293	164	164	
1.2.2.2	CARRIER PIPE	1,011	460	108	
1.2.2.3	PRETARGET ENCLOSURE	2,326	358	765	
1.2.2.4	TARGET TUBE ENCLOSURE	2,334	3,463	1,045	
1.2.2.5.1	TARGET CAVERN & SHAFT	4,337	1,382	938	
1.2.2.5.2	TARGET SERVICE BUILDING	1,026	960	960	
1.2.2.6	DECAY PIPE	4,330	4,273	3,977	
1.2.2.7.1	DUMP CAVERN & SHAFT	2,256	1,812	1,713	
1.2.2.7.2	DUMP SERVICE BUILDING	77	77	77	
1.2.2.8.1	EXPERIMENTAL CAVERN & SHAFT	4,596	3,283	4,347	
1.2.2.8.2	EXPERIMENT SERVICE BUILDING	1,679	1,724	1,724	
		26,380	20,240	18,102	
	Subcontractors OH & Profit	3,957	3,036	2,715	
	Testing Services (flat sum)	625	625	625	
1.2.3	EDIA	6,502	5,019	4,503	
	Contingency	4,121	3,181	2,854	
	Management Reserve	4,121	3,181	2,854	
	TOTAL	45,706	35,283	31,653	

Numi Target Hall Plan 14aMar95

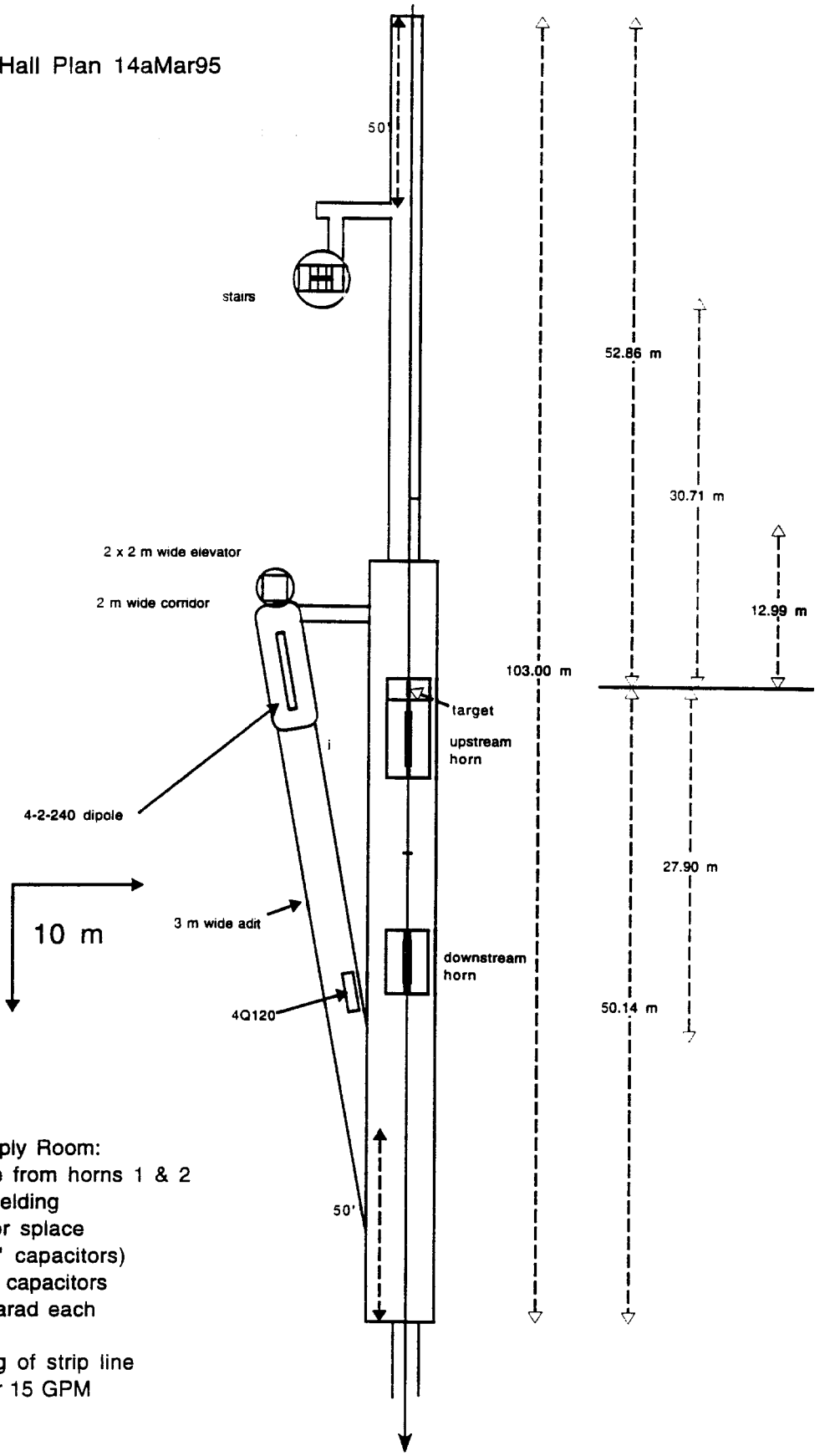

Horn Power Supply Room:

1. equi-distance from horns 1 & 2
2. moderate shielding
3. 15 x 15' floor splace
   (20"x20"x5' capacitors)
   approx. 100 capacitors
   3000 microfarad each
   7 Klb total
4. water cooling of strip line
   and capacitor 15 GPM

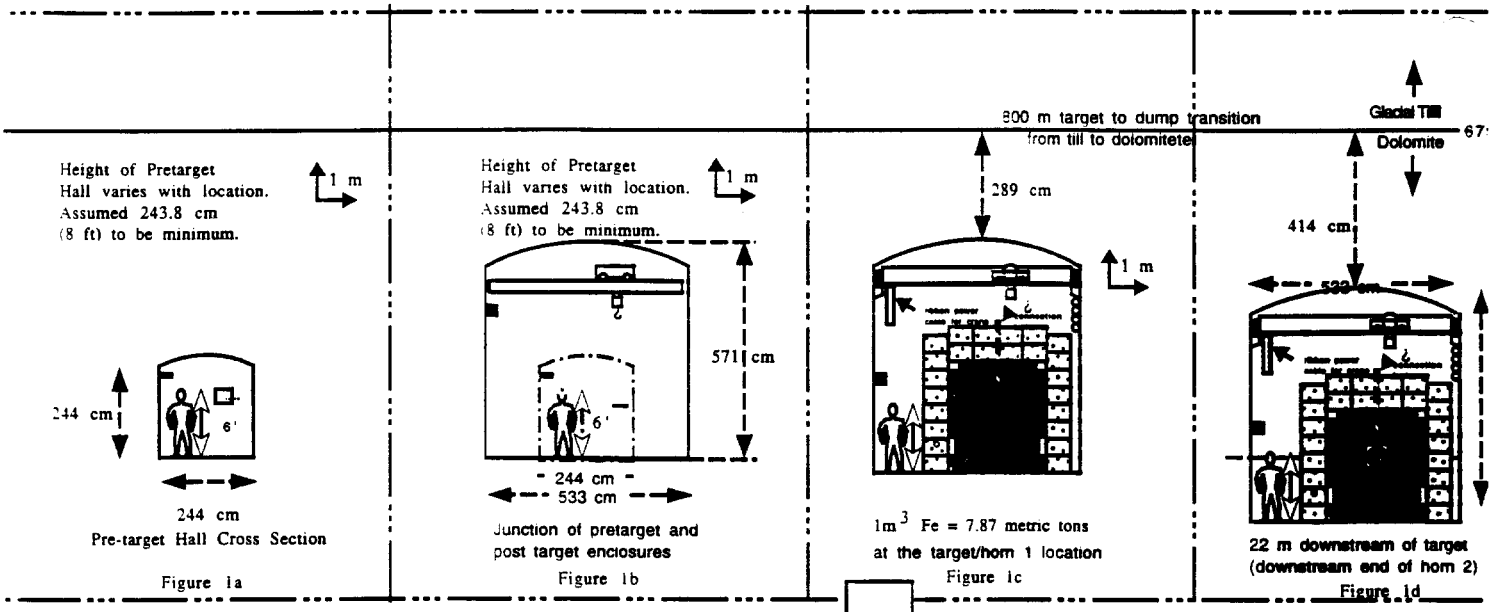

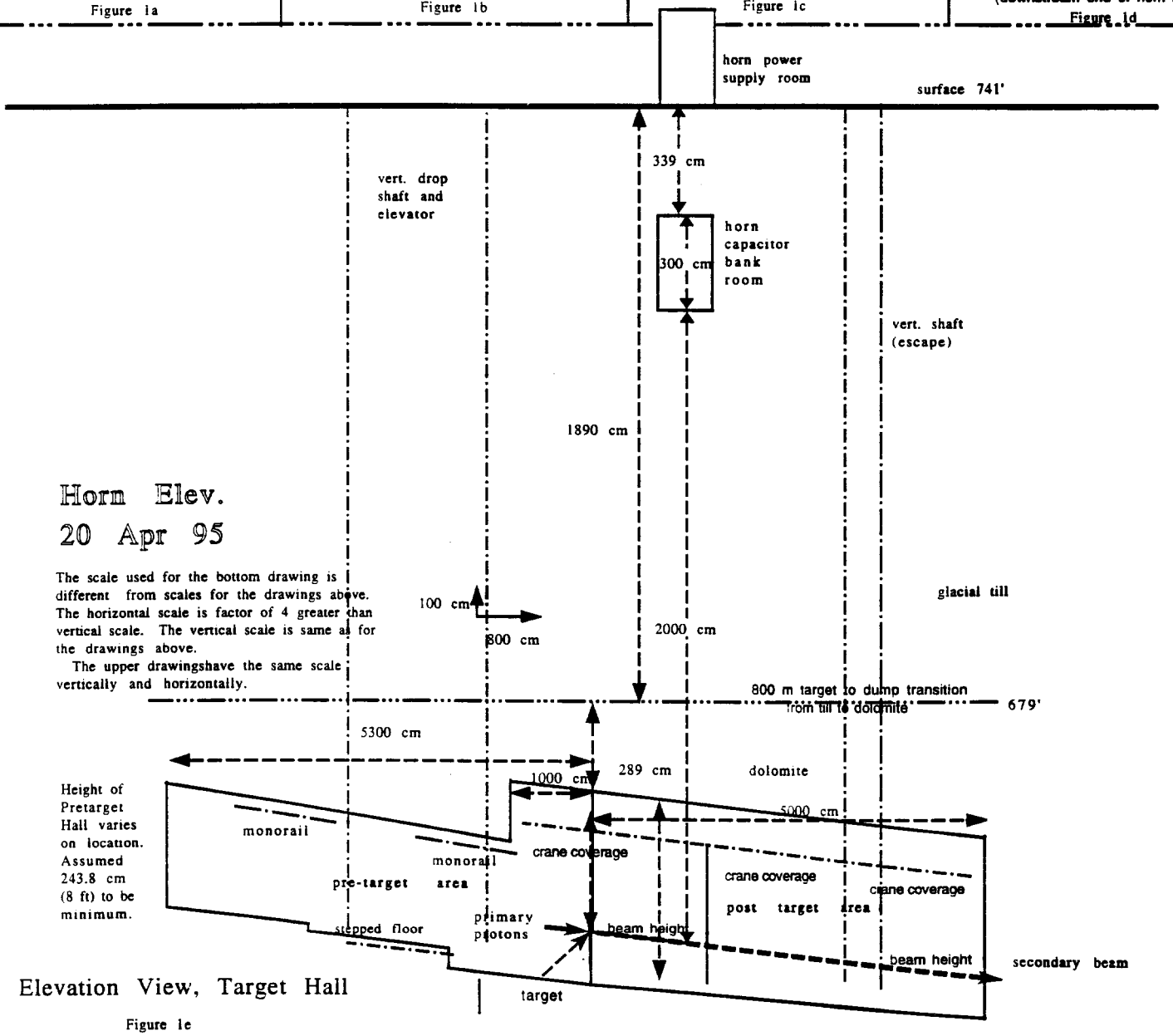

Elevation View, Target Hall

Figure 1e

at the target location

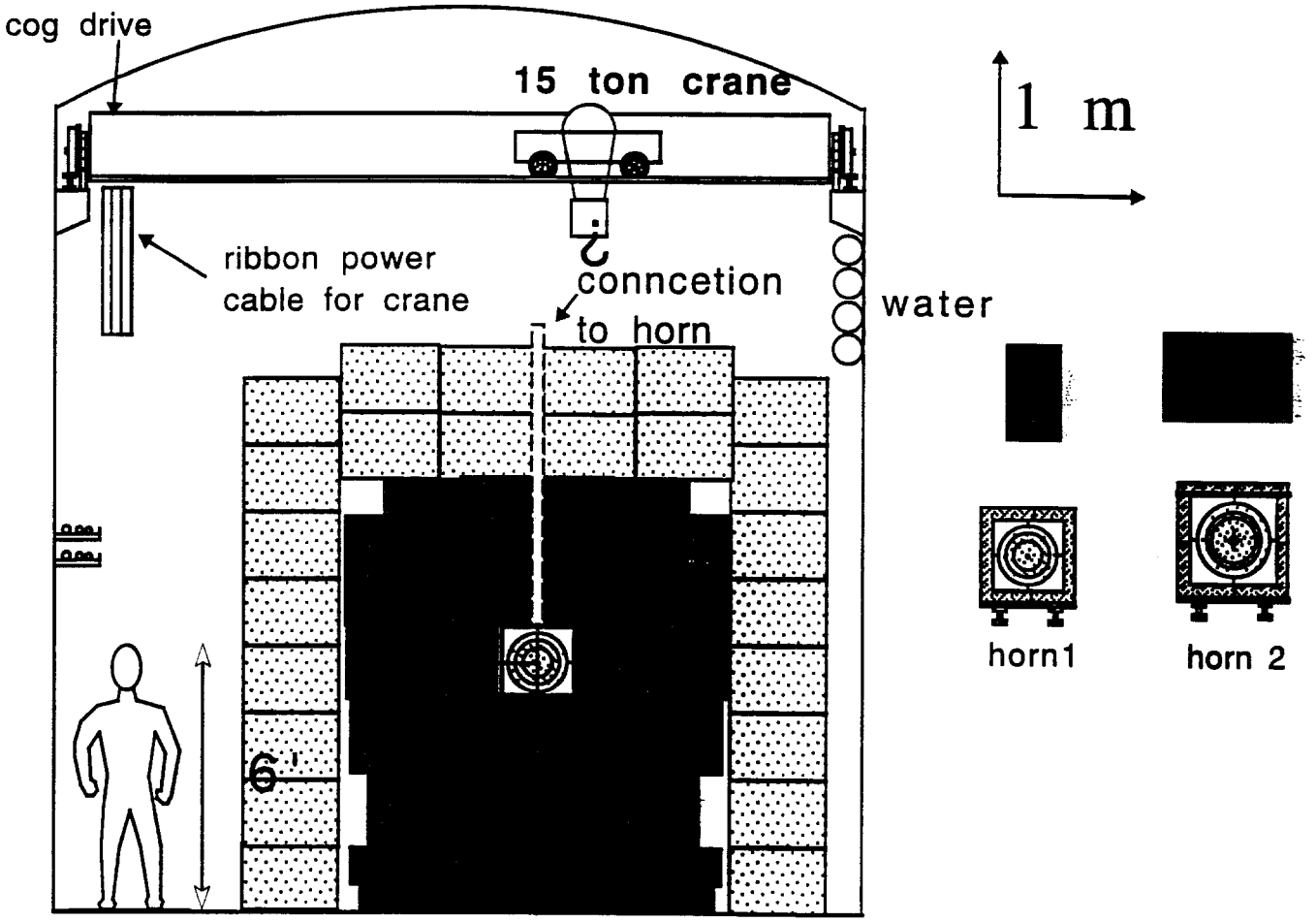

$1m^3$ Fe = 7.87 metric tons = 8.677 short tons
$1m^3$ concrete = 2.373 metric tons = 2.616 short tons

WBS Costing Elements for NuMI Technical Systems

WBS 1.1 Technical Cost Estimate	Number	Unit	Unit Cost(K$)	Cost(K$)	Sub-Total(K$)	Total(K$)
1.1.2 Beampipe to Target Enclosure						64
1.1.2.1 Roughing Pump	1	Each	35		35	
1.1.2.2 Diffusion Pump	1	Each	25		25	
1.1.2.3 End Flanges & Windows	2	Each	2		4	
1.1.3 Primary Beam						752.48
1.1.3.1 Magnets					121.2	
1.1.3.1.1 Dipoles	8	Each	0	0		
1.1.3.1.2 Quads	3	Each	0	0		
1.1.3.1.3 Trims	2	Each	2	4		
1.1.3.1.4 Stands	13	Each	2	26		
1.1.3.1.5 Installation	52	Crew Hr	0.6	31.2		
1.1.3.1.6 Alignment Sight Pipes	2	Each	30	60		
1.1.3.2 Power Supples					121.4	
1.1.3.2.1 Dipoles	2	Each	0	0		
1.1.3.2.2 Quads	3	Each	0	0		
1.1.3.2.3 Trims	2	Each	3	6		
1.1.3.2.4 Circuit Breakers/Panels	7	Each	2	14		
1.1.3.2.5 Cable Trays	1200	Feet	0.007	8.4		
1.1.3.2.6 Cable Tray Installation	1200	Feet	0.05	60		
1.1.3.2.7 Cables	7000	Feet	0.003	21		
1.1.3.2.8 Cable Installation	7000	Feet	0.0015	10.5		
1.1.3.2.9 Cable End Terminations	30	Each	0.05	1.5		
1.1.3.2.10 PS Controllers	7	Each	0	0		
1.1.3.3 Water System					108.6	
1.1.3.3.1 Heat Exchanger	1	Each	19	19		
1.1.3.3.2 LCW Pipes	1200	Feet	0.015	18		
1.1.3.3.3 Fittings	1	Lot	6	6		
1.1.3.3.4 Valves	40	Each	0	0		
1.1.3.3.5 Pipe Installation	60	Crew Hr	0.6	36		
1.1.3.3.6 RAW System	1	Each	16	16		
1.1.3.3.7 RAW Installation	16	Crew Hr	0.6	9.6		
1.1.3.3.8 ICW parts	1	Lot	4	4		
1.1.3.3.9 LCW Pumps	3	Each	0	0		
1.1.3.4 Vacuum System					91.2	
1.1.3.4.1 Beampipe & Bellows	100	Feet	0.2	20		
1.1.3.4.2 Roughing Pump	1	Each	35	35		
1.1.3.4.3 Diffusion Pump	1	Each	25	25		
1.1.3.4.4 Valves	2	Each	5	10		
1.1.3.4.5 Gauges/Cables	6	Each	0.2	1.2		
1.1.3.5 Controls					106	
1.1.3.5.1 Racks	2	Each	1	2		
1.1.3.5.2 Crates	2	Each	4	8		
1.1.3.5.3 Computer Link	1	Each	1	1		
1.1.3.5.4 FIRUS & CATV	1	Each	10	10		
1.1.3.5.5 Safety Interlocks	6000	Feet	0.0015	9		
1.1.3.5.6 Interlock Electronics	1	Lot	9	9		
1.1.3.5.7 Electricians	20	Crew Hr	0.6	12		
1.1.3.5.8 Local Control System	1	Each	55	55		
1.1.3.6 Instrumentation					57.68	
1.1.3.6.1 Beam Position Monitors	4	Each	4	16		
1.1.3.6.2 Loss Monitors	4	Each	0.02	0.08		

1.1.3.6.3 SWICs	2	Each	0	0		
1.1.3.6.4 Large Area SWIC	1	Each	5	5		
1.1.3.6.5 Split Plate Ion Chamber	1	Each	3	3		
1.1.3.6.6 Electronics	12	Each	2	24		
1.1.3.6.7 Cables	4800	Feet	0.002	9.6		
1.1.3.7 Reclaimation of Existing Equipment					146.4	
1.1.3.7.1 Magnets(36)	144	Crew Hr	0.6	86.4		
1.1.3.7.2 Power Supplies(15)	60	Crew Hr	0.6	36		
1.1.3.7.3 PS-4 Water System	40	Crew Hr	0.6	24		
1.1.4 Horn Beam						1491
1.1.4.1 Target	1	Each	10		10	
1.1.4.2 Steel Shielding	100	Ton	0.7		70	
1.1.4.3 Limestone Shielding	18	Blocks	2		36	
1.1.4.4 Horn 1	1	Each	200		200	
1.1.4.5 Steel Sheielding	300	Ton	0.7		210	
1.1.4.6 Limestone Shielding	54	Blocks	2		108	
1.1.4.7 Horn 2	1	Each	200		200	
1.1.4.8 Steel Sheielding	200	Ton	0.7		140	
1.1.4.9 Limestone Shielding	36	Blocks	2		72	
1.1.4.10 Installation	120	Crew Hr	0.6		72	
1.1.4.11 Horn Power Supply System					285	
1.1.4.11.1 Power Supply	2	Each		0		
1.1.4.11.2 Capacitor Bank	1	Each	120	120		
1.1.4.11.3 Cap Bank(Structural)	1	Each	40	40		
1.1.4.11.4 SCR Switches & Trnsdtrs	8	Each	5	40		
1.1.4.11.5 Firing Circuits & Controls	1	Each	10	10		
1.1.4.11.6 Dischg Restr & Safety	1	Each	15	15		
1.1.4.11.7 Installation	100	Crew Hr	0.6	60		
1.1.4.12 PC Data Logger/Controller	1	Each	10	10	10	
1.1.4.13 Helium System	150	Feet	0.2	30	30	
1.1.4.14 Limestone Shielding(between Horns)	24	Blocks	2	48	48	
1.1.5 Dichromatic Beam						1144
1.1.5.1 Target	1	Each	10		10	
1.1.5.2 Lithium Lens	1	Each	42		42	
1.1.5.3 Transformer	1	Each	57		57	
1.1.5.4 Lithium Lens Power Supply	1	Each	270		270	
1.1.4.5 Dipoles	2	Each	70		140	
1.1.4.6 Quadrupoles	5	Each	44		220	
1.1.4.7 Magnet Power Supplies	7	Each	40		280	
1.1.4.8 Primary Proton Dump	1	Each	125		125	
1.1.6 Dump Enclosure						528.98
1.1.6.1 Primary Proton Dump					165.4	
1.1.6.1.1 Steel	100	Ton	0.7	70		
1.1.6.1.2 Copper	0.8	Ton	10	8		
1.1.6.1.3 Machining	100	Hr	0.04	4		
1.1.6.1.4 Underground Assembly	40	Crew Hr	0.6	24		
1.1.6.1.5 Installation	24	Crew Hr	0.6	14.4		
1.1.6.2 Water System					45	
1.1.6.2.1 Heat Exchanger	1	Each	19	19		
1.1.6.2.2 RAW Water System	1	Each	26	26		
1.1.6.3 Vacuum(At Target & Dump Enclosure)					156.8	
1.1.6.3.1 Roughing Pump	2	Each	35	70		
1.1.6.3.2 Diffusion Pump	2	Each	25	50		
1.1.6.3.3 Valves Between Pumps(35")	2	Each	12	24		
1.1.6.3.4 End Flanges & Windows	2	Each	3	6		
1.1.6.3.5 Safety Doors	2	Each	3	6		
1.1.6.3 6 Guages/Cables	4	Each	0.2	0.8		

1.1.6.4 Controls						96.1	
	1.1.6.4.1 Racks	1	Each	1	1		
	1.1.6.4.2 Crates	1	Each	4	4		
	1.1.6.4.3 Computer Link	1	Each	1	1		
	1.1.6.4.4 FIRUS & CATV	1	Each	10	10		
	1.1.6.4.5 Safety Interlocks	7000	Feet	0.0015	10.5		
	1.1.6.4.6 Interlock Electronics	1	Lot	9	9		
	1.1.6.4.7 Electricians	16	Crew Hr	0.6	9.6		
	1.1.6.4.8 Control System(Extn. of Upsm)	1	Each	51	51		
1.1.6.5 Instrumentation						65.68	
	1.1.6.5.1 Beam Position Monitors	4	Each	4	16		
	1.1.6.5.2 Loss Monitors	4	Each	0.02	0.08		
	1.1.6.5.3 SWICs	2	Each	0	0		
	1.1.6.5.4 Large Area SWIC	1	Each	10	10		
	1.1.6.5.5 Split Plate Ion Chamber	1	Each	6	6		
	1.1.6.5.6 Electronics	12	Each	2	24		
	1.1.6.5.7 Cables	4800	Feet	0.002	9.6		
					GRAND TOTAL		3980.46

Switching between Wide–band and Narrow–band beams

The NuMI (Neutrinos with the Main Injector) neutrino beam target hall has been designed to accomodate both a wide–band beam (WBB) using horns as the beam focusing devices and a narrow–band beam (NBB) using a lithium lens and conventional magnets as the focusing devices. The MINOS collaboration intends to use both beams in the proposed experimental program. The layouts of each beam are schematically illustrated in Figure 1. The components are placed to scale along the beam direction but not in the orthogonal direction.

The primary proton beam from the Main Injector travels through a two foot diameter beam pipe into the pre-target hall. The WBB primary proton beam must be on the beam axis pointing to Soudan. However, since the NBB has its bend plane in the vertical plane, the NBB primary proton beam has a trajectory that is approximately one foot higher than the WBB at the target. The switch from the WBB to the NBB will require that all of the pre-target dipoles and quadrupoles move up so that the primary protons will strike the NBB target. The magnet stands for the pre-target beam line will be designed so that the vertical movement necessary to switch beams will be to pre-determined locations. The method chosen will allow precise alignment for each beam and the movement and final location will be repeatable within the desired precision.

The shielding concept for the target and beam lines includes the use of modular shielding blocks of steel and calcium carbonate, marble or limestone, placed around the beam line elements. The steel will be $\sim$ one meter thick radially around the target and the horns. Radially out from the steel will be $\sim$ one meter of calcium carbonate. These shielding materials and thicknesses will allow personnel access to the target hall with the beam off. The thickness of each shielding material will be chosen such that calculations of radiation exposure indicate that the dose rate will be $\sim$ 10 - 100 mrem/hour with the beam off. The modular design of the shielding allows rapid disassembly in order to replace failed components or switch beams using the overhead crane in the target hall.

The targets for the WBB and NBB are different designs. The depth of field for the focus of the horn allows the use of a long thin target while the depth of field for the focus of the lithium lens requires a more conventional target. The target pile is designed to allow the placement and removal of the NBB target in minimal time and with minimal radiation exposure. Shielding blocks will be rearranged at the target location to accomplish this.

Figures 2 and 3 illustrate the minor shielding configuration changes necessary to switch from the WBB to the NBB. For ease of switching the beams the steel surrounding Horn 1 will be made 1.25 m thick with the inner radius steel piece 0.25 m thick. The inner piece will be removed and stored in a lead coffin in order to install the lithium lens, quadrupole Q1 and dipole B1. The alignment base that Horn 1 sits on will be designed to hold the lithium lens in a pre-aligned position. The conventional magnets will either be installed to pre-determined locations with their stands or the stands will be permanently installed. The supports for the He filled beam pipe present in the WBB will be designed to accept the B1 and Q2 magnet stands as an addition to them. Both the WBB and NBB will need to be installed and aligned before any beam is put on target in order to insure that a switch between them will allow the placement of the beam elements onto pre-determined locations.

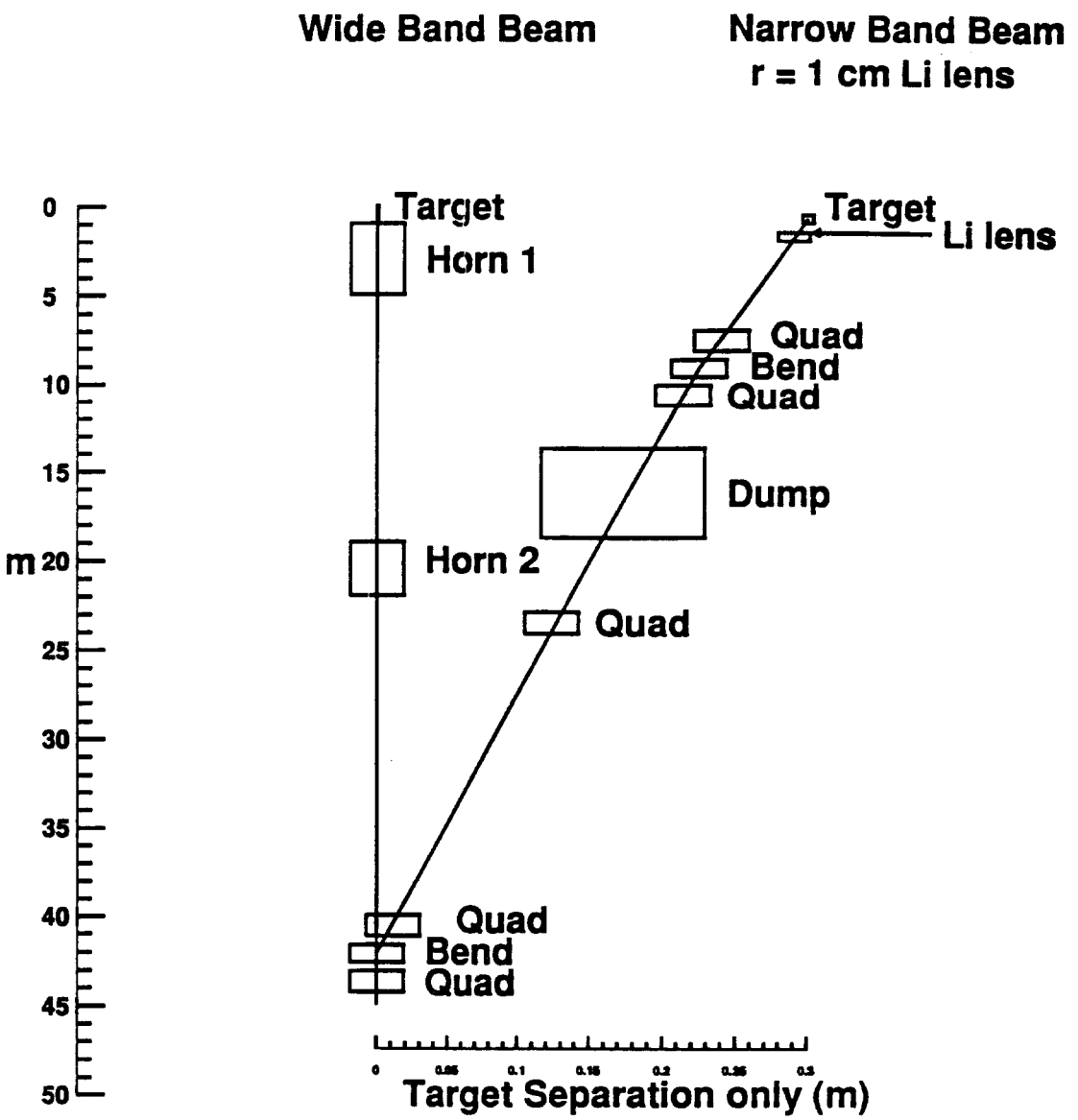

Figure 1: Schematic diagram of the wide–band and narrow–band beams. The figure is not to scale in the direction perpendicular to the beamline.

All of the connections for power, water and instrumentation will be made on top of the shielding. For example, the strip line for the horn will rise vertically from the contact points on the horn the height of the shielding (2 m) and be connected to the power supply through flexible connections to the rest of the strip line. The design of the connections brought out the top of the shielding is inspired by the successful design and operation of the Fermilab anti-proton source beam line. Personnel will be able to disconnect each element from the rest of the world with minimal radiation exposure. The activated elements may then be removed from a remote location using the target hall's overhead crane and placed in a protected container and location.

When the decision is made to switch from one beam to the other the proton beam will be turned off. The target hall, with calcium carbonate as a component of the shielding, will need to cool off for 7-10 days before personnel will be allowed to enter the hall for the purpose of switching the beams. The full cool off period is not required for the replacement of a failed horn or lithium lens since the replacement system for them is designed to allow remote handling and minimal radiation exposure to personnel. After the 7-10 day radiation cool off period, it is estimated that 9 shifts over a minimum of 5 days will be necessary to switch the WBB to the NBB. The work will begin at the downstream end of the hall and proceed upstream to allow further radioactive decay to cool off the more highly activated elements closer to the target. The need for additional radiation protection, such as lead curtains over radiation hot spots, is currently undergoing careful evaluation.

The NBB proton dump will be placed in the initial installation of the beam line and remain there until the line is disassembled. The dump will have a removable core that allows the WBB He filled pipe to fit. When the NBB is installed the core will be replaced. It may be the last element of the NBB to be installed since with it absent there is line of sight horizontally for alignment. An alignment strategy that will allow verification that the elements are in the proper location will be adopted after discussions with alignment experts.

The design of the beam elements and their supports will allow the neutrino beam to be switched from WBB to NBB in approximately 2-3 weeks of calendar time. Careful engineering of the two beam lines with a design goal of ease of installation is critical for adhering to the replacement time estimate of two weeks. The major stumbling block to a more rapid replacement is the radiation cool off period necessary before extensive personnel access. The choice of calcium carbonate as a shielding material makes the cool off time as short as possible.

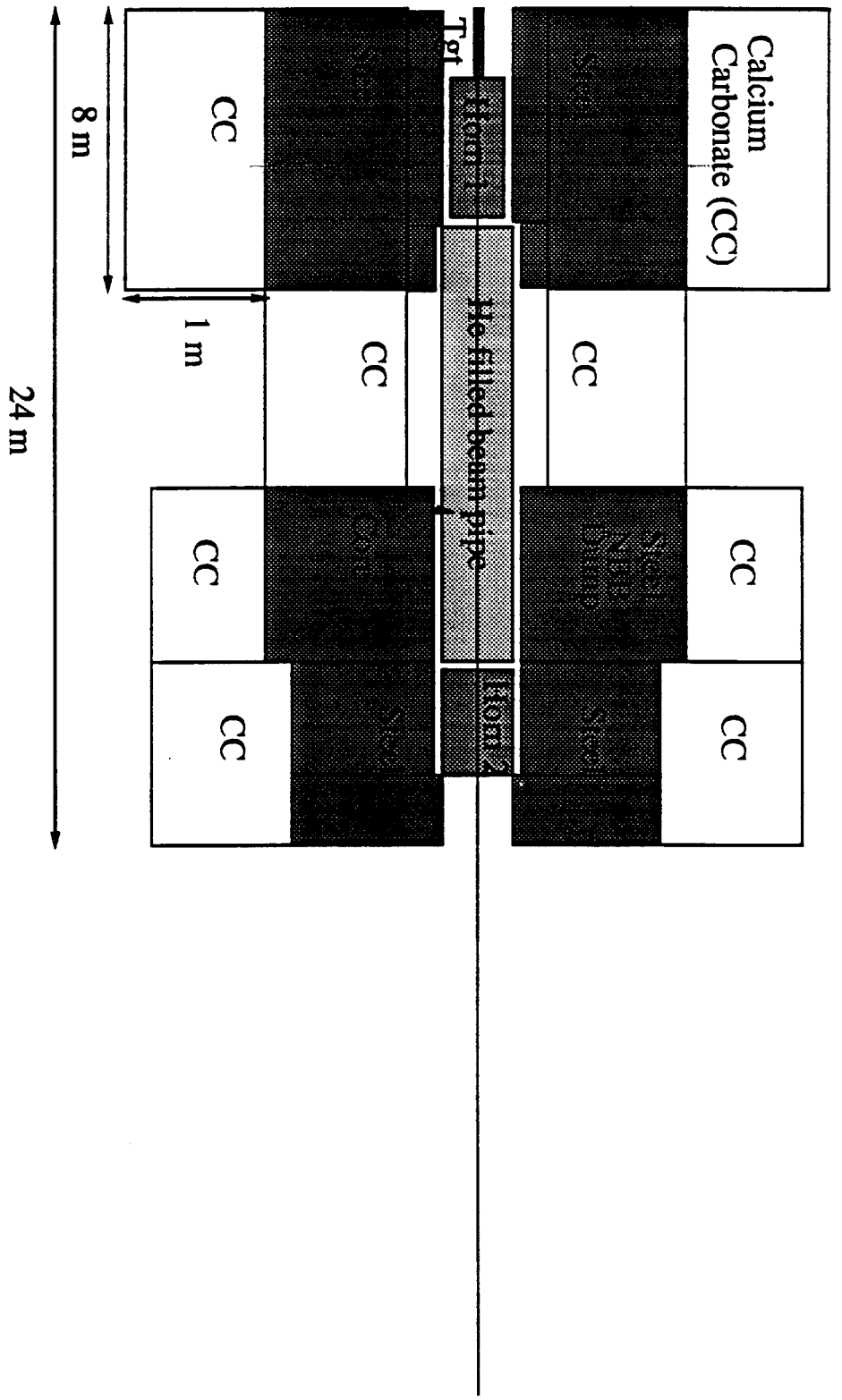

Figure 2: The layout of the WBB and the shielding design for it viewed from the top with the top shielding removed.

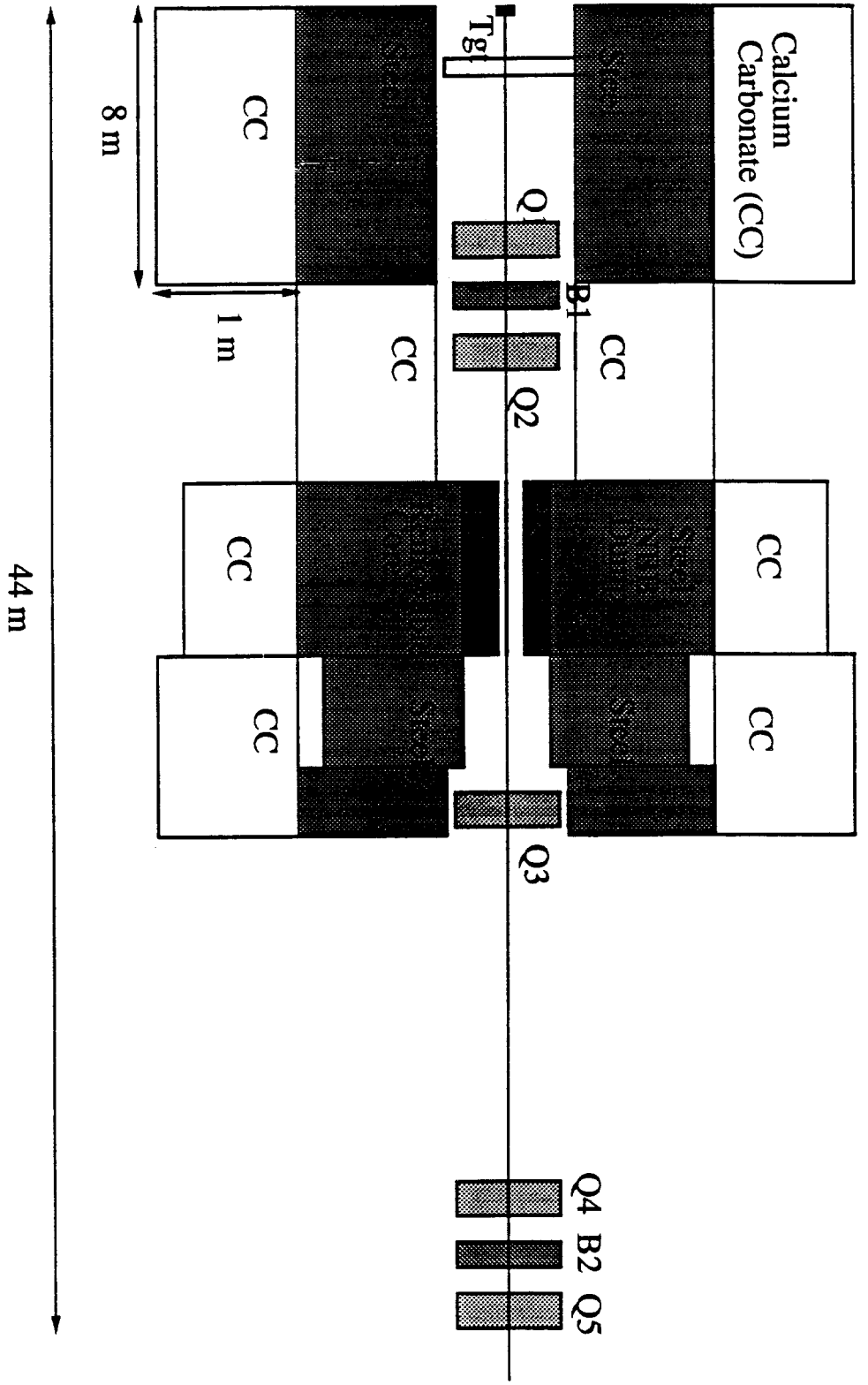

Figure 3: The layout of the NBB and the shielding design for it viewed from the top with the top shielding removed.

Maintenance of the neutrino beamline

All of the power, water and instrumentation connections to the beam line elements will be made outside of the shielding. The connections that are within the shielding and, therefore, within a high radiation environment will be designed to be radiation hard. The replacement of a failed beam line element can be accomplished in a timely manner, as has been described for the switching of the WBB to the NBB. There are design criteria for the replacement of the beam elements judged most likely to fail and a well designed beam will be one in which any failure may be quickly rectified.

The ability to keep the beam line operational depends on the designs of the elements. The design specifications for each will include the current knowledge of radiation hard materials and possible failures due to radiation exposure. The designs will have a philosophy of a low maintenance, success oriented beam line.

known precisely in advance, but we have assumed that we will be able to fit the charged K fraction to better than 2% using the 10^9 charged current neutrino events in the near detector. There is also a 1% systematic error from the uncertainty in the K_{e3} branching ratio. A more conservative estimate of the total systematic error on the ν_e fraction is 10%.

The MINOS beam monitor - near detector system is a vital part of the long baseline experiment, specifically designed to meet its needs and problems, using a technology similar to that of the far detector. E-803, because of its limited transverse dimensions and possible serious acceptance problems at low energies, could not by itself meet the needs of MINOS, but in the regions where it is most effective it could provide a very useful check on the performance of the MINOS beam monitor. In any event, a careful Monte Carlo study of E-803 capabilities would be very important. With regard to the topics discussed here it would seem that the E-803 downstream spectrometer and the MINOS beam monitor could very nicely complement each other. Not only would E-803 serve as a check on the MINOS beam monitor (and *vice versa*), but the MINOS beam monitor measurement of the ν_e beam content and energy distribution could be quite useful for E-803 if, for example, ν_e oscillates into ν_τ in the E-803 sensitive region.

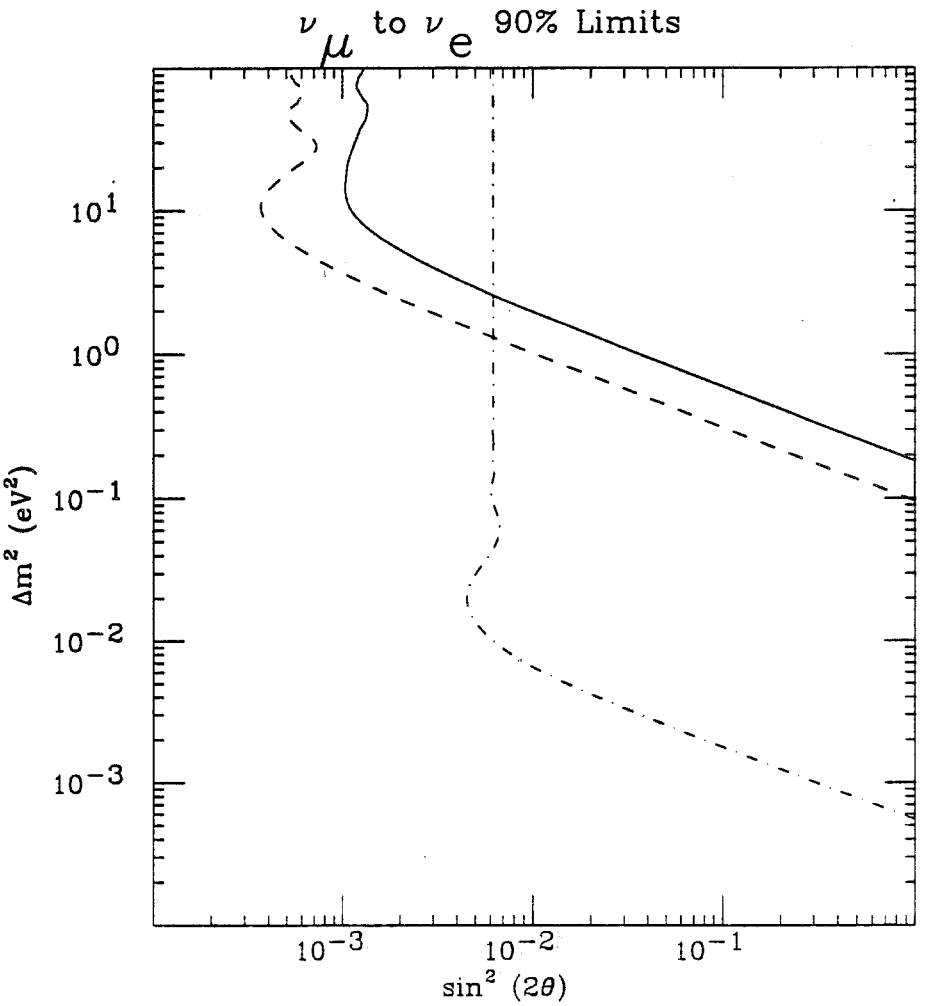

Figure 28: $\nu_\mu \rightarrow \nu_e$ sensitivity plots for MINOS and COSMOS. The dash-dot curve is the 90%CL limit that MINOS can set using its far detector. The solid curve is the limit that both COSMOS and the MINOS near detector could set using all electron events and is dominated for both experiments by the systematic error in the beam. An estimate of this error is described in the text. The dashed curve is for both experiments cutting on $E_\nu < 15\ GeV$.

3.8 Question #8

"The Committee would like to see further justification that astrophysical measurements can be made which compete favorably with those from underground laboratories. If possible without added expense, these are an added bonus of the MINOS experiment."

The MINOS collaboration has necessarily focussed on the accelerator-based oscillation experiment in its preparation of the P-875 proposal. However, it is clear that construction of a detector of the scale of MINOS in a deep-underground location will provide several interesting capabilities for nonaccelerator measurements. Such capabilities can provide further justification for construction of the detector, especially if no extra detector construction costs are involved. Any additional cost will be relatively small compared to the cost of implementing the primary measurement capabilities of MINOS. However, one of the most useful additions will be an active veto shield (discussed below). Such a shield will cost in the range of $2M.

An evaluation of the nonaccelerator capabilities of MINOS requires a projection of the expected results from existing or near-existing underground detectors. Detectors which we anticipate will offer direct competition to possible measurements in MINOS include Super-Kamiokande, MACRO, and one of several possible deep-underwater Cerenkov detectors which are currently being developed and may come into operation in the next five years (DUMAND, AMANDA, NESTOR, Baikal). Super-Kamiokande will offer excellent measurement capabilities and statistics for low-energy (less than a couple of GeV) contained neutrino interactions. By the time that MINOS is ready to acquire data, Super-Kamiokande will already have collected 4 years of data. MACRO is currently the largest-area underground detector and offers excellent muon reconstruction capabilities for both upgoing and downgoing muons. By the time MINOS acquires data, MACRO will have 5-6 years of data with the full detector. Since MACRO has a larger surface area with fine granularity, MINOS will likely not compete in measurements which are in direct competition with MACRO's primary physics goals. These include measurements of the integral flux of upgoing muons and studies of downward-going single and multi-muon events. Finally, the 10 kT mass of MINOS will severely limit its ability to compete with the deep-underwater Cerenkov detectors, which are being designed with extremely large masses specifically to study high-energy neutrino astronomy.

The nonaccelerator measurements divide into two major categories, neutrino measurements and other astro-particle physics. Because we have thus far focussed on the needs of the accelerator based experiment, we have not yet calculated in detail the possibilities for the nonaccelerator measurements. Hence, the examples that we list here should not to be taken as clearly demonstrated measurement capabilities. We list here only measurements in which we think MINOS can add significantly to the information coming from other detectors. There are a number of other topics where MINOS will add little to existing measurements other than to repeat them with an independent set of systematic errors; these are not discussed here.

The key to understanding the unique measurements available to MINOS comes in under-

standing the unique detector properties that MINOS brings to the ensemble of underground experiments. First, MINOS will have a magnetic field which has never before been implemented in such a large underground detector. This will allow muon momentum measurement up to about 200 GeV/c for a wide range of zenith and azimuth angles and up to several hundred GeV/c for muons traversing the detector along the long axis. Second, MINOS will offer very large mass (about one-fourth that of Super-Kamiokande) with fine-grained tracking readout. In addition, MINOS is a very thick detector which will provide many absorption lengths for electromagnetic and hadronic showers. These features will allow measurements on atmospheric neutrino interactions which will not be possible with any of the existing or proposed underground detectors. Finally, we envision the possibility that active detectors capable of nanosecond timing will be installed in at least some of the detector plane locations and/or as an active shield around the detector. As described below, we believe that such timing can add considerably to the nonaccelerator measurement capabilities.

Muon energy measurement in the TeV region will require shower energy reconstruction. The energy loss for muons with energies greater than a few hundred GeV is dominated by bremsstrahlung and pair production. These processes are stochastic in nature but the probability of production of observable electromagnetic showers by multi-TeV muons propagating through several meters of iron is relatively high. Energy loss by muons up to 1 TeV has been measured by the CCFR collaboration [9] and up to 10 TeV by the MUTRON collaboration [10]. These measurements give good agreement with calculations of energy loss for muons up to these energies [11].

The average energy loss for muons with energy greater than 1 TeV rises linearly with the energy. Furthermore, thicknesses of iron in the range of several meters to tens of meters are sufficiently great that energy losses will not be the result of a single hard interaction but will usually result from several or many smaller-but-observable, shower-inducing interactions. For example, a muon of 10 TeV energy travelling through 10 m of MINOS (average density 5.2 g/cm^3) will lose 500 GeV of energy on average. About 280 GeV of this energy will be in the form of pair production with most of the remainder coming from hard bremsstrahlung. An electromagnetic shower with at least 300 MeV of energy will be produced every 40 cm on average, making muons of this energy give tracks in the detector which are almost continuously 'hairy'. The rate of electromagnetic showers per decade of energy is almost constant up to a shower energy of about 100 GeV so that on average, muons of this 10 TeV energy will suffer a few energy losses with tens of GeV of energy. Since MINOS is sufficiently thick to completely absorb several such showers, it will be possible to combine the average energy loss, the energy distribution of resolvable showers, and the 'hairiness' of the remainder of the track to achieve a rough energy measurement capability for TeV and higher energy muons. We have made preliminary estimates of the energy resolution obtainable by these methods and conclude that for multi-TeV muons a logarithmic resolution should be achievable. Such a resolution would be entirely adequate for most studies involving ultra-high-energy cosmic-ray muons.

The neutrino measurements for which we believe MINOS will add substantially to the information obtainable from other large detectors are listed in Table 3. Most of these measurements will require a detailed analysis of the acceptance and properties of MINOS as a function of zenith and azimuth angle since MINOS is not a homogeneous detector. One of the most significant of these areas is measurement of the NC/CC ratio for neutrinos in the

several GeV range. An explicit calculation for this has been performed and has already been discussed in the P-875 proposal[1]. In addition, the magnetic field of MINOS will allow the determination of the charge of the muons from ν_μ CC events. These measurements will be unique to MINOS. The capability of each detector is listed in a rough way in Table 3. Also listed in Table 3 is whether the MINOS measurement will require or benefit from nanosecond timing in the main detector or in an active shield. As can be seen, most of these measurements will at least benefit from such capabilities and many of the most interesting measurements demand the capability of an active shield. Hence, this physics will not come for free but the additional cost is modest given the substantial investment which MINOS would already represent. The only neutrino result available with no active shield will be measurement of ν_μ CC events where the muon is clearly slowing (and therefore bending more) as it crosses the detector.

Some possibilities for astro-particle physics measurements are listed in Table 4. These topics are based on observations on downgoing muons through the detector. The detector features of interest for these events are good tracking ability (angular resolution), fine granularity for multi-track reconstruction in muon bundles, time-of-arrival of muons within a bundle and measurement of muon energies at the detector. Most muons arriving deep underground have originated from energetic ($E_p > 10$ TeV) primary cosmic-ray interactions in the upper atmosphere. Questions which can be addressed include the composition of very-high-energy cosmic rays, the interactions at these energies, possible point source objects which create particles that produce muons in the earth's atmosphere, and prompt production of muons from other particle interactions or heavy flavor production.

Although direct measurements of the primary cosmic-ray spectrum and composition have been made for energies up to a few hundred TeV, higher energy measurements require indirect measurements by studying the shower products. High energy muons which penetrate deep into the earth are of interest since they typically result from decays of particles early in the shower production process. Hence, they are more directly tied to the primary particle and the initial interactions than shower products deeper in the atmosphere. Some of the most interesting questions involve muons originating from cosmic rays with energies above 'the knee' (about 8000 TeV) in the spectrum. If these cosmic rays are of extra-galactic origin, then the composition should be almost purely protons. However, if they are not purely protons, that implies very strong (and unknown) acceleration mechanisms within our galaxy.

The indirect study of the cosmic-ray composition in this energy regime is greatly complicated by uncertainties in the interaction properties of the primary constituents. The usual tools employed for these studies (in MACRO and Soudan 2 for example) are muon multiplicities and separations, along with surface detectors which measure the total energy of the associated atmospheric EM shower. MINOS will have roughly the same granularity as MACRO but will add the ability of a logarithmic measurement of TeV-and-above muon energies. This additional handle may prove valuable in separating the effects of interactions and composition at very-high primary energies. Some enhancement of the existing surface array at Soudan could prove useful for these measurements as well. If nothing else, measurement of the muon energy spectrum in the multi-TeV region will be a unique addition to our catalogue of information on cosmic rays. This could be of particular interest for muons arriving at large zenith angles which could result from prompt production either via heavy

MINOS Measurement	Other Detectors and Data			MINOS Requirements	
Neutrino Physics	Deep Water/Ice Cerenkov	Super-Kamio-kande	MACRO	Active Shield	Internal Timing
Atm. ν_e contained events from 1-20 GeV E_ν out to $\pm 60°$ from horizontal; $\frac{dN}{dE}$, $\frac{dN}{d\theta}$	*?	**1	*	+++	+
Atm. ν_μ contained events from .5-20 GeV E_ν out to $\pm 80°$ from horizontal; $\frac{dN}{dE}$, $\frac{dN}{d\theta}$	*?	**2	*	+	+
$\nu/\overline{\nu}$ ratio for above				+	+
Atm. NC contained events from 2-20 GeV E_ν out to $\pm 60°$ from horizontal; $\frac{dN}{dE}$, $\frac{dN}{d\theta}$		*		+++	++
Ratio of NC/CC events with oscillation sensitivity down to $\Delta m^2 = 10^{-4} eV^2$		*		+++	++
$\frac{d^2N}{dE\,d\theta}$ for upgoing muons from 1-200 GeV E_μ	**3	*4	*5	+++	+
$\nu/\overline{\nu}$ ratio for above				+++	+
ν point-source search in multi-TeV range using upgoing muons and log(E) from showers	***6	*		+++	+

*= small capability.
**= moderate capability.
***= substantial capability.
+= slight improvement with this capability.
++=considerable improvement with this capability.
+++=essential for this measurement.
1: It is unclear how well Super-Kamiokande can separate ν_e and NC events in the multi-GeV region.
2: The Super-Kamiokande range measurement cuts off at ~10 GeV muon energy.
3: Threshold energy about 10 GeV.
4: Energy measurement only for $E < 10\ GeV$.
5: Energy measurement only for $E < 2\ GeV$ and $E > 80\ GeV$ for a small area.
6: Detectors don't exist yet; capabilities uncertain.

Table 3: Nonaccelerator neutrino measurement capabilities for MINOS compared to other experiments in the year 2000. The first column lists those areas in which MINOS is likely to yield useful data. The next three columns show the capabilities of competing experiments. The last two columns indicate whether an active shield and/or internal timing are needed for MINOS.

flavor production or strong interactions of particles such as neutrinos at very high energy.

Downgoing muons are certainly of interest if they come from point sources. It is unclear whether any such sources exist but if they do exist it seems that the muons arriving from these sources are episodic. In that case, it is of interest to have as many detectors employed as possible in order to make coincident observations when such bursts are reported. Only with several simultaneous observations (or lack thereof) on such bursts will we finally answer the question about whether muon point sources really exist. MINOS may add an additional twist with the capability of muon energy measurement.

Two possible measurements which require capabilities beyond the reference design for MINOS are muon time-of-arrival and a search for a gravitational collapse within the galaxy. If the active detector planes within MINOS have sub-nanosecond timing capabilities, then the time of arrival of individual muons within a muon bundle could be measured to a precision of about 50-100 ps. Production of heavy particles in cosmic-ray interactions which subsequently decay giving muons could result in delayed muons arriving at the detector. The timing capabilities of MINOS would be about ten times better than MACRO for these events. Finally, if a scintillator-readout, low-Z portion of MINOS is built, it should be possible to search for neutrinos coming from a gravitational collapse within our galaxy. Depending on the properties of the low-Z detector, MINOS could have the second largest (behind Super-Kamiokande) active mass for such interactions of any operating detector. Although galactic supernovae are predicted to occur only once every few decades, the potential benefits of such observations are sufficiently large that it is important to always have some operational detectors capable of observing the neutrino burst from such an event.

MINOS Measurement	Other Detectors and Data			MINOS Requirements	
Astro-particle Physics	Deep Water/Ice Cerenkov	Super-Kamio-kande	MACRO	Active Shield	Internal Timing
Downgoing muon bundles with E_μ measured up to 100 GeV and logarithmic $E_\mu > 1\ TeV$				+	
Downgoing single muons with E_μ measured up to 100 GeV and logarithmic $E_\mu > 1\ TeV$	*1	*1		+	
Muon astronomy with/without energy cuts	**2	**2	**2	+	
Search for delayed muons within a bundle down to 50 ps			*3	+	+++
Search for neutrinos from a gravitational collapse within our galaxy (4)	?	***	**		

*= small capability.
**= moderate capability.
***= substantial capability.
+= slight improvement with this capability.
++=considerable improvement with this capability.
+++=essential for this measurement.
1: Water Cerenkov detectors may have a high probability for mistaking muon. bundles for high-energy muons which shower.
2: Even without energy cuts, the possibly episodic nature of muon point sources. makes overlap in operating detectors desirable.
3: Timing resolution of about 500 ps.
4: Requires a low-Z scintillator readout in MINOS.

Table 4: Astro-particle physics measurement capabilities for MINOS compared to completed or running experiments in the year 2000. The first column lists those areas in which MINOS is likely to yield useful data. The next three columns show the capabilities of competing experiments. The last two columns indicate whether an active shield and/or internal timing are needed for MINOS.

4 Errata for the February 1995 MINOS Proposal

1. Page 32, fourth line under Equation 3.1: (a) Change "10 T/m" to "1000 T/m," (b) Change "0.67 m" to "0.62 m."

2. Page 37, first line of the Figure 3.3 caption: delete "ν_μ and"; the figure shows only ν_τ event rates.

3. Page 99, first line: change "22% of an interaction length" to "22% of a radiation length."

4. Page 99, third line from bottom of page: change "7,500 A" to "7,500 Amp-turns."

5. Page 101 (Fig. 6.4) and page 104 (Fig. 6.5): the angle between the beam and the Soudan 2 detector modules is incorrectly shown as being close to 45 deg. The angle between the beam and the drift tubes (horizontal in Fig. 6.4) should be 26 deg.

6. Page 112, fourth line after Eq. 7.3: the units of energy loss should be $GeV/(g/cm^2)$, or $GeV g^{-1} cm^2$.

7. Pages 113-115: the calculation of magnetic resolution described here is incorrect. The radiation length for pure iron was used in Eq. 7.5, instead of the radiation length for iron plus chamber gaps. Consequently the magnetic resolution curve in Figure 7.5 is incorrect.

8. Page 115, final sentance: change 10^{-5} to 10^{-4}.

9. Page 129, Eq. 8.6: change "$-3.8dT$" to "$-2.8dT$".

10. Page 131, third line of the "Electron neutrino" subsection, the errors given on near and far values of the ratio $(\nu_e + \overline{\nu}_e)/\nu_\mu$ ($\pm 0.009\%$ and $\pm 0.023\%$ respectively) are the statistical errors from the Monte Carlo simulation (as stated in the text). The systematic uncertainties in the measurements of these numbers will be substantially larger, and are *not* shown.

11. Page 176, Fig. 8.25: The labels on curves "A" and "B" are interchanged. Curve "A" uses longitudinal cuts and is for statistical errors only. Curve "B" is for the cc/total test and includes systematic errors.

12. Page 193-210 (throughout Chapter 12): all costs are given in FY 1995 dollars.

13. Page 237, Ref. 18: the new Kamiokande results were not published in the proceedings of the Eilat conference (although they were presented orally).

14. Page 237, Ref. 24: (Y. Fukuda *et al.*): change p. 205 to p. 237.

References

[1] The MINOS Collaboration, "P-875: A Long-baseline Neutrino Ocillation Experiment at Fermilab," February 1995.

[2] D. Crane, G. Koizumi, A. Malensek, J. Morfin, T. Toohig, "Response to PAC question No. 2 relating to the NuMI beam line," Fermilab report NuMI-L-80, April 1995.

[3] P.F. Harrison, D.H. Perkins and W.G. Scott, "Threefold Maximal Lepton Mixing and the Solar and Atmospheric Neutrino Deficits", submitted to Phys. Lett. B, December (1994); also C. Giunti, C.W. Kim and J.D. Kim, "Atmospheric Neutrino Problem in Maximally Mixed Three Generations of Neutrinos", DFTT-54-94, submitted to Physics Letters B, October (1994).

[4] Y. Fukuda *et al.*, Phys. Lett. **B335**, 237 (1994).

[5] D.C. Carey and V.A. White, "NUADA, the Fermilab Neutrino Flux Program," Note PM0011, Fermilab, June 1975.

[6] A. Malensek, Fermilab internal report FN-341, and private communication.

[7] C. L. Wang, "Empirical formula for pion production in proton-proton collisions up to 1500 GeV/c", Phys. Rev. **D7**, 2609 (1973) and C. L. Wang, "Pion production in high energy collisions", Phys. Rev. **D10**, 3876 (1974).

[8] Cocconi *et al.*, Nucl. Phys **B128**, 397 (1977).

[9] S. Sakumoto *et al.*, Phys. Rev. **D45**, 3045 (1992).

[10] K. Mitsui *et al.*, Nuovo Cimento **A73**, 235 (1983).

[11] W. Lohmann, *et al.*, "Energy Loss of Muons in the Energy Range 1-10000 GeV", CERN Yellow Report 85-03, 1985.